Advanced Processes for 193-nm Immersion Lithography

Yayi Wei
Robert L. Brainard

SPIE PRESS
Bellingham, Washington USA

Library of Congress Cataloging-in-Publication Data

Wei, Yayi.
Advanced processes for 193-nm immersion lithography / Yayi Wei and Robert L. Brainard.
p. cm.
Includes bibliographical references and index.
ISBN 978-0-8194-7557-2 (alk. paper)
1. Immersion lithography. 2. Semiconductors--Etching. 3. Integrated circuits--Design and construction. I. Brainard, Robert L. II. Title.
TK7872.M3W45 2009
621.3815'31--dc22

2008050743

Published by

SPIE
P.O. Box 10
Bellingham, Washington 98227-0010 USA
Phone: +1 360.676.3290
Fax: +1 360.647.1445
Email: Books@spie.org
Web: http://spie.org

Printed in the United States of America.

Contents

Preface

The benefits of using liquids in optical microscopes were first demonstrated in the 1880s. A century later, in the 1980s, experiments with immersion technology demonstrated its potential for use in modern lithography. In 2002, when 157-nm lithography was delayed by a host of technical problems, the development of 193-nm immersion lithography for use in fabricating integrated circuits gained momentum. The development of 193-nm immersion lithography (193i) occurred much faster than did any previous lithographic technology. Currently, 193i is widely used to manufacture advanced microelectronic devices at the 45-nm node. The entire transition from proof of concept to delivery of a mass production tool took only about four years.

This rapid growth was possible because of the combined efforts of all sectors of the lithography community, including the manufacturers of scanners, materials, and integrated circuits. Much of the research critical to the rapid advancement of 193i has been published in the last few years in various journals and proceedings. One of the goals of this book is to summarize this information so that those new to the field as well as current practitioners may increase their understanding of this important technology.

Thus, while actively involved in evaluating new materials, equipment, and processes for 193i imaging, Yayi Wei began writing the manuscript for this book. During the summer of 2008, Robert Brainard, a researcher developing new resist materials, joined Yayi as his coauthor to help prepare the manuscript. Their collaboration resulted in this timely monograph that presents the knowledge critical for establishing high-yield cost-effective 193i processes and materials. The text can be used as course material for graduate students of electrical engineering, material sciences, physics, chemistry, and microelectronics engineering. It can also be used to train engineers involved in the manufacture of integrated circuits.

A large portion of this book is concerned with the challenges and opportunities of water-based 193-nm immersion lithography. The first chapter provides a broad overview of 193i lithography. The second chapter describes the track where most of the processes occur. The book continues with descriptions of the interactions between the immersion fluid (water) and the resist in terms of contact angle, leaching of resist components, and topcoats. It also provides a comprehensive summary of various immersion-related defects and defect-reduction strategies. It covers topics that were originally developed in “dry” lithography and are extendable to immersion 193-nm lithography, discussing

strategies for antireflection control, shrink processes, trim processes, double exposure, double patterning, and line-edge roughness. The book concludes with a chapter describing research efforts aimed at further extensions of immersion lithography to higher numerical aperture (NA) and resolution through the development of high-index lithography. Discussion of some topics (e.g., optical theory of hyper-NA) was kept brief when well described in other monographs.

The knowledge of 193i is still growing and will continue to mature as it is used more frequently in mass production. We appreciate any suggestions from our readers on how to update this material. Your input will help us improve subsequent editions of this book.

Yayi Wei
Altamont, New York

Robert L. Brainard
College of Nanoscale Science and Engineering
University at Albany, State University of New York

January 2009

Acknowledgments

Without a doubt, the knowledge presented in this book was collectively generated by the entire lithography community. The authors would like to express their sincere gratitude to the individuals in this community who provided enormous support during preparation of the manuscript, both by sharing their most recent results and by suggesting improvements to the content and organization of the material. Many of the figures in this book are direct reprints from their publications.

We are especially grateful to David Back, Stefan Brandl, Frank Goodwin, Antje Laessig, Brian Martinick, Michael Sebald, Nickolay Stepanenko, and Lars Voelkel of Qimonda, Karen Petrillo and Chris Robinson of IBM, Peter Benson and Rich Housley of Micron, Uzo Okoroanyanwu and Harry Levinson of AMD, Michael Tittnich of Albany Nanotech, and Ralph Dammel of AZ Electronic Materials. We also thank Dara Burrows and Tim Lamkins of SPIE Press for their patience and encouragement. The authors particularly thank Lisa C. Brainard and Chien-Hsien Sam Lee for the many hours of expert help in editing and revising the various drafts of this book.

List of Acronyms and Abbreviations

193i	193-nm immersion lithography
193i+	high refractive index 193-nm immersion lithography
α	absorption coefficient
a-C	amorphous carbon
AFM	atomic force microscope
alt. PSM	alternating phase-shift mask
ARC	antireflective coating
ArF	argon fluoride
att. PSM	attenuated phase-shift mask
BARC	bottom antireflection coating
BEOL	back end of line
BIM	binary intensity mask
CA	contact angle
CAR	chemically amplified resist
CARL	chemical amplification of resist lines
CD	critical dimension
CDU	critical dimension uniformity
CGS	centimeter-gram-second system
CMP	chemical-mechanical planarization
CNAR	critical normalized aspect ratio
C-SOH	carbon spin-on hard mask
CVD	chemical vapor deposition
DBARC	developer-soluble BARC
DE	double exposure
DI	deionized
DIW	deionized water
DLP	dynamic leaching procedure
DOE	design of experiment
DOF	depth of focus
DP	double patterning
DRAM	dynamic random access memory
DUV	deep ultraviolet
E_0	dose to clear
EBR	edge bead removal
EDX	energy dispersive x-ray spectrometry
EL	exposure latitude

ESCA	electron spectroscopy for chemical analysis
EUV	extreme ultraviolet
F_2	fluorine
FCCD	first collapse critical dimension
FEM	focus exposure matrix
FEOL	front end of line
FIB	focused ion beam
FOV	field of view
FT	film thickness
FTIR	Fourier transform infrared spectroscopy
GBARC	graded bottom antireflection coating
GIS	gas injector system
HF	hydrofluoric acid
HM	hard mask
HMDS	hexamethyldisilizane
IBR	intrinsic birefringence
IC	integrated circuit
IL	interferometric lithography
i-line	365-nm wavelength lithography
ILS	image log-slope
IMR	intrinsic material roughness
IR	infrared
ITRS	International Technology Roadmap for Semiconductors
KrF	krypton fluoride
λ	wavelength
LC-MS	liquid chromatography mass spectroscopy
LER	line-edge roughness
LWR	line-width roughness
MB	mixing bake
MEEF	mask error enhancement factor
Mw	molecular weight
NA	numerical aperture
NAR	normalized aspect ratio
NILS	normalized image log-slope
NR	neutron reflectometry
OAI	off-axis illumination
OL	overlay
OPC	optical proximity correction
OPD	optical path difference
PAB	post-apply bake
PAG	photoacid generator
PDB	post-develop bake
PEB	post-exposure bake
PGME	propylene glycol monomethyl ether
PGMEA	propylene glycol monomethyl ether acetate

POR	process of record
POU	point of use
ppb	parts-per-billion
ppt	parts-per-trillion
PSD	power spectral density
PSZ	perhydropolysilazane
PW	process window
PWP	particles per wafer pass
QCM	quartz crystal microbalance
QSPR	quantitative structure property relationship
RCA	receding contact angle
RDA	resist development analyzer
RELACS	resolution enhancement lithography assisted by chemical shrink
RI	refractive index, n
RMS	root mean square
rpm	rotation per minute
SA	swing amplitude
SADP	self-aligned double patterning
SAFIER	shrink assist film for enhanced resolution
SBR	stress birefringence
SEM	scanning electron microscope
Si-BARC	silicon-containing bottom antireflection coating
SIMS	secondary-ion mass spectroscopy
Si-SOH	silicon spin-on hard mask
SOC	spin-on carbon
SSQ	silsesquioxane
SWA	sidewall angle
TARC	top antireflective coating
TC	topcoat
TE	transverse electric
T_g	glass transition temperature
TGP	thermal gradient plate
TM	transverse magnetic
TMAH	tetramethylammonium hydroxide
TOF-SIMS	time of flight–secondary-ion mass spectroscopy
UCP	ultra-casting predispense
UPW	ultrapure water
VUV	vacuum ultraviolet
WEE	wafer edge exposure
WEXA	water extraction and analysis
WM	watermark
XPS	x-ray photoelectron spectroscope

Chapter 1
Immersion Lithography and Its Challenges

As the microelectronics industry continues to follow Moore's law, the demand to print ever smaller features continues. Figure 1.1 shows a roadmap of lithographic technologies from the past, as well as possible technologies of the future. The microelectronics industry has progressed from 365-nm (i-line) to 193-nm (ArF) lithography. Currently, both "dry" and immersion 193-nm lithography are being used to manufacture today's fastest integrated circuits. For several years (~2000–2004), the development of 157-nm lithography was pursued but eventually was abandoned. Although EUV lithography is capable of printing high-resolution images, advances in supporting technology (source power, resists, masks) have been slow and EUV lithography is not yet ready for high-volume manufacturing. Immersion 193-nm lithography (193i) has emerged as the successor to 193-nm dry imaging and is the subject of this book. The rise of 193i actually pushed 157-nm lithography off the roadmap. Double patterning of immersion 193-nm images will most likely follow 193i single patterning.

The immersion technique was first introduced by Carl Zeiss in the 1880s to increase the resolving power of the optical microscope. Introduction of the immersion technique into modern lithography was suggested in 1980s.[1] The technique attracted the IC industry's attention in 2002, when 157-nm lithography

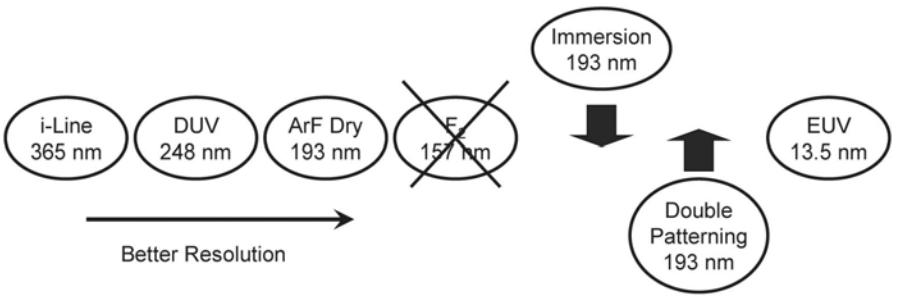

Figure 1.1 193-nm immersion lithography (193i) and 193-nm double patterning have filled the need for higher-resolution technologies, as EUV lithography is not yet ready for high-volume manufacturing.

was delayed by several technical problems, such as strong pellicle and resist absorptions. Since then, the development of 193i has been incredibly rapid.

1.1 Basics of Photolithography

Photolithography is central to the manufacture of microelectronic devices. In this process, light is projected through a mask onto a silicon wafer covered with a photosensitive film, or photoresist (Fig. 1.2). Photoresists can be either positive or negative tone. When a positive photoresist is imaged, the areas exposed to the light are removed. The resulting resist pattern on the wafers is a duplicate of the pattern on the mask, where opaque regions on the mask correspond to the remaining resist pattern on the wafer. After the photolithographic process, the pattern is usually measured using a scanning electron microscope (SEM) to ensure that the size and location of the printed features meet specifications. This measurement of features is called metrology. Finally, the wafer is released for further processing: etch, implantation, or film deposition. A typical process flow of photolithography consists of (a) photoresist coating, (b) post-apply bake (PAB), (c) exposure, (d) post-exposure bake (PEB), and (e) development (see Fig. 1.2). The steps (a) and (b) can be repeated for bottom antireflection coating (BARC) and topcoat (TC) to form a BARC / resist / TC stack before exposure. The exposure is accomplished in the exposure tool, while all other steps are processed in the coating / baking / developing system called the track. The track and exposure tool are usually linked to avoid the manual transportation of wafers and to reduce the delay between exposure and PEB.

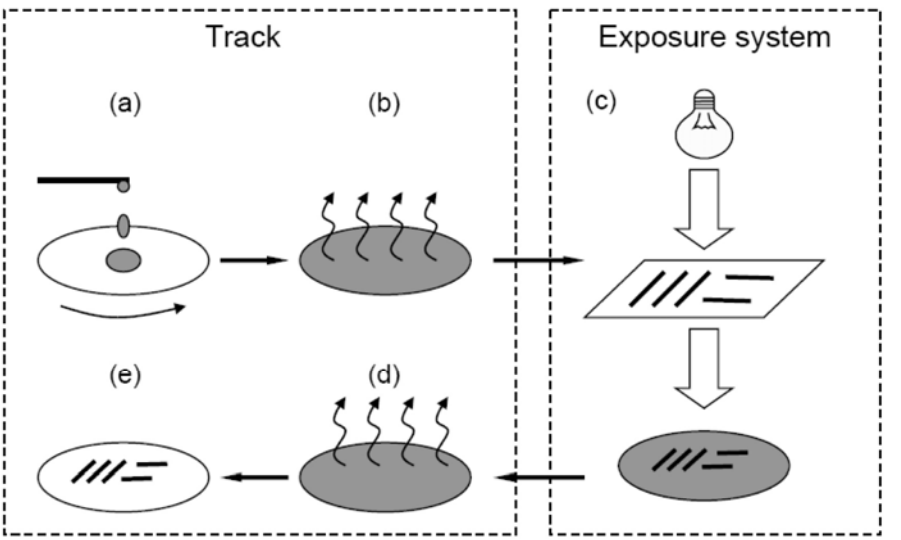

Figure 1.2 Simplified process flow of photolithography: (a) photoresist coating, (b) post-apply bake, (c) exposure, (d) post-exposure bake, and (e) development. Steps (a) and (b) can be repeated for bottom antireflection coating (BARC) and topcoat (TC) to form a BARC / resist / TC stack before exposure.

1.1.1 Resolution of the exposure system

The photolithographic system can be simply described with Köhler illumination (Fig. 1.3).[2] The light source is located in the focal plane of the condenser lens. After passing through the condenser lens, the light shines on the mask, generating diffraction orders of 0, ±1, ±2, etc. The size of the projection lens will determine which of the diffraction orders will be collected and projected onto the focal plane (wafer surface) by the optical system. The convergence of the diffraction orders forms the image of the mask patterns on the wafer. A larger lens (larger NA as defined below) will have greater resolving power, since it will be able to collect more diffraction orders. The ratio of the pattern size in the mask to its image can be adjusted by the projection optics. Currently, the ratio is 4:1 in almost all 193-nm lithography systems.

The optics of Köhler illumination is a standard topic for optics textbooks and is beyond the scope of this monograph.[2] However, we describe the basic principles as they relate to 193-nm immersion lithography. The resolution capability of the system—the minimum feature that can be printed—is described by the Rayleigh equation:

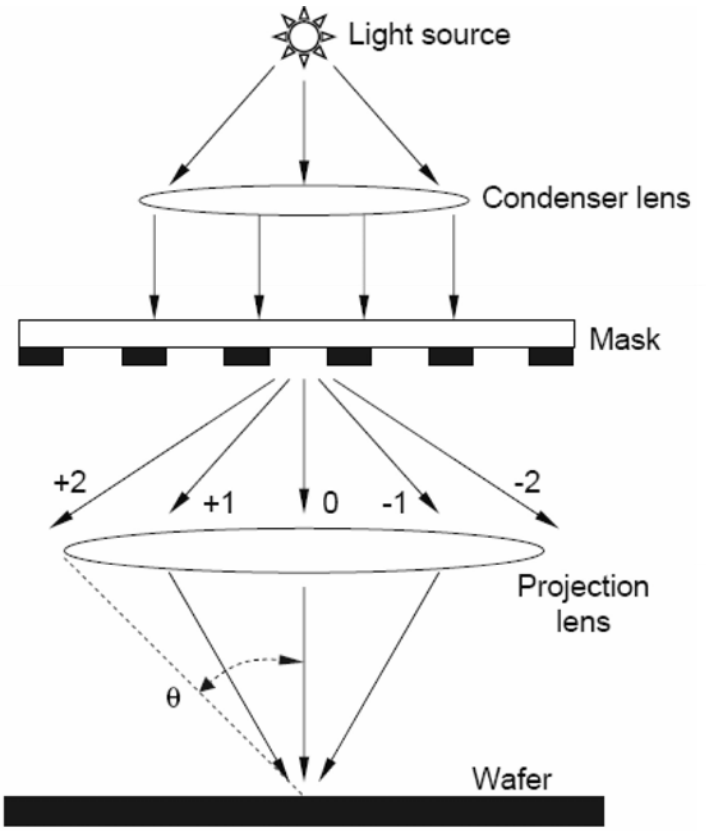

Figure 1.3 Koehler illumination of a photolithographic system. The illumination source can also be located off the optical axis, in a setup called off-axis illumination.[3]

$$\text{Resolution} = k_1 \frac{\lambda}{\text{NA}} = k_1 \frac{\lambda}{n \sin\theta} \tag{1.1}$$

where k_1 is a constant (described below), λ is the wavelength of the exposure light in the vacuum, and NA is the numerical aperture of the projection lens (defined as $n\sin\theta$). Theta (θ) is the maximum incident angle on the wafer (as labeled in Fig. 1.3) and is a measure of the capture angle of the projection lens; n is the refractive index of media between the projection lens and the wafer surface. With 193-nm dry lithography, air is in the gap between the lens and wafer; therefore, $n = 1$.

Equation (1.1) shows how resolution of the lithographic system can be improved by reduction of the wavelength λ of the exposure light and/or by increasing the numerical aperture (NA) of the projection lens. Indeed, the electronics industry has improved resolution by developing imaging tools based on successively shorter wavelengths: g-line (436 nm), i-line (365 nm), DUV (248 nm), to ArF (193 nm). Similarly, resolution has been improved by creating exposure tools with greater NAs for each wavelength. For 193-nm dry imaging, the lenses have increased from 0.6NA, 0.75NA, 0.85NA to 0.93NA. In addition to the wavelength reduction and the increase of NA, the resolution can also be enhanced by optimization of the process parameters, including illumination settings, mask design, and resist process. These contributions can be included in the k_1 factor; therefore, k_1 is also called a process factor.

The k_1 factor can be used to simply assess the difficulty of printing specific feature sizes with a specific exposure tool. A larger k_1 factor generally means that the lithographic process control will be easier and the yield will be higher. Usually, a k_1 factor above 0.30 is needed for production and k_1 cannot typically go below 0.25.[4] A lithographic process in which $0.25 < k_1 < 0.30$ is difficult and requires very aggressive resolution enhancement techniques. This kind of low-k_1 process is useful during early process development. For example, a 193-nm exposure tool with 0.85NA used for production at the 90-nm half-pitch node ($k_1 = 0.396$) could also be used for advanced development of 65-nm half-pitch processes ($k_1 = 0.286$). Once the 0.93NA tool became available, the 65-nm process could be transferred to this new tool.

1.1.2 Step and scan

To effectively increase the exposure field size, the concept of step and scan has been introduced into modern exposure systems.[5] Instead of projecting the whole mask to the wafer, the exposure system scans the mask. The mask is illuminated only by an illumination slit as sketched in Fig. 1.4. To obtain exposure of all mask patterns, the mask stage can be moved in one direction along the focal plane relative to the optical system, i.e., the exposure light scans the mask. In response, the wafer stage moves simultaneously in the opposite direction with a quarter of the speed. In a modern 193-nm production tool, the reticle stage has a scan speed of about 2000 mm/s and the wafer stage has a scan speed of about 500 mm/s. High scanning speeds allow faster exposures, thereby increasing the throughput. After

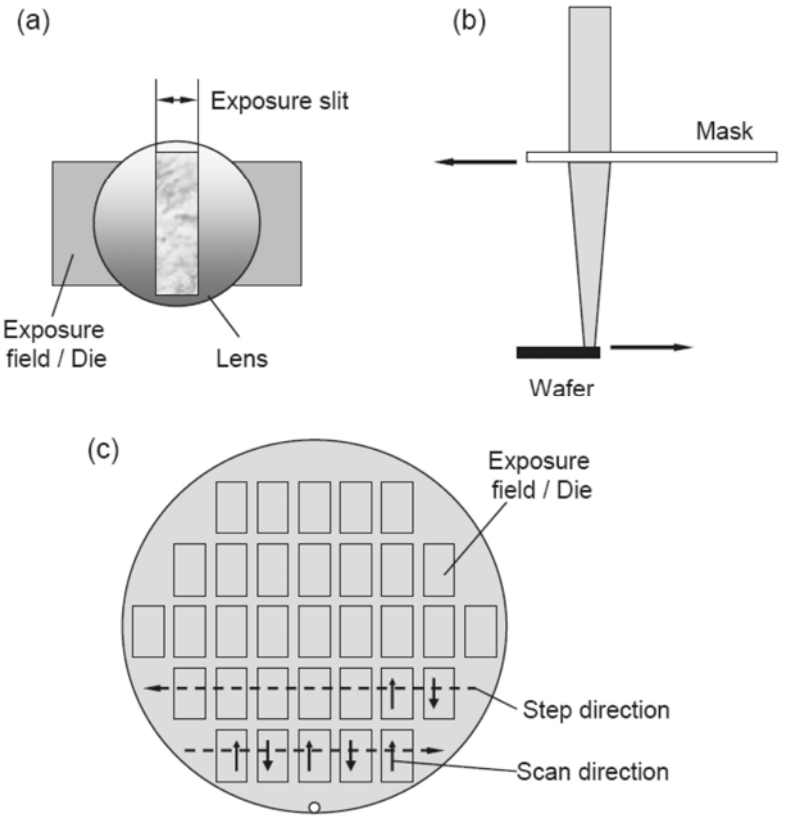

Figure 1.4 Concept of step and scan. (a) Top-view diagram of the scan exposure, (b) side-view diagram, and (c) typical step-and-scan movement of the exposure head over a wafer.

finishing the scan, the exposure system steps to the next field. A typical movement of the exposure head over a wafer (called routing) is sketched in Fig. 1.4 (c). With the step-and-scan technique, the maximum exposure field size (i.e., chip size) is no longer limited by the lens diameter. The exposure field size of 193-nm production tools is required by ITRS to be 26 mm × 33 mm.[6] This slit projection approach makes the exposure less sensitive to lens aberrations, since only a portion of the lens is used at any given time during exposure.

1.2 Immersion Lithography and Its Advantages

Typically, the projection optics and the wafer stage occur in air or in a vacuum, in order to reduce the light absorption, which means the refractive index n in Eq. (1.1) is 1.0 and NA = $\sin\theta$. The numerical aperture is, therefore, entirely decided by the size of the projection lens and cannot be bigger than 1, and more practically is $\leq$ 0.93. Immersion technology provides another way to increase the NA: by increasing n. The gap between the last lens element and the resist can be filled with a liquid and all liquids have much higher refractive indices n than air.[7] Values of n

can vary from 1.28 to 1.75 at 589-nm light for typical organic liquids. Conveniently, the index of refraction of water is 1.33 at 589 nm and 1.44 using 193-nm light. Figure 1.5 shows a diagram of the 193-nm immersion (193i) exposure head with its final lens and wafer.

The water that fills the gap between the projection lens and the wafer is supplied by an immersion water handling system and must be free of bubbles and particles. Regular cleanroom deionized (DI) water is connected to this special immersion water handling system. The water handling system reduces elemental contamination and silica to parts-per-trillion (ppt) levels, degasses the water, provides ultraviolet treatment to kill bacteria, maintains the water temperature and flow, removes particulates, and accommodates in-line metrology. The water flow under the exposure head is constant, even when the tool is idle. The system keeps the water fresh and clean and prevents deposition of contaminants. The design of the exposure head is very critical for immersion scanner performance.[8,9] The design must contain the water in the gap between the final lens element and the resist, forming the water meniscus. This water meniscus must move easily with the exposure head across the wafer without leaving water droplets behind. Minimizing water evaporation is another objective. Evaporation will cause temperature fluctuations, causing the wafer to shrink.[10] Dry exposures are not subjected to this temperature variation and, therefore, cause a significant overlay mismatch between layers exposed with immersion and those exposed on dry tools.

Two configurations have been considered for 193-nm immersion lithography: bath and shower. In the bath configuration, the whole wafer is immersed in a water bath. In the shower configuration, the water is confined to the area on the wafer immediately below the exposure head (Fig. 1.5), while the rest of wafer stays dry. Therefore, the immersion has no conflict with the wafer alignment and the leveling sensors.[11] This design makes it easier to maintain a high throughput than does the design of the "bath" configuration and has, therefore, been universally adopted by immersion tool suppliers. The technical challenge in the shower configuration is at the wafer edge. When the exposure head moves across the wafer edge,

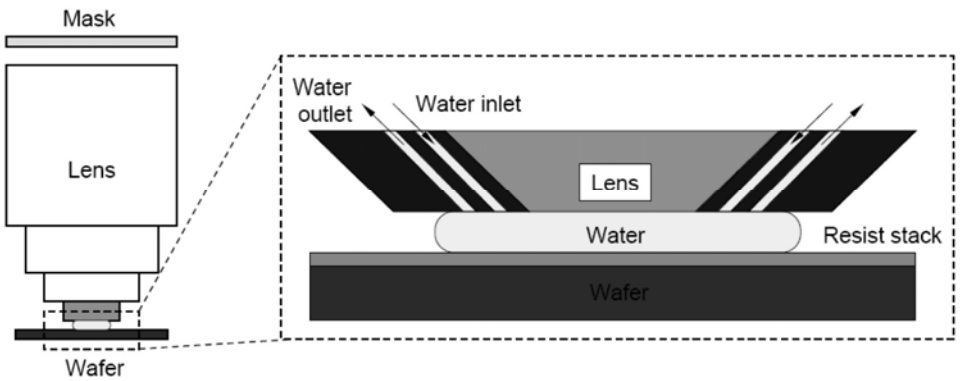

Figure 1.5 Shower design for an immersion 193-nm (193i) exposure head. Water fills the gap between the final lens and the wafer.

water leakage may occur and air bubbles may be generated. A special wafer stage has been designed to address these issues.

Despite these technical challenges, the development of 193i has been incredibly fast. In the immersion workshop organized by SEMATECH in July 2003, scanner suppliers showed their development plans for 193i scanners. SEMATECH and its member companies then reorientated their development resources from 157 nm to 193i.[12] In 2004, 193i full-field scanners modified from dry tools (0.75NA and 0.85NA) were available for early immersion process evaluation and learning. In 2007, tools with NAs of 1.3 and 1.35, which are the maximum achievable with water immersion, became available on the market.

Compared to 157-nm lithography, the advantage of 193i is obvious. The change to immersion imaging has had a powerful effect on resolution, since the effective wavelength of the exposure light in water is 134 nm, which, according to Eq. (1.1), provides better resolution potential than does 157 nm lithography. Additionally, much of the technical infrastructure was already in place, greatly reducing the time needed to implement this technology. Excimer laser sources and mask designs for 193-nm dry lithography were applicable to 193i and the regular 193-nm resists demonstrated good lithographic performance with immersion.

1.2.1 Depth-of-focus improvement

Depth-of-focus (DOF) is another important parameter that measures the performance of a photolithographic system. DOF is a measure of the sensitivity of the imaging system to variations in distance between the lens and the resist film plane. The lithographic process yield is highly dependent on the magnitude of the DOF. The resist coating may not be perfectly planar, as production wafers often have many embedded patterns and structures. Although chemical-mechanical planarization (CMP) has been implemented to planarize these surfaces, significant surface topography variation can still exist. The exposure DOF must be larger than the wafer topography, so that the wafer surface is in the focal range across the whole wafer and the size of the printed features (critical dimension or CD) can be well controlled across the wafer to within ±10%.

The immersion technique can improve the exposure DOF. The water in the gap between the final lens and wafer changes the optical paths of the exposure light beams. Figure 1.6 compares two-beam interference exposures for dry and "wet" situations. The exposure beams pass through the air or water gap and are focused on the wafer surfaces. Refractions occur at the interface of lens–air for the dry exposure or lens–water for the immersion exposure. According to Snell's law, the following relation dictates the refraction angles:

$$n_{\text{lens}} \sin\theta_1 = n_{\text{air}} \sin\theta_2 = n_{\text{water}} \sin\theta_3 = \text{NA}, \tag{1.2}$$

where θ_1 is the incident angle at the interface and θ_2 and θ_3 are the refractive angles corresponding to dry and immersion, respectively. It is obvious from Eq. (1.2) that

the refractive index of water alone does not change the NA. However, the water does reduce the refractive angle, i.e., $\theta_2 > \theta_3$, significantly increasing the DOF of the image.

In a high-NA situation, exposure light can have a high incident angle on the resist surface, i.e., the paraxial approximation cannot be applied. (The paraxial approximation assumes that the light beam makes a small angle θ to the optical axis of the optical system and lies close to the axis throughout the optical system. This approximation allows that $\sin\theta \approx \theta$ and $\tan\theta \approx \theta$ (θ is in radians) for calculation of the beam's path.) The contribution of high incident angle beams must be included.[13,14] Figure 1.7 shows a spherical image wavefront. The focal point of the image wave is at P_0, i.e., R_0P_0 (0 order beam) = RP_0 (first order beam). When out of focus, rays traveling at larger angles undergo a larger phase change than do rays traveling at smaller angles. As a result, the phase difference between the 0 order and first order beams will result in a blurred image. Assuming the defocus value is δ at point P, the optical path difference (OPD) between the two beams (R_0P and RP) is

$$\mathrm{OPD} = R_0P - RP = \delta - (RP - RP_0) \approx \delta(1-\cos\theta). \tag{1.3}$$

The maximum tolerable OPD during exposure is a quarter of the wavelength, i.e., $\mathrm{OPD} \le \lambda/4$. At the OPD of λ/4, the zero and first diffracted orders would be exactly 90 deg out of phase with each other. The DOF is defined as the focus range that allows the maximum tolerable OPD; therefore,

$$\mathrm{DOF} = 2\delta = \frac{k_2}{2} \cdot \frac{\lambda}{1-\cos\theta}, \tag{1.4}$$

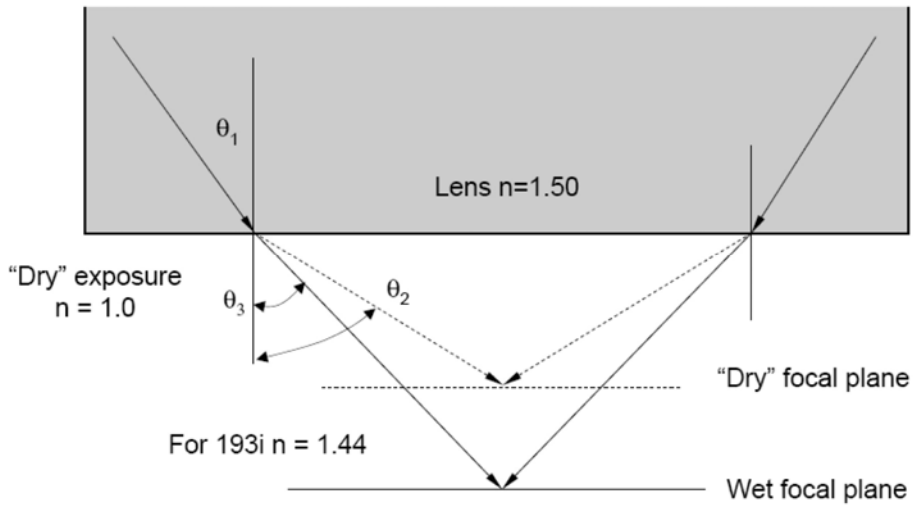

Figure 1.6 Optical paths of two-beam interference for both dry and 193i exposures.

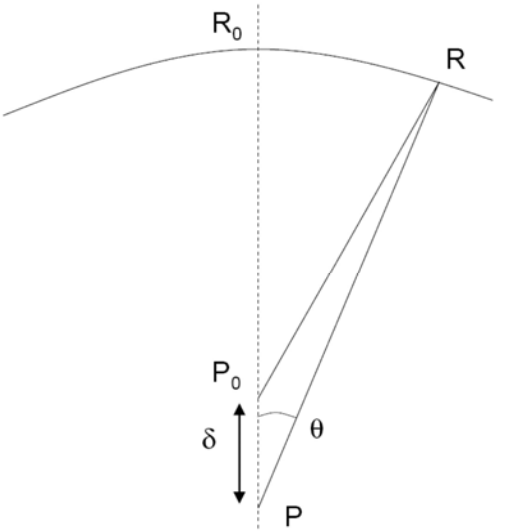

Figure 1.7 Optical path of a spherical image wavefront. The focal point of the image wave is at P_0, i.e., $R_0P_0 = RP_0$.

where k_2 (<1) is a factor. In the water immersion situation, the wavelength of the exposure light is reduced, as λ/n_{water} and the incident angle θ in Eq. (1.4) can be replaced by NA. The high-NA version of the DOF is

$$\mathrm{DOF} = \frac{k_2}{2} \cdot \frac{\lambda}{n - \sqrt{n^2 - \mathrm{NA}^2}} . \tag{1.5}$$

In a low-NA situation, the paraxial approximation can be used: $\sin\theta << 1$. Equation (1.5) can be simplified to a more familiar form

$$\mathrm{DOF} = k_2 \cdot \frac{n\lambda}{\mathrm{NA}^2} = k_2 \cdot \frac{\lambda}{n \sin^2 \theta} . \tag{1.6}$$

The refractive index n of the media between the projection lens and wafer contributes to the DOF. Contributions of the illumination setting and mask to the DOF are included in the factor k_2. Even with the same NA and λ, the DOF can be enhanced by using off-axis illumination or alternating phase-shift mask (alt. PSM).

The DOF enhancement of water immersion versus dry exposure can be calculated from Eq. (1.5). Assuming both the immersion and dry exposures have the same NA and process factor k_2, we have

$$\frac{\mathrm{DOF}_{193i}}{\mathrm{DOF}_{dry}} = \frac{1-\sqrt{1-\mathrm{NA}^2}}{n_{water}-\sqrt{n_{water}{}^2-\mathrm{NA}^2}} = \frac{1-\sqrt{1-\mathrm{NA}^2}}{n_{water}\left[1-\sqrt{1-(\mathrm{NA}/n_{water})^2}\right]}. \quad (1.7)$$

The improvement in DOF is at least the refractive index of the fluid and gets larger for the smaller pitches.[14] For example, 90-nm dense lines were printed by a dry lithography and an immersion tool with the same mask and illumination settings (0.75 NA). About 1.8 × DOF was obtained with the immersion exposure.[15] Historically, an increase in imaging resolution is obtained by reduction of exposure wavelength. This was always accompanied by the DOF loss, as indicated by Eq. (1.6). With immersion technology, not only does the imaging resolution improve, but the DOF also increases at the same resolution.

1.2.2 Water as the immersion fluid

The choice of immersion fluid is first based on transparency to 193-nm light.[16] The absorption coefficient α of water is only 0.036 cm^{-1}. This is the "base 10" coefficient, i.e., $I = I_0 \cdot 10^{-\alpha x}$. The refractive index of water at 193 nm is 1.44, which would effectively decrease its wavelength to 134 nm, indicating a 17% potential resolution improvement using water immersion at 193 nm, when compared to 157-nm conventional imaging for identical air-NA values.

In many ways, water is a nearly perfect immersion fluid. It has been an essential component in fabrication ever since the beginning of high-volume manufacturing. DI water is plumbed into every track, since the water rinse is a standard process step after development. Additionally, water has many other properties that make it nearly ideal. It has a low viscosity, is stable under the 193-nm wavelength exposure, and does not react with the lens material. In addition, water's refractive index is relatively insensitive to changes in temperature. At 193 nm, $dn/dT = -10^{-4}$/°C, which means 0.01° C temperature fluctuation causes n change of 10^{-6}. With 1-mm working distance, this will cause a defocus of ~1 nm.[17] As a part of the optical system, the physical and chemical properties of water have been investigated in detail. Further results can be found in other publications.[18]

1.2.3 Hyper-NA and high refractive index immersion (193i+)

Another advantage of the immersion technique is that it enables hyper-NA 193-nm immersion lithography in which the optics have numerical apertures greater than 1.0. The NA of a dry exposure system cannot exceed 1.0. With the air gap between the lens and wafer, the maximum incident angle θ_1 at the lens–air interface is limited to $\sin^{-1}(1/n_{lens})$ (Fig. 1.8(a)). Otherwise, if the light beams have an incident angle larger than $\sin^{-1}(1/n_{lens})$, light will be reflected instead of being refracted. This is called total internal reflection and limits the size of lenses in

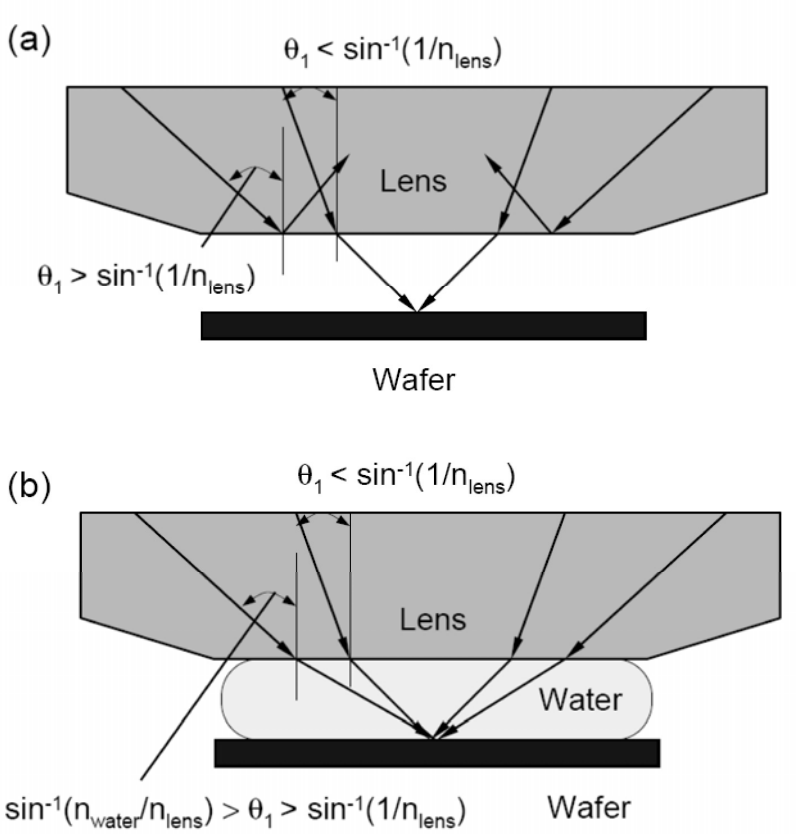

Figure 1.8 (a) The maximum incident angle at the lens–air interface is $\sin^{-1}(1/n_{\text{lens}})$. Beams with incident angle > $\sin^{-1}(1/n_{\text{lens}})$ are totally reflected. (b) With water in the gap, the maximum incident angle increases to $\sin^{-1}(n_{\text{water}}/n_{\text{lens}})$.

193-nm dry steppers. With water immersion, however, the maximum incident angle θ_1 can be $\sin^{-1}(n_{\text{water}}/n_{\text{lens}}) \approx 68$ deg (Fig. 1.8(b)). This enables a larger lens design. Currently, 193i full-field exposure systems with a maximum NA of 1.35 are available on the market and can provide lithography solutions down to 45-nm half-pitch.

Can we realize higher than 1.35NA by introducing high refractive index fluid (> 1.44 at 193-nm wavelength) into the exposure system? Figure 1.9 shows a stack lens / immersion fluid / resist / BARC system that mimics the immersion exposure head. According to Snell's law, $n_{\text{lens}} \sin\theta_1 = n_{\text{fluid}} \sin\theta_3 = n_{\text{resist}} \sin\theta_4$.

As labeled in Fig. 1.9, $\theta_{1,3,4}$ are the incident angles of the exposure beam at the interfaces of lens and fluid, fluid and resist, and resist and BARC (topcoat is not included in this discussion), respectively. Accordingly, the maximum effective NA is equal to the lowest value of n_{lens}, n_{fluid}, or n_{resist}. Further increases in NA are limited by the refractive index of lens, fluid, and resist. Therefore, high refractive index materials are the key to further increases in NA.

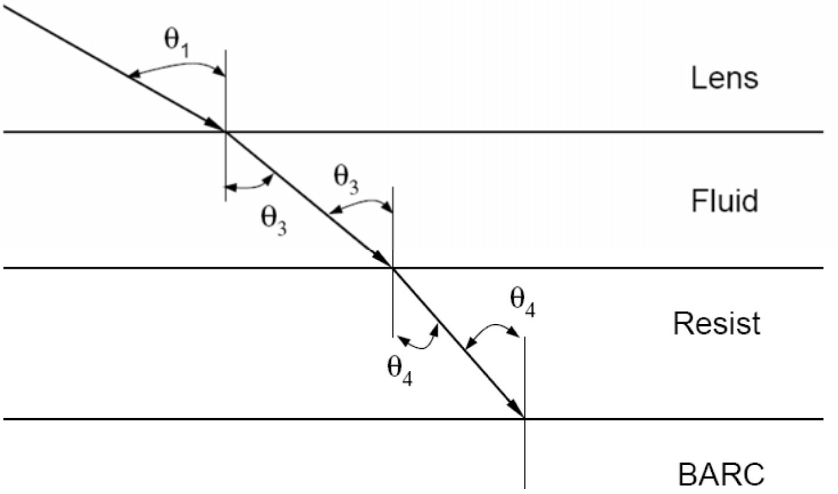

Figure 1.9 Optical path of the exposure beam in lens/immersion fluid/resist/BARC system.

Encouraged by the great success of water immersion, researchers are developing various high refractive index (RI) materials, including high-RI immersion fluids, high-RI lens materials, and high RI resists. A high-RI fluid of n = 1.65 is now available and ready to be tested by scanner suppliers[19] and various high-RI lens materials have been screened. Initial results have demonstrated that LuAG (lutetium aluminum garnet) has an RI of ~2.2 and may be a strong candidate for a high-RI lens material.[20] Introduction of sulfur into photoresist polymers can significantly increase their refractive index.[21] 193i with water as immersion fluid is commonly referred to as first-generation 193i. Second-generation 193i with immersion fluids of n = 1.65 and lenses of n = 2.0 are being pursued and are expected to achieve NAs of 1.55. Third-generation 193i is also being investigated and is currently targeting an NA of 1.65. Based on these initial studies, 193i+ is becoming an option for the 32-nm half-pitch node.[22] However, development efforts on high-RI immersion have been much reduced since the summer of 2008. Double exposure or double patterning are believed to be viable solutions for the 32-nm half-pitch node or even for the 22-nm node before the availability of EUV.

Table 1.1 shows the NA values of various 193-nm exposure tools. The k_1 factor is calculated (CDλ/NA) for each technology node. Beyond 45-nm half-pitch, an immersion tool with a high refractive index (193i+) will be needed.

1.3 Challenges for the 193i Process

Apart from the gains of enhancing the DOF and enabling hyper-NA lens design, 193i brings various process challenges. The first challenge is leaching, where the photoacid generator (PAG), base quencher, and other small molecular components in the resist can leach into the water. This leaching not only degrades

Table 1.1 193-nm lithography tools with NA = 0.75–1.35 have been used in IC manufacturing. The high refractive index tool (193i+) is not yet available.

		NA								
		193nm			193nm water immersion				193i+	
	k_1	0.75	0.85	0.93	1.07	1.2	1.3	1.35	1.55	1.80
Half-pitch size	130nm	0.505	0.573	0.620						
	90nm	0.350	0.396	0.429	0.499	0.560				
	65nm		0.286	0.310	0.360	0.404	0.438			
	45nm					0.280	0.303	0.315		
	32nm								0.257	0.298

the resist performance, but also contaminates the water. The contaminated water can further contaminate the lens and wafer stage of the scanner. Water can also permeate into the resist film, causing resist swelling and changing its photochemical properties. Prior to the availability of low-leaching resists, topcoat was an effective solution to blocking the leaching and, to some extent, the water uptake.

1.3.1 Topcoat versus non-topcoat

Topcoat is spin-coated onto a resist and is transparent at 193-nm. It serves as a barrier layer that enables the regular 193-nm resists (i.e., dry resists) to be used in the wet process. The topcoat layer is removed after exposure/PEB and before pattern development. According to their solubility in regular aqueous TMAH (tetramethylammonium hydroxide) developer, there are two types of topcoats: solvent-based and developer-soluble. Solvent-based topcoats can be removed only with specific topcoat solvents. Additional process steps and track modules are required to remove the topcoats (Fig. 1.10(a)). Therefore, developer-insoluble topcoats were not suitable for use in high-volume manufacturing and the development of developer-soluble topcoats quickly followed. Developer-soluble topcoats can be dissolved by regular aqueous TMAH developer; therefore, the topcoat removal step can be done in the develop module and integrated into the development step (Fig. 1.10(b)). However, compatibility of the resist and topcoat has to be considered and the process parameters have to be aligned in order to obtain the best lithographic process window.

Resist processes without topcoats are preferred for introduction of 193-nm immersion lithography into mass production. These simplified processes, as sketched in Fig. 1.10(c), do not need separate coating and baking steps for the topcoat material and thereby reduce cost of ownership and offer fewer sources of defects. Conventional 193-nm resists optimized for dry 193-nm imaging are not generally suitable for use in immersion tools without topcoats, since the dry resist components typically show water solubility and leach into the water. Leaching of the components that are present before, or as a result of, exposure can deteriorate lithographic performance. The selection of components for single-layer 193-nm immersion resists that can be used without top coatings is challenging, since both minimized leaching behaviors in water and superior overall lithographic performance need to be achieved simultaneously. Material innovation is the key for non-topcoat processes to supercede topcoat processes.

1.3.2 Immersion defectivity

Immersion-related defects are another challenge in the 193i process. The water between the front lens and the resist forms a meniscus that moves with the exposure head across the resist surface. Various physical and chemical interactions between the water and the resist stack occur, possibly leading to water immersion-related defects. Bubbles in the water can distort the exposure image; water droplets left on the wafer surface may deteriorate the local resist performance; and water can transport particles to the wafer surface and deposit there. With an unoptimized 193i process, approximately 4–20% more defects may be added to a wafer than may be added in dry 193-nm lithography.[23] These immersion defects will limit process yields, and therefore, must be understood and their numbers reduced before 193i processes can be used in high-volume manufacturing.

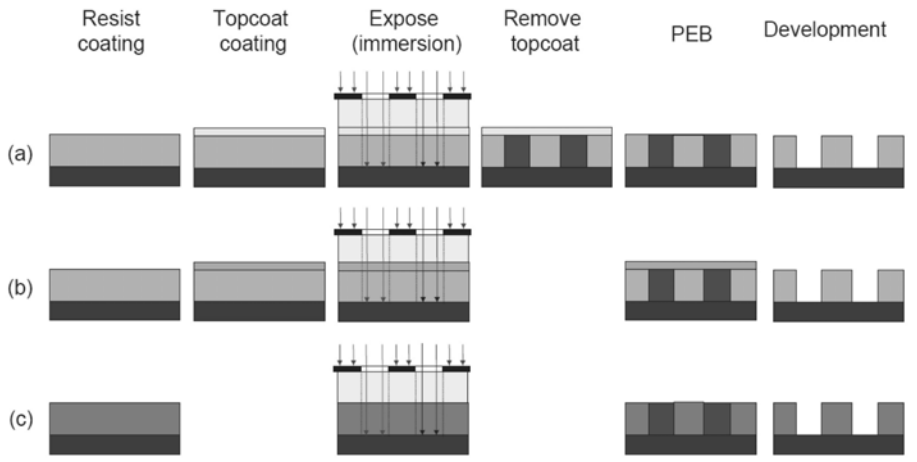

Figure 1.10 Process flow comparison of resist stack (a) with solvent-soluble topcoat, (b) with developer-soluble topcoat, and (c) without topcoat.

1.3.3 Imaging at hyper-NA

With the hyper-NA 193i exposure, the maximum incident angle of the exposure light on the resist stack is high. For example, corresponding to 1.3NA, the maximum incident angle is $\sin^{-1}(1.3/1.44) = 64.5$ deg, while at 0.75NA of 193i, the maximum incident angle is only about 31.4 deg. The high incident angle will cause the contrast loss of the transverse magnetic (TM) imaging component. Figure 1.11 shows a diagram of the two-beam interference. The electric field of the incident beams $\mathbf{E}$ can be divided into two components: one is in the incident plane, the TM model ($\mathbf{E}^{\mathrm{TM}}$); and another is perpendicular to the incident plane, the transverse electric (TE) model

$$(\mathbf{E}^{\mathrm{TE}}):\ \mathbf{E}_1 = \mathbf{E}_1^{\mathrm{TE}} + \mathbf{E}_1^{\mathrm{TM}} \text{ and } \mathbf{E}_2 = \mathbf{E}_2^{\mathrm{TE}} + \mathbf{E}_2^{\mathrm{TM}}. \tag{1.8}$$

After being focused on the wafer surface, the total light intensity is

$$I = |\mathbf{E}_1 + \mathbf{E}_2|^2 = |\mathbf{E}_1^{\mathrm{TE}} + \mathbf{E}_2^{\mathrm{TE}}|^2 + |\mathbf{E}_1^{\mathrm{TM}} + \mathbf{E}_2^{\mathrm{TM}}|^2. \tag{1.9}$$

The TE components ($\mathbf{E}_1^{\mathrm{TE}}$ and $\mathbf{E}_2^{\mathrm{TE}}$) are parallel to each other and their superposition has no relation to the incident angle. However, the TM components ($\mathbf{E}_2^{\mathrm{TE}}$ and $\mathbf{E}_2^{\mathrm{TE}}$) form an angle of 180 deg $-2\theta_3$ and the superposition depends on the incident angle by a factor of $\cos(2\theta_3)$. At hyper-NA exposure, the $\cos(2\theta_3)$ is much smaller than 1 and destroys the TM contrast. Therefore, illumination with only the TE component—TE polarized illumination—has been suggested for hyper-NA exposure.

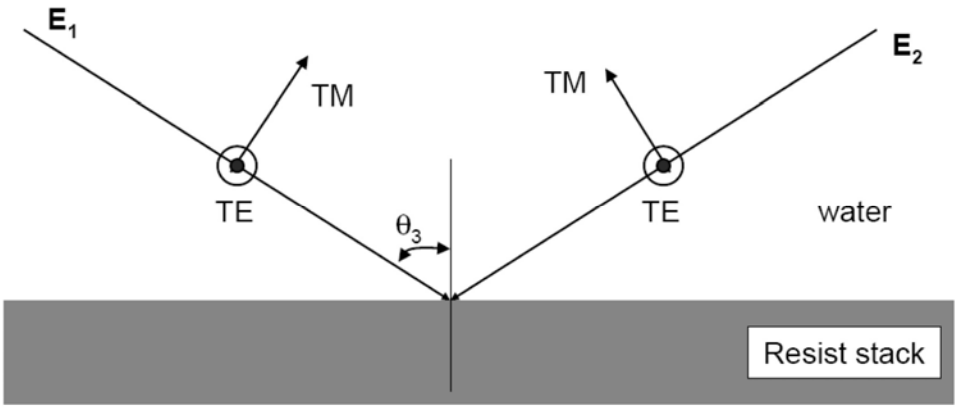

Figure 1.11 Two-beam interference. Electric field of the incident beams $\mathbf{E}$ can be divided into two components: TE and TM. The TM components cannot form enough contrast at hyper-N

The high incident angle will also lead to a high reflection at the interfaces of the resist stack and make reflectivity control very difficult. The incident angles of the exposure lights are scattered in a broad range, especially when patterns with different pitches are exposed. To reduce the reflection of light with different incident angles is extremely challenging for a single-layer BARC. Different BARC strategies have been proposed for the hyper-NA imaging, for example, the thick organic BARC approach and the double-layer BARC approach.[24] In order to prevent line collapse, the resist film thickness is typically 2–3x the CD. For example, at 45-nm half-pitch, the resist film thickness is about 100–120 nm. Such a thin resist film can no longer provide enough etch resistance. Si-containing material and spin-on carbon have been developed to work both as a BARC and as an etch mask.

References

1. B. J. Lin, "The future of subhalf-micrometer optical lithography," *Microcircuit Engineering* **87**, Sept. 1987.
2. See for example: M. Born and W. Wolf, *Principles of Optics*, Pergamon Press, Oxford (1980).
3. See for example: A. K.-K. Wong, *Resolution Enhancement Techniques in Optical Lithography*, SPIE Press, Bellingham, WA (2001).
4. K. Suzuki, B. W. Smith, *Microlithography: Science and Technology*, Second Edition, CRC Press (2007).
5. H. Sewell, "200 nm deep-UV lithography using step-and-scan," *Microelectronic Engineering*, **35**, Issue 1-4 (March 1997) 177–183.
6. *International Technology Roadmap for Semiconductors*, 2007 Edition, Lithography section.
7. "Typical organic compounds have refractive indices from 1.28 to 1.75 using 589 nm light." *CRC Handbook of Chemistry and Physics*, Ed.: Robert Weast, 67th Edition (1986).
8. D. Flagello, J. Mulkens, B. Streefkerk, and P. Graeupner, "The benefits and limitations of immersion lithography," *J. Microlith., Microfab., Microsyst.*, **3**, 104 (2004).
9. S. Owa and H. Nagasaka, "Advantage and feasibility of immersion lithography," *J. Microlith., Microfab., Microsyst.*, **3**, 97, 2004.
10. ASML's presentation in 193i symposium Oct. 2006 in Kyoto, Japan.
11. B. Streefkerk, J. Baselmans, W. Gehoel-van Ansem, J. Mulkens, C. Hoogendam, M. Hoogendorp, D. Flagello, H. Sewell, and P. Graeupner, "Extending optical lithography with immersion," *Proc. SPIE* **5377**, 285–305 (2004).
12. See for example, the proceedings of International Symposium on Immersion and 157nm Lithography, Vancouver, Canada, 2004.
13. B. J. Lin, "The k_3 coefficient in nonparaxial λ/NA scaling equations for resolution, depth of focus, and immersion lithography," *J. Microlith., Microfab., Microsyst.*, **1**, 7 (2002).

14. C. A. Mack and J. D. Byers, "Exploring the capabilities of immersion lithography through simulation," *Proc. SPIE* **5377**, 428–441 (2004).
15. Y. Wei, K. Petrillo, S. Brandl, F. Goodwin, P. Benson, R. Housley, and U. Okoroanyanwu, "Selection and evaluation of developer-soluble topcoat for 193nm immersion lithography," *Proc. SPIE* **6153**, 615306 (2006).
16. B. W. Smith, "Immersion optical lithography at 193nm," *Future Fab Intl*., **15**, July, 2003.
17. M. Switkes, R. R. Kunz, M. Rothschild, R. F. Sinta, M. Yeung, and S.-Y. Baek, "Extending optics to 50nm and beyond with immersion lithography," *JVST* **B21**(6), Nov./Dec. 2003, 2794–2799.
18. M. Switkes, R. R. Kunz, R. F. Sinta, M. Rothschild, P. M. Gallagher-Wetmore, V. J. Krukonis, and K. Williams, "Immersion liquids for lithography in the deep ultraviolet," *Proc. SPIE* **5040**, 690–699 (2003).
19. Y. Wang, T. Miyamatsu, T. Furukawa, K. Yamada, T. Tominaga, Y. Makita, H. Nakagawa, A. Nakamura, M. Shima, S. Kusumoto, T. Shimokawa, and K. Hieda, "High-refractive-index fluids for the next generation ArF immersion lithography," *Proc. SPIE* **6153**, 61530A (2006).
20. J. H. Burnett, "High-index materials for 193 nm immersion lithography," Presentation at International Symposium on Immersion Lithography, Kyoto, Oct. 2006.
21. I. Blakey, W. Conley, G. A. George, D. J. T. Hill, H. Liu, F. Rasoul, and A. K. Whittaker, "Synthesis of high refractive index sulfur containing polymers for 193-nm immersion lithography: a progress report," *Proc. SPIE* **6153**, 61530H (2006).
22. M. van den Brink, "The only cost-effective extendable lithography option: EUV," Presentation at EUV symposium, Barcelona, Oct. 2006.
23. U. Okoroanyanwu and H. Levinson, "193nm immersion lithography defects," Presentation at the SEMATECH 2nd 193nm Immersion Symposium, Brugge, Belgium, Sept. 14, 2005.
24. M. Colburn, S. Halle, M. Burkhardt, S. Burns, N. Seong, D. Goldfarb, and DE Team, "Process challenges for extension of H_2O immersion lithography to hyper-NA," SEMATECH Litho Forum 2006.

Chapter 2
Process Steps in the Track

The track is a necessary tool for lithographic processing, providing all of the material processes (coating, baking, rinsing, and developing) except exposure. Typically, in a mass production environment, the track is linked to an exposure tool to increase the process efficiency and reduce delays. The linked track and scanner are sometimes called the litho-cell or the litho-cluster. The track is made up of several modules; each module does one specific process with its respective chemicals. Photoresists and solvents are connected from a chemical storage cabinet to the module via pipelines, filters, and pumps. Before processing wafers on the track, a process flow must be defined.

Depending on the process requirements, various modules can be assembled. For example, a track used for 193-nm lithography consists of at least one coating module for BARC, one coating module for resist, one coating module for topcoat, several bake modules for post-apply bakes and post-exposure bake, and more than one development module. If more process steps are needed, more modules can be added. If the process needs to use the solvent-soluble topcoat for immersion, a topcoat coating module and a topcoat removal module must be added into the track design.

This chapter covers the main process modules: coating, baking, and developing. Each process module consists of various process steps. For each process step, we review its purpose, its possible failure mechanisms, and some solutions to these failure mechanisms. Resist line collapse, blob defects, and surfactant rinse are associated with the development module, and are, therefore, also included in this chapter. Immersion lithography requires some additional process modules. These immersion-specific requirements, as well as track performance monitoring, make up the last part of this chapter.

2.1 Coating Module

A coating module consists of a spin table and several dispense nozzles for different materials. Solvents are introduced into the module for pre-wetting the wafer surface, removing the edge bead, and rinsing the back side of the wafer. Figure 2.1(a) shows a diagram of a coating module, also called a coating bowl or a coating cup, due to its shape. Although BARCs, resists, and topcoats all have dedicated coating cups, the configuration and process steps for each coating are

almost the same. The techniques discussed in this section are applicable to all of these coatings unless specified otherwise.

The coating module recipe consists of several process steps. Figure 2.1(b) shows a typical process flow in the coating module. However, not all of the steps in Fig. 2.1(b) are necessary for a specific coating process. After the wafer is loaded on the spin table, the first process step is a pre-wet. A solvent nozzle moves to the wafer center and dispenses the solvent while the wafer spins at a low speed. Before the solvent becomes dry, the material (BARC, resist, or topcoat) is dispensed. The pre-wet helps to carry the material to the wafer edge, promoting better coating uniformity. However, the pre-wet solvent has to be carefully chosen; it should not degrade the film previously coated or deposited on

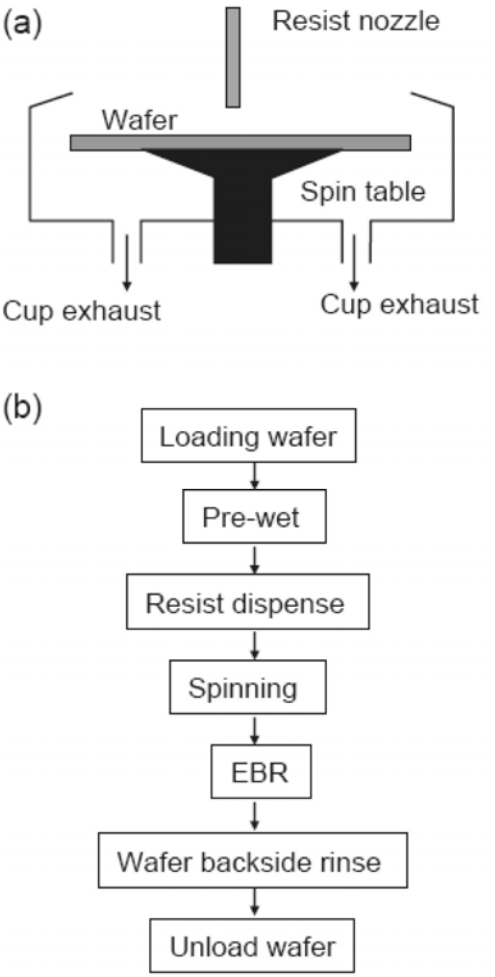

Figure 2.1 (a) Diagram of a coating module. (b) Universal process flow in the coating module. Edge bead removal (EBR) and backside rinse are typically performed simultaneously.

the wafer. For example, the pre-wet with PGMEA (propylene glycol monomethyl ether acetate) is prohibited when coating some resists, because the solvent may elute photoacid generators out of the resist film and degrade its lithographic performance.

2.1.1 Material dispense

The three chemicals used in a manufacturing fab (BARC, resist, or topcoat) are typically called materials. These materials are dispensed from a nozzle at the center above the wafer (Fig. 2.1(a)). During dispensing of the material, the wafer can either spin at a specified speed or not spin. Introduction of material to a spinning wafer is called a dynamic dispense; introduction of materials when the wafer is not spinning is called a static dispense.

The material is pumped to the nozzle from a container. The volume of each dispense can be adjusted by the pump recipe (typically 1–4 mL for a 300-mm wafer). After the material is dispensed on the wafer, the wafer is typically set to a low spin speed in order to allow the resist to cover the whole wafer, and is then accelerated to a high spin speed to attain target thickness and uniformity. For example, a 193-nm resist is dispensed on the wafer with a spin speed of 100 rpm and a dispense volume of about 3 mL. After the resist is dispensed, the wafer is first accelerated to 500 rpm for 3 seconds and then to 1750 rpm for 45 seconds. This acceleration speed has only a minor effect on the resist thickness and uniformity[1] and is usually set to the maximum available value of above 10,000 rpm/s. Figure 2.2 shows the spin speeds and dwell times in each step. Using this recipe, a target thickness of 220 nm with 3σ of less than 2.5 nm can be obtained on a 300-mm wafer.

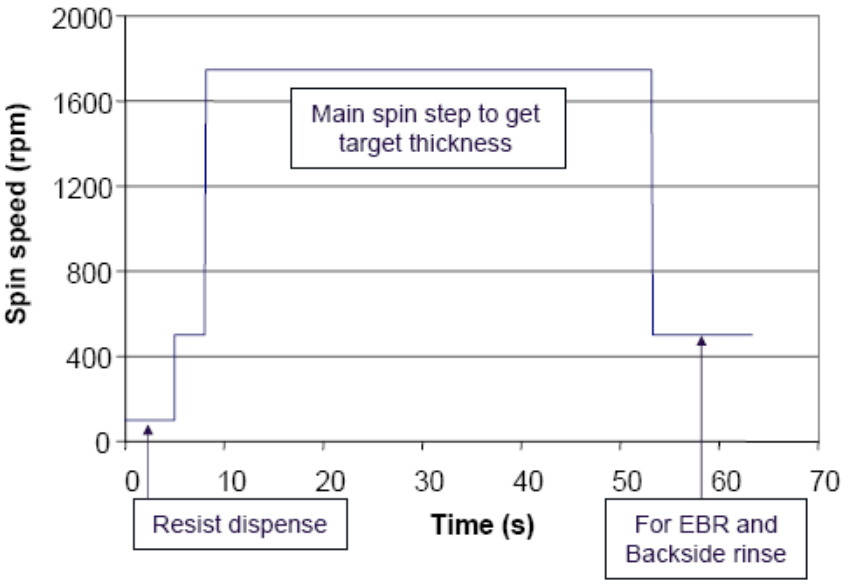

Figure 2.2 Example of a spin speed setting in a coating module.

2.1.2 Viscosity of materials

In addition to the spin speed, the material viscosity is another important factor that affects film thickness and uniformity; appropriate viscosity is needed to reach target thickness and uniformity. Usually, the spin speed is set in the range of 800–3000 rpm for the coating of 300-mm wafers. When spin speeds are set too low, losses in uniformity can occur. When spin speeds are set too high, mechanical break-down of the wafer or the spinner may result.

Viscosity can be thought of as internal friction. Friction is a force acting along the direction of travel. The SI unit of viscosity is $N \cdot s/m^2$, or Poiseuille, and is abbreviated as PI. The centimeter-gram-second system (CGS) unit of viscosity is $dyne \cdot s/cm^2$, also known as Poise and abbreviated as P. In practice, the industry uses the centi-Poise (cP) or one-hundredth of a Poise, because water has a viscosity of 1.002 cP at 20° C, which is very close to 1.

1 Poiseuille (PI) = 10 poise (P) = 1000 cP,
1 P = 0.1PI, and
1 centi-Poise (cP) = 0.01 poise (P).

Viscosity values of some common fluids are listed below.

air @ 18° C:	0.0182 cP
acetone @ 20° C:	0.3 cP
methyl alcohol @ 20° C:	0.597 cP
benzene @ 20° C:	0.652 cP
ethyl alcohol @ 20° C:	1.2 cP

Most 193-nm resists have a viscosity of ~1.8 cP, which will reach thicknesses of 150–300 nm with spin speeds of 800–3000 rpm. By adding more or less solvent (e.g., PGMEA), the viscosity can be adjusted to meet the required target thickness.

2.1.3 Film thickness

The physics behind spin coating involves a balance between centrifugal forces controlled by the spin speed and viscosity of the resist, which is determined by the solvent content[2,3] and the molecular weight of the polymer. Solvent evaporation is another important factor that affects the film thickness. Once the resist is dispensed on the wafer, solvent evaporation begins. The evaporation rate determines how fast the resist film loses fluidity and becomes a solid. Therefore, the dwell time of the high-speed spinning has to be long enough to ensure solidification of the resist film. The evaporation rate is not a constant; it increases with the spin speed and exhaust flow rate. This is because the air flow at the surface of the resist film increases with spin speed and because increasing the exhaust flow rate decreases the partial pressure of the solvent in the coating chamber.

The relationship between the spin speed ω and the resist film thickness *t* can be expressed as

$$t = c \cdot 1/\sqrt{\omega}\,, \tag{2.1}$$

where *c* is the material factor. Equation (2.1) is used in the process setup to predict the spin speed for a target thickness. This equation is generally applicable to most resists, BARCs, and topcoats.

In practice, process engineers must use the basic principles described here, in combination with experimentation, to arrive at the best process for a specific material and application. A good coating recipe should not only reach the target thickness and uniformity, but must also consume the minimum amount of material. This material saving is especially important for large volume production. A typical production fab processes 30,000 wafers per week; each wafer may need 30 lithographic levels. Saving 1 mL resist per coating means a total savings of 900 liters of resist per week.[4]

2.1.4 Reduction of material consumption

Reduction of photomaterials consumption while maintaining coating quality is becoming a major challenge for process and equipment engineers. The biggest disadvantage of the spin coating process is lack of material efficiency. An excessive amount of material is used to prevent coating discontinuities caused by the fluid front drying prior to reaching the wafer edge. Typical spin coating processes utilize < 20% of material dispensed onto the wafer, while > 80% is thrown off the wafer into the coating bowl and sent to waste treatment.[5]

Pre-wetting the substrate is the most common way to reduce material consumption. An example of a pre-wetting process is coating topcoat (TCX041) onto the resist film.[6] Traditionally, the TC is coated without pre-wet and requires ~3.0-mL TC to fully cover a 300-mm wafer. However, the use of a 2.5-mL solvent pre-wet followed by 1.0 mL of TC will fully coat a 300-mm wafer. Lithographic results indicate that a film stack coated using this pre-wet process performs as well as a film stack coated by the non-wetting process.

Other technologies have been developed and implemented to reduce material consumption. One example is the use of dispensing nozzles with smaller diameters. Normal dispensing nozzles have a diameter of 1.5 mm with a minimum dispense volume of 0.6–0.75 mL per coating. A small dispensing nozzle with a diameter of 0.5 mm can reduce the dispense volume to 0.4 mL per coating, while meeting both thickness and uniformity specifications.[5]

Another approach to reducing resist consumption is to use the ultra-casting pre-dispense technique (UCP),[7] in which the resist is dispensed twice in one coating recipe. Each dispense drops only < 1 mL of the resist. The first dispense is performed at high spin speed. At the high spin speed, due to high centrifugal force, the resist is quickly cast over the entire wafer, creating a resist interface on the substrate. The second dispense occurs at low spin speed. A minimal resist is

needed to form a uniform resist film, because surface tension has been much reduced by the first resist dispense. The time interval between the two dispenses is about 1 second. Figure 2.3 shows how the spin speed changes in the coating process. The total resist consumption of the two-dispense process is smaller than that of the traditional one-dispense process.

2.1.5 Coating imperfections and defects

The spin coating process is required in order to produce a clean and uniform resist film. Nonoptimized coating processes may result in thickness deviation and introduction of coating defects.[8] Three of the most common coating defects are summarized in the next sections.

2.1.5.1 Comets

Small particles on the wafer will impede resist flow during spin coating, forming comet defects. Figure 2.4 shows an optical microscopic image of a typical comet defect. The radial resist flow generated by the centrifugal force is blocked by the particle. The disturbed flow forms a comet pattern at the particle site. Therefore, the root cause of comet defects is foreign particles on the wafer surface.

Depending on particle size, comet defects are typically in the range of several nanometers to hundreds of microns. The particles may come from the wafer itself or be left over from previous processes. Dirty environments can also cause particles to be on the wafer. In addition, chemical segregation and precipitation may occur in the resist bottle, forming clusters and particles. With poor filtration, these clusters and particles can be delivered to the wafer surface. Therefore,

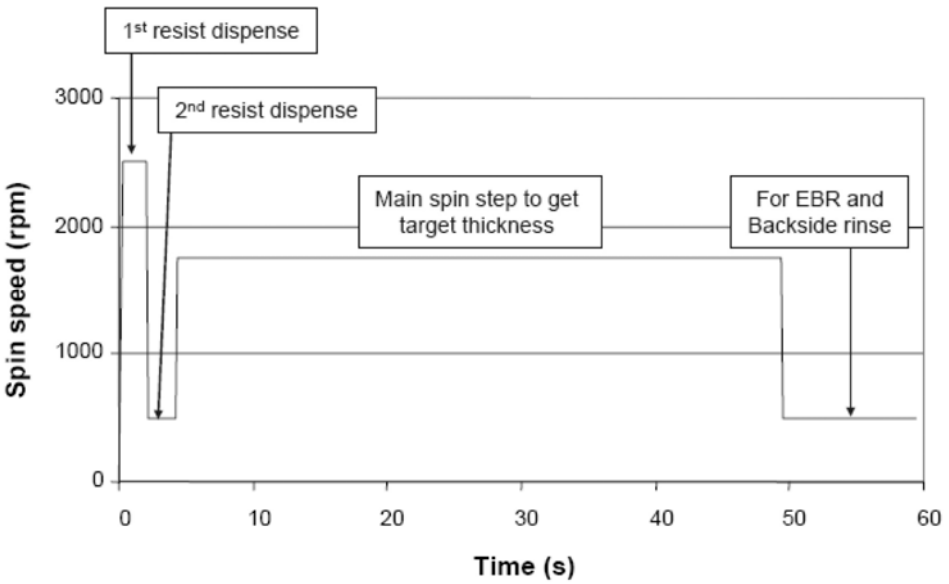

Figure 2.3 Two-dispense process for resist coating.

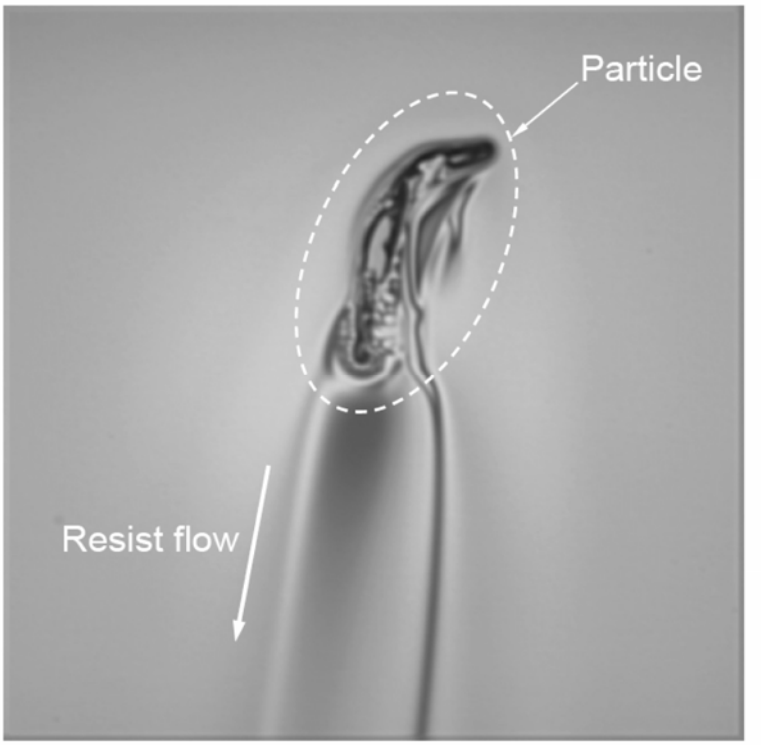

Figure 2.4 Optical microscopic image of a coating defect: a comet.

thoroughly cleaning the wafer before coating, as well as coating the wafer in an enclosed environment with filtered ventilation and installing suitable resist filters are the key measures for reduction of comet defects.[9]

2.1.5.2 Striations

Striations are radially oriented resist stripes and are severe coating failures that show the existence of coating nonuniformity in an angular direction. Striations usually start near the center of the wafer and become broader toward the wafer edge. Figure 2.5 shows an optical microscopic image of typical striations.

Striations are most often caused by lack of wetting. The interaction of a hydrophobic surface with a polar solvent in the resist (e.g., ethyl lactate) will result in poor wetting. Centrifugal force pushes the resist across the wafer surface, leaving some coating stripes behind. Striations may also occur when the resist dispense volume is too low. In this case, the dispensed resist volume is too small to cover the whole wafer. Each drop of the resist forms a radial stripe and the stripes cannot form a continuous film. Fast evaporation of the solvent has also been blamed for striations. Solvent evaporation changes the composition in the resist surface layer and therefore changes its surface tension. According to the results reported in literature,[10,11] surface tension variation can lead to striations.

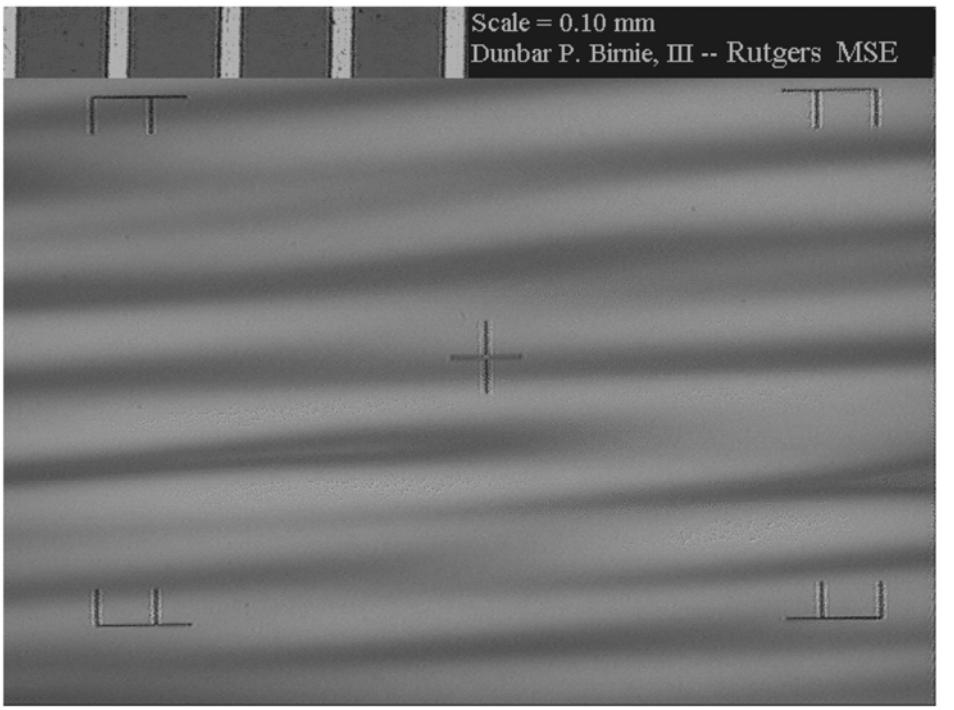

Figure 2.5 Optical microscopic image of a coating defect: striations. (Reprinted by permission from Ref. 8.)

2.1.5.3 Edge bead and backside contamination

During spin coating, excess material is pushed to the wafer edge by centrifugal force and most of the material flies off the wafer's edge. However, surface tension prevents all of the resist from leaving the wafer. Additionally, the wafer edge moves at the highest velocity and has the highest air flow. Excess resist can dry and form a bump around the entire edge of the wafer. This is called the edge bead (Fig. 2.6). If the substrate is not a circular shape (e.g., is square or rectangular), the excess resist will be pushed to the corners where a thicker film will be formed. In addition to the edge bead formation, the resist is likely to wrap around the wafer edge and contaminate the backside of the wafer, as well.

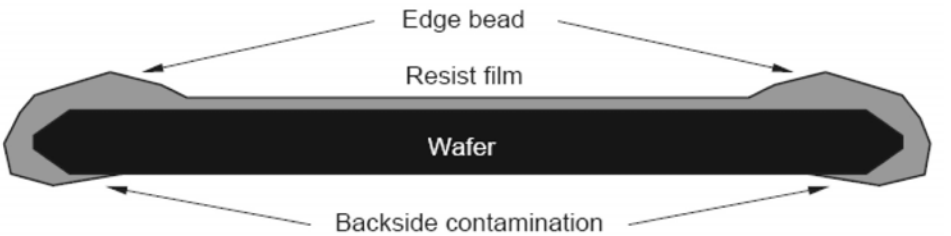

Figure 2.6 Sketched profile of resist film with edge beads and backside contamination.

Presence of the edge bead can lead to various problems in subsequent processes.[12] After post-apply bake, the edge bead can contaminate hot plates, wafer handlers, and stages. Accumulation of material on the back side of the wafer can also disturb the leveling readings in the exposure tool and generate "hot spots" during exposure. Due to these undesirable effects, most lithographic processes employ edge bead removal (EBR) and back rinse processes immediately after spin coating. The EBR is done by spraying the beaded edge with the solvent while the substrate spins, as sketched in Fig. 2.7. The solvent dissolves the edge bead along the wafer periphery. The EBR nozzle is titled so that the solvent sprays toward the wafer edge. The centrifugal force casts away the dissolved resist and solvent. To better remove the edge bead, resist manufacturers have developed special EBR solvents; instead of simply using the resist solvent, they add some chemical components to make the EBR solvent more effective at removing the edge bead.[13] The backside rinse process is similar: the solvent is sprayed from the bottom of the coating chamber during spinning (Fig. 2.7) and dissolves the resist contaminants on the backside of the wafer.

The nonuniform resist film can also be removed from the wafer edge by an optical method called wafer edge exposure (WEE). After resist coating and post-apply bake, the wafer is sent to the WEE module, where the wafer edge is exposed by a broadband light, but not removed. After pattern exposure and PEB, the resist at the wafer edge is removed in the development process. The WEE process cannot be used for the BARC film, as this film is not photosensitive.

The advantage of the chemical EBR is that it can remove both photoresists and organic antireflective coatings (ARCs) with the appropriate EBR solvents. The disadvantage of the chemical EBR is that it can splash onto critical areas of the wafer. Solvent splashing issues have been shown to result in missing-pattern defects. Yield loss caused by the EBR solvent splash is increasingly reported by modern fabs.[14] The position and tilting angle of the EBR nozzle and the solvent flow must be optimized in order to address this splashing issue.

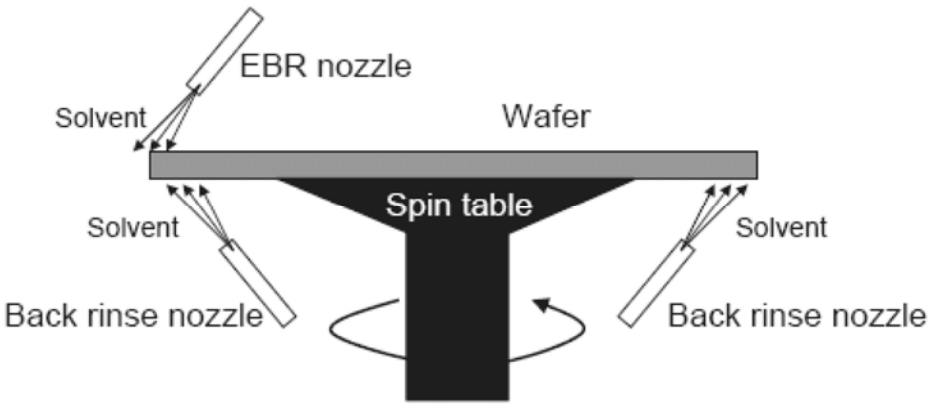

Figure 2.7 Diagram of EBR and back rinse setup.

2.1.6 Material drying at the nozzle

After dispensing material, the nozzle is moved back to its home position where it sits above a solvent bath. The purpose of the solvent bath is to immerse the nozzle tip in solvent vapor and prevent material from drying at the nozzle tip (Fig. 2.8). However, most ArF resist solvents are so volatile that early solvent bath changes were unable to prevent resist drying at the nozzle tip. Dried resist at the nozzle tip not only blocks the flow of resist, but can also fall from the tip onto the wafer, causing particle defects. Numerous reports have demonstrated that a significant number of particle defects can be traced back to the coating process. Proper cleaning of resist dispense nozzles has proven to be effective in reducing particle defect counts. New solvent bath designs have been proposed to increase the vapor pressure around the nozzle by raising the inlet of solvent.[15]

2.1.7 Alternative coating techniques

Resist coating is a key process step in lithography. Though spin coating is a mainstream technology, alternative coating methods have been developed. For example, in scan coating, the resist is dispensed from a nozzle with 30- to 100-μm dispense holes.[16] The nozzle continuously scans in one direction while the wafer steps in the other direction (Fig. 2.9). After the resist is scan coated onto the substrate, the liquid resist film is dried in reduced pressure. This separation of the coating and drying processes allows separate control of solvent evaporation and film formation.

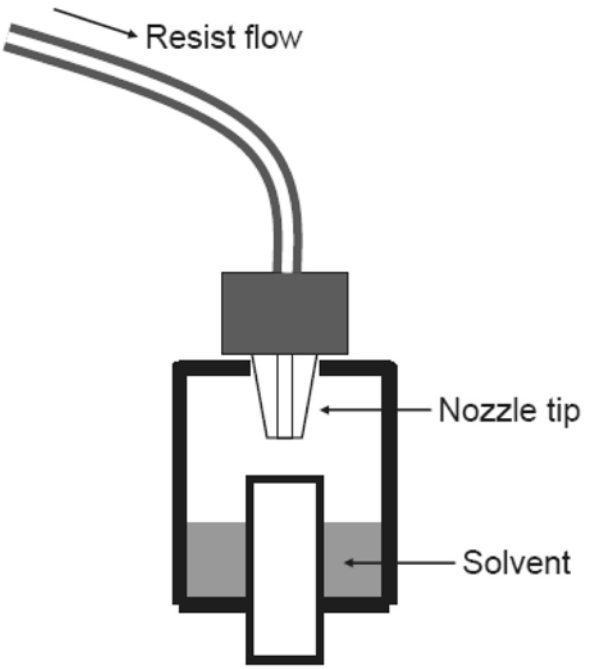

Figure 2.8 Diagram of the resist nozzle at its home position.

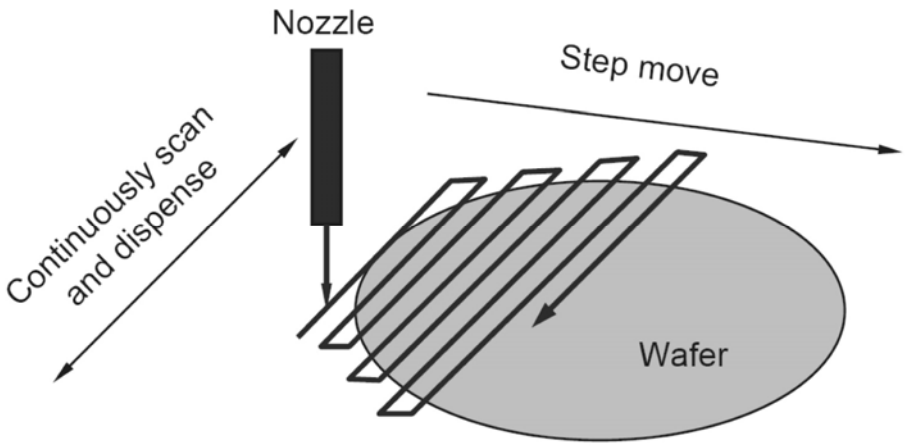

Figure 2.9 Diagram of the scan coating.

Different coating techniques will affect material performance. One study showed that scan coating better distributes photoacid generator (PAG) than spin coating does.[16] In this study, the spin-coated resist film was shown to have a lower PAG concentration at the surface than it had in the bulk of the resist film. By contrast, films coated by the scan method were shown to have a much more uniform PAG concentration throughout the thickness of the film. The depth profile of PAG concentration has significant effect on the lithographic performance of the resist film.

2.2 Baking Module

Since the 1980s, hotplates have become the primary method of baking wafers, replacing ovens for this purpose. Hotplates have several advantages over ovens; they offer high throughput, better heating uniformity, and reduced particle contamination. In the hotplate bake process, the resist film is baked from the bottom, preventing the formation of a skin over the surface, which is a severe issue in oven bake processes. In a typical bake process, the hotplate is first heated to the bake temperature, then the wafer is loaded, coming in close contact with the hotplate. The retention time (bake time) is usually about one minute. In a typical process flow, wafers are baked several times. Post-apply bakes (PABs), also known as “soft-bakes,” drive solvent from films after spin coating to solidify the films. BARCs, resists, and topcoats are all subjected to PABs after coating. Post-exposure bakes (PEBs) thermally activate the deprotection reactions occurring in resists after exposure. Tracks have several bake modules offering various bake temperatures. The following sections discuss key issues for engineers and tool owners working on baking modules.

2.2.1 Temperature uniformity

The temperature of a hotplate must be very accurately and precisely controlled. The PEB process of 193-nm lithography typically requires that hotplate temperatures be controlled to an accuracy of ± 0.1° C and to less than ± 0.5° C across the plate. In addition to potential hotplate temperature nonuniformity, the wafer itself may introduce bake nonuniformity. Since the processed wafers have some degree of nonflatness, hot spots are created at positions where the wafer touches the hotplate and cold spots are created at positions where the wafer does not touch the hotplate. To compensate for the curvature of the wafer, a vacuum is connected to the hotplate to pull the wafer into closer contact with the hotplate.[17]

Instead of being in direct contact with the hotplate, a wafer can also be suspended to within 25–100 μm of the hotplate surface, so that a small air gap is formed (Fig. 2.10). This setup is called proximity baking.[18] Hotplates must be adjusted to higher temperatures or baked for longer times to compensate for the heat loss caused by the air gap. The proximity bake provides a higher degree of uniformity than does the contact bake, especially for backside-contaminated wafers. Proximity baking also offers the unique advantage of allowing hotplate processing without touching the backside of the wafer, thereby avoiding cross-contamination between the wafer and the hotplate.

2.2.2 Temperature variation across the hotplate during thermal ramp

Bake temperature variation across the hotplate results in poor CD uniformity across the wafer. Temperature variation across the hotplate is often observed during thermal ramps.[19] As shown in Fig. 2.11, the temperature at the center of the hotplate increases more slowly than the temperature at the edge. The hotplate reaches a thermal equilibrium after ~4 minutes, when the temperature variation across the plate almost disappears. Similar nonuniformity has also been observed during chilling. Experimental results have demonstrated that this thermal nonuniformity causes CD variation across the wafer.[19] Process engineers and tool owners must be very careful that thermal uniformity is maintained across the wafer and from wafer to wafer during all of the bake steps, but most importantly, during PEB. The most direct solution is to have hotplates dedicated to each necessary temperature, so that temperature ramps can be minimized; even so,

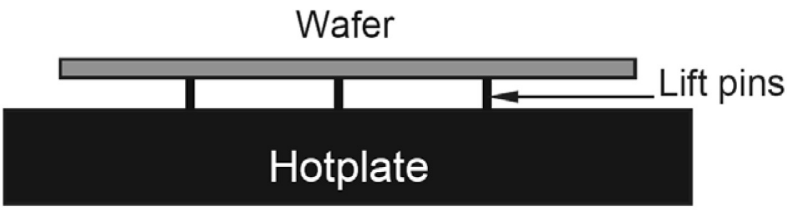

Figure 2.10 Proximity baking: wafer is lifted 25–100 μm above the hotplate.

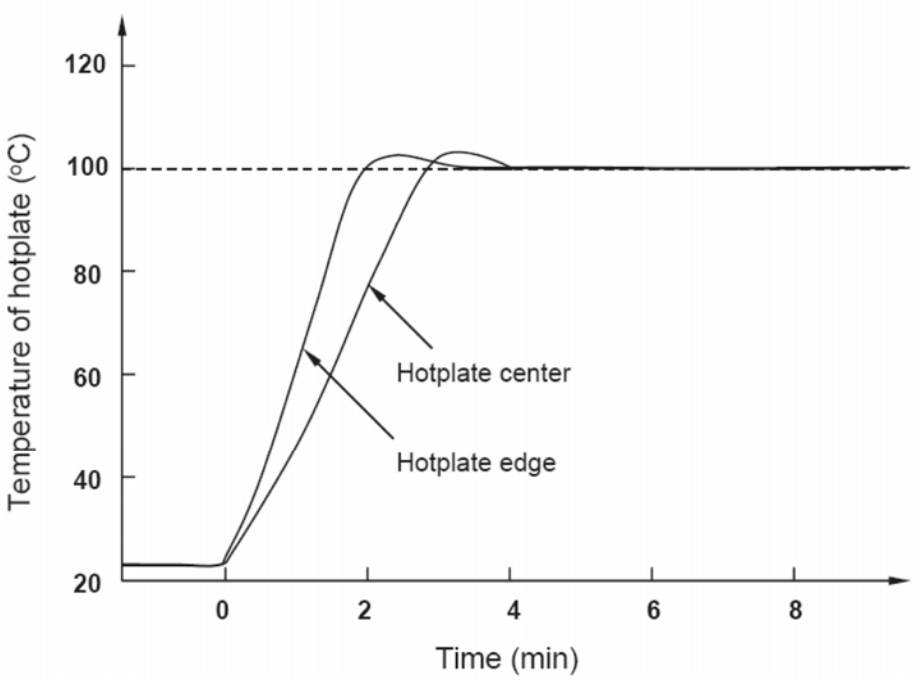

Figure 2.11 Temperatures at the center and at the edge of a hotplate during heat up. The hotplate starts to heat up at $t = 0$ and the target temperature is set to 100° C.

the heat capacity of the wafer can cause the hotplate to cool down. New hotplate designs with better heat-exchange properties have been developed to address this problem.[20,21]

2.2.3 Hotplates with temperature gradients

When considering process development, hotplates with controllable temperature gradients are very useful for achieving bake temperature optimization. More specifically, to determine the PEB temperature sensitivity of a resist, exposed wafers need to be baked at different temperatures. This is typically done using multiple wafers—one temperature per wafer. A new hotplate capable of generating a temperature gradient has been designed: the thermal gradient plate (TGP).[22]

The TGP is made of a machined block of aluminum placed on top of a conventional hotplate or on another heat source (Fig. 2.12). Temperature distribution across the plate can be measured using a silicon wafer with probes embedded in an array across the wafer (called a thermal map system).[23] The temperature decreases in the X-direction and is uniform along the Y-direction in the wafer area. The range of the temperature gradient can be adjusted by changing the heat source temperature and the type and degree of active cooling at the end of the TGP, as well as by changing the displacement along the gradient direction from the heat source.

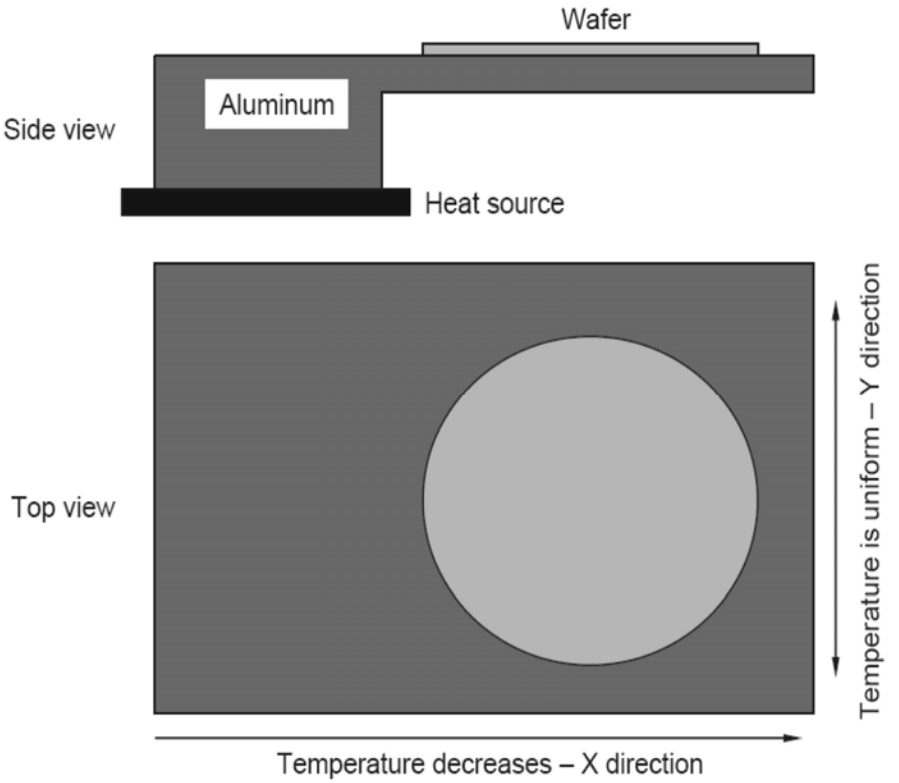

Figure 2.12 Thermal gradient hotplate. (Reprinted by permission from Ref. 22.)

With the TGP, a substrate can be baked across a range of temperatures, allowing multiple experiments to be run in parallel. The number of wafers required to optimize the bake temperature of a given process is significantly reduced. Exposure conditions are the same for all of the dies. The PEB is performed with the TGP; the PEB temperature sensitivity can be obtained from the single wafer. As suggested in Ref. 22, the wafer can also be rotated 90 deg for another bake. For example, the PAB can be performed with the temperature gradient in one direction and the PEB can be performed with the wafer rotated 90 deg. In this way, the effect of a full PAB and PEB temperature matrix can be explored using only one wafer.

2.2.4 Sublimation at high-temperature post-apply bakes

During low-temperature post-apply bakes, solvent is driven from the freshly spin-coated films, which do not cause problems unless they condense on the hotplate cover. During high-temperature bakes (i.e., for BARC PABs), however, temperatures are typically ~200° C and solid compounds can sublimate from the film. With nonoptimized exhaust systems, these outgassed chemicals can condense on the internal walls of the baking chamber or directly back onto the wafer, forming defects. Depositions on the chamber internal wall can flake off,

forming particle defects with diameters of 0.16–0.2 μm on subsequent wafers. These sublimation defects were first observed as a result of BARC baking, since the temperature of BARC PAB is high, typically above 200° C.

Particle defects associated with high-temperature BARC PAB were studied by mounting a quartz plate over a wafer on a hotplate.[24] The chemical components outgassed from the BARC sublimed and were deposited on the quartz plate. Infrared (IR) spectral analysis of the quartz plate revealed that the deposits were low molecular weight additives such as cross-linkers. The sublimation rate was measured using a quartz crystal microbalance (QCM) positioned over the wafer in the bake chamber. The resonant frequency of a QCM is very sensitive to the mass of its acoustic resonator. The deposition of outgassed components onto the acoustic resonator was monitored as a function of time, in order to determine the sublimation rate from the BARC film.

Obviously, the solution to the sublimation problem was to redesign bake chambers with better exhaust systems, and as a temporary solution, two-step baking was widely used. Wafers were first baked at intermediate temperatures for short times, (e.g., 120° C / 45 s), then, the wafers were sent to high-temperature hotplates. The intermediate-temperature bakes removed the first outgassed components and significantly reduced the exhaust burden of high-temperature hotplates. Although this approach showed a decrease in sublimation defects, it also caused a loss in throughput.

2.2.5 Chemical flare during post-exposure bake

Outgassing during post-exposure bake can be another problem. Photoacids are generated in resist films during exposure. Some of the photoacids can be volatilized during the PEB process and redeposit on adjacent unexposed areas, causing variations in CD. This phenomenon is called chemical flare.[25]

Time of flight–secondary ion mass spectroscopy (TOF-SIMS) has been used to investigate the change in resist surface composition after exposure and PEB. The results indicate that some resists show significant photoacid migration from exposed to unexposed areas, but that other resists exhibit less migration. The outgassing rates of photoacids depend on their volatilities and local concentrations. In the 193i process, the use of topcoat may mitigate this chemical flare. Furthermore, resist designs that minimize leaching and acid diffusion length may also help to reduce the volatility of the photoacid.

Increasing the exhaust flow has been demonstrated to be an effective method for reducing chemical flare and sublimation defects. In a mass production environment, it has been found that CD drifts and defect counts increase with increasing service time of hotplates.[26] These observations have been attributed to the blockage of the exhaust flow by the deposition of outgassed chemical components. After cleaning of the exhaust lines, CD and defect counts can generally be brought back to target values. The design of new bake chamber covers with larger exhaust openings seems to be an effective solution to this problem (Fig. 2.13).[26]

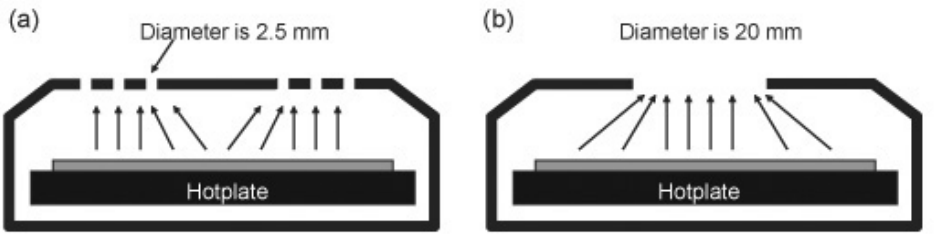

Figure 2.13 Hotplate chamber with (a) small exhaust openings and (b) large exhaust openings.

2.3 Development

Resist development is performed in development bowls equipped with spin tables and nozzles for dispensing developer, DI water, and possibly, surfactant. Wafers are loaded onto spin tables and aqueous developer is dispensed onto the wafer surface. For positive resists, exposed areas are dissolved by the developer and the patterns appear (Fig. 2.14). Then, DI water is dispensed onto the wafer to stop the development and to remove the developer. The retention time of developer on the wafer is defined as the development time. Finally, the wafer is spun until dry.

2.3.1 Developer dispense

There are two main methods to dispense the aqueous developer: static and dynamic. During a static dispense, the wafer is motionless while the developer is dispensed by the develop arm (Fig. 2.15(a)). The arm moves across the wafer and the aqueous developer is released from the nozzles on the bottom of the arm. The aqueous developer forms a puddle covering the wafer surface. The develop arm can scan across the wafer once (single puddle) or twice (double puddle). During a dynamic dispense, the wafer spins at slow speed while the developer is dispensed from a nozzle located in the center of the spin table (Fig. 2.15(b)). The developer flows radially, driven by centrifugal force. Development occurs in both methods as soon as the developer is in contact with the resist.

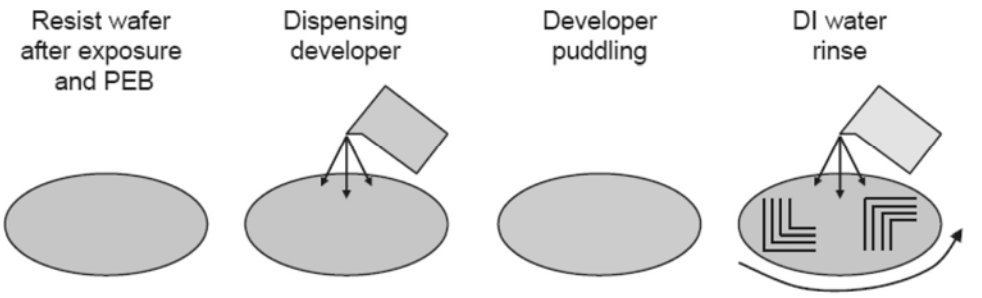

Figure 2.14 Process flow of a simple development.

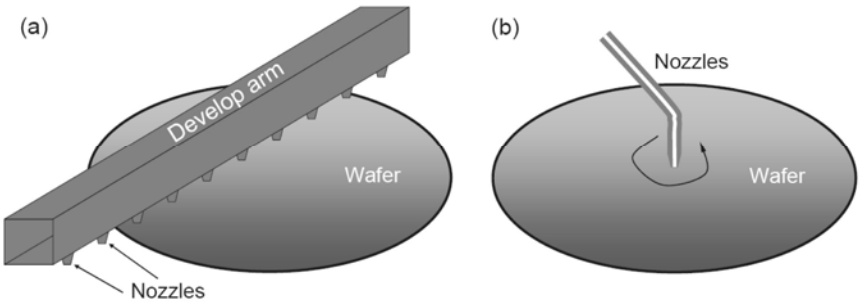

Figure 2.15 Diagram of (a) static dispense and (b) dynamic dispense.

The performance of static and dynamic dispense methods was investigated and compared for 193-nm dry lithography. It was concluded that both nozzles give similar CD uniformity and defect counts. However, for the immersion process, the situation is different. To reduce watermark defects (see Chapter 6 for details), 193i processes use very hydrophobic resists with static water contact angles of over 90 deg. These hydrophobic resists are incompatible with simple puddle development using aqueous TMAH developers. The aqueous developer beads up due to surface tension and does not cover the whole wafer, resulting in a loss in CD uniformity.

Dynamic dispense of developer addresses this issue. Wafers are spun while the developer is dispensed at the wafer center. The centrifugal force overcomes surface tension to pull the TMAH developer across the wafer surface. Key parameters are the developer dispense rate (flow rate at the nozzle) and wafer spin speed, both of which need to be optimized for different resist stacks. Dynamic dispense of developer is primarily used in the 193i process and provides better CD uniformity and defect counts. In addition to the dispense methods demonstrated in Fig. 2.15, the developer can be dispensed by other methods; one example involves a setup in which the developer puddle can be formed by a rotating develop arm.

2.3.2 Optimization of development time

Development time is a key process parameter. Because the development process of 193-nm lithography is simply adopted from the 248-nm process with the same concentration of developer (2.38 wt% tetramethylammonium hydroxide (TMAH)), the development time must be optimized in order to obtain the best performance for each 193-nm resist.

In one study, puddle time was optimized for imaging of 90-nm dense lines.[27] First, the exposure latitude (EL) and DOF versus puddle time were determined as a function of development time for three different resists (Fig. 2.16). Although the dense-line patterns were completely formed during the first 10 seconds of development, the EL and DOF of Resists A and B were found to be relatively

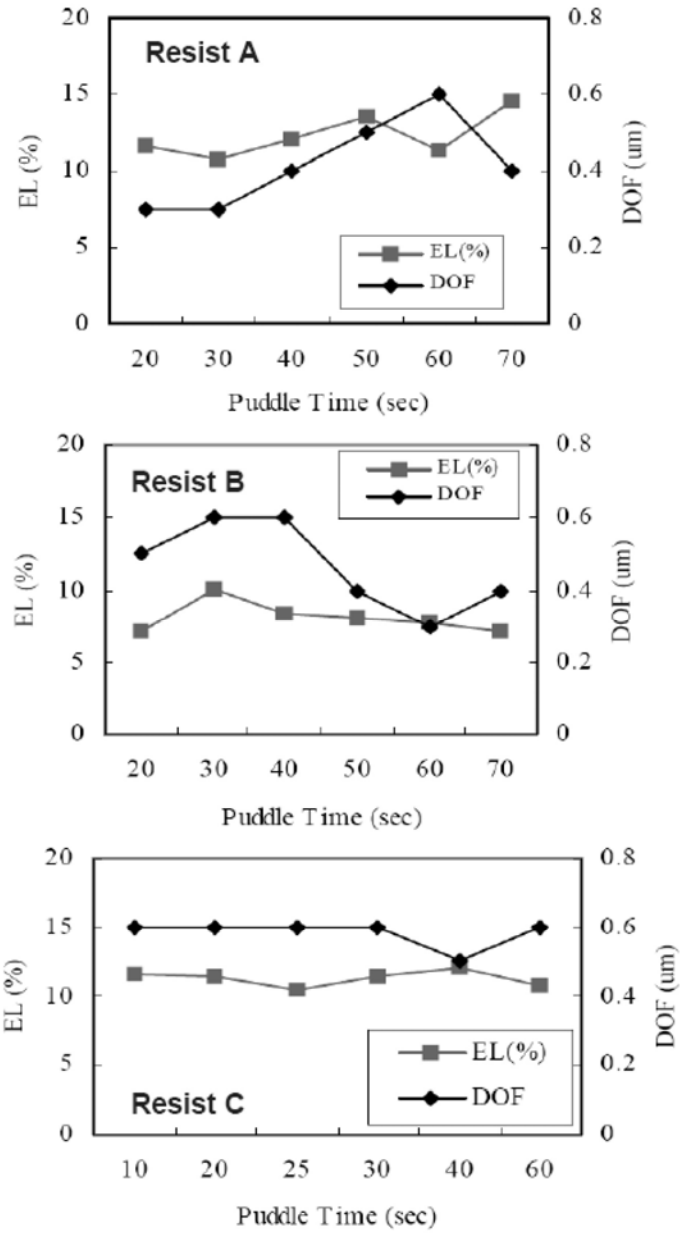

Figure 2.16 Measured EL and DOF versus puddle time for three different resists. (Reprinted by permission from Ref. 27.)

sensitive to the length of puddle time (low puddle-time latitude), whereas the EL and DOF of Resist C seemed relatively insensitive to puddle-time. Resist C was selected for additional experiments to characterize its performance sensitivity to development time, including: line-edge roughness (LER), cross-wafer CD uniformity (CDU), mask error enhancement factor (MEEF), and resist pattern

profile. Figure 2.17 shows the measured LER and resist pattern profile change with the puddle time. Finally, defect counts versus puddle time was evaluated and the optimum puddle time was identified.

Other researchers performed similar experiments. In one case,[28] the wafers were exposed with focus exposure matrix (FEM) and sent to the development module. The Bossung plot was measured versus different development parameters, such as scan direction of the developer arm and developer puddle time. The optimum development parameters were obtained at the point where the Bossung plot does not change with a small dose variation. Figure 2.18 shows the Bossung plots before and after the optimization of development parameters.

2.3.3 Deionized water rinse process

The deionized (DI) water rinse serves two functions: to stop development and to remove particles generated during development. The wafer spins during the rinse so that centrifugal force can assist in removing particles. Figure 2.19 shows a simple sequence for a rinse process. Sometimes, to get improved particle removal, more complex rinse processes are used. For example, the spin speed of the wafer can be alternated between high and low speeds. This acceleration/deceleration cycle can be repeated several times as shown in Fig. 2.20. The "spin-speed oscillation" rinse has been shown to reduce the counts of defects introduced during development.

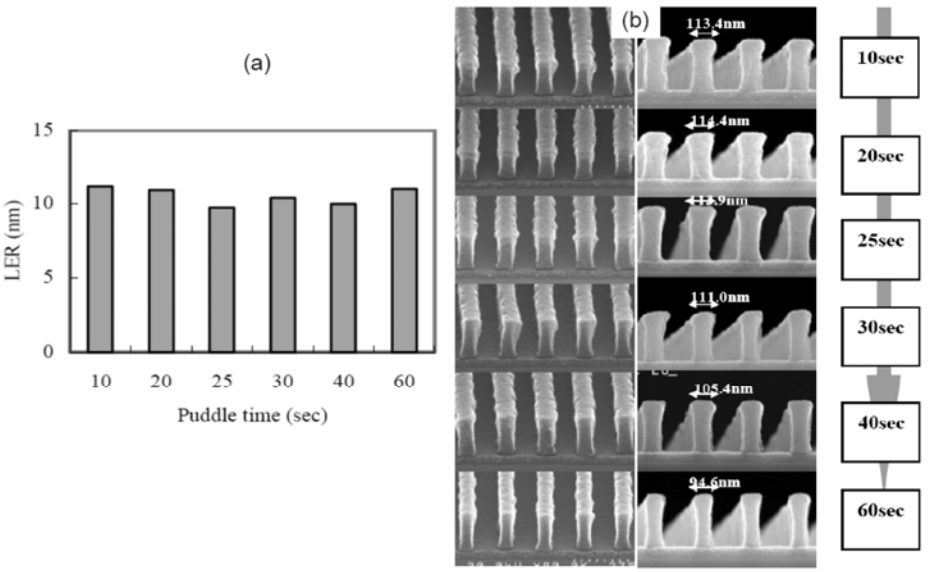

Figure 2.17 LER and cross-sectional images of resist pattern profile change with the puddle time. (Reprinted by permission from Ref. 27.)

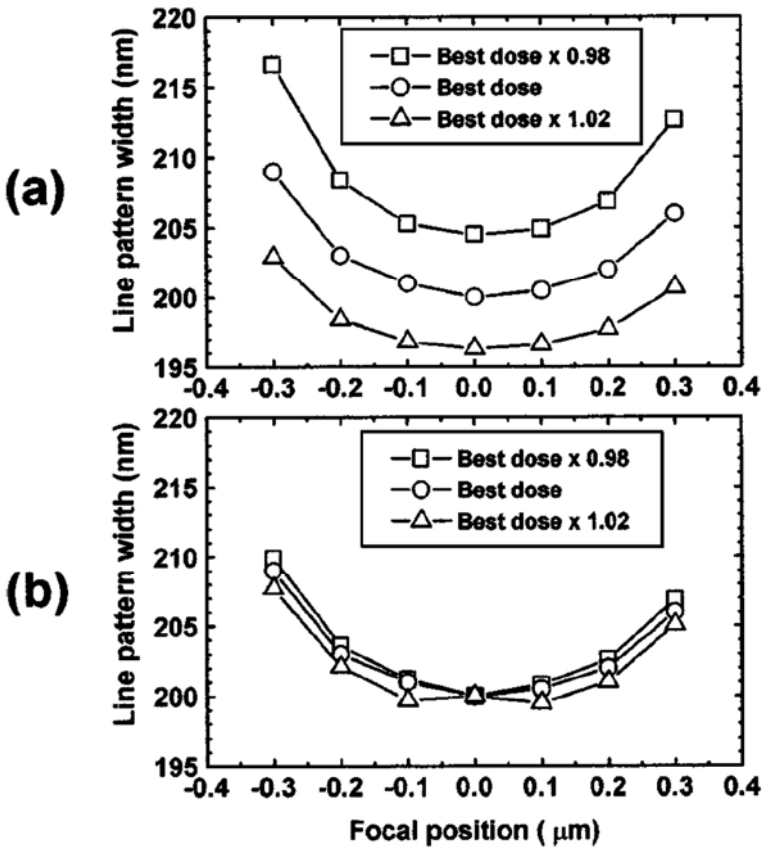

Figure 2.18 Bossung plot of a line pattern (a) before and (b) after optimization of development parameters. (Reprinted by permission from Ref. 28.)

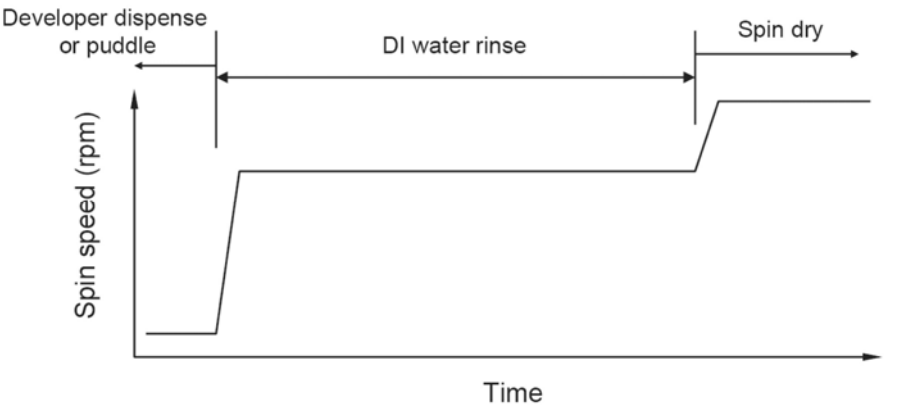

Figure 2.19 Simple sequence for a rinse process.

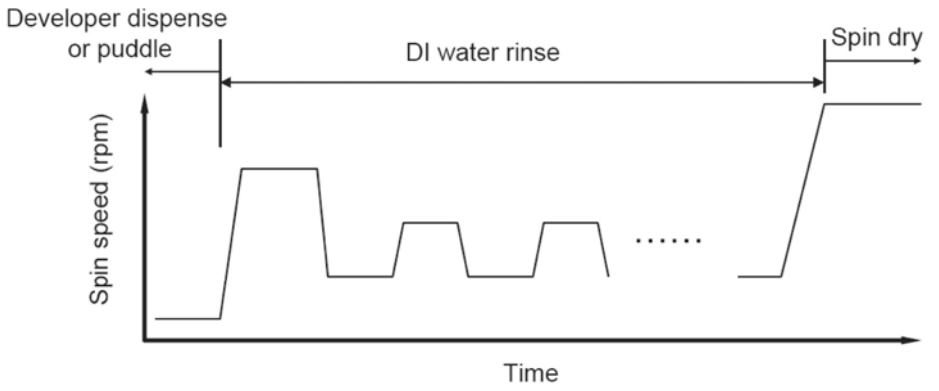

Time (s)	Speed (rpm)	Acceleration (rpm/s)	Dispense	Rinse Arm
…	…	…	…	…
1.5	1200	1200	DI water	Center
4	1200	1200	DI water	Center
3	500	1400	DI water	Center
3.6	2000	15000	DI water	Center
3	500	3000	DI water	Center
4.1	3000	25000	DI water	Center
10.5	4000	2000		Home
1	0	4000		Home

Figure 2.20 Sequence of the “spin-speed oscillation” rinse.

2.4 Resist Line Collapse and Corrective Measures

As the water dries after the rinse, surface tension from receding water pulls on the resist features. In the case where the drying pattern is symmetric, the force is cancelled out. With asymmetric drying patterns, the water dries faster on one side than on the other and a net force is generated on the pattern.

2.4.1 Mechanism of line collapse

Resist line collapse refers to the deformation (bending), fracture, and/or peeling of photoresist structures from the substrate. It is mainly caused by DI water capillary forces acting on the structures during drying. Detailed theoretical analysis of the capillary forces can be found in Refs. 30–32. In a simple case, two resist lines are near each other and water fills the gap between the lines (Fig. 2.21). The pressure induced by the meniscus of the DI water between the lines can be explained by the following equation:

$$\Delta P = \frac{2\gamma \cos\theta}{S}, \tag{2.2}$$

where γ is surface tension, θ is contact angle, and S is the space size. This pressure tends to bend the resist lines toward each other. The resist lines suffer from the stress as

$$\sigma = \frac{6\gamma (H/L)^2 \cos\theta}{P}, \tag{2.3}$$

where H/L is the aspect ratio of the resist line and P is the pitch (and equals $S+L$) (Fig. 2.21).

Capillary force increases with aspect ratio H/L and water surface tension γ, but decreases with contact angle θ. Therefore, hydrophobic resists generate less capillary force and give reduced levels of pattern collapse. The surface tension of water at room temperature is about 0.072 N/m. The counterforce is the resist stiffness or mechanical strength, which is described by the Young's modulus, E and has a range of 2–6 GPa. In general, materials with a higher glass transition temperature (T_g) have higher Young's moduli. Novolak resists have the highest moduli and ArF resists have the lowest.[30]

Mack did a quantitative calculation of ArF resist line collapse by assuming that a resist line from an ArF resist has an E/σ ratio of ~35 nm^{-1} and a water–resist contact angle of about 60 deg.[30] For a resist thickness of 141 nm, the target feature is 45 nm 1:1 dense lines. With increasing dose, the resist lines become narrower and aspect ratio increases. Before the resist line CD reaches 40.5 nm (–10% CD error), the surface tension of the rinse water will cause the lines to collapse. One conclusion from this work is that pattern collapse is becoming an increasingly important factor in limiting the size of the process window in 193-nm lithography.

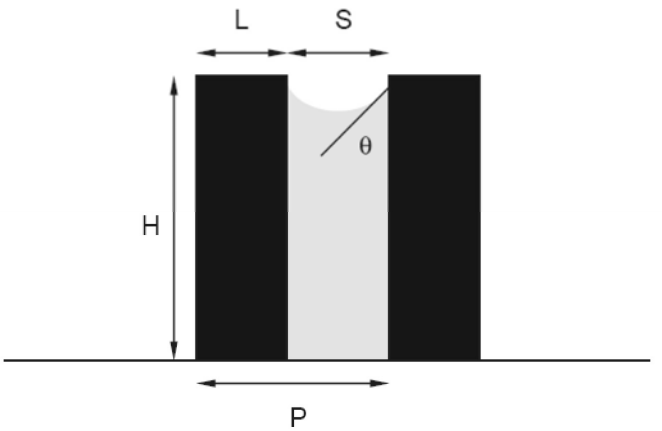

Figure 2.21 Two resist lines are near each other and water fills between the lines.

2.4.2 Surfactant rinse to reduce line collapse

A simple solution to line collapse is to reduce the aspect ratio of the resist pattern. However, this approach causes problems with etch resistance. Sufficient resist thickness is needed to provide enough etch resistance for transferring the patterns to the substrate. Other approaches include coating the resist on a pre-wet BARC surface or using shorter development times. Pre-wetting of the BARC surface with solvent immediately before resist coating can enhance the resist adhesion to the BARC. Line collapse can be caused by the intrusion of developer into the resist–BARC interface. Shorter development time has been suggested in order to suppress the developer intrusion, thereby reducing line collapse.[33]

The most effective approach for reducing line collapse is to reduce the surface tension of the rinse water and increase the contact angle (Eq. (2.3)). Addition of small concentrations of surfactants to rinse water can reduce its surface tension.[34] The results of such tests are showed in Fig. 2.22. The surface tension is dramatically reduced when a small amount of the surfactant is added. With further increases in surfactant concentration of up to 6x the control, the surface tension levels off to about 0.4 of that of water, indicating that a further increase of surfactant concentration beyond 6x is a waste of material.

The surfactant rinse process is typically introduced after DI water rinse. Before the DI water dries, the surfactant water is dispensed on the wafer and replaces the DI water, filling the gaps between the resist patterns. However, it has been reported that this surfactant rinse can be absorbed by 193-nm resists, causing swelling. In contrast, hydrophilic resists may partially dissolve in surfactant solutions, even under low surfactant concentrations.[34] Therefore, compatibility of resist and surfactant must be evaluated before implementation of the surfactant rinse approach.

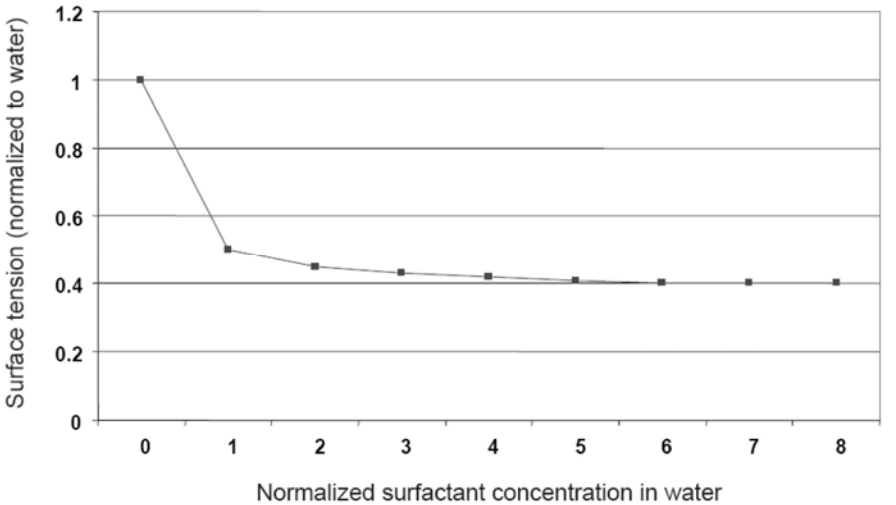

Figure 2.22 Surface tension reduction with increased surfactant concentration.

2.4.3 Evaluation of the line-collapse process margin

The effectiveness of the surfactant rinse can be compared to the effectiveness of the pure DI water rinse. First, two resist-coated wafers are exposed at the best focus as a function of dose (energy meander). One wafer is rinsed with a pure DI water rinse process, while the other is rinsed with surfactant-containing DI water. With increased dose, the CDs decrease and their aspect ratios increase. At a certain point, line collapse starts, as labeled in the darker gray in Fig. 2.23. With the surfactant rinse process, the line collapse occurs at a much higher dose.

The concept of normalized aspect ratio (NAR) was introduced in order to quantitatively describe line collapse.[35,36] The NAR is defined as the pattern aspect ratio divided by the pitch (i.e., NAR ≡ nominal resist thickness/(measured line CD)(pitch)). With increasing dose, the NAR increases to a critical value (CNAR), at which point line collapse begins. For better statistics, collapsed patterns are counted in each die to determine the collapse percentage. Figure 2.24 shows collapse percentage versus NAR for standard developer plus DI-water-rinsed wafer and surfactant-rinsed wafer for 100-nm dense line and spaces. The surfactant rinse clearly increases the CNAR.

It is also possible to evaluate the line collapse process window (PW). For this evaluation, wafers are exposed as a function of focus and dose (i.e., focus exposure matrix or FEM) and processed with DI water and surfactant rinses. This PW includes only dies for which no line collapse is observed (Fig. 2.25). The surfactant rinse process significantly increases the line-collapse process window. To realize a process window with maximum practicality, the line-collapse PW must overlap the 10% CD tolerance process window.

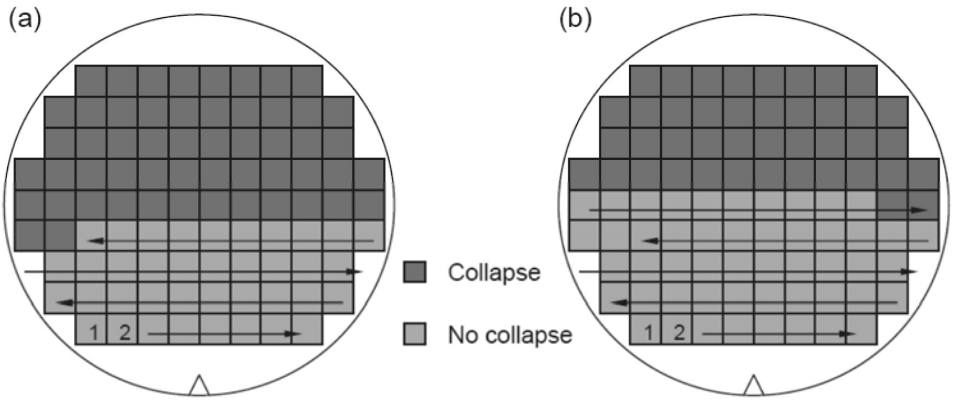

Figure 2.23 Line-collapse map of (a) standard developer plus DI water rinse process and (b) developer plus surfactant rinse process. The arrows indicate the direction of exposure dose.

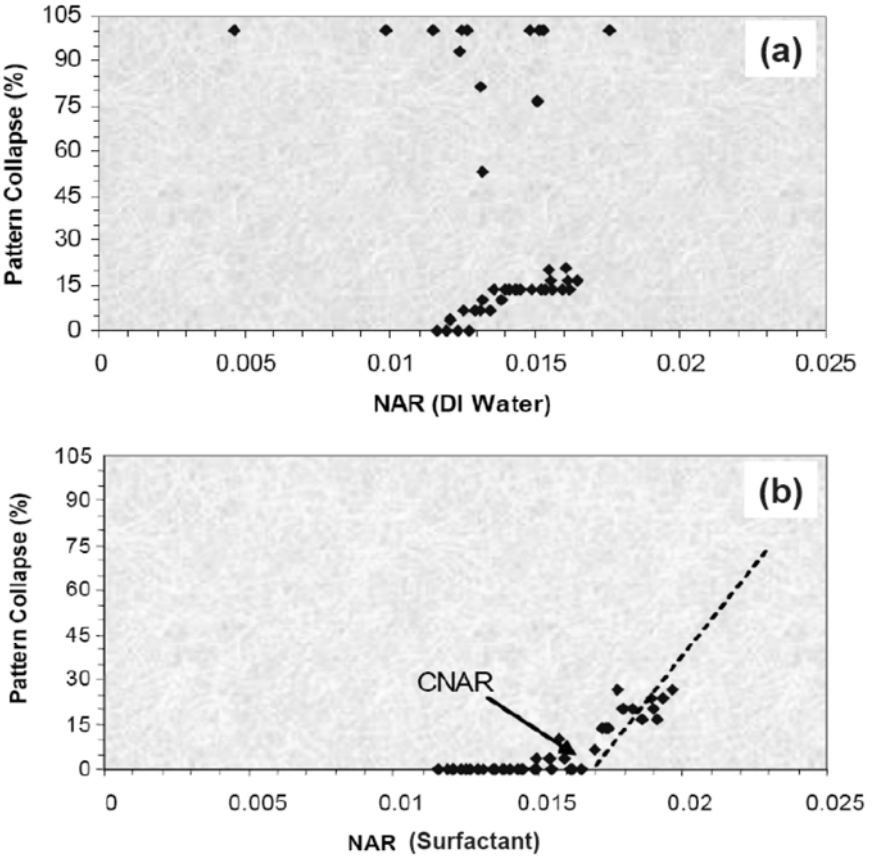

Figure 2.24 Pattern collapse percentage versus normalized aspect ratio for (a) DI water rinse and (b) surfactant rinse processes. (Reprinted by permission from Ref. 36.)

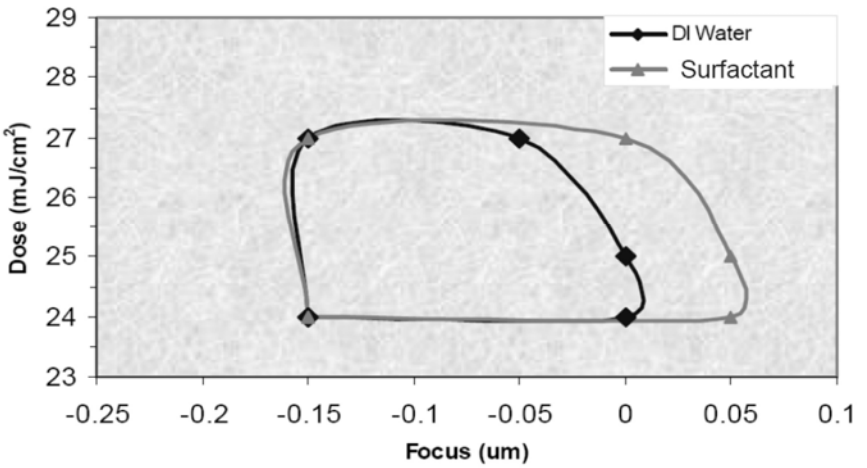

Figure 2.25 Plot of line-collapse PW. No line collapse occurs in dose and focus range surrounded by the curve. (Reprinted by permission from Ref. 36.)

2.5 Blob Defects

Blob defects, also known as satellite spot defects, are primarily found in low pattern density areas.[37] These defects are several microns to hundreds of microns across (Fig. 2.26). Blob defects have been observed in both 248- and 193-nm resists and appear after development. The formation mechanism of these defects is complicated and still not completely understood. However, some studies successfully used energy dispersive x-ray spectrometry (EDX) and Raman spectroscopy to determine that these defects have approximately the same chemical composition as the original resist films. Additional studies indicate that blob defects originate from partially deprotected resist polymers.[38] The partially deprotected polymers cannot completely dissolve in the developer and form particles and clusters there, then deposit back to the resist surface, forming blob defects. Formation of blob defects has also been explained as originating in the DI water rinse. The DI water rinsed on the wafer surface abruptly changes the pH value of the developer puddle—the so-called pH value shock. The pH value shock changes the solubility of the deprotected resist in the developer and part of the dissolved resist precipitates and forms the blob defects.[39,40] Formation of blob defects is also linked with the electrochemical property of the surface.

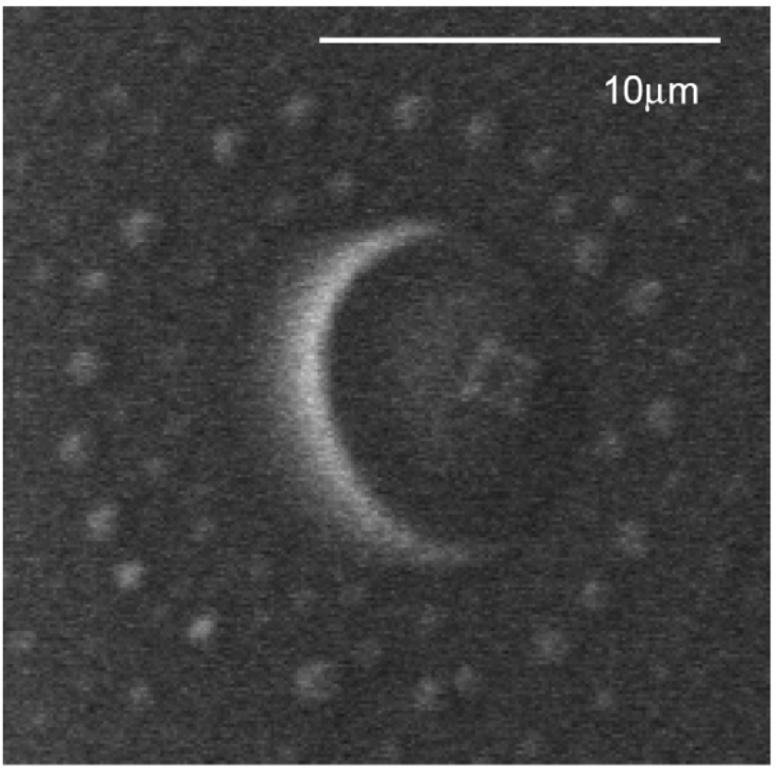

Figure 2.26 SEM image of a blob defect.

2.5.1 Reduction of blob defects by process optimization

The numbers of blob defects can be reduced by changing the dissolution rate of the deprotected polymers. If a resist polymer has a high dissolution rate in the developer, the amount of undissolved polymer suspended in the developer is small, which helps to reduce the numbers of observed blob defects. However, increasing the dissolution rate requires a change of resist formulations.

Incorporating multiple development cycles has been shown to be an effective method for reducing defect counts.[41] One cycle consists of a full development procedure: developer puddle, DI water rinse, and spin dry (Fig. 2.27). For a KrF resist, a 3x development cycle removes about half of the blob defects; 4x and 5x development reduces the defects to 0. For an ArF resist, a > 3x development circle reduces the defect counts to 0. The results also show that increasing the DI water rinse time or repeating DI water rinse and dry cycles helps reduce defect counts, but not as effectively as repeating the development cycle.

2.5.2 Surfactant rinse to reduce blob defects

Surfactant rinse is an effective approach for reducing blob defect counts. The surfactant adsorbs to the substrate and around the resist clusters. A repulsive force (zeta potential) forms between the substrate and the dispersed resist clusters, preventing deposition of the resist clusters on the substrate.[42] Further rinsing can easily remove the particles and clusters. A mechanism diagram is shown in Fig. 2.28. The surfactant can be added to the aqueous developer, forming surfactant developer; alternatively, the surfactant can be added to the DI water rinse.

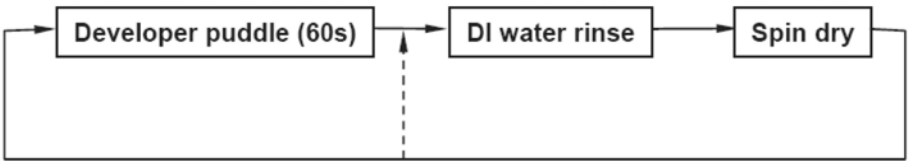

Figure 2.27 Flow of one cycle of development.

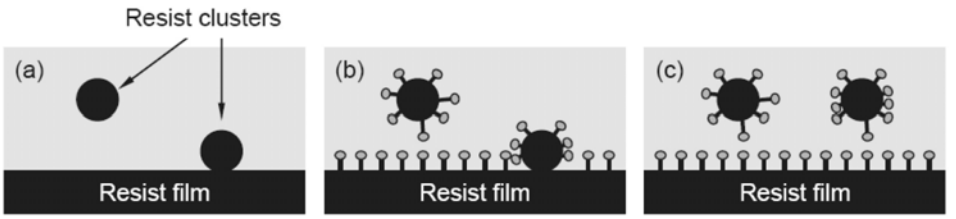

Figure 2.28 How surfactant prevents blob defect formation. (a) Low-solubility resist clusters in developer. (b) Surfactant molecules attach to the resist surface and surround the resist clusters. (c) The repulsive force prevents deposition of the resist clusters.

As described in previous sections, surfactant rinses have been introduced to reduce line collapse or blob defects. Apparently, it is impractical to implement two separate surfactant rinses, due to capital equipment, software costs, and reduced throughput. Therefore, bifunctional surfactant rinses have been developed that are capable of reducing both line collapse and defects.[36] These bifunctional surfactants help to meet two goals simultaneously, further justifying their use in standard IC processing. Furthermore, new types of surfactant rinses have been designed to reduce the line-edge roughness.

2.6 193-nm Immersion-Specific Track Process

In addition to the coating, baking, and development steps associated with resists and BARCs, 193-nm immersion lithography requires additional unique process steps:

1. Topcoat coating and baking,
2. DI water rinse before exposure (pre-rinse) to remove the leaching components,
3. DI water rinse after exposure (post-rinse) to reduce the watermark defects, and
4. Topcoat removal (only needed for solvent-soluble topcoat).

Figure 2.29 shows a diagram of a typical 193-nm dry lithography process flow. The immersion-specific process steps included in the right column require more modules in the track.

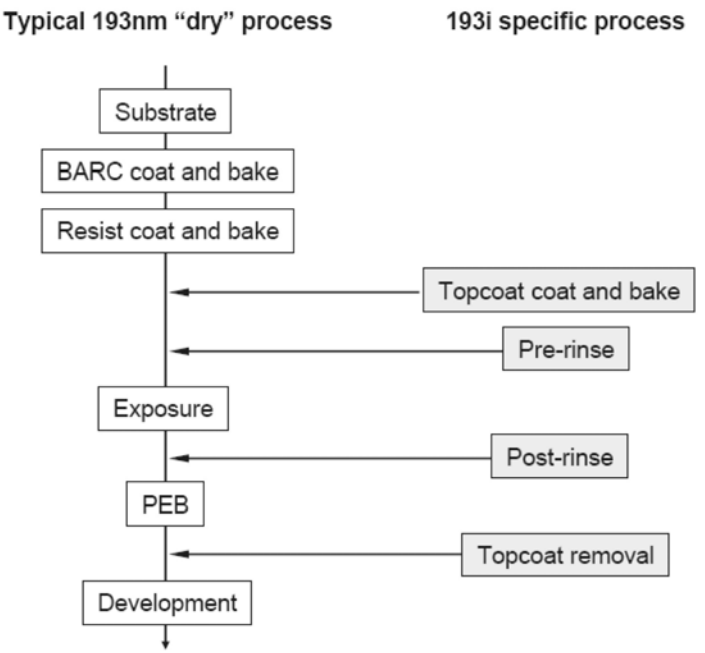

Figure 2.29 Typical 193-nm dry lithography process flow and 193i-specific process steps.

These additional process steps are not necessary for all 193i lithographic approaches; for example, resists specifically designed for 193i may not need topcoats. If a resist shows very good imaging but slightly unacceptable levels of leaching without topcoat, then the pre-rinse process can be used to flush away the leaching components before exposure. The leaching level of the pre-rinsed wafers is reduced to about 12% of the leaching level of nonrinsed wafers.[43] Developer-soluble topcoats do not require a separate step for removal; this step is integrated into the development step.

To maintain a stable process, track performance must be monitored regularly. The resulting data must be frequently reviewed to detect degradation in overall performance, as well as differences between tracks.[44] This performance monitoring is not unique to 193i; however, 193i lithography utilizes more complicated processes than do previous technologies, so upholding rigorous standards is even more critical. Quality degradation of each process step in the track can lead to 193i yield loss. Complete history data of track performances have been proven to be very helpful in identifying the root cause of 193i yield loss. Usually, track performance is monitored by using the baseline process. Every day, several wafers and a certain amount of tool time are dedicated to this work. Typically, the performance of each of the following six parameters is monitored.

2.6.1 Coating uniformity and stability

Wafers are coated with the baseline materials: BARC, resist, or topcoat. Film thicknesses across the wafer are measured because average film thickness and 3σ must be within the specifications. Advanced tracks have *in situ* film thickness measuring modules, enabling film thickness measurements without removing the wafer from the track.

2.6.2 Particle count after coating

The defect counts of the coated wafers also need to be measured. Wafers coated with each material—BARC, resist, or topcoat—must be measured separately. These results indicate how many defects are introduced by each coating process.

2.6.3 Across-wafer CD uniformity (CDU)

The baseline process wafer, using baseline materials (BARC/resist/topcoat) and baseline process conditions, is exposed at a fixed dose and focus across the wafer. CDs are measured at each die across the wafer. The average CD and 3σ must be within the specifications. If needed, dense lines, isolated lines, or contact holes can be exposed and measured.

2.6.4 PEB plate matching

Resist performance is very sensitive to PEB temperature, and for 193-nm resists, the PEB temperature sensitivity can be 1–5 nm/°C. Several hotplates in a track

can be used for the PEB process. To minimize CD deviation, these hotplates need to be matched. Two or more wafers are exposed and processed in exactly the same way, except that different PEB hotplates are used. CDs across the wafers are measured to determine average CD and 3σ. The differences reflect performance deviation between the hotplates.

2.6.5 Developer cup matching

To allow a certain flexibility in designing the process flow, a track typically has more than one develop module. These develop modules need to be monitored in order to ensure that they have the same performance. This performance check is called developer cup matching and is similar to the process for hotplate matching. Two or more wafers are exposed and processed in exactly the same way, except in different develop modules. CDs across the wafers are measured to determine the average CD and 3σ. The differences reflect performance deviation between the developer cups.

2.6.6 Batch trend evaluation

A batch trend evaluation is a procedure in which a batch of wafers (typically 25) is processed using the baseline process. The CDU (average CD and 3σ) across the wafers or defect counts are measured and plotted in order to determine the CDU or defect count variation as a function of wafer order. This evaluation helps determine process stability.

References

1. M. Cecchi, H. Smith, and D. Braun, "Method to optimize polymer film coating for polymer LED displays," *Synthetic Metals*, **121**, Issue 1–3, 1715–1716 (2001).
2. A. G. Emslie, F. T. Bonner, and L. G. Peck, "Flow of a viscous liquid on a rotating disk," *J. Appl. Phys.*, **29**, Issue 5, 858–862 (1958).
3. D. Meyerhofer, "Characteristics of resist films produced by spinning," *J. Appl. Phys.*, **49**, Issue 7, 3993–3997 (1978).
4. G. Standley , B. Kidd , and K. Hartman, "Advanced photoresist dispense valve control technology," *Proc. SPIE* **6153**, 61534O (2006).
5. X. Li, T. Lehmann, and W. Greene, "Stability of photo resist coating performance of small dispense nozzle size in photolithographic spin coating process," *Proc. SPIE* **6153**, 61533A (2006).
6. H. Nakagawa, K. Goto, M. Shima, J. Takahashi, T. Shimokawa, K. Ichino, N. Nagatani, H. Kyoda and K. Yoshihara, "Process optimization for developer soluble immersion topcoat material," *Proc. SPIE* **6519**, 651923 (2007).
7. T. W. Peterson, "VOC emissions reduction from lithographic process," Presentation from webpage http://www.erc.arizona.edu/.
8. http://www.coatings.rutgers.edu/.

9. H. Zhang, J. Andrews, X. Man, P. Antle, R. Buschjost, M. Ayubali, "Membrane compatibility for nanofiltration applications in DUV lithography," *Solid State Technology*, February, 2008.
10. D. E. Haas and D. P. Birnie III, "Real-time monitoring of striation development during spin-on-glass deposition," *Proc. of Am. Ceramic. Soc. Symposium on Sol-Gel Commercialization and Application*, May 2000.
11. J. A. Britten and I. M. Thomas, "Non-Newtonian flow effects during spin coating large-area optical coatings with colloidal suspensions," *J. Appl. Phys.*, **71**, Issue 2, 972–979 (1992).
12. I. Jekauc, M. Watt, T. Hornsmith, and J. Tiffany, "Necessity of chemical edge bead removal in modern day lithographic process," *Proc. SPIE* **5376**, 1255–1263 (2004).
13. J. E. Oberlander, E. S. Sison, C. Traynor, and J. Griffin, "Development of an edge bead remover (EBR) for thick films," *Proc. SPIE* **4345**, 475–483 (2001).
14. M. Randall, M. Linnane, C. Longstaff, K. Ueda, and T. Winter, "A universal process development methodology for complete removal of residues from 300-mm wafer edge bevel," *Proc. SPIE* **6153**, 61533C (2006).
15. G. Lee, H. Kim, E. Lee, M. Kim, S. Kim, C. Bok, H. Kim, S. Moon , and J. Kim, "The suppression method of powder formation in ArF photoresist," *Proc. SPIE* **6153**, 61533F (2006).
16. H. Shinya, T. Ishii, Y. Wakamoto, S. Sugimoto, and T. Kitano, "Evaluation of resist-film property by scan and spin coating," *Proc. SPIE* **5376**, 939–950 (2004).
17. S. Goto, A. Morita, K. Oyama, S. Hori, K. Matsuchika, and H. Taniguchi, "Post exposure bake unit equipped with wafer shape compensation technology," *Proc. SPIE* **6519**, 651937 (2007).
18. N. Ramanan, A. Kozman and J. B. Sims, "On the differences between wafer and bake plate temperature uniformity in proximity bake: a theoretical and experimental study," *Proc. SPIE* **3999**, 890–898 (2000).
19. A. Hisai, K. Kaneyama, and C. Pieczulewski, "Optimizing CD uniformity by total PEB cycle temperature control on track equipment," *Proc. SPIE* **4690** 754–760 (2002).
20. Y. Terashita, M. Shizukuishi, H. Shite, H. Kyoda, K. Oshima, and K. Yoshihara, "Critical dimension control in 90nm–65nm node," *Proc. SPIE* **5376**, 1264–1273 (2004).
21. S. Goto, K. Matsuchika, and A. Hisai, "The new bake plate optimized for a PEB process," *Proc. SPIE* **6153**, 61534N (2006).
22. C. E. Larson and G. M. Wallraff, "Combinatorial resist processing studies," *Proc. SPIE* **5376**, 1165–1173 (2004).
23. http://www.sensarray.com/public/products/products.html.
24. Y. Hiroi, T. Kishioka, R. Sakamoto, D. Maruyama, T. Ohashi, Y. Sakaida, H. Watanabe, Y. Nakajima, and S. Kimura, "BARC (bottom anti-reflective coating) for immersion process," Presentation at ISIL 2006, Kyoto, Japan, Oct. 2006.

25. T. Wallow, M. Plat, Z. Zhang, B. MacDonald, J. Bernard, J. Romero, B. La Fontaine, and H. J. Levinsona, "Characterization of photoacid redeposition in 193-nm photoresists," *Proc. SPIE* **6519**, 65190T (2007).
26. S.-F. Tsai, Y.-S. Chiu, C.-H. Chien, H.-Y. Gao, and C.-Y. Ku, "Effect of PEB exhaust on resist CD for DUV process," *Proc. SPIE* **5376**, 1157–1164 (2004).
27. H. Lee, J. Shin, H. Kim, S. Woo, H. Cho, and W. Han, "Evaluation of puddle time effect and optimization of development process in 193-nm lithography," *Proc. SPIE* **5376**, 1115–1122 (2004).
28. S. Ito and K. Hayasaki, "Monitor and control for development technology," J. *Vac. Sci. Technol.*, **B21**(6), 3177–3180, Nov./Dec. 2003.
29. N. L. Brakensieka, P. Zhang, D. King, and C. Ghelli, "Advanced rinse process alternatives for reduction of photolithography development cycle defects," *Proc. SPIE* **5753**, 241–251 (2005).
30. C. A. Mack, "Pattern collapse," *Microlithography World*, Nov. 2006, 16–17.
31. T. Tanaka et al., "Mechanism of resist pattern collapse during development process," *Jap. J. Appl. Phys*., **32**, Part 1, No. 12B, 6059–6064 (1993).
32. J. Simons, D. L. Goldfarb, M. Angelopoulos, S. Messick, W. M. Moreau, C. Robinson, J. J. de Pablo, and P. F. Nealey, "Image collapse issues in photoresist," *Proc. SPIE* **4345**, 19–29 (2001).
33. M. Sanada, O. Tamada, A. Ishikawa, and A. Kawai, "Analysis for collapse behavior of resist pattern in short develop time process using atomic force microscope," *Proc. SPIE* **5753**, 988–995 (2005).
34. S. Masuda, M. Kobayashi, W.-K. Kim, C. Anyadiegwu, M. Padmanaban, R. R. Dammel, K. Tanaka, and Y. Yamada, "Effect of the rinse solution to avoid 193-nm resist line-collapse: a study for modification of resist polymer and process conditions," *Proc. SPIE* **5376**, 819–829 (2004).
35. P. Zhang, M. Jaramillo, Jr., D. M. King, M. B. Rao, B. L. O'Brien, and B. F. Ross, "Surface conditioning solutions for pattern collapse reduction," *Proc. SPIE* **5376**, 807–812 (2004).
36. M. Sanada, M. Sugiyama, M. Jaramillo, Jr., P. Zhang, and S. Cassel, "Formulated surface conditioners to enhance the non-collapse window and maintain defect control: a bi-functional approach for sub-100-nm lithography," *Proc. SPIE* **6153**, 615331 (2006).
37. L. Ng and H. K. Lim, "Defect density control on 'satellite spots' or chemical stains for DUV resist process," *Proc. SPIE* **4690**, 679–689 (2002).
38. Y. Ono, T. Shimoaoki, R. Naito, and J. Kitano, "Behavior of chemically amplified resist defects in TMAH solution (3)," *Proc. SPIE* **5376**, 1206–1214 (2004).
39. S. Skordas, R. L. Burns, D. L. Goldfarb, S. D. Burns, M. Angelopoulos, C. J. Brodsky, M. C. Lawson, C. Pillette, J. J. Bright, R. L. Isaacson, M. E. Lagus, and V. Vishnu, "Rinse additives for defect suppression in 193nm and 248nm lithography," *Proc. SPIE* **5376**, 471–481 (2004).
40. G. Mirth, "Reduction of post-develop residue using optimal developer chemistry and develop/rinse processes," *Proc. SPIE* **2635**, 268–275 (1995).

41. M. Harumoto, A. Yamaguchi, and A. Hisai, “Mechanism of post develop stain defect and resist surface condition,” *Proc. SPIE* **6519**, 65193F (2007).
42. O. Miyahara, T. Shimoaoki, R. Naito, K. Yoshihara, and J. Kitano, “Defect reduction by using a new rinse solution for 193-nm conventional and immersion lithography,” *Proc. SPIE* **6153**, 61533K (2006).
43. R. R. Dammel, G. Pawlowski, A. Romano, F. M. Houlihan, “Resist component leaching in 193 immersion lithography,” *Proc. SPIE* **5753**, 95–101 (2005).
44. M. Deguchi, K. Tanaka, N. Nagatani, Y. Miyata, M. Yamashita, Y. Minami and Y. Matsuyama, “Critical dimension control for prevention of wafer to wafer and module to module difference,” *Proc. SPIE* **5376**, 1274–1281 (2004).

Chapter 3
Resist Leaching and Water Uptake

One unique aspect of 193i lithography is the use of water situated between the final lens element and the resist. The resist stack (with or without topcoat) on the wafer is dynamically exposed through this water with the step-and-scan process. The photoacid generator (PAG), quencher, and other small molecular components of the resist may leach into the water. These leached components contaminate the water and may degrade resist performance. The contaminated water can additionally contaminate the lens and wafer stage of the scanner. To master these leaching problems, we must understand the dynamics of resist leaching and the transportation of leached contaminates in the immersion water, as well as the impact of these contaminants on the lens during exposure.

Additionally, water can penetrate the topcoat and diffuse into the resist film, causing the topcoat or the resist to swell, which, in turn, affects their lithographic performance. This chapter specifically addresses the following issues: (1) leaching test methods, (2) leaching dynamics, (3) leaching with 193-nm exposure, (4) pre-rinse to partially remove leached contaminants, (5) lens contamination caused by resist leaching, and (6) water uptake in resist film.

3.1 Leaching Test Methods

A general approach to evaluating the leaching characteristics of a resist involves several steps. First, a puddle of DI water is formed on the surface of the resist stack. After a specific amount of time, the water in the puddle is sent for analysis. The leaching test measures the amount of resist components that have leached into the water over time. Various methods of immersing the resist film and extracting the water sample have been developed and reported;[1] however, the results have been inconsistent with variability as high as 2–3x. So far, no standard test method or specifications for leaching have been accepted by the entire 193i community. However, these are worthwhile goals and more reliable methods continue to be sought.[2]

3.1.1 Water extraction

Figure 3.1 shows a simple water extraction test method.[3] Although this method is not recommended, it gives a basic example of water extraction. A beaker with a wide opening (crystallizing dish) holds a specific volume of DI water (Fig. 3.1(a)). A silicon wafer coated with resist or resist stack is placed face down covering the beaker mouth (Fig. 3.1(b)). The beaker and the wafer are flipped over and the water covers the resist surface (Fig. 3.1(c)). The immersion area or resist leaching area is equal to the size of the beaker opening. After a specific amount of time, the beaker is flipped back to its normal position and the water is collected for analysis (Fig. 3.1(d)). To investigate the time dependence of leaching, a series of experiments can be conducted as a function of retention time.

Two recommended methods for this investigation are the water extraction and analysis (WEXA) technique described by IBM[4] and the dynamic leaching procedure (DLP) developed at IMEC.[5] Figure 3.2(a) shows a diagram of the bottom view of a Teflon lid in the WEXA design. In the test, the lid covers the resist surface and the evacuation hole is connected to a vacuum pump. The gap between the wafer and the lid is filled with water. Water flows along the rectangular channel, reaching the outlet. The contact time with water can be varied by adjusting the flow rate and the size of the channel. The water flowing out of the outlet hole is collected for analysis.

Figure 3.2(b) is a diagram of how the DLP works. A resist-coated wafer is loaded onto the wafer stage. A showerhead dispenses a specific volume of water across the resist surface. Then, the water in the showerhead is collected for analysis. The retention time of water contact can be varied by adjusting the speed.

3.1.2 Water sample analysis

Water samples can be analyzed for resist components using various chemical analytical methods that have different sensitivities toward certain components. The best analytical method must be chosen for each compound. For example, sulfonates of PAG can be detected separately by liquid chromatography mass

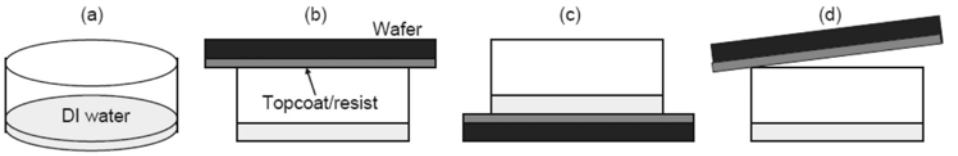

Figure 3.1 Simple method of extracting a water sample from the resist surface using a crystallizing dish.

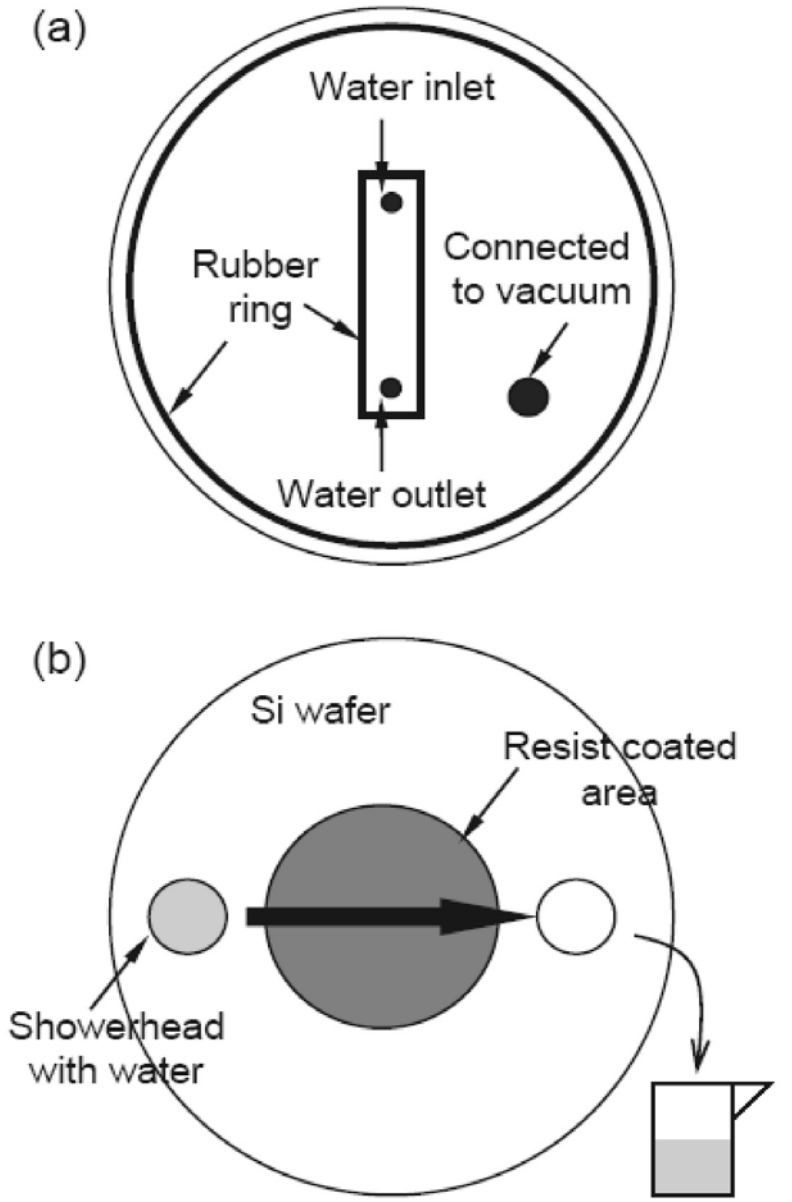

Figure 3.2 Diagrams of (a) WEXA cover design (bottom view) and (b) how DPL works.

spectroscopy (LC-MS) with a detection limit of 0.2 ng/mL or ppb. The dynamic leaching rate (ng/cm^2s) can be determined from quantitative measurements, contact area, and immersion time. SEMATECH experiments suggest that the PAGs are most likely to leach from the film and also impose the greatest danger to the lens.[6] Experimental results from resist vendors also support this suggestion.

3.2 Leaching Dynamics

3.2.1 Leaching dynamics described by the single-exponential model

The rate of leaching has been shown to be nonlinear. The resist components (primarily PAGs) leach faster at the onset of the contact with water. Radioactive labeling studies and early kinetics studies with limited time resolution have shown that leaching reaches a limiting value within a few seconds after water contact.[6] The concentration C of PAG in water versus the water contact time t can be approximately described by an exponential relation:

$$C = C_{\infty}(1-e^{-\beta t}), \tag{3.1}$$

where C_{∞} is the saturated PAG concentration and β is the time constant.[7] The leaching rate dC/dt changes with time. At initial time $t = 0$, the leaching rate has the maximum value—$dC/dt\,|_{t=0} = C_{\infty}\beta$, which is called the dynamic leaching rate. Both C_{∞} and $C_{\infty}\beta$ can be obtained from the C–t curve (Fig. 3.3).

3.2.2 Leaching dynamics described by the double-exponential model

Detailed measurements and data analysis suggest that the best fit of the leaching-rate data is obtained using two exponential functions. This is know as the double-exponential model:[5]

$$C = C_{\infty 1}(1-e^{-\beta_1 t}) + C_{\infty 2}(1-e^{-\beta_2 t})\,. \tag{3.2}$$

$C_{\infty 1} + C_{\infty 2}$ is the saturated concentration and β_1 and β_2 are the time constants. Figure 3.4 shows the leaching amount of anion from PAR-817 resist as a function of the water contact time. These results were measured via the DLP method at IMEC. Both the single-exponential model (Eq. (3.1)) and the double-exponential

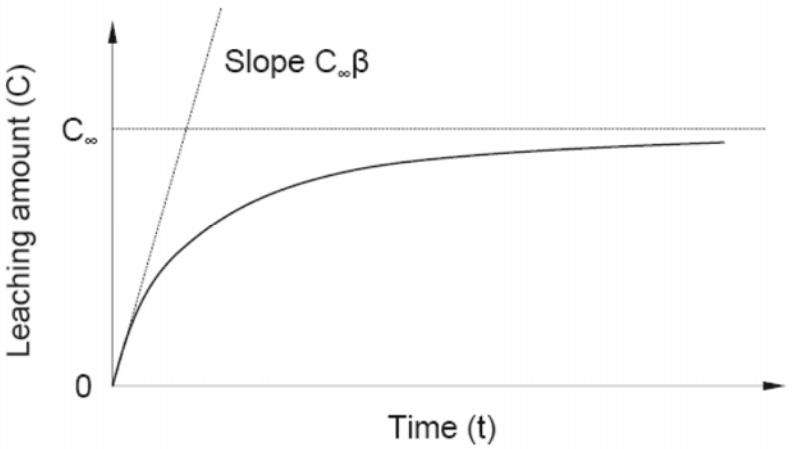

Figure 3.3 Dynamic model of PAG leaching.

model (Eq. (3.2)) were used to fit the measured data points shown in Figs. 3.4(a) and (b)). The correlation coefficients (R^2) show that the double-exponential model fits the original data better than the single-exponential model.

The double-exponential model suggests two processes, one fast and one slow, that could play a role in resist leaching. The fast leaching process occurs immediately after the water contacts the resist and reaches saturation within a few seconds, while the slow leaching process lasts much longer, up to 5–20 minutes. The fast process may be a result of PAG that has accumulated near the resist–air interface during spin-coating and baking. The slow process may be a result of PAG leaching from within the bulk of the resist.[8] This mechanism explains why some residual leaching can be observed even after long pre-soaks. Finite element modeling suggests that PAG initially located at the surface quickly diffuses into the water.[9] However, the diffusion coefficients of PAG in the bulk are much smaller than they are within the surface region. These results are consistent with the experimental observations that leaching is best described by two time constants (Eq. (3.2)). One corresponds to the leaching of PAGs from the surface, the other corresponds to the leaching of PAGs from the bulk.

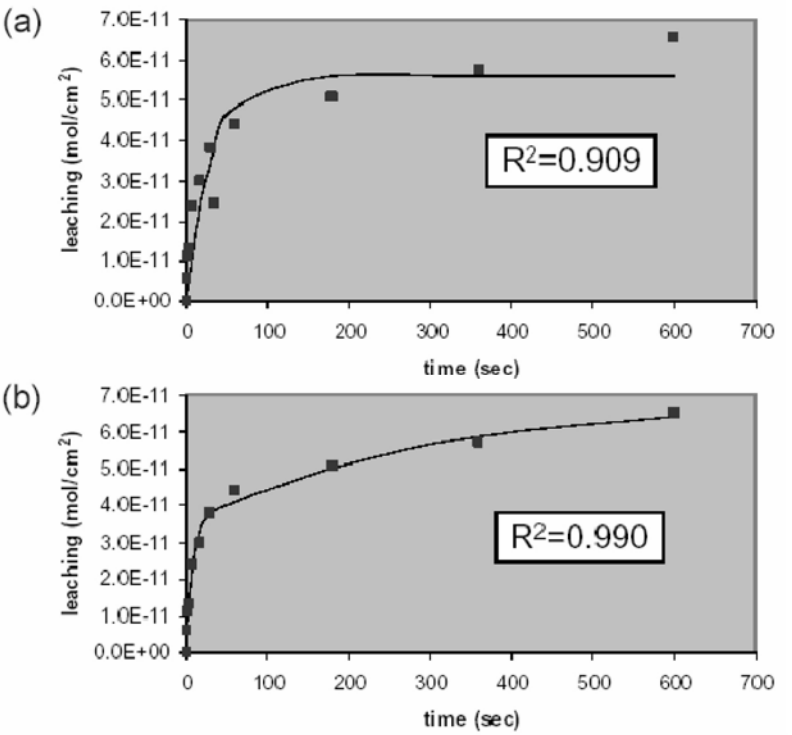

Figure 3.4 Leaching amount of anion from PAR-817 resist as a function of the water contact time (square dots in the graphs). The curve in (a) is the fitted results ($C_\infty = 5.6 \times 10^{-11}$mol/cm^2, $\beta = 0.033s^{-1}$) using the single-exponential model. The curve in (b) is the fitted results ($C_{\infty 1} = 3.5\times10^{-11}$mol/cm^2, $\beta_1 = 0.15s^{-1}$; $C_{\infty 2} = 3.4\times10^{-11}$mol/cm^2, $\beta_2 = 0.0035s^{-1}$) using the double-exponential model. (Reprinted by permission from Ref. 5.)

In a full-field 193-nm immersion scanner, the exposure head stays in one field for only a few seconds. Therefore, the fast leaching process is a particularly important factor in understanding lens contamination. The single-exponential model and dynamic leaching rate proposed in Eq. (3.1) are sufficient for studying leaching kinetics relevant to lens contamination. The slow leaching occurs in the time scale of 1–20 minutes and may play a role in the formation of watermark defects.

3.2.3 Leaching specifications recommended by scanner suppliers

The dynamic leaching rate is a measure of how quickly a resist component leaches from the film after it contacts water. In the manufacturing environment, this value is more important than the saturated leaching value, because the water, lens, and resist are in close proximity only for a short time before the water is flushed from the system. Immersion water flows continuously through the 193i scanners so that the leached components are flushed from the system. Therefore, the dynamic leaching rate is a better measure of the concentration of resist components in the water near the lens. Tolerances for dynamic leaching rate are a function of the exposure head design and the water flow rate.

Table 3.1 shows dynamic leaching rate specifications published by ASML, Canon, and Nikon. Nikon has designed an exposure head that allows the water to flow from the top (lens) to the bottom (resist surface).[10] Water is contaminated by the resist downstream from the lens, enabling Nikon to relax its early leaching specifications by a factor of 15. Hopefully, additional improvements in exposure head designs will enable additional relaxation of leaching specifications in the future.

3.2.4 Comparing saturation leaching results

Determining saturation leaching levels is much easier than determining dynamic leaching rates, since analytical measurements can be made offline to determine saturation values. Therefore, most 193-nm immersion researchers have in-house capabilities for measurement of saturation leaching levels of resist samples. However, the details of these techniques differ from site to site and the absolute values of saturated leaching generally differ. Nonetheless, correlations can be established. The leaching values of six resist samples were measured at two different locations. Figure 3.5 shows the results obtained at one location plotted

Table 3.1 Leaching rates suggested by scanner suppliers.[10,11]

	ASML	Canon	Nikon
PAG leaching	1.6×10^{-12} mol/cm^2/s	1.0×10^{-11} mol/cm^2/s	5×10^{-12} mol/cm^2/s
Amine leaching	-	-	2×10^{-12} mol/cm^2/s

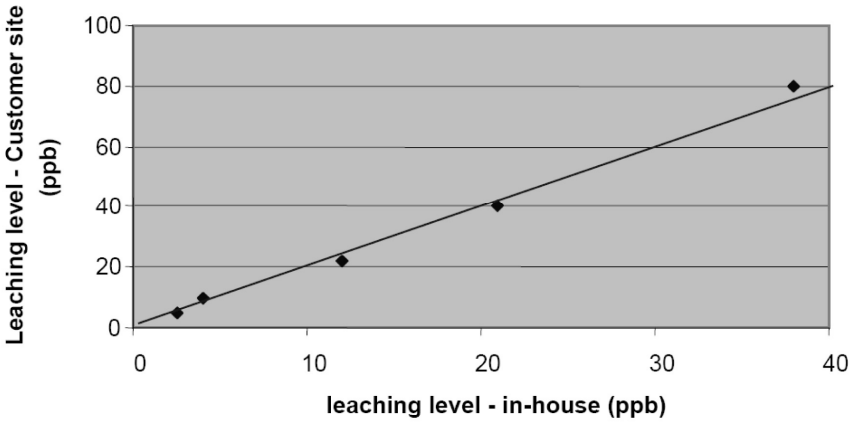

Figure 3.5 Leaching test results comparison between different sites for the same samples.

against results obtained at the other location. The absolute values of the results tested in one location differ from those tested at the other location, but a linear correlation exists between the two sets of results. For the same resist sample, the PAG leaching level measured at one site is about 2x that of the other. These results show that it is possible to calibrate the leaching results between sites.

3.3 Leaching with 193-nm Exposure

The leaching tests discussed so far in this chapter were done without exposure. With exposure to 193-nm light, it is reasonable to expect that leaching levels increase. Unfortunately, to collect water samples directly after exposure is not easy and requires a special setup (Fig. 3.6). A small volume of DI water is dispensed and confined on the resist surface, forming a puddle. The apparatus controls the exposure area and exposes the resist through the water.

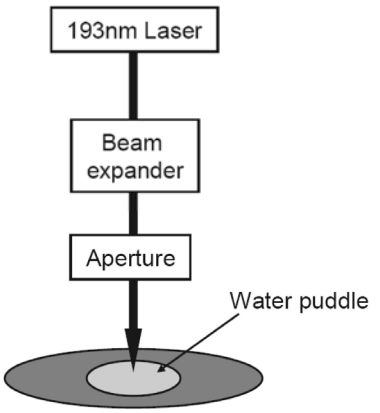

Figure 3.6 Exposure system for leaching water collection.

In one study, a variety of resists or resist/topcoat stacks were exposed with different doses and evaluated for leaching. After exposure, water samples were collected and analyzed (Fig. 3.7). The PAG components of C1 and C4 were traced. Topcoat TC1 is such an effective leaching barrier that no leaching was detected, even at the exposure doses as high as $3E_0$. The leaching was higher without topcoat. With increased doses from 0 to $3E_0$, all of the data, except for resist1/TC1 stack, showed more C1 and C4 leached into water. However, the increased value is less than 15%.

The results in Fig. 3.7 suggest that with exposure, leaching is about 15% higher than it is without exposure. Surprisingly, exposure to 193-nm light does not dramatically increase leaching. Similar results were reported for leaching levels of three resist stacks.[12] Exposure increased leaching levels by only 25–100% over unexposed samples. For this reason, scanner suppliers have agreed to allow unexposed leaching tests as sufficient criteria for judging which samples can be exposed on scanners.[2]

3.4 Pre-Rinse to Partially Remove Leached Contaminants

The development of 193i resists is still in progress. The requirements of both low leaching and high resolution make resist development very difficult. For example, low activation energy resists are baked at low PEB temperatures and generally have smaller acid diffusion lengths, improving resolution, but tending to result in higher leaching levels.

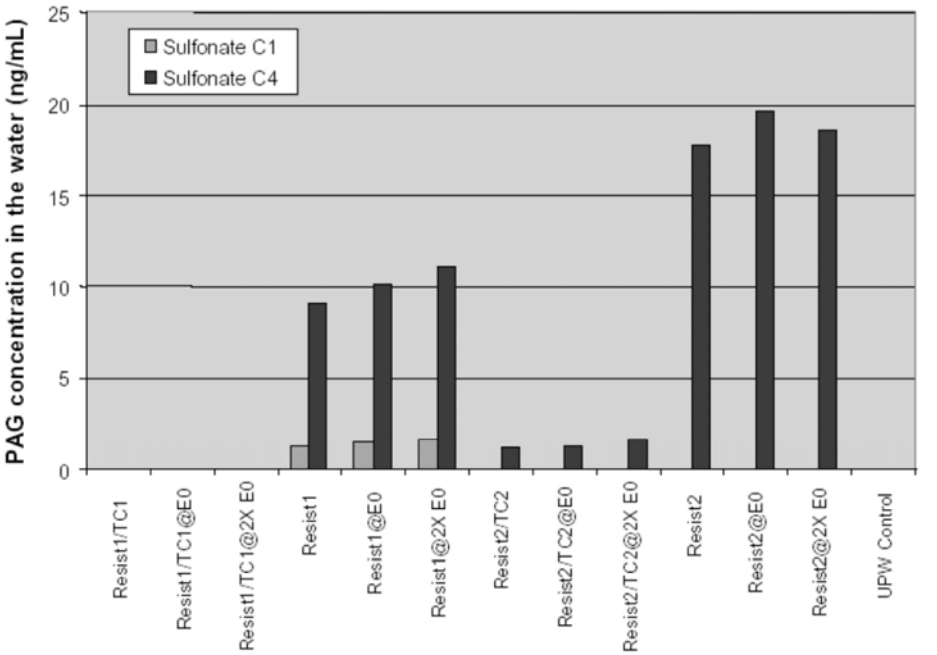

Figure 3.7 Leaching tests of resist samples with and without topcoat under different exposure doses (detection limit ~0.2 ng/mL). Sulfonate C1 is FC-122 and sulfonate C4 is PFBS.

Because some experimental resists exceed leaching thresholds, topcoats can be used to protect resists from leaching. Rinsing of the resist film by DI water before exposure has also been investigated as an alternative method to address this issue. DI-water rinses can wash away significant amounts of the leaching components. Leaching levels of pre-rinsed wafers can be reduced to ~12% of that of nonrinsed wafers. Similarly, the leaching time constant β can be decreased by a factor of about two.[7] Before the availability of low-leaching and high-performance 193i resists, "high leaching" 193-nm resists in combination with DI water pre-rinses were used. Figure 3.8 shows a typical process flow.

One major concern is the extent to which pre-rinse steps change resist sensitivity. To evaluate this, open frame exposures with a dose meander were carried out on wafers with different pre-rinse times of 0, 10, and 30 seconds. The maximum pre-rinse time of 30 seconds was selected, based on the assumption that leaching occurs within the first 30 seconds of water contact.[13] After development, the thickness of the remaining resist was measured as a function of dose. The resist thickness versus dose curves (contrast curves) shows no significant changes as a result of pre-rinse (Fig. 3.9). Similar results were obtained for a dry resist sample, which had a leaching level of ~24 ppb.

It is surprising that these contrast curves did not change with rinsing prior to exposure, since PAGs leach out of the film as soon as it contacts the water. We suspect that the flow of water through the exposure head provides the answer. The water is confined between the lens and the wafer. The water flow continues through the exposure head both during the exposure and between exposures. When the exposure head moves to the next die, before the exposure starts, the die is flushed by the water, providing an "intrinsic flush" prior to exposure.

According to simulation results,[14] this intrinsic flush occurs in about 1–2 seconds. Apparently, the intrinsic flush removes sufficient amounts of PAG from the resist prior to exposure so that the pre-rinse has no effect.

3.5 Lens Contamination Caused by Resist Leaching

Contamination of immersion water by the resist will, in turn, contaminate the lens. During exposure to 193-nm light, components in the water may absorb photons and decompose into other chemical species. These chemical compounds

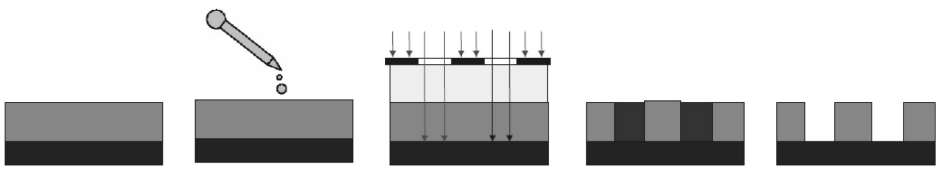

Figure 3.8 Process flow with pre-rinse.

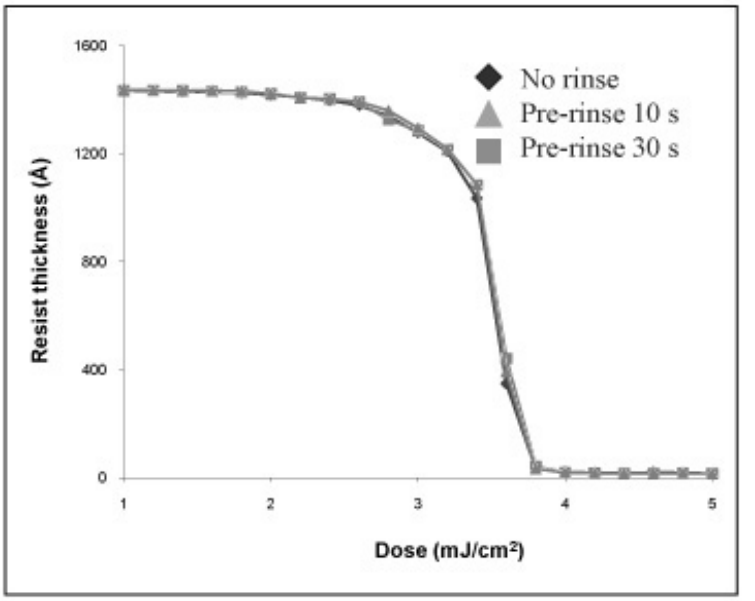

Figure 3.9 Contrast curves of a 193i resist with different pre-rinse times. The resist sample has a leaching of ~12 ppb.

may have limited solubility in water and form deposits on the lens surface. Quantitative analysis of the leach-induced lens contamination is important to the design of immersion heads and for establishment of leaching specifications. Optimization of immersion head design should minimize contact between leaching components and lens, ultimately allowing for more relaxed leaching specifications for the resists.

3.5.1 Simulation results

In a simplified immersion system (Fig. 3.10(a)), water fills the gap between the lens and a wafer moving at a scan speed of ~500 mm/s. A theoretic model from the University of Wisconsin was used to predict the concentration distribution of contaminants throughout the gap region.[15] The geometry of the gap is defined by its length (L = 4 cm) and height (h = 1 mm) (Fig. 3.10(a)).

Due to the concentration gradient and bulk fluid motion, the motion of contaminant species can be defined by the following flow equation (under the assumption of inertia-free and parallel flow):

$$\rho \frac{\partial u}{\partial t} = \mu \frac{\partial^2 u}{\partial y^2}, \tag{3.3}$$

where u is the velocity of water, ρ is the density of water, and μ is the viscosity of water. The boundary conditions for Eq. (3.3) are $u(y = 0, t)$ = scan speed (500

mm/s) and $u(y = h, t) = 0$. Thus, the equation for contaminant transportation is defined as

$$\rho u \frac{\partial C}{\partial x} = \rho D \frac{\partial^2 C}{\partial y^2}, \tag{3.4}$$

where C is the local concentration of the contaminant species and D is the diffusion coefficient of the contaminant species in the water. The boundary conditions for Eq. (3.4) are $C(x, y = h, t) = 0$ and $C(x, y = 0, t) = \text{constant}$ (corresponding to the leaching value). The concentration distribution in the gap can be calculated by Eqs. (3.3) and (3.4). Figure 3.10(b) shows the concentration of the leached component from 0 to 12 seconds after the initiation of the scan. The model predicts that the contaminant will reach the lens in about 10 seconds.

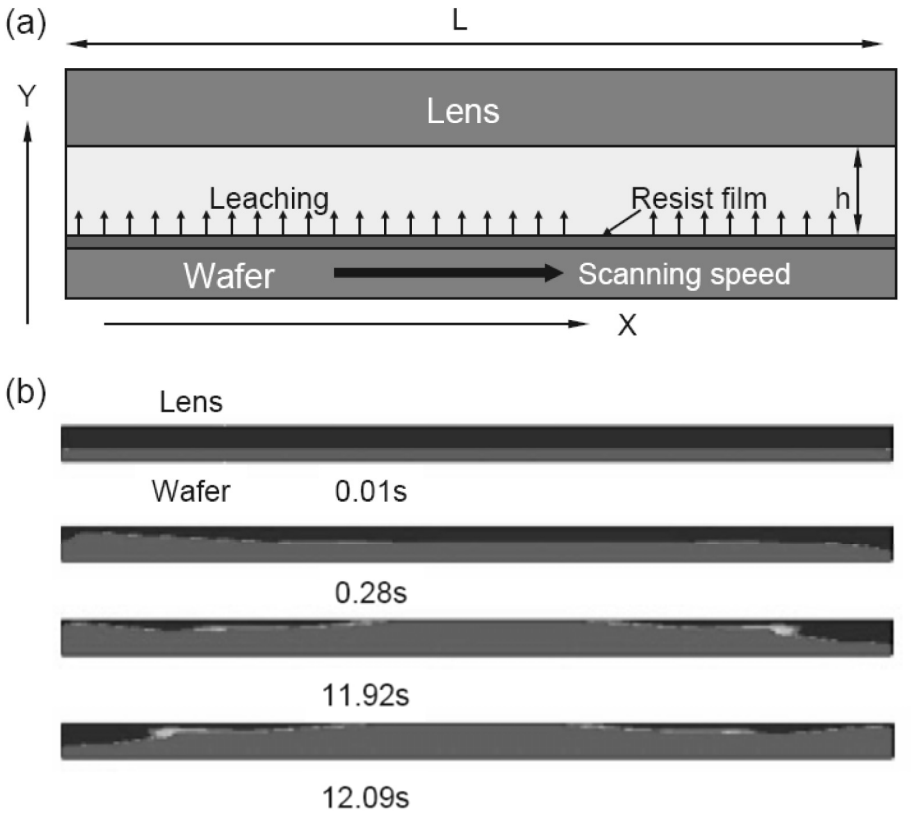

Figure 3.10 (a) Contamination transport model for 193-nm immersion lithography. (b) Concentration distribution at various times relative to the initiation of the scanning process (assuming the resist component is released (leaching) at 10 ng/cm^2 and its diffusion coefficient in water is 10^{-9} m^2/s). (Reprinted by permission from Ref. 15.)

In reality, full-field immersion scanners have much more complicated immersion head designs than were described in the simplified model. In scanners, the injection and extraction of immersion water will most likely disturb the parallel flow described by the simplified model. Nonetheless, the qualitative conclusion that the chemicals leached from the resist will arrive at the lens within the timeframe of the exposure is relevant to the design of full-field scanners.

3.5.2 Controlled immersion contamination

Irradiated by 193-nm photons, the chemical components in the water may decompose into water-insoluble species and deposit onto the lens surface, resulting in transmission degradation of the lens. Controlled-contamination experiments were designed to study lens contamination during exposure.[16–19] Figure 3.11 shows a diagram of the experimental setup. PAG as a contaminant is injected into ultrapure water (UPW) (18 MΩ-cm). This contaminated water flows through a cell with two windows. The windows are made from the 193-nm lens materials (fused silica or CaF_2) with protective coatings. 193-nm light illuminates the water through the windows (Fig. 3.11). To accelerate the contamination process, the exposure dose is very high and the contaminant concentration is increased. After exposure, the transmission of the window is measured and the transmission loss is obtained.

Figure 3.12 shows the results reported by a group at the Massachusetts Institute of Technology (MIT).[19] In their experiment, the immersion cell has two 3-mm thick windows separated by a 2-mm gap. PAG (TPS-PFBS), which has a solubility of 2300 ppm in water, was tested. A syringe pump was used to inject PAG into the water upstream of the test cell, generating concentration levels of 3–3000 ppb. No deposition was observed without laser light, as the contamination precursor (PAG) is soluble in water. However, deposition of the contaminants did occur with exposure, but primarily *upstream* of the location of the 193-nm exposure area.

The authors offered the following explanation of the result.[19] The laser light initiates two opposing reactions: forward (contamination) and reverse (cleaning). During the forward reaction, the PAG undergoes photodecomposition, creating insoluble photoproducts. At the time of formation, these photoproducts diffuse to the surface of the windows, forming deposits. During the reverse reaction, the water photolyzes to form hydrogen peroxide (H_2O_2). H_2O_2 can then react

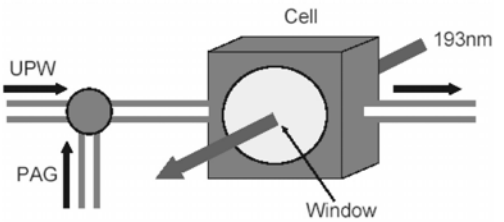

Figure 3.11 Setup of the controlled contamination experiment with 193-nm exposure.

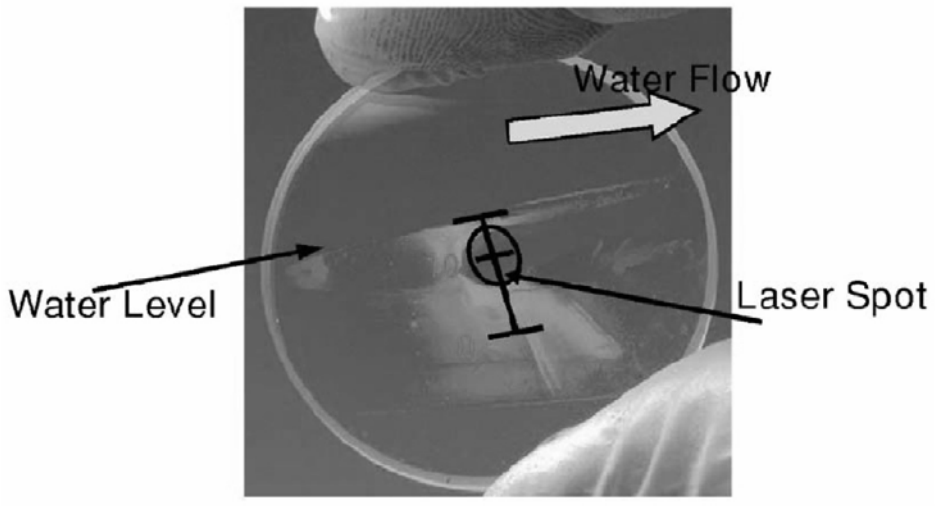

Figure 3.12 Contamination pattern formed after 193-nm exposure of 100 ppm of TPS-PFBS in water. (Reprinted by permission from Ref. 19.)

thermally or photochemically with the insoluble deposits to generate water-soluble products. In the directly exposed area, the dose is high, creating high concentrations of H_2O_2. The H_2O_2 generated at the exposed area not only cleans the local contamination, but also flows downstream, cleaning the downstream areas. No difference was found between contamination of fused silica and coated CaF_2 optics at the same exposure conditions.

Similar results were obtained by another group[18,20] that also observed the deposition of contaminants occurring primarily *around* the exposed areas, but not in the areas of highest exposure. Additionally, they found that contamination builds up at the immersion nozzle, resulting in increased pressure and decreased flow rate.

3.5.3 *In situ* cleaning of the immersion system

In situ cleaning is a process in which a cleaning solvent is injected into the immersion water so that it flows through the immersion system. The concept here is the same as the concept in the controlled-contamination experiment in Fig. 3.11. The cleaning solvent removes deposits and cleans the immersion water handling system. Depending on the purpose, various cleaning solvents can be used. For example, introducing CO_2 gas into the immersion water flow can kill bacteria growing in the system. This type of cleaning is preferred from the customer's point of view, because the contaminated system can be cleaned without disassembling the exposure head and the water handling system, reducing downtime.

Figure 3.13 shows the results of one cleaning study using an apparatus similar to the one shown in Fig. 3.11.[18,20] The apparatus is filled with PAG-contaminated water and exposed across an area of 2×5 mm^2. Transmittance is measured across an area of 5×10 mm^2. The leaching components deposited on the lens are cleaned with a special lens-friendly cleaning fluid that is water soluble and has a neutral pH. Figure 3.13(b) shows the transmittance values measured before exposure, after exposure, and after *in situ* cleaning. Before exposure, the window has an average transmittance of ~83%; however, after exposure the transmittance is reduced. The transmittance loss is related to the exposure dose and contaminant concentration. For the dose of 2.7 million pulses and a contaminant level of 10 ppm, a transmittance loss of 28% is observed. After exposure, the lens is flushed with the cleaning fluid for 10 minutes and most of the transmittance is recovered. For a dose of 4 million pulses and a contaminant level of 2 ppm, the transmittance loss from the light-contaminated lens is totally recovered after cleaning. Further spectral analysis indicates that the transmittance spectrum is completely recovered (Fig. 3.13(c)). In the case of a more heavily contaminated lens, transmission loss cannot be completely recovered after the cleaning. These results show the importance of cleaning before too much contamination is deposited.

In situ cleaning can also remove deposits in water injection and extraction nozzles. Experiments have shown that water pressure, which increases with contamination, can be restored with *in situ* cleaning.[20]

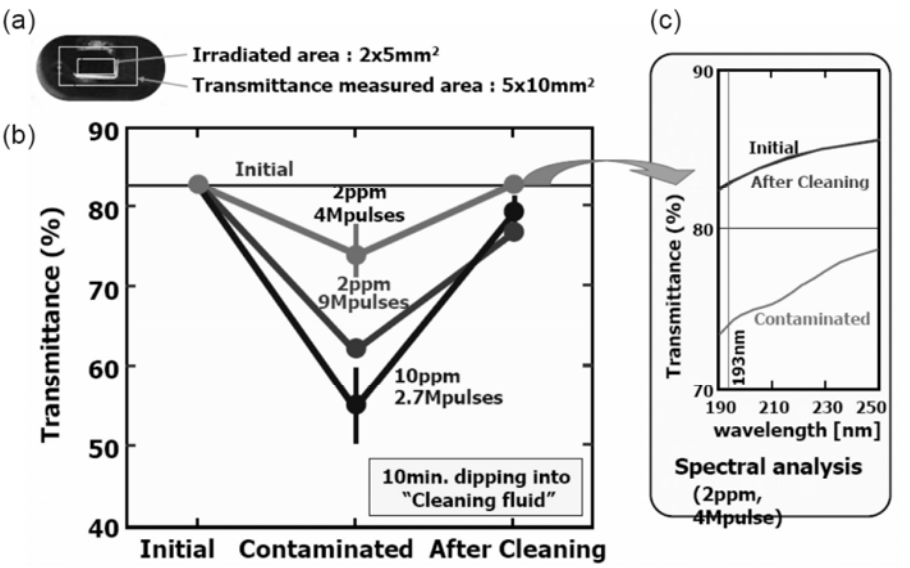

Figure 3.13 Lens contamination and cleaning experiment. (a) Exposure area and transmittance measured area. (b) Transmittance values measured before exposure, after exposure, and after cleaning. Within the figure, the exposure dose and contaminant level are labeled. (c) Transmittance spectra of the window before exposure, after exposure with 2 million pulses and 2 ppm contaminant level, and after cleaning. (Reprinted by permission from Ref. 18.)

3.6 Water Uptake in Resist Film

In addition to the leaching of resist components into water, water can also diffuse into resist films, changing their reactivity. This water diffusion may occur even through a topcoat layer, as water may easily penetrate the topcoat layer and reach the resist film. This phenomenon can be explained by diffusion theory.

3.6.1 Diffusion theory

Assuming that the diffusion of water in the resist film follows Fick's law, the diffusion behavior and water uptake can be modeled using the following equation:

$$\frac{M_t}{M_\infty} = 1 - \frac{8}{\pi^2}\sum_{n=0}^{\infty}\frac{i}{(2n+1)^2}\exp\left[-\frac{(2n+1)^2\pi^2 Dt}{L^2}\right], \tag{3.5}$$

where M_t is the mass uptake at time t, M_∞ is the ultimate mass uptake at time $t = \infty$, D is the water diffusion coefficient, and L is the film thickness.[21,22] At the initial phases of the diffusion process (for approximately $M_t/M_\infty < 0.6$), Eq. (3.5) can be simplified to a linear relationship versus the square root of time:

$$\frac{M_t}{M_\infty} = \frac{2}{L}\left(\frac{Dt}{\pi}\right)^{1/2}. \tag{3.6}$$

3.6.2 Quartz crystal microbalance to measure water uptake

Water uptake by resist films can be experimentally measured using quartz crystal microbalances (QCMs). QCMs are piezoelectric transducers widely used in electrochemistry (Fig. 3.14(a)). Resonant frequency varies linearly with the mass of the device. The QCM converts from a change in mass (Δm) to a change in resonant frequency (ΔF), which is an easily measured signal,

$$\Delta F = -k\,\Delta m, \tag{3.7}$$

where k is a coefficient and is dependent on the crystal and the circuit. This method is very useful because of its high mass sensitivity and can be used in real time to make *in situ* measurements. A frequency shift of 1 Hz corresponds to a mass change of 1 ng.

Figure 3.14(b) shows the heart of a QCM instrument, which is a thin quartz crystal with a gold pad on each side. The gold pads form a pair of electrodes for electric measurements. The surface of the gold pad is flat and suitable for resist coating. The diameter of the crystal is in the range of several centimeters. The resist stack is spin coated on the front surface of the crystal, covering the gold pad. Following post-apply bake (PAB), the resist-coated crystal is loaded into the QCM. The device can be soaked in a water bath and its resonant frequency is measured over time.

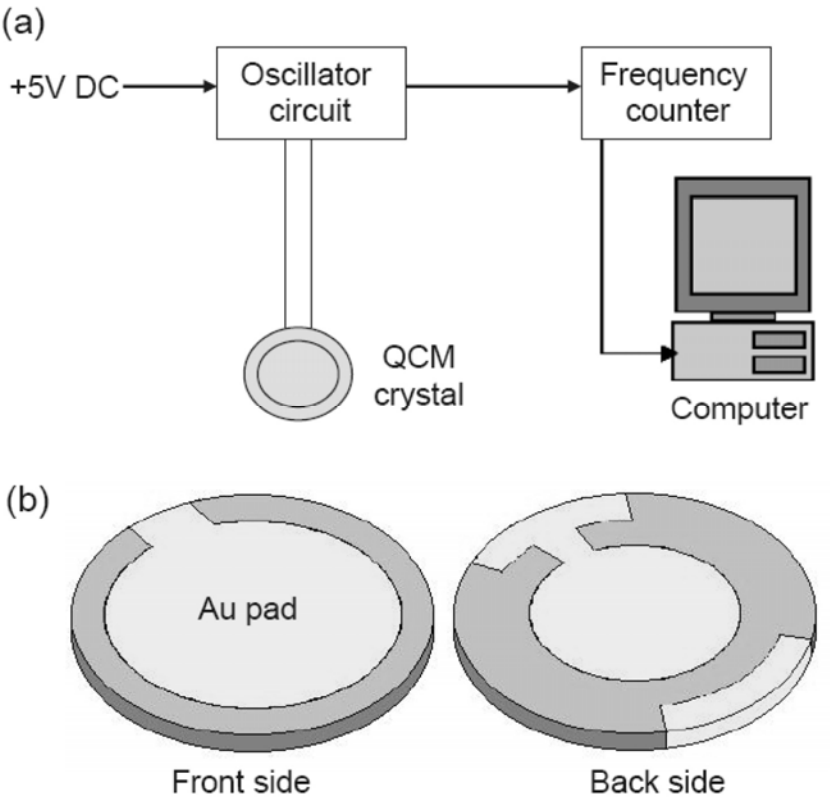

Figure 3.14 (a) Diagram of the quartz crystal microbalance (QCM). (b) Quartz crystal with gold pads.

Experimental results demonstrate that the diffusion of water into photoresist films is a very rapid process, with most of the water uptake occurring within the first few seconds of exposure to water. The water uptake and absorption in resists is dependent on a variety of factors, including polymer molecular weight and the nature of the polymer substitute groups.[23] At the beginning stage of water contact, the water diffusion follows Fick's law and is effectively described by Eq. (3.6). Water uptake is very sensitive to temperature. Figure 3.15 shows the resonant frequency of the resist-coated QCM device soaked in water at different temperatures.[24]

The study in Ref. 24 demonstrated that an increase in water temperature from 23 to 40° C leads to a ~20-fold increase in water uptake. This result indicates that the water diffusion coefficient D in the resist increases with temperature increase. Additional experiments demonstrate that diffusion coefficients decrease with increasing PAB temperature and contact time t with water. Resist films treated by DI-water rinse have smaller diffusion coefficients. Thus, water diffuses more readily into hydrophilic resists than into hydrophobic resists and also diffuses

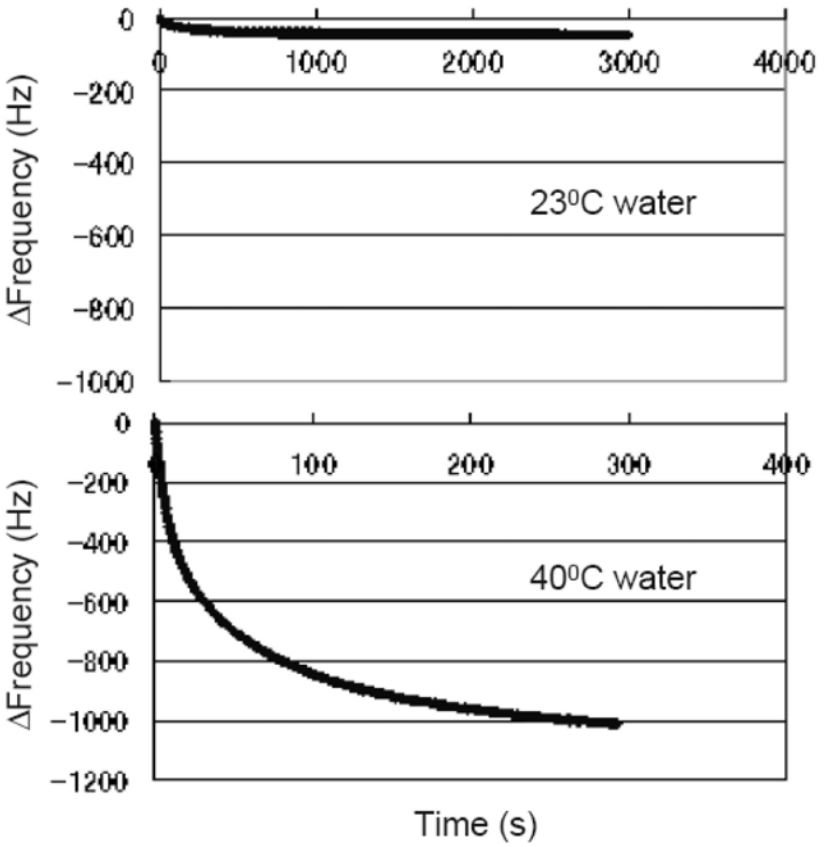

Figure 3.15 Resonant frequency of the resist-coated QCM device soaked in water at different temperatures. (Reprinted by permission from Ref. 24.)

more readily into resist films containing high molecular weight polymers than into resist films containing low molecular weight polymers. Similarly, water diffusion coefficients are larger in develop-soluble topcoats than they are in solvent-soluble topcoats.[25] Additionally, solvent remaining in resist films plays an important role in the extent of water penetration.[26]

Water diffuses into resist films, making them thicker; however, it does not change the roughness of the resist films. During PEB, water evaporates out of the resist. This process changes the resist surface roughness and resist-patterned LER. The roughness is proportional to the amount of water that diffused in the resist, i.e., $\sim M_t \sim t^{1/2}$. Therefore, it is possible to estimate how much water has diffused into the resist film by measuring the resist surface roughness.[27]

In addition to using the QCM, water uptake can also be measured by ellipsometry.[23] Resist film thickness measured by ellipsometry can be compared under wet and dry conditions. The difference corresponds to the amount of water uptake. Additionally, AFM (atomic force microscopy) can be used to measure variations in surface roughness in the resist caused by water uptake.

References

1. See for example, presentations at the Leaching Measurement Workshop of International Symposium on Immersion Lithography, Kyoto, Japan, Oct. 2006.
2. R. Gronheid, C. Baerts, S. Caporale, J. Alexander, B. Rathsack, S. Scheer, K. Ohmori, and B. Rice, *World-wide Standardization Effort on Leaching Measurement Methodology*, 4th International Immersion Symposium, Keystone, Colorado, Oct. 8–11, 2007.
3. T. Miyamatsu, Y. Wang, M. Shima, S. Kusumoto, T. Chiba, H. Nakagawa, K. Hieda, and T. Shimokawa, "Material design for immersion lithography with high refractive index fluid (HIF)," *Proc. SPIE* **5753**, 10–19 (2005).
4. W. Hinsberg, G. Wallraff, C. Larson, B. Davis, V. Deline, S. Raoux, D. Miller, F. Houle, J. Hoffnagle, M. Sanchez, C. Rettner, L. Sundberg, D. Medeiros, R. Dammel, W. Conley, "Liquid immersion lithography: evaluation of resist issues," *Proc. SPIE* **5376**, 21–33 (2004).
5. R. Gronheid, "Towards standardization of the leaching measurement methodology," Presentation at the Leaching Measurement Workshop of International Symposium on Immersion Lithography, Kyoto, Japan, Oct. 2006.
6. W. Conley, R. J. LeSuer, F. F. Fan, A. J. Bard, C. Taylor, P. Tsiartas, G. Willson, A. Romano, and R. Dammel, "Understanding the photoresist surface-liquid interface for ArF immersion lithography," *Proc. SPIE* **5753**, 64–76 (2005).
7. R. R. Dammel, G. Pawlowski, A. Romano, and F. M. Hoilihan, "Resist component leaching in 193 immersion lithography," *Proc. SPIE* **5753**, 95–101 (2005).
8. M. Ercken, N. Stepanenko, R. Gronheid, P. Foubert, M. Kocsis, C. Delvaux, N. Vandenbroeck, J. De Backer, and I. Pollentier, "Current status of immersion dedicated resists: Are they ready?" Interface 2006, San Diego.
9. B. M. Rathsack, S. Scheer, Y. Kuwahara, J. Kitano, R. Gronheid, and C. Baerts, "Finite element modeling of PAG leaching and water uptake in immersion lithography resist materials," *Proc. SPIE* **6923**, 692315 (2008).
10. H. Kohno, H. Nagasaka, H. Akiyama, K. Nakano, S. Watanabe, and S. Owa, Presentation at International Symposium on Immersion Lithography, Brugge, Belgium, Sept. 2005.
11. B. Streefkerk, C. Wagner, R. Moerman, J. Mulkens, I. Bouchoms, F. Van de Mast, P. Vanoppen, F. De Jong, T. Modderman, and B. Kneer, Presentation at International Symposium on Immersion Lithography, Brugge, Belgium, Sept. 14, 2005.
12. E. Tenaglia, D. De Simone, P. Canestrati, G. Cotti, "ArF photo-resist benchmarking when using immersion tool for dense trenches pattern," San Diego, *Interface 2006.*

13. Y. Wei, N. Stepanenko, A. Laessig, L. Voelkel, and M. Sebald, "Evaluation of 193-nm immersion resist without topcoat," *Proc. SPIE* **6153**, 615305 (2006).
14. I. Pollentier, M. Ercken, P. Foubert, and S. Y. Cheng, "Resist profile control in immersion lithography using scatterometry measurements," *Proc. SPIE* **5754**, 129–140 (2005).
15. G. F. Nellis, M. S. El-Morsi, C. Van Peski, and A. Grenville, "Contamination transport in immersion lithography," *J. Microlith., Microfab., Microsyst.*, **5**(1), 013007, (2006).
16. V. Liberman, S. T. Palmacci, D. E. Hardy, M. Rothschild, and A. Grenville, "Controlled contamination studies in 193-nm immersion Lithography," *Proc. SPIE* **5754**, 148–153 (2005).
17. S. Owa, H. Nagasaka, Y. Ishii, and S. Hirukawa, "Full-field exposure tools for immersion lithography," *Proc. SPIE* **5754**, 655–668 (2005).
18. M. Kobayashi, H. Nakano, M. Arakawa, T. Chibana, Y. Matsuoka,Y. Kawasaki, and M. Tanabe, "Future and present aspects of a 193-nm immersion scanner," Presentation at 193nm Immersion Symposium, Kyoto, Japan, Oct. 2006.
19. V. Liberman, M. Rothschild, S. T. Palmacci, and A. Grenville, "Impact of photoacid generator leaching on optics photocontamination in 193-nm immersion lithography,**"** *J. Microlith., Microfab., Microsyst.*, **6**(1), 013001 (2007).
20. M. Kobayashi, H. Nakano, M. Arakawa, M. Tanabe, K. Toyoda, T. Chibana, Y. Matsuoka, and Y. Kawasaki, "Contamination and particle control system in immersion exposure tool," *Proc. SPIE* **6520**, 652014 (2007).
21. C. M. Berger and C. L. Henderson, "The effect of humidity on water sorption in photoresist polymer thin films," *Polymer*, **44**, 2101–2108 (2003).
22. T. Hoskins, P. J. Roman, P. J. Ludovice, and C. L. Henderson, "Equilibrium water uptake and diffusion behavior in model polynorbornene photoresist polymers," *Proc. SPIE* **5753**, 851–861 (2005).
23. M. Carcasi, S. Hatakeyama, K. Nafus, R. Moerman, Y. van Dommelen, P. Huisman, J. Hooge, S. Scheer, and P. Foubert, "Defectivity reduction by optimization of 193-nm immersion lithography using an interfaced exposure-track system," *Proc. SPIE* **6153**, 61533J (2006).
24. S. Kanna, H. Inabe , K. Yamamoto, S. Tarutani , H. Kanda , W. Kenji, K. Kodama, and K. Shitabatake, "Non-topcoat resist design for immersion defectivity reduction," Presentation at Immersion Symposium, Kyoto, Japan, Oct. 2006.
25. M. Toriumi, C. Matsubara, A. Otoguro, and T. Itani, "Diffusion mechanism of water for immersion lithography," *Proc. SPIE* **6153**, 615311 (2006).
26. T. Niwa, S. Scheer, M. Carcasi, M. Enomoto, T. Tomita, K. Hontake, H. Kyoda, and J. Kitano, "Behavior and effects of water penetration in 193-nm immersion lithography process materials," *Proc. SPIE* **6519**, 651922 (2007).

27. S. I. Ahn, J. H. Kim, and W. C. Zin, “The effect of water contact and evaporation on the roughness of photoresist for immersion lithography,” *Proc. SPIE* **6153**, 615326 (2006).

Chapter 4
Contact Angle of Water on Resist Stacks

In a 193-nm immersion scanner, the water is confined to the gap between the front lens and the wafer, forming a water meniscus. This water meniscus stays with the exposure head as the wafer moves at peak speeds of ~500 mm/s (Fig. 4.1). The movement of the wafer applies a frictional force to the bottom of the water meniscus. This force changes the shape of the water meniscus, forming an advancing side and a receding side. To maintain a clean process, the water meniscus must keep its shape and move easily on the wafer surface without leaking water and leaving water droplets behind. Therefore, a hydrophobic resist surface is essential to the success of immersion lithography.

Both static and dynamic contact angles on resist surfaces have been investigated and the research on these angles has been beneficial to resist designers, scanner designers, and process engineers. This chapter covers the following topics: definitions of static and dynamic contact angles, dynamics of the water meniscus, experimental results from the model immersion head, water leakage mechanisms, contact angle measurement methods, and process-induced contact angle changes.

4.1 Definition of Static and Dynamic Contact Angles

The contact angle (CA) of water on the resist surface is a very important parameter in 193i lithography and is defined as the angle at which a water and air interface meets the resist surface. Figure 4.2 shows a water droplet resting on

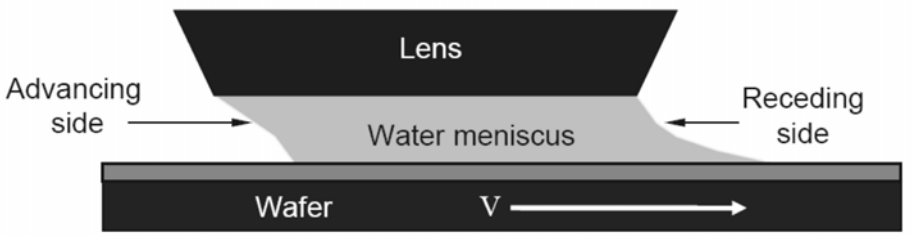

Figure 4.1 Sketched diagram of the water meniscus in the exposure head.

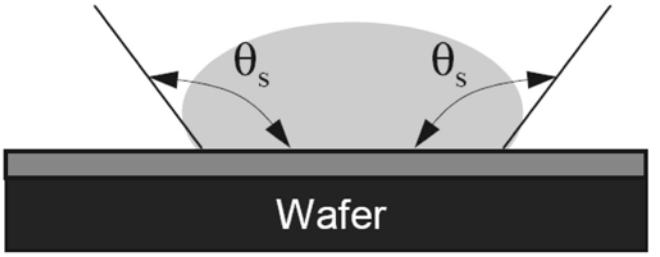

Figure 4.2 Definition of static water contact angle θ_s on a resist surface. The wafer is flat and horizontal.

a flat horizontal resist surface. The water contact angle is labeled as θ_s. A high contact angle means that the surface is hydrophobic (water resisting) and water is easily moved across it. A low contact angle means the surface is hydrophilic (water loving). The static contact angle of water on a typical 193-nm dry resist is 40–70 deg. A static contact angle is measured using a water droplet that is stationary on the wafer surface.

In a 193i scanner, the water meniscus stays with the exposure head as the wafer moves (Fig. 4.1). The static contact angle is insufficient to describe the shape of the water meniscus as the wafer moves beneath it; therefore, dynamic contact angles must be used. Dynamic contact angles can be defined in several ways. For this discussion, we use the definition associated with the model of the immersion exposure head. Figure 4.3 shows the advancing contact angle, labeled as θ_a, and the receding contact angle, labeled as θ_r. These notations are used to describe the water contact angles in the front and rear of the meniscus at a wafer scan speed of *v*. The advancing and receding contact angles are affected by the water viscosity, the resist surface hydrophobicity, the gap height *h*, and the wafer scan speed *v*.

Note that the exposure head sketched in Fig. 4.3 is only a simple model used to analyze the water meniscus and its interaction with the wafer. In this model, water is confined between the lens and the wafer by its surface tension. In real 193i scanners, the exposure heads are much more complicated and include features that control the confinement and circulation of the water. Obviously, the predictive capabilities of this model must be demonstrated before its results can be trusted.

4.2 Dynamics of the Water Meniscus

The dynamics of the water meniscus has been investigated in detail by the University of Wisconsin and SEMATECH.[1–3] The meniscus is defined simply as a volume of liquid with surface tension σ, density ρ, and viscosity μ. The gap has a height *h* formed between a stationary flat lens and a wafer with velocity *v*, as

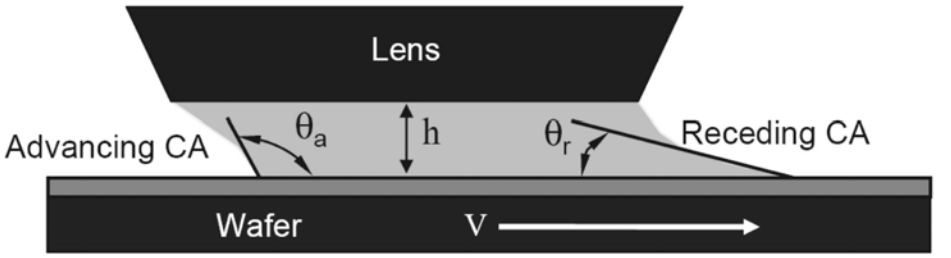

Figure 4.3 Dynamic contact angles of the water meniscus in the exposure head: θ_a (advancing contact angle) > θ_s (static contact angle) and > θ_r (receding contact angle).

sketched in Fig. 4.3. The shape of the meniscus is established by the shearing of the liquid between the lens and the substrate. Fluid dynamics can determine the relationship between the dynamic contact angles and the static contact angle. For example, the advancing contact angle θ_a and receding contact angle θ_r can be expressed as

$$\theta_a = \theta_s + \frac{9\mu v}{\sigma} \ln\left(\frac{h}{L_s}\right), \tag{4.1}$$

$$\theta_r = \theta_s - \frac{9\mu v}{\sigma} \ln\left(\frac{h}{L_s}\right), \tag{4.2}$$

where L_s is a microscopic length scale called the slip length.[1] Equations (4.1) and (4.2) quantitatively describe how the dynamic contact angles are related to the height of the water gap h, the velocity of the wafer stage v, the viscosity μ, the surface tension σ of the water, and the hydrophobicity of the resist surface.

Figure 4.4 shows the results of numerical calculations using Eqs. (4.1) and (4.2).[2] By increasing the scan speed, the receding contact angle decreases and the advancing contact angle increases. A hysteresis region at $v = 0$ is caused by the surface tension and the viscosity of water. At critical points, when the meniscus starts to move on the wafer, the advancing and receding contact angles are defined as static advancing and receding contact angles ($\theta_a|_{v=0}$, $\theta_r|_{v=0}$) (Fig. 4.4). The receding contact angle is highly correlated with the number of water droplets left on the resist surface. Resists with smaller receding contact angles will generally leave more water droplets on the wafer. When the receding contact angle θ_r approaches 0 deg, water film pulling occurs and a thin film of water is left behind. (This is an effective technique for painting, but is a failure mechanism for 193i lithography.) A large receding contact angle is necessary to prevent the formation of water droplets.

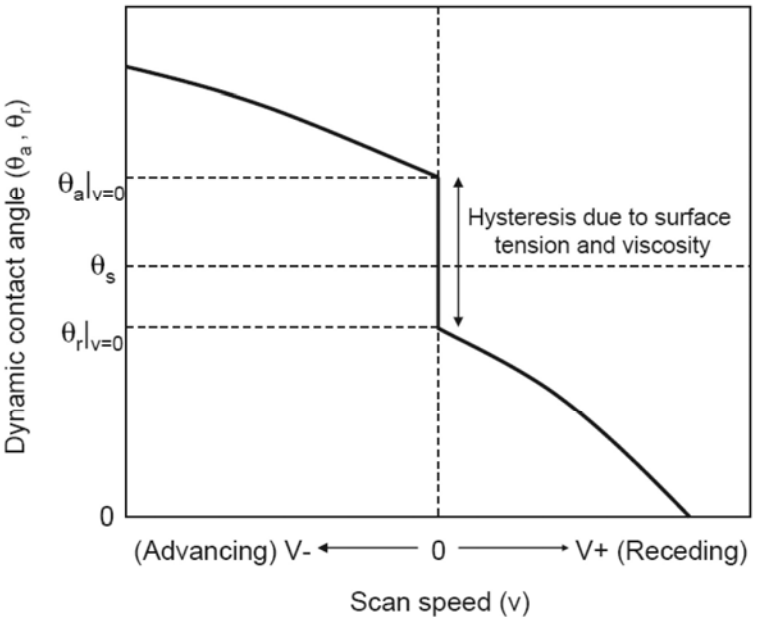

Figure 4.4 Dynamic model of the correlation between dynamic contact angle and scan speed.

4.3 Experimental Results from the Model Immersion Head

A device with a model immersion head was designed to study the water meniscus.[1] The experimental setup (Fig. 4.5(a)) consists of a fluid management system, a substrate, and a translation stage. The apparatus is enclosed in a nitrogen-purged environment so that atmospheric contamination and humidity can be controlled. The fluid management system is held in close proximity to the moving substrate with the height adjusted through a digital micrometer. The velocity of the wafer with respect to the fluid management system is controlled by the translation stage. The camera images the meniscus from the side, in the plane of the wafer. Such an image is illustrated in Fig. 4.5(b). By increasing the magnification of the images, the dynamic contact angles can be measured.

The advancing and receding contact angles are measured as a function of meniscus volume (Fig. 4.6(a)). The gap height and scanning speed are set at 250 mm and 100 mm/s, respectively. Adding more water to the meniscus does not change the measured values of the dynamic contact angles. This result indicates that the dynamic contact angles are not sensitive to deviations in the volume of the meniscus in this apparatus. The dynamic contact angles are also measured as a function of gap height (Fig. 4.6(b)). The scan speed is set at 100 mm/s and the water volume is nominal. The dynamic contact angles increase slightly with gap height, indicating the extent of the sensitivity of the contact angles to the gap height.

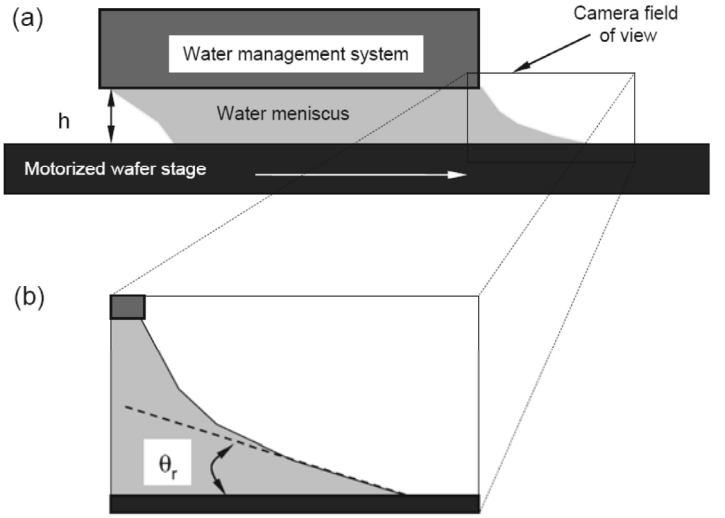

Figure 4.5 (a) Diagram of the setup of the water meniscus test. (b) Local image acquisition to obtain the dynamic contact angles.

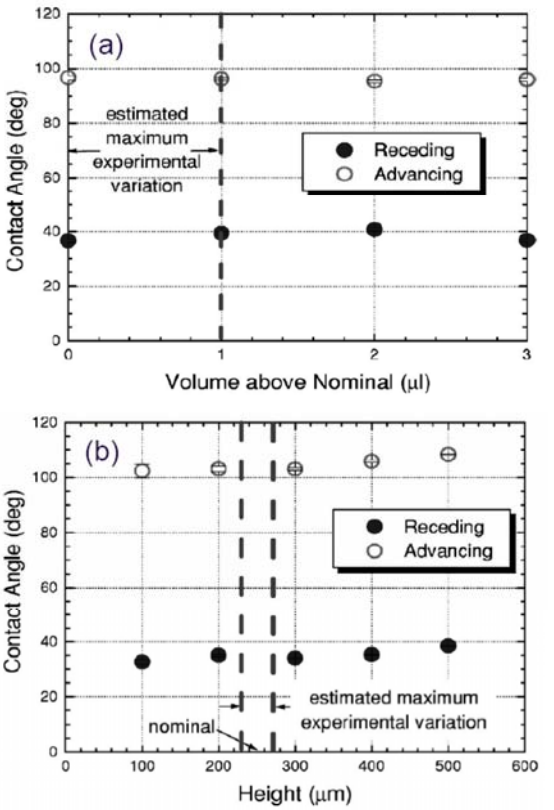

Figure 4.6 Sensitivity of measured dynamic contact angles (a) to the change in volume of the water meniscus (h = 250 μm, v = 100 mm/s) and (b) to the gap height (at nominal water volume, v = 100 mm/s). (Reprinted by permission from Ref. 1.)

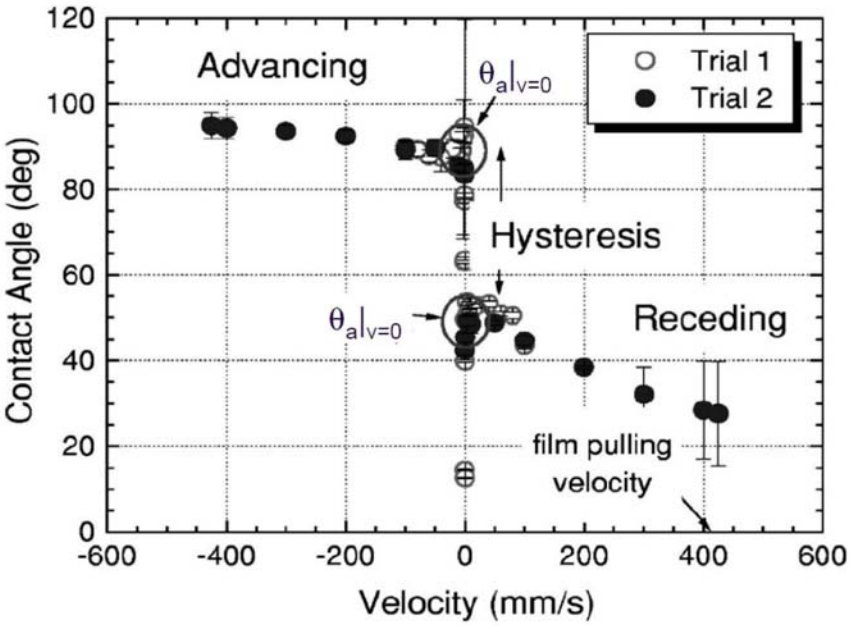

Figure 4.7 Measured dynamic contact angles versus scan speed (at nominal water volume and h = 250 μm). (Reprinted by permission from Ref. 1.)

Figure 4.7 shows the measured dynamic contact angles versus scan speed. The measured curve has the same shape and features as predicted theoretically (Fig. 4.4) and an hysteresis was observed as predicted. The static advancing and receding contact angles were measured as ~90 and 50 deg, respectively, in this resist-coated wafer.

4.4 Leakage Mechanism of the Water Meniscus

The ultimate goal for investigating contact angles is to reduce the probability of both water leakage from the meniscus and bubble formation at full scan speed. For a given exposure head design, the hydrophobicity of the resist greatly influences the tendency of the water to stay with the exposure head when the wafer is moving at high velocities. Hydrophobic resist surfaces have low wetting energies, giving water a high mobility and enabling it to stay with the showerhead at high wafer velocities. In contrast, hydrophilic resist surfaces have high wetting energies with water, preventing the meniscus from staying with the exposure head without some leakage. As a result, water droplets are left behind, forming circularly shaped defects. Two conditions result in water loss from the meniscus: film pulling and inertial instability, each of which is explained below.[4]

The receding contact angle continuously decreases with the scan speed until it reaches 0 deg, at which point a film of water is left on the wafer. The scan speed corresponding to a receding angle of 0 deg is called the film pulling speed. This film pulling behavior readily occurs on hydrophilic surfaces.

The receding contact angle decreases with the scan speed, but only to a certain value. Further increases in scan speed do not change the receding angle, but induce a failure of water confinement and the liquid loss occurs suddenly. Inertial instability occurs when the water in the meniscus cannot be contained by surface tension. This situation is observed with intermediate or high contact angle surfaces.

In general, four factors can cause a decrease in critical scan speed: (1) decreases in surface tension, (2) increases in viscosity, (3) increases in liquid density, and (4) decreases in the hydrophobicity of the surface. Among the four factors, hydrophobicity of the resist surface has the clearest effect on critical scan speed.

4.5 Methods for Measuring Contact Angles

The dynamic contact angles defined in Fig. 4.3 are critical to understanding the shape of the meniscus and its relationship to surface hydrophobicity. However, it is impractical to evaluate every resist using the hysteresis test depicted in Fig. 4.3. Therefore, several simpler contact angle measuring methods have been assessed.[5] Among them, the tilting wafer and captive drop methods have proven the most useful for evaluating the hydrophobicity of resist surfaces and for measuring dynamic water contact angles.

4.5.1 Tilting wafer method

A setup of the tilting wafer method, also called the Sessil drop method, is shown in Figure 4.8. A ~50-μL drop of water is dispensed onto a wafer that is coated with resist or topcoat. The wafer is tilted slowly, for example, 1 deg/s. Immediately prior to the sliding of the droplet, the contact angles at the front and rear of the droplet are measured. These angles correspond to, but are not equal to, static advancing and static receding contact angles—$\theta_a|_{v=0}$ and $\theta_r|_{v=0}$. Because the water confinement on the tilted wafer is completely based on surface tension, this method is much simpler than the exposure head model. The wafer tilting angle at which the droplet starts sliding is called the sliding angle.

The receding contact angles from various resists or topcoats have been measured using the tilting wafer method. The defect counts or watermarks have also been measured from these resists or topcoats exposed by full-field scanners. Much data comparing defect counts versus surface hydrophobicity has been accumulated.[6,7] These experimental results show that receding contact angles of at least 70 deg are required to avoid leaving behind water droplets at full scan speeds. However, increasing resist hydrophobicity may be accompanied by undesirable side effects. For example, hydrophobic resists tend to have small dissolution rates in the standard aqueous TMAH developer, which is > 99% water. The resist formulation must be optimized to give the best lithographic performances in all aspects.

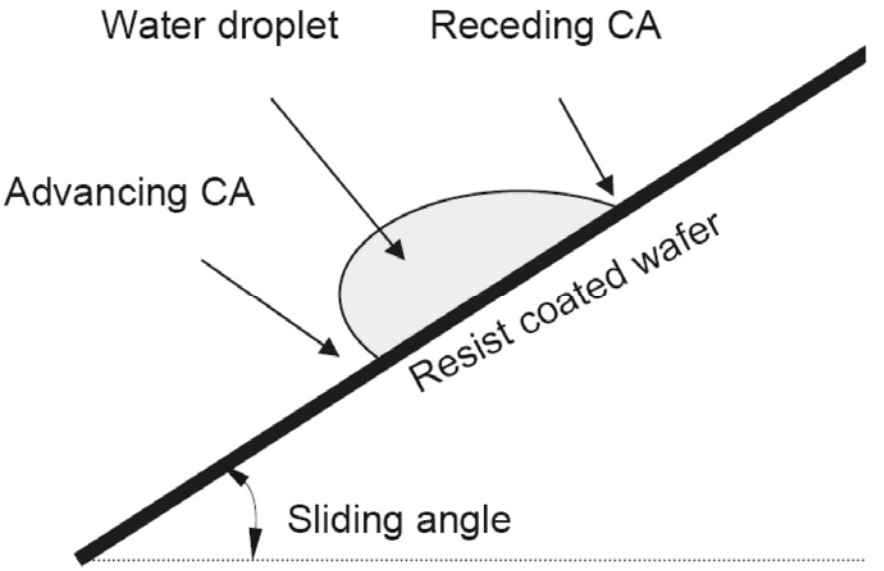

Figure 4.8 Tilting wafer (or Sessil drop) method for measuring dynamic contact angles (CAs).

Additionally, contact angles measured using the tilting wafer method are sensitive to environmental humidity, the volume of the droplet, and the tilting speed of the wafer. Detailed protocols must be agreed on in order to reduce the deviation of test results.

4.5.2 Captive drop method

It has been reported that the captive drop method tends to be less sensitive to experimental details than is the tilting wafer method. In this technique, a small nozzle with a diameter of ~0.3 mm is held ~0.5 mm above the substrate surface. Water is injected onto the substrate, forming a droplet. The water is slowly injected at a speed of ~300 μL/min and the surface of the water droplet expands outward. The advancing contact angle θ_a is measured at the three-phase contact point (water–air–substrate) (Fig. 4.9(a)). The receding contact angle θ_r is measured by pulling the water back into the nozzle at a speed of ~600 μL/min, as the size of the droplet contracts. The surface of the droplet moves inward and the receding contact angle θ_r is measured at the three-phase contact point (Fig. 4.9(b)).

The contact angles measured from the captive drop test show dependence on the speed of water injection and suction. A study showed that the shape of the water droplet changes over time during withdrawal.[8] Immediately after suction begins, the height of the water droplet decreases and the diameter stays the same (Fig. 4.10(a)), leading to a slow decrease in receding angle, over time. After

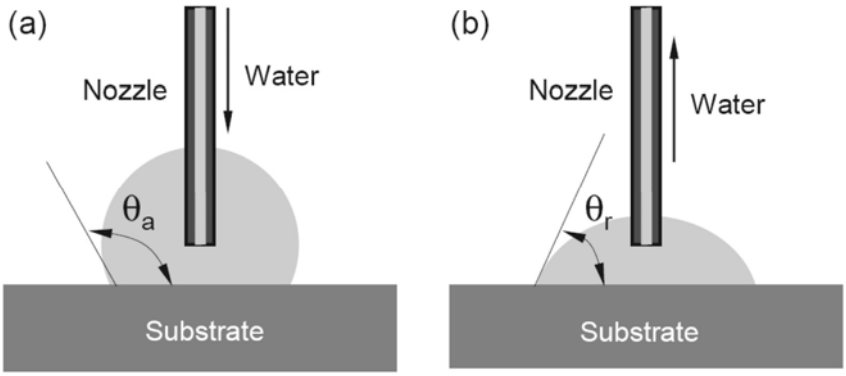

Figure 4.9 (a) Advancing θ_a and (b) receding θ_r contact angles in the captive drop test.

the height of the droplet has been reduced to a critical value, the receding angle stays constant (Fig. 4.10(b)). Finally, the water droplet is removed completely and the receding angle versus time is measured (Fig. 4.10(c)). Reliable receding angles are obtained in this plateau region.

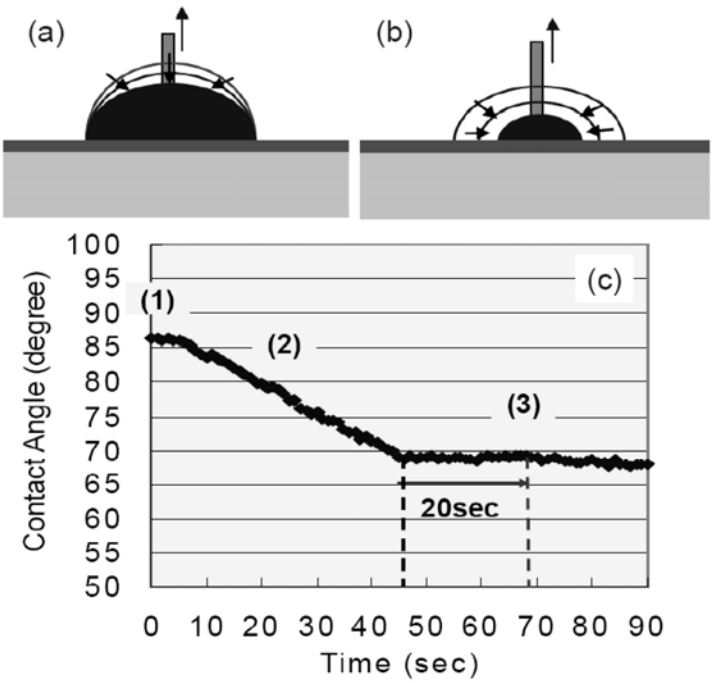

Figure 4.10 (a) and (b) Sketched diagrams showing how the shape of a water droplet changes over time. (c) The measured receding contact angle over time. A 25-μL DIW droplet was placed on a sample wafer and then drawn up through a microsyringe at the speed of 10 μL/min. The labels (1), (2), and (3) in (c) indicate time periods. (Reprinted by permission from Ref. 8.)

4.5.3 Wilhelmy plate method

The Wilhelmy plate is a method commonly used to measure the surface tension of a fluid, but can also be used to measure contact angles.[5] A resist-coated substrate is held vertically and immersed in water (Fig. 4.11(a)). The substrate is held stationary to measure the static contact angle θ_s (Fig. 4.11(b)). The substrate is pushed into the water to measure the advancing contact angle θ_a (Fig. 4.11(c)). The receding contact angle θ_r is measured when the substrate is pulled slowly out of the water.

4.5.4 Correlation between static and dynamic contact angles

The static and dynamic contact angles are correlated with each other as described by Eqs. (4.1) and (4.2). A surface with a high static contact angle usually has a large dynamic contact angle. However, this is not always the case, as other parameters also play roles in Eqs. (4.1) and (4.2). Experimental results have demonstrated that some topcoats have high static angles but small receding angles. Figure 4.12 shows the measured contact angles from three different topcoats (TC1, TC2, and TC3) using the tilting wafer method. The static contact angles measured for TC1, TC2, and TC3 are very similar (80, 81, and 78 deg, respectively), but the receding angles are 36, 51, and 62 deg, respectively. Therefore, dynamic contact angles must be measured in order to properly evaluate resist stacks.

4.6 Process-Induced Contact Angle Variation

The surface hydrophobicity of resists and topcoats is a function of their chemical composition; i.e., hydrophobocity is an intrinsic material property and depends on

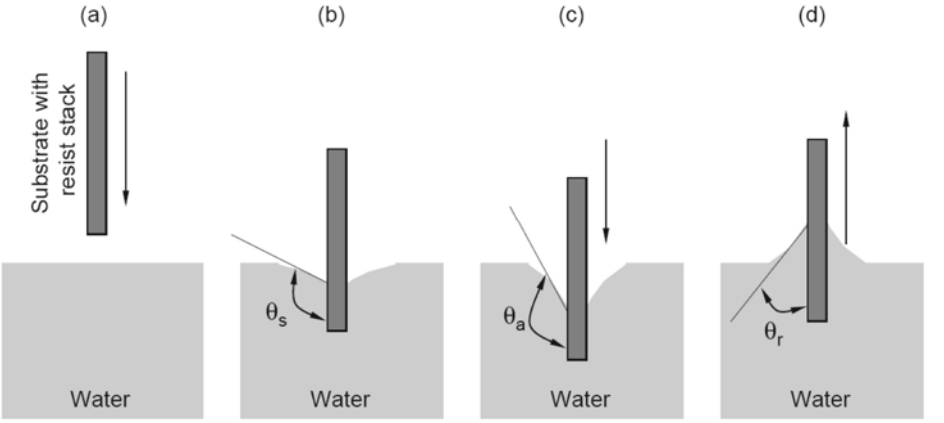

Figure 4.11 Wilhelmy plate method used to measure contact angles. (a) Substrate dips into the water bath. (b) Substrate stands still in the water and the static contact angle θ_s is measured. (c) Substrate is pushed farther into the water and the advancing contact angle θ_a is measured. (d) Substrate is pulled out of the water and the receding contact angle θ_r is measured.

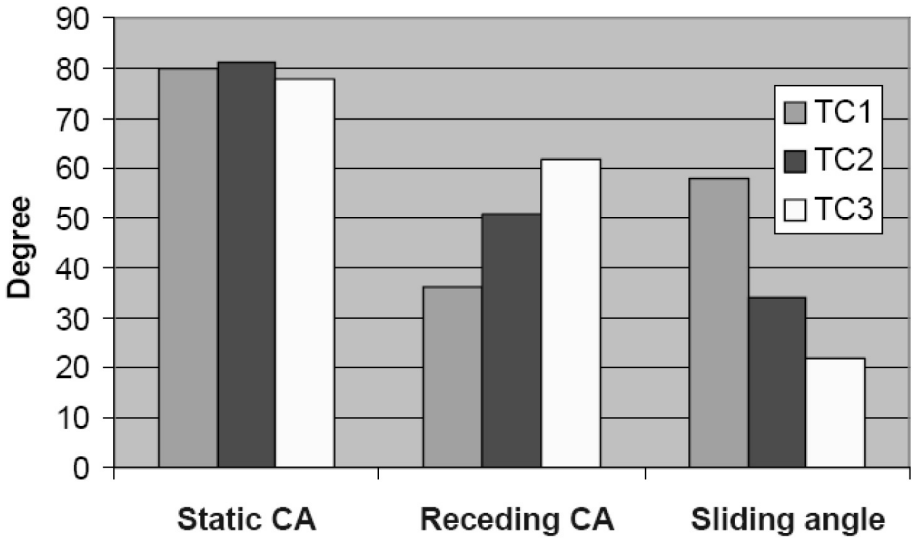

Figure 4.12 Contact angles measured from three different topcoats.

the chemical's surface structure. Physical or chemical treatments can modify the chemical structure of the surface components, resulting in a change in surface hydrophobicity.

4.6.1 Surface modification by exposure

The contact angle of water on a resist surface can change as a result of exposure. Exposure to 193-nm photons not only generates photoacids, but also can induce outgassing of resist components. These physical and chemical reactions may alter the surface hydrophobicity of the resist, causing a change in contact angle.

It has been observed that exposure can cause a distinctive change in dynamic contact angles, without causing changes in static contact angles. For example, the receding contact angle, sliding angle, and static contact angle of one resist were measured *before exposure* to be 51, 20, and 75 deg, respectively. *After exposure*, they were measured to be 44, 26, and 75 deg, respectively. The resist surface gets more hydrophilic after exposure, as determined by the dynamic measurements, whereas the static contact angle remains unchanged.

Exposure-induced changes in dynamic contact angles are very much smaller on topcoat surfaces. This may be attributed to the physical and chemical properties of the topcoat and is probably due to the fact that topcoats are generally not photosensitive. Figure 4.13 shows the contact angles measured from the resist and from the topcoat before and after open frame exposures. Reduction of static contact angles and receding contact angles are observed on the resist. For the topcoat, only ~1-deg changes in the dynamic contact angles are observed.

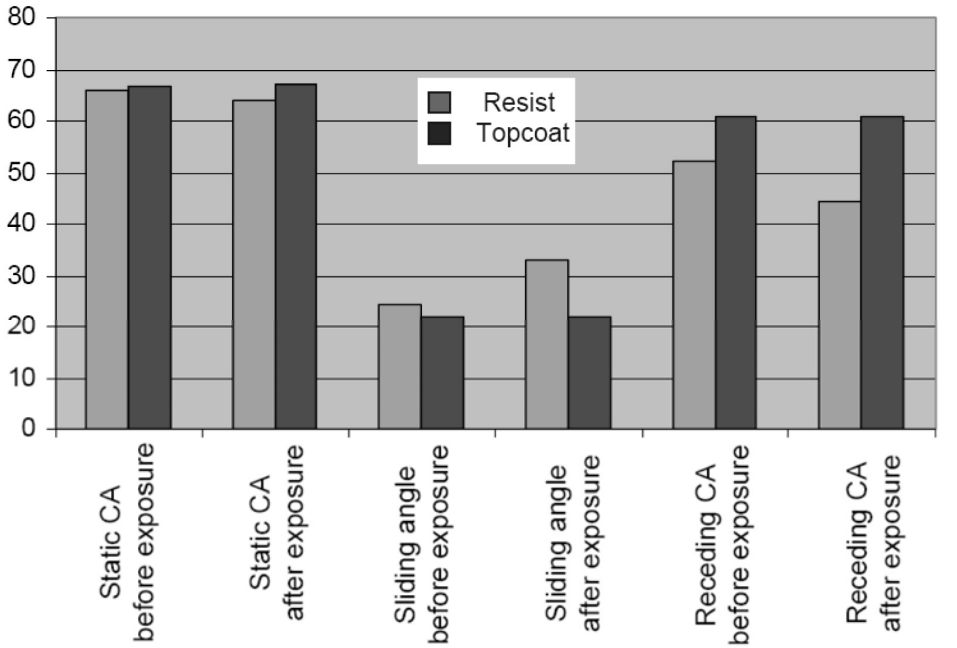

Figure 4.13 Measured contact angles from one resist and one topcoat before and after exposures.

4.6.2 Surface modification by rinse liquid

Resist surface treatment with surfactant before exposure was proposed[9] and serves two functions. First, it washes away the quickly leachable components from the resist surface. This mechanism was explained in the previous chapter on leaching. Second, it increases hydrophobicity of the surface, increasing contact angles. For example, surfactant treatment of a resist increases the receding contact angle from 50 to 66 deg and increases the static contact angle from 75 to 81 deg.

Surfactant rinse treatments of resists are capable of yielding high receding contact angles during exposure and yielding low static contact angles during development. This special process lowers watermark and blob defect counts. However, the effectiveness of the rinse process heavily depends on successfully matching the properties of the rinse chemical to the properties of the resist.

References

1. S. Schuetter, T. Shedd, K. Doxtator, G. Nellis, C. Van Peski, A. Grenville, S.-H. Lin, and D. C. Owe-Yang, "Measurements of the dynamic contact angle for conditions relevant to immersion lithography," *J. Microlith., Microfab., Microsyst.*, **5**, No.2 (2006).

2. C. Van Peski, A. Grenville, R. Engelstad, G. Nellis, T. Shedd, S. Schuetter, K. Doxtator, S.-H. Lin, and D. C. Owe-Yang, "Film pulling and meniscus instability as a cause of residual fluid droplet," Presentation at the 2nd Immersion Symposium, Brugge, Belgium, Sept., 2005.
3. H. Burnett, T. Shedd, G. Nellis, M. El-Morsi, and R. Engelstad, "Control of the receding meniscus in immersion lithography, *J. Vacuum Sci. Tech. B*, **23**, No. 6, 2611–2616 (2005).
4. T. A. Shedd, S. D. Schuetter, G. F. Nellis, and C. van Peski, "A correlation for predicting film-pulling velocity in immersion lithography," Presentation at Photomask Japan 2006.
5. E. Rame, "The interpretation of dynamic contact angles measured by the Wilhelmy plate method," *J. Colloid Interface Sci.*, **185**, No. 1, 245–251 (1997).
6. See for example: S. Owa, H. Nagasaka, Y. Ishii, K. Shiraishi, and S. Hirukawa, "Full-field exposure tools for immersion lithography," *Proc. SPIE* **5754**, 655–668 (2005).
7. S. Kanna, H. Inabe, K. Yamamoto, T. Fukuhara, S. Tarutani, H. Kanda, W. Kenji, K. Kodama, and K. Shitabatake, "Materials and process parameters on ArF immersion defectivity study," *Proc. SPIE* **6153**, 6153–58 (2006).
8. N. Matsumura, N. Sugie, K. Goto, K. Fujiwara, Y. Yamaguchi, H. Tanizaki, K. Nakano, T. Fujiwara, S. Wakamizu, H. Takeguchi, H. Arima, H. Kyoda, K. Yoshihara, and J. Kitano, "Process development for high scan speed ArF immersion lithography," *Proc. SPIE* **6923**, 69230D (2008).
9. P. Foubert, M. Kocsisa, R. Gronheida, S. Kishimura, A. Soyano, K. Nafus, N. Stepanenko, J. De Backer, N. Vandenbroeck, and M. Ercken, "Measurement and evaluation of water uptake by resists, topcoats and stacks and correlation with watermark defects," *Proc. SPIE* **6519**, 65190E (2007).

Chapter 5
Topcoat and Resist Processes for Immersion Lithography

Practitioners of 193-nm immersion lithography use three topcoat approaches: solvent-soluble topcoats, developer-soluble topcoats, and no topcoat. Topcoats are coated over resists to prevent the components in the resists from leaching into water. After exposure, topcoats are removed using either a solvent (solvent-soluble) or a developer (developer-soluble). Application of topcoats enables the use of 193-nm dry resists for the immersion process. These 193-nm dry resists are widely used in production; however, they typically have high levels of leaching.

Early in the development of 193i, when low-leaching and high-performance 193i resists were not available, topcoats were a practical and viable solution. They worked with dry resists and were removed after development. Downstream processes, such as etch, did not need to be changed. Therefore, the developer-soluble topcoat processes were relatively easy to integrate into manufacturing lines and remain the most commonly used processes today. In contrast, solvent-soluble topcoats have never been used in mass production because they are made from fluoropolymers that require toxic solvents for removal. Additionally, solvent-soluble topcoats require dedicated modules for coating and removal.

Resist processes without topcoats have always been the preferred approach. The elimination of a topcoat simplifies the process, eliminates the coat and bake steps for the application of topcoats, reduces the cost of ownership, and eliminates one source of defects. Conventional dry 193-nm resists are not suitable for use in immersion lithography without topcoats, because their components leach into water and contaminate the exposure head. In order for a resist to be suitable for use without a topcoat, it must simultaneously meet the requirements of low leaching and superior lithographic performance.

This chapter focuses on methods for processing developer-soluble topcoats and resists without topcoat. It covers the following topics: selection of developer-soluble topcoats, process optimization of developer-soluble topcoat and resist stack, new approaches for developing topcoats, resist processes without topcoat, and new approaches for high-performance 193i resists.

5.1 Selection of Developer-Soluble Topcoat

In general, developer-soluble topcoats consist of at least one solvent plus a polymer that meets the target dissolution rate in aqueous alkaline developer. Photoacid generators can be added to the formulation to compensate for acid diffusion from the resist film during exposure and PEB. A successful topcoat must fulfill many requirements, but most importantly, it must be compatible with the resist. These requirements and compatibility issues have been gradually understood through collaborative efforts between lithographers and resist chemists. The best topcoat and resist stacks are identified using the following general procedure. First, the topcoat and resist stacks are tested for leaching. Leaching tests ensure that the topcoat effectively prevents resist components from leaching into the water (see Chapter 3 for details). Second, the topcoat must be physically and chemically compatible with the resist film. Various combinations of topcoats and resists must be investigated for their performance in the process window, line-edge roughness (LER), and pattern profile. The best combination is identified, and finally, process parameters (typically bake temperatures) of the selected topcoat and resist stacks are optimized for best performance.

5.1.1 Refractive index and thickness of topcoat

In the immersion exposure, the topcoat layer is between the immersion water and the resist (Fig. 5.1). Exposure light can be reflected from the interface between immersion fluid and topcoat as well as from the interface between topcoat and resist. The refractive index of the topcoat n_{TC} and its thickness t must be optimized in order to minimize the reflections at the interfaces so that more light reaches the resist.[1]

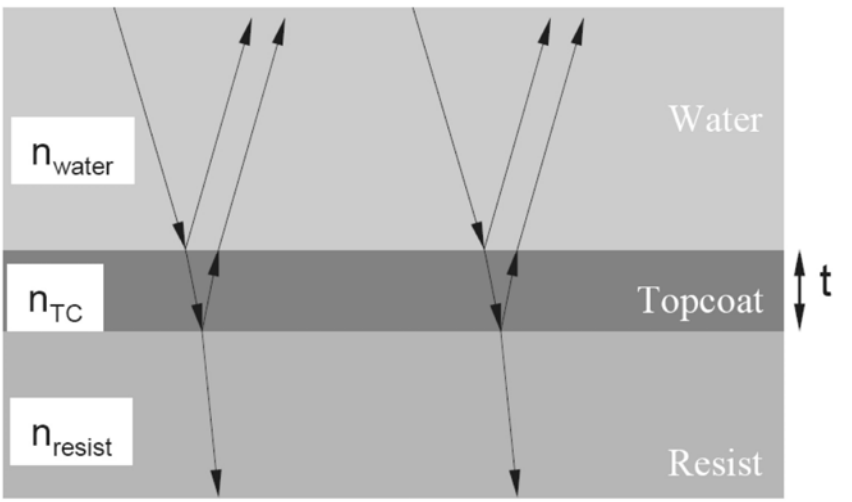

Figure 5.1 Reflection of exposure light at interfaces of water/topcoat, topcoat/resist, and resist/substrate.

Assuming that the water and the resist layers are semi-infinite and the light incident angle is small (low NA), the destructive interference requires the following conditions:

$$n_{TC} = (n_{water} \cdot n_{resist})^{1/2}, \quad (5.1)$$

$$t = m\,\lambda/(4\,n_{TC}), \quad (5.2)$$

where n_{TC}, n_{water}, and n_{resist} are the refractive indices of the topcoat, water, and resists at 193-nm wavelength, and m is an integer. Equation (5.1) ensures that the light intensity of reflected light components are matched and Eq. (5.2) ensures that the reflected light components have opposite phases.[2] Table 5.1 shows the refractive index and recommended thickness of topcoats from major vendors. Typically, the topcoats are 30–100 nm thick.

193-nm resists generally have refractive indices of ~1.7 and water has a refractive index of ~1.44 at 193-nm wavelength. From Eq. (5.1), the ideal refractive index of a topcoat for water immersion is calculated as ~1.55. With n_{TC} of 1.55, the ideal topcoat thickness is calculated from Eq. (5.2) as a multiple of 31 nm. The topcoat film selected based on Eqs. (5.1) and (5.2) can function not only as a leaching protective layer, but also as a top antireflective coating (TARC). The total reflectivity at the resist surface and its swing amplitude are much reduced by the topcoat film. The dose-to-size of a resist stack with an optimized topcoat is smaller than that of the same resist stack without topcoat film. Similar experimental results indicate that the topcoat process can improve the CD uniformity on a topographic wafer.[3]

For high-incident (high NA) angles, the calculations for optimum thickness are much more complicated. Swing curves and reflectivity must be simulated as a function of topcoat thickness in order to understand the contributions from light from all incident angles (from 0 to maximum NA).[4] In general, the simulation results demonstrate that higher NAs require thicker topcoat films, corresponding to the first reflective minima.

Apart from optical requirements, the topcoats must be thick enough to serve as barriers to leaching of the resist components. Depending on the permeability of the topcoat and its coating uniformity, the resist leaching level is typically

Table 5.1 Refractive index and recommended thickness of experimental topcoats.

	TC1	TC2	TC3	TC4	TC5	TC6	TC7	TC8
n_{TC} (Measured)	1.53	1.54	1.48	1.62	1.42	1.47	1.51	1.38
$\lambda/(4n_{TC})$ (nm) (Calculated)	31.5	31.3	32.6	29.8	34.0	32.8	31.9	35.0
Recommended thickness (nm)	30	90	40	30	50	32	30	40

evaluated as a function of the thickness of the topcoat (Fig. 5.2). Leaching levels generally decrease nonlinearly with topcoat thickness. Target thicknesses of topcoats are set based on acceptable levels of leaching. If the topcoat film is below target thickness, the topcoat will not sufficiently protect against leaching.

It is obvious that topcoats must be transparent. However, a small amount of absorption can be beneficial, as it can absorb some flares (which is a scattered light generated during exposure). Assuming that the light intensity before entering the film is $I_{0,}$ and it is attenuated to I after traveling a distance of x in the film, the light attenuation in the polymer film is

$$I = I_0 \cdot e^{-\alpha x}, \tag{5.3}$$

where α is the absorption coefficient, which is equal to the Dill B parameter. The value of α multiplied by the film thickness is called optical density. The Dill B parameter can be calculated as

$$Dill\ B = \frac{4\pi}{\lambda} k\ . \tag{5.4}.$$

Most 193-nm topcoats have k values of ~0.01, which is the imaginary part of the refractive index. According to Eq. (5.4), Dill B is calculated as about 0.64 μm^{-1} for the topcoats. The relationships in Eqs. (5.3) and (5.4) are also applicable to resist films.

5.1.2 Chemical compatibility of topcoat and resist

The topcoat solvent should not dissolve the resist. Otherwise, the solvent will partially dissolve the resist surface during the topcoat coating process, forming an

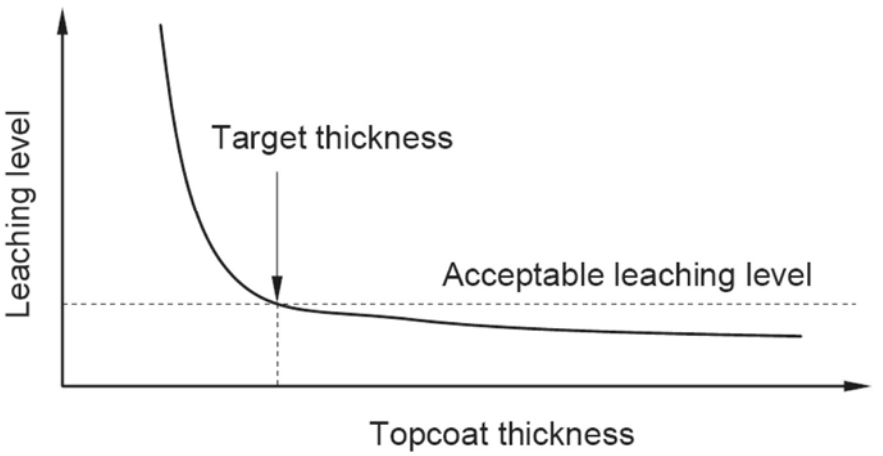

Figure 5.2 Diagram of leaching level versus topcoat thickness.

intermixed layer.[5] While most 193-nm resists use PGMEA or PGME as solvents, topcoats generally use alcohol-based solvents.

An effective method for evaluating the solvent compatibility between resist and topcoat is to measure the "dark loss" of the resist. The resist is first coated on a substrate and its thickness is measured, then the topcoat is coated over the resist film. After the post-apply bake, the topcoat is removed by developer and the resist thickness is measured again. The dark loss is the difference between the resist thickness before and after removing the topcoat and is called the dark loss because no exposure is involved in the measurement. Figure 5.3 shows the dark loss of various resists caused by different topcoats.[6] The topcoats are all developer-soluble, i.e., the topcoat removal process was done in a develop bowl by aqueous TMAH developer. All combinations of six resists and three topcoats were tested. Dark loss of resists without topcoat was also measured. Except for Resist-B and Resist-D, all resists without topcoat demonstrated negligible dark loss in the developer. Topcoat TC-B induces large resist losses, especially in combination with Resist-C (Fig. 5.3(b)). In general, higher resist dark losses indicate that resist films are at least partially removed by the topcoat solvent during the coating of the topcoat.

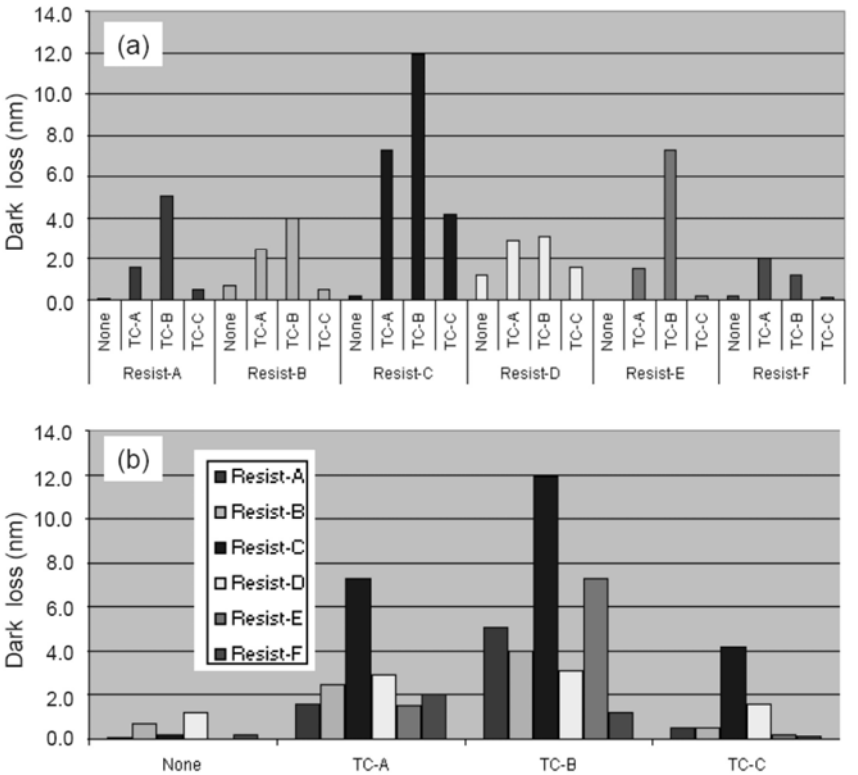

Figure 5.3 Dark loss of resists caused by different topcoats. The topcoats are all developer-soluble, i.e., the topcoat removal process was done in a develop bowl by aqueous TMAH developer. Dark loss of resists without topcoat was also measured.

In addition to dark loss tests, solvent compatibility can also be evaluated using solvent rinse experiments. Resist films can be directly rinsed with various types of topcoat solvents, for example, alcohols or ethers (developer-soluble topcoat), or hydrocarbons (solvent-soluble topcoats). The resist thickness loss and surface roughness are measured after the solvent rinse process.[7] Incompatible topcoat solvents show more resist loss and generate rougher resist surfaces.

Figure 5.4(a) shows the resist loss caused by a topcoat solvent rinse. The resist loss was measured from resists with different acrylates and molecular weights. In Fig. 5.4(a), high resist loss was observed in the resists with high acryl rates and low molecule weights. While alcohol solvents induce the most resist loss, hydrocarbon solvents induce the least resist loss. Surface roughness values of resists rinsed with different solvents are shown in Fig. 5.4(b). The rinse with ethers (Solvent-E2) has the least effect on the resist surface roughness.

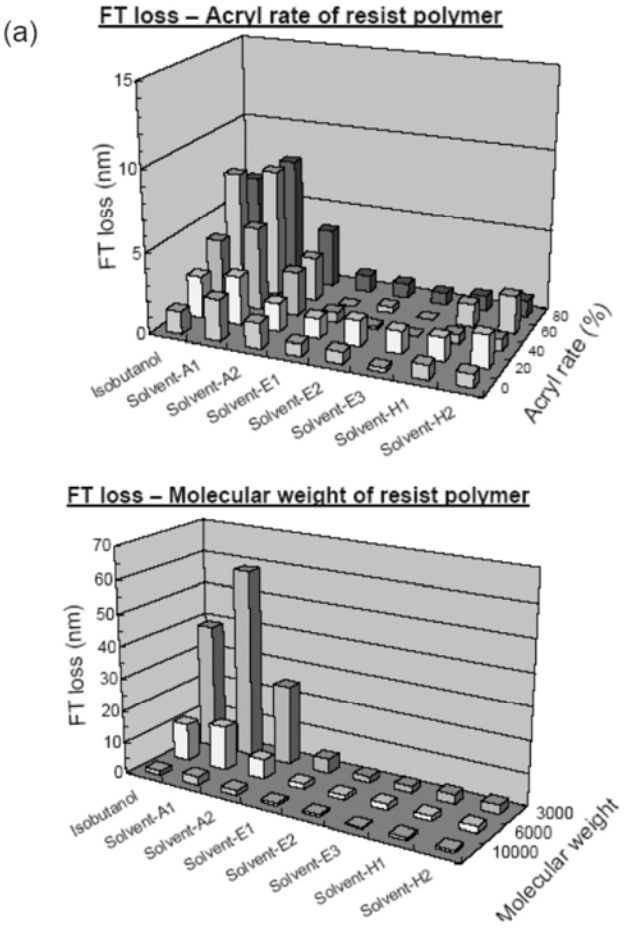

Figure 5.4 (a) Resist loss caused by topcoat solvent rinse. Solvents A1 and A2 are alcohols; solvents E1, E2, and E3 are ethers; solvents H1 and H2 are hydrocarbons. (Reprinted by permission from Ref. 7.)

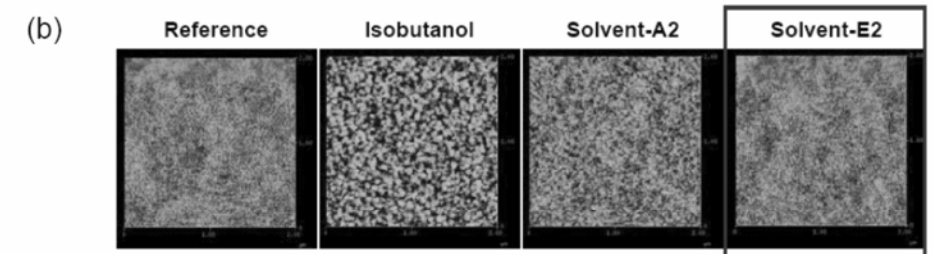

	Reference	Isobutanol	Solvent-A2	Solvent-E2
FT loss	-	3.0	1.8	1.6
Ra	0.750	1.247	0.795	0.791
Rrms	0.952	1.558	1.074	0.977
Rz	7.776	14.289	15.532	7.622

Figure 5.4 (b) Resist surface roughness after the solvent rinses. The AFM field is 2 μm × 2 μm. R_a is the average roughness; R_{rms} is the root-mean-square roughness; R_z is the z-range roughness. (Reprinted by permission from Ref. 7.)

Solvent incompatibility can occur when the resists and topcoats are supplied by different vendors. In this situation, the topcoat supplier may not fully understand the solvent system of the resist, and vice versa. To plumb a new topcoat, special attention must be paid to solvent cleaning procedures for the line. The line must be purged by the topcoat solvent to completely remove any residual solvents that may be incompatible with the topcoat, causing it to precipitate and generate particles.

5.1.3 Dissolution rate of developer-soluble topcoat in developer

The topcoat is removed after PEB and before the development of the resist. Developer-soluble topcoats are removed by aqueous TMAH developers in the develop module. Blob defects are generated during topcoat removal in 193i processes, just as they are generated during the development of 193-nm dry resists. For 193i, topcoat blob defects are typically composed of topcoat materials that have redeposited on the surface during the removal of topcoat. The mechanism for formation of blob defects is complex and is still under investigation (see Chapter 2 for more details). To reduce the numbers of blob defects, it is essential to use topcoats with high dissolution rates.

Dissolution rate monitors can be used to measure dissolution rates. As shown in Fig. 5.5, a wafer coated with topcoat is immersed in a bath filled with the aqueous TMAH developer. A light beam shines on the wafer where it is reflected, both at the topcoat surface and at the interface between the topcoat and the wafer. The reflected beams form interference patterns that are detected by a sensor (Fig. 5.5(a)). As the topcoat film dissolves, the intensity of the reflected beams oscillates between the maxima (constructive interference) and minima (destructive interference) (Fig. 5.5(b)). Following these changes in thickness over

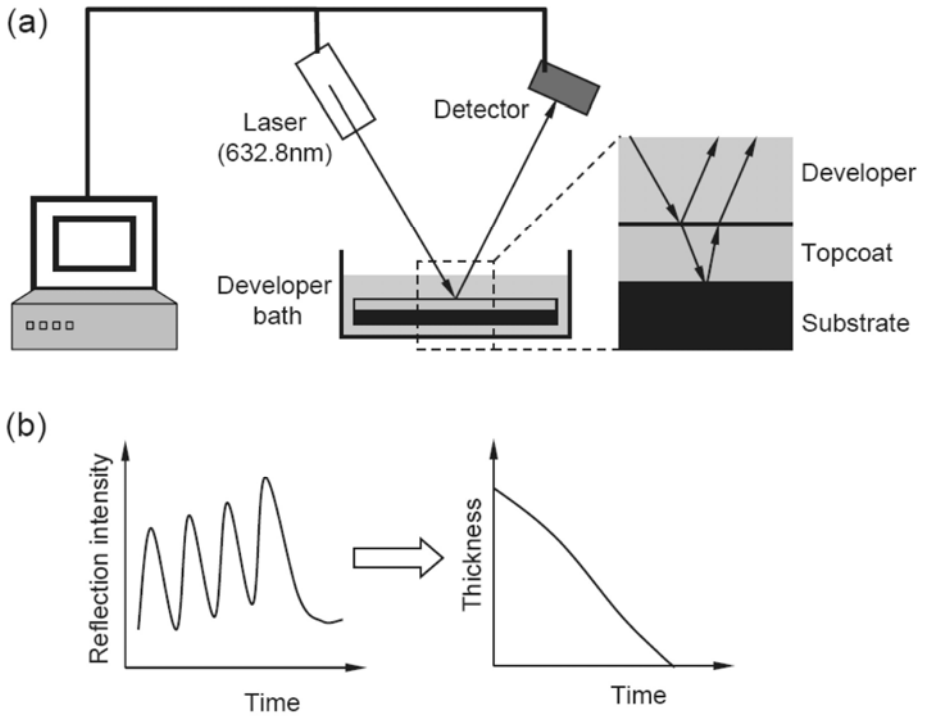

Figure 5.5 (a) Setup of a dissolution rate monitor and light interference at the interfaces. (b) Measured reflection intensity over time and transformation of the film thickness change over time.

time gives the dissolution rate.[8] Dissolution rates of most topcoats are in the range of 100 to 1000 nm/s.

Although topcoats with *high* dissolution rates are expected to yield *fewer* blob defects, they are expected to yield *more* watermark defects. As previously discussed, materials with high dissolution rates typically have hydrophilic surfaces with high wetting energies. These surfaces prevent efficient confinement of the water meniscus, causing an increased tendency for water droplets to form behind the exposure head, leaving watermarks. Therefore, an ideal developer-soluble topcoat would have both high dissolution rate in developer and high water contact angle (Fig. 5.6).

In contrast, the requirement to simultaneously meet high dissolution rates in aqueous developers and high hydrophobicity does not apply to the solvent-soluble topcoat. The solvent-soluble topcoat is removed by a dedicated solvent and can be designed to be very hydrophobic to water and still have a high dissolution rate in the solvent.

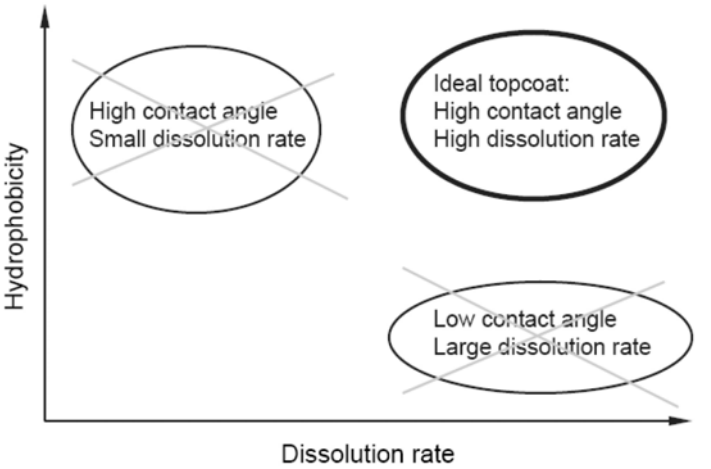

Figure 5.6 Diagram displaying the compromise between hydrophobicity and dissolution rate of the topcoat.

5.1.4 Advanced developer-soluble topcoats

A clever approach to addressing the "contradictory requirements" of high hydrophobicity and high dissolution rate is to blend the hydrophobic additives into the developer-soluble topcoat. This approach is called polymer blending.[9–11] The hydrophobic additives are fluorinated polymers that are hydrophobic and have low surface energies. During spin-coating and PAB, they migrate to the top surface of the film, forming a hydrophobic surface, while the bulk of the topcoat film is acid rich and retains its ability to dissolve quickly. Figure 5.7(a) shows a diagram of the concept and Fig. 5.7(b) shows a test topcoat (graded topcoat B) that is made by blending two such polymers (fluorinated polymer B and sulfonic acid polymer B) in a ratio of 50:50. Graded topcoat B demonstrated a hydrophobic surface with a receding contact angle of 70.2 deg and a good dissolution rate of 160 nm/s.

In theory, the approach of polymer blending splits the polymer design burden of high hydrophobicity and high dissolution rate. The surface hydrophobicity is realized by the fluorinated polymer and the bulk dissolution rate is realized by the acidic polymer. By carefully engineering the component polymers and their blending ratio, a topcoat can be generated that meets the contradictory requirements.

5.2 Lithographic Assessment of Developer-Soluble Topcoats with Resists

After the optical and chemical compatibility of the topcoat and the resist are confirmed, the lithographic performance of the stack must be evaluated. To date, there are no universal developer-soluble topcoats that are compatible with all

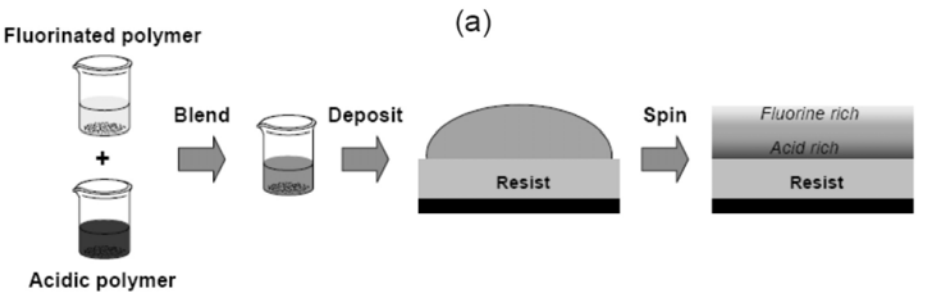

(b)

Polymer	Adv. CA	Rec. CA	Tilt Angle	Dissolution Rate
Fluorinated polymer B	92.1°	72.9°	18.0°	10.4 nm/s
Sulfonic acid polymer B	83.4°	42.1°	37.9°	570 nm/s
Graded topcoat B (50:50 blend)	91.8°	70.2°	19.1°	160 nm/s

Figure 5.7 (a) Diagram showing the concept of polymer blending. (b) One example of the topcoat generated by polymer blending. (Reprinted by permission from Ref. 11.)

193-nm resists, despite the attractiveness of such a product. Many developer-soluble topcoats are available that have been evaluated in combination with various resists. The best combination of resist and topcoat can be identified by comparing overall lithographic performance.

5.2.1 Lithographic assessment

In one study, the lithographic performance of resist and topcoat stacks was evaluated using a binary intensity mask.[12] For all imaging experiments, the BARC (AR40) was 90 nm and the illumination condition was annular 0.55/0.85 and 0.75NA. Process windows for 90-nm line / 90-nm space features were printed and inspected. Figure 5.8 shows the top-down images of 90-nm line / 90-nm space features for different combinations of resists and topcoats. Images were taken at the best dose and focus. The top-down images reveal that most topcoats will work with multiple resists; however, some incompatible interactions were also observed. For example, Resist A and Topcoat 4 produced lines that are broken and distorted (Fig. 5.8).

The line-edge roughness (LER) of the resist lines in Fig. 5.8 are plotted in Fig. 5.9 and sorted by resist (Fig. 5.9(a)) and topcoat (Fig. 5.9(b)). The LER from the worst combination of resist and topcoat (Resist A / TC4) was omitted. LER seems to be consistent for each resist, although topcoats do have some influence on the final outcome, but with a smaller range.

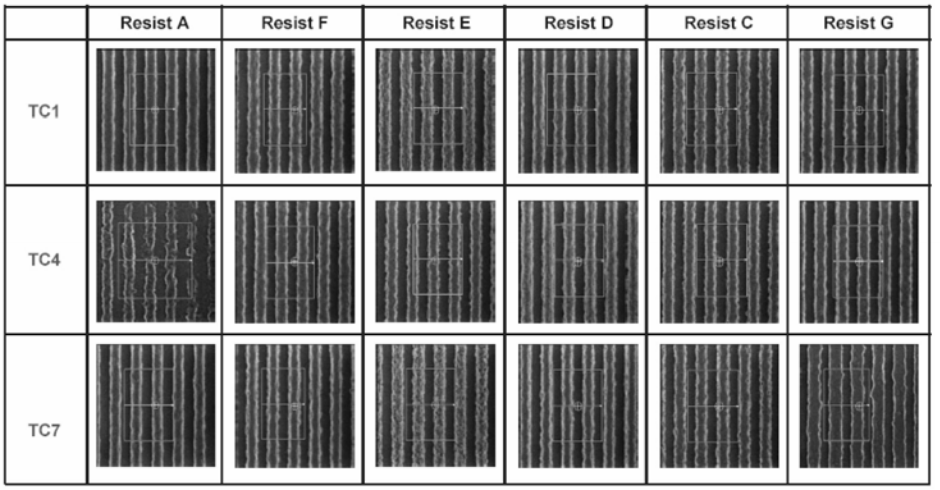

Figure 5.8 Top-down images of 90-nm line / 90-nm space features taken from different resist/topcoat stacks. The field of view is 1 μm × 1 μm.

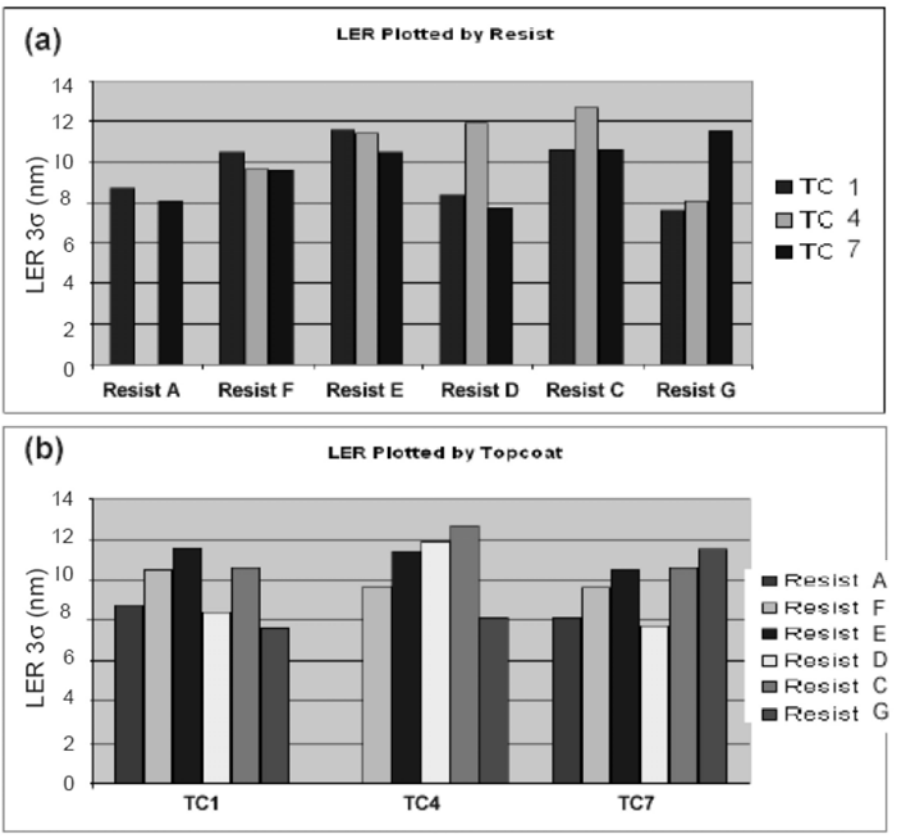

Figure 5.9 LER 3σ of the resist lines in Fig. 5.8.

Process windows are plotted in Fig. 5.10. A negative bias of 20 nm was added to the CDs measured by the CD-SEM (i.e., 110 nm measured by the CD-SEM corresponds to the 90-nm target). CD tolerance was set ±10%. Two resist / topcoat stacks have no process windows: Resist A / TC4 and Resist G / TC7. The biggest process window was obtained from the stack of Resist A / TC1.

Cross-sectional SEMs are essential for evaluating the profile and top loss of the resist lines. Figure 5.11 shows the cross-sectional images of resist and topcoat combinations at best dose and focus. Note that different resists were coated at different thicknesses, as recommended by the vendors. In general, the profiles of most patterns are acceptable, with top-rounding observed in some resist patterns. The incompatible combination of Resist A with Topcoat 4 shows significant levels of loss, with the final height of the resist pattern less than 40% of its original thickness.

The heights of resist patterns in Fig. 5.11 were measured and calculated. The exposed resist losses reported in Fig. 5.12 are the differences between nominal resist film thicknesses and their corresponding pattern heights. For comparison, the exposed resist loss is sorted by topcoats (Fig. 5.12(a)) and resists (Fig. 5.12(b)), separately. The combination of Resist A and Topcoat 4 shows catastrophic imaging failure. All of the other combinations show adequate performance through imaging.

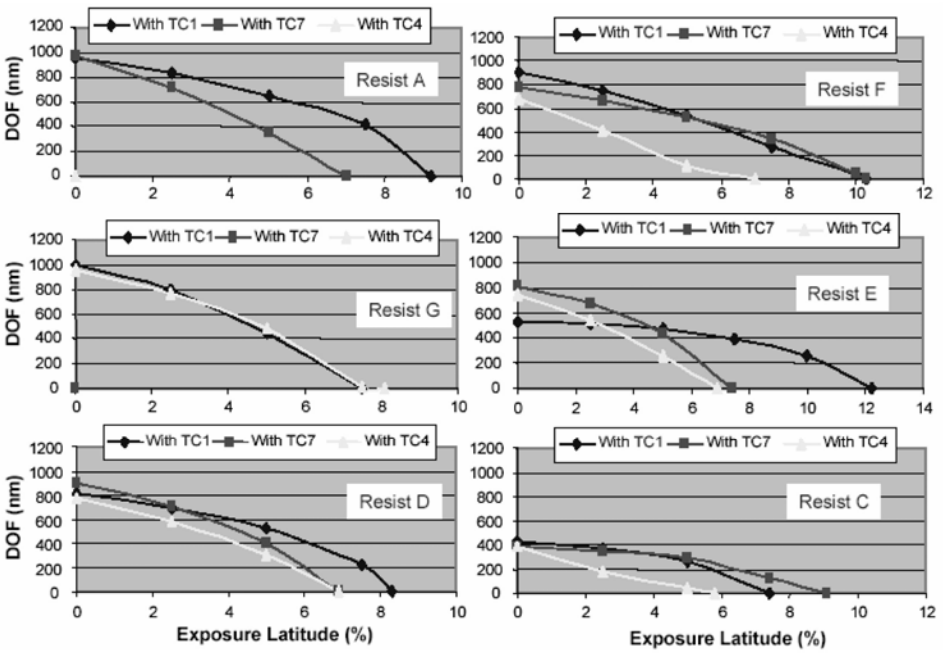

Figure 5.10 Process window of resist and topcoat combinations.

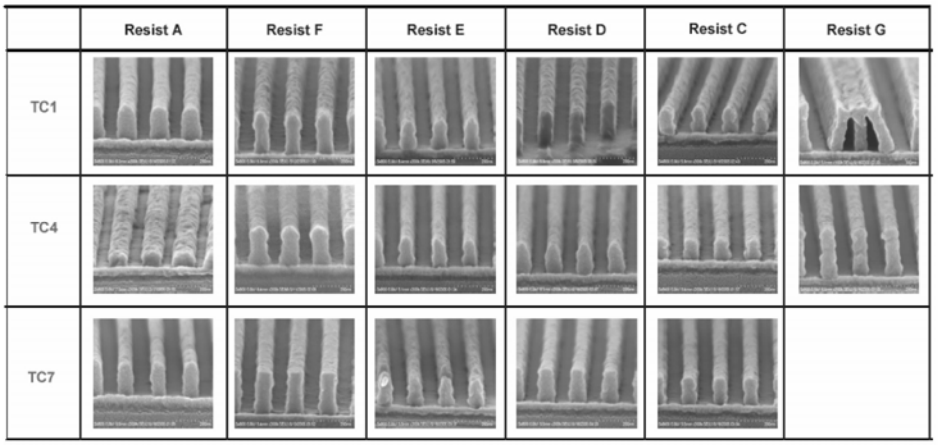

Figure 5.11 Cross-sectional images of 90-nm / 90-nm dense features from different resist and topcoat combinations at best dose and focus.

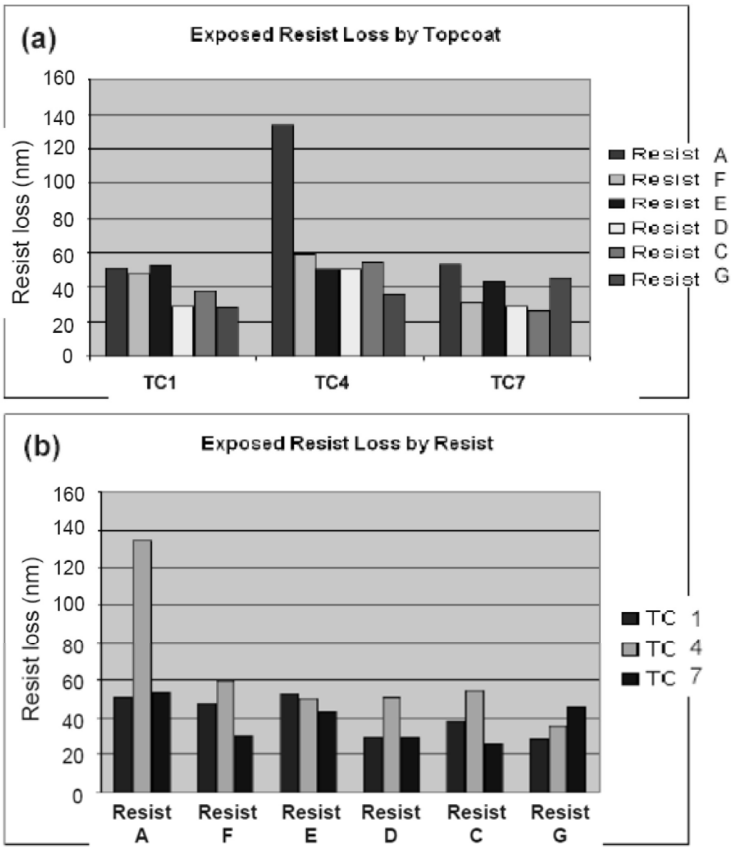

Figure 5.12 Exposed resist loss (resist film thickness – height of the resist pattern) for different resist and topcoat combinations. (a) Sorted by topcoats. (b) Sorted by resists.

5.2.2 Exposed resist loss by developer-soluble topcoat

The resist losses shown in Fig. 5.12 were measured from the resist lines that correspond to the opaque areas in the line/space patterns on the mask. However, the aerial images are not perfect square waves and the resist in these lines absorbs some stray light. Because of the effects of stray light and acid diffusion, the top losses in Fig. 5.12 are larger than the dark losses shown in Fig. 5.3.

To further investigate resist film loss, open frame exposures are carried out and contrast curves are measured for stacks of Resist A with Topcoats 1, 2, and 3 (Fig. 5.13). The stack with TC3 loses the most thickness and the stack with TC1 loses the least. Figure 5.13 also shows that the resist dark loss is negligibly small for all three topcoats. This suggests that the topcoat-induced resist loss has some interaction with the exposure/deprotection chemistry.

The stacks of Resist A and Topcoats 1, 2, and 3 were exposed at the same dose and focus for 90-nm / 90-nm dense patterns. The CD of the resist patterns was measured and plotted (Fig. 5.14(a)). With Topcoat 3, the average CD of the resist patterns is the smallest, which again suggests that Topcoat 3 gives enhanced resist sensitivity. Cross-sectional images are taken of the resist patterns with different topcoats (Fig. 5.14(b)). About 50 nm of resist loss is measured from the Resist A / Topcoat 3 stack, while with Topcoat 1, the resist loss is only about 30 nm.

5.2.3 PEB delay of 193i process with developer-soluble topcoats

Usually, amine contamination is a concern for chemically amplified resists. Amines exist in the environment and react with the photoacids generated during exposure, leading to losses in resist sensitivity. Longer delays between exposure and PEB typically result in T-topping of resist patterns and/or increases in CD. However, topcoats may be capable of producing additional benefits to the imaging process by protecting resists from amine contamination.

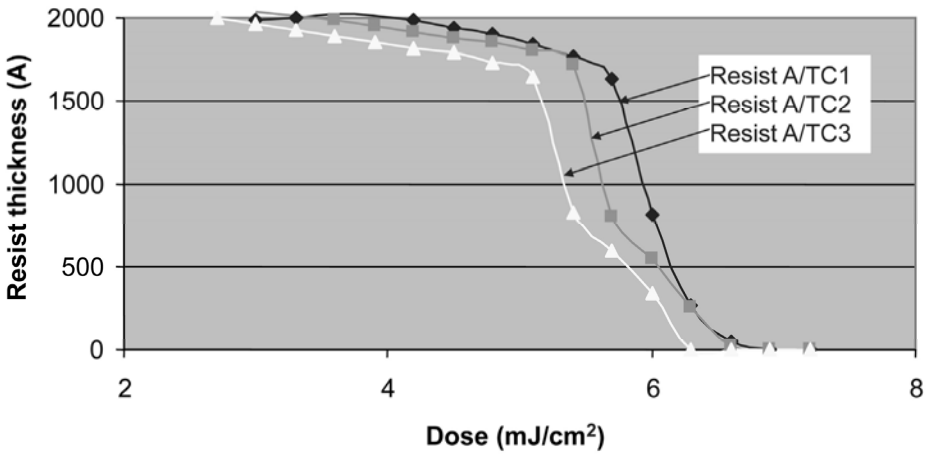

Figure 5.13 Contrast curves measured from stacks of Resist A / different topcoats. The resist film thickness before exposure is 200 nm.

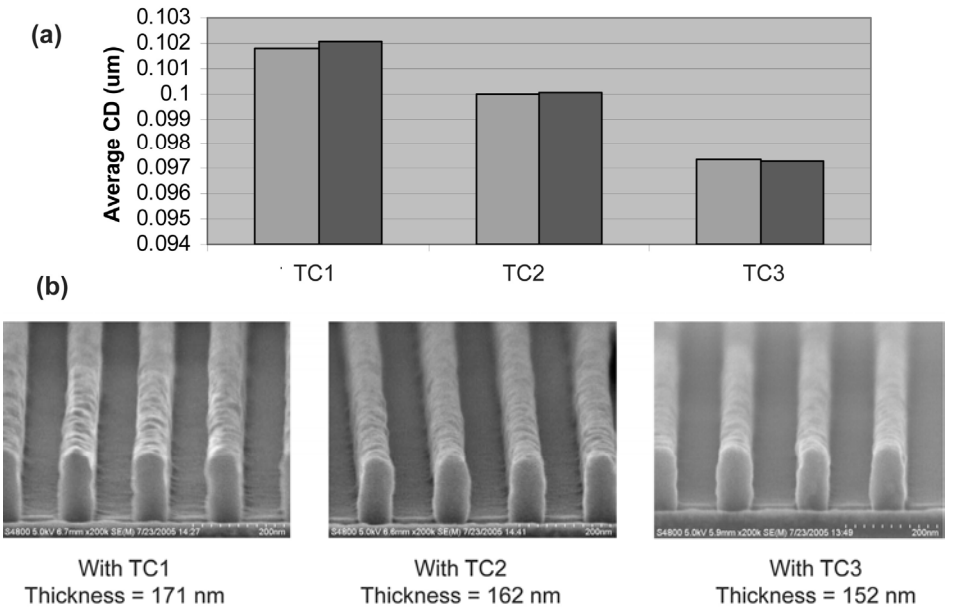

Figure 5.14 (a) Average CD measured from 90-nm / 90-nm resist stacks with different topcoats. (b) Cross-sections of resist stacks in (a).

Figure 5.15 shows the experimental results from one post-exposure delay study.[12] The resist film has a thickness of 220 nm and the developer-soluble topcoat has a thickness of 30 nm. Wafers were exposed at constant dose and focus and stored in the track for delays of 1, 5, and 15 minutes prior to PEB and development. The track and scanner are linked and have an amine level of ~1 ppb. The CDs of 90-nm / 90-nm and 80-nm / 80-nm resist patterns were measured across the wafer. To better monitor changes in resist profile, the CDs at both the top and the bottom of the resist lines were measured. The CDs were averaged across the wafer and plotted in Fig. 5.15 as a function of PEB delay time. As expected, all CDs were unchanged as a function of PEB delay time up to 15 minutes, which suggests that the topcoat can also serve as a contamination barrier layer.

5.3 Optimization of Developer-Soluble Topcoat Processes

Developer-soluble topcoats interact with resists, affecting the ultimate imaging capability of the stack. Therefore, the processing of developer-soluble topcoat/resist stacks must also be optimized. Each process step can have a significant impact on the ultimate imaging capability of the stack. For example, the resist/topcoat stack must be baked three times: resist PAB, topcoat PAB, and PEB. The PAB steps remove most of the solvents from the resist and topcoat. The solvent evaporation from the resist can also affect the PAG distribution, as well as other components. PEB affects deprotection, diffusion of photoacid, and the dissolution rate of topcoat in the developer. Thus, the bake temperatures must be optimized to obtain the best resist performance.

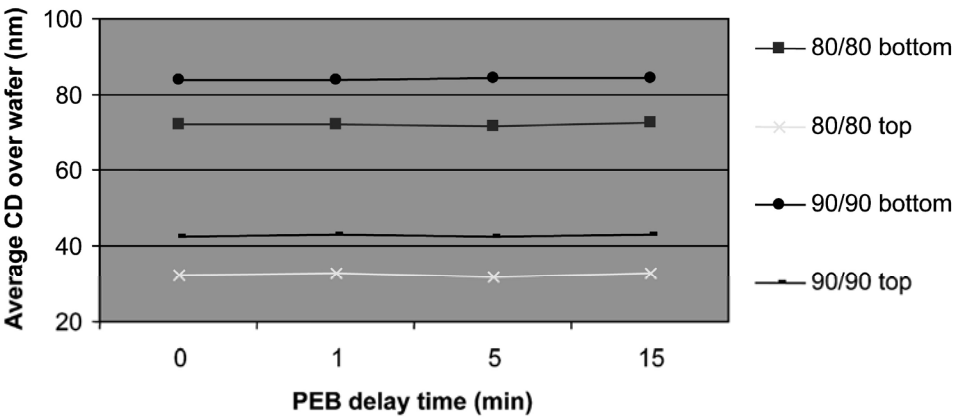

Figure 5.15 Measured average CD across the wafer versus PEB time delay. Because of the rounded tops of these resists, the CDs measured at the top of the lines are much smaller (25–42 nm) than the CDs near the bottom (75–85 nm). The topcoat prevents direct contact of amine with the resist film, leading to CD stability versus PEB delay.

The stack of 51-nm ArF1C5D (BARC), 230-nm JSR1682, and 30-nm TCX007 was selected for a design of experiments (DOE) exploring bake temperatures, with all other parameters kept constant. In addition to the bake temperatures recommended by vendors, the DOE matrix includes 5° C above and below the resist PAB and PEB temperatures, as well as 10° C above and below the topcoat PAB temperature (Fig. 5.16). Contrast curves were measured as a function of bake temperatures (Fig. 5.17(a)). The shape of the contrast curves appears to be highly sensitive to bake temperature, especially in the shoulder where the temperature combination of 105° C / 80° C / 110° C (PAB temperature of resist / PAB temperature of topcoat / PEB temperature) gives the smallest resist loss. Figure 5.17(b) shows the cross-sectional images of the resist patterns resulting from bake temperatures of 105° C / 80° C / 110° C and vendor-recommended temperatures (process of record (POR): 110° C / 90° C / 115° C). The resist pattern produced using the POR bake temperatures has about 10 nm more resist loss than that produced using bake temperatures of 105° C / 80° C / 110° C.

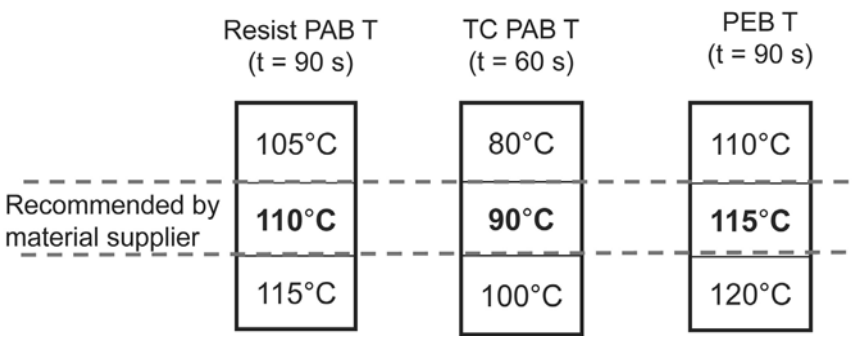

Figure 5.16 Bake temperature setting for the design of experiments.

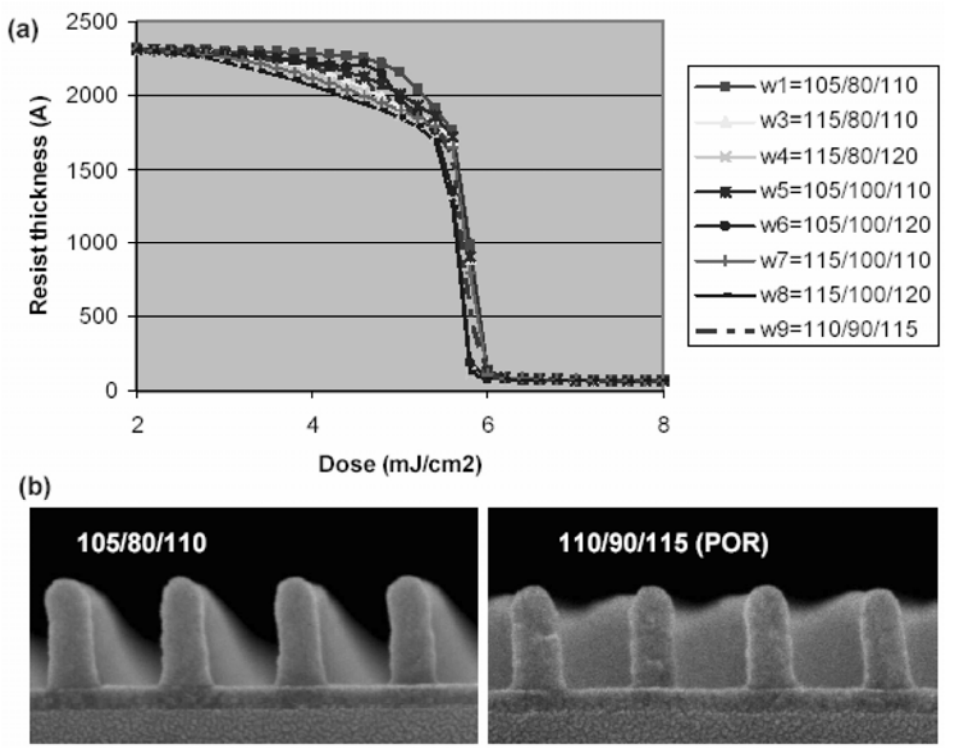

Figure 5.17 (a) Contrast curves measured at different bake temperatures. (b) Cross-sectional images of resist patterns processed at bake temperatures of 105° C / 80° C / 110° C and POR temperatures (110° C / 90° C / 115° C). Exposure conditions (illumination setting, NA, mask, dose, and focus) are the same for all of the wafers.

The optimized PAB temperatures for both the resist and the topcoat are lower than those recommended by the vendor (POR), while the PEB temperature remains the same. The reason the PAB temperatures needed to be decreased may have to do with PAG distribution within the resist. In the resist PAB step, thermal energy drives the resist solvent to the surface, where it evaporates, and part of the PAG in the bulk of the resist is also dragged to the resist surface by the movement of the solvent. During the topcoat PAB step, the resist solvent may further evaporate, causing additional PAG movement to the resist surface. The resist PAB temperature recommended by the vendor was originally optimized for dry 193-nm lithography; however, for the immersion process, the topcoat PAB is added. With POR temperatures, the resist is generally over-baked by the topcoat PAB. Thus, more PAG is moved to the resist and topcoat interface. High concentrations of PAG at the interface cause extra resist loss after exposure and development, as observed. In principle, the resist PAB temperature is the same as that of the dry lithography process, if the PAB of the topcoat can be omitted. However, this is not preferred, since the barrier performance of the topcoat decreases with decreasing bake temperatures.

5.4 193i Resists without Topcoats

Resist process without top protection coatings is thought to be the ultimate solution for 193-nm immersion lithography. This simplified process does not require the additional coat and bake steps required by the topcoat process; therefore, the cost of ownership and some sources of defects are reduced. In the early stages of the development of 193-nm immersion lithography, it was projected that the topcoat would play only a transitional role in the immersion process before low-leaching high-performance resists could be developed. The surface hydrophobicity requirements discussed previously for topcoats are also applicable to the 193i resist without topcoat. Similarly, other requirements such as high resolution, low defect counts, and etch selectivity must obviously be met in order for these more advanced resists to be useful in high-volume manufacturing.[13]

Table 5.2 provides a list of target values needed for 193i resists without topcoat. These values provide guidelines for the design of 193i resists; however innovation is the key to the successful development of high-performance 193i resists. Resist suppliers are actively pursuing the development of 193i resists capable of meeting all of these requirements.

5.4.1 Intrinsic topcoats: balancing immersion needs with high-resolution performance

The addition of self-segregating additives to photoresists is one interesting approach for converting dry resists into immersion resists. The additives are fluorine-containing compounds that are hydrophobic and have low surface energies. During coating and PAB, the hydrophobic compounds diffuse and

Table 5.2 Performance guidelines for 193i resist without topcoat.

Factors	Items	Recommended values	Comments
Surface hydrophobicity	Static CA	$>90^0$	To prevent the water leakage from the meniscus
	Receding CA	$>70^0$	
Leaching	Dynamic leaching rate	Meet the requirements of scanner suppliers	See, for example, Table 1 in Chapter 3
Defectivity	Defect count after coating	$<0.01/cm^2$	Totally ~50 defects per 300mm wafer
	Defect count with pattern	$<0.03/cm^2$	
Litho performance	Thickness	70-150nm	Meet the imaging requirements of 45nm hp node
	LWR	$3\sigma<2.4$nm	
	Resolution	~45nm hp	
Etch	Etch selectivity	Similar to current "dry" resist	

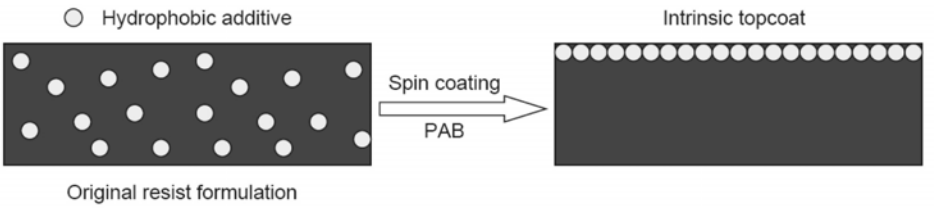

Figure 5.18 A sketched diagram of surface segregation forming intrinsic topcoat.

concentrate at the surface of the film (Fig. 5.18). The hydrophobic surface layer blocks leaching of resist component from bulk, and is therefore called an intrinsic topcoat.[14] This approach is based on the same concept as the polymer blending for topcoats approach, which was explained in Section 5.1.4

The advantage of the intrinsic topcoat approach is obvious. It offers a straightforward method for converting high-performance 193-nm dry resists into immersion resists. In principle, the simple addition of hydrophobic compounds to conventional dry resist should lead to the formation of intrinsic topcoats. These intrinsic topcoats should improve surface hydrophobicity and prevent leaching from the bulk without significant degradation of the original lithographic performance of the dry resists. This approach has attracted a lot of attention from resist suppliers.[15–20]

Typically, small amounts of additives (0.5–5 wt% of resist solids) are added to resist formulations. These additives must be soluble in resist solvents in order to form uniform solutions. Phase segregation occurs mainly during the spin-coating step.[10] Figure 5.19 shows significant reductions in leaching levels by the addition of compounds E or F. The leaching results are largely independent of PAB, suggesting that phase separation occurs in the coating step.

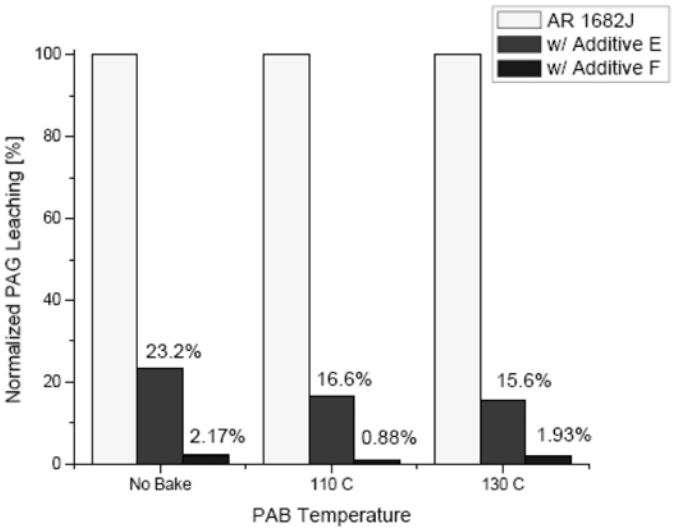

Figure 5.19 Leaching levels measured from 193-nm dry resist AR1682J with or without additives and baked at different temperatures. (Reprinted by permission from Ref. 10.)

The tendency for additives to segregate at the surface is highly dependent on the relative surface energies of the additives and the resist polymer; lower surface energy of the additives leads to better segregation. The concentration of additives versus depth can be determined using electron spectroscopy for chemical analysis (ESCA) by monitoring the fluorine peaks while sputtering.[17] Figure 5.20(a) shows the depth profile of fluorine measured from the resist film with various additives. The surface analysis shows that the fluoropolymer enrichment layer is only several nanometers thick. The static and dynamic contact angles of the resist film with these additives were also measured (Fig. 5.20(b)). Additive E shows the strongest tendency to segregate to the surface and produces the most hydrophobic resist surface.

It has been reported that fluorine additives can be as high as ~10 wt% of the resist polymer without degrading lithographic performance.[20] However, the gains in hydrophobicity of the resist surface begin to diminish at high additive

(a)

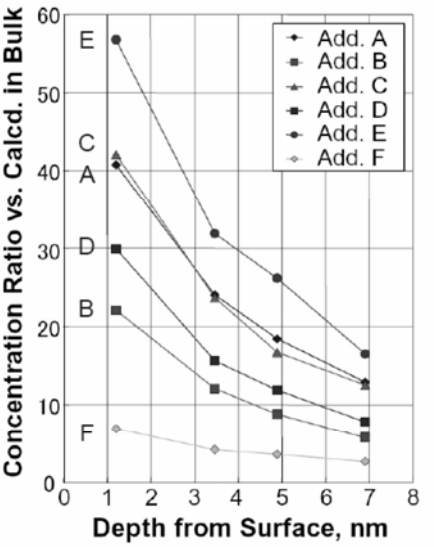

(b)

Additive	Static C.A.	Advancing C.A.	Receding C.A.
A	79.3°	89.2°	57.5°
B	70.6°	91.0°	34.1°
C	80.2°	89.6°	67.0°
D	79.7°	90.4°	62.9°
E	100.7°	103.0°	94.1°
F	69.0°	82.0°	44.0°
None	66.1°	78.5°	44.9 °

Figure 5.20 (a) Surface density of additives measured by ESCA analysis. (b) Static and dynamic contact angles of the resist films. (Reprinted by permission from Ref. 17.)

levels.[18,20] Similar behavior was observed for leaching tests. Figure 5.21 shows receding contact angles and leaching levels from resists as a function of additive loading. The chart demonstrates that with the increase of additives, the receding contact angles quickly become saturated and the leaching levels become leveled.

One of the difficulties arising from the use of self-segregating additives is that the resist surface may no longer be wet by the TMAH developer and the fluoropolymer additives may not be soluble in the developer. Typically, these additives have small dissolution rates in developer, leading to high blob defect counts. Selection of the right additives and optimization of their loading amounts are the keys to addressing this issue.

5.4.2 Resolution limits of resists

The resolution capability of a lithographic process depends on the resolution of the optics (described by the aerial image contrast) and the resist performance. The aerial image is projected onto the resist film during exposure, resulting in the generation of photoacids in the exposed areas. To activate the deprotection process, resists must be baked at elevated temperatures after exposure (PEB). High temperature increases the rate of acid diffusion and blurs the aerial image, leading to a loss in resolution. Acid diffusion length and exposure latitude are highly correlated, i.e., the longer the diffusion length, the narrower the exposure latitude.[21]

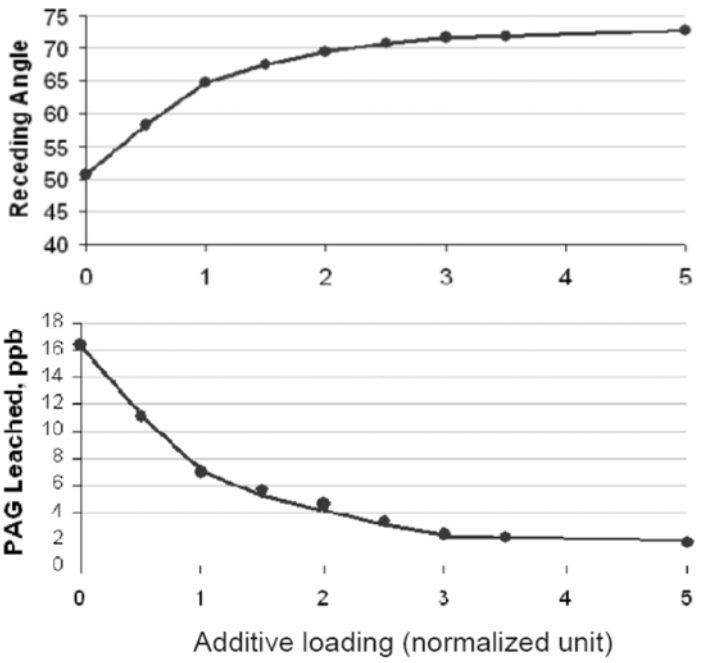

Figure 5.21 Receding contact angle and PAG leaching as functions of the additive loading in the resist. (Reprinted by permission from Ref. 18.)

The concentration profiles of the acids play important roles in determining the final profiles of the resist images. Yet, these concentration profiles change with time during the PEB bake, because they diffuse and are annihilated by the quencher base. The acid diffusion rates must be slower than the deprotection reaction so that the acid molecules can react with sufficient protecting groups before diffusing into regions of higher base. Therefore, the diffusion is a reaction-limiting step, in which Fick's diffusion law cannot be used.[22] In addition to bake temperature and quencher loading, the sizes of the acids and protecting groups also affect acid diffusion.[23] There are various methods for measuring the acid diffusion length.[24,25] In one such method, a resist is coated over a polymer film (without PAG) and the top resist film acts as an acid feeder layer. After exposure and PEB, the thickness loss of the bottom layer indicates how deep the acid diffuses. This thickness loss is correlated with acid diffusion length;[26] typically, ~10–40 nm of resist thickness is lost.[27]

Evidence from interferometric lithography (IL) at 193-nm immersion suggests that advanced chemically amplified resists can resolve 35- to 45-nm dense lines. Resist patterns with sub-45-nm half-pitch have been demonstrated with the 1.3NA immersion tool at exposure doses of 20–30 mJ/cm^2.[28] However, theoretical analysis predicts that acid diffusion will eventually prevent further resolution improvement, because the key lithographic performance parameters (line-edge roughness, photospeed, and resolution) are interdependent, meaning that one cannot be improved without sacrificing the performance of the others.[29]

References

1. M. Slezak, R. Hung, and Z. Liu, "Swing curve suppression," *Solid State Technology*, July 1, 2004.
2. R. Dammel, Anti-Reflective Coatings: Theory and Application, SPIE short course #118, 2007.
3. T. Kodama, T. Nakata, M. Fujimoto, M. Yamana, S. Nagahara, M. Miyasaka, T. Tamura, K. Yoshimochi, and T. Uchiyama, "Development of immersion lithography processes for 55-nm node device mass production," Presentation at 3rd International Symposium on Immersion Lithography, Kyoto, Japan, Oct. 2006.
4. T. A. Brunner and N. Seong, "High numerical aperture lithographic imagery at the Brewster angle," *J. Microlitho. Microfab., Microsyst.*, **1**, 188 (2002).
5. K. Petrillo, K. Patel, M. Slezak, and G. Dabbagh, "Formulating materials that are compatible with high-performance immersion lithography," *Micro Magazine*, July 2005.
6. K. Petrillo, R. Housley, P. Benson, F. Goodwin, Y. Wei, S. Brandl, and B. Martinick, "Topcoat compatibility studies: What you wanted to know about resist–topcoat compatibility but were afraid to ask," Presentation at the SEMATECH 2nd 193nm Immersion Symposium, Brugge, Belgium, Sept. 14, 2005.

7. T. Ando, S. Maemori, S. Yokoi, T. Takayama, K. Ishizuka, T. Hirano, J. Yokoya, and K. Ohmori, "Synthesis of topcoat process for 193nm immersion lithography: a progress report," Presentation at 3rd International Symposium on Immersion Lithography, Kyoto, Japan, Oct. 2006.
8. V. Q. Pham, N. Rao, and C. K. Ober, "Swelling and dissolution rate measurements of polymer thin films in supercritical carbon dioxide," *J. Supercritical Fluids*, **31**, Issue 3, Nov. 2004, 323–328.
9. N. Shirota, Y. Takebe, T. Sasaki, S.-Z. Wang, and O. Yokokoji, "Development of new materials based on fluoropolymers for 193-nm immersion lithography," Presentation at 3rd International Symposium on Immersion Lithography, Kyoto, Japan, Oct. 2006.
10. D. Sanders, L. Sundberg, H. Ito, P. Brock, R. Sooriyakumaran, H. Truong, and R. Allen, "New materials for surface energy control of 193 nm photoresists," Presentation at 4th Immersion Symposium, Keystone, Colorado, 2007.
11. D. P. Sanders, L. K. Sundberg, P. J. Brock, H. Ito, H. D. Truong, R. D. Allen, G. R. McIntyre, and D. L. Goldfarb, "Self-segregating materials for immersion lithography," *Proc. SPIE* **6923**, 692309 (2008).
12. Y. Wei, K. Petrillo, S. Brandl, F. Goodwin, P. Benson, R. Housley, and U. Okoroanyanwu, "Selection and evaluation of developer-soluble topcoat for 193nm immersion lithography," *Proc. SPIE* **6153**, 615306 (2006).
13. S. Mimotogi, F. Uesawa, M. Tominaga, H. Fujise, K. Sho, M. Katsumata, H. Hane, A. Ikegami, S. Nagahara, T. Ema, M. Asano, H. Kanai, T. Kimura, and M. Iwai, "Performance of immersion lithography for 45nm-node CMOS and ultra-high density SRAM with 0.25μm^2," *Proc. SPIE* **6520**, 652008 (2007).
14. L. K. Sundberg, D. P. Sanders, R. Sooriyakumaran, P. J. Brock, and R. D. Allen, "Contact angles and structure/surface property relationships of immersion materials," *Proc. SPIE* **6519**, 65191Q (2007).
15. K. Sasaki, T. Nakamura, T. Hirayama, H. Shimizu, Y. Utsumi, T. Hirano, M. Irie, K. Endo, T. Yamada, N. Motoike, K. Oshita, and K. Omori, "Defect reduction with topcoat less photo resist for 193nm immersion lithography," Presentation at ISIL2006.
16. M. Padmanaban, G. Lin, S. Chakrapani, T. Kudo, and R. Dammel, "Recent advances in 193nm resists for dry and wet applications," 4th International Immersion Symposium, Keystone, Colorado, Oct. 11, 2007.
17. K. Wada, S. Kanna, and H. Kanda, "Novel materials design for immersion lithography," *Proc. SPIE* **6519**, 651908 (2007).
18. S. Wu, A. Tseng, B. Lin, C. C. Yu, B.-J. Lu, W.-S. Liao, D. Wang, V. Vohra, C. B. Xu, S. Caporale, and G. Barclay, "Non-topcoat resist design for immersion process at 32-nm node," *Proc. SPIE* **6923**, 692307 (2008).
19. N. Shirota, Y. Takebe, S.-Z. Wang, T. Sasaki, and O. Yokokoji, "Development of non-topcoat resist polymers for 193-nm immersion lithography," *Proc. SPIE* **6519**, 651905 (2007).

20. I. Takemoto, N. Ando, K. Edamatsu, Y. Fuji, K. Kuwana, K. Hashimoto, J. Funase, and H. Yokoyama, "Tailoring surface properties of ArF resists thin films with functionally graded materials (FGM)," *Proc. SPIE* **6519**, 65191X (2007).
21. S. A. Robertson, S. Yamada, and J. M. Leonard, "Fundamental parameter extraction for a dry/immersion hybrid photoresist for contact hole applications," *Proc. SPIE* **6153**, 615312 (2006).
22. C. A. Mack, "The lithography expert: diffusion and resolution," *Microlithography World*, May 2006.
23. T. Kawakami, T. Nagai, Y. Nishimura, M. Shima, S. Kusumoto, and T. Shimokawa, "Various factors of the image blur in chemically amplified resist," *Proc. SPIE* **6519**, 65193K (2007).
24. Y. Kishikawa, M. Kawashima, A. Ohkubo, Y. Iwasaki, S. Takeuchi, M. Yoshii, and T. Honda, "Assessment of trade-off between resist resolution and sensitivity for optimization of hyper-NA immersion lithography," *Proc. SPIE* **6520**, 65203L (2007).
25. C. Grant Willson, "Chemically amplified resist resolution," Presentation at 2006 Litho Forum, Vancouver, BC.
26. J. H. Kim, C. H. Lee, S. B. Park, W. M. Kim, S. S. Moon, K. M. Kim, S. Y. Lee, S. Yoon, Y. H. Kim, and S. M. Chon, "Influence of activation energy on LER in chemically amplified KrF photoresists," *Proc. SPIE* **5376**, 790–800 (2004).
27. T. Honda, Y. Kishikawa, Y. Iwasaki, A. Ohkubo, M. Kawashima, and M. Yoshii, "Influence of resist blur on ultimate resolution of ArF immersion lithography," *J. Microlith., Microfab., Microsyst.* **5**, No. 4, 043004 (2006).
28. E. C. Piscani, S. Palmer, and C. Van Peski, "Demonstration of sub-45nm features using azimuthal polarization on a 1.30NA immersion microstepper," *Proc. SPIE* **6520**, 652025 (2007).
29. G. M. Gallatin, "Resist blur and line edge roughness," *Proc. SPIE* **5754**, 38–52 (2005).

Chapter 6
Immersion Defects and Defect-Reduction Strategies

Defectivity is the most important issue yet to be resolved in order to move 193i lithography into high-volume manufacturing. Typically, unoptimized 193i processes have 4–20% more defects than dry 193-nm processes have. Defects can be introduced by the scanner, the track, the materials, or the process. In general, sources of defects that are present in dry 193-nm lithographic processes are also present in immersion 193i lithography. For example, coating defects introduced during BARC and resist coating processes are commonly observed in both dry and immersion 193-nm lithography. Optimized 193-nm dry processes can serve as starting points for 193i processes.

Unfortunately, however, immersion processes introduce additional sources of defects. During exposure, the immersion water may contain particles or insoluble compounds that can be deposited onto the wafer, forming defects. Bubbles in the water can scatter the exposure light, distorting the aerial images and forming bubble defects in the resist pattern. Topcoats can also introduce additional material-related defects, including particles from the topcoat itself or microbridges caused by intermixing problems between resist and topcoat layers.

Defects can also be introduced by the wafer edge. Resist or topcoat films at the edge of the wafer can peel off to generate particles. These particles may be brought to the wafer center by the movement of the immersion exposure head. Watermark defects are generated by water leakage from the meniscus and are unique to the 193i process. This chapter focuses on these immersion-related defects. The formation mechanism of each defect type is analyzed with the help of simulation and experimental results. A series of defect reduction methods are proposed based on these defect mechanisms.

6.1 The Basics of Defect Detection

After the lithographic process, the desired patterns must be printed in all locations, faithfully reproducing the mask pattern. Any deviations from the desired patterns are called defects. Examples of defects include missing pattern segments, pattern scum, and particles. Defect detection includes the use of optical microscopes, scanning electron microscopes (SEMs), and die-comparison

techniques. In general, the wafers are loaded into the defect inspection tools, then the microscopic images of each die are obtained and compared. These images should be identical. Any inconsistent spots are indicative of possible defects. The positions of these defects in the wafer are recorded by the tool, forming a defect map. This step is called defect inspection. The defect map is transferred to a high-resolution SEM, where each defect can be inspected and/or chemically analyzed. This step is called the defect review, during which defects are categorized based on their shapes and sizes. The defect density is the total number of defects divided by the area of inspection. Continuous improvement in the resolution and accuracy of defect-detection technology to keep up with each lithographic node is a challenge to the defect-metrology community.[1] Detailed descriptions of the configuration and function of defect-detection equipment is beyond the scope of this book.

6.1.1 ITRS defectivity requirements

The detection limit of defect sizes is usually set to about 60% of the half-pitch of each technology node. This means that defect sizes smaller than ~60% of the half-pitch are considered to have negligible effects on lithographic yields.

Table 6.1 lists the defect detection limits and defect count specifications for various technology nodes recommended by the ITRS.[2] For each technology node, targets are set for minimum defect size and maximum allowable defect counts. These two numbers are set both for resist-coated wafers without exposure (coating defects) and for patterned resist film (patterned defects). Typically, the patterned defect counts are higher than the coating defect counts because the additional process steps that occur after resist coating introduce additional defects.

With the shrinkage of technology nodes, the pattern sizes become smaller and the pattern density increases. Thus, the miniaturized defects that could be neglected in previous nodes must be addressed. High-sensitivity defect inspection tools must be developed for these defect applications.

Table 6.1 Recommendations for defect detection limits and defect counts for various technology nodes.[2]

DRAM half-pitch node (nm)	80	70	65	57	50	45	40	36
Flash half-pitch node (nm)	76	64	57	51	45	40	36	32
Logic half-pitch at M1 level (nm)	90	78	68	59	52	45	40	36
Defects in spin-coated resist film (#/cm^2)	0.01	0.01	0.01	0.01	0.01	0.01	0.01	0.01
Minimum defect size in spin-coated resist film (nm)	50	45	40	35	30	30	20	20
Defects in patterned resist film (#/cm^2)	0.05	0.04	0.04	0.03	0.03	0.03	0.02	0.02
Minimum defect size in patterned resist film (nm)	50	45	40	35	30	30	20	20

6.1.2 A systematic approach for identifying the sources of defects in the immersion process

Most immersion processes are modifications of established dry processes. The starting dry baseline process must be stable and optimized for low defect counts. The immersion process deviates from the dry process beginning with the coating of the topcoat. Thereafter, the PAB, the immersion exposure, the topcoat removal, and the development are all steps that differ from the dry process steps and can lead to additional sources of defects. Therefore, a systematic approach for investigating immersion-related defects is to inspect the wafer after each of these new immersion-related process steps (Fig. 6.1).[3] By comparing results, it is possible to identify the defects introduced during a specific process step. The defect review yields the SEM images of the defects, providing information about the mechanism of their formation.

6.1.3 Particle per wafer pass test

The particle per wafer pass (PWP) test is a routine method for evaluating the cleanliness of the immersion scanner. In this test, a blank wafer with very low defect counts (premeasured) is sent through the immersion track and scanner without a pattern exposure. After cycling through the immersion tool, the wafer

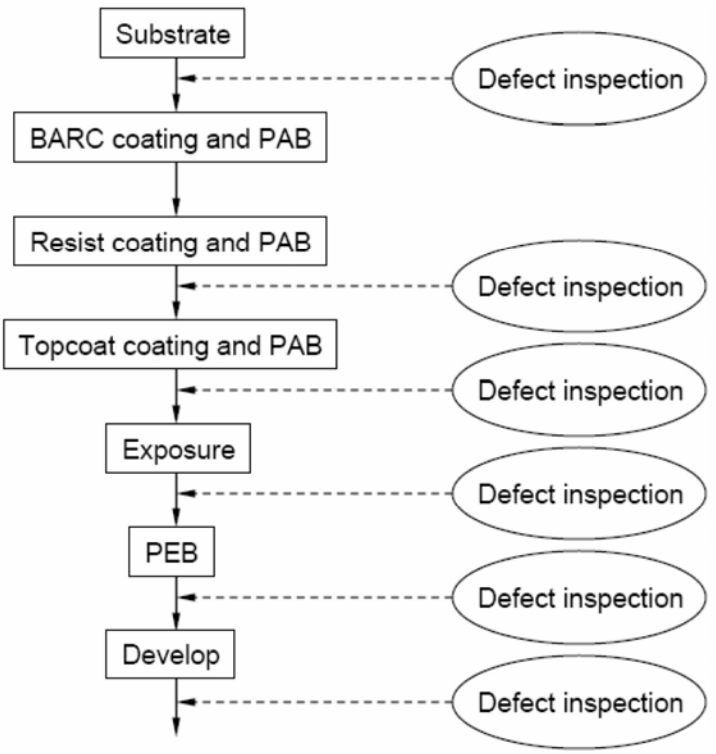

Figure 6.1 Defect inspection is placed after each process step for defect monitoring.

is inspected for defects. This test determines if the immersion head adds any defect patterns to the wafer. The defect maps resulting from several PWP tests are averaged to yield defect maps with good signal-to-noise ratio.

6.2 Quality of the Immersion Water

The immersion water is in direct contact with the wafer during exposure, therefore its quality affects the defect counts of the wafers. In general, immersion water must be bubble-free and extremely clean. Bubbles in the water can reflect and refract exposure light, leading to distortion of the aerial image. Any particles or unwanted chemicals in the water may either deposit on the wafer or react with the resist, causing increased defect counts.

To meet purity requirements, standard clean-room deionized water (DIW) with high resistivity (> 18.2 MΩ-cm) must be further purified before it can be used in the scanner. The further treatment includes ultrapure (UP) DIW polishing and conditioning. The schematic of the water treatment system is shown in Fig. 6.2 and consists of filters, temperature control units, degassing units, and UV light exposure units. Filtration removes particles larger than 30 nm. The degassing unit reduces the concentration of dissolved gases to suppress bubble formation. Oxygen content in the water is reduced from its room-temperature saturation value of ~10 ppm to < 70 ppb.[4]

UV light kills bacteria. Organics in the DIW must be reduced from the incoming parts-per-billion (ppb) levels to parts-per-trillion (ppt) levels.[5] Otherwise, the organics will deposit on the lens, causing haze and impairing lens performance. In addition, organics can absorb 193-nm light from the stepper, causing defects. The output water from the purification system has a resistivity of > 18 MΩ-cm, elemental contamination of ppt levels on anions and cations to below 10–30 ppt, and total oxidizable carbon (TOC) < 50 ppt. To prevent bacterial growth in the water supply line, the system must also be periodically sanitized.

Water flow is computer controlled to deliver a stable flow of deionized water to the illuminated area. The movement of water must be optimized to prevent the attachment of bubbles to the wafer or the lens. The temperature control unit stabilizes the water temperature to a target temperature of 20.5° C, with an accuracy of < 0.01° C.[5] In order to control water flow, each scanner has a unique set of specifications that are optimized specifically for the design of each exposure head.[6]

Figure 6.2 Schematic of the immersion water treatment system.

6.3 Appearance of Bubble Defects

Bubble defects are caused by air bubbles in the immersion water and act as small lenses during exposure. They change the local aerial image and cause pattern distortion in the surrounding areas. Figure 6.3(a) shows a bubble attached to a resist surface and Fig. 6.3(b) shows a bubble suspended in the immersion water. The bubbles scatter the aerial image, forming circularly shaped defects in the final resist pattern.

6.3.1 Simulation results

Systematic experiments with bubble defects are difficult to perform, since there is no particular method for positioning a bubble on a resist surface to see what the defect pattern looks like. Thus, simulation is the best way to predict the shape and fine structures of the bubble defects. The quantitative relationships between bubbles and imaging have been simulated by various groups[7,8] whose results provide information helpful in identifying bubble defects on exposed wafers.

6.3.1.1 Floating bubbles

Because the refractive index of air is less than that of water, the air bubble floating in the immersion water functions as a divergence lens, as sketched in Fig. 6.3(b). At certain angles, the exposure light is totally reflected at the surface of air bubble. Figure 6.4 shows the scattered light distribution of air bubbles with diameters of 2, 1, and 0.5 μm.[7] The light beam shines on the air bubble with an intensity of I_0. The bubble scatters the light and forms fringes in the forward direction (Fig. 6.4(a)). The fringes projected on the resist surface are symmetrical in the lateral direction. The main feature to note is that the light intensity is attenuated directly beneath the bubble. As the bubble size decreases, the scattered irradiance in the forward directions becomes more uniform.

To verify the effectiveness of these simulations, polystyrene spheres have been used to mimic air bubbles in the immersion water of an interference lithography system.[7] It was found that the overall impact of a floating bubble on the image depends on its distance from the resist surface—the larger the

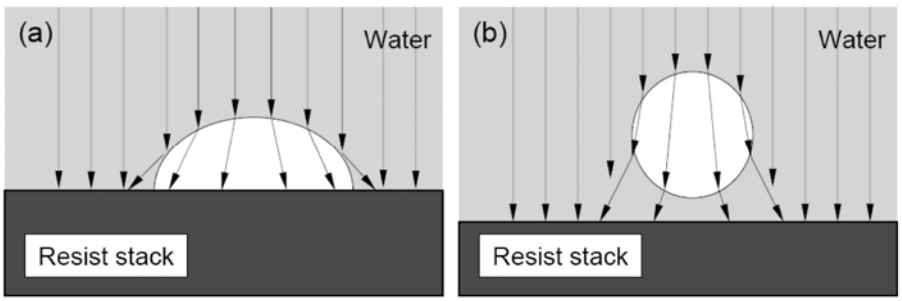

Figure 6.3 Air bubble (a) on the resist surface and (b) floating in the immersion water. The bubble acts as a lens during exposure.

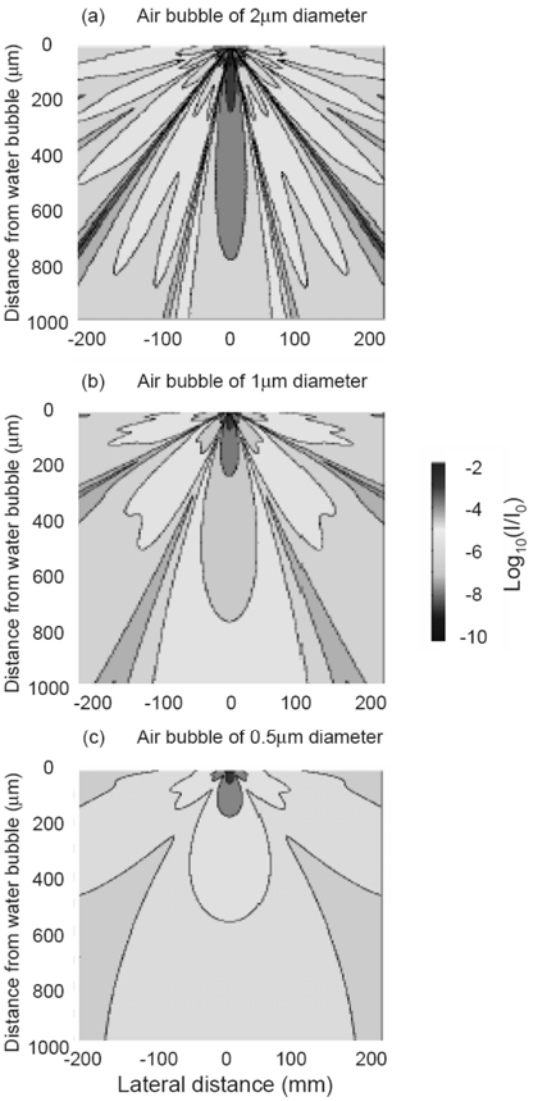

Figure 6.4 Distribution of scattered light intensity by air bubbles with diameters of (a) 2 μm, (b) 1 μm, and (c) 0.5 μm. (Reprinted by permission from Ref. 7.)

distance, the weaker the impact. Neither 2- nor 0.5-μm polystyrene spheres positioned > 0.3 mm away from the resist produced images. These results suggest that small free-floating air bubbles in the immersion water do not cause imaging defects.

In full-field immersion scanners, the wafer scan speed is about 500 mm/s during exposure. Air bubbles in the water are almost static during exposure, while the wafer passes quickly underneath. The fast wafer movement and constant water flow reduce the shadow effect of the floating bubble on the resist

surface. According to fluid dynamics, free-floating bubbles have very short lifetimes. However, due to surface confinement, the lifetimes of air bubbles attached on the resist surface may be longer. Therefore, air bubbles attached to resist surfaces pose much greater threats to defect-free imaging.

6.3.1.2 Bubbles attached to the resist surface

The effects of bubbles attached to resist surfaces have been simulated.[8] Figure 6.5 shows the results of this study as a grayscale plot of scattered light intensity. The bubble is 400 nm in diameter and the exposure pattern is 100-nm dense lines.

The most noticeable effect is the reduction of image intensity in the resist-surface plane under the bubble. From the center to the edge of the bubble, the image intensity gets lower. Even if there is an underexposed (but printed) line/space (L/S) pattern in the central area of the bubble, one could expect that at the edge, the L/S pattern would be completely missing. The bubble also seems to have some 'magnifying' effect on the incident L/S pattern, which leads to a distortion in the center of the bubble defect. Outside of the bubble, the imaging intensity is increased at certain locations.

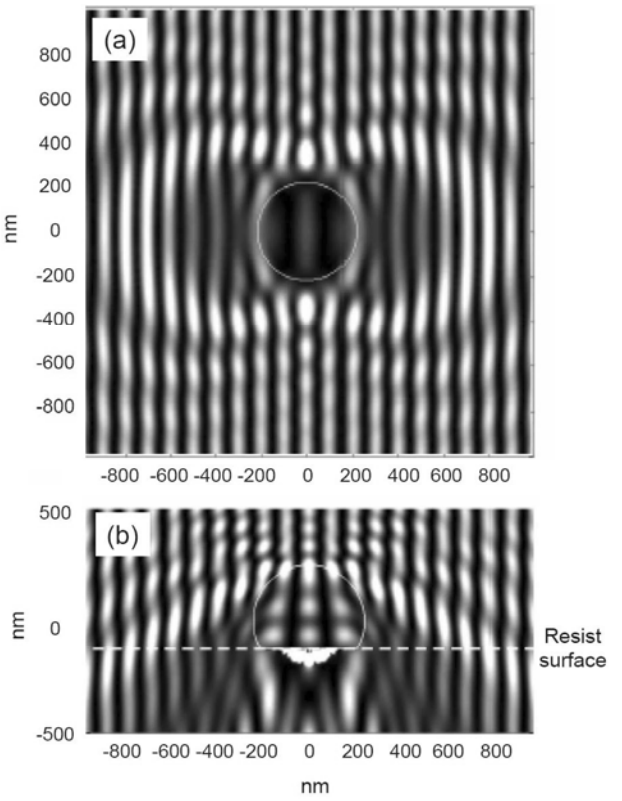

Figure 6.5 Aerial image of 100-nm dense lines in the vicinity of an air bubble. The air bubble is 400 nm in diameter. (a) Intensity at the resist surface. (b) Intensity profile view. (The dotted straight line labels the resist surface.) (Reprinted by permission from Ref. 8.)

6.3.1.3 Shape effect of the attached bubble

The bubbles attached to the resist surface may have a range of different shapes, from "curved" to "flat." A bubble model was built to investigate how the shape of the bubble affects the aerial images (Fig. 6.6).[8] The bubble is semispherical with a diameter of D and is attached to the resist surface with a height of H ($D > H$). The ratio of H/D defines the shape of the bubble. Another parameter is W, which defines the size of the bubble projected on the resist surface.

Figure 6.7 shows the simulation results of bubbles with W = 500 nm and H/D = 3/4, 1/2, and 1/4. The gray circles indicate the edge of the bubble on the resist surface. The reduction of the image intensity under the bubble becomes less severe as the bubble becomes flatter (from H/D = 3/4 to H/D = 1/4). For the 3/4 bubble, the unprinted area is larger than the actual (lateral) size of the bubble. For the 1/2 bubble, the unprinted area more or less corresponds to the area of the bubble on the resist surface. In the 1/4 bubble, there is some imaging 'under' the bubble, even though the image is significantly underexposed. Outside of the area covered by the bubble, some of the lines are actually overexposed with bright white spots around the bubble.

If the bubble is small and trapped between two resist lines, it causes a reduction in image intensity, resulting in resist scumming in the space area beneath the bubble. This may cause microbridge defects. With an increase in the diameter of the bubble, the impact on imaging increases. Simulation shows that 80-nm diameter bubbles positioned over 100-nm 1:1 dense patterns can cause the spaces not to clear.[8] These simulations provide insight useful for distinguishing between circularly shaped defects caused by bubbles and circularly shaped defects caused by other sources of defects.

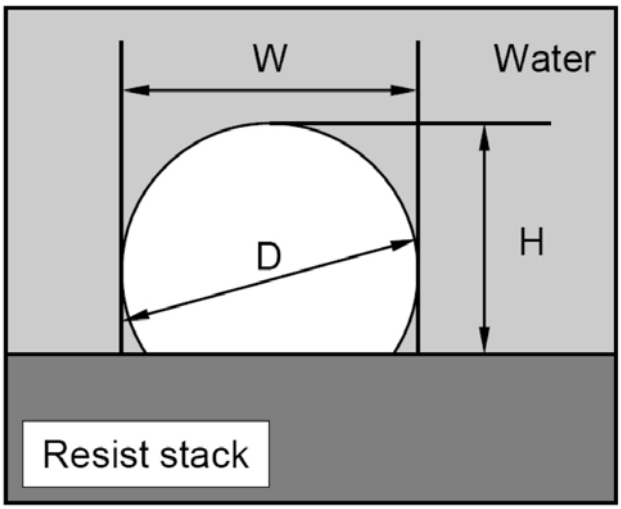

Figure 6.6 The shape of the bubble is defined by D (diameter), H (height), and W (lateral size of the bubble projected on the resist surface).

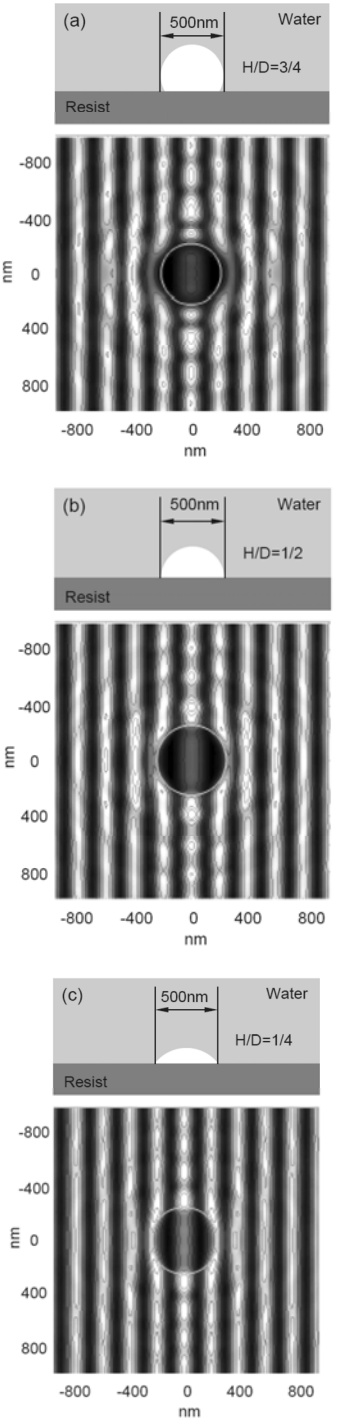

Figure 6.7 Simulation results of bubbles with different curvatures. The size of the bubbles projected on the resist surface is 500 nm with (a) *H*/*D* = 3/4, (b) *H*/*D* = 1/2, and (c) *H*/*D* = 1/4. (Reprinted by permission from Ref. 8.)

6.3.2 Bubble defects observed in resist patterns

In our experimental work, we found that bubble defects can have diameters as large as 10–20 μm. Figure 6.8 shows a typical bubble defect on a line and space pattern. The bubble is circular with a diameter of about 9 μm. As predicted by simulation, the bubble causes underexposure in the local area. In the center of the defect, image modulation is visible, but the pitch of the dense line/space is 308 nm (Fig. 6.8). This amplification ratio is ~1.4 (the target pitch of the dense line/space is 220 nm). From the center moving to the edge, the image modulation diminishes until it disappears at the edge of the bubble. Another interesting feature of bubble defects is that they tend to be symmetrical. In Fig. 6.8, the defect is symmetrical in the X and Y directions; at the left and right edge (circled areas), residuals of the resist lines have the same shape.

In general, the areas surrounding the bubble defect are overexposed. Looking closely, intensity fringes can be observed outside the circularly shaped defect (Fig. 6.9(a)). Surrounding the defect, the resist is completely developed, making the edge of the bubble defect very sharp and clear. A short distance from the edge, the resist line appears, indicating a lower local dose. Moving farther away, the resist line gets narrower, indicating a higher local dose, as labeled in Fig. 6.9(a).

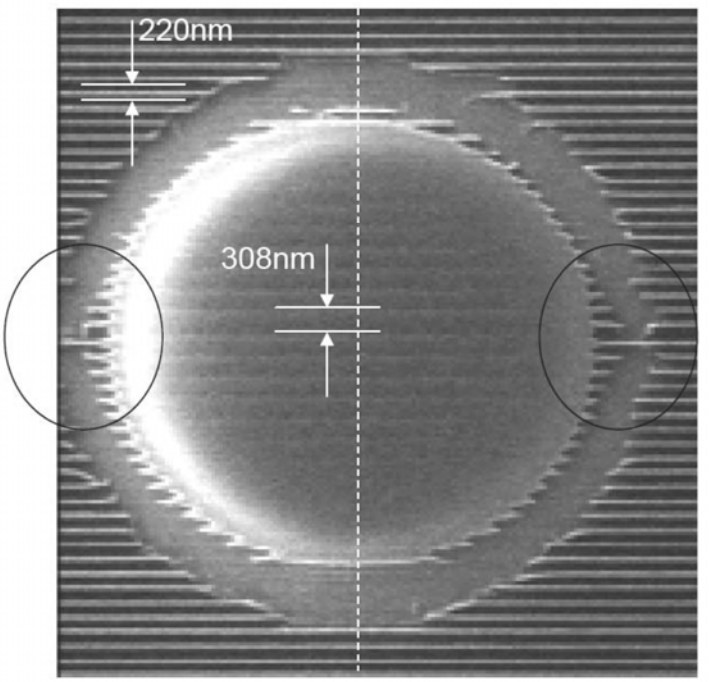

Figure 6.8 SEM image of a big bubble defect with a diameter of about 9 μm. The bubble defect is symmetrical in the X and Y directions. At the left and right edge (the circled areas), residuals of the resist lines have the same shape. The pitch of the line/space pattern is 220 nm in all images.

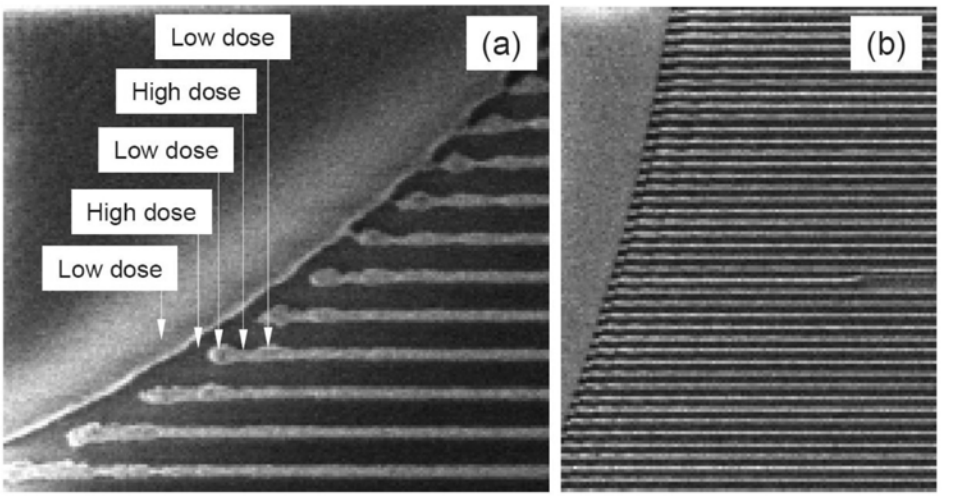

Figure 6.9 SEM images taken at the edge of bubble defects with (a) high magnification and (b) low magnification. The pitch of the line/space pattern is 220 nm in all images.

The resist line-width variation shows spatial periodic behavior, which corresponds to dose modulation. Yet farther from the defect, the dose modulation gets weaker and finally becomes invisible. The fringe pattern caused by dose modulation can be better observed at low magnification (Fig. 6.9(b)). Obviously, the dose modulation is derived from the effect of the bubble on the exposure light.

Conceptually, this redistribution of light by the bubble can be considered in terms of energy conservation. The total exposure energy in and around the bubble defect can be thought of as a constant that equals the average dose × area of the region. The light striking the bubble is diffracted so that the intensity beneath the bubble is decreased and the intensity around the bubble is increased.

A straightforward method for identifying bubble defects is to print wafers with open fields using doses that are slightly below or slightly above the dose-to-clear E_0 of the resist. For the lower dose ($< E_0$), the bubble will scatter the light so that the dose surrounding the bubble will be larger than $E_{0,}$ the bubble, thereby, showing itself as a cleared ring in the resist. Conversely, if the exposure dose is slightly above E_0, the bubble will manifest as a circular resist island.

From our experience with defect inspection, bubble defects with diameters > 2 μm are relatively easy to identify, since the imaging modulation is clear, leaving ample information on the resist pattern. The challenge is to identify small bubble defects, as the reflection and refraction of exposure light by small bubbles is much less distinctive than it is by big bubbles. Therefore, the features described in previous paragraphs are not clearly visible in circularly shaped defects generated by small bubbles. A defect caused by a 100-nm bubble may appear to be a small bridge connecting two resist lines.

6.4 Origins of Bubbles

Bubbles in immersion water scatter the exposure light and generate defects in the resist film. The best way to reduce bubble defects is to reduce bubbles suspended in the water as well as bubbles attached to the surface of the resist. Incomplete degassing of water in the supply system and poor exposure head design can lead to bubbles forming in the water during exposure. Outgassing of the resist stack can also generate bubbles.

6.4.1 Bubbles from the water supply

Bubble formation occurs when gas-saturated water shifts to a state of over-saturation, due to changes in pressure or temperature. This mechanism suggests that degassing should be an efficient method for preventing bubble formation. Liquid handling systems must be carefully designed to avoid creating air bubbles by leaking air into the system or by outgassing from the materials of manufacture.

6.4.2 Outgassing of resist during exposure

Outgassing of the resist during exposure is a process that has been known for many years and is still under investigation.[9] In general, the decomposition of both polymer protecting groups and photoacid generators during exposure can result in the formation of volatile compounds. Experiments were conducted to determine if bubbles were formed as a result of resist outgassing.[10] Resist-coated wafers were exposed in water using 2–20 mJ/cm^2 193-nm light and inspected immediately with a high-resolution CCD camera to search for bubbles (Fig. 6.10). No bubble formation was observed.

These results suggest that exposure-induced outgassing from typical 193-nm resists should not be the source of bubbles in the immersion water. Perhaps the amount of outgassing is small or the outgassed components are water soluble. Nonetheless, bubble formation from 193-nm outgassing should be considered a real possibility, as high-outgassing 248-nm resists have been shown to create bubbles during immersion exposure conditions. Careful selection of low-outgassing resists should help to avoid the formation of bubbles during exposure.

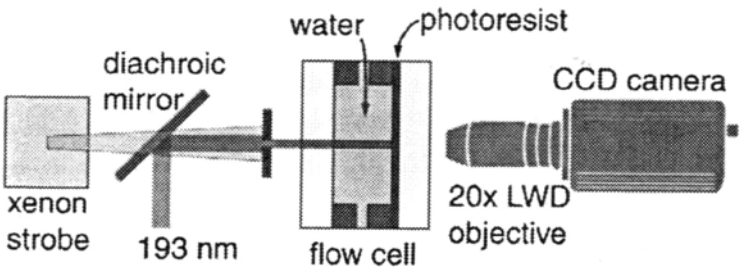

Figure 6.10 Schematic setup of bubble-imaging experiment. The camera is focused through the rear window of the cell on the resist–water interface. (Reprinted by permission from Ref. 10.)

6.4.3 Entrapment of bubbles on the wafer surface

The water meniscus moves with the exposure head on the wafer surface from die to die. The movement distorts the water meniscus, forming advancing and receding contact angles. Due to this movement, the advancing contact angle is bigger than the static contact angle. It was suspected that bubbles could be entrained by the moving wafer at the three-phase liquid–wafer–ambient interface (Fig. 6.11). Observation of water droplets on tilted wafers suggests that water droplets can either slide or roll across surfaces.[11] Rolling tends to occur on hydrophobic surfaces that are more likely to entrap bubbles, while sliding tends to occur on hydrophilic surfaces. Additionally, water uptake (swelling) in the resist film is also related to the tendency to entrap bubbles;[11] increased water uptake generally leads to decreased bubble entrapment. However, increased water uptake also introduces other issues, for example watermark defects.[12]

Researchers further suspected that ridges or trenches in the resist may also trap bubbles as the liquid flows over them. The movement of the water meniscus across topography was simulated,[13–15] and it was found that bubble formation occurs only for extreme geometries and flow conditions. Manufacturing scan speeds, contact angles, and feature profiles are anticipated to be well within these extreme ranges and bubbles should not be formed.[13] Experiments with etched substrates (1-μm wide and 0.5-μm deep trenches) verified the simulated results, since no bubble entrapment on the topographic surface was observed using a model immersion head.[14]

Bubble formation on topographic wafers was experimentally investigated using a full-field immersion scanner.[15] Wafers with typical logic and DRAM patterns were used in the tests. Both bare Si and SiO_2 wafers were tested. The total number of bubbles and the cross-wafer distribution of bubbles were the same for flat and topographic wafers. Wafer maps showed that bubbles were concentrated near the edges of wafers and that the edge effects were much greater than the effect of topography. These results suggest that surface topography plays a negligible role in the formation of bubbles.

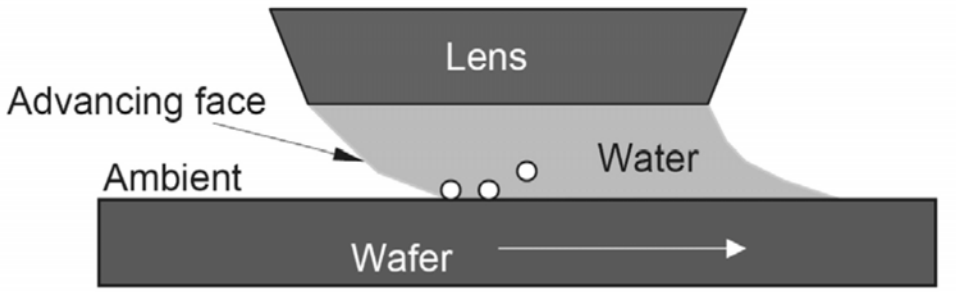

Figure 6.11 Bubbles can be entrained by the moving wafer at the three-phase liquid–wafer–ambient interface.

6.4.4 Exposure head design

In addition to the bubble sources previously discussed, bubbles can be introduced by poorly designed exposure heads that can cause turbulence and entrap bubbles. Air flow used to confine the water meniscus may also inject bubbles into water. In order to reduce the creation of bubble defects, scanner suppliers have created new designs that they claim are bubble-free.[16,17]

6.5 Defects Caused by Transparent Particles and Blisters

Because the refractive index of air (~1.0) is smaller than that of water (~1.44 at 193 nm), air bubbles act as divergent lenses, causing the areas beneath the bubbles to be underexposed. As previously explained, air-bubble defects appear as circular underexposed regions in the resist pattern. However, overexposed regions with circular shapes are often observed in 193-nm immersion resist patterns. Figure 6.12 shows SEM images of two circularly shaped overexposed regions. The defects have diameters of about 550 nm in Fig. 6.12(a) and about 1.65 μm in Fig. 6.12(b).

Careful inspection of Fig. 6.12 reveals that the resist lines surrounding the overexposed areas are a little wider than the nondefect areas (underexposed ring between the white circles). In addition, the resist lines in the defect area in Fig. 6.12(b) shift toward the center. These defects are sometimes called antibubble defects because their appearance seems to be opposite to that of bubble defects. Figure 6.13 shows another SEM image of the antibubble defect with dotted lines added to show the center of the outside lines. While the center resist line aligns well with the resist line outside of the defect (labeled by a thick dotted line in Fig. 6.13), the upper portion of the resist lines shifts downward toward the center, while the lower portion of the resist lines shifts upward toward the center. It

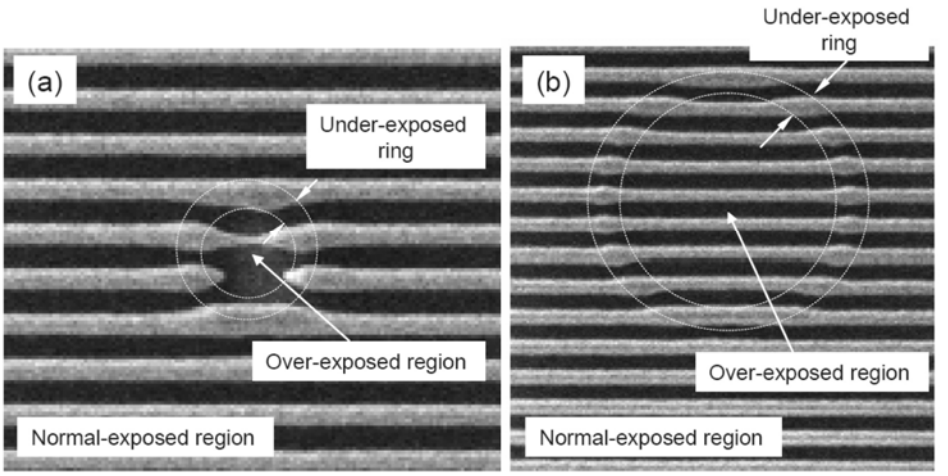

Figure 6.12 SEM image of a circularly shaped overexposed region: the “antibubble” defect. The white dotted circles are added to the images to outline the shape of the defects. The pitch of the dense lines is 220 nm.

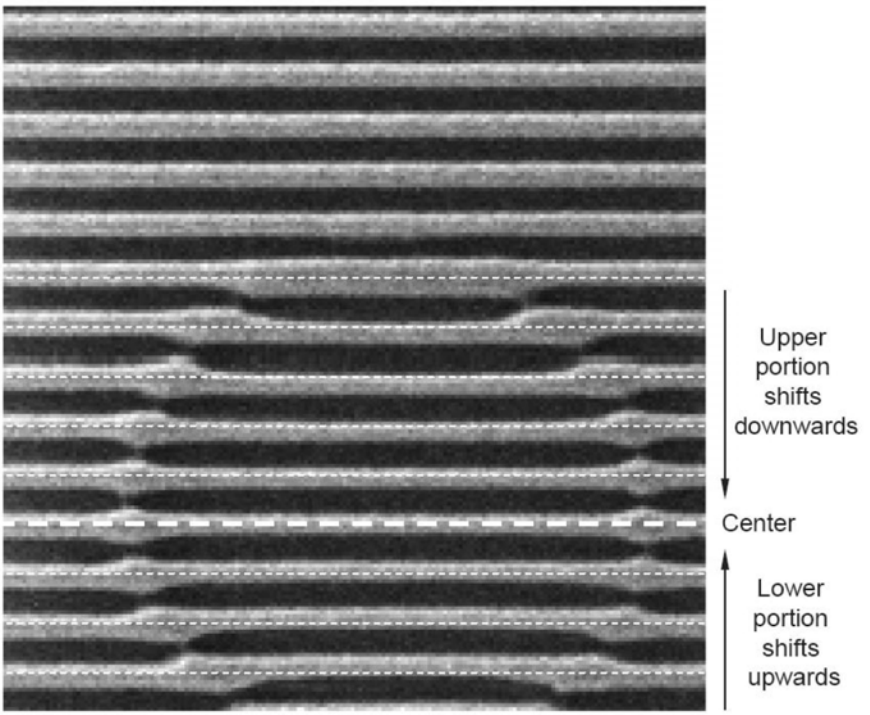

Figure 6.13 SEM image of antibubble defect with dotted lines added to the figure to serve as references.

appears that the distance the line shifts is proportional to the line's distance from the center. These antibubble defects are not watermarks. As will be explained in the next chapter, water droplets left on the resist surface will reduce the local resist sensitivity, resulting in T-topping.

6.5.1 Formation of antibubble defects

The antibubble defect can be caused when an extraneous piece of resist or topcoat is deposited on the resist or topcoat film surface. These particles are typically transparent to 193-nm light and act as microlenses during exposure. Since the refractive index of resist (n ~1.7) or topcoat (n ~1.55) is larger than that of water, the particle will cause the light to converge, resulting in overexposed areas beneath the particle.

Figure 6.14(a) shows a diagram of the resist particle working as a convex microlens. The original exposure light with a dense line pattern is refracted by the transparent sphere (resist or topcoat particle) to converge as it reaches the resist surface underneath the sphere. Thus, the refracted line pattern shifts toward the center and the unrefracted line pattern remains unchanged. Resist lines at the edge of the defect are broader than the original lines because of the misalignment of the refracted beam and the unrefracted beam (Fig. 6.14(a)). This generates an

underexposed ring surrounding the defect, as labeled by a white circle in Fig. 6.14(b). All features observed in antibubble defects can be predicted by the model in Fig. 6.14(a).

The refracted angle of the exposure light is related to the shape and curvature of the particle. In general, particles with high curvatures generate defects with high overexposures and large pattern shifts. For example, the defect in Fig. 6.14(b) was generated by a particle with high curvature, while the defect in Fig. 6.13 was generated by a particle with low curvature and is called a "flat resist bump."

Defects generated by resist particles were first observed in 248-nm lithography.[18] With a 6% attenuated phase-shift mask (att. PSM) in a dark area, a particle may converge the attenuated light, causing the local dose under the particle to be larger than E_0. This will print a hole on the blank resist. For example, a resist has an E_0 of 4.5 mJ/cm^2 and is imaged with a dose of 45 mJ/cm^2 in the bright areas. If a resist ball with a diameter of 1.5 μm is deposited over a dark area, it will print a hole in the resist with a diameter of 1 μm. Since the reticle is 6% att. PSM, the local dose beneath the resist ball is $45 \times 6\% \times (\pi 0.75^2)/(\pi 0.5^2) = 6.1$ mJ/cm^2, which is larger than the E_0 of 4.5 mJ/cm^2. If a 3% att. PSM were used, the hole would not have been created, because the local dose would have been about 3 mJ/cm^2 < E_0.

Antibubble defects are similar to air bubble defects, although air bubbles diverge the exposure light and generate underexposed areas, while resist or topcoat particles converge the exposure light and generate overexposed areas beneath the particle. This is the reason defects generated by resist or topcoat particles are called antibubble defects.

6.5.2 Sources of resist or topcoat particles and bumps

Resist or topcoat particles are most frequently generated during coating, as dirty coating bowls are the major source of resist particles. During coating, excess resist is spun off the wafer, some of which will deposit on the wall of the coating bowl. This resist may dry and form particles. During coating of subsequent wafers, the high spin speed will create turbulence and a partial vacuum near the wafer, drawing resist particles to the wafer surface. Figure 6.15 shows a series of diagrams describing this particle generation process. The same process can occur during the coating of topcoats.

Resist and topcoat particles are not necessarily spherical in shape. Generation of these particles can be reduced by optimizing coating recipes. For example, increasing the exhaust flow and frequent cleaning of the coating bowl will reduce the formation of coating defects.

In addition to the transparent particles, nonuniform coatings may also generate antibubble defects. Specifically, nonuniformly coated topcoat may create curved bumps that will converge the exposure light, generating antibubble

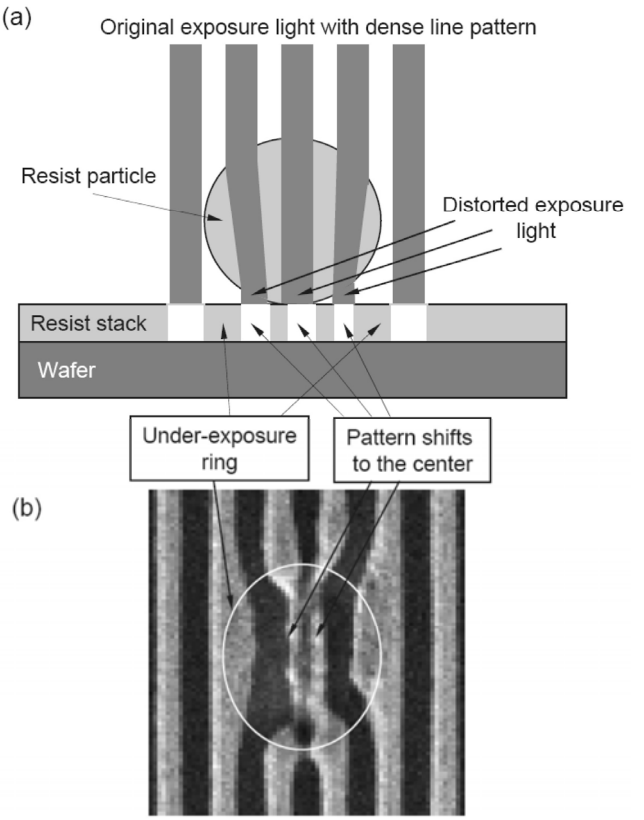

Figure 6.14 (a) Diagram of the resist particle working as a convex microlens. (b) Corresponding top-down SEM image of the defect.

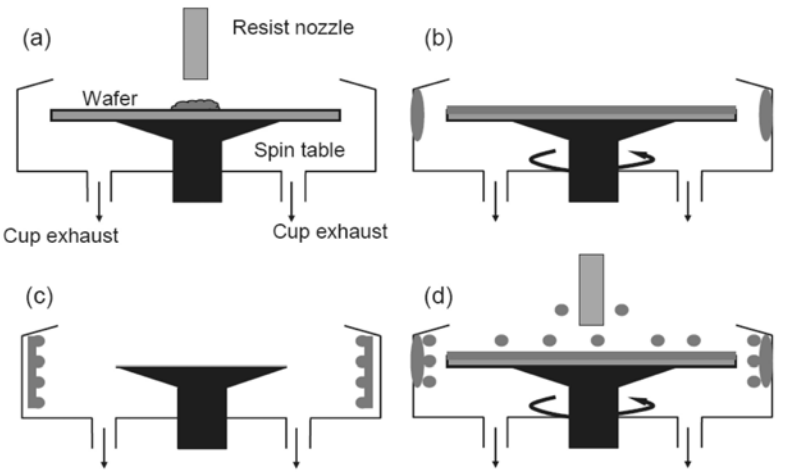

Figure 6.15 Formation of resist particles on the wafer surface. (a) Resist is dispensed on the wafer surface. (b) During spin coating, excessive resist is deposited on the wall of coating bowl. (c) Resist deposited on the wall dries and peels off, forming particles. (d) Resist particles are sucked toward the wafer during spin coating of the next wafers.

defects in the resist. Figure 6.16(a) shows a “flat” topcoat bump and demonstrates how it refracts the exposure light. Figure 6.16(b) shows a SEM image of the corresponding defect.

6.5.3 Blisters

Transparent particles and nonuniform coatings are not immersion-specific; they exist in dry lithography as well. However, the immersion process introduces additional ways to create the transparent particles or bumps. Water can penetrate the topcoat film in some spots where it can accumulate at the topcoat–resist interface, forming a topcoat-enclosed water bubble or blister (Fig. 6.17). Experiments also demonstrate that water may penetrate directly into resist films, enlarging the polymer volume to form a resist bump.[19] Water droplets were dispensed onto a resist surface, and later the surface was inspected. It was observed that water penetrated into the resist and circularly shaped bumps were

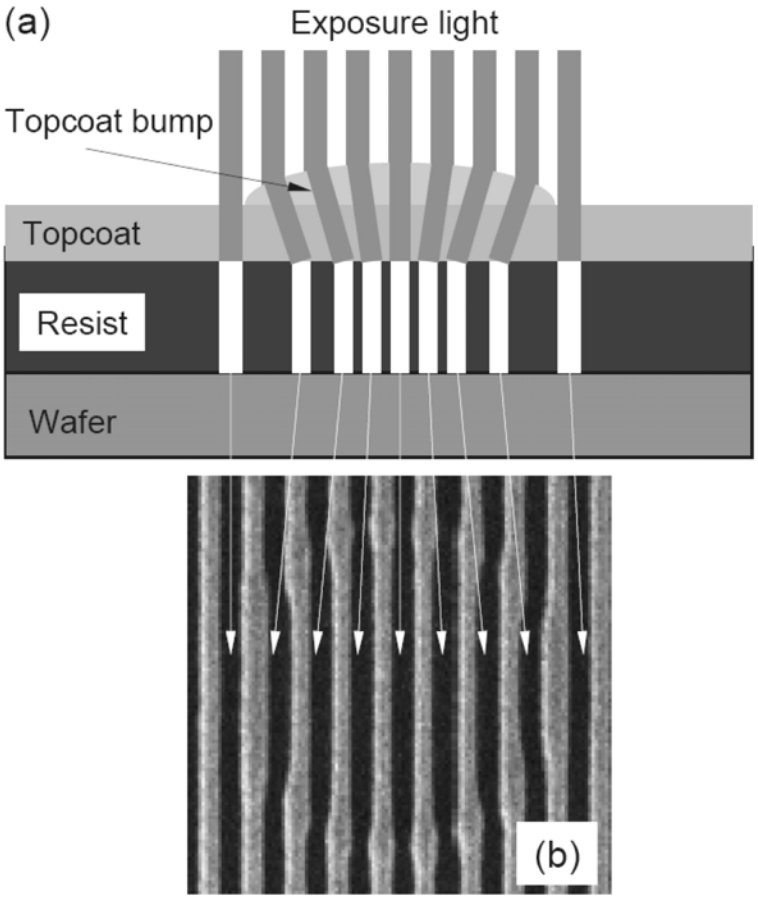

Figure 6.16 (a) Topcoat bump refracts the exposure light and generates a defect. (b) SEM image of a corresponding defect.

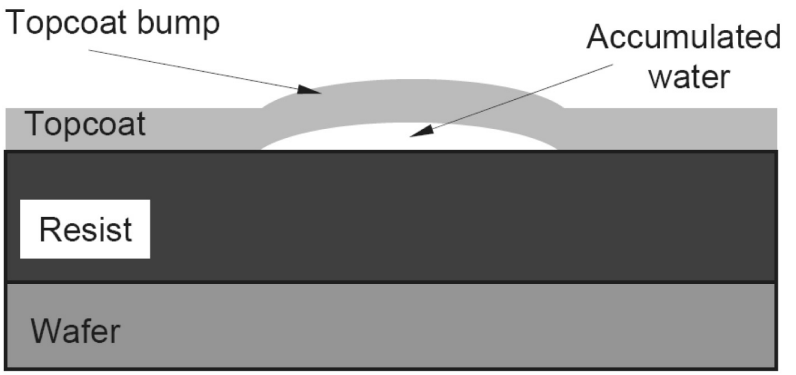

Figure 6.17 Water penetrates the topcoat film and accumulates at the interface of topcoat and resist, forming a blister.

formed (Fig. 6.18(a)). Figure 6.18(b) shows a SEM image of a resist bump caused by water penetration. Material innovation is the key to reducing these types of defects.

The lithographic impact of topcoat blisters has been simulated[20,21] and the effect is the same as that of transparent particles (Fig. 6.19). Topcoats with hydrophobic surfaces and better compatibility between topcoats and resists help to prevent water penetration and accumulation at this interface. It has also been reported that resist swelling and topcoat blistering are strongly dependent on process conditions.[22] The use of higher PAB temperatures for topcoats and resists reduces the frequency of swelling and topcoat blister defects. Topcoat thickness and coating methods are also related to blister defect counts. Small cavities and bubbles in the topcoat dispense system may act as nucleation sites for blister formation.[23]

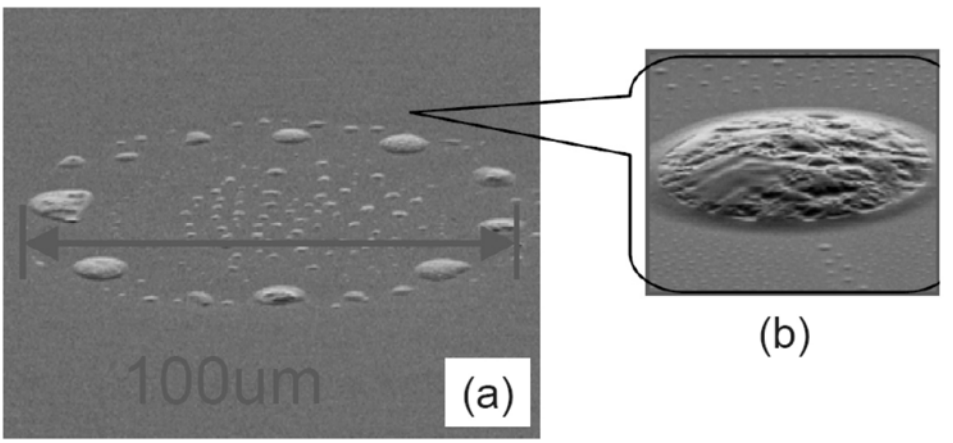

Figure 6.18 SEM images of (a) resist surface that was immersed in the water and (b) resist bump caused by water penetration. (Reprinted by permission from Ref. 19.)

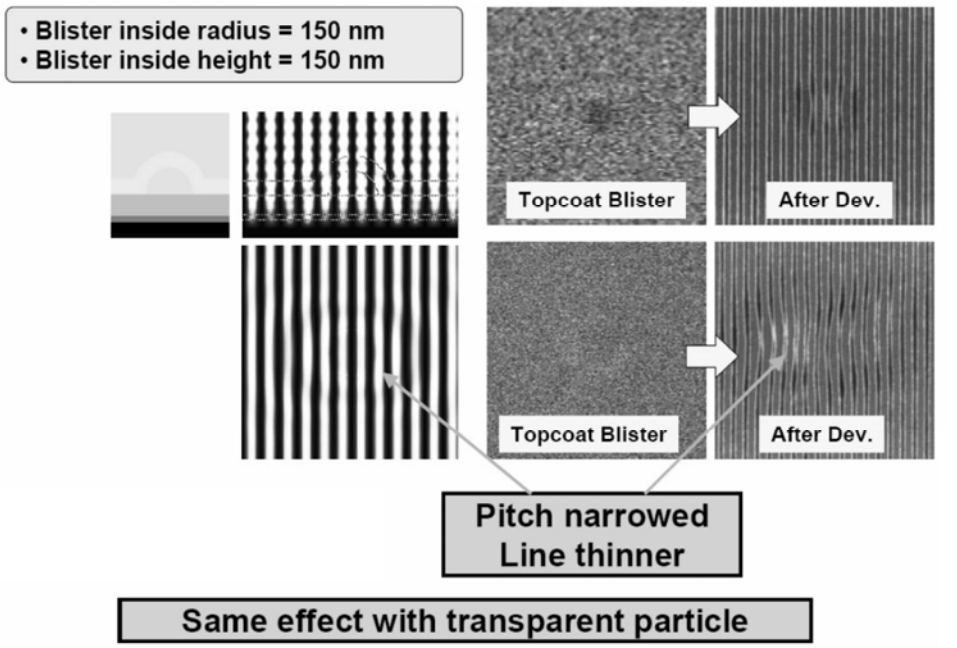

Figure 6.19 Simulation results of a topcoat blister. (Reprinted by permission from Ref. 21.)

6.6 Watermark Defects

Although having similar circular shapes, watermark defects are formed by processes that are completely different from bubble defect formation processes. Water droplets can be left in the trail behind the exposure head as it moves across the wafer. Menisci with smaller receding contact angles tend to leave more water droplets.[24] The photoacid generated during exposure, as well as other resist components, can leach into the water droplet (Fig. 6.20). Water can also penetrate into the resist film. Thus, leaching and water uptake can change the local resist photosensitivity. If the water droplet is present during PEB, the elevated temperatures can enhance local chemical reactions, causing changes to the local photochemistry, and leading to watermark defects.

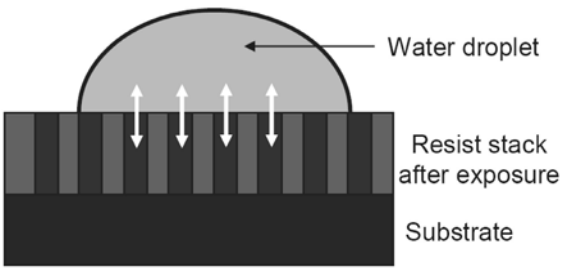

Figure 6.20 Water droplet left on the resist surface after immersion exposure changes the local resist sensitivity.

6.6.1 Mechanism of watermark defects: water droplets cause local resist photosensitivity losses

The effect of water droplets on local resist sensitivity has been experimentally investigated.[19,25] After open frame exposures, drops of DI water are manually dispensed onto resist stacks. The water droplets on resist surfaces are dried during PEB. Resist dissolution rates are determined using a quartz crystal microbalance (QCM), comparing regions with and without treatment by water droplets (Fig. 6.21). The frequency change Δf is proportional to the resist loss. The slope of Δf versus development time gives the resist dissolution rate. The results indicate that the dissolution rate in the region treated with water droplets is lower than the dissolution rate in the untreated region.

The time-of-flight–secondary ion mass spectroscopy (TOF–SIMS) method was also used to compare water droplet regions and nondroplet regions after PEB and before development.[19] The signal of the blocking group was measured across a water-dropped region (Fig. 6.22). The results show that high blocking group signals were measured in the water droplet region, suggesting that deblocking reactions were inhibited by the droplets of water. Therefore, the mechanism of watermark defect formation must be related to the interaction of local resist and water. This interaction reduces the local resist sensitivity and involves no optical reflection/refraction. It is worth mentioning that another mechanism based on leaching has been proposed to explain the formation of watermark defects. This mechanism suggests that leaching of acid or amine occurs when water droplets are left on the resist surface. As the water droplet gets smaller due to water

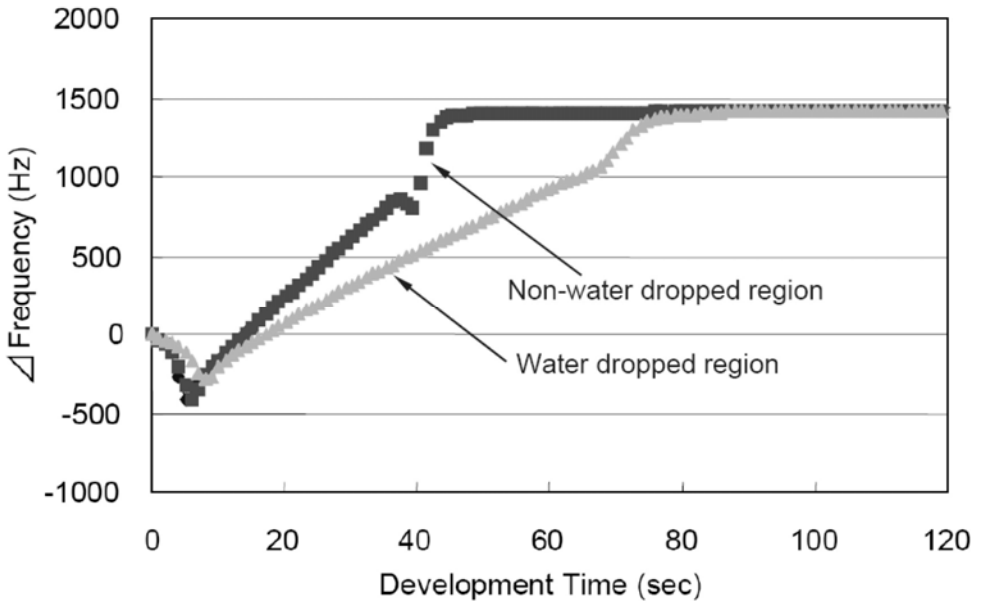

Figure 6.21 QCM measurements of resist dissolution rate at the water droplet region versus the nondroplet region. (Reprinted by permission from Ref. 19.)

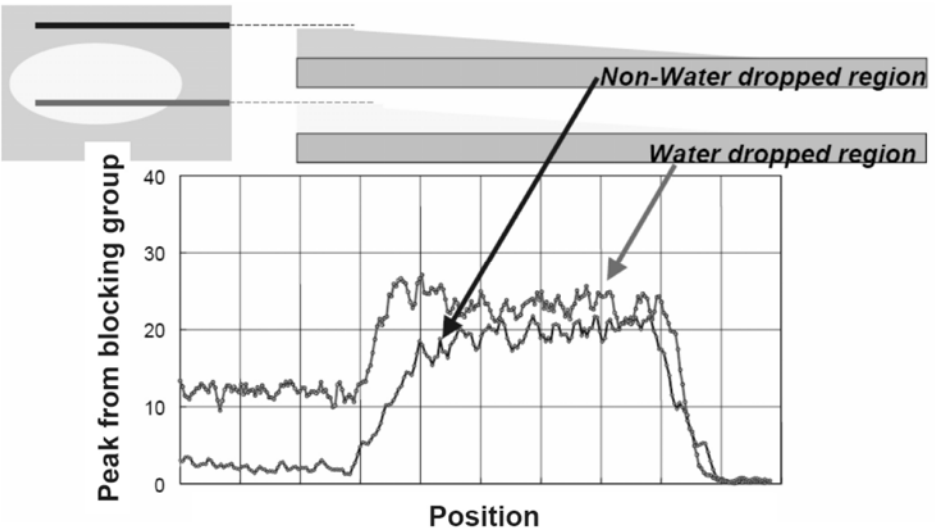

Figure 6.22 TOF-SIMS results at water droplet and nondroplet regions. (Reprinted by permission from Ref. 19.)

evaporation, the acid or amine concentration increases. This mechanism predicts two types of watermark defects: circular overexposed areas and circular underexposed areas. If the leaching rate of the acid is greater than that of the amine, the evaporation of water will eventually lead to a higher localized acid concentration and form circular overexposed areas. If the leaching rate of the amine is larger than that of the acid, the circular underexposed areas should be formed. However, this mechanism has not been supported by experimental results.

6.6.2 SEM images of watermark defects

Figure 6.23 shows a top-down SEM image of a typical watermark defect. The outline of the defect is circular, as labeled by the dotted circle. In the center, resist lines are thick and almost touching. Away from the defect center, resist lines gradually thin until they become the same width as the lines in the unaffected regions. This is quite different from bubble defects, which generally show sharp transitions at the defect edges. Although the resist lines swell in the watermark area, the pitch remains the same, as shown by the thin dotted lines in Fig. 6.23. Pattern amplification and fine fringes are not observed, since watermark defects are caused by chemical interactions between water droplets and resist—not by optical effects.

To obtain three-dimensional information about watermark defects, local cross-sections of watermark defects were prepared using a focused ion beam (FIB) instrument.[26] A dual FIB/SEM instrument equipped with a gas injector system

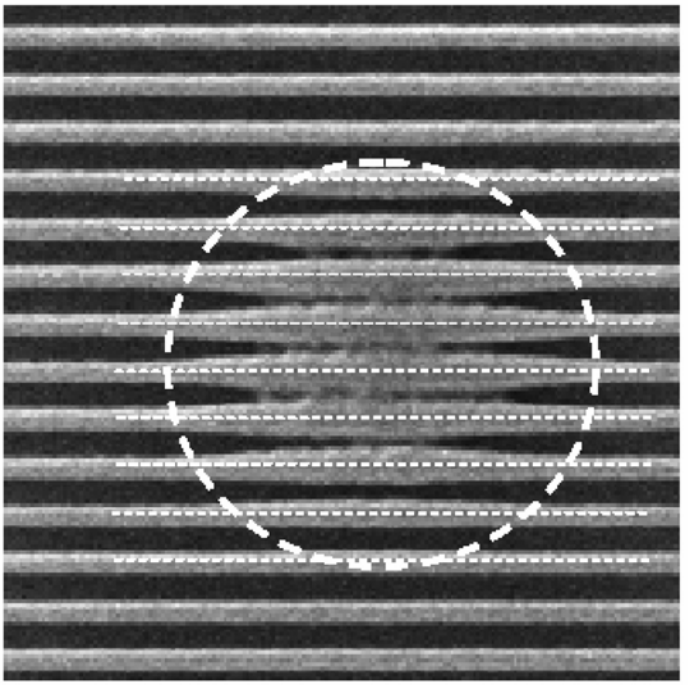

Figure 6.23 Top-down SEM image of a typical watermark defect. The pitch of the dense line is 220 nm.

(GIS) was used. First, a thin platinum film of ~100 nm was coated over the defect area. Then, a finely focused ion beam milled away a precise amount of material from the defect area. The sidewall or profile exposed by the milling process is essentially a precise cross-section of the defect. After ion-beam milling, the tool was switched to SEM mode and the wafer was tilted. High-resolution cross-sectional images were taken at a titling angle of 45 deg.

Figure 6.24(b) shows the cross-sectional image. For comparison, a top-down image of the defect is included in Fig. 6.24(a). A platinum film was coated on the pattern to give contrast (Fig. 6.24(b)). Additionally, the platinum covers the resist lines and fills the spaces. The resist lines appear dark in the image. T-topping of the resist lines is observed in the defect area, as framed by the dotted box. In the center of the defect, the T-topping is so extensive that the adjacent resist lines contact each other, forming cavities that prevent the coating of platinum in the space regions. This cross-sectional image clearly shows that the watermark defects are actually formed as a result of T-topping, due to losses in resist sensitivity at the surface. This result is highly consistent with the theoretical prediction previously described.

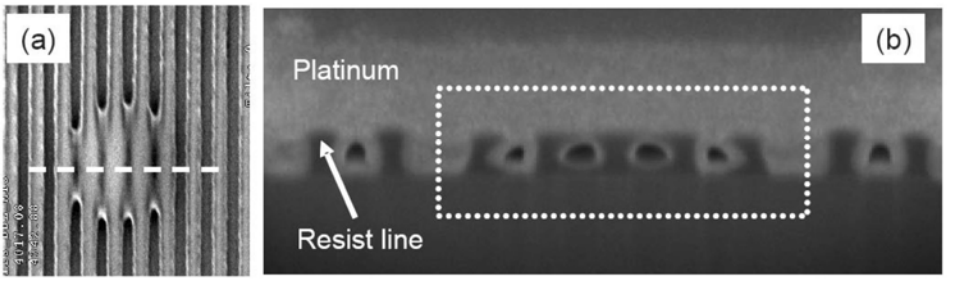

Figure 6.24 (a) Top-down image of a watermark defect that has been cross-sectionally imaged in (b). The dotted line labels where the cross-section was made using FIB technology. The pitch of the dense lines is 220 nm. (b) Cross-sectional images of the watermark defect. A platinum layer was locally coated on the pattern. The wafer was tilted 45 deg.

For comparison, a cross-sectional image of a bubble defect using the same FIB technique was obtained. Figure 6.25(a) shows the image before FIB milling. The characteristic features of the bubble defects are clearly observed (i.e., circular underexposed area with magnified patterns in the center). The dotted line in Fig. 6.25(a) shows the position of FIB milling and Fig. 6.25(b) shows the image after FIB milling. In the defect area, below the platinum film, a solid resist film was observed, as framed by the dotted box in the figure. This result further confirms that bubble defects are formed by underexposure, because they diverge the exposure light, reducing the exposure light intensity under the bubble.

6.6.3 Other evidence of watermark defects

Watermark defects also leave other evidence on the wafer. Immersion water invariably contains some impurities. One mL of water containing 2 ppt of iron (2.2×10^{10} Fe atoms) could form one 640-nm × 640-nm × 640-nm iron cube if all of the water were evaporated or could form dozens of particles in the 100- to 200-nm range.[27] Figure 6.26(a) shows a SEM image of several particles resulting from the evaporation of a droplet of water on a silicon wafer. Therefore, it is expected that there should be some dry residuals associated with watermark defects. After PEB, however, dry residuals might be washed away by the developer or by the DI water rinse. We searched our database of defect images and found a few watermark defects that were accompanied by particles (Fig. 6.26(b)). We expect that the particle sticking on the defect surface is the dry residual of the water droplet.

6.6.4 How resist components and process parameters affect the formation of watermark defects

Because the details of the physical and chemical interactions leading to the loss of resist sensitivity under water droplets are still not completely understood, this

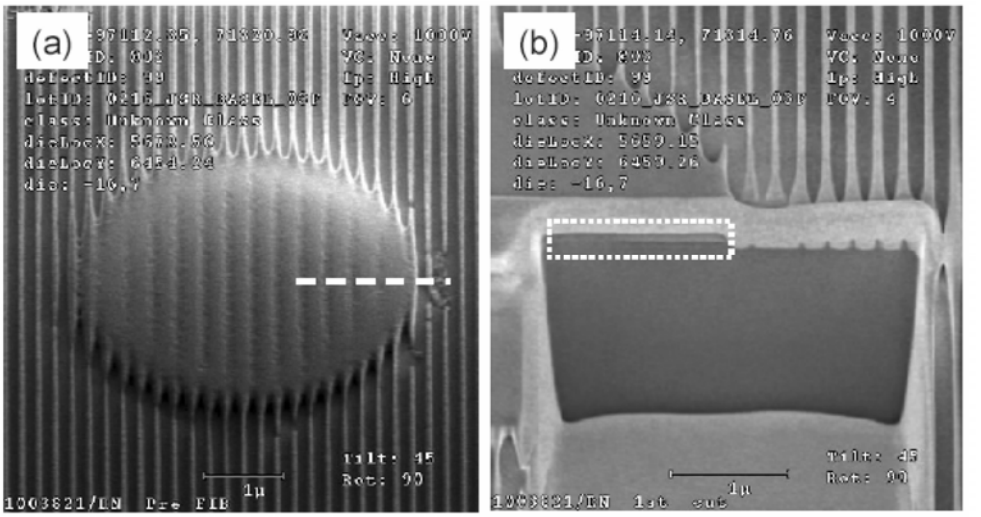

Figure 6.25 Images of a bubble defect taking by a FIB/SEM tool. The wafer was tilted 45 deg. (a) Before FIB milling. (b) After FIB milling.

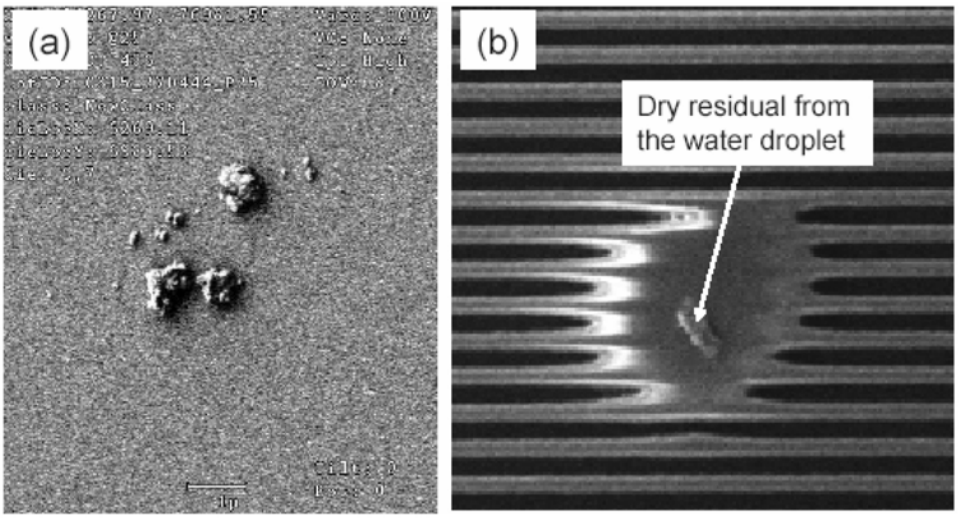

Figure 6.26 (a) Dry residuals of a water droplet on a bare-Si wafer. (b) SEM image of a watermark defect. The particle on the surface is believed to be the dry residual from the water droplet.

is an area of active experimental investigation. These experiments explore the roles played by resist composition and processing conditions in the formation of watermark defects. However, these experiments have been done across different resist and topcoat platforms and the results are somewhat ambiguous.[28] A summary of these results follows.

The studies reveal no clear correlations between leaching levels of the resist and the number of watermark defects. However, higher levels of PAG or base tend to decrease the frequency of watermark formation. Various PAGs also result in different watermark defect counts. Further experiments suggest that the formation of watermark defects on resist films is related to the activation energy and hydrophobicity of the resist.[29] High activation energy and hydrophilic resists tend to have more watermark defects; however, increasing the PEB temperature reduces the number of watermark defects.

The correlation between the watermark defect and the water uptake is still unclear, partly due to the difficulty of measuring the uptake of water. Specifically, water uptake (swelling), occurring as a result of interaction with a water droplet, is different from interaction with a meniscus. Due to surface tension, the pressure inside a water droplet P_1 is higher than the outside pressure P_2 (Fig. 6.27). Assuming that the water droplet has a spherical shape, the pressure difference is calculated as follows:

$$P_1 - P_2 = \gamma \cdot \frac{2}{R}, \tag{6.1}$$

where γ is the water surface energy and R is the radius of the sphere. This is called the Laplace equation. R can be calculated from the height a and width $2b$ of the droplet as

$$R = \left(\frac{b^2}{a} + a \right) / 2 . \tag{6.2}$$

From Eq. (6.1), the Laplace pressure ($P_1 - P_2$) increases with decreasing size of the water droplet. Immediately before the water droplet dries out, the Laplace pressure increases to a maximum value.[30] This pressure may help the water penetrate into the resist film.

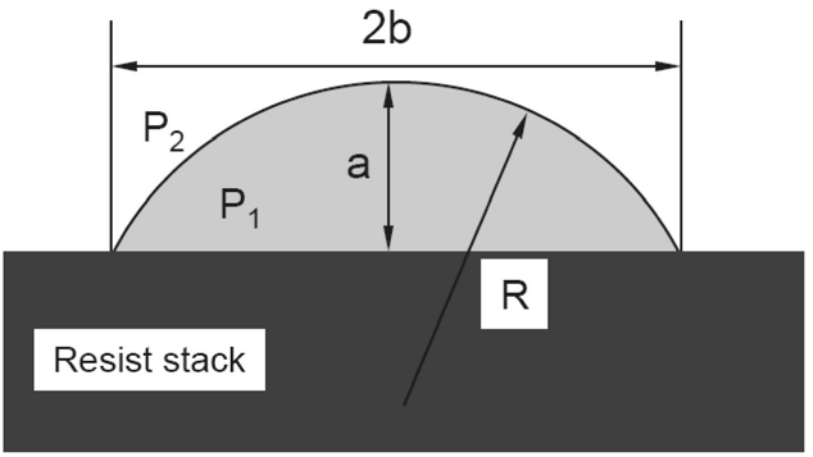

Figure 6.27 Diagram of a water droplet on the resist film.

6.7 Strategies for Reducing Watermark Defects

The first strategy for reducing the number of watermarks is to minimize the number of water droplets left behind. Such efforts include optimization of immersion head design to give better water confinement and utilization of hydrophobic resists. If droplets are left behind, they should be removed from the resist surface as quickly as possible. Thus, the second strategy is to rinse the wafer with DI water prior to the PEB, effectively removing water droplets before they cause any damage to the resist. To reduce the retention time of water droplets, rinse modules are typically installed at the interface between the immersion scanner and the track. The third strategy is to select a resist that demonstrates certain watermark-proof characteristics.

6.7.1 Hydrophobic surfaces help reduce watermarks

In an immersion scanner, the water meniscus moves with the exposure head. The shape of the meniscus can be defined by the dynamic contact angles, which describe the water contact angles in the front (advancing contact angle θ_a) and the rear (receding contact angle θ_r) of the meniscus. Smaller receding contact angles lead to an increasing number of water droplets left behind. If the receding contact angle is zero, a continuous film of water is left behind. This condition is called "film pulling." To reduce the numbers of droplets left behind, the receding contact angle must be large. Large receding contact angles can be achieved by increasing the hydrophobicity of the resist or topcoat surface.

The density of watermark defects was measured as a function of topcoat hydrophobicity (Fig. 6.28).[31,32] Defect counts decrease dramatically with increasing surface hydrophobicity. As the receding contact angle exceeds 70 deg, defect counts approach those of 193-nm dry processed wafers. Therefore, it has been suggested that a receding contact angle of 70 deg is required in order to avoid leaving behind water droplets at full scan speeds. When printing contact holes, photosensitivity losses caused by water droplets lead to missing contact holes. By using topcoats with higher hydrophobicity, the missing-hole defects can be reduced. Figure 6.28(b) shows the measured defect (missing-hole) counts at the contact level from different topcoat processes. The results show that the hydrophobic topcoat (TC-H) has the lowest density of watermark defect counts. These results clearly underscore the importance of hydrophobic surfaces in reducing the number of watermark defects (Fig. 6.28).

The number of water droplets left behind the meniscus increases with decreasing receding contact angle (RCA). Numerous experiments have shown that the density of droplets versus the RCA is nonlinear and can be approximately described by the curve in Fig. 6.29.[34] These curves show a sharp transition region that is very sensitive to small changes in receding contact angle. This transition generally occurs for contact angles of 50–60 deg. However, for conditions that are more likely to produce a higher density of water droplets, such as high scan speeds or proximity to the wafer edge, the transition region can

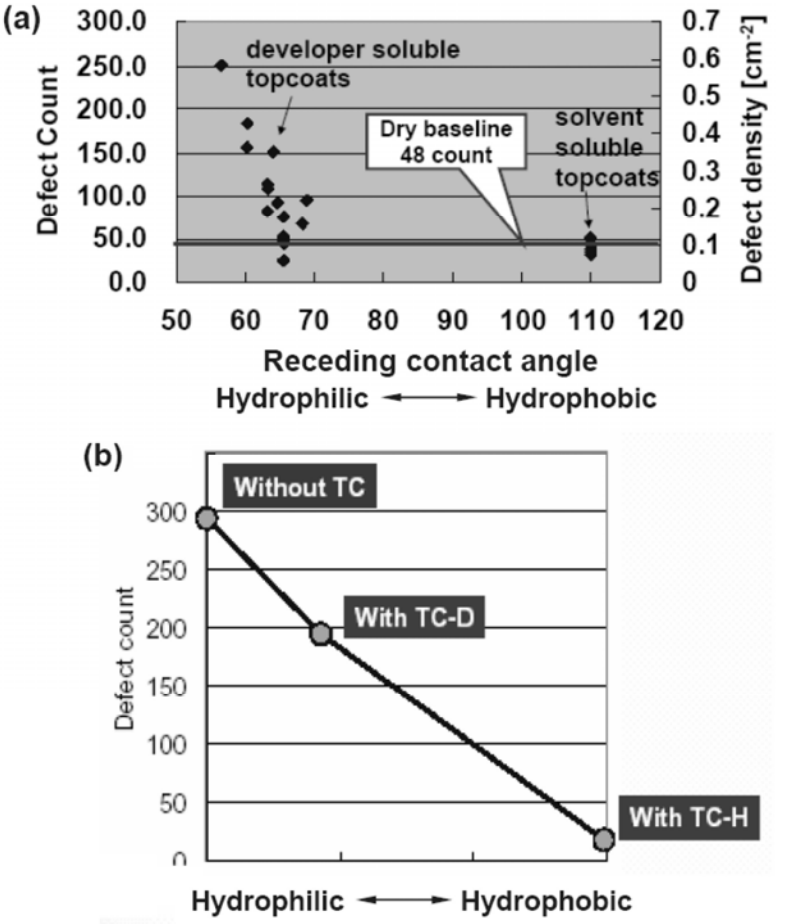

Figure 6.28 (a) Watermark defect counts measured from various topcoats. The topcoats are characterized by the receding contact angle. (Reprinted by permission from Ref. 31.) (b) Defect (missing-hole) counts at contact level measured from different topcoat processes. (Reprinted by permission from Ref. 33.)

occur at higher RCAs. Therefore, in order to minimize droplet density at which the meniscus is metastable, higher RCAs are required.

Although hydrophobic surfaces have fewer watermark defects, they tend to have higher bubble defects, since air bubbles are easily entrapped when the advancing contact angles are high. Thus, there is a trade-off between the number of watermark defects and the number of bubble defects. Fortunately, many scanner vendors have announced exposure heads with bubble-free designs.[16,17] If bubble entrapment can be solved with advanced designs of exposure heads, topcoat or resist vendors can increase the material hydrophobicity to reduce watermark defects. Typical 193-nm dry resists have static angles of ~60 deg and receding contact angles of ~40 deg. New 193i resists can have receding contact angles of ~80 deg.

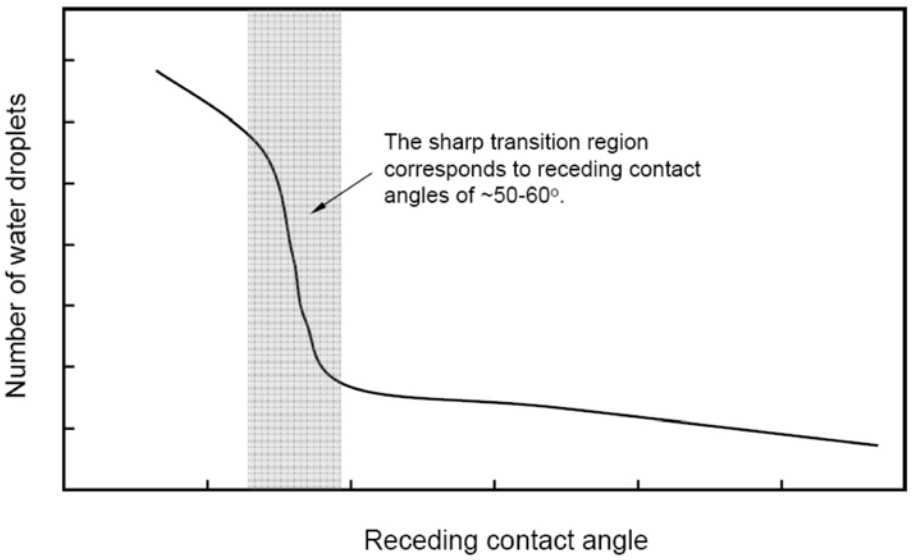

Figure 6.29 The expected "quantitative" relationship between the receding contact angle and number of water droplets. (Data from Ref. 34.)

Another side-effect of increasing the hydrophobicity of developer-soluble topcoats is that hydrophobic topcoats tend to have lower dissolution rates in developer. Unfortunately, however, high dissolution rates are required to reduce blob (satellite) defects. As mentioned earlier, blob defects are typically composed of topcoat or resist materials that have redeposited on the surface during development or rinse steps. Although hydrophobic surfaces will generally have fewer watermark defects, they are likely to have more blob defects. This issue can be addressed by using the polymer blending technique. Small quantities of fluoropolymers in hydrophilic topcoat or resist will migrate to the surface, forming a hydrophobic surface layer, while the bulk remains hydrophilic. This technique may lead to ideal developer-soluble topcoats that have hydrophobic surfaces but dissolve quickly in developer.

6.7.2 Optimization of routing paths and scan speeds of immersion heads

The shape of the water meniscus is highly dependent on the scan speed. Higher scan speeds lead to smaller receding contact angles, typically resulting in the formation of higher densities of water droplets on the wafer. Figure 6.30 shows the defect density measured from the wafers exposed at different scan speeds.[35] Although the scanner has an early exposure head design, the results show that high scan speeds lead to higher defect counts.

Development of exposure heads with ideal water confinement is an attractive goal; however, some level of water leakage appears to be unavoidable.

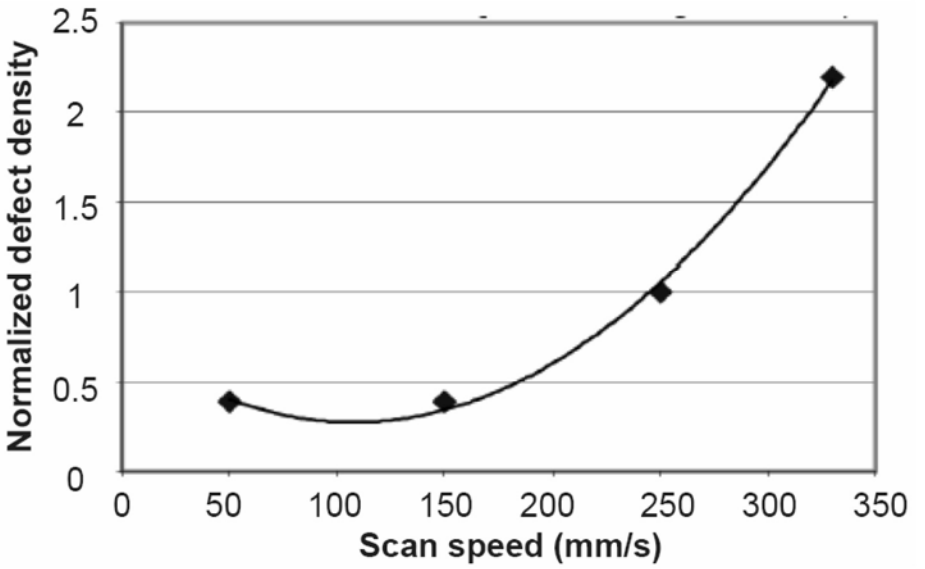

Figure 6.30 Defect density measured from the wafers exposed at different scan speeds. This scanner has an early exposure head design. (Reprinted by permission from Ref. 35.)

Immersion heads have complex designs that are circular in shape and surround the bottom lens element. Inwardly directed air jets are used to better confine the meniscus (Fig. 6.31).[36] The water circulation and air confinement systems may

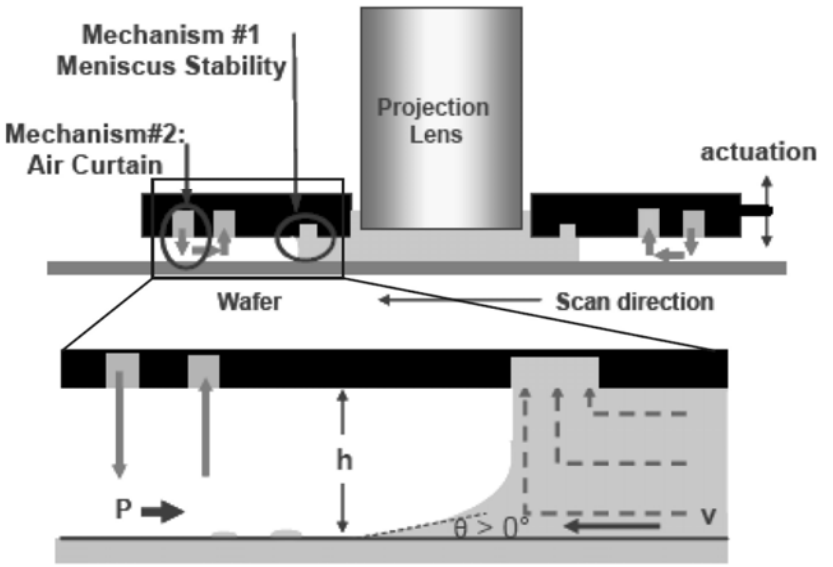

Figure 6.31 Sketch of an immersion head design. (Reprinted by permission from Ref. 36.)

introduce additional turbulence into the water meniscus. Even when the exposure head is stopped, water leakage and watermark defects are observed at the edge of the immersion head.[37,38] In these studies, with no exposure, the immersion heads are moved to the wafer centers and held steady for a couple of minutes. This is called hovering. Defects with a ring signature were observed in these wafers (Fig. 6.32). The ring, which indicates the water leakage at the edge of the immersion head, matches the size of the immersion head: the longer the hovering time, the more water leakage occurs.

These results show that the contact time between the immersion head and the wafer should be minimized (Fig. 6.32). An effective way to reduce watermark defect counts is through optimization of the movement path of the exposure head over the wafer surface in a method called "routing." The movement of the exposure head consists of two parts: the step and the scan. The coverage area of an immersion head is larger than the exposure field. The key to the optimization of routing is, therefore, to minimize the number of times the exposure head passes through any point.

Figure 6.33 shows three different exposure routes: one normal route and two special routes.[39] The normal route is widely used for dry exposures and is the default setting for 193i scanners. Special routes 1 and 2 were designed to reduce defect counts. The short light-gray arrows in Fig. 6.33 show the scan direction in each die. The dies are labeled according to the exposure order. In both the normal route and the special route 1, the scan directions in neighboring dies are opposite. As soon as the exposure head finishes the first die exposure and steps to the second die, it is ready for the next scan. This helps to improve the exposure throughput. In contrast, in special route 2, all dies are scanned in the same direction. When the exposure head finishes the first die exposure and steps to the second die, it is not ready for the second scan, so the reticle stage needs to first move back to the starting position.

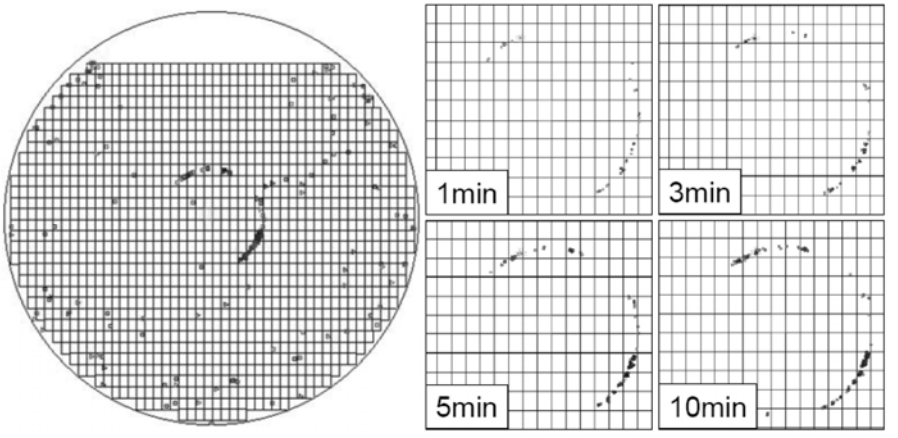

Figure 6.32 Wafer defect maps after immersion head hovering for different times. On the left is the whole wafer map and on the right are amplifications (the immersion head hovered for 1, 3, 5, and 10 min) in the wafer center. (Reprinted by permission from Ref. 37.)

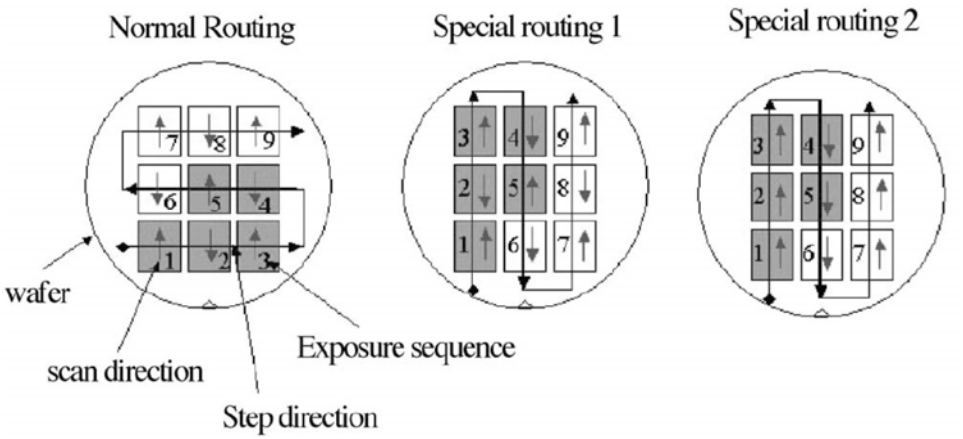

Figure 6.33 Normal exposure routing and two special routings. The normal routing is adopted from the dry process. The special routings were designed to reduce watermark defect counts. (Reprinted by permission from Ref. 39.)

Defect counts are measured for the wafers processed by the three different routes. Special route 2 gives the lowest defect count, but the throughput is the smallest because there is a delay between passes, as the exposure head has to realign. The normal route has the highest defect count. Geometric calculations show that some points between the dies were wet several times by the exposure head using this normal route. Special route 2 minimizes the number of times the points between the dies were wet.

Before exposure, the exposure head may need to move across the wafer stage for alignment. The concept of minimizing the multiple wetting areas is applicable to alignment as well; it is better to avoid moving the exposure head across the wafer during alignment.

6.7.3 DI water rinse process

Rinsing wafers with DI water immediately before and after exposure (pre- and post-rinses) can reduce the density of watermark defects.[40] While pre-rinses change the surface state and reduce the probability of droplet formation, post-rinses remove water droplets. If droplets remain on the surface too long, the post-rinses are no longer effective.

The effectiveness of DI water rinsing has been evaluated by various groups[41] who determined that pre- and post-rinses can reduce watermarks. The effectiveness of the rinse largely depends on the resist stack. For some resists, the rinsing reduces defect counts by up to 80%. For other resists, only < 5% reduction is observed. Such dependency on materials has been attributed to water uptake and continues to be an active area of investigation. Due to its effectiveness, rinse modules for performing rinses before and after exposure have been added to advanced tracks.

One issue with this approach is that rinse processes can change the resist sensitivity, as shown by contrast curve studies.[42] This is especially true for the post-rinse process. Figure 6.34 shows cross-sectional images taken from the wafers with and without a 30-second post-rinse. The resist profiles resulting from the process without the rinse show top-rounding, indicating resist loss, whereas the resist profiles resulting from the process with the rinse have flat tops. Further experiments demonstrate that the DI water rinse may also affect cross-wafer uniformity (CDU) and line-edge roughness (LER) deviations. Therefore, before new rinse steps can be added to reduce watermark defects, the effect of these changes must be fully considered.

6.7.4 Other rinse processes

In addition to DI water rinses, rinsing resists with other solutions has been proposed. For example, rinsing resist films with surfactant before exposure can increase the resist surface hydrophobicity (see Chapter 4 for details). Some experimental results demonstrate that post-rinsing the resist film with a weak acid (so-called acid rinse) is more effective at removing the watermark defects than is a DI water rinse.[43]

Figure 6.35 shows the comparison results of two resists: TARF-Pi6-001 and PAR IM850. First, water droplets were dispensed on the resist surfaces. After delays of 0–4 min, the wafers are rinsed with DI water and inspected for watermarks. Rinsing with DI water is more effective at removing watermarks from the resist TARF-Pi6-001 than from PAR IM850. Even after retention times of up to 4 min, the water droplets on TARF-Pi6-001 can be effectively removed using the DI water rinse. For the resist PAR IM850, the acid rinse is more efficient at removing watermarks from the resist surface than is a DI rinse. One challenge associated with the implementation of the acid rinse is the need to redesign the configuration of the track, since the acid rinse module may need a separate drain system.

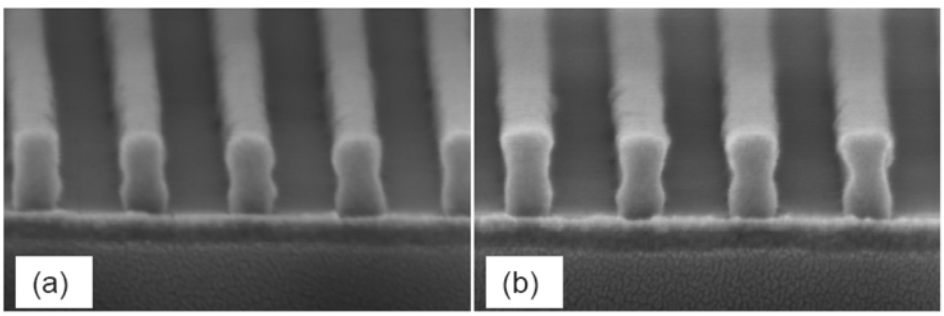

Figure 6.34 Cross-sectional images of 90-nm / 90-nm pattern processed (a) without rinse and (b) with a 30-second post-rinse. Both chips were tilted at the same angle with magnification of 200 K.

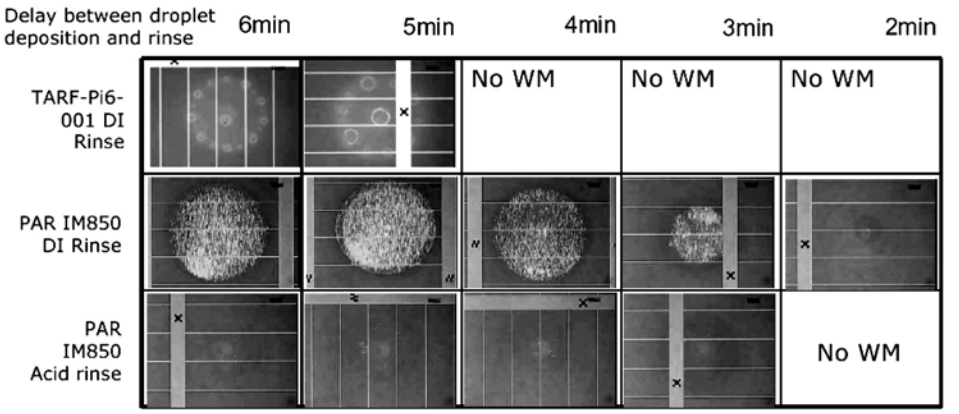

Figure 6.35 Rinse-effect comparison. (Reprinted by permission from Ref. 43.)

6.8 Particles

Particles are another major source of defects observed in 193i-processed wafers and are found in both patterned and nonpatterned fields. Particles may have various shapes and sizes, from several nanometers to tens of micrometers. Particle defects are not unique to 193i lithography; however, some additional particle sources exist only in the 193-nm immersion process.

6.8.1 Particles from the immersion water

The water used for immersion inevitably contains particles and impurities. Particles in the water can deposit on the wafer surface allowing unwanted chemical components in the water to aggregate on the wafer surface. Therefore, the immersion water must be ultrapure with very low levels of particles and impurities. Clean-room DI water must be further treated and filtered before it can be used in exposure heads. Scanner suppliers provide detailed specifications for immersion water.

Apparently, particles suspended in immersion water are less likely to generate optical defects on the pattern. Considering the 500-mm/s wafer scan speed and the flow rate of the water, the particles in the water are almost static during exposure while the wafer quickly passes underneath. The resist image would contain stripes if the suspended particles were printed; however, stripe-like defects are not observed. Simulations show that the projected image of a particle will be too out of focus to print if it is too far from the resist surface. Only particles with H/D ratios < ~50 (H is distance of the particle from the resist surface and D is diameter of the particle) will print images on the resist film.

6.8.2 Particles from the wafer stage

Another potential source of particles is the wafer stage. After the wafer is loaded on the wafer stage, the exposure head must move across the wafer stage for

alignment. While the water meniscus moves with the exposure head across the wafer stage, particles on the wafer stage can be picked up by the water meniscus and transported to the wafer (Fig. 6.36). Particles on the wafer stage may come from previously processed wafers. After extended use during production, the wafer stage inevitably contains particles and deposited films.

Polystyrene and silica nanoparticles were intentionally deposited onto bare silicon wafers or resist-coated wafers. Particle distributions were measured before and after passing through the immersion scanner. Changes in distribution indicate how particles are picked up and redeposited by the immersion head. It was found that the rate of particle pickup decreases monotonically with increased scan speed. Although there is almost no redeposition at either low or high scan speeds, the redeposition rate reaches a maximum at medium scan speeds.

Routine cleaning of the wafer stage and immersion head has been proposed to reduce particle counts. Wafer stages and immersion heads can be cleaned either by wiping with a solvent or by using an *in situ* cleaning technique.[44] For example, a special cleaning fluid can be injected into the immersion head, which is then scanned across the stage at very slow speeds so that the water meniscus can pick up and flush away particles. Figure 6.37 shows the results of the particle per wafer pass (PWP) tests before and after the *in situ* cleaning procedure. These results demonstrate that tool cleaning can reduce defect counts by 75%.[21,37]

6.8.3 Wafer edge

The movement of the water meniscus can pick up loose flakes or particles along the wafer edge. The thickness of the resist stack changes from several hundred nanometers to zero, forming slopes. Figure 6.38(a) is a sketch of the edge of a wafer, which consists of top and bottom bevels and an apex. Particles and loose flakes are easily generated in this region. For example, some resists or topcoats have poor adhesion on bare silicon. If the resist film is coated beyond the edge of the BARC film, the resist film on bare silicon can easily form loose flakes. Figure 6.38(b) shows a side view of film peeling from the wafer edge. The resist film peels along the apex and bevel regions. Typically, this film peeling is only present at the edge, and therefore is difficult to detect by the conventional top-

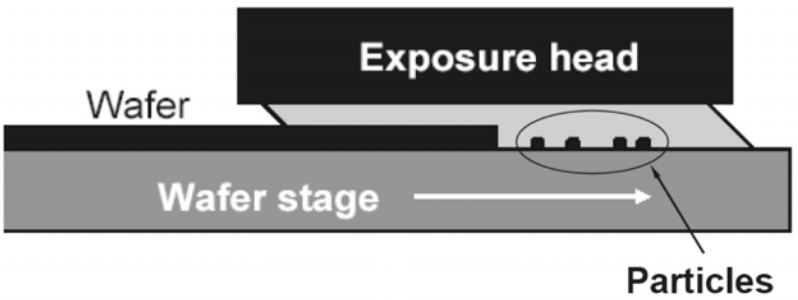

Figure 6.36 Diagram of particles on the wafer stage picked up by the water meniscus.

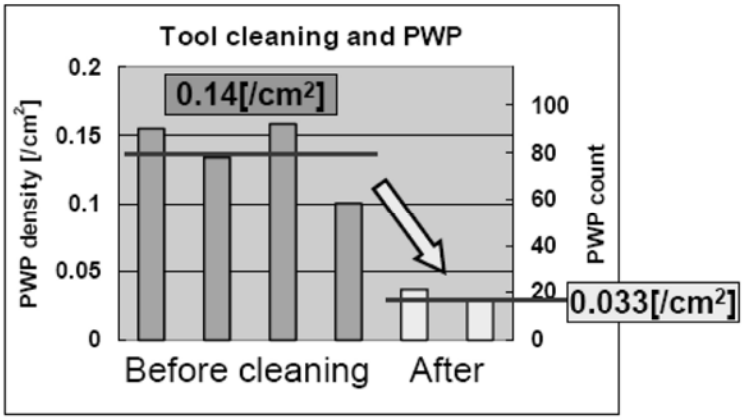

Figure 6.37 PWP (particle per wafer pass) test results before and after the *in situ* cleaning procedure. (Reprinted by permission from Ref. 21.)

down inspection methods. Thus, a special tool dedicated to edge inspection is needed.[45] When the exposure head moves across the wafer edge, it wets not only the near-edge top surface, but also the curved wafer edge and even part of the bottom surface. Particles and peeled films can be released from this area and redeposited either on the wafer or on the wafer stage.

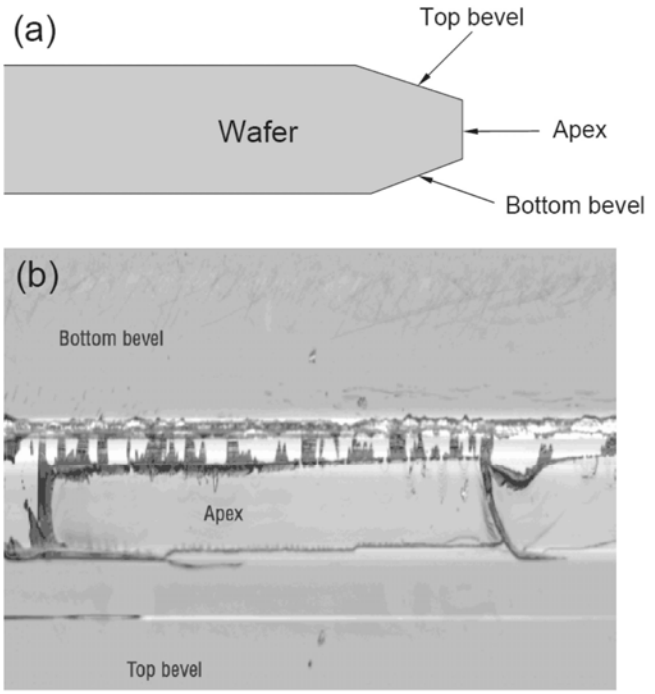

Figure 6.38 (a) Diagram of a wafer edge. (b) Side-view image of a wafer edge. (Reprinted by permission from Ref. 45.)

A point near the edge of a wafer coated with resist and topcoat was inspected by optical microscopy. The wafer was then loaded into a full-field scanner and the exposure head was moved across the selected point near the wafer edge. The point was inspected again by optical microscopy. Figure 6.39 shows optical microscopic images of the wafer edge region before and after treatment by the exposure head. Particles clearly visible at the edge (Fig. 6.39(a)) disappeared after being scanned by the exposure head (Fig. 6.39(b)). The particles were carried by the water meniscus to the wafer center.

To reduce film peeling at the edge of wafers, good adhesion of resist or topcoats is essential. For integrated wafers, the adhesion between BARC and the film stack on the wafer can be weak. Special chemical treatment may be required to enhance adhesion. The adhesion of topcoats to various substrates, such as bare Si, SiON, and poly-Si, was systematically investigated.[46,47] It was found that some topcoats have good adhesion to the substrate, while others do not. Changing coating conditions and/or PAB of the topcoats cannot effectively enhance adhesion. Treating wafers with special chemicals can enhance topcoat adhesion.

The edge bead removal (EBR) process should remove loose flakes and keep the edge region clean and inert to the effects of the water meniscus. Optimization of the EBR process is a tedious, yet necessary step in reducing defects. The best processes can be obtained only through numerous tests and are material dependent.[21,48] Figure 6.40 shows experimental results in which different EBR layouts and their impact on pattern defects counts are evaluated. The BARC/resist/topcoat was coated on bare Si (Figs. 6.40(a) and (c)) or on HMDS-treated (Fig. 6.40(b)) wafers with different EBR layouts. The wafers were cycled through the immersion scanner and the defect counts were measured and compared. Results show that with the wrong EBR layout (Fig. 6.40(a)), the resist or topcoat can be flushed away from the wafer, thus causing a huge number of particle defects. The best EBR strategy is to put both the resist and the topcoat on the BARC (Fig. 6.40(b) and (c)), with or without the use of adhesion

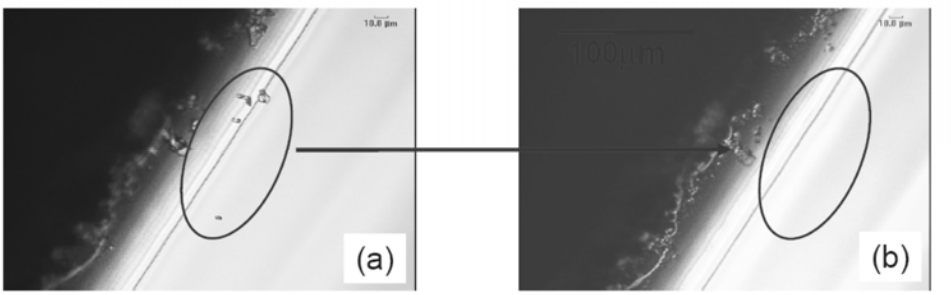

Figure 6.39 Optical microscopic images at the wafer edge (a) before being scanned by exposure head and (b) after being scanned by exposure head.

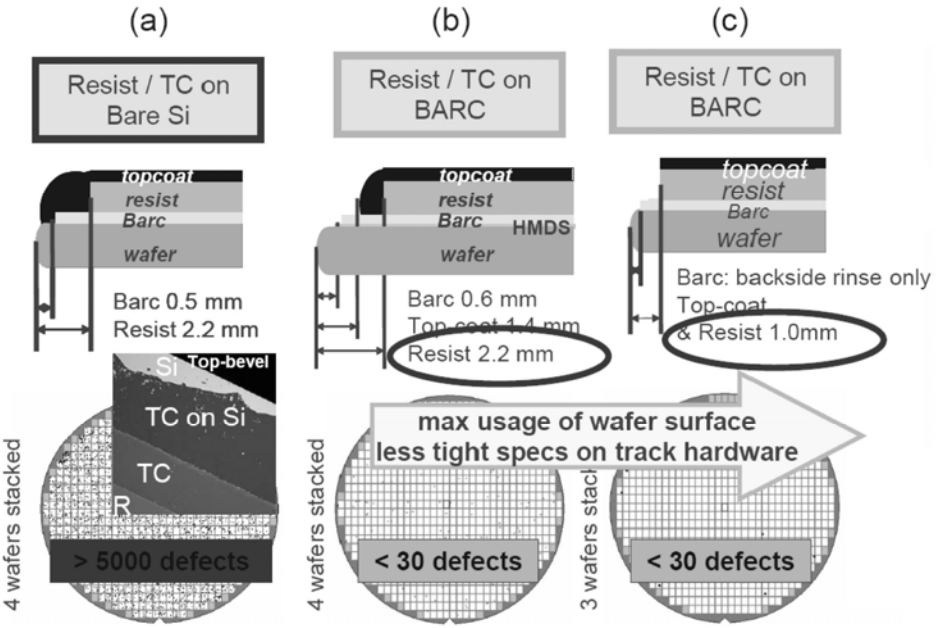

Figure 6.40 Different EBR layouts and their impact on pattern defects counts. (Reprinted by permission from Ref. 20.)

promotion with HMDS prior to the coating of the BARC.[36] This assures the best adhesion to the wafer with minimal particle contamination from the edge.

To further reduce the particles at the bevel region, polishing the edge after material coating has been suggested. Early tests showed a particle reduction of > 60%.[20]

The severity of film peeling at the edge largely depends on the choice of substrate and film material. Not only resist and topcoat, but also poorly adhering films such as oxide, nitride, low-*k* films, etc., can peel off at the wafer edge, especially with the force generated by the movement of the water meniscus. Also, one must pay extra attention to transport- and handling-related damage to the wafer edge. Rework processes typically result in an increased presence of scratches (usually at the lower bottom bevel). These defects can pose risks when the immersion head is passing over the wafer.[45]

6.9 Pinholes in Ultrathin Films of Topcoat or Resist

Topcoats are very thin coatings, typically thinner than 90 nm. Spin coating of ultrathin films (< 100 nm) can be a challenge. The polymer solution must have the right viscosity in order to reach the target thickness with a reasonable spin speed. In addition, contamination and imperfections in the substrate can result in the formation of nucleated holes in the film, called pinhole defects.

Pinholes in topcoat films allow the resist film to be directly exposed to the immersion water. Water can penetrate the holes, reaching the resist film, and resist components can leach out through the hole. These compounds can change the local resist chemistry and form defects. An atomic force microscope (AFM) was used to investigate the pinholes in various topcoat films.[11] Figure 6.41 shows AFM images in different locations across the wafer. In some topcoats, pinholes as large as 100 nm were observed.

The pinhole densities in resist films were investigated as a function of thickness.[49] The resist was spin coated onto 80-nm thick chromium films on glass substrates at different thicknesses. Following the PEB, samples were immersed in a Cr etch solution for 60 seconds. The resist films served as etch masks to block the etch process. At the pinhole sites, however, the Cr etch solution had direct contact with the Cr film and etched the Cr film. After the Cr etch process, the resist films were stripped by rinsing with acetone. The pinholes in the resist film were transferred to the Cr film. The samples were then examined for pinhole density measurement with a transmission optical microscope. It was observed that the thinner resist films had higher densities of pinholes. The pinhole density was roughly inversely proportional to the square of the film thickness. Below a thickness of 100 nm, the pinholes introduced a defect density of > 4 /cm^2, which corresponds to a total defect count of ~2800 on a 12-in wafer. The scaling relation depended strongly on the type of material and on the process conditions. Optimization of the material and the process parameters effectively reduced the pinhole density.

6.10 Microbridging Defects

Microbridging defects are undeveloped sections of resist that form bridges between adjacent resist lines. These defects are often observed in dense line features and are usually < 300 nm (Fig. 6.42). Microbridging defects were first observed in resist patterns printed using 193-nm dry lithography. The defects were attributed to the BARC process[50] and small particles that block the exposure light. Wafers processed using immersion lithography show much higher counts

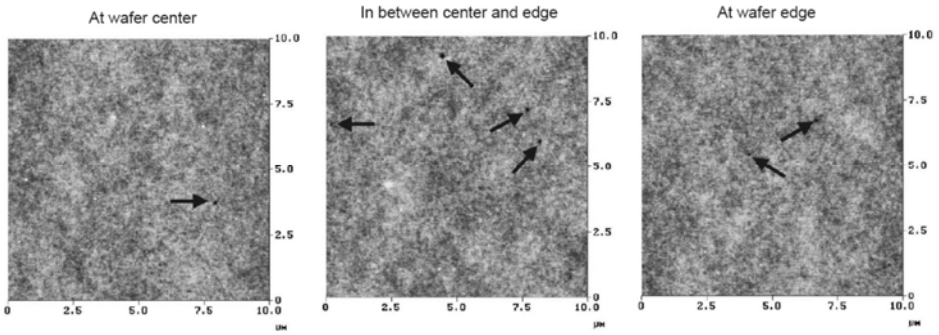

Figure 6.41 AFM images of topcoat film at different locations on the wafer. The arrows in the images are pointed at the pinholes. (Reprinted by permission from Ref. 11.)

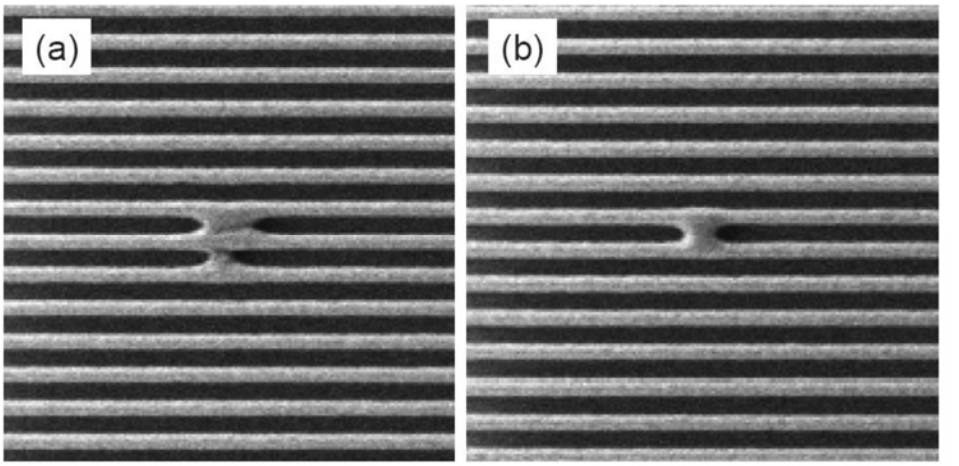

Figure 6.42 SEM images of typical microbridging defects. The pitch of the dense lines is 220 nm.

of microbridging defects than those processed using 193-nm dry lithography. This indicates that the 193-nm immersion process has additional sources of microbridging defects.

Auger spectroscopy has been used to perform *in situ* analysis of microbridging defects.[51] The chemical composition of microbridges is similar to that of the resist pattern. This result seems to suggest that the microbridges are actually resist residues, or at least, the majority of the microbridging is from the resist. However, microbridging defects can be generated by several different mechanisms.

6.10.1 Microbridging caused by microbubbles

As described in a previous section, a bubble attached to the resist surface can refract and scatter exposure light, reducing its local intensity. Simulation shows that a bubble of ~80-nm diameter attached over a 100-nm 1:1 dense line/space pattern can cause the spaces not to open.[8] However, with such a small bubble, other features characteristic of scattered light (e.g., fringes around defects) are not detected. These microbubbles may be the result of either resist outgassing or the delivery system of the immersion water.

6.10.2 Opaque particles

Microbridging can also be generated by opaque particles attached to the resist surface that can block the exposure light and cause small underexposed spots. After development and rinse, the particles may be washed away, leaving behind underexposed spots that appear as microbridging defects. Several experimental results suggest that these opaque particles may result from particulate contaminants in the resist.[52] These substances do not react during exposure

or PEB, so by optimizing the filtration process, specifically the point-of-use (POU) filters, they can be removed and microbridging defect counts can be reduced.

6.10.3 Intermixing layer between resist and topcoat

It has been reported that intermixing layers may be formed at the interface between developer-soluble topcoats and resists.[53] These intermixing layers result from the diffusion of chemical components during bake. In some resist and topcoat combinations, the intermixing layer has a low dissolution rate in developer.[54] Figure 6.43 shows a dissolution rate curve measured from a topcoat and resist stack by a resist development analyzer (RDA). The wafer coated with the resist and topcoat was first flood-exposed and then sent to development.

The development of topcoat and resist occurs in three stages. The topcoat and resist dissolve quickly during the initial and final stages. Between the topcoat and resist, the intermixed layer dissolves slowly (marked with an oval in Fig. 6.43). The formation of this intermixing layer has been blamed for bridging defects on the resist pattern.

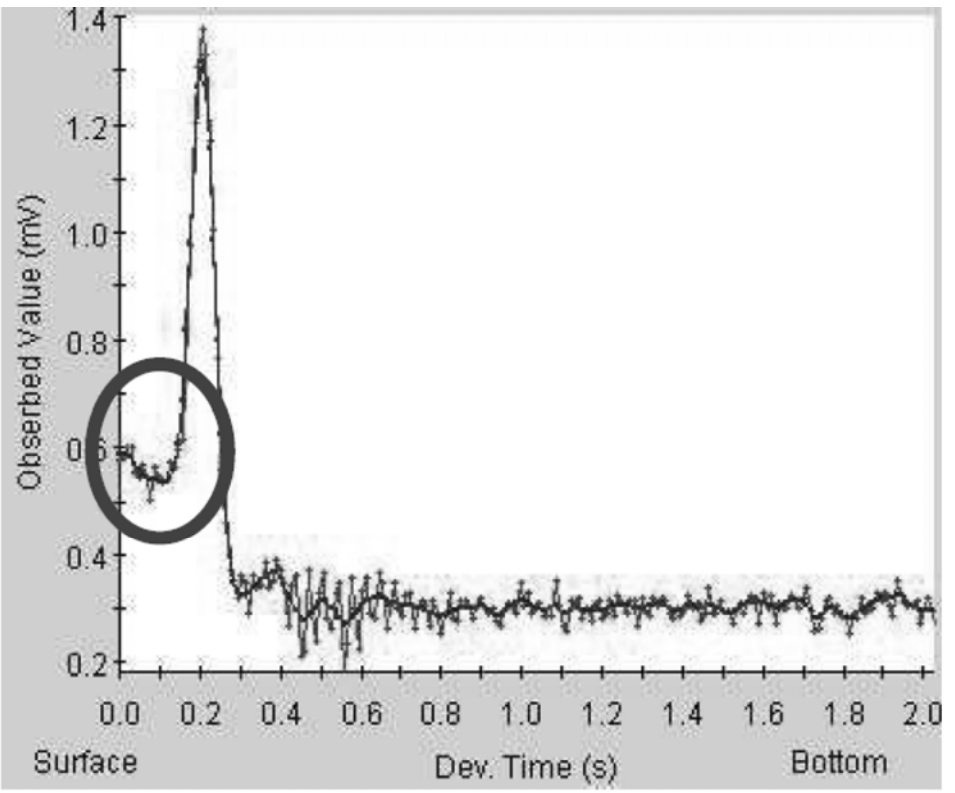

Figure 6.43 Resist development analyzer (RDA) results of a developer-soluble topcoat and resist stack. The oval marks the low dissolution rate period, which corresponds to the intermixing layer. (Reprinted by permission from Ref. 54.)

6.11 Summary

Bubbles, transparent particles, topcoat blisters, watermarks, particles, and pinholes on topcoat have been identified as 193-nm immersion-related defects. Bubbles, water blisters, and watermarks are unique to the immersion process. Although particles and pinholes are observed on dry processed wafers, the immersion process provides additional complexity. After development, these defects may appear in a number of different ways. Some defects may look alike, but are generated by different mechanisms (e.g., watermark defects and bubble defects are all circular in shape). The mechanisms for formation of immersion defects have been shown to originate in the scanner, in the material (BARC/resist/topcoat), or as a result of the process setup. Based on these mechanisms, various strategies have been proposed to reduce these immersion-related defects. Table 6.2 outlines the various defects and appropriate reduction strategies.

As a result of the combined efforts of scanner suppliers, material suppliers, and IC manufacturers, the defect counts of 193i processed wafers are approaching those of dry 193-nm processed wafers. Immersion-dedicated tracks with rinse modules are available on the market and immersion heads with better water confinement have been installed in full-field scanners. With advanced immersion cell and developer-soluble topcoat processes, 55-nm dense lines with defect densities as low as $< 0.03/cm^2$ have been obtained.[55]

Lithography generally has the luxury of rework; wafers that fail in CD or OL (overlay) can be sent back for rework. Resist patterns can be removed and sent back to be coated with resist and exposed again. Strategies involving the rework of wafers that have failed in defect counts, however, are still not fully developed. Clearly, there is no sense in reworking wafers if the original defect densities cannot be reduced. Process engineers must first categorize the defects measured from the wafers and compare these with specifications. For example, if the watermark defect counts are higher than the specifications and dominate the total defect counts, the wafer can be re-exposed at slower scan speeds or can be processed in combination with a more hydrophobic topcoat. Understanding defect formation mechanisms is critical to implementing the rework route for wafers that fail to meet defect specifications.

Table 6.2 Various immersion-related defects and reduction strategies.

Defect type	Immersion uniqueness	Appearances	Mechanisms	Reduction strategies
Bubble	yes	1. Circular with diameters of 1–100 µm 2. Underexposed with sharp edges 3. Pattern amplification 4. Fine outside fringes	Exposure light scattered by air bubbles: optical effect	1. Optimization of exposure head design (commitment from scanner suppliers) 2. Optimization of topcoat or resist contact angle
Transparent particle/ Topcoat blister	Transparent particle was observed in the dry process	1. Circular or oval-shaped with an average diameter of 0.5–5 µm 2. Low-dose ring	Exposure light scattered by transparent particles or bumps/blisters: optical effect	1. Filtration optimization 2. Regular cleaning of coating bowl 3. Better coating uniformity 4. Selection of topcoat with low water uptake
Watermark	yes	1. Circular with diameter of 100 nm–10 µm 2. T-Topping in the center	Local resist sensitivity loss caused by the water droplet: local chemical effect	1. Selection of resist with high receding contact angle 2. Better routing and post-rinse 3. Reduction of scan speed
Particle	Observed in both dry and immersion-processed wafers	Sizes range from several tens of nanometers to hundreds of micrometers	Water meniscus picks up particles or loose flakes from wafer stage and wafer edge	1. High quality immersion water 2. Routine cleaning of wafer stage 3. Material adhesion and EBR optimization
Pinhole	Observed in both dry and immersion-processed wafers	1. Circular with diameter ≈ 100 nm 2. Underexposed	Local resist leaching causes sensitivity loss	1. Selection of topcoat with better coating uniformity 2. Better compatibility between topcoat and resist

References

1. B. Bunday, M. Godwin, P. Lipscomb, D. Patel, M. Bishop, J. Allgair, and A. C. Diebold, "Meeting manufacturing metrology challenges at 90 nm and beyond," *Micro Magazine* Aug./Sept. 2005.
2. *International Technology Roadmap for Semiconductors (ITRS)*, 2005 Edition and 2007 Edition, Lithography Section.
3. J.-Y. Yoon, Y.-K. Jang, H.-W. Kim, S.-W. Choi, and W.-S. Han, "Studies on the defectivity of 193nm immersion lithography for sub-50nm node and beyond," 4th International Immersion Symposium, Keystone, Colorado, Oct. 8–11, 2007.

4. V. Liberman, M. Switkes, M. Rothschild, S. T. Palmacci, J. H. C. Sedlacek, D. E. Hardy, and A. Grenville, *Proc. SPIE* **5754**, 646–654 (2005).
5. M. E. Clarke, A. Xia, J. Smith, and B. Parekh, "Point-of-use ultrapure water for immersion lithography," *Clean Rooms*, Jul. 1, 2006.
6. M. Ali, D. Ashworth, P. Baker, J. Cashmore, S. Fuller, M. Gower, N. McEntee, E. Piscani, A. Rudack, and D. Stark, "Design and performance of a hyper-NA 193nm immersion microstepper system," Presentation at 3rd 193i Symposium, Kyoto, Oct. 2006.
7. Y. Fan, N. Lafferty, A. Bourov, L. Zavyalova, and B. W. Smith, "Study of air bubble induced light scattering effect on image quality in 193 nm immersion lithography," *Proc. SPIE* **5377**, 477–486 (2004).
8. P. De Bisschop, A. Erdmann, and A. Rathsfeld, "Simulation of the effect of a resist-surface bound air bubble on imaging in immersion lithography," *Proc. SPIE* **5754**, 243–253 (2005).
9. See for example, R. R. Kunz, "Photoresist outgassing: A potential Achilles heel for short wavelength optical lithography?" *Proc. SPIE* **5376**, 1–15 (2004).
10. M. Switkes, M. Rothschild, T. A. Shedd, H. B. Burnett, and M. S. Yeung, "Bubbles in immersion lithography," *J. Vacuum Sci. & Tec. B* **23**(6), Nov./Dec. 2005, 2409–2412.
11. M. Terai, T. Kumadaa, T. Ishibashib, T. Hagiwarab, T. Hanawab, T. Andoc, T. Matsunobed, K. Okadad, Y. Murajid, K. Yoshikawad, and N. Mand, "Mechanism of immersion-specific defects with high receding angle topcoat," *Proc. SPIE* **6519**, 65191S (2007).
12. Y. Wei, K. Petrillo, S. Brandl, F. Goodwin, P. Benson, R. Housley, and U. Okoroanyanwu, "Selection and evaluation of developer-soluble topcoat for 193nm immersion lithography," *Proc. SPIE* **6153**, 615306 (2006).
13. A. Wei, M. El-Morsi, G. Nellis, A. Abdo, and R. Engelstad, "Predicting air entrainment due to topography during the filling and scanning process for immersion lithography," *J. Vacuum Sci. & Tec. B* **22**(6), Nov./Dec. 2004, 3444–3449.
14. H. B. Burnett, A. C. Wei, M. S. El-Morsi, T. A. Shedd, G. F. Nellis, C. Van Peski, and A. Grenville, "Modeling and experimental investigation of bubble entrapment for flow over topography during immersion lithography," *J. Microlith., Microfab., Microsyst.* **5**(1), 013008, Jan.–Mar. 2006.
15. M. Kocsis, P. De Bisschop, M. Maenhoudt, Y.-C. Kim, G. Wells, S. Light, T. DiBiase, "A methodology for the characterization of topography induced immersion bubble defects," *Proc. SPIE* **5754**, 154–163 (2005).
16. B. Streefkerk, C. Wagner, et al., "Advancements in system technology for the immersion lithography era," Presentation at 2nd International Symposium on Immersion Lithography, Brugge, Belgium, Sept. 14, 2005.
17. K. Nakano, S. Nagaoka, and S. Owa, "Defectivity data taken with a full-field immersion exposure tool," Presentation at 2nd International Symposium on Immersion Lithography, Brugge, Belgium, Sept. 14, 2005.

18. S.-F. Tsai, C.-Y. Chen, C.-C. Chang, T.-W. Huang, H.-Y. Gao, and C.-Y. Ku, "Micro-lens induced pattern defect in DUV resist," *Proc. SPIE* **5376**, 1149–56 (2004).
19. S. Kanna, H. Inabe, K. Yamamoto, S. Tarutani, H. Kanda, W. Kenji, K. Kodama, and K. Shitabatake, "Non topcoat resist design for immersion defectivity reduction," Presentation at 3rd International Symposium on Immersion Lithography, Kyoto, Japan, Oct. 2006.
20. J. W. Cromwijk, M. B. Mantecon, N. Boudou, H. Boom, Y. van Dommelen, C. Grouwstra, J. Mulkens, M. Pieters, S. Uzunbajakau, and S. Wang, "Defects performance and stability for immersion lithography at 45 nm and beyond," Presentation at 4th International Symposium on Immersion Lithography, Keystone, Colorado. Oct. 8–11, 2007.
21. K. Nakano, H. Kato, M. Yoshida, S. Nagaoka, T. Fujiwara, Y. Iriuchijima, and S. Owa, "Analysis and improvement of immersion defectivity using volume production immersion lithography tool," Presentation at 4th International Symposium on Immersion Lithography, Keystone, Colorado, Oct. 8–11, 2007.
22. K. Ban, S. Park, C. Bok, H. Lim, J. Heo, H. Chun, J. Kang and S. Moon, "Study on the reduction of defects in immersion lithography," *Proc. SPIE* **6519**, 65191V (2007).
23. W. B. Alexander, K. T. O'Dougherty, W. Liu, H. Yan, and K. Mikkelsen, "Reducing bubbles and particles associated with photoresist packaging materials and dispense systems," *Proc. SPIE* **6519**, 651939 (2007).
24. C. Van Peski, A. Grenville, et al., "Film pulling and meniscus instability as a cause of residual fluid droplet," Presentation at the 2nd International Symposium on Immersion Lithography, Brugge, Belgium, Sept. 14, 2005.
25. S. Kanna, H. Inabe, K. Yamamoto, T. Fukuhara, S. Tarutani, H. Kanda, W. Kenji, K. Kodama, and K. Shitabatake, "Materials and process parameters on ArF immersion defectivity study," *Proc. SPIE* **6153**, 6153–8 (2006).
26. Y. Wei, S. Brandl, F. Goodwin, and D. Back, "193nm immersion-related defects and strategies of defect reduction," *Future-Fab Internl*., 65–68, Jan. 2007.
27. C. Robinson, D. Corliss, J. Barns, K. Cummings, H. Jansen, B. Lee, R. Watso, J. Woodbeck, F. Goodwin, Y. Wei, P. Benson, R. Housley, and U. Okoroanyanwu, "Immersion lithography water quality learning at Albany," Presentation at 2nd International Symposium on Immersion Lithography, Brugge, Belgium, Sept. 14, 2005.
28. P. Foubert, M. Kocsis, R. Gronheid, S. Kishimura, A. Soyano, K. Nafus, N. Stepanenko, J. De Backer, N. Vandenbroeck, M. Ercken, "Measurement and evaluation of water uptake by resists, top coats and stacks and correlation with watermark defects," *Proc. SPIE* **6519**, 65190E (2007).
29. H. Nakagawa, A. Nakamura, H. Dougauchi, M. Shima, S. Kusumoto, T. Shimokawa, "Improvement of watermark defect in immersion lithography: mechanism of watermark defect formation and its reduction by using alkaline soluble immersion topcoat," *Proc. SPIE* **6153**, 61531R2 (2006).

30. T. Niwa, S. Scheer, M. Carcasi, M. Enomoto, T. Tomita, K. Hontake, H. Kyoda, and J. Kitano, "Behavior and effects of water penetration in 193-nm immersion lithography process materials," *Proc. SPIE* **6519**, 651922 (2007).
31. S. Owa, H. Nagasaka, K. Nakano, and Y. Ohmura, "Current status and future prospects of immersion lithography," *Proc. SPIE,* **6154,** 515408 (2006).
32. T. Ando, K. Ohmori, et al., "Defect studies of resist process for 193nm immersion lithography," *Proc. SPIE* **6153,** 615309 (2006).
33. T. Kodama, T. Nakata, M. Fujimoto, M. Yamana, S. Nagahara, M. Miyasaka, T. Tamura, K. Yoshimochi, and T. Uchiyama, "Development of immersion lithography processes for 55-nm node device mass production," Presentation at 3rd International Symposium on Immersion Lithography, Kyoto, Japan, Oct. 2006.
34. M. Kocsis, D. Van Den Heuvel, R. Gronheid, M. Maenhoudt, D. Vangoidsenhoven, G. Wells, N. Stepanenko, M. Benndorf, H.-W. Kim, S. Kishimura, M. Ercken, F. Van Roey, S. O'Brien, W. Fyen, P. Foubert, R. Moerman, and B. Streefkerk, "Immersion specific defect mechanisms: findings and recommendations for their control," *Proc. SPIE* **6154**, 615409 (2006).
35. U. Okoroanyanwu and H. Levinson, "193nm immersion lithography defects," Presentation at 2nd International Symposium on Immersion Lithography, Brugge, Belgium, Sept. 14, 2005.
36. J. Mulkens, B. Streefkerk, H. Jasper, J. de Klerk, F. de Jong, L. Levasier, and M. Leenders, "Defects, overlay and focus performance improvements with five generations of immersion exposure systems," *Proc. SPIE* **6520**, 652005 (2007).
37. S. Brandl, R. Watso, B. Pierson, S. Holmes, Y. Wei, K. Petrillo, K. Cummings, and F. Goodwin, "Investigation of immersion related defects using pre- and post-wet experiments," *Proc. SPIE* **6154**, 61540T (2006).
38. F.-J. Liang, H. Chang, L.-H. Shiu, C.-K. Chen, L.-J. Chen, T.-S. Gau, and B. J. Lin, "Immersion defect reduction (1): analysis of water leaks in an immersion scanner," *Proc. SPIE* **6520**, 65204U (2007).
39. F.-J. Liang, L.-H. Shiu, C.-K. Chen, L.-J. Chen, T.-S. Gau, and B. J. Lin, "Defect reduction with special routing for immersion lithography," *J. Microlith. Microfab. Microsyst. letters*, Jan.–Mar. 2007 **6**(1).
40. M. Carcasi, S. Hatakeyama, et al., "Defectivity reduction by optimization of 193nm immersion lithography using an interfaced exposure-track system," *Proc. SPIE* **6153,** 61533J (2006).
41. See for example, K. Matsunaga, T. Kondoh, H. Kato, Y. Kobayashi, K. Hayasaki, S. Ito, A. Yoshida, S. Shimura, T. Kawasaki and H. Kyoda, "Defectivity reduction studies for ArF immersion lithography," *Proc. SPIE* **6519**, 65191T (2007).
42. Y. Wei, N. Stepanenko, A. Laessig, L. Voelkel, and M. Sebald, "Evaluation of 193nm immersion resist without topcoat," *J. Microlith. Microfab. Microsyst*., Jul.–Sep. 2006.
43. M. Kocsisl, R. Gronheid, A. Soyano, P. Foubert, K. Nafus, M. Maenhoudt, N. Stepanenko, S. Kishimura, "Watermark defects: underlying mechanisms and recommendations for their control," Presentation at 3rd International Symposium on Immersion Lithography, Kyoto, Japan, Oct. 2006.

44. K. Nakano, H. Kato, T. Fujiwara, K. Shiraishi, Y. Iriuchijima, S. Owa, I. Malik, S. Woodman, P. Terala, C. Pelissier, and H. Zhang, "Immersion defectivity study with volume production immersion lithography tool," *Proc. SPIE* **6520**, 652016 (2007).
45. S. Vedula, F. Burkeen, A. Somanchi, and I. Pollentier, "Influence of immersion lithography on wafer edge defectivity," *Solid State Technology*, Feb. 2008.
46. D. Kawamura, T. Takeishi, K. Matsunga, E. Shiobara, Y. Oonishi, and S. Ito, "Pattern defect study using cover material film in immersion lithography," *Proc. SPIE* **6153**, 61531Q (2006).
47. E. Ng and J. Hooge, "A multi-tiered approach to 193 nm immersion defect reduction through track process adjustments," *Proc. SPIE* **6519**, 651926 (2007).
48. T. Fujiwara, J. Ishikawa, T. Kawakubo, Y. Ishii, H. Kyoda, S. Wakamizu and T. Shimoaoki, "Adapting immersion exposure to mass production by adopting a cluster of novel resist-coating/developing and immersion-exposure equipment," *Proc. SPIE* **6519**, 65190C (2007).
49. S. W. J. Kuan, C. W. Frank, C. C. Fu, D. R. Allee, P. Maccagno, and R. F. W. Pease, "Ultrathin polymer films for microlithography," *J. Vac. Sci.& Tec. B* **6**(6), p. 2274, Nov./Dec. 1988.
50. M. Randall, C. Longstaff, et al, "Minimizing wafer defectivity during high temperature baking of organic films in 193nm lithography," *Proc. SPIE* **6153**, (2006).
51. M. Enomoto, S. Hatakeyama, T. Niwa, T. Tomita, H. Kyoda, J. Kitano, S. Shimura, and T. Kawasaki, "193nm immersion process defect generation and reduction mechanism investigation using analytical methods," *Proc. SPIE* **6153**, 61533L (2006).
52. T. Umeda, J. Yokoyama, N. Iguchi, Y. Mizuno, and S. Tsuzuki, "Study on effective property of point of use filter for defectivity reduction in 75nm ArF lithography and 120nm KrF lithography," Presentation at Interface 2006.
53. S. Kishimura et al., "Impact of water and top-coats on lithographic performance in 193-nm immersion lithography," *Proc. SPIE* **5752**, 20–30 (2005).
54. N. Stepanenko, H.-W. Kim, S. Kishimura, D. Van Den Heuvela, N. Vandenbroecka, M. Kocsisa, P. Fouberta, M. Maenhoudta, M. Erckena, F. Van Roeya, R. Gronheida, I. Pollentiera, D. Vangoidsenhovena, C. Delvauxa, C. Baertsa, S. O'Brienf, W. Fyena, and G. Wellsa, "Top coat or no top coat for immersion lithography?" *Proc. SPIE* **6153**, 615304 (2006).
55. K. Goto, Y. Yamaguchi, T. Fujiwara, K. Nakano, Y. Ishii, H. Kyouda, and J. Kitano, "Adapting non topcoat process to high volume manufacturing," Presentation at 4th International Symposium on Immersion Lithography, Keystone, Colorado, Oct. 8–11, 2007.

Chapter 7
Antireflection Coatings and Underlayer Technology

Exposure light passes through resist films and may reflect off the substrate. The reflected light interferes with the incoming exposure light and generates standing waves in the direction normal to the wafer surface. These standing waves have a period of a quarter of the wavelength divided by the index of refraction n_{Resist}. Thus, the reflected light causes a corrugated profile in the resist pattern and makes CD control very difficult. If the substrate has patterns, the patterns underneath the resist film may reflect exposure light differently from the way unpatterned areas reflect exposure light, leading to poor CD uniformity across the wafer.

Antireflection coatings (ARCs) have been introduced to control reflection. These ARCs can be located either below the resist film (bottom antireflection coatings or BARCs) or above the resist film (top antireflection coatings or TARCs). TARCs control the reflection at the top resist surface. They are organic solutions that are spin-coated onto the resist surface. BARCs are specifically useful on pattern or topographic substrates and control the reflection from below. BARCs can consist of either organic or inorganic materials. Inorganic BARCs are deposited via chemical vapor deposition (CVD) methods (e.g., SiON films). Organic BARCs are spin-coated onto the substrate and then baked at high temperatures to remove solvent and to cross-link the film.

The disadvantage of inorganic BARCs is that they cannot be removed by solvent and so cannot be reworked. Usually, after pattern transfer, the inorganic film stays on the wafer and becomes part of the film stack. In contrast, the spin-on organic BARCs are more process-flexible and can be easily removed with solvent or plasma etch. Their viscosities can be adjusted, enabling different coating thicknesses from several tens to several hundreds of nanometers.

Due to their fluid nature, organic BARCs may fill the wafer surface topography and planarize surfaces. Some organic BARCs are optimized for this purpose and are called planarizing BARCs. The coating performance of BARCs is strongly related to the molecular weight of their polymers, their viscosity, and their solvent content. While low molecular weight polymers can easily fill vias and help planarize surface topography, high molecular weight polymers can provide more uniform coverage over surface topography and are called

conformal BARCs. The CVD method deposits inorganic films that are conformal to the surface topography of the substrate. This chapter focuses on various organic spin-on BARC and TARC processes. The introduction of the immersion technique enables hyper-NA, where NA > 1. At this high NA, the incident angle of the exposure beams is larger than 44 deg and the reflection issue becomes much more severe. Advanced strategies for reflection control must be developed to address this issue.

As pattern size continues to decrease, so does the film thickness of photoresists. At the 45-nm half-pitch node, resist thicknesses of 70–130 nm are recommended by the ITRS roadmap. Such thin resists can no longer provide enough etch resistance for transferring the pattern to the substrate. Hard masks (HMs) have been widely adopted as a solution. First, the thin resist pattern is transferred to the HM layer during etch, where the etch rate of the HM is much larger than that of the resist. Then, the pattern is transferred from the HM to the substrate (using different etch chemistry), where the etch rate of the substrate is much larger than that of the HM. Traditionally, the HM is an inorganic material deposited using CVD. More recently, however, the spin-on HM has been developed and widely accepted by IC manufacturers.

Spin-on hard masks are supplied as chemical solutions. They are spin-coated onto substrates and baked to remove solvent. These coat and bake steps are easily installed in standard tracks without the need for CVD tools. Most spin-on hard masks can be reworked by stripping with solvents to further reduce the cost of the process. Spin-on HMs are typically coated between the resist/BARC stack and the substrate. They can also be designed to have some antireflection properties. Thus, the combination of BARCs and HMs can have better antireflection control; however, the development of BARC technology has not been limited to reflection control. In fact, the name “BARC technology” is not enough to describe this field and the more general “underlayer technology” may now be the better term. The “underlayer” simply means all layers under the resist film. This chapter reviews advanced underlayer technologies, as well as top antireflection coatings (TARCs).

7.1 General Requirements for Conventional Bottom Anti-reflection Coatings (BARCs)

7.1.1 Optical requirements

Assuming a resist film is coated on a substrate without any antireflection coatings, exposure light will be reflected at the resist surface and at the interface of the resist and the substrate. The interference of the exposure beams and the reflected beams generates a periodic variation in light intensity along the vertical direction of the resist film, creating a standing wave profile. The standing wave has a period of a quarter of the wavelength in the resist ($\lambda_{Resist}/4$). Its swing amplitude (SA) is strongly related to the reflectivity at both the resist top (R_T) and the resist bottom (R_B):

$$\mathrm{SA} \approx \frac{\sqrt{\mathrm{R_T} \cdot \mathrm{R_B}}}{\mathrm{EL}} \cdot e^{-\alpha D}. \tag{7.1}$$

In Eq. (7.1), EL is the exposure latitude of the lithographic process, D is the thickness of the resist, and α is the absorbance of the resist. The presence of the standing waves generates a CD variation and the dispersion of the CD is directly linked to the swing amplitude (SA) of the standing wave. It is possible to minimize the SA by decreasing R_B or R_T (use BARC or TARC) or by increasing the absorbance α of the resist (dyed resists).[1]

The BARC film is coated on the substrate underneath the resist film to reduce the reflection at the resist bottom. Figure 7.1 shows the propagation of light beams in a resist and BARC stack. Working properly, the BARC film causes the destructive interference between the incident beams and the reflected beams at the bottom of the resist film. A detailed optical calculation can be applied here to find parameters for the destructive interference.[2] At a small incident angle, the calculations are simple:

$$n_{\mathrm{BARC}} = \sqrt{n_{\mathrm{Resist}} \cdot n_{\mathrm{Substrate}}}, \tag{7.2}$$

$$t_{\mathrm{BARC}} = k \cdot \frac{\lambda_{\mathrm{BARC}}}{4}. \tag{7.3}$$

In Eqs. (7.2) and (7.3), n_{BARC}, n_{Resist}, and $n_{\mathrm{Substrate}}$ are the refractive indices of the BARC, resist, and substrate, respectively, k is an integer factor, and λ_{BARC} is the light wavelength in the BARC, which equals 193 nm/n_{BARC}. These are labeled in Fig. 7.1, as well. In the case of a large incident angle corresponding to a high NA exposure, Eqs. (7.2) and (7.3) are not applicable and detailed calculations are needed to find the optimum thickness and refractive index.

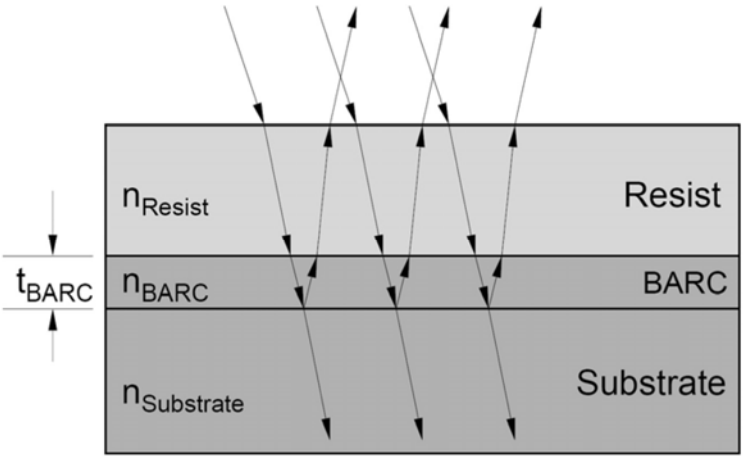

Figure 7.1 Propagations of light beams in a resist and BARC stack.

7.1.2 Thermal cross-linking

After BARC films are coated on a substrate, they are cross-linked using high-temperature bakes. Not only is this cross-linking important to the overall lithographic performance of the resist and the BARC stack, but also it enables the use of the pre-wet process and prevents erosion of the BARC film during resist coating.

A simple method for evaluating the cross-link performance of an ARC uses a solvent rinse. After PAB, the BARC film is soaked by the resist solvent (for example, PGMEA), for 60 seconds. The thickness of the BARC film is measured before and after the solvent soak. Figure 7.2 plots the results of such an experiment.[3] Without the solvent soak, the BARC maintains a similar thickness at different bake temperatures from 150 to 220° C. With the solvent soak, the thickness loss is observed with the BARC film baked at the temperature < 180° C, which indicates incomplete cross-linking. At a bake temperature ≥ 180° C, the film is cross-linked and the thickness remains at a constant value throughout the solvent soak.

The cross-linking can also be checked using FTIR. The FTIR spectrum of BARC films is measured before and after high-temperature bakes. A reduction of the alcohol band from 3100 to 3500 cm^{-1} indicates that cross-linking occurred.

7.1.3 Sublimation test

After coating, BARC films must be baked at high temperatures, typically around 200° C, to ensure that cross-linking is complete. At such high temperatures, outgassing of chemical components of the BARCs can be a problem. In general,

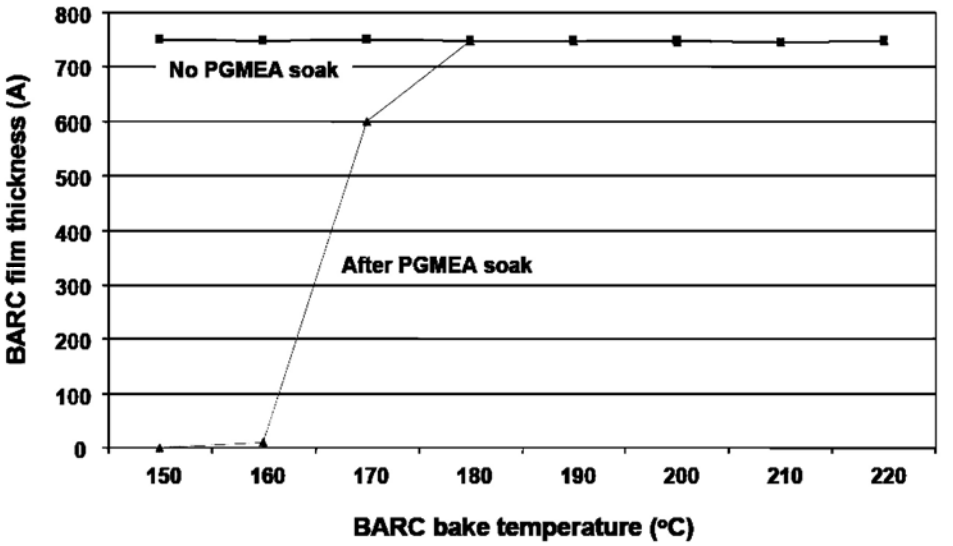

Figure 7.2 BARC film thickness variation after solvent soak. The BARC film was baked for 90 seconds.

outgassing is caused by solvents, residual monomers, and other small molecules in the BARC formulation. When large amounts of outgassing occurs, the exhaust system may not always be evacuated quickly enough, so the outgassed components condense on the inner wall of the baking chambers. These condensates can be solids that may peel off and drop onto subsequent wafers, resulting in cross-contamination. Therefore, BARC formulations must be tested for outgassing by what is called the sublimation test.

Sublimation tests consist of two parts.[4] One test identifies the outgassing components, while the other determines the outgassing rate. A wafer coated with a BARC film is loaded onto a hotplate with a quartz plate above it (Fig. 7.3(a)). During the bake, the chemical components outgas from the BARC film and deposit onto the quartz plate. The quartz plate is sent for transmission spectral analysis, such as FTIR, to identify the composition of the chemicals deposited on the plate.

Figure 7.3(b) shows the apparatus for measuring the outgassing rate. A funnel-shaped collector is placed over the wafer and a vacuum pump is connected to the collector. The outgassed components are forced to pass near a

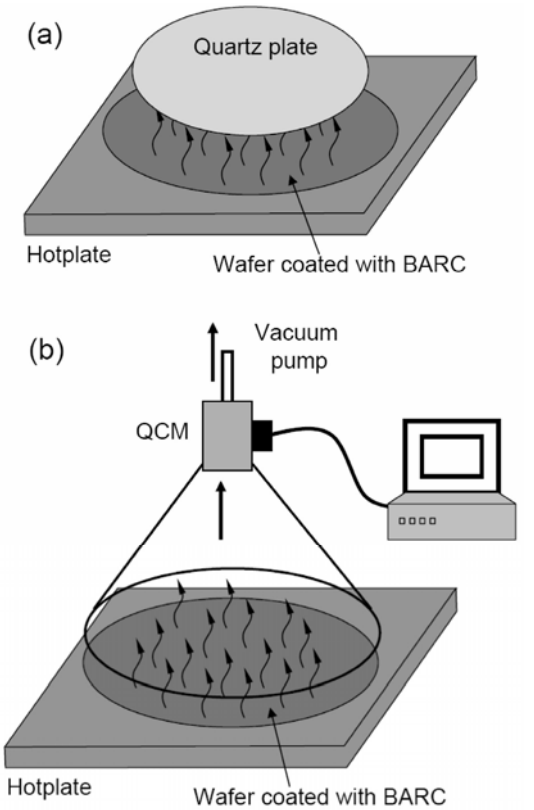

Figure 7.3 Sublimation test of the BARC film. (a) Setup for testing the outgassing components. (b) Setup for testing the outgassing rate.

QCM (using a vacuum pump. Some of the chemical components deposit onto the QCM detector, causing a decrease in the resonant frequency. By measuring the frequency change over time, the outgassing rate can be obtained.

7.1.4 Resist compatibility

As sketched in Fig.7.1, the BARC film is located between the resist film and the substrate and, therefore, must be compatible with the resist. The compatibility has two criteria from the perspective of lithography performance. First, after exposure and development, the resist patterns on the BARC surface should have no footing. Second, the BARC surface must be optimized to reduce blob defects.

7.1.4.1 Resist footing

Resist footing occurs when the bottom of the resist film loses photosensitivity. After exposure, photoacids are generated in the resist. These acid molecules can diffuse into or pass through the BARC film and react with the ions in the substrate (e.g., SiON hard mask) (Fig. 7.4). Similarly, amines in the substrate can penetrate the BARC and poison the resist. By increasing the BARC thickness, amine poisoning can be suppressed and resist footing reduced. However, thicker BARCs are not preferred, due to their effect on pattern transfer during etch. Therefore, better barrier performance of BARC material must be designed.

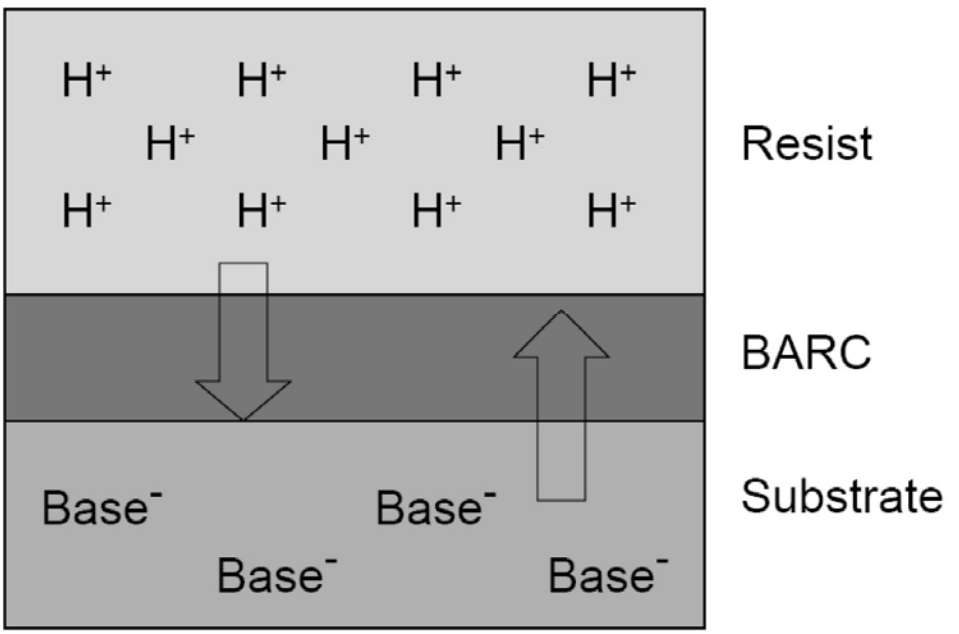

Figure 7.4 Sketched mechanism of resist poisoning.

7.1.4.2 Control of blob defects

The root cause of blob defects is pH shock occurring during development and DI water rinse. Blob defects occur when resist particles or clusters in the developer redeposit on the surface. Increasing the surface affinity of BARC to developer helps to reduce the precipitation of resist clusters onto the BARC surface during development and rinse.[4]

7.1.5 Etch rate of organic BARCs

Organic BARCs are generally not soluble in standard aqueous developers. After development of the resist, the BARC must be opened by etch. Thus, etch resistance is a very important parameter for BARCs. A typical organic BARC formulation consists of a polymer, a chromophore, a cross-linker, and a thermal acid generator in a suitable organic solvent. Etch rates of BARC films depend on all of the components within the formulation; however, the polymer is thought to have the largest impact, since it is present in the largest amount. The Ohnishi parameter has been used to model the etch rates of BARC polymers. This model was originally proposed in 1983 and has been widely accepted.[5] According to the Ohnishi model, etch rate is proportional to the Ohnishi parameter as

$$\text{Etch rate} \propto \frac{N_T}{N_C - N_O}\ , \tag{7.4}$$

where N_T, N_C, and N_O are the total number of atoms, carbon atoms, and oxygen atoms in the polymer. As seen in Eq. (7.4), high carbon content in the BARC polymer leads to lower etch rates, while high oxygen content leads to higher etch rates. The etch rate for a BARC film under a patterned resist film is found to be about 51 to 74% of its blank etch rate.[6]

Recently, several modifications have been made to the Ohnishi model. These modified models include the contributions of other elements, such as nitrogen and fluorine, to the etch rate. More nitrogen atoms lead to smaller etch rates in oxygen etches, but lead to higher etch rates in fluorine etches.[7]

7.2 Challenges to Antireflection Control for Hyper-NA Exposure

193-nm water immersion scanners have numerical apertures as high as 1.35. These hyper-NA (> 1) projection lenses are capable of collecting light beams with large diffraction angles. The smallest dense patterns on the mask diffract the light at the largest angles. These light beams are converged by the projection lens on the resist surface with large incident angles (Fig. 7.5). Small lenses are able to collect the diffraction orders from larger features (Fig. 7.5(a)), whereas larger lenses are needed to collect the diffraction orders from the smallest patterns (Fig. 7.5(b)). The maximum incident angle of exposure beams can be calculated from the NA value as

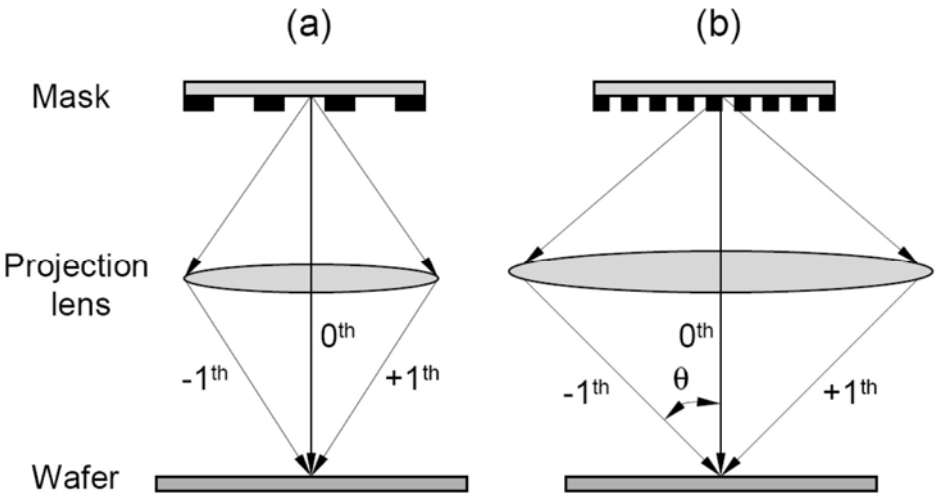

Figure 7.5 (a) Patterns with large pitch in the mask generate small diffraction angles that can be collected by a small projection lens. (b) Small patterns in the mask generate large diffraction angles and require a large projection lens to collect the diffraction orders.

$$\theta = \sin^{-1}\left(\frac{\mathrm{NA}}{n}\right). \tag{7.5}$$

In Eq. (7.5), n is the refractive index of the media between the projection lens and the wafer. For 193i, $n = 1.44$. At NA = 1.35, the maximum incident angle on the resist surface is about 70 deg.

The high incident angles characteristic of higher-NA 193i exposures impose challenges to antireflection control, especially for masks with both small dense and isolated features, since the incident angle on the resist surface for the dense and isolated features is in a broad range of 0 to $\sin^{-1}$(NA/1.44), depending on the pitch value. It is becoming very difficult to simultaneously reduce the reflections from all light beams using a single-layer BARC. A simulation was done with a single-layer BARC and 1.35NA exposure of 45-nm 1:1 dense and isolated lines. Figure 7.6 shows the reflectivity at the resist–BARC interface with various BARC thicknesses. The reflectivity minimum for the dense and isolated features is located at different thicknesses as labeled. One cannot find an optimum BARC thickness that can reduce the reflectivity to less than 0.5% for both dense and isolated lines. The requirement of < 0.5% is commonly suggested by IC manufacturers.

In addition, at the high incidence angle, the reflectivity at the resist–BARC interface also depends on light polarization, i.e., the reflectivity versus incident angle is quantitatively different for various polarization components. Figure 7.7 shows the calculated reflectivity at the resist–BARC interface as a function of incident angle for both X and Y linear polarizations. In the figure, the stack is a

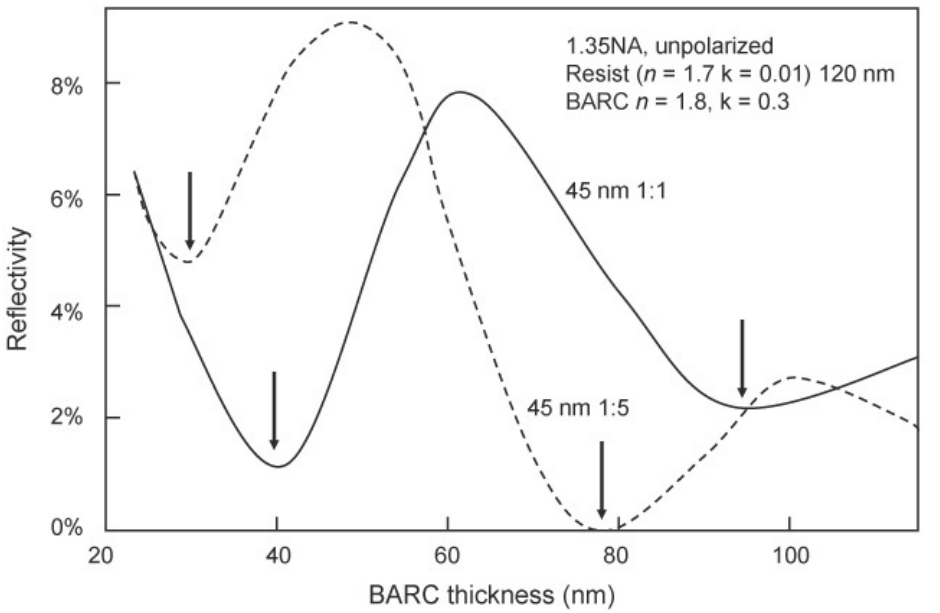

Figure 7.6 Reflectivity at the resist–BARC interface for different BARC thicknesses. The arrows indicate the reflectivity minima.

representative stack. The angle of the incident light is plotted on the X axis as $n_{resist}\sin\theta$, where n_{resist} is the refractive index of the resist and θ is the angle of incident light at the resist–BARC interface. Figure 7.7 demonstrates that the reflectivity of X- and Y-polarized light is different when the incident angle is away from zero. As a result, the BARC process also has to be optimized for each polarization.

The challenges to the antireflection control at hyper-NA were first recognized before hyper-NA tools became available. It was generally agreed that a single-layer BARC process can be optimized to provide enough reflective control for only one pitch. If one wants to simultaneously expose patterns with various pitches, more aggressive antireflection control strategies are needed for hyper-NA exposure. Although the use of conventional single-layer BARC processes is the primary strategy used in mass production, more advanced antireflection control strategies are being developed.[8]

7.3 Spin-on Dual-Layer BARCs and Graded Spin-on BARCs

7.3.1 Spin-on dual-layer BARCs

Compared to one layer of BARC, two layers of organic BARC can provide better reflective control during hyper-NA exposures. The use of two different BARC layers is not a totally new idea. Many CVD films that have antireflective functions (e.g., SiON) are widely used as hard masks (HMs) in film stacks. A

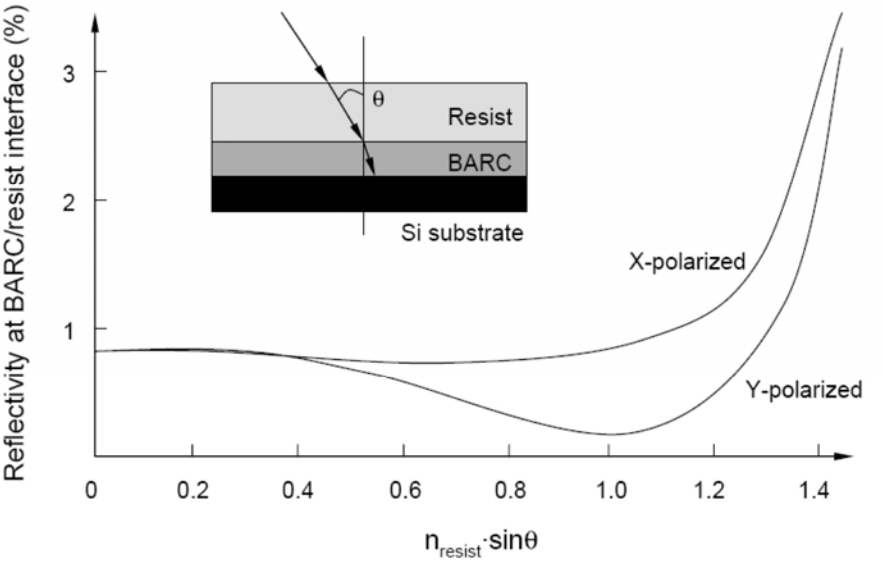

Figure 7.7 Reflectivity at the interface of resist–BARC as a function of incident angle for both X and Y linear polarizations. n_{resist} is the refractive index of the resist and θ is the light incident angle at the resist–BARC interface. The resist film has a thickness of 220 nm with n = 1.7 and k = 0.02; the BARC film has a thickness of 51 nm with n = 1.8 and k = 0.5.

conventional organic BARC coated over a CVD film gives better reflection control than does the organic BARC by itself. However, this hybrid of inorganic and organic approaches lacks process flexibility. A CVD process is needed for the inorganic film but the inorganic film cannot be removed after the lithography process.

In the case of spin-on dual-layer BARCs, two different BARC layers are spin-coated onto the substrate (Fig. 7.8). The n, k, and thickness t of the BARC layers are optimized to obtain a minimum reflection over the pitch.

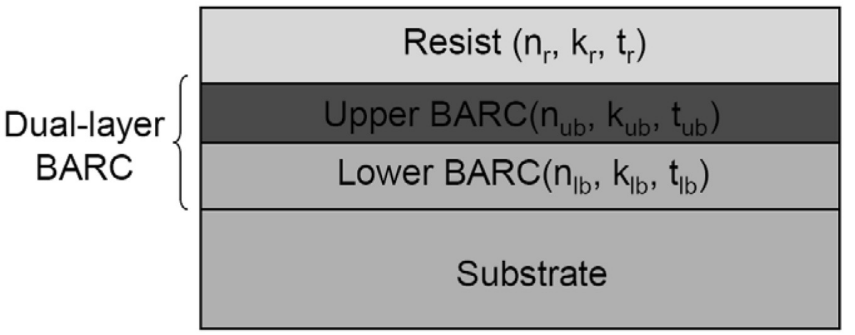

Figure 7.8 Dual-layer organic BARC stack is obtained by spin-coating two layers of BARC on the substrate. The upper layer has optical parameters of n_{ub}, k_{ub}, and a thickness of t_{ub}. The lower layer has optical parameters of n_{lb}, k_{lb}, and a thickness of t_{lb}.

The lower layer is a planarization BARC and has a high *k* value, while the upper layer has a low *k* value. The low-*k* upper layer enables high transparency of exposure light for absorption to occur at the lower layer. It works in an attenuation mode and offers better reflection control over pitches.[9] Figure 7.9(a) shows an example of dual-layer BARC materials. The dual-layer BARC was coated on a poly-Si substrate, and a 1.35NA scanner was used to expose 40-nm lines with various pitches. Figure 7.9(b) shows the reflectivity of the exposure light at the top of the dual-layer BARC with the change of total BARC thickness. The results demonstrate that the reflectivity of all pitches reaches a minimum of < 0.5% at the region close to 80-nm thickness. For comparison purposes, a normal second minimum BARC is also used for simulation and gives different optimum thicknesses for every pitch (Fig. 7.9(b)).

The dual-layer BARC has been evaluated for lithographic performance.[10] Dual-layer BARCs demonstrate better exposure latitude and dose stability through illumination configuration, as compared to single-layer BARCs. In considering etch, the two BARCs are designed to have similar etch rates in order to avoid potential complication of etch CD control.

(a)

	n@193nm	k @193nm
Upper layer	1.72	0.20
Lower layer	1.87	0.61

(b)

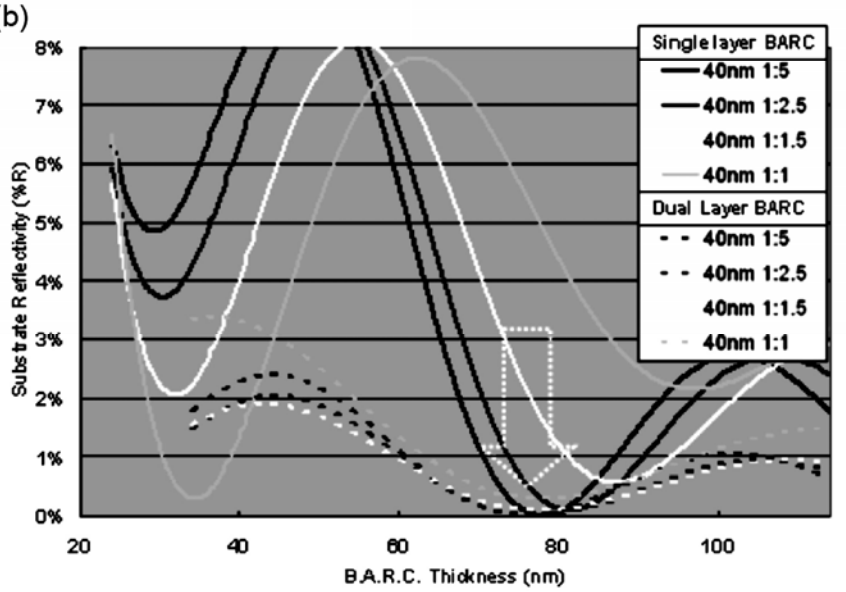

Figure 7.9 (a) Parameters of a dual-layer BARC sample. (b) Reflectivity versus the total BARC thickness for various pitches. The dotted arrow in (b) indicates a common reflectivity minimum for all pitches. (Reprinted by permission from Ref. 9.)

From the perspective of material suppliers, the dual-layer BARC processes are ready; they do not require the invention of any new material platforms. Thus, various organic BARCs with broad ranges of optical parameters and etch performance are available and constitute part of the existing product portfolios of BARC suppliers. In practice, only simulation is needed to identify the appropriate materials and thicknesses. However, the introduction of spin-on dual-layer BARC processes into mass production appears to be much more complicated. Compared to single-layer processes, the dual-layer approaches require additional material and additional coat and bake steps. As the total thickness of the dual-layer BARC approaches the thickness of the resist film, issues of etch selectivity become more critical.

7.3.2 Graded spin-on BARCs

Usually BARC films have uniform optical parameters throughout their depth. Theoretical calculations, however, suggest that BARCs can provide better reflection control if their refractive indices change continuously as a function of depth. This type of BARC is called graded BARC (GBARC).

Graded BARCs were first realized as inorganic film deposited by CVD.[11] They were prepared by treating silicon nitride films with oxygen plasma so that the oxygen composition could be gradually decreased through the silicon nitride film. Consequently, the optical constants of the film also gradually changed. As a result, a reflectivity of less than 1% was obtained with CVD graded BARC.

Graded spin-on BARCs were prepared by blending polymers (Fig. 7.10).[12] Two polymers were designed, one targeted as the top component (near the resist film) and another targeted as the bottom component (near the substrate). The etch selectivity and cross-linking functionality must be incorporated into the polymer designs. As a general design, the bottom polymers are relatively hydrophilic with k values > 0.5 at 193 nm. This ensures good adhesion to the substrate and higher light absorption. In contrast, the top polymer contains fluorinated moieties and has a smaller k of < 0.5 at 193 nm. It also has low surface energy and good etch selectivity. The two polymers are formulated in an organic solvent together with a thermal acid generator (TAG) and cross-linker (XL). After spin coating and PAB, the top polymer self-segregates to the surface and the bottom polymer moves to the bottom. Intermixing of the two polymers occurs between the two, and a continuous increase of k from the top to the bottom in the BARC film is obtained.

For different resists and substrates, the top and bottom polymers must be designed to optically match. General rules are:

- Index n of the top of the graded BARC $\cong$ n of the resist.
- k of the top of the graded BARC << k of the bottom of the graded BARC.
- Index n of the bottom of the graded BARC $\cong$ n of the substrate.

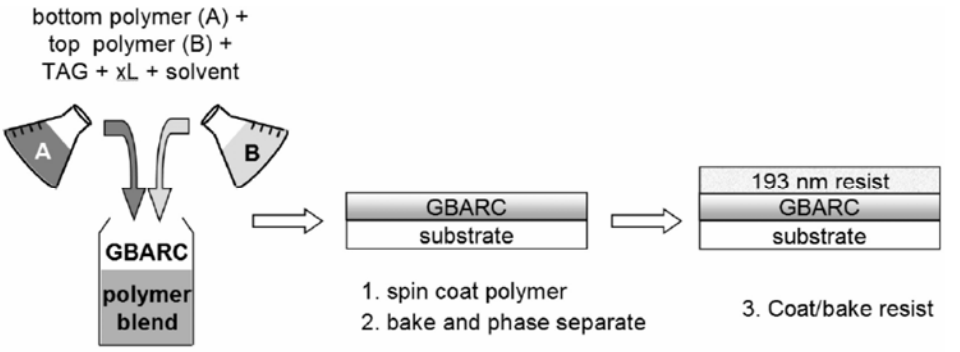

Figure 7.10 Design concept of graded spin-on BARC (GBARC) and its process flow. (Reprinted by permission from Ref. 12.)

Various samples with thickness < 50 nm were prepared and coated on different substrates. The improvement of through-pitch DOF, exposure latitude, and cross-sectional profiles was demonstrated.[12]

From the process perspective, there are obvious advantages to spin-on graded BARCs, one being that they have the same process flow as conventional single-layer BARCs. To realize the same reflectivity control, the graded BARC can be made much thinner than a conventional single-layer BARC. This provides an extra etch thickness budget for pattern transfer to the substrate. The problems that accompany the development of graded BARCs will be solved primarily through the design of new polymers.

7.4 Si-containing BARC and Spin-on Carbon

ArF resists inherently give poorer etch resistance than do KrF resists. Therefore, etch masks are occasionally required for transfering the resist pattern to the substrate. The most popular hard mask for Si or SiO_2 substrate is the amorphous carbon (a-C) film, which has several advantages, such as high etch selectivity and durability in preventing damage during strip. Traditionally, a SiON layer is deposited over the a-C layer. Then, BARC and resist are spin-coated on for the lithographic process. The SiON serves as a hard mask for the a-carbon film. However, SiON and a-C films are deposited by CVD, adding to the process steps that increase the complexity, cost of ownership, and turn-around time. Si-containing BARC (Si-BARC) and spin-on carbon (SOC) are developed to simplify the process.[13] Both Si-BARC and SOC materials are dissolved in organic solvents and spin-coated onto the substrate. A variety of other names are used for the Si-BARC and SOC, such as Si-containing hard mask (Si-HM), Si spin-on hard mask (Si-SOH), and C spin-on hard mask (C-SOH).

7.4.1 Process flow of the resist/Si-BARC/SOC trilayer

The SOC is first spin-coated onto the substrate. After the post-apply bake, the Si-BARC is spin-coated onto the SOC film. The SOC material typically has 80–90

wt% carbon content and a thickness between 100 and 300 nm. The stack of resist/Si-BARC/SOC forms a trilayer structure, as shown in Fig. 7.11(a). The Si-BARC replaces the combination of BARC film and SiON film in the traditional process and typically has a thickness of 20–100 nm with a Si content of 15–45 wt%.

Figure 7.11 shows the process flow of the trilayer. After the lithographic process, the resist pattern is formed (Fig. 7.11(b)). The wafer is etched with a halogen plasma to transfer the pattern from the resist film to the Si-BARC film (Fig. 7.11(c)). Residuals of the resist film may be left on the Si-BARC. Then, oxygen plasma is introduced to etch the SOC film for transfer of the pattern from the Si-BARC film to the SOC film (Fig. 7.11(d)). The resist residuals are removed by the oxygen plasma and residuals of the Si-BARC remain on the SOC film. Finally, the etch chemistry is switched back to halogen plasma to transfer the pattern from the SOC film to the Si substrate (SiO_2 or SiN) (Fig. 7.11(e)). This transfer of patterns to the substrate by etches is sometimes called "dry development." All of these plasma etch processes are accomplished in one etch chamber with one recipe. Both the Si-BARC film and the SOC film function as hard masks to transfer patterns from the resist to the Si substrate.

The trilayer process has been evaluated by many groups, so numerous results are available. Taking the work shown in Fig. 7.12 as an example, the trilayer stack has 200-nm resist / 100-nm Si-BARC / 200-nm SOC with Si content of 35 wt%.[14] First, 80-nm dense lines are printed in the resist film. Next, the lithography performances are obtained and compared to the traditional CVD hard mask stacks (resist/BARC/SiON/a-C), as shown in the table in Fig. 7.12. The resist on the Si-BARC stack provides a similar lithographic performance to that of a resist in a traditional CVD stack, indicating that the resist is compatible with the Si-BARC and the stack can provide effective antireflective control. Figure 7.12 shows the top-down and cross-sectional SEM images taken during the etch processing steps. The pattern in Si-BARC film (Fig. 7.12(b)) shows slightly tapered profiles with the resist residuals visible in the image. The pattern in the Si-BARC film is subsequently transferred to the SOC film by oxygen-based chemistry.

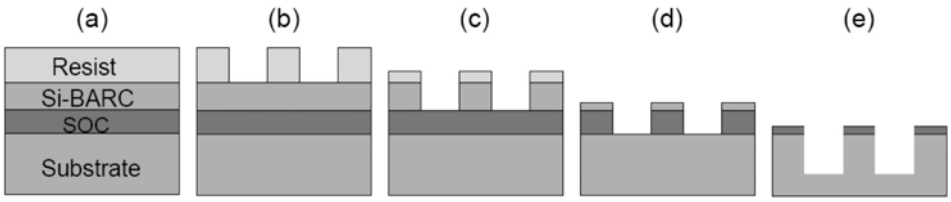

Figure 7.11 Process flow of the trilayer Si-BARC approach. (a) Trilayer stack of resist/Si-BARC/SOC on substrate. (b) Resist pattern after lithographic process. (c) The resist pattern is transferred to the Si-BARC film by halogen plasma etching. (d) The pattern is transferred from Si-BARC to SOC film by oxygen plasma etching. (e) The pattern is transferred from the SOC film to the Si substrate (SiO_2 or SiN) by halogen plasma etching.

	MFHM Process	BARC Process
EL (%)	12.8	13.4
DOF (μm)	≥0.2	≥0.2
FCCD (nm)	66.4	67.5
LWR (3σ)	5.4	3.2

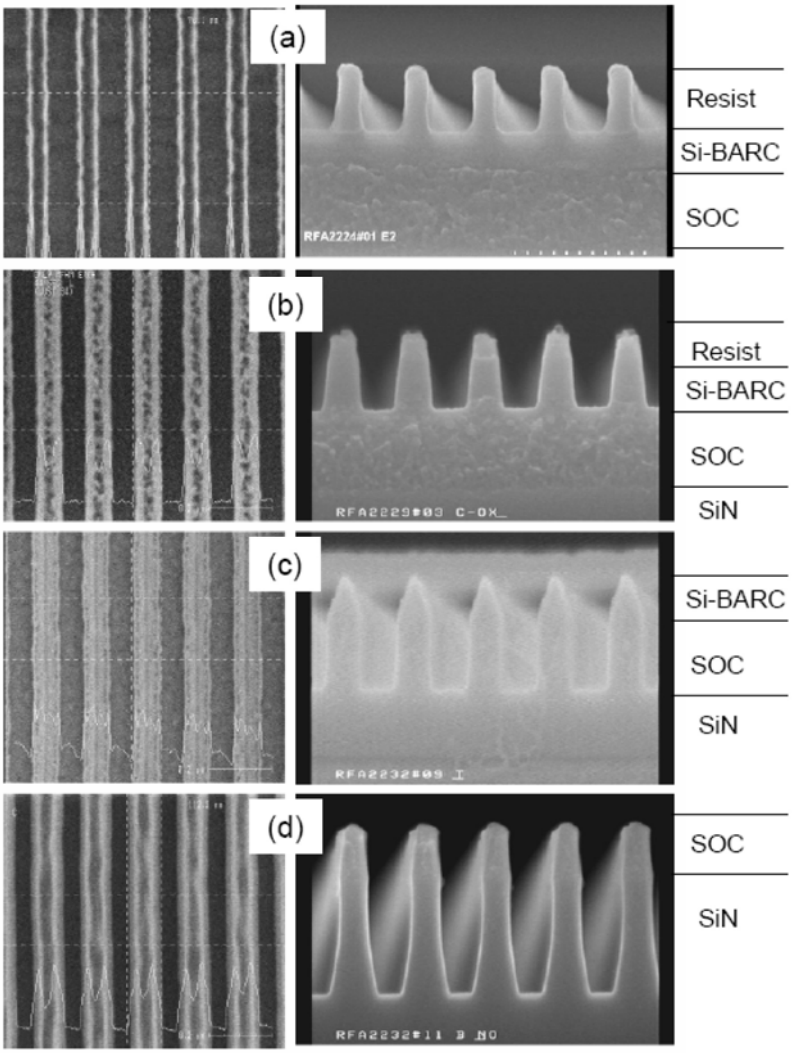

Figure 7.12 Top-down and cross-sectional SEM images at pattern transferring steps: (a) post development, (b) after opening the Si-BARC, (c) after opening the SOC, and (d) after etching the SiN substrate. The half-pitch of the pattern is 160 nm. The table shows the lithographic performance comparison of the Si-BARC process (resist/Si-BARC/SOC) and the traditional process (resist/BARC/SiON/a-C). FCCD stands for first collapse critical dimension, which is a maximum CD after pattern collapse when overexposed (at the best focus). (Reprinted by permission from Ref. 14.)

7.4.2 Consideration of antireflection control

Both Si-BARC and SOC films are spin-coated onto a substrate, providing good surface planarization. Their thickness and optical parameters must be optimized to provide dual-BARC reflective control. The mask contains various patterns with different pitches and the incident angle of exposure light on the resist surface ranges from 0 to the full numerical aperture ($\sin^{-1}$(NA/1.44)). Ideally, a BARC stack should be optimized so that the reflectivity at the resist–BARC interface is minimized for all possible incident angles.

A method has been developed to optimize stack parameters over broad incident angles.[15] First, the n and k ranges of the Si-BARC and SOC are defined by the availability of the samples. Si-BARC film thickness (FT) is in the range of 20–70 nm to cover the first minimum. The thickness of SOC film is assumed to be three times that of the Si-BARC layer, which corresponds to the expected etch selectivity. The reflectivity at the Si-BARC surface is calculated and averaged over all incident angles from 0 to $\sin^{-1}$(1.35/1.44) for 193i. The average reflectivity is obtained for all points in the parameter space ($n_{\text{Si-BARC}}$ = 1.6–1.8, $k_{\text{Si-BARC}}$ = 0–0.4, $\text{FT}_{\text{Si-BARC}}$ = 20–70 nm, n_{SOC} = 1.5–1.9, k_{SOC} = 0.3–0.7). The results are sorted by using the threshold of the average reflectivity < 0.5%. Corresponding to one specific parameter, for example $n_{\text{Si-BARC}}$ = 1.7, the occurrence of the reflectivity < 0.5% is counted and plotted in Fig. 7.13.
From Fig. 7.13, the trilayer stack with the Si-BARC (n = 1.70, k = 0.175, and FT = 40 nm) and the SOC (n = 1.80, k = 0.40, and FT = 120 nm) can provide the best reflection control on a SiO_2 substrate with a typical ArF resist of n = 1.7 and k = 0.2 in hyper-NA exposures. The same simulation method can be applied to other thickness ratios of Si-BARC and SOC films.

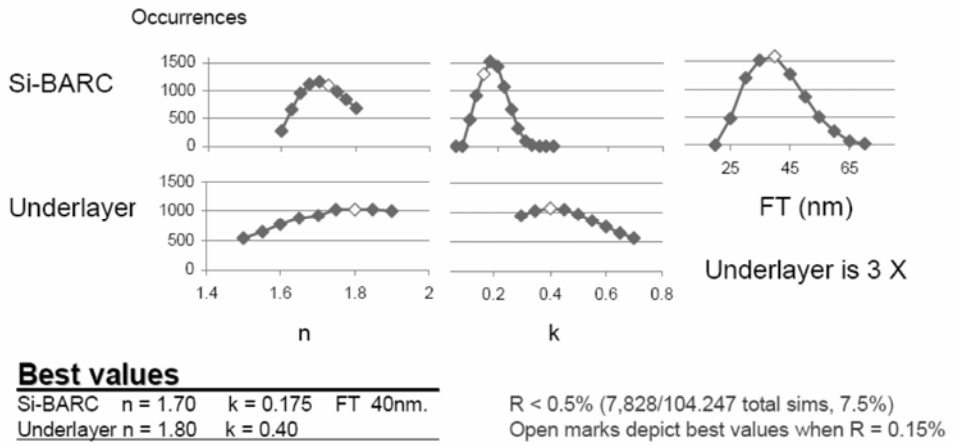

Figure 7.13 Simulation results for the best optical indices and film thicknesses (FTs) based on minimizing reflectivity (R) for a trilayer stack with Si-BARC FT between 20 and 70 nm and SOC (underlayer) FT that is three times the Si-BARC FT. (Conditions: 193-nm Y-polarized light, resist n = 1.7, k = 0.02, the substrate is SiO_2, and the reflectivity is averaged through angle 0 < NA < 1.35.) (Reprinted by permission from Ref. 15.)

7.4.3 Etch selectivity

Etch selectivity in the trilayer process must be broken into two parts. One part is for the transfer of the resist pattern to the Si-BARC in halogen plasma (such as CF_4) and the other part is for transferring the Si-BARC pattern to the SOC film in oxygen plasma. In general, the Si-BARC has a higher etch rate in the halogen chemistry, while the resist has a lower etch rate. This high selectivity enables a thin resist process. In contrast, the Si-BARC has a lower etch rate in the oxygen chemistry and the SOC has a higher etch rate.

Although the exact etch rates can be modified by the details of etch recipes, the Si content in the Si-BARC is the key to achieving the highest etch selectivity. First-generation Si-BARC has a Si content of 15–25% and the second generation has boosted the Si content to 35–40%.[16] It is widely known that photoresists are quickly etched in oxygen-based plasmas (such as SO_2/O_2) and slowly etched in halogen-based plasmas. The Si-BARC interacts with oxygen-based plasma differently from the way it interacts with fluorocarbon plasma.[17] Figure 7.14 shows the bulk etch rates of a Si-BARC sample in SO_2/O_2 and C_xF_y chemistry.

The results in Fig. 7.14 demonstrate that in a SO_2/O_2 environment, etch stops quickly. This is because the Si component in the Si-BARC film forms a protective layer of SiO_2 that slows the etch process. Thus, Si-BARC shows a significantly slow etch rate and etch-stopping capability against SO_2/O_2 gas plasma. However, in the C_xF_y chemistry, the Si-BARC thickness decreases linearly with etch time and the slope of the curve (the etch rate) is ~5 nm/s. Such a clear difference in the etch rates in SO_2/O_2 and C_xF_y confirms that the Si-BARC can serve as an etch mask for transferring a pattern from a regular resist to the SOC. Further experimental results demonstrate that the higher the Si content, the better the etch selectivity.[18] To provide a reference, the ratio of the etch rates of

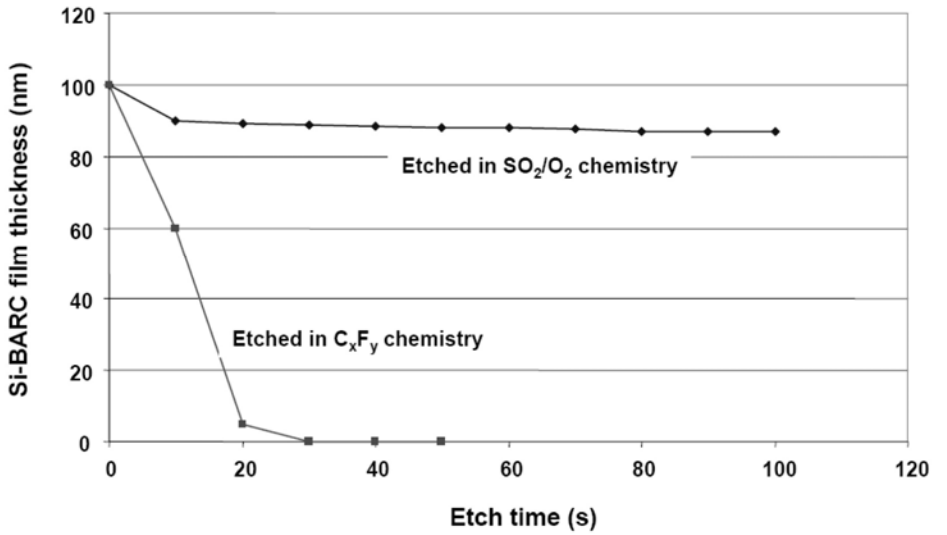

Figure 7.14 Bulk etch rates of Si-BARC film in SO_2/O_2 chemistry and in C_xF_y chemistry.

an advanced Si-BARC and regular ArF resists in CF_4 plasma is about 3:1 and the ratio of the etch rates of an advanced SOC and Si-BARC in oxygen plasma is about 35:1.

Many technical details are associated with Si-BARC and SOC etch. For example, the pattern may deform during etching and lead to increases in line-edge roughness.[19] The etch selectivity of SOC relative to Si-BARC is very high, thus, significant amounts of Si-BARC may remain after SOC etch and generate defects during the etching of the substrate. These issues are beyond the scope of this book and will not be discussed further.

7.4.4 Resist compatibility and the tetralayer approach

One of the challenges in the trilayer process is achieving resist compatibility. Footing in the resist patterns gets worse as the percentage of silicon in the Si-BARC increases. This problem has been attributed to the rough surface of Si-BARC or to the fact that acid diffuses from the resist into the Si-BARC.[20] Two methods have been suggested to reduce footing. One is to increase the cross-linking of the base polymer in Si-BARC and the other is to reduce the surface roughness of the Si-BARC.

A stripping test with the resist solvent can be used to evaluate the extent of cross-linking of the Si-BARC. The same test is used for conventional BARCs. The Si-BARC is first coated onto a Si substrate and baked. The resist solvent (e.g., PGMEA) is dispensed on the Si-BARC film, forming a puddle for 30–60 seconds to mimic the resist dispense time, and is then spun dry. The Si-BARC thickness is measured before and after this solvent process.[21]

To temporarily solve the compatibility issue between the resist and the Si-BARC, an additional thin organic BARC layer can be coated between them to serve as an isolation layer (Fig. 7.15). The entire stack on the substrate has four layers (resist/BARC/Si-BARC/SOC) and is called a tetralayer or quadlayer. The tetralayer approach enables universal resist compatibility. Although one extra layer of BARC gives better antireflection control, the drawback is the increased cost and complexity of the additional process steps.

Etch performance of the tetralayer approach has been evaluated.[22] The stack has the following specifications: the BARC thickness of 30 nm, the Si-BARC thickness of 70 nm, and the SOC thickness of 200 nm. The Si-BARC is a silsesquioxane- (SSQ) type resin that contains a chromophore cross-linking group, with a high Si-containing group (> 30 wt%) to increase etch selectivity in the SOC layer. The SOC, which has a carbon content > 85 wt%, is an acrylate-type polymer containing large amounts of aromatic rings for high etch selectivity versus the substrate. The tetralayer approach is similar to the trilayer approach in that fluorinated gas chemicals such as CF_4, CHF_3, and C_4F_8 are used to transfer patterns from the resist film to the Si-BARC. The oxygen chemistry is

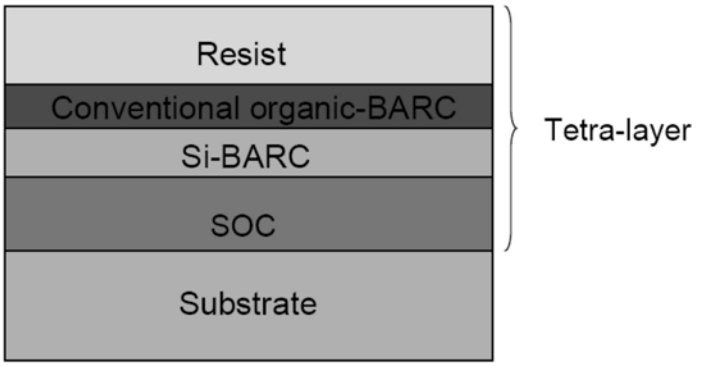

Figure 7.15 Tetralayer on the substrate: resist/BARC/Si-BARC/SOC.

used to transfer patterns from the Si-BARC to the SOC. A regular BARC open step is added at the beginning of the etch recipe to open the thin organic BARC. The etch rates of the thin BARC, Si-BARC, SOC, SiO_2, SiN, and poly-Si are measured at various etch conditions and calculated for etch selectivity (Table 7.1). The results demonstrate that (1) the thin organic BARC and Si-BARC etch about 1.4 faster than do the resist in CF_4 plasma, (2) the SOC etches 30 times faster than does the Si-BARC in oxygen plasma, and (3) the SOC etches 15.1, 5.9, and 4.9 times faster than do the SiO_2, SiN, and poly-Si, respectively.

7.4.5 Storage stability and solvent rework capability

Si-BARCs tend to have poor shelflives because the silanol groups can react with each other, leading to molecular weight increases or the formation of gel-type particles.[23] Thus, Si-BARC samples must be tested for shelflife so that the

Table 7.1 Etch selectivity of each material in the tetralayer approach. (Reprinted by permission from Ref. 22.)

Sample	CF_4 *1	O_2 *2	CHF_3/Ar *3		Cl_2 *4
	Sample rate / ArF resist rate	Sample rate / Si-ARC rate	SiO_2 rate / Sample rate	SiN rate / Sample rate	Poly-Si rate / Sample rate
ArF resist	1.0	-	7.8	3.0	2.4
SiO_2	-	-	1.0	0.4	-
SiN	-	-	2.6	1.0	-
Poly-Si	-	-	-	-	1.0
Thin BARC	1.4	-	-	-	-
Si-ARC	1.4	1.0	-	-	3.4
SOC	0.7	30.0	15.1	5.9	4.9

*1: CF_4=90sccm, 50mtorr, 100W, 30degC, 60sec.; ES401 (Nippon scientific Co. LTD.).

*2: O_2=40sccm, 60mtorr, 100W, 25degC, 60sec.; RIE-10NR (samco).

*3: CHF_3/Ar=40sccm/120sccm, 60mtorr, 280W, 25degC, 90sec.; RIE-10NR (samco).

*4: Cl_2=30sccm, 30mtorr, Top/Bottom=350W/50W, 30degC, 60sec.; TCP9400SE (Lam Research)

molecular weight (Mw), film thickness, water content, and liquid particle counts (LPCs) remain constant for at least 6 months at 20° C or for 1 month at 40° C.[24]

Similarly to resists, both Si-BARC and SOC films are claimed to be strippable by solvents, thereby, making the rework route applicable to the trilayer process. The reasons for reworking these films include failures in CD, overlay, and defect counts. In practice, there are two rework strategies applicable to the trilayer (Fig. 7.16). The first strategy is to remove only the resist (Fig. 7.16(a)). This process is accomplished by soaking the trilayer in a resist solvent that removes the resist film and leaves Si-BARC and SOC cross-linked films behind. Before recoating the resist film, the wafer is typically baked at ~100° C to dehydrate the films. The second strategy is to remove the entire stack via either a traditional oxygen ashing process or with a Piranha solution (H_2SO_4/H_2O_2) wet rework process (Fig. 7.16(b)).[25] These rework processes should not cause any damage to the substrate and should not fall outside of the specification in the particle counts.

7.4.6 Thick Si-BARC ("etch screw") process

In addition to the trilayer and tetralayer processes, Si-BARC opens another process option for reflection control, called the thick BARC process. The mechanism of reflective control of thin organic BARCs is mainly the destructive interference between incident light and reflected light. For thin-layer BARCs, even a small variation in thickness results in rapid increases in reflectivity. By contrast, light absorption is the main mechanism of reflection control in thick BARCs. For a thick BARC, 99% of 193-nm light entering the BARC will be absorbed, making the lithographic process highly insensitive to thickness variations of the underlying film stack. Thus, the optical constants of the substrate are unimportant to the overall result. Simulation was performed with a stack of resist/thick BARC/Si substrate.[3] The resist has a thickness of 230 nm, a refractive index of $n = 1.7$, and $k = 0.02$. The BARC has a refractive index of $n = 1.75$ and $k = 0.21$. The Si-substrate has a refractive index of $n = 0.88$ and $k = 2.78$ at 193 nm. The results demonstrate that if the BARC thickness is ~200 nm, a reflectivity of < 1% can be achieved for 1.2NA exposures.

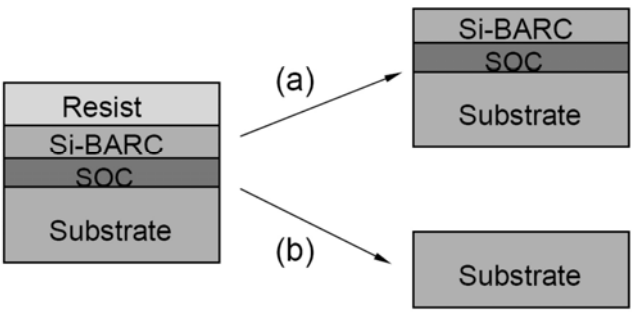

Figure 7.16 Rework strategies for the resist/Si-BARC/SOC trilayer: (a) removing the resist film only and (b) removing the whole stack.

However, the challenge to the thick BARC process lies in the etch process. Conventional organic BARCs have nearly the same etch rates as 193-nm resists. How can such thick BARCs be opened without completely consuming the resist film? One possible answer is the use of Si-BARCs, since their etch rate ratio to the resist is greater than 3:1 and far exceeds that of organic BARCs.

The concept of using a thick Si-BARC for contact hole printing has been demonstrated.[3] Figure 7.17(a) shows a diagram of the process flow. After development and before etch, top-down and cross-sectional images are taken of the resist pattern (Fig. 7.17(b)). The average CD of the contact holes in the resist film is about 145 nm. After etch and cleaning, the final patterns are inspected again (Fig. 7.17(c)). A final CD of 125 nm is obtained in the substrate. The CD shrinkage is attributed to the tapered Si-BARC profiles shown in Fig. 7.17(a).

The CD shrinkage shown in Fig. 7.17 is about 20 nm. This value is comparable to the shrinkages obtained by most CD shrink processes. Further increases in the thickness of Si-BARC and SOC should produce more shrinkage in CD. This process is called the "etch screw."

Alternatively, the stack can be a thin Si-containing resist on top of a thick organic BARC. This results in another type of resist development: bilayer resists with thick organic underlayers. The imaging layer is a Si-containing photosensitive polymer. Although these imaging layers are continuously being improved, their resolution and image contrast are typically inferior to those of conventional single-layer resists. Further material development and evaluation are ongoing.[26]

7.5 Gap-Fill Materials

Gap-fill materials are most commonly used in the back end of line (BEOL) lithographic processes, especially in the dual-damascene process. In general, dual-damascene widely uses the via-first approach. In this process, deep vias are formed first, then trenches are patterned on top of the vias. Due to high aspect ratios of the vias, conventional BARCs cannot completely fill the holes, and voids are formed at the bottom of the vias (Fig. 7.18(a)). BARC films are typically thicker in areas with isolated vias than they are in areas with dense vias (Fig. 7.18(b) and (c)). This thickness variation leads to degradation in CD uniformity across the wafer.

Gap-fill material is designed to fill deep vias during spin coating, after which, the post-apply bake drives the solvent out, forming a solid film. This gap-fill material also prevents over-etching of the underlying metal at the base of the vias while the trench is being etched. The alternative option to the dual-damascene process is the trench-first process, in which the gap-fill material is used to fill the trenches and planarize the surface for the via-patterning processes.

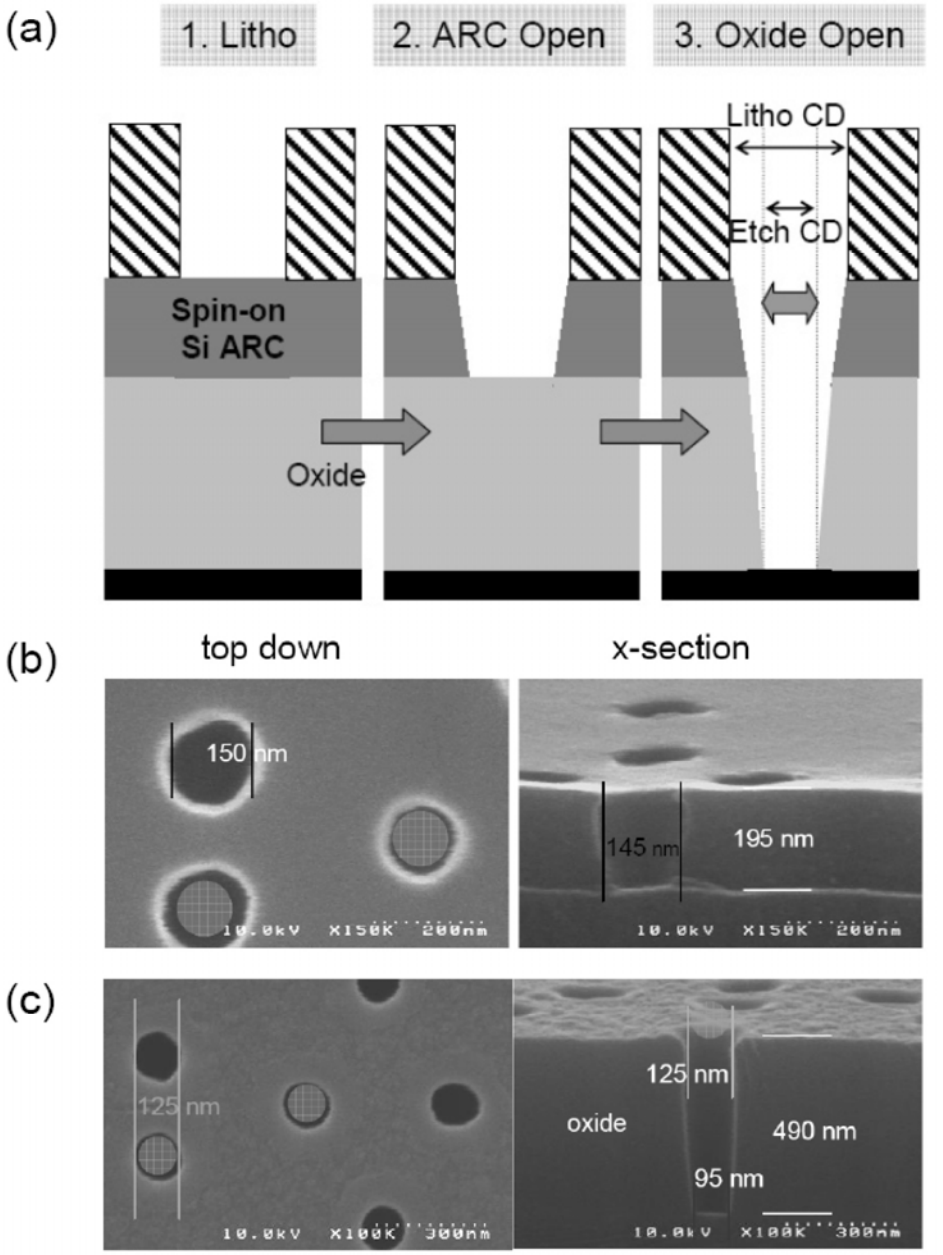

Figure 7.17 (a) Process flow of the thick Si-BARC process for contact hole patterning. (b) Top-down and cross-sectional SEM images after development and before etch. (c) Top-down and cross-sectional SEM images after etching and cleaning processes. (Reprinted by permission from Ref. 3.)

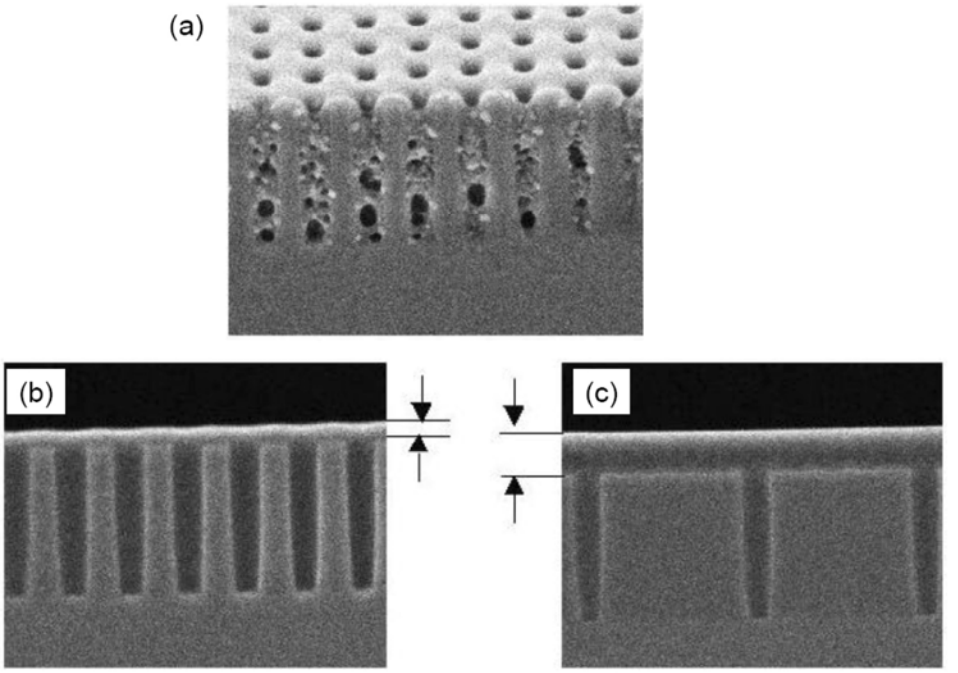

Figure 7.18 SEM images of vias filled with a conventional BARC. The diameter of the vias is about 180 nm and the depth is about 900 nm. (a) Voids are observed in the vias. The BARC film is thinner in the (b) dense area than in the (c) isolated area. (Reprinted by permission from Ref. 27.)

7.5.1 Process flow of gap-fill materials

A popular gap-fill strategy is the dry etch-back process, shown in Fig. 7.19. The gap-fill material should be thick enough to ensure complete filling of the gaps. Vias or trenches are filled first with a thick spin-on film. The cross-linking occurs during the post-apply bake, typically at high temperatures. In the area of dense vias, more gap-fill material is reflowed into the vias, while, in the area of isolated vias, less material is needed to fill the vias. Thus, the gap-fill material is thicker in the area of isolated vias than it is in the area of dense vias, as shown in Fig. 7.19(b). Next, an oxygen-plasma etch is used to remove the excess material, leaving only filled vias or trenches. The BARC and resist are then coated. After exposure and development, the gap-fill material, along with the BARC film, is removed by dry etch. The drawback of this type of gap-fill materials is obvious: dry etch is needed before the coating of the BARC and the resist.

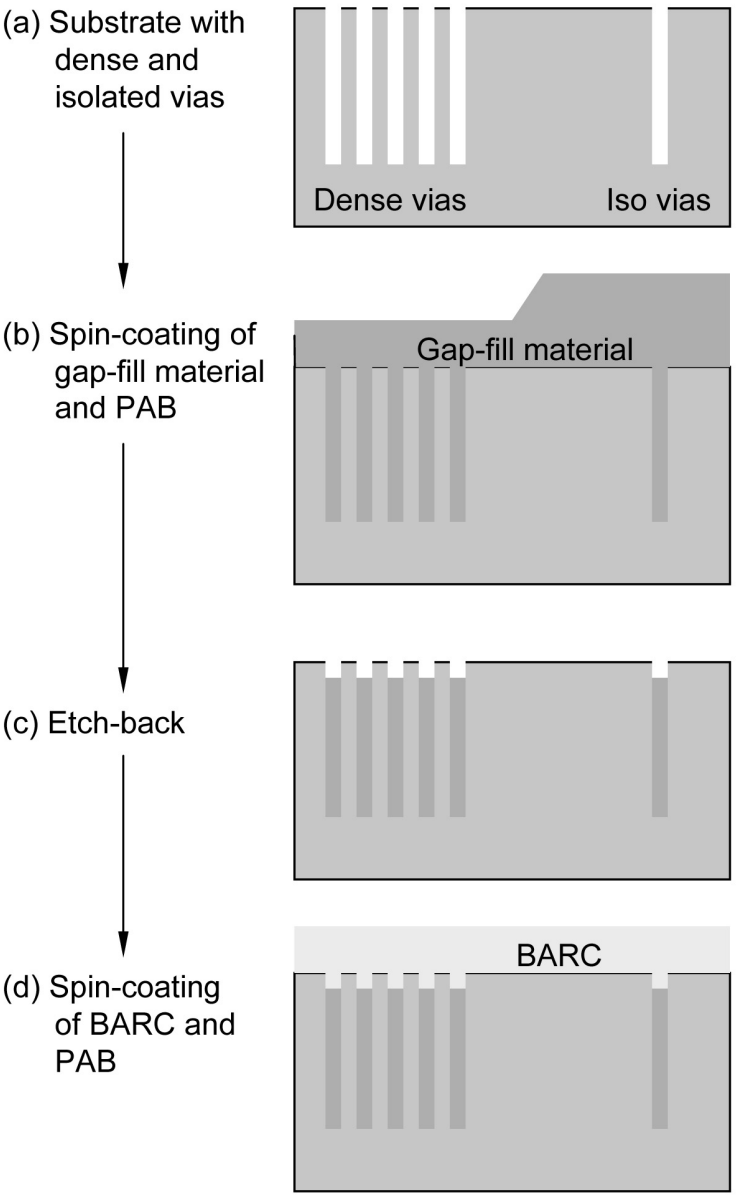

Figure 7.19 Process flow of gap-fill material in the dry etch-back process.

Developer-soluble gap-fill materials were designed as an alternative to the conventional gap-fill approach.[28,29] This type of material requires relatively low PAB temperatures because no cross-linking is needed. Then, the etch-back process is performed using a standard aqueous developer. This step, called the wet-recess, replaces the etch-back process and eliminates the need to transfer wafers between etch and photo bays; therefore, developer-soluble gap-fill materials are preferred for use in production.

7.5.2 Evaluation of filling capability

The filling capability of these materials can be evaluated by measuring the thickness uniformity across the wafer. The gap-fill material and BARC films are coated on via-patterned wafers following the process flows shown in Fig. 7.19. The BARC thicknesses at the wafer center and near the wafer edge are measured for dense pattern regions, isolated pattern regions, and unpatterned regions. Ideally, the BARC thickness across the wafer and for different pattern densities should be the same. This is called global planarization. In reality, the thickness values have a distribution. The standard deviation of the thickness values across the wafer is used to quantitatively assess the filling capability. Depending on the CDU budget, a global planarization of < 20 nm is required for an advanced BEOL lithographic process. The gap-fill capability for trenches has been evaluated and reported.[30]

Before the etch-back process, the thickness of the gap-fill material in sparsely patterned areas is different from that in densely patterned areas. These thickness variations are called the thickness bias, which is a function of the viscosity of the material, the spin speed, acceleration, air flow, and bake conditions.[31] During the high-temperature bake, the polymer can both reflow and cross-link. The gap-fill materials usually have glass transition temperatures (T_gs) between 20 and 150° C. When the curing temperature of the film is above the polymer's T_g, the polymer becomes less viscous and is able to reflow. This thermal reflow smoothes the surface and reduces thickness nonuniformity. At the same time, cross-linking takes place, slowing the movement of the polymer. Thus, increases in the bake temperature can be either beneficial or harmful to the filling capability, since thermal reflow and cross-linking are in competition with each other. If the activation energy of thermal flow is larger than that of the cross-linking reaction, the thickness bias will decrease with bake temperature. If the case is the opposite, the thickness bias will increase with increasing bake temperature. Table 7.2 shows the measured iso-dense bias from two BARC materials. The results indicate that the activation energy for cross-linking of ARC81 is larger than its activation energy for thermal flow. The opposite is true for DUV52.

Table 7.2 Iso-dense bias of ARC81 and DUV52 coatings at different bake temperatures. (Reprinted by permission from Ref. 31.)

Bake temperature (°C)	Iso/dense Bias (nm)	
	ARC81	DUV52
225	-	245
205	274	246
175	263	256
150	242	274
135	248	331

7.5.3 Chemical compatibility and etch rate

Gap-fill materials do not need to have antireflection properties; however, they should not be soluble in the BARC solvent. If they are soluble, intermixing will occur, altering the optical performance of the BARC film. A strip test must be performed to assess the resistance of the gap-fill materials to the BARC solvent. In this test, the gap-fill material is spin-coated on a Si wafer and baked. Then, the wafer is soaked in the BARC solvent for 30 seconds (for example). The film thicknesses before and after the soak are measured and compared. Typically, a thickness loss of less than 10 nm is considered acceptable.[27]

Gap-fill materials typically have high etch rates both in the oxygen etch-back process and in the BARC open process. For developer-soluble gap-fill materials, the cured film must be soluble in standard developer. While the dissolution rates can be adjusted by the PAB temperature, the dissolution rate of the material inside the vias is typically smaller than that of the bulk material.[32]

7.6 Top Antireflective Coatings (TARCs)

Conventional organic BARCs are not imageable or soluble in aqueous developers, and pattern transfer into BARCs is typically accomplished by an etch process that is downstream from lithography. The etch recipe must open the BARC layer before the substrate may be etched. However, for implant levels, etch is not a downstream process. To open BARC films, wafers must be sent to etch chambers for additional processing. Top antireflective coatings (TARCs) have been designed to address this issue. Figure 7.20 shows a typical TARC process flow. The resist is coated over a substrate primed by hexamethyldisilizane (HMDS). Then, the TARC, which is transparent to the exposure light, is coated over the resist film. TARCs are usually base-soluble polymers that are removed by standard aqueous tetramethylammonium hydroxide (TMAH) developer during development.

As shown in Fig. 7.20, the TARC process is very similar to the developer-soluble topcoat process in 193-nm immersion lithography. The main function of TARCs is to provide reflection control (as opposed to providing a barrier to leaching and water uptake). Thus, the major concerns related to the use of TARC films are optical performance and chemical compatibility with the resist.

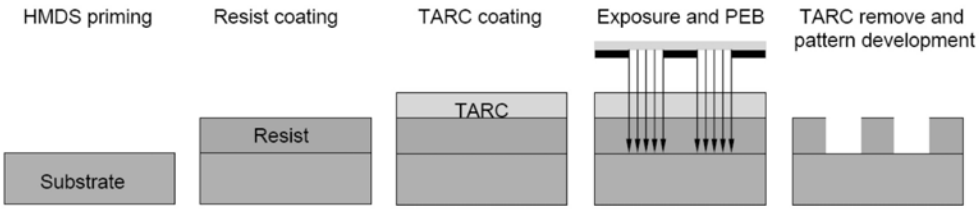

Figure 7.20 A typical TARC process flow. The TARC is aqueous soluble and is removed in the development step.

7.6.1 Optical performance of TARC films

TARCs reduce reflectivity through destructive interference. The thickness and refractive index of the TARC must be carefully controlled to meet the destructive interference conditions. Assuming that the TARC has no absorption, the conditions for destructive interference are

$$n_{\mathrm{TARC}} = \sqrt{n_{\mathrm{air}} \cdot n_{\mathrm{resist}}} \quad \text{and} \tag{7.8}$$

$$t_{\mathrm{TARC}} = \frac{1}{4} \cdot \frac{\lambda}{n_{\mathrm{TARC}}}. \tag{7.9}$$

In Eqs. (7.8) and (7.9), n_{TARC}, n_{resist}, and n_{air} are the reflective indices of TARC, resist, and air, and λ is the exposure light, which is 193 nm. 193-nm resists typically have refractive indices of ~1.7 and $n_{\mathrm{air}} = 1$. Thus, the ideal refractive index for TARCs is about 1.3 and the ideal thickness is about 37 nm for 193-nm exposures.

Most 193-nm TARCs have refractive indices around 1.4. Design of TARCs with refractive indices of ~1.3 may not be technically feasible. In order to provide enough solubility in the aqueous base, TARC polymers must have sufficient polar groups, such as fluorocarbinols, carboxylic acids, sulfonic acids, sulfonamides, or other hydroxyl groups. These polar groups, unfortunately, increase the n value of the polymers to above 1.4.[33] Fluoropolymers are ideal materials for TARCs because of their high transparency, since fluorinated compounds are much more transparent to 193-nm light than are conventional alkanes.[34] Two approaches have been used to reduce n value: (1) incorporation of air into the polymer films to form nanoporous structures and/or (2) incorporation of fluorine into the polymers. However, the hydrophobicity of fluorine groups decreases the solubility of these polymers in aqueous developer.

7.6.2 Chemical compatibility and coating issues

Because TARCs are coated on resist films, they must be chemically compatible with the resist and, specifically, the acid levels in the two layers must match. While too much acid in the TARC will result in resist loss and degradation of pattern profile, too little acid will result in T-topping.

TARCs usually contain surfactants to improve coating uniformity and stability. The surfactants will encapsulate microbubbles during filtration and dispense. These microbubbles in TARC film lead to microlensing effects during exposure. To remedy this problem, TARCs often require double dispense techniques to minimize the formation of bubbles in the coatings and the buildup of bubbles in the dispense pump.[35] Due to their excellent wet-ability, TARCs can protect resist layers from airborne contamination and improve uniformity during the development process.

7.6.3 Absorbing TARCs

Highly absorbing polymers have recently been developed for use as absorbing TARCs.[33] The absorbing TARCs have k values greater than zero, thus, the optimum refractive index equation of $n_{TARC} = (n_{air} \cdot n_{resist})^{1/2}$ and the optimum TARC thickness equation of $t = \lambda/4n_{TARC}$ are no longer valid. Detailed simulation is needed to find the reflectivity at the TARC surface.

Figure 7.21(a) shows the simulations of reflectance versus the refractive index for several k values (extinction coefficients). For minimum reflectance when $k = 0$ (transparent TARC), n is around 1.3; however, when $k = 0.14$ (absorbing TARC), n is around 1.34–1.35. The advantage of using the absorbing TARC is that the ultralow n (i.e., 1.3), is no longer required. Figure 7.21(b) shows the simulations of reflectance versus TARC thickness for $n = 1.34$ and various k values. The minimum reflectance shifts to thinner TARC thickness with higher k value. When $k = 0$, the optimum TARC thickness is around 36–37 nm. When $k = 0.15$, the optimum is around 27 nm. At this thickness, the transmittance is around 76%. Even though absorbing TARCs absorb a certain amount of light, the exposure energy loss is not expected to cause significant losses in throughput and one can compensate for the losses by selecting resists with higher sensitivity.

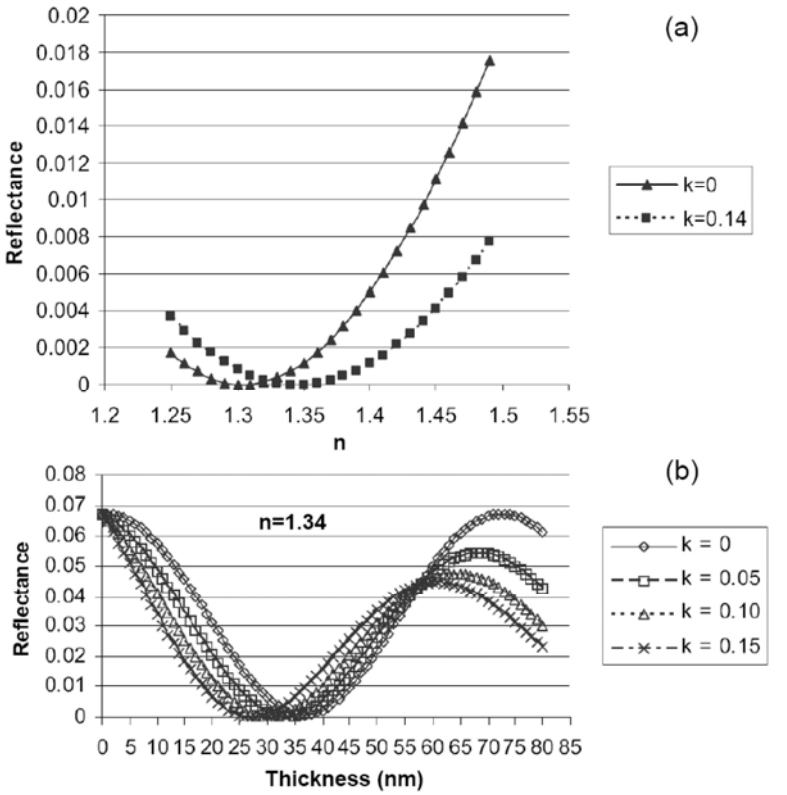

Figure 7.21 Reflectance at the TARC surface as a function of (a) the refractive index and (b) the TARC thickness, respectively. (Reprinted by permission from Ref. 33.)

7.7 Developer-Soluble BARCs (DBARCs)

TARCs provide reflection control only at the top surface of the resist. For the same resist and exposure conditions, BARCs provide better reflection control than TARCs provide, especially on topographic substrates.[36] Thus, developer-soluble BARCs (DBARCs) have been developed for implant levels. There are two types of DBARCs: nonphotosensitive and photosensitive. Nonphotosensitive DBARCs can be dissolved by standard aqueous developer without exposure and photosensitive DBARCs have solubility in the developer only after exposure, as do resists. Because of its solubility in developer, the open process on the BARC is accomplished together with the resist development; therefore, DBARCs are also called wet-BARCs.

7.7.1 Nonphotosensitive DBARCs

Nonphotosensitive DBARCs are soluble in aqueous developers. During development, the exposed resist is first dissolved and then the DBARC film is dissolved. The optimum DBARC thickness is determined from the curve of reflectivity versus thickness. Usually, the first minimum that corresponds to several tens of nanometers is selected.

Achieving good pattern profiles from nonphotosensitive DBARCs is a challenge. Nonphotosensitive DBARCs dissolve isotropically in developer. They tend to form either undercut or footing profiles (Fig. 7.22). The DBARC in the center of the space typically dissolves faster than the DBARC dissolves near the sides, resulting in footing (Fig. 7.22(a)). With longer development times, the developers dissolve the DBARC underneath the resist pattern, forming undercut profiles (Fig. 7.22(c)). These problems limit the resolution of nonphotosensitive DBARCs, which typically cannot achieve better resolution than 150 nm. Since 150-nm pitch falls in the resolution capability of KrF exposures, nonphotosensitive DBARCs are most often used in KrF processes.

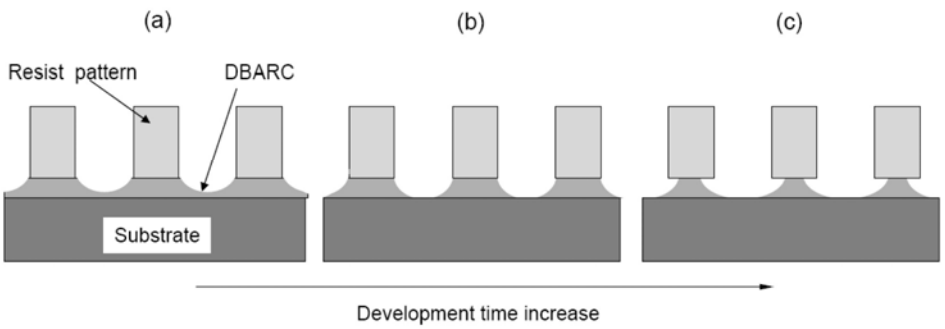

Figure 7.22 Isotropic dissolution of nonphotosensitive BARC in the standard aqueous TMAH developer. Development time increases from (a) to (c).

One method for controlling the DBARC profile is to vary the PAB temperature. Typically, higher PAB temperatures give lower dissolution rates. Figure 7.23 shows the dissolution rate versus bake temperature curve measured for a nonphotosensitive DBARC.[37] Cross-sectional SEM images of the patterns obtained at different bake temperatures are also included in the figure. These images demonstrate that profiles can be optimized through careful selection of bake temperature. Due to its sensitivity to bake temperature, nonphotosensitive DBARCs are also called "thermal-BARCs."

7.7.2 Photosensitive DBARCs

Photosensitive DBARCs or photo-DBARCs are exposed at the same time as the resists are exposed and both layers are subsequently removed by developer. Photo-DBARCs offer the potential for anisotropic development and should provide less undercut and line-collapse problems than nonphotosensitive DBARCs provide.

7.7.2.1 Photospeed match with resist

Photosensitive BARCs typically contain polymers, cross-linkers, photoacid generators (PAGs), quenchers, and solvents. The PAB removes solvent and causes the polymer to cross-link. To achieve the best pattern transfer, the photospeeds of the resist and of the BARC must be matched. The E_0 values of the resist and the DBARC should be close. The PAB temperature of the DBARC is often used to adjust the photospeed. Cross-sectional images are required for judging pattern profiles.

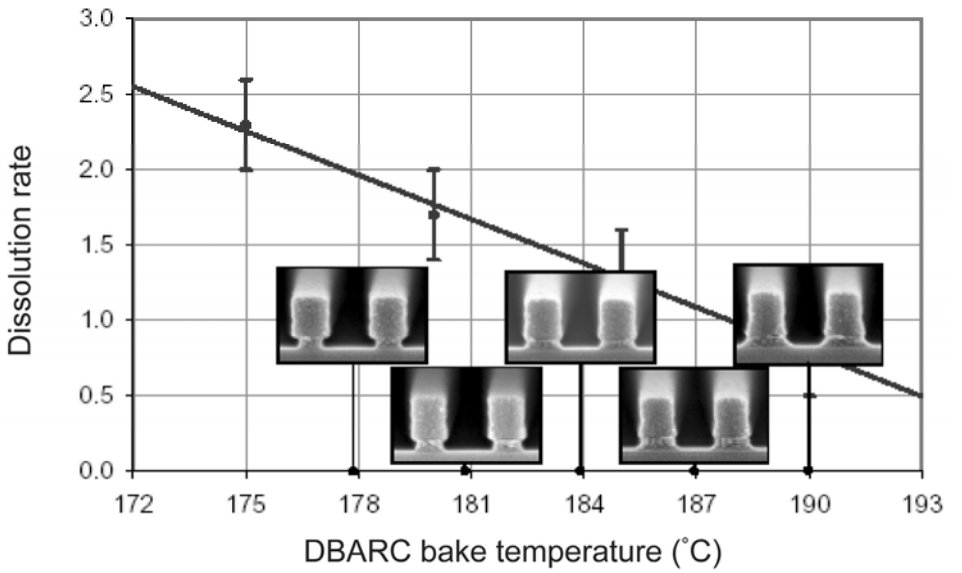

Figure 7.23 Dissolution rate versus bake temperature curve measured from a nonphotosensitive DBARC. Cross-sectional SEM images of the patterns obtained at different bake temperatures are included. (Reprinted by permission from Ref. 37.)

7.7.2.2 Chemical compatibility

One of the technical challenges of working with photosensitive DBARCs is their compatibility with resists. Resist solvents can cause changes in DBARC sensitivity. DBARC films rinsed by PGMEA become less photosensitive.[38] Thus, DBARC formulations require some process optimization for each new resist. Pattern profiles of the resist/DBARC stack can be optimized by adjusting exposure dose and PEB temperatures.

References

1. V. Farys, S. Warrick, C. Chaton, and J.-D. Chapon, "ARC stack development for hyper NA imaging," *Proc. SPIE* **6520,** 65204O (2007).
2. H. A. Macleod, *Thin-Film Optical Filters*, Hilger, Bristol, UK (1986).
3. S. Burns, D. Pfeiffer, A. Mahorowala, K. Petrillo, A. Clancy, K. Babich, D. Medeiros, S. Allen, S. Holmes, M. Crouse, C. Brodsky, V. Pham, Y.-H. Lin, K. Patel, N. Lustig, A. Gabor, C. Sheraw, P. Brock, and C. Larson, "Silicon containing polymer in applications for 193nm high NA lithography processes," *Proc. SPIE* **6153**, 61530K (2006).
4. Y. Hiroi, T. Kishioka, R. Sakamoto, D. Maruyama, T. Ohashi, T. Ishida, S. Kimura, Y. Sakaida, and H. Watanabe, "BARC (bottom anti-reflective coating) for immersion process," *Proc. SPIE* **6519**, 651928 (2007).
5. H. Gokan, S. Esho, and Y. Ohnishi, "Dry etch resistance of organic materials" *J. Electrochemical Soc.*, **130**, 143 (1983).
6. H. Zhuang, D. Abdallah, Z. Xiang, H. Wu, J. Shan, P.-H. Lu, M. Neisser, E. J. Karwacki, B. Ji, and P. R. Badowski, "The effects of etch chemistry on the etch rates of ArF BARC products," *Proc. SPIE* **6153**, 61530N (2006).
7. R. Huang and M. Weigand, "Plasma etch properties of organic BARCs," *Proc. SPIE* **6923**, 69232G (2008).
8. M. Colburn, S. Halle, M. Burkhardt, S. Burns, N. Seong, D. Goldfarb, and DE Team, "Process challenges for extension of H_2O immersion lithography to hyper-NA," Presentation at Litho Forum 2006, Vancouver BC, May, 2006.
9. Z. Xiang, H. Zhuang, H. Wu, J. Shan, D. Abdallah, J. Yin, S. Mullen, H. Yao, E. Gonzalez, and M. Neisser, "Organic ArF bottom anti-reflective coatings for immersion lithography," *Proc. SPIE* **6519**, 651929 (2007).
10. E. C. Piscani, S. Palmer, and C. Van Peski, "Demonstration of sub-45nm features using azimuthal polarization on a 1.30NA immersion microstepper," *Proc. SPIE* **6520**, 652025 (2007).
11. See for example, H.-L. Chen, W. Fan, T.-J. Wang, F.-H. Ko, R.-S. Zhai, C.-K. Hsu, and T.-J. Chuang, "Optical-gradient antireflective coatings for 157-nm optical lithography applications," *Applied Optics*, **43**, Issue 10, 2141–2145 (2004).

12. D. Goldfarb, S. Burns, L. Vyklicky, D. Pfeiffer, A. Lisi, K. Petrillo, J. Arnold, D. Sanders, A. Clancy, R. Lang, R. Allen, D. Medeiros, D. OweYang, K. Noda, S. Tachibana, and S. Shirai, "Graded spin-on organic bottom antireflective coating for high NA lithography," *Proc. SPIE* **6923**, 69230V (2008).
13. J. D. Meador, D. Holmes, M. Nagatkina, R. Puligadda, D. Gum, R. Bennett, S. Sun, and T. Enomoto, "New materials for 193nm trilayer imaging," *Proc. SPIE* **5376**, 1138–1148 (2004).
14. K. Lee, S. Kim, G. Lee, S. Lee, J. Cho, W. Kim, C. Bok, H. Kim, S. Moon, and J. Kim, "Development of multi-function hard mask to simplify process step," *Proc. SPIE* **6153**, 61532V (2006).
15. D. J. Abdallah, D. Mckenzie, A. Timko, A. Dioses, F. Houlihan, D. Rahman, S. Miyazaki, R. Zhang, W. Kim, H. Wu, L. Pylneva, P.-H. Lu, M. Neisser, R. R. Dammel, and J. J. Biafore, "Spin-on trilayer approaches to high NA 193nm lithography," *Proc. SPIE* **6519**, 65190M (2007).
16. D. C. Owe-Yang, T. Yano, T. Ueda, M. Iwabuchi, T. Ogihara, and S. Shirai, "Development of high-performance tri-layer material," *Proc. SPIE* **6923**, 69232I (2008).
17. V. Sipani, Y. Hishiro, and M. Abatchev, "Fundamental characterization of silicon-containing spin-on hardmask for 193nm photolithography," *Proc. SPIE* **6153**, 61532U (2006).
18. D. J. Abdallah, P.-H. Lu, M. Neisser, R. D. Dammel, W.-K. Kim, M. Zhang, and J. J. Biafore, "Dual layer spin-on approaches to high NA antireflection," Presentation at 3rd Immersion Symposium, Kyoto, Japan, Oct. 2006.
19. Y. Ono, T. Ishibashi1, A. Yamaguchi1, T. Hanawa, M. Tadokoro, K. Yoshikawa, K. Yonekura, K. Matsuda, T. Matsunobe, Y. Fujii, and T. Tanaka, "Development of high-performance multi-layer resist process with hardening treatment," *Proc. SPIE* **6519**, 65192O (2007).
20. H. Harada, K. Yonemura, T. Tanaka, D. Kawana, N. Yamashita, and K. Ohmori, "Progress of hard mask material for multi-layer stack application," *Proc. SPIE* **6519**, 65190N (2007).
21. Y. Sakaida, S. Takei, M. Nakajima, S. Kimura, T. Sakaguchi, K. Hashimoto, and H. Imamura, "Multi-layer BARCs for hyper-NA immersion lithography process," *Proc. SPIE* **6519**, 65192A (2007).
22. M. Nakajima, T. Sakaguchi, K. Hashimoto, R. Sakamoto, T. Kishioka, S. Takei, T. Enomoto, and Y. Nakajima, "Design and development of next generation bottom anti-reflective coatings for 45nm process with hyper NA lithography," *Proc. SPIE* **6153**, 61532L (2006).
23. S. K. Kim, S. H. Lim, D. Kim, S. R. Koh, M. Kim, H. C. Yoon, D. S. Uh, J. S. Kim, and T. Chang, "Silicon-based anti-reflective spin-on hardmask materials with improved storage stability for 193 nm lithography," *Proc. SPIE* **6519**, 65190O (2007).
24. J. Kennedy, S. Xie, R. Katsanes, K. Flanigan, S. Mukhopadhyay, B. Wu, E. Rutter, Jr., and M. Slezak, "A high Si content middle layer for ArF trilayer patterning," *Proc. SPIE* **6923**, 69230W (2008).

25. S. Turner, "Rework/stripping of multilayer materials for FEOL and BEOL integration using single wafer tool techniques," *Proc. SPIE* **6519**, 65192Q (2007).
26. B. Osborn, G. Quinto, C. Cheung, F. Wang, C. Gabriel, F. Cheung, F. Tsai, and A. Minvielle, "A modified bilayer resist approach for 45 nm flash lithography," *Proc. SPIE* **6923**, 69230Y (2008).
27. S. Takei, Y. Sakaida, and T. Shinjo, "Effect of solvents and cross-link reaction group concentration on via filling performance in gap fill materials," *Proc. SPIE* **6519**, 65192V (2007).
28. A. Qin, D. M. Sullivan, and R. Huang, "New developer-soluble gap-fill material with fast plasma etch rate," *Proc. SPIE* **6153,** 61532T (2006).
29. R. H. Hsu, I. H. Huang, L. C. Lin, and B. S.-M. Lin, "Global planarization of gap-filling process for low-k dual damascene applications," *Proc. SPIE* **5753**, 1158–1169 (2005).
30. C. Washburn, N. Brakensiek, A. Guerrero, K. Edwards, C. Stroud, and N. Chapman, "Wet-recess process optimization of a developer-soluble gap-fill material for planarization of trenches in trench-first dual damascene process," *Proc. SPIE* **6153**, 61532K (2006).
31. R. Huang, "Study of iso/dense bias of BARCs and gap-fill materials on via wafers," *Proc. SPIE* **6153**, 61532M (2006).
32. R. Huang, D. Sullivan, A. Qin, and S. Brown, "Advanced developer-soluble gap-fill materials and applications," *Proc. SPIE* **6519**, 65192T (2007).
33. W.-S. Huang, W. H. Heath, R. Kwong, W. Li, K. Patel, and P. R. Varanasi, "New 193nm top antireflective coatings for superior swing reduction," *Proc. SPIE* **6153**, 61530S (2006).
34. T. Yamashita, T. Hayami, T. Ishikawa, T. Kanemura, and H. Aoyama, "Novel low reflective index fluoropolymers based top anti-reflective coatings (TARC) for 193-nm lithography," *Proc. SPIE* **6519**, 65192U (2007).
35. T. Couteau and M. Carcasi, "Topside anti-reflective coating process and productivity improvements on KrF lithography," *Proc. SPIE* **6153**, 61533H (2006).
36. T. C. Bailey, J. Maynollo, J. J. Perez, I. Popova, and B. Zhang, "Evaluation of ArF lithography for 45nm node implant layers," *Proc. SPIE* **6519**, 65190S (2007).
37. C. Washburn, A. Guerrero, R. Mercado, D. Guerrero, and J. Meador, "Process development for developer soluble bottom anti-reflective coatings (BARCs), Presentation at Interface 2006, Oct. 31, 2006.
38. M. Toukhy, J. Oberlander, S. Mullen, P. H. Lu, and M. Neisser, "Radiation sensitive developable bottom anti reflective coatings (DBARCs) for 193nm lithography," *Proc. SPIE* **6519**, 651936 (2007).

Chapter 8
Resist Shrink and Trim Processes

The ultimate resolution of lithography can be improved by improving the optics of the exposure system. Various techniques are used to obtain better aerial image contrast, such as off-axis illumination, phase-shift masks, and optical proximity correction. The resolution can also be improved by using better resists and by optimizing the methods for processing them. These are the traditional ways to improve lithographic resolution according to the Rayleigh equation, which states that resolution cannot be better than $k_1\lambda/\mathrm{NA}$.

In addition to the traditional approaches, various innovative techniques have been implemented to further boost resist pattern resolution. The techniques are all based on treatment of the resist patterns after development. These so called "shrink processes" use special physical or chemical processes to convert optically derived resist patterns into ultrafine patterns that are beyond optical resolution limits. For example, a resist film printed with a contact-hole pattern can be baked slightly above the glass transition temperature (T_g) of the resist so that it gets soft and starts to flow, resulting in smaller contact holes. This process is called thermal reflow. Another method is to submerge the resist patterns into chemicals that react at the surface of the resist patterns, resulting in conformal "growth" of the resist patterns.

Shrink processes are capable of boosting the resolution of a process by one or two technology nodes without the need to purchase new exposure tools. For example, an ArF scanner with 0.75NA can print contact holes with diameters of 120 nm. Thermal reflow can further shrink the diameter to below 100 nm, which is in the resolution regime of a 0.93NA ArF tool. Implementation of the shrink process at some critical levels can help reduce costs, leading to a gain in technological leadership. Because of its huge potential for cost savings, shrink technology has attracted attention beyond lithographers, having also been adopted in film deposition processes. Plasma-assisted shrink processes have been used to shrink contact holes prior to etch.

Shrink processes actually "shrink" the open areas of the pattern by expanding/growing the resist area. These processes are more applicable to the lithographic levels where the space CD is crucial, such as the contact level or the first metal level. At gate levels, resist line CD is crucial and trim processes can be

used. The resist pattern is etched in a plasma chamber using an isotropic mode so that the resist pattern is trimmed in both lateral and vertical directions. This "trimming" process can reduce the resist line CD with minimal loss of resist thickness and minimal degradation of pattern profile. For example, the trim process can reduce a 90-nm resist line to 50 nm, which is particularly desirable for the gate level.

Shrink and trim processes are not unique to immersion lithography. They can be used to treat resist patterns obtained by various lithographic technologies including i-line, KrF, ArF, and even electron-beam lithography. However, neither shrink nor trim processes change the pitch of the patterns. The pitch is solely decided by the exposure. This chapter focuses on the shrink processes that are applicable to ArF lithography. The trim process falls mainly in the territory of etch technology, and therefore will be discussed only briefly in this chapter.

8.1 Resist Thermal Reflow

The thermal reflow process involves heating a wafer above the glass transition temperature (T_g) of the resist. When a resist is heated above T_g, the polymer chains are able to move to more thermodynamically preferred orientations. Near contact holes, the resist flows toward the open space, leading to a reduction in CD (Fig. 8.1). The thermal reflow process is simple and can achieve very high levels of shrinkage, ranging from 20 to 60 nm, depending on the resist and the patterns. Shrinkage of isolated contact holes can be ~20 nm more than shrinkage of similar holes in a dense pattern. This is called shrinkage bias. The extent of shrinkage and the shrinkage bias are sensitive to bake temperature and the resist material. Additionally, thermal reflow typically results in a degradation of the pattern profile.

8.1.1 Behavior of thermal reflow

Contact-hole patterns are ideal for reflow processes because their pattern density is typically low and enough resist material is available to reflow. This process has been evaluated by various groups. One group studied a resist coated to 300 nm over a BARC (PAB 100° C / 90 s).[1] Contact patterns were exposed by an ArF scanner (0.75NA). The PEB was 105° C for 90 seconds and the resist was

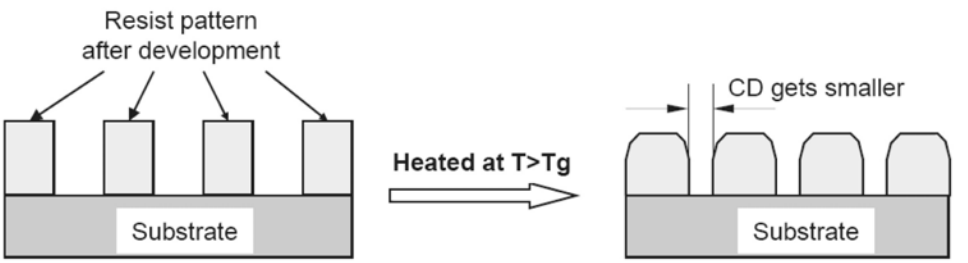

Figure 8.1 Process flow of the resist thermal reflow. The CDs of contact holes decrease.

developed in a standard developer for 30 seconds. After development, the contact holes had a diameter of 110 nm with pitches from 200 to 2000 nm. Thermal reflow bakes used temperatures of 150–170° C. Figure 8.2(a) shows the measured shrinkage value versus bake temperature at different pitches. The shrinkage value was defined as the CD difference before and after the reflow bake. Contact holes can be easily shrunk from 110 to 100 nm by performing the thermal reflow process at about 161° C. Larger shrinkage was observed at higher bake temperatures. The flow rates (defined as shrinkage/bake temperature) of isolated and dense holes were 6.4 and 1.4 nm/°C, respectively, at a bake temperature of about 161° C. The shrinkage values clearly depend on pitch (i.e., the pattern density). Figure 8.2(b) shows top-down SEM images of contact holes before and after thermal reflow at 161° C. Larger shrinkage was observed near isolated holes. The results presented in Fig. 8.2 clearly demonstrate that shrinkage during thermal reflow depends on the bake temperature and pitch.

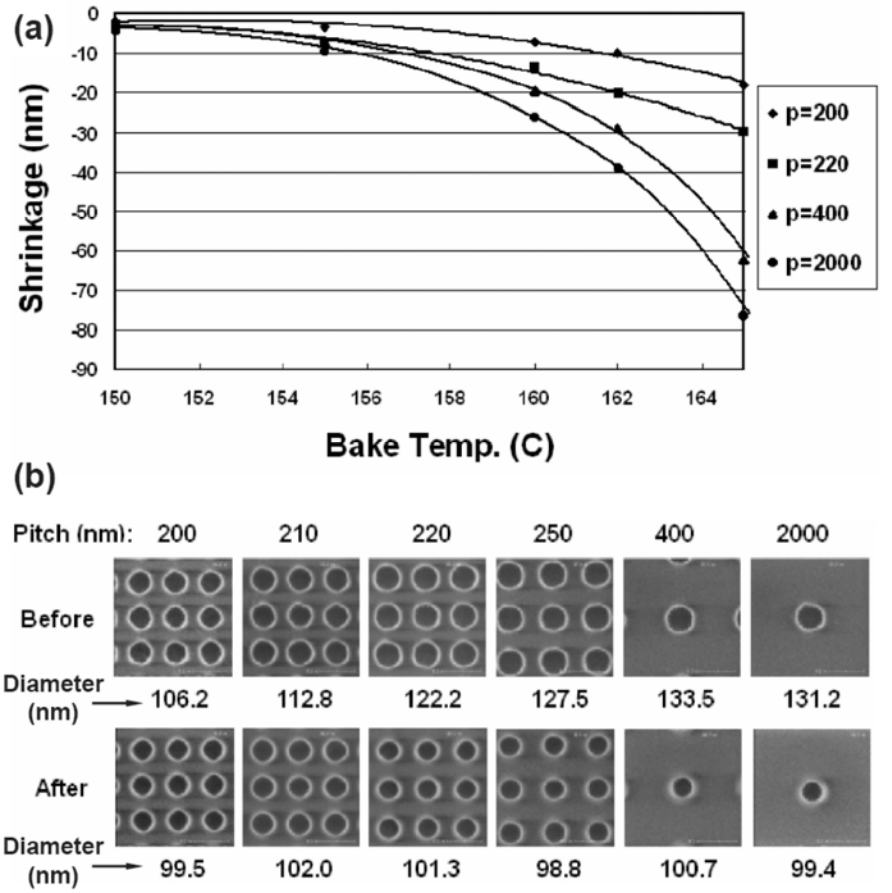

Figure 8.2 (a) Shrinkage value measured as a function of bake temperature at different pitches. The contact holes have a diameter of 110 nm before the reflow bake process. (b) Top-down SEM images of contact holes before and after the thermal bake at 161°C. The numbers below the images are the diameters of the holes. (Reprinted by permission from Ref. 1.)

Thermal flow generally improves both the LER of resist patterns and CD uniformity across the wafer. In the study discussed above, the standard deviations of CDU for 100-nm isolated and dense holes after the reflow were only 1.95 and 1.77 nm, respectively.

Figure 8.3 shows cross-sectional SEM images of dense contact holes before and after reflow for two different resists. Reflow degrades the pattern profile because it rounds the tops of the profiles. During high-temperature bakes ($T > T_g$), the resists soften and flow. The top corners of the patterns round and flow downward, due to the effects of surface tension. Top rounding has been observed for almost all thermally reflowed resist patterns, as demonstrated by Resists A and B (Fig. 8.3). Another profile degradation is called "foot pinning," in which the bottom of the resist pattern appears to be pinned to the substrate and does not move during reflow (e.g., Resist B in Fig. 8.3(b)), resulting in an undercut profile. Resist A, on the other hand, does not appear to exhibit foot pinning (Fig. 8.3(a)). The adhesion and/or wet-ability between the resist and the substrate (BARC) play a role here. Therefore, careful selection of resist and BARC materials may reduce the amount of foot pinning observed.

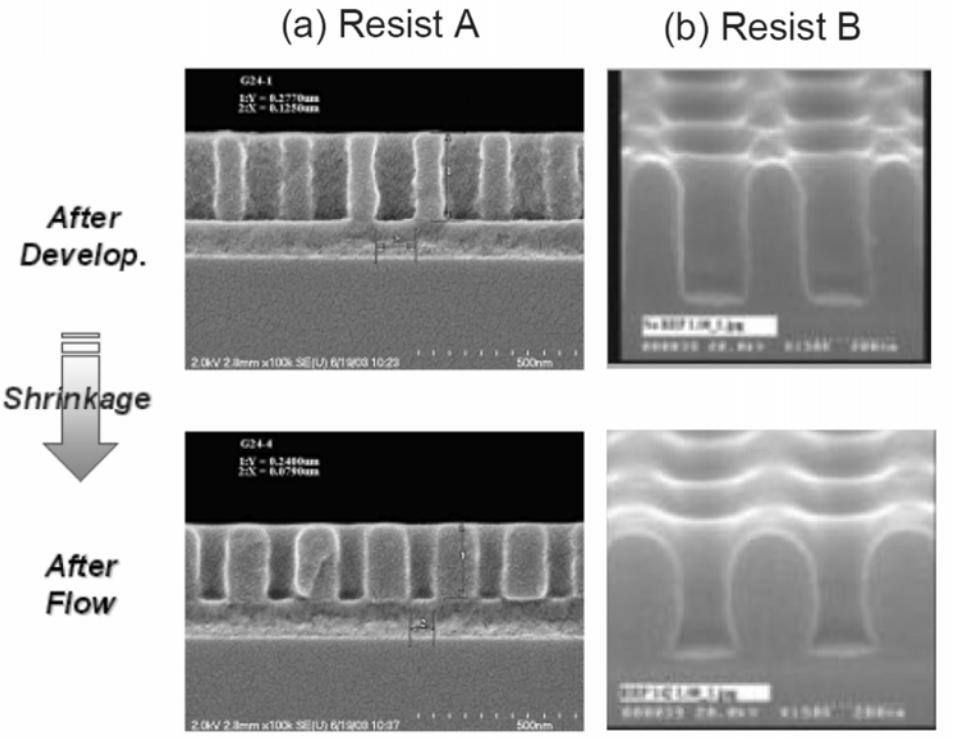

Figure 8.3 Cross-sectional images of dense contact holes before and after the reflow bake: (a) Resist A and (b) Resist B. (Reprinted by permission from Refs. 1 and 2.)

8.1.2 Reflow bake temperature

Resists must have low T_gs in order to be capable of thermal reflow without decomposition. For 193-nm resists with high T_gs, reflow bake temperatures may be too close to their thermal decomposition temperatures to be used. In this case, thermal decomposition may lead to bubble formation or other serious issues.[3]

It has been found that shrinkage in X and Y directions may be different for elongated holes. As bake temperature increases, the CD difference between the X and Y directions diminishes and elongated holes tend to become circular (Fig. 8.4). This issue must be addressed before the reflow process can be applied to elongated holes.

8.1.3 Optical proximity correction (OPC) for thermal reflow

Shrinkage from thermal reflow exhibits a proximity effect, where the shrinkage value depends on the pattern density. This dependency can make the design of the layout very difficult. Introduction of bias into the mask to compensate for the proximity effects of shrinkage has been proposed and is called thermal reflow optical proximity correction (OPC).[2,4] In the lithographic process, including the thermal reflow, mask error enhancement factor (MEEF) can be divided into

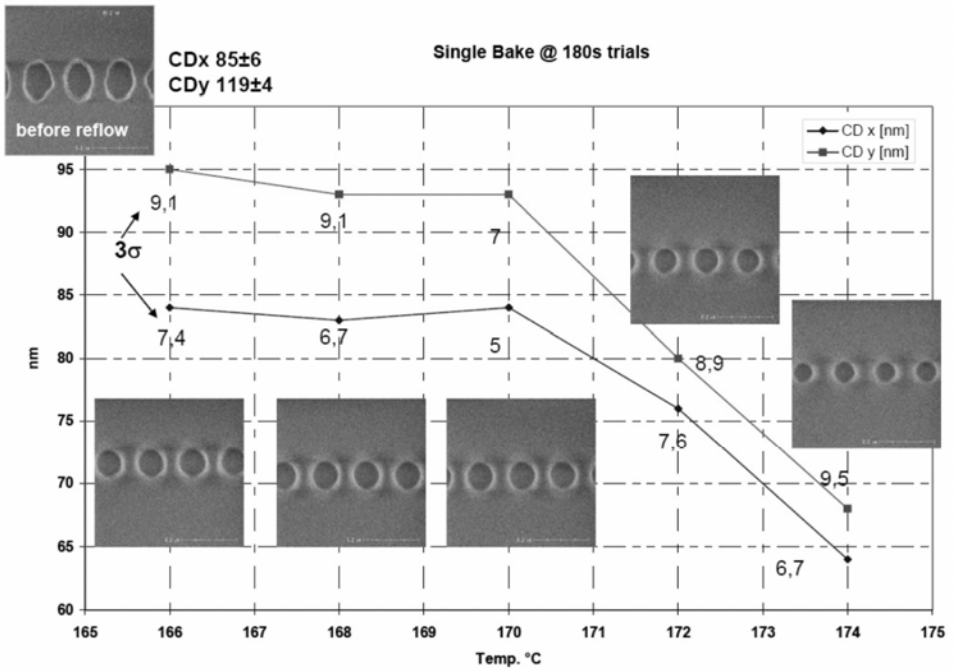

Figure 8.4 Change of CDs in X and Y directions of an elongated hole as a function of bake temperatures. The bake duration is 180 seconds. The top-down image corresponding to each bake temperature point is included. The roughness of the holes was measured and the value of 3σ is labeled in the figure. (Reprinted by permission from Ref. 3.)

MEEF after the development and MEEF after the thermal reflow. The algorithm for the thermal reflow model is

$$\frac{CD_{\text{wafer}}}{CD_{\text{mask}}/M} = \left(\frac{CD_{\text{develop}}}{CD_{\text{mask}}/M}\right) \cdot \left(\frac{CD_{\text{wafer}}}{CD_{\text{develop}}}\right), \tag{8.1}$$

where M is the imaging reduction ratio, CD_{develop} is the CD after development and before thermal reflow, and CD_{wafer} is the CD after thermal reflow. The factors that affect the shrinkage are bake temperature, bake time, resist identity, resist volume surrounding the contact hole, and initial contact size and shape. The shrinkage can be expressed as

$$\Delta CD = CD_{\text{develop}} - CD_{\text{wafer}} = f(T_{\text{b}}, V_{\text{n}}, K_{\text{r}}), \tag{8.2}$$

where T_{b} is the bake temperature, V_{n} is the resist volume surrounding the hole, and K_{r} is the resist identity. To a first-order approximation, these factors are not correlated with each other and thermal shrinkage can be simplified as

$$\Delta CD = f(T_{\text{b}}) \cdot f(V_{\text{n}}) \cdot f(K_{\text{r}}), \tag{8.3}$$

where $f(T_{\text{b}})$ is the thermal shrinkage factor due to temperature, $f(V_{\text{n}})$ is the thermal shrinkage factor due to resist volume surrounding the hole, and $f(K_{\text{r}})$ is the thermal shrinkage factor due to the resist.

This model was incorporated into the OPC for 65-nm contact holes. A large bias was introduced for isolated holes, since isolated holes are printed much larger than dense holes are printed. After reflow, the bias was compensated by shrinkage proximity effects and identical CDs were obtained in both dense and isolated areas, as shown in Fig. 8.5.

As is well known, isolated holes have smaller DOF than dense holes within a lithographic level. The ability to print isolated holes at larger CDs (larger than the CDs at which dense holes can be printed) should certainly improve the overall process windows. This is an additional advantage of the thermal reflow process.

The OPC model for thermal reflow has been further improved to include resist adhesion effects.[5] Further application of the reflow process to line and space patterns has been proposed.

8.2 Chemical Shrink

Although thermal reflow is a physical process that does not involve chemical reactions, shrinkage can also be affected using chemical reactions. One such chemical shrink technology is the resolution enhancement lithography assisted by a chemical shrink process (RELACS), developed by AZ Electronic Materials. In

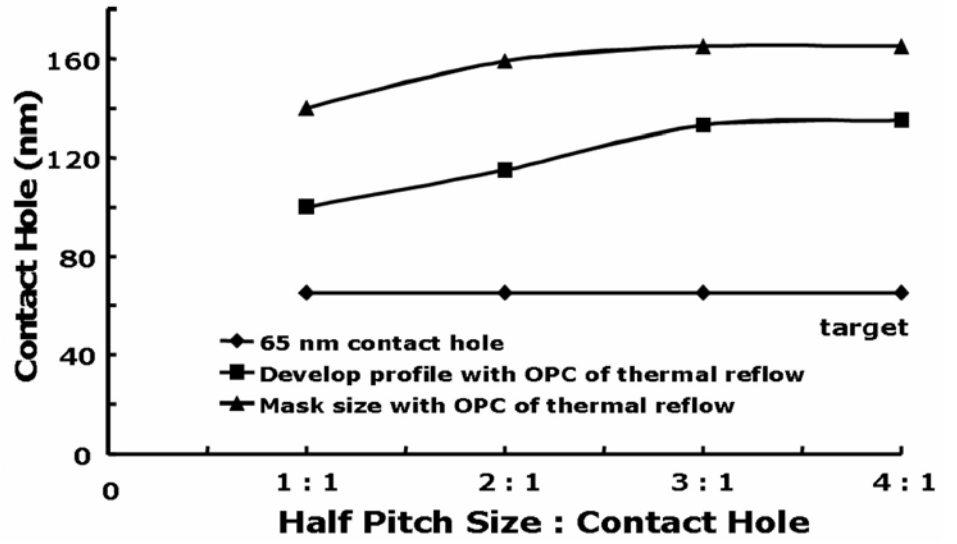

Figure 8.5 Simulation results of the reflow OPC for 65-nm contact holes. (Reprinted by permission from Ref. 4.)

the RELACS process, the resist pattern is coated with a shrink material and then baked. This step is called mixing bake or shrink bake. The bake temperature must be lower than the T_g of the resist in order to prevent resist thermal reflow. The shrink material contains polymers and cross-linkers,[7] is water soluble, and does not cause dissolution damage to the resist patterns during overcoating. At elevated temperatures, the photoacid in the resist film diffuses into the shrink material, reacting with the cross-linker. After bake, a water-insoluble layer is formed at the resist interface. The formation of this layer leads to shrinkage in CD. The non-cross-linked shrink material is removed by rinsing with DI water (Fig. 8.6).

8.2.1 Shrinkage behavior

The amount of chemical shrinkage is related to the extent of chemical reaction at the interface, which, in turn, is dependent on the shrinkage material, the resist, and the temperature of the mixing bake. For a given resist and shrink material, the amount of shrinkage can be adjusted by the bake temperature. Figure 8.7 shows the CD shrinkage of contact holes after the RELACS process as a function of the mixing bake temperature.[7] With increases in bake temperature from 100 to 160° C, the shrinkage increases from about 13 to 37 nm.

The amount of shrinkage obtained by the chemical shrinkage process appears to occur without proximity effect. This is because the shrink reaction occurs at the interface and the bulk of the resist film is not involved. Figure 8.8 shows CD versus pitch curves measured before and after the RELACS treatment. The mixing bakes (MBs) are set at temperatures of 100, 130, and 155° C. The shrink

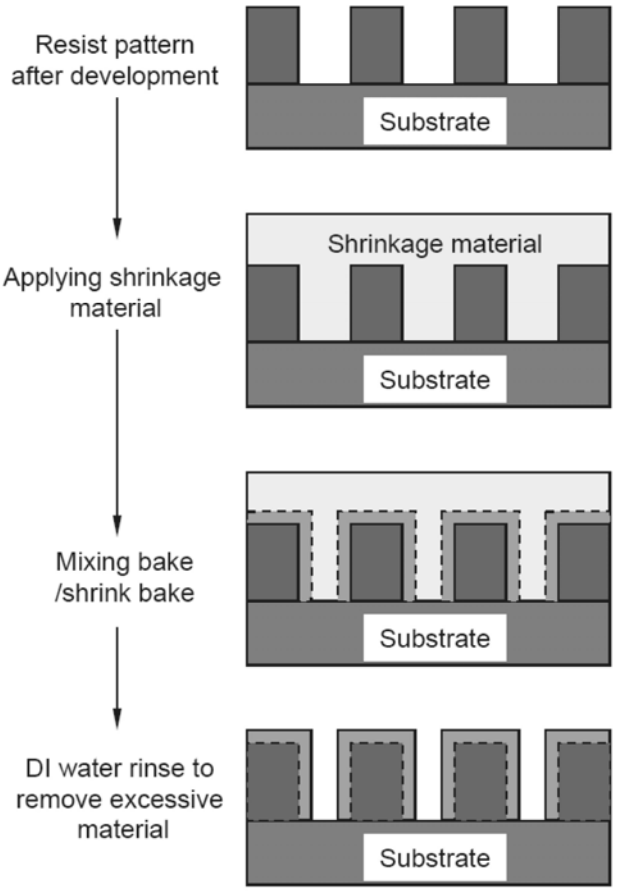

Figure 8.6 Process flow of the chemical shrink.

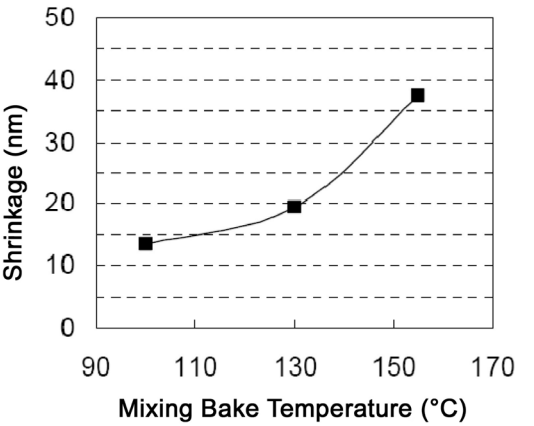

Figure 8.7 CD shrinkage of contact holes after the RELACS process as a function of the mixing bake temperature. The initial resist thickness is 464 nm and the mixing bake time is 70 seconds. (Reprinted by permission from Ref. 7.)

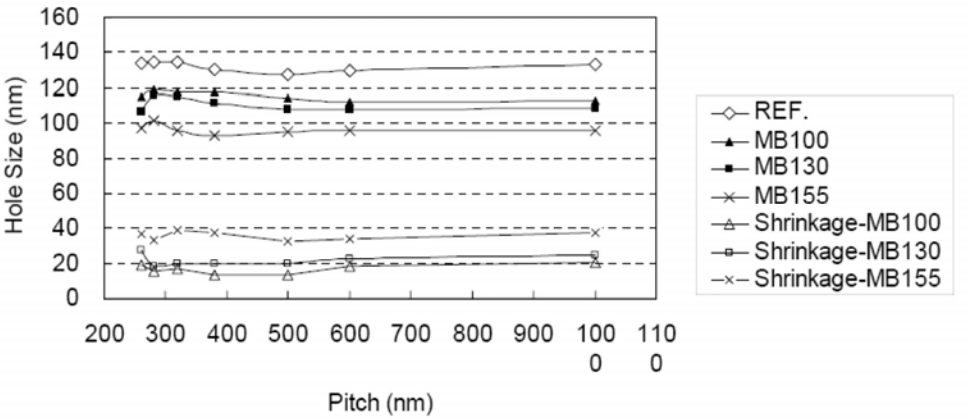

Figure 8.8 Diameter of contact holes and shrinkage amounts plotted as a function of pitch, shown before (labeled as REF.) and after the RELACS processes. The RELACS mixing bakes were performed for 70 seconds at 100, 130, and 155º C, respectively. (Reprinted by permission from Ref. 7.)

values are also plotted in Fig. 8.8. With variations in pitch, the shrinkage values are almost the same and fluctuation is less than 10 nm. The RELACS shrinkage is insensitive to initial pattern sizes. The curve of CD value versus exposure dose is measured before and after the RELACS process (Fig. 8.9(a)). With increasing dose, contact holes increase in size, but the amount of shrinkage remains the same. Figure 8.9(b) shows both top-down and cross-sectional SEM images before and after the RELACS process. The RELACS process appears to uniformly add a layer to the resist profile.

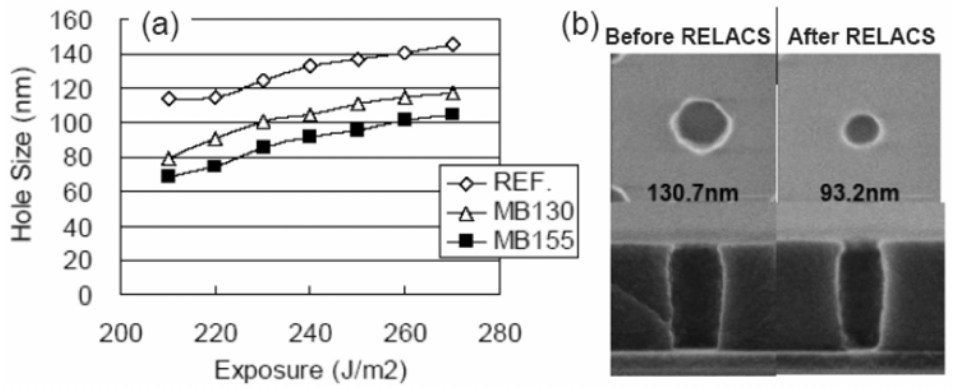

Figure 8.9 (a) CD value versus exposure dose curves measured before and after the RELACS process. (b) Top-down and cross-sectional SEM images before and after the RELACS process. (Reprinted by permission from Ref. 7.)

The RELACS shrinkage in X and Y directions was measured for elongated holes as a function of the mixing bake temperature, as shown in Fig. 8.10.[8] The same temperature dependence was observed, independent of direction. This result further demonstrates the uniform growth of the chemical shrink process.

Due to good shrinking uniformity over pitch, chemical shrink processes have attracted strong interest. In addition to RELACS, other chemical shrinkage processes have been developed.[9–11] For example, a new water-soluble coating material is a solution of two water-soluble polymers and a base.[11] One polymer is a proton-donor polymer (or polyacid) having acid groups such as carboxyl acids on each repeat unit. The other is a proton-acceptor polymer (or polybase) having heteroatoms with lone electron pairs on each repeat unit. The shrink mechanism is based on interpolymer complex (IPC) and zipper gel principles and is, therefore, called IPC-based chemical attachment process (ICAP). This process demonstrates about 40-nm shrinkage at 145° C, without forming microbridges. In addition to water-soluble shrink materials, shrink material that can be dissolved in an alcohol-based casting solvent has been developed. The shrink material is compatible with resist solvent; thus, resist or BARC coating bowls can be used to process the overcoating. Though the shrink materials and chemical reactions leading to the shrinkage may be different, these chemical shrink processes have similar process flows and performance characteristics, such as shrink uniformity and pitch independency.

8.2.2 Defectivity issues

Minimization of defects may be the most significant challenge to implementation of chemical shrink processes. Coating of shrink materials over resist patterns introduces additional sources of defects. Extra attention must be paid to the storage, plumbing, filtration, and coating of the shrink materials. Furthermore, resist clusters and particles may remain on the wafer surfaces. These particles come from a partially deprotected polymer (as discussed previously) and do not

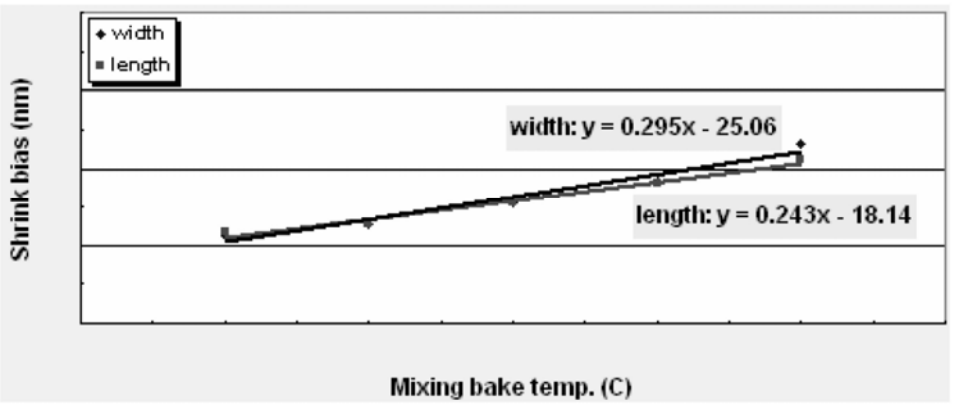

Figure 8.10 RELACS shrinkage values in X (width) and Y (length) direction versus the bake temperature for elongated hole. (Reprinted by permission from Ref. 8.)

dissolve in developer, nor are they completely removed during DI water rinse. The resist clusters contain photoacid and can react with the shrink materials to increase in size. Increasing the temperature of the mixing bake can result in increases in defect counts.

8.3 Shrink Assist Film for Enhanced Resolution (SAFIER)

The SAFIER process, developed by TOK (Tokyo Ohka Kogyo Co.), has the same process flow as RELACS (Fig. 8.6). Patterned resists are coated with SAFIER and then baked. Excess material is removed using a DI water rinse. However, the shrinking mechanism is different from the RELACS process, as it involves both physical and chemical reactions. The SAFIER aqueous solution consists of thermo-responsive copolymers that facilitate resist flow during the bake.[12] With the help of SAFIER film, the profile degradation due to resist thermal flow is significantly reduced. The SAFIER process can achieve large shrinks, ranging from 20 to 80 nm.

Like the shrinkage during thermal reflow, the shrinkage due to the SAFIER process is a function of bake temperature and pitch. Figure 8.11 shows shrinkage of trench patterns as a result of the SAFIER process. The patterns in the mask have a nominal line CD of 120 nm with various pitches. After lithographic and/or SAFIER processes, the trench CD in the wafer is measured through pitch and plotted as a function of pitch. The shrinkage clearly depends on the bake temperature and the pitch. The shrinkage is about 40 nm in the dense areas, and 80 nm in the isolated areas. A difference in shrinkage between X and Y directions for an elongated hole has also been observed.[13]

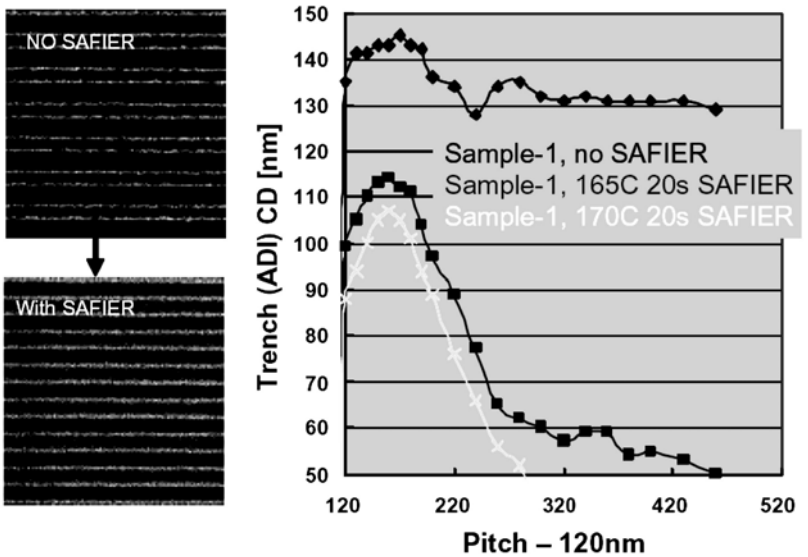

Figure 8.11 Trench CD measured before and after the SAFIER process at bake temperatures of 165 and 170° C for various pitches. (Reprinted by permission from Ref. 12.)

8.4 Shrinking via Fluorination Process

Fluorination is a gas-phase shrink process. Although thermal reflow, chemical shrink (RELACS), and SAFIER processes can each be performed in a track, wafers must be transported out of the litho cell to be fluorinated. Wafers with resist patterns are treated with dilute fluorine gas in a process chamber under conditions near room temperature and near atmospheric pressure. During fluorination, fluorine diffuses into the resist and replaces hydrogen (Fig. 8.12). Because C-F bonds (1.35 Å) are longer than C-H bonds (1.09 Å), the substitution leads to a uniform swelling of the resist film, thereby shrinking holes or trenches in the resists.[14] The table in Fig. 8.12 shows the increase in polymer film thickness after fluorination for three types of polymers. The rate of this diffusion-driven reaction is proportional to process time and pressure. Process time can be decreased if pressure is increased, while still achieving the same extent of resist swelling.

Figure 8.13 shows the amount of fluorine in a blanket resist film versus depth as a function of fluorination time, as determined using secondary-ion mass spectroscopy (SIMS). The profiles show that fluorine penetrates to a depth of ~70 nm after 5 min and continues in a roughly linear fashion. Wafers were processed in the chamber for 3–8 min.

This fluorination process has several advantages over other shrink technologies: (1) It can achieve above 25-nm shrinkage with small through-pitch effects (less than ~ 5 nm iso-dense shrink bias).[14] (2) The process creates more

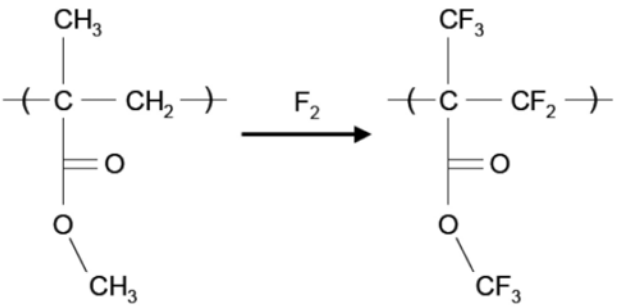

Resist	Thickness (nm) No F_2	Thickness (nm) 5min F_2	Delta (nm)	% change
PHS	242.2	271.5	29.3	12.1%
PMMA	251.7	257.3	5.6	2.2%
novolac	237.7	301.9	64.2	27.0%

Figure 8.12 Substitution of H in poly(methyl methacrylate) for F. The table shows the change in thickness due to gas-phase fluorination for PHS, PMMA, and novolac films. (Reprinted by permission from Ref. 15.)

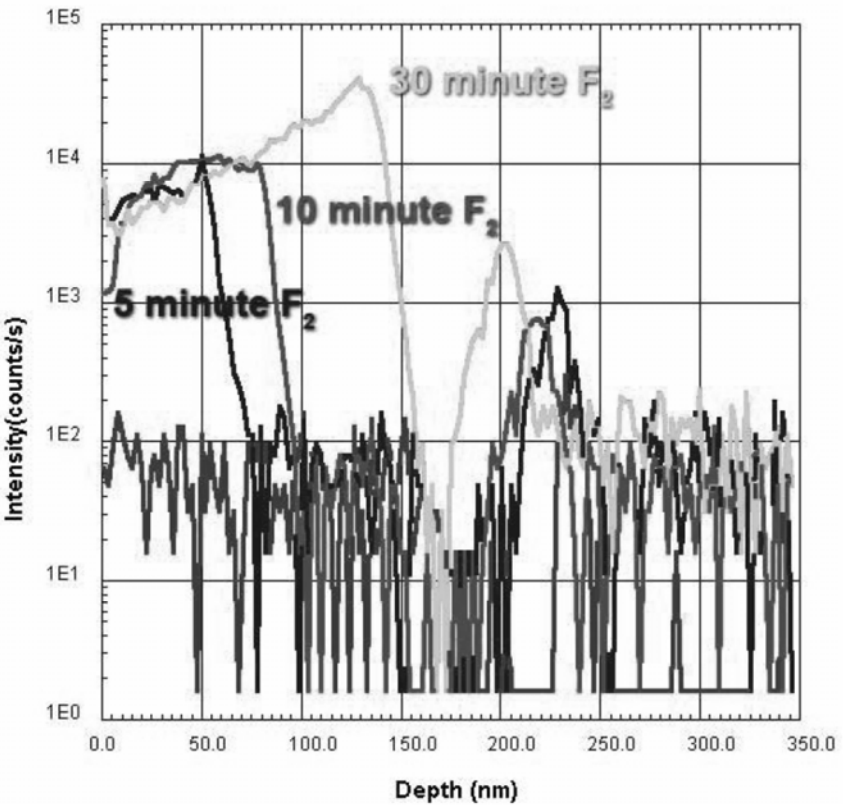

Figure 8.13 SIMS depth profile of F atoms in the resist film after different fluorination process times. (Reprinted by permission from Ref. 16.)

vertical line-end profiles, which in turn, lead to less pullback in subsequent etch processes. Thus, line end-to-end spacing is observed to improve by as much as 27% after the polysilicon gate etch.[15] (3) Fluorination can increase resist hardness and improve its mechanical stability. Although fluorinated resists have high resistance to implantation,[16] their etch rates are 10–40% worse (faster) than the nonfluorinated samples.[17]

8.5 Shrinking via Silylation Process

The silylation process is based on a bilayer resist system consisting of a thin imaging layer and a thick underlayer. The imaging layer is a Si-containing resist (e.g., silsesquioxane (SSQ)) with typical thicknesses of < 100 nm. The underlayer is a nonphotosensitive organic polymer such as polyhydroxystyrene, phenyl(meth)acrylate, or novolak. Figure 8.14 shows the process flow. After exposure and PEB, the wafer is developed with the standard aqueous developer to form the imaging pattern. This step is called the "wet" development. Then a dry-etch process, called the "dry" development, is applied to open the underlayer.

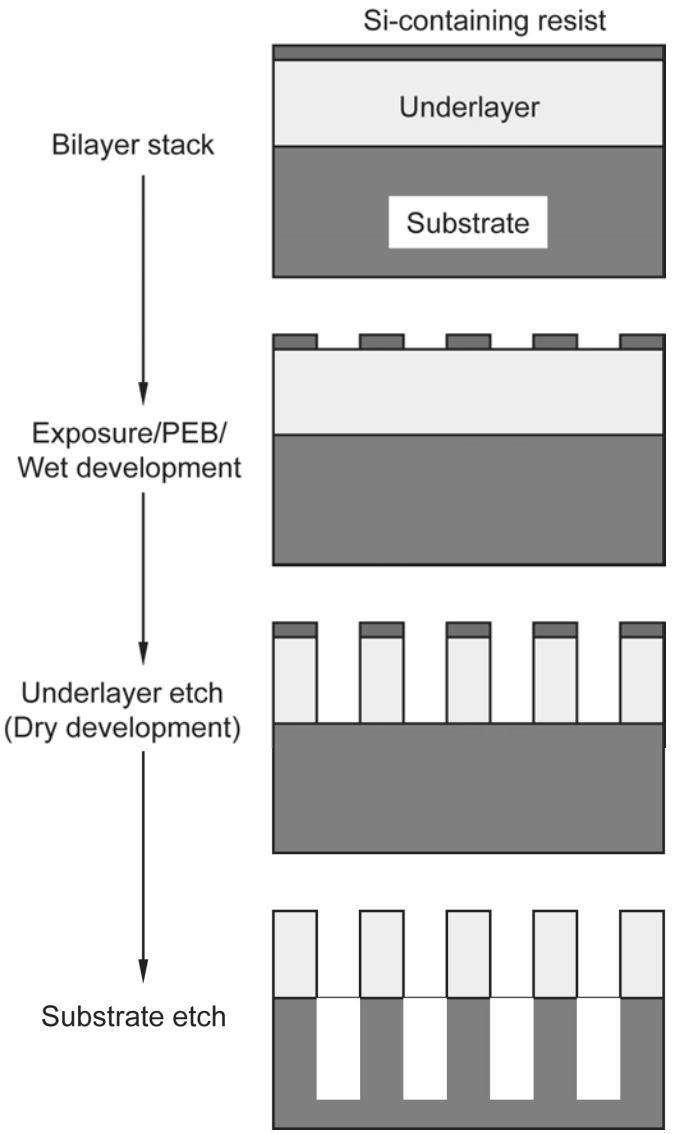

Figure 8.14 Process flow with the bilayer resist system.

This bilayer process offers higher etch selectivity than traditional single-layer resist processes offer. The etch selectivity between the Si-containing resist and the underlayer is greater than 1:4 in the oxygen-based plasma. The etch selectivity between the underlayer polymer and the Si substrate can be above 1:3 in the fluorine-based plasma. Such high etch selectivity enables the use of thin imaging layers and results in high aspect-ratio patterns in the substrate. The thin imaging layer offers a reduction in line collapse and slightly larger process windows. The thick underlayer works as a planarization BARC, effectively reducing the swing curve effect caused by the substrate topography.

As an option, a shrink process can be combined with this bilayer imaging system. After wet development of the imaging layer, the resist pattern can be treated with a silylation liquid or gas. This silylation process introduces additional Si into the imaging layer, leading to swelling of the resist patterns. This is called the chemical amplification of resist lines (CARL) process and was originally developed by Sebald et al.[18] The CARL process can shrink contact holes by 20 to 60 nm with no through-pitch bias.

However, the bilayer system has several weak points, so further improvements are needed.[19] The CARL process can be used only with specific resists and requires the additional cost of the silylation chemicals. The Si-containing resist may outgas Si-containing compounds during exposure, causing lens contamination. The resist formulations must be carefully designed to minimize the Si outgassing. Other concerns include the rework of Si-containing resists. Additional rework chemistry is needed to effectively remove the resist and to obtain clean substrates without defects or particles. Si-containing thin resists are also subject to large dark losses. Increasing development time causes the size of resist features to decrease.[20] During pattern transfer from the underlayer to the substrate, resist residuals can form "flowers" over the trench, blocking the substrate etch.

8.6 Plasma-Assisted Shrink

As mentioned at the beginning of this chapter, because of its cost saving potential, shrinkage technology has been adopted in film deposition processes, resulting in the development of plasma-assisted shrink processes (Fig. 8.15).[21] In a plasma chamber, a layer of polymer is conformally deposited on all exposed surfaces, resulting in the shrinkage of pattern. This is called the plasma-assisted shrink. Deposition can be cycled several times to reach shrinkage targets, after which, the wafer is loaded into an etch chamber, where it can be anisotropically etched. The etch consumes the polymer at the top of the resist features, but leaves the polymer on the sidewalls intact.

Figure 8.16 (a) shows the CD values of contact holes after lithography and after the plasma-assisted shrink process as a function of exposure dose. The mild, moderate, and aggressive shrinks correspond to 3, 5, and 7 deposition cycles, respectively. In Fig. 8.16(a), the shrinkage value appears to increase slightly with the original size of the contact holes. More shrinkage values are obtained with longer deposition cycles (Fig. 8.16(b)). A shrinkage value over 50 nm is obtained with 7 deposition cycles. Top-down and cross-sectional images of contact patterns in a 290-nm oxide layer are showed in Fig. 8.16(c). The nominal CD of the contact holes in the mask is 100 nm and the pitch is 240 nm. It appears that the shrink process does not degrade the profile of the final pattern. The improvement of CD uniformity is also observed with the shrinking process. After lithography, the average CD was 106.5 nm with $3\sigma = 3.6$ nm; after the moderate shrink and etch, the final average CD was reduced to 39.3 nm with $\sigma = 2.2$ nm.

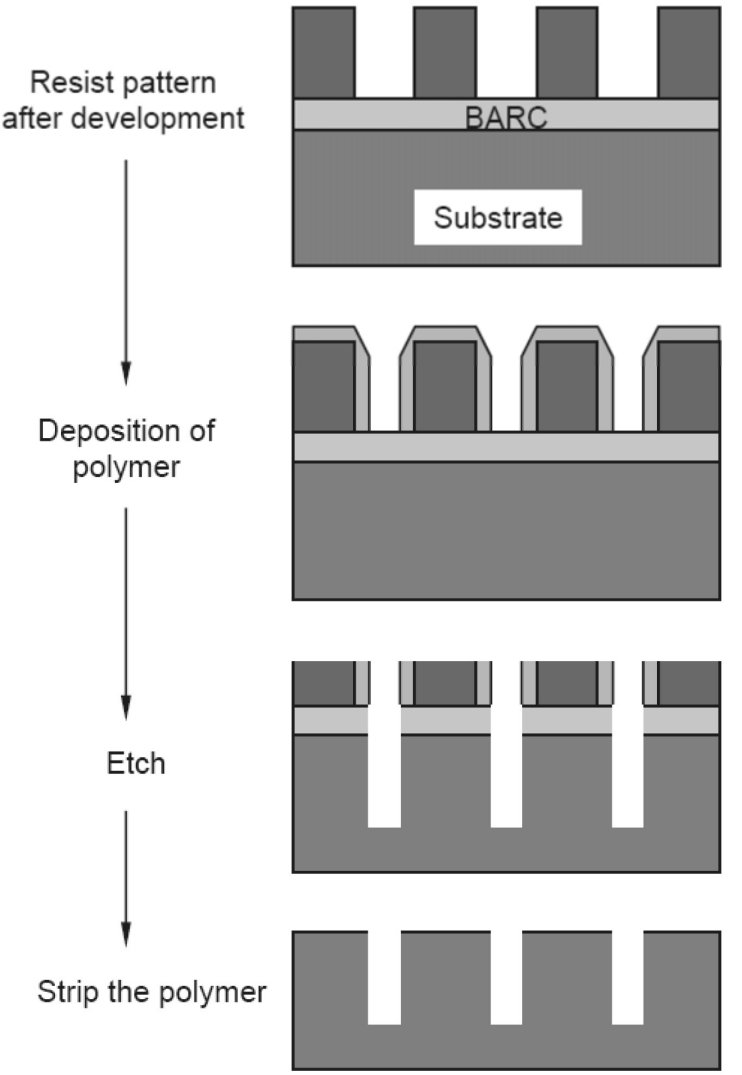

Figure 8.15 Process flow of the plasma-assisted shrink.

Figure 8.17 shows the dependence on pitch of CD shrinkage. In the test performed in Ref. 21, OPC was included in the mask, and contact holes with uniform CDs over the pitch were obtained after lithography. The difference in shrinkage values for the dense patterns and for the isolated patterns introduces additional iso-dense bias. This is because more polymers can be deposited in isolated holes than in dense holes, a condition called the loading effect. With fine tuning of the etch recipe, the iso-dense bias can be partially eliminated after the etch process.

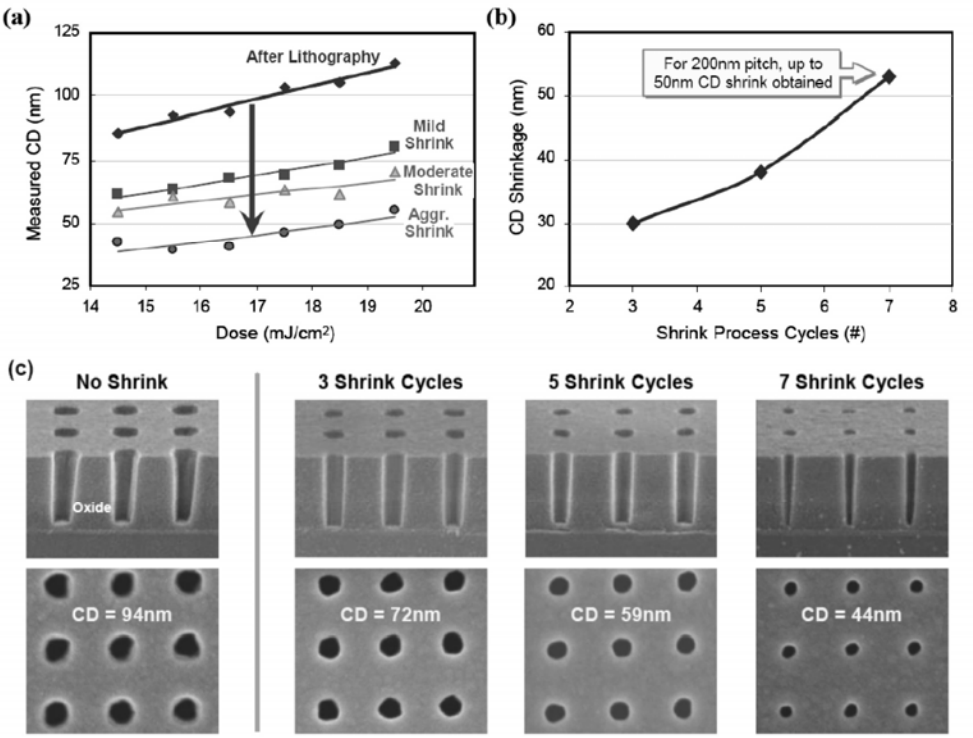

Figure 8.16 (a) The measured CD as a function of the dose after lithography and after the plasma-assisted shrinking process. (b) Shrinkage value versus the number of deposition cycles. (c) Cross-sectional images of the contact patterns in a 290-nm oxide layer. The nominal CD of the contact holes in the mask is 100 nm and the pitch is 240 nm. Top-down images are also included. (Reprinted by permission from Ref. 21.)

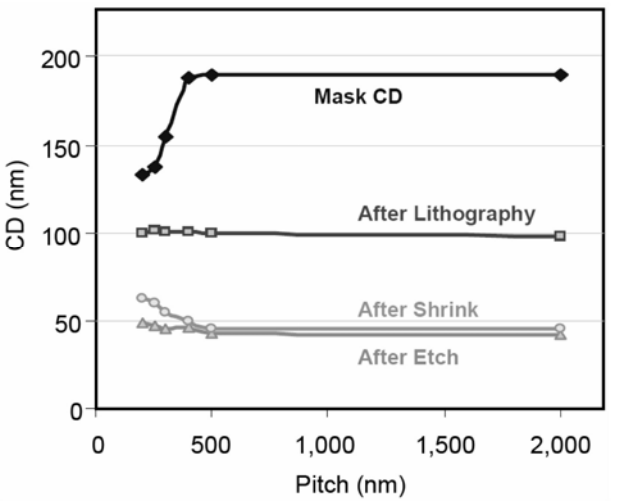

Figure 8.17 Contact hole CD over pitch in the mask, after lithography, after shrinking deposition, and after the final etch process. (Reprinted by permission from Ref. 21.)

The plasma-assisted shrink process is primarily used in the BEOL for contacts and trenches. In the FEOL, trim processes can be used to shrink gate CDs.[22] After lithography, the resist patterns are trimmed in a plasma chamber. The etch chemistry is adjusted to etch the sidewalls of the resist patterns. After the trim process, CDs of the resist patterns are much reduced. The trimming process can be integrated into the BARC open step before the substrate etch.

8.7 Evaluation of Shrink Processes

Shrinkage processes have been primarily used to reduce the size of contact holes; however, these methods have also been applied to trenches. Aggressive off-axis illumination gives better resolution and depth of focus when printing contact holes, but is also accompanied by detrimentally large iso-dense bias. However, some shrink processes can counteract the iso-dense bias occurring during resist imaging, because the bias is in the opposite direction. Depending on design and process assumptions, the requirements for the shrinking processes may vary from fab to fab. In general, the following shrink performance characteristics must be evaluated and understood:

1. Shrinkage dependence on initial CD (X and Y directions) and pitch must be evaluated. Typically, it is better for the shrinkage to be independent of initial CD and pitch. Otherwise, complicated OPC must be added to the mask design to compensate for shrinkage bias. As noted above, however, some iso-dense bias could be beneficial.
2. The shrink material must have good etch resistance in order to avoid CD transfer issues.
3. The shrink material should not introduce excessive defects and must be easily removed by the rinse process without leaving particles.
4. It should be possible to modulate the shrink value by adjusting the process parameters (e.g., the mixing bake temperature). Although these process control variables should provide some process flexibility, sensitivity to these variables should not be too high.
5. The shrinking process should not degrade the resist pattern profile.

8.8 Trim Processes

Trim processes are implemented in plasma-etch chambers. The trim process steps for gate level are illustrated in Fig. 8.18. Oxygen is the main etch gas in the resist trim process, as it etches the polymers isotropically. The BARC film is opened at the same time because it has a similar etch rate to that of photoresists in the oxygen-plasma environment. The resist CD can be further reduced during the BARC over-etch step. After the trim process, the polysilicon film is etched anisotropically using fluorine etch gases. The trimmed resist pattern serves as the etch mask during the polysilicon etch.

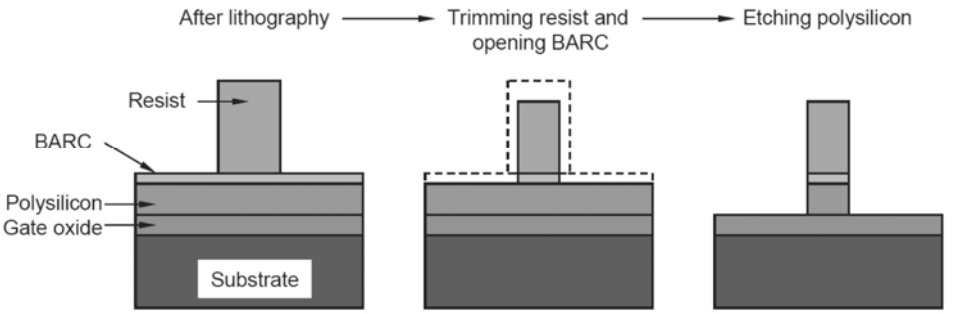

Figure 8.18 Trim process flow for gate level. Oxygen-plasma is used to simultaneously trim the resist pattern and open the BARC.

To achieve vertical sidewalls and provide control over the ratio of lateral versus vertical etch rate, halogens such as HBr, HCl, or fluorocarbon gases are added to the oxygen-plasma during the trim process. The trim rate difference between dense and isolated lines can be adjusted by varying the concentration of these gas additives.[23]

The reduction of resist line CD, or trim rate, depends on the etch chemistry, the plasma condition, and the trim process time. It is mainly limited by the resist consumption because a certain amount of resist must remain in order to provide enough etch resistance during the polysilicon etch. For the 65-nm node, the resist line width delivered at pattern is between 60 and 70 nm, while the final transistor gate length is usually targeted between 35 and 45 nm. The 15- to 35-nm CD difference can be bridged by the trim process.[24] A successful trim process must fulfill the following requirements:

1. CD uniformity across the wafer is improved, or, at minimum, no degradation of the CD uniformity occurs.
2. No degradation of pattern LER and LWR occurs.
3. Minimal trim bias occurs between dense and isolated lines.
4. No degradation of the resist pattern profiles occurs, and some resist remains after the trim process.
5. CD reduction is linearly dependent on trim time (i.e., a linear trim curve is preferred). The linearity enables accurate process control.

References

1. S.-H. Lin, J.-M. Teng, J.-H. Chen, C.-H. Chen, and B.-C. Ho, "How to print 100 nm contact hole with low NA 193 nm lithography," *Proc. SPIE* **5376**, 1091–1099 (2004).
2. J.-E. Lee, D.-G. Kim, K. B. Kim, M.-R. Jung, H.-Y. Kang, J.-S. Kim, J.-Y. Hong, and H.-K. Oh, "Reflow modeling for elongated contact hole shape," *Proc. SPIE* **6153**, 61533T (2006).

3. R. Tiron, C. Petitdidier, C. Sourd, D. De Simone, G. Cotti, E. Annoni, and B.Mortini, "Resist evaluation for contact hole patterning with thermal flow process," *Proc. SPIE* **6519**, 65193A (2007).
4. S.-K. Kim, "OPC of resist reflow process," *Proc. SPIE* **6153**, 61530Y (2006).
5. J.-M. Park, J.-E. Lee, M.-S. Kim, J.-H. Kim, J.-S. Kim, S.-M. Lee, J.-T. Park, C.-K. Bok, S.-C. Moon, S.-W. Park, J.-Y. Hong, and H.-K. Oh, "Photoresist adhesion effect of resist reflow process," *Proc. SPIE* **6519**, 65193O (2007).
6. J.-M. Park, I. An, and H.-K. Oh, "Resist reflow process for arbitrary 32nm node pattern," *Proc. SPIE* **6923**, 69233A (2008).
7. M. Terai, T. Kumada, T. Ishibashi, T. Hanawa, N. Satake, and Y. Takano, "Newly developed RELACS materials and process for 65 nm nodes," *Proc. SPIE* **6153**, 61532I (2006).
8. W. H. Hsieh, H. J. Liu, W. B. Wu, C. L. Shih, and J. P. Lin, "Proximity effect correction for the chemical shrink process of different type contact holes," *Proc. SPIE* **6519**, 65193E (2007).
9. M. Slezak, R. Ayothi, and Z. Liu, "Achieving 45 nm HP without a wavelength change, *Semiconductor International*, 2/1/2007.
10. T. Abe, T. Kimura, T. Chiba, M. Shima, S. Kusumoto, and T. Shimokawa, "Contact hole shrink process with novel chemical shrink materials," *Proc. SPIE* **5753**, 206–212 (2005).
11. M. Hata, J.-H. Hah, H.-W. Kim, M.-H. Ryoo, S.-G. Woo, and H.-K. Cho, "Novel chemical shrinkage material for small contact hole and small space patterning," *Proc. SPIE* **5753**, 214–221 (2005).
12. C. Wallace, J. Schacht, I. H. Huang, and R. H. Hsu, "Optimization of resist shrink techniques for contact hole and metal trench ArF lithography at the 90nm technology node," *Proc. SPIE* **5376**, 238–244 (2004).
13. S.-H. Kim, H.-D. Kim, S.-H. Lee, C.-M. Park, M.-H. Ryoo, G.-S. Yeo, J.-H. Lee, H.-K. Cho, W.-S. Han, and J.-T. Moon, "Realization of sub-80nm small space patterning in ArF photolithography," *Proc. SPIE* **5376**, 1082–1090 (2004).
14. R. Peters, P. Montgomery, C. Garza, S. Filipiak, T. Stephens, and D. Babbitt, "A novel contact hole shrink process for the 65-nm-node and beyond," *Proc. SPIE* **5753**, 195–205 (2005).
15. R. D. Peters, P. K. Montgomery, and P. J. Stout, "Gas-phase fluorination of resist for improving line-end pullback during etch," *Proc. SPIE* **6153**, 61532X (2006).
16. P. K. Montgomery, R. D. Peters, C. Garza, T. Breeden, M. Azrak, J. Jiang, and K. Kim, "Improved ion implantation masking through photoresist fluorination," *Proc. SPIE* **6153**, 61532Y (2006).
17. P. K. Montgomery, R. Peters, C. Garza, J. Cobb, B. Darlington, C. Parker, S. Filipiak, and D. Babbitt, "Reduction of line edge roughness and post resist trim pattern collapse for sub 60 nm gate patterns using gas-phase resist fluorination," *Proc. SPIE* **5753**, 1024–1033 (2005).

18. M. Sebald, J. Berthold, M. Beyer, R. Leuschner, C. Noelscher, U. Scheler, R. Sezi, H. Ahne, and S. Birkle, "Application aspects of the Si-CARL bilayer process," *Proc. SPIE* **1466**, 227–237 (1991).
19. M.-H. Jung, H.-W. Kim, J. Hong, S.-G. Woo, H.-K. Cho, and W.-S. Han, "Performance of SSQ type ArF bi-layer resist in 80-nm node DRAM line and space fabrication," *Proc. SPIE* **5376**, 1100–1106 (2004).
20. L. Voelkel, M. Heller, M. Markert, and I. Vermeir, "Challenges of introduction of a 193nm bilayer system into sub-90nm L/S fabrication," *Interface* (2004).
21. M. Op de Beeck, J. Versluijs, Z. Tőkei, S. Demuynck, J.-F. De Marneffe, W. Boullart, S. Vanhaelemeersch, H. Zhu, P. Cirigliano, E. Pavel, R. Sadjadi, and J. Kim, "A novel plasma-assisted shrink process to enlarge process windows of narrow trenches and contacts for 45nm node applications and beyond," *Proc. SPIE* **6519**, 65190U (2007).
22. J.-Y. Kim, J.-Y. Jang, J.-H. Kim, and K. Kim, "Transistor fabrication for sub-90 nm transistor by using trim technology at ArF light source," *Proc. SPIE* **6153**, 61532Z (2006).
23. E. Pargon, O. Joubert, T. Chevolleau, G. Cunge, S. Xu, and T. Lill, "Mass spectrometry studies of resist trimming processes in HBr/O_2 and Cl_2/O_2 chemistries," *J. Vac. Sci. Technol. B* **23**(1), 103–112 (2005).
24. Y. Gu, J. B. Friedmann, V. Ukraintsev, G. Zhang, T. Wolf, T. Lii, and R. Jackson, "Characterization of bending CD errors induced by resist trimming in 65 nm node and beyond," *Proc. SPIE* **6518**, 651826 (2007).

Chapter 9
Double Exposure and Double Patterning

193-nm water immersion can provide lithographic solutions as far as the 45-nm half-pitch node. Double exposure and double patterning have emerged as leading candidates to fill the technology gap between water immersion and EUV lithography. Early test results have demonstrated that key technical challenges to double patterning, such as tight overlap requirements and strict CD control, are being solved, while novel materials for double exposure are being quickly developed. It is widely believed that double exposure and double patterning can provide viable patterning solutions to the 32-nm half-pitch node, with possible extensions to the 22-nm node. This chapter covers various approaches of double exposure and double patterning. At the time of this writing (Fall 2008), double exposure and double patterning are undergoing rapid growth and many new approaches are being explored. Although this chapter is as comprehensive as possible, an exhaustive list is not practical.

9.1 Introduction

9.1.1 Double exposure (DE)

Double exposure (DE) refers to exposing the resist-coated wafer twice to create one resist pattern. No etching process is used between the two exposures. Two process approaches for DE have been explored:

A. **Two exposures of the same resist using different masks.** After the two exposures, the wafer is sent to PEB and development. The process flow is abbreviated as Resist 1 / Exposure 1 / Exposure 2.

B. **Two separate exposure/develop processes using different masks.** The process flow is abbreviated as Resist 1 / Exposure 1 / Develop 1 / Resist 2 / Exposure 2 / Develop 2. Some additional processes may be applied somewhere between steps to “freeze” the 1st resist pattern so that it can withstand the 2nd lithographic process.

However, to implement approach A (exposing the same resist twice), one must be cautious about the total aerial image contrast. The total aerial image intensity is the sum of both exposures; flare also contributes to the total intensity. For example, to print 50-nm dense lines using a positive resist, the exposure prints a 50-nm space with a 150-nm line and the 2nd exposure prints the same pattern, shifted 100 nm from the first lines. After PEB and development, a dense pattern of 50 nm / 50 nm is obtained. The advantage of this approach is that each exposure is required to resolve a pitch of only 200 nm and the same resist film is used twice. Additionally, the illumination conditions can be optimized separately for each exposure. However, if the tool has insufficient aerial image contrast and/or significant levels of flare, the total light intensity in the dark areas could be above the deprotection threshold E_0 of the resist, causing total resist loss (Fig. 9.1(a)). An exposure tool with much higher aerial image contrast and lower flare is needed for this simple approach of "spatial frequency doubling" (Fig. 9.1(b)). With higher contrast and reduced flare, the total aerial image has enough contrast to be resolved by the resist. Alternatively, an extremely nonlinear resist can also make this process viable. The nonlinear resist must have almost zero resist loss under high levels of flare. The development of such nonlinear resists is an attractive topic being actively pursued by several research organizations.[1]

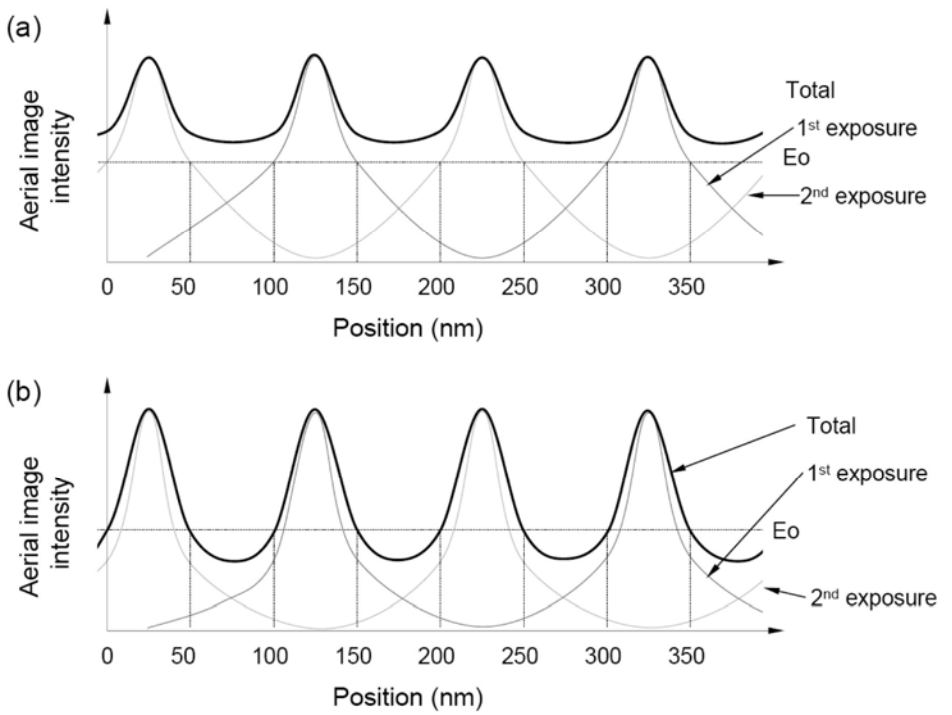

Figure 9.1 Aerial image intensity of the double exposure (DE) with one layer resist. (a) Low aerial image contrast in single exposure leads to the total resist loss after the DE. (b) High aerial image contrast is required to ensure sufficient total image contrast.

Approach B was developed to overcome the difficulties of approach A. In this approach, the resist pattern obtained from the 1st lithographic step is treated with a "freeze" process so that the coat, exposure, and development steps of the 2nd resist do not damage the initially formed resist pattern. Several approaches have been described that entail freezing the 1st resist pattern by physical or chemical means. The frozen resist pattern is photo-inactive and does not interact with the 2nd resist at any time during the process. After the 2nd lithographic step, the two resist patterns work together as an etch mask for the substrate etch. The whole process can be accomplished in one integrated process flow in a lithography cluster (scanner and track).

9.1.2 Double patterning (DP)

Double patterning (DP) takes a more conservative approach to preserving the 1st pattern. In the double patterning process, an etch step is added between the two lithographic processes. The resist pattern from the 1st lithographic process is transferred to a hard mask (HM) layer by an intermediate etch process. Then, the wafer is sent back to the lithographic cell to process the 2nd pattern. During the 2nd lithographic process, the 1st pattern is preserved by the HM. The 2nd pattern is transferred to the HM by another etching process. So, the major difference between DE and DP is that DP has an etching process inserted between the two exposures, while the etch process for DE occurs after both exposures.

Compared to DE, DP can be more easily implemented with the conventional 193-nm resist process. Resists need not be freezable or nonlinear. The increase in process steps is an obvious disadvantage, particularly since the wafer must be sent to the etch equipment between lithography steps, thereby reducing throughput. This chapter will review various DE and DP processes.

9.1.3 Resolution capability of DE/DP

Theoretically, either DE or DP can double the resolving power of 193-nm lithography. This means that the process factor of k_1 in the Rayleigh equation can be half the current value. DP has demonstrated a k_1 factor of ~0.16,[2] which is beyond the resolution limit of advanced 193-nm lithography ($k_1 > 0.25$) and beyond what is considered to be practically achievable in mass production ($k_1 > 0.3$). Therefore, the DE/DP process could provide resolution for a 45-nm half-pitch node using a 0.93NA scanner and could resolve 32-nm half-pitch using a 1.3NA 193i tool. For quite some time, EUV lithography has been considered the primary option for imaging in the 32-nm node. However, DE/DP in combination with 193-nm immersion provides another lithographic solution to the 32-nm half-pitch node and, in fact, has taken over as the prime candidate.[3]

9.1.4 Challenges

DE/DP processes have many more steps than traditional single-exposure processes. More process steps means lower yields and lower throughput. Figure

9.2 shows a diagram of the process steps in the DE and DP approaches. From the viewpoint of throughput and process cost, DE with one resist is preferred.

Overlay (OL) control is another challenge that must be faced with DE or DP processes. 193-nm scanners typically have 3σ overlay specifications of ±15 nm in both X and Y directions. Obviously, the overlay capability of exposure tools must be improved in order for DE/DP processes to be viable. Otherwise, overlay errors between exposures will be transferred into CD variation in the DE/DP process. This can be explained using the double trench patterning process (Fig. 9.3). The misalignment of the 2nd to 1st exposure (Δ) causes a shift in HM pattern, which directly results in the deviation of *line*-CD from the target CD to CD ± Δ. At the 45-nm half-pitch node, the minimum target CD is 45 nm. If 10% CD variation is acceptable, the overlay must be controlled to less than 4.5 nm. Full-field 193-nm scanners with tight overlay specifications dedicated to DE/DP processes are being developed with overlay capabilities of 4 nm.[4] Although the *space*-CD is not affected by the misalignment, the location of the spaces is shifted (Fig. 9.3), causing image placement error for spaces.

In addition to tight overlay control, DE/DP tools must also have exceptional image quality.[5] Although the pitch in the 1st and 2nd exposures is twice that of the final pitch (e.g., the left part of Fig. 9.3), the printed trench widths are the same as the final space widths. The tools must resolve small trenches at relatively large pitches. Therefore, tools capable of imaging 70-nm dense lines and spaces (140-nm pitch) may not be suitable for imaging 35-nm dense lines and spaces using DE/DP, because each individual exposure must resolve 35-nm lines or trenches, even though the pitch is still 140 nm. Thus, in addition to tight overlay specifications, DE/DP tools must have lower aberrations, better image quality, and better stability.

The decision on how to split the patterns into two masks is another challenge that will require new rules to be developed. In addition, optical proximity correction (OPC) must be implemented in each mask. The pattern-splitting issue

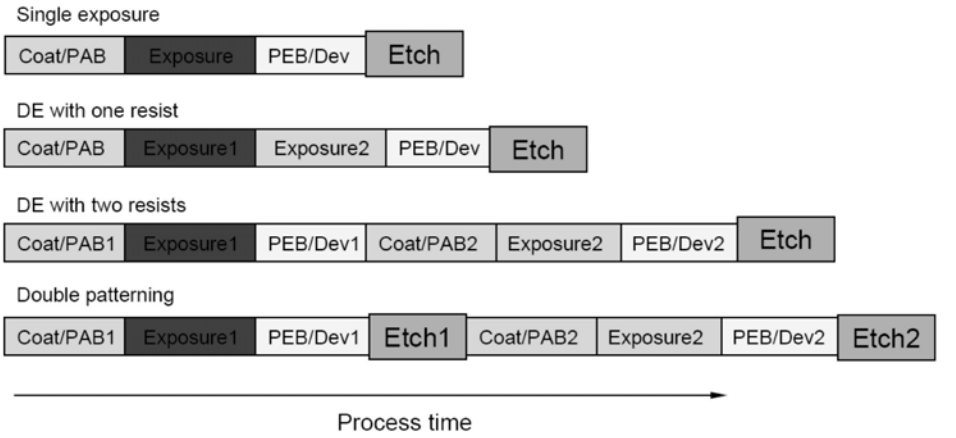

Figure 9.2 Process steps in various DE/DP approaches.

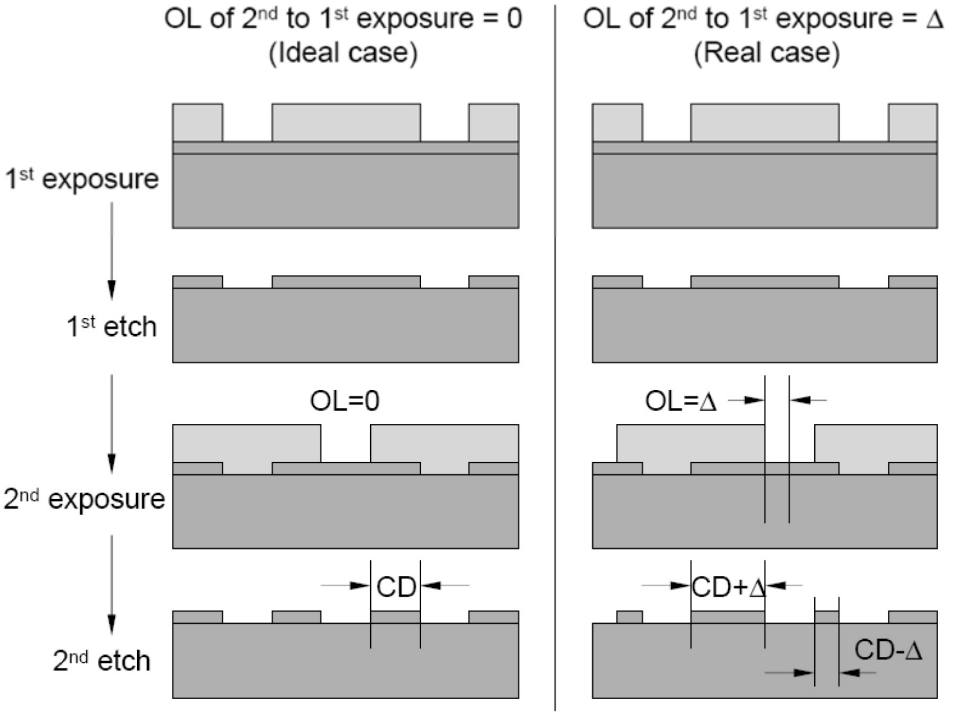

Figure 9.3 In the double trench patterning process, the overlay (OL) error is transferred into CD deviation for lines and is transferred into image placement error for spaces.

has proven to be challenging for arbitrary designs. In general, pattern stitching is easier for flash and more difficult for logic, with DRAM (dynamic random access memory) falling somewhere between the two. Pattern splitting reduces the pattern density in each mask, which is beneficial to mask manufacturing.

9.2 Double Exposure with One Resist Layer

Double exposure with one resist layer is the simplest and the most cost-effective process among various approaches to DE and DP. However, the double exposure of one resist film typically leads to unacceptable losses in image contrast, unless nonlinear resists are used. Double exposure with one resist layer could be a viable process if each exposure could be optimized to avoid losses in image contrast. One successful example involves alternating phase-shift masks (PSMs), in which the critical layer (e.g., polygate) is split into two masks and the lithographic processes are optimized separately. The most critical part—the gates—is patterned using a dark-field alternating PSM, as it provides the best resolution and CD control. The less critical parts—the local interconnect lines and gate trim-out regions—are patterned using a binary mask.

9.2.1 Combination of interference and projection (regular) lithography

Researchers at MIT Lincoln Laboratory developed a new double-exposure process they named "hybrid optical maskless lithography" (HOMA). In this process, first, an interferometric exposure is used to create high-resolution dense resist gratings. Then, a conventional optical trim exposure customizes the grating into patterns that are useful for semiconductor integrated circuits (ICs).[6] Two exposures are performed in the same resist, prior to PEB and development.

Interference can provide excellent aerial image contrast with process latitudes that greatly exceed those of projection optics. The HOMA method is a combination of high-resolution maskless (optical interferometer) and low-resolution optical projection. Both exposures are capable of very high throughputs. Figure 9.4 shows the proof-of-concept results. Exposures are performed in the same resist prior to PEB and development. Figure 9.4(a) shows the 45-nm half-pitch grating pattern imaged by Lincoln Lab's 157-nm interferometric system and Fig. 9.4(b) is the resist pattern after the trim exposure with a 248-nm projection tool to "erase" several grating lines. The resist is sensitive to both 157- and 248-nm wavelengths.

One key challenge to the HOMA process lies in deciding on how to split the patterns into dense lines and trim parts. The decision is based on the assumption that circuit patterns can be formed from simple grating patterns that can be trimmed by an additional exposure. Making use of the HOMA method for semiconductor lithography will certainly have implications for the design process. All critical features, gates, contacts, and metal will need to be placed on a coarse grid. Contacts can be printed out with crossed grating exposures using a negative-tone resist.

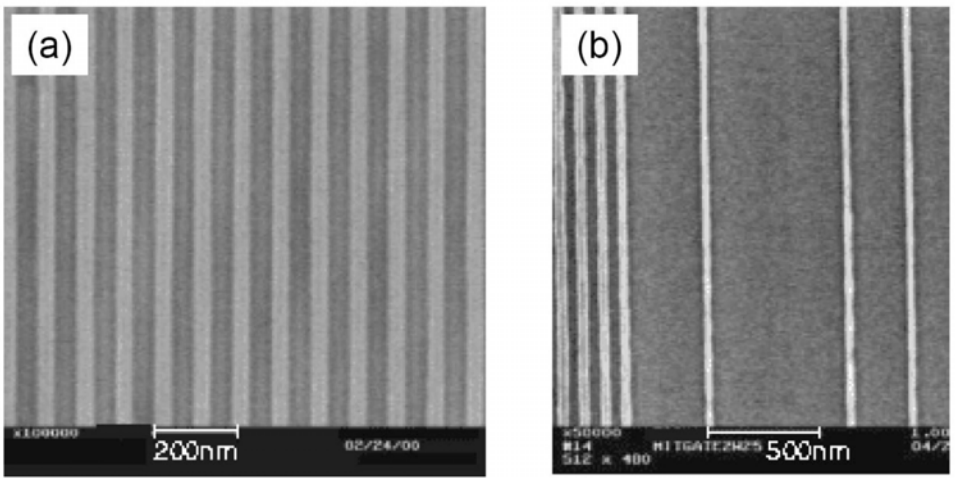

Figure 9.4 Top-down images of (a) 45-nm dense resist lines obtained by the interference exposure and of (b) the resist pattern after the trim exposure. (Reprinted by permission from Ref. 6.)

A similar approach was separately named "composite optical lithography" (COOL).[7] COOL uses less expensive interference lithography tools to form an initial pattern at the minimally required pitch and the 2nd exposure uses lower resolution lithography to form the required layout. The process using a negative resist is demonstrated in Fig. 9.5. The dense lines are exposed first (PSM mask is used as the interference lithography emulator). The 2nd exposure forms the bridge patterns. Finally, the wafer is sent to PEB and development.

9.2.2 Exposures with X-dipole and Y-dipole illuminations

Dipole is an aggressive off-axis illumination process that provides better aerial image contrast than conventional or annular illuminations can provide, in directions perpendicular to the dipole orientation (Fig. 9.6). X-dipole illumination gives the best resolution for vertical lines (Fig. 9.6(a)) and Y-dipole illumination gives the best resolution for horizontal lines (Fig. 9.6(b)). However, X-dipole does not give good resolution for horizontal lines, nor does Y-dipole for vertical lines. Thus, double exposure is proposed for effective imaging of both horizontal and vertical lines. A level consisting of both horizontal and vertical lines can be split into two masks. One mask has only vertical lines and the other mask has only horizontal lines. The 1st exposure is done with Mask 1 and the X-dipole illumination and the 2nd exposure is done with Mask 2 and the Y-dipole illumination.

Alternatively, these vertical and horizontal lines can be exposed once by C-quad illumination and one mask with both vertical and horizontal lines, as sketched in Fig.9.6(c). Compared to the double exposure approach, the C-quad illumination introduces additional flare and causes a degradation in image contrast.[8]

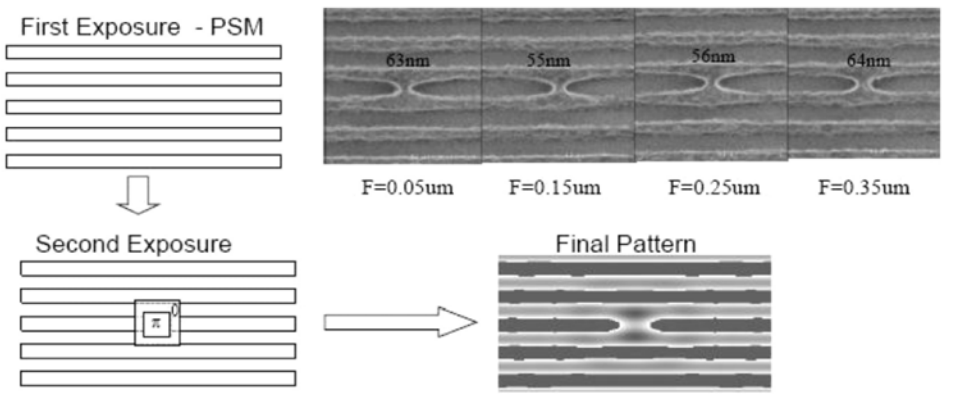

Figure 9.5 Demonstration of exposing one resist film twice to obtain the desired pattern (negative resist, 0.85NA 193-nm tool). (Reprinted by permission from Ref. 7.)

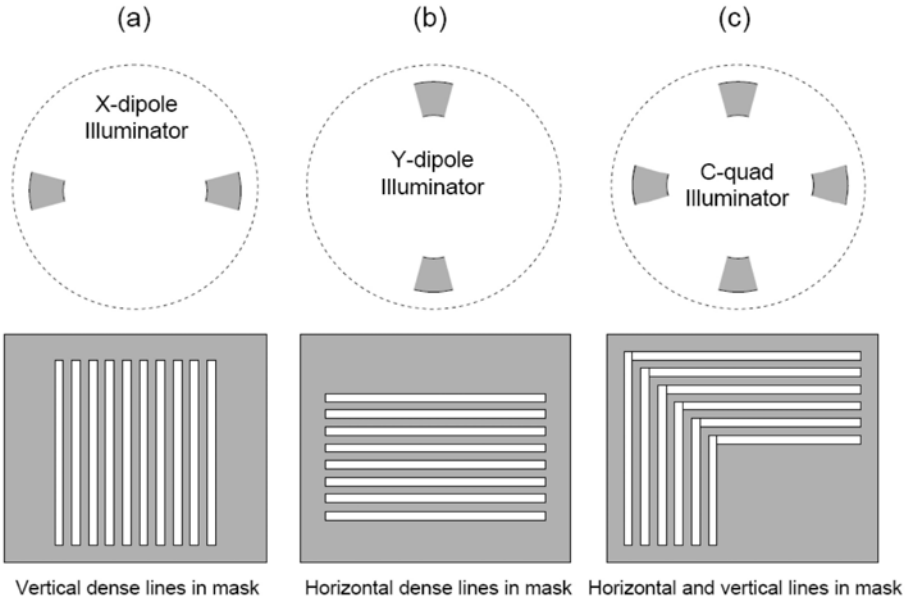

Figure 9.6 (a) X-dipole illumination gives the best resolution for vertical dense lines. (b) Y-dipole illumination gives the best resolution for horizontal dense lines. (c) C-quad illumination can be used to resolve both vertical and horizontal lines with degraded imaging contrast.

Figure 9.7 shows the experimental results of double exposures with X- and Y-dipole illumination.[9] The design has both horizontal and vertical lines and is split into two masks. One has all of the horizontal lines that were imaged using Y-dipole illumination. The other has all of the vertical lines that were imaged using X-dipole illumination. The top-down image of the final pattern is shown in Fig. 9.7.

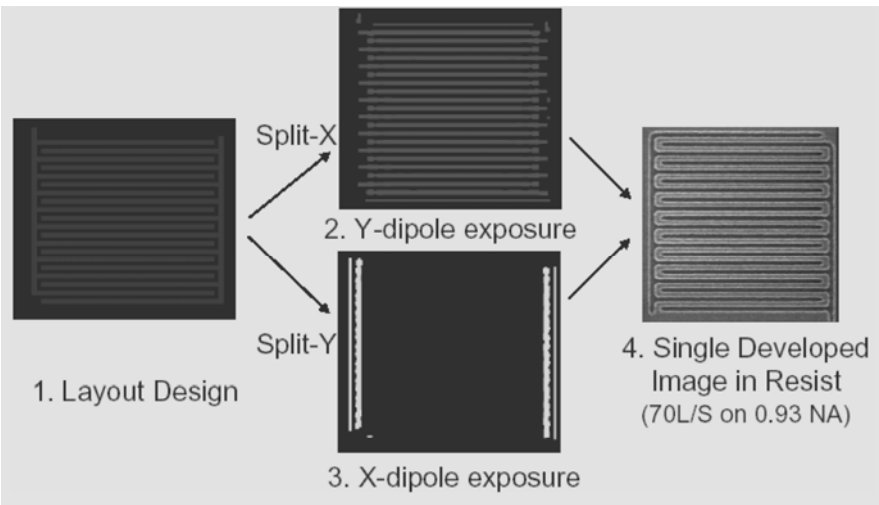

Figure 9.7 Dipole decomposition of the layout. (Reprinted by permission from Ref. 9.)

For complex mask layouts, OPC must be used in order to ensure pattern fidelity under dipole illumination. Figure 9.8 shows an example of OPC use.[10] The target layout is split into an X-dipole mask and a Y-dipole mask. The OPC is added to each mask to ensure image fidelity during exposure.

9.2.3 Image-assisted double exposure

Double exposure uses two masks and (possibly) two illuminations. The combined aerial images are a linear superposition of the aerial image intensities from the individual exposures. The residual energies from the exposures must be shielded in order to guarantee good combined aerial image fidelity. To reach this goal, inverse lithography has been developed to assist in the designs of Masks 1 and 2.[11] Inverse lithography attempts to synthesize the mask (input) that results in the desired wafer pattern (output), by inverting the forward model from mask to wafer (Fig. 9.9). The masks designed by this method should give superior contrast to the combined aerial images, without concern for the residual energies from the previous exposure.

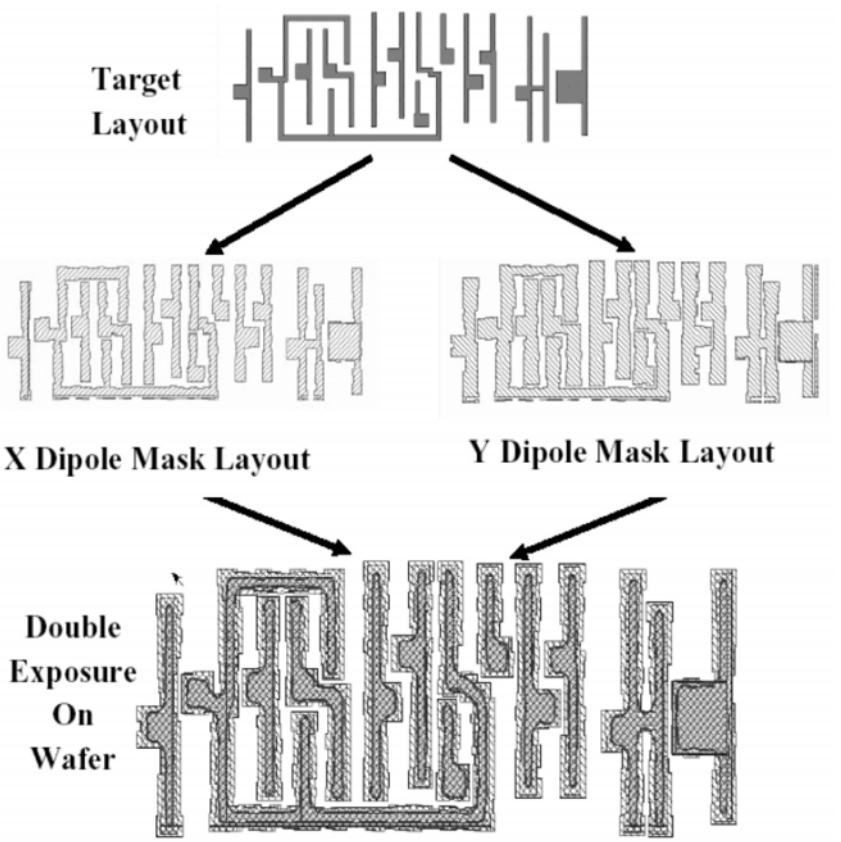

Figure 9.8 OPC is introduced into the dipole-decomposed layouts. (Reprinted by permission from Ref. 10.)

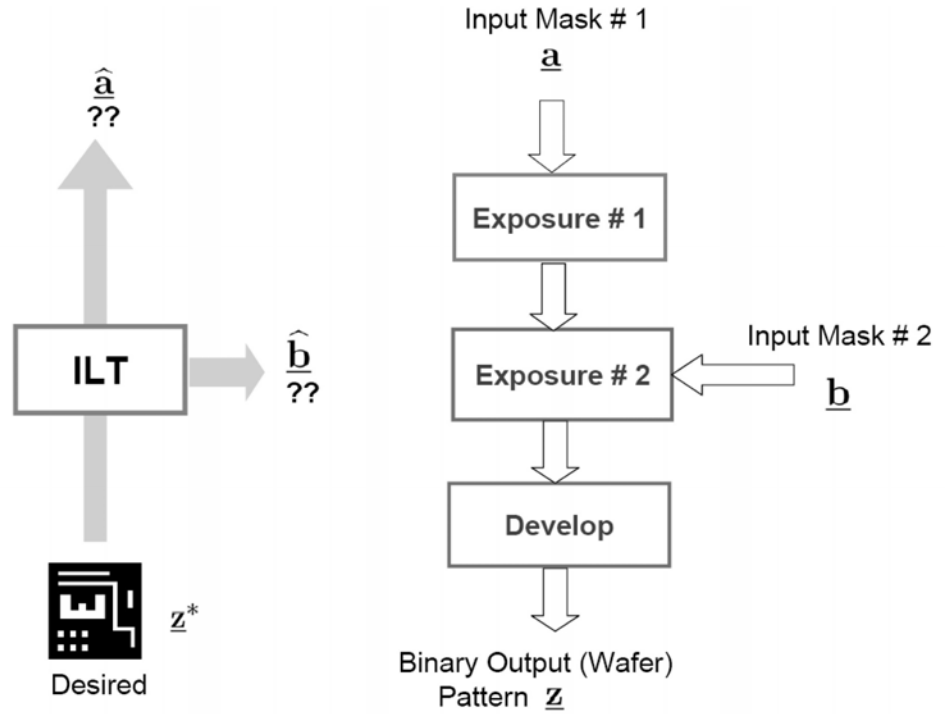

Figure 9.9 Inverse lithography is employed to design the masks for the double exposure. (Reprinted by permission from Ref. 11.)

Unlike the decomposition of X- and Y-dipole exposures, which simply splits the vertical and horizontal lines between masks, the imaging-inverse calculation splits the gray-level aerial image into two (overlapping) parts. The resulting imaging-inverse solution may not be unique.

Figure 9.10 shows an example of such an image-assisted double exposure. In this test, Contacts A and B must be patterned on a resist film. The aerial image of the 1st exposure (1st mask + annular illumination) is simulated and the aerial image intensity is lower for Contact A than for Contact B. The 2nd mask and illumination condition were designed to enhance the contrast of the combined aerial image.

The effect of misalignment between the two exposures was evaluated.[12] The overlay (OL) of the 2nd exposure was systematically shifted in both the X and Y directions to determine the effect on the top-down SEM images and CDs of the contact holes. Figure 9.11(a) shows the top-down images at the OL shift from –15 nm to +15 nm and Fig. 9.11(b) shows the measured CD value versus the OL shift. The results suggest that the double exposure can provide acceptable results within the OL shifts of ±10 nm.

Both simulation and experiment clearly show that double-exposure imaging can provide better process windows and pattern profiles than can single-exposure

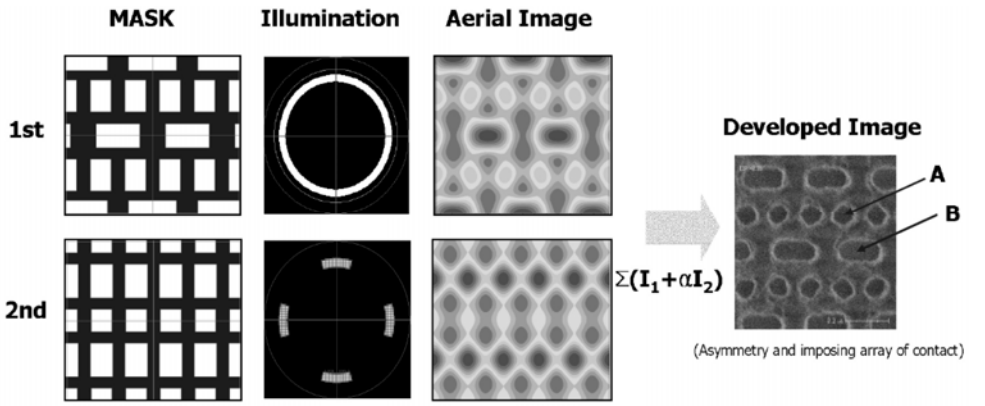

Figure 9.10 Image-assisting double exposure. (Reprinted by permission from Ref. 12.)

imaging. However, to get the best imaging possible, the doses of the 1st exposure (E_1) and the 2nd exposure (E_2) must also be optimized so that the "effective first-order efficiency" can be as large as possible.[12] The effective first-order efficiency is defined as follows:

$$\text{Effective First Order Efficiency} = \frac{A_1 + (E_2 / E_1)A_2}{1 + (E_2 / E_1)}, \tag{9.1}$$

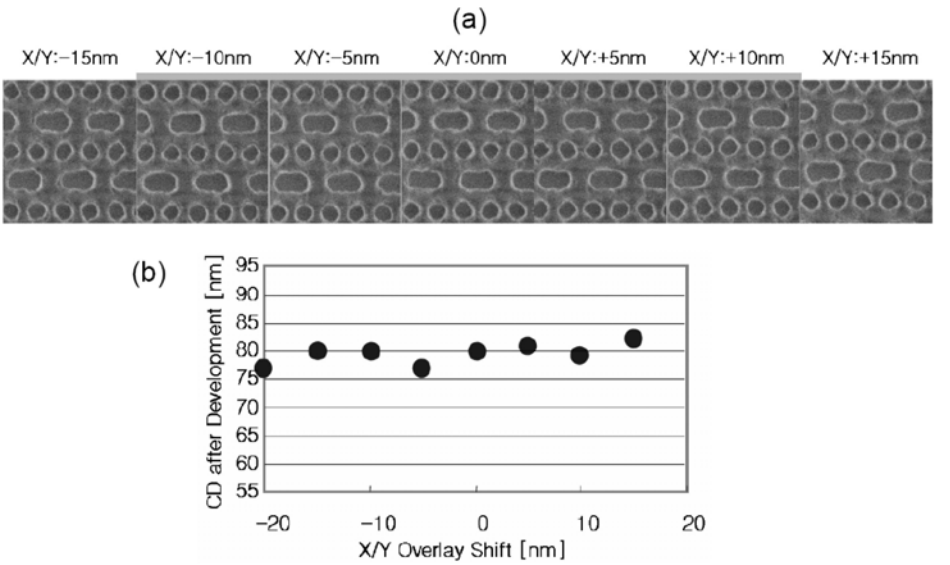

Figure 9.11 Misalignment effect between the two exposures. (a) Top-down images at different overlay (OL) errors. (b) Measured CD value as a function of OL. (Reprinted by permission from Ref. 12.)

where A_1 and A_2 are the first-order efficiencies of the 1st and 2nd exposures. Assuming 0 and ±1 diffraction orders are the only ones to pass through the lens, A_1 is the intensity ratio between the 0 and ±1 diffraction orders in the 1st exposure; A_2 is the intensity for the 2nd exposure.

9.2.4 Other approaches

Among various DE/DP approaches, the DE with one layer of resist has the fewest process steps and is the most cost effective. This approach has attracted a lot of attention and various new approaches have been proposed in theory.[13] The key to the success of these approaches is the availability of innovative materials. For example, contrast-enhancement layers (CELs) have been proposed as coatings over the resist stack. The CEL would absorb enough light to prevent the flare from reaching the resist film. It has been theoretically predicted that CELs would simply allow spatial frequency doubling (Fig. 9.1) to work with current 193-nm resists.

9.3 Double Exposure with Two Full Lithographic Processes

This section summarizes various approaches of double exposure with two full lithographic processes: Resist 1 / Exposure 1 / Develop 1 followed by Resist 2 / Exposure 2 / Develop 2. A special process may be added between the lithographic processes to freeze the 1st resist pattern so that it can remain unaffected during the processing of the 2nd resist. This freezing process should be accomplished in the track to reduce the delay time and increase throughput.

9.3.1 Double exposure with positive and negative resists

Double exposure processes have been developed employing both positive and negative resists. The 1st lithographic step uses the positive resist. Then, the negative resist is coated over the 1st resist pattern. A dehydration bake may be needed before coating the negative resist. Both resist films share the same BARC layer. Finally, the hard mask and substrate etches are integrated into one process step. Figure 9.12 shows the process flow.

In a specific example, the positive resist is TOK Pi06-001ME and the negative resist is TOK N3001. The solvents used for each resist are different in order to prevent intermixing. Therefore, the Pi06-001ME resist is not dissolved by the N3001 solvent system.[14] Exposure of the negative resist is done using a dark-field mask in the area between the previously printed resist lines. The flare is absorbed by the negative resist before it reaches the positive resist pattern. The flare level is sufficiently low that it does not activate cross-linking of the negative resist. Enough image contrast is expected with this approach. In comparison, if a positive resist were selected for the 2nd exposure, a bright-field mask would be used and the flare generated by the 2nd exposure would overexpose the 1st resist pattern (Fig. 9.12). In this approach, additional processes to freeze the 1st resist pattern are not required. Figure 9.13 shows top-down SEM images of 60-nm

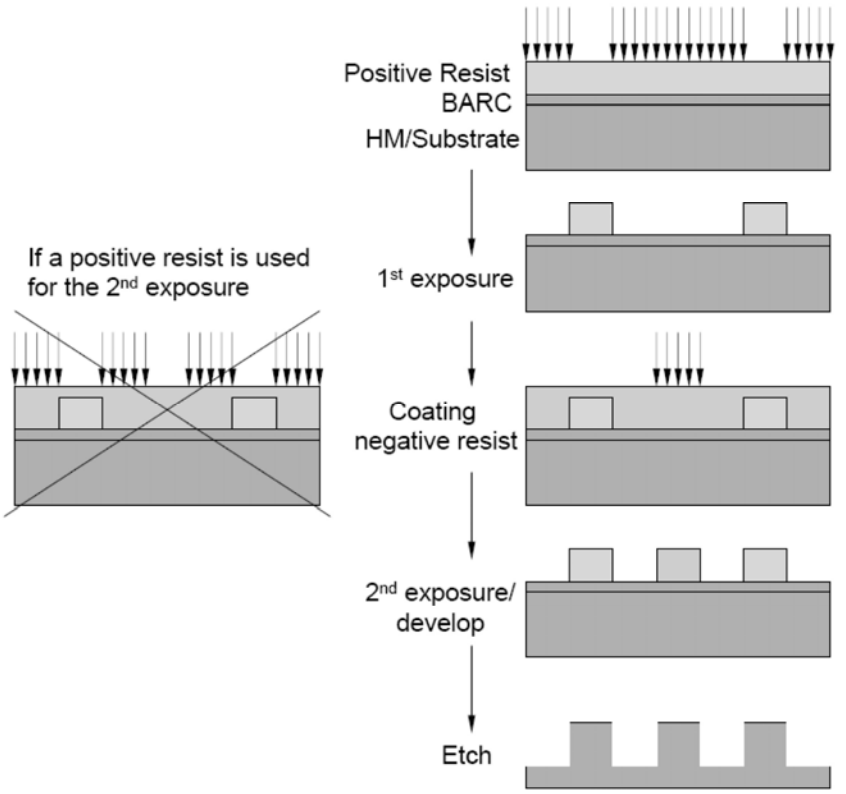

Figure 9.12 Process flow of DE with positive and negative resists.

half-pitch dense lines (Fig. 9.13(a)) and 36-nm half-pitch dense lines (Fig. 9.13(b)) obtained from this double-exposure process.[14]

A successful double exposure process that uses positive and negative resists must have the following characteristics:

1. The coating of the negative resist should not damage the patterns generated by the 1st exposure. The two resists should use different types of solvents and no intermixing should occur at the interface. The diffusion of resist components between resists must be minimized and should not cause problems.
2. The positive resist patterns must survive the 2nd exposure and development. Minimal resist loss is required.
3. The two resists must have similar lithographic performance characteristics, including high resolution and low LER.
4. Because the etch resistance of positive and negative resists is typically different, the etch process must be carefully optimized. Although the CDs of the two resist patterns are the same, the final CD in the substrate might be different.

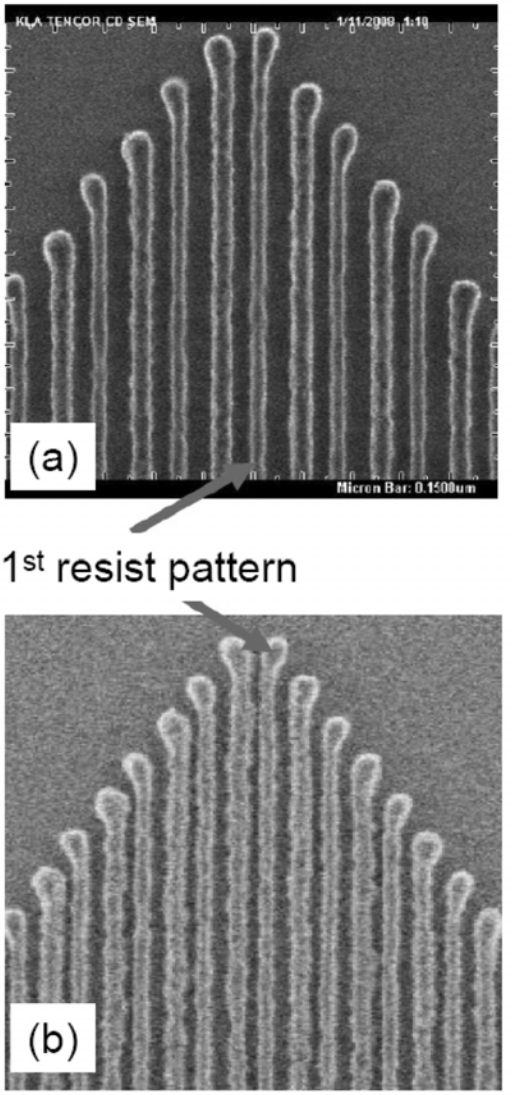

Figure 9.13 Top-down SEM images of (a) 60-nm half-pitch and (b) 36-nm half-pitch dense lines. The patterns were obtained by the double exposures with positive and negative resists. (Reprinted by permission from Ref. 14.)

9.3.2 Freezing of the 1st resist pattern

"Freeze" processes have been developed to preserve the 1st resist patterns during the 2nd lithographic process. After the 1st lithographic process, the resist pattern is treated using either a physical or a chemical step. These treatments can include high-temperature bakes, chemical fluid rinses, or ion implantations. After treatment, the resist pattern should be unaffected by the 2nd lithographic processes. Depending on the resist and the treatment method, the "freezing"

mechanism can be either removal of the photoactive components in the resist pattern or formation of a protective surface layer on the pattern. After the 2nd lithographic process, the 2nd resist pattern together with the preserved 1st resist pattern work as an etch mask for either the HM opening or the substrate etch. This section covers the various approaches of freezing the 1st resist pattern.

9.3.2.1 Freezing technique with a surface-protecting layer

In this approach, a thin protective layer that covers the 1st resist pattern is formed. Figure 9.14 shows the process flow. After the 1st lithographic processes, a chemical freeze material is coated on the resist pattern. The freeze material is composed of resin, cross-linker, and solvents.[15,16] The wafer is baked and rinsed, leaving an ultrathin cross-linked layer on the outside of the resist features. The cross-linking reaction is catalyzed by acid on the resist surface. The acid may be the result of thermal decomposition of the PAG or may simply come from the initial exposure step. After the 1st resist has been frozen, the 2nd resist is coated. During the 2nd lithographic process, the cross-linked freezing material preserves the 1st resist pattern.

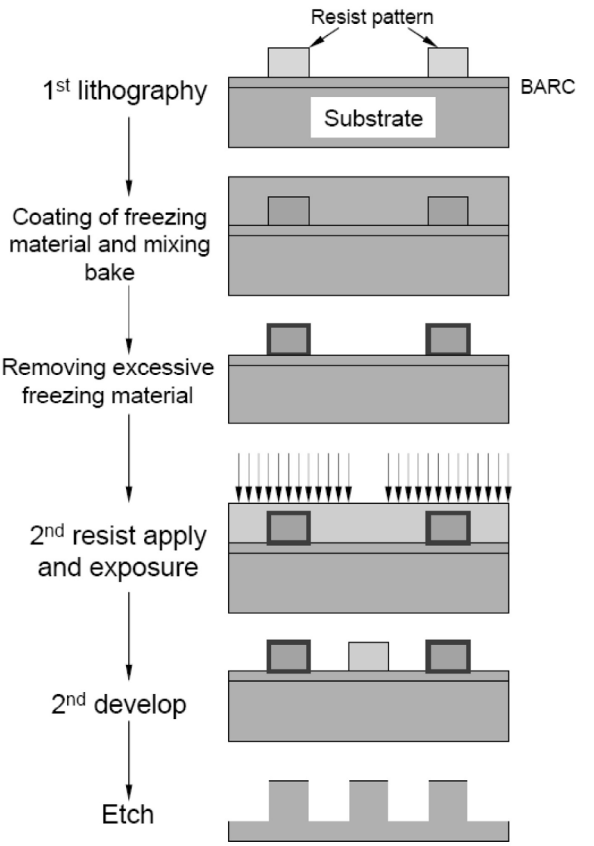

Figure 9.14 Process flow of the pattern freezing approach.

Figure 9.15 shows top-down SEM images measured at each step of the double exposure, using the protective-layer approach.[15] This process is used to print two target features: 40-nm and 32-nm dense lines. The 1st lithographic step generates the patterns of 40-nm lines with 160-nm pitch or 32-nm lines with 128-nm pitch. Then, the lines are frozen and the 2nd lithographic process produces the target patterns. The CDs of the resist lines are measured and labeled (Fig. 9.15).

One key challenge of this process is minimizing CD variation between process steps. First, the cross-linking layer tends to increase the line CD; the higher the bake temperature, the more the CD increases.[16] Second, the bake temperature is about 150° C. At such a temperature, the resist pattern begins to shrink, leading to a decreasing CD of the 1st resist pattern.[15] As a result of these two effects, an approximately 2-nm reduction in resist CD is observed after the freezing process. Third, the CD of the 1st resist pattern increases during the 2nd lithographic process. Apparently, the 2nd resist causes a CD increase in the 1st resist pattern. CD increases of ~4 nm have been observed (Fig. 9.15).

Obviously, this approach would be much more successful if the CD of the 1st pattern remained unchanged during the 2nd lithographic process. Optimization of the freeze material and the temperature, or of the time of the freeze bake, is being pursued to address the issue of CD variation. If the issue is not successfully addressed by adjusting the freeze parameters, OPC will be required to compensate for the CD variations.

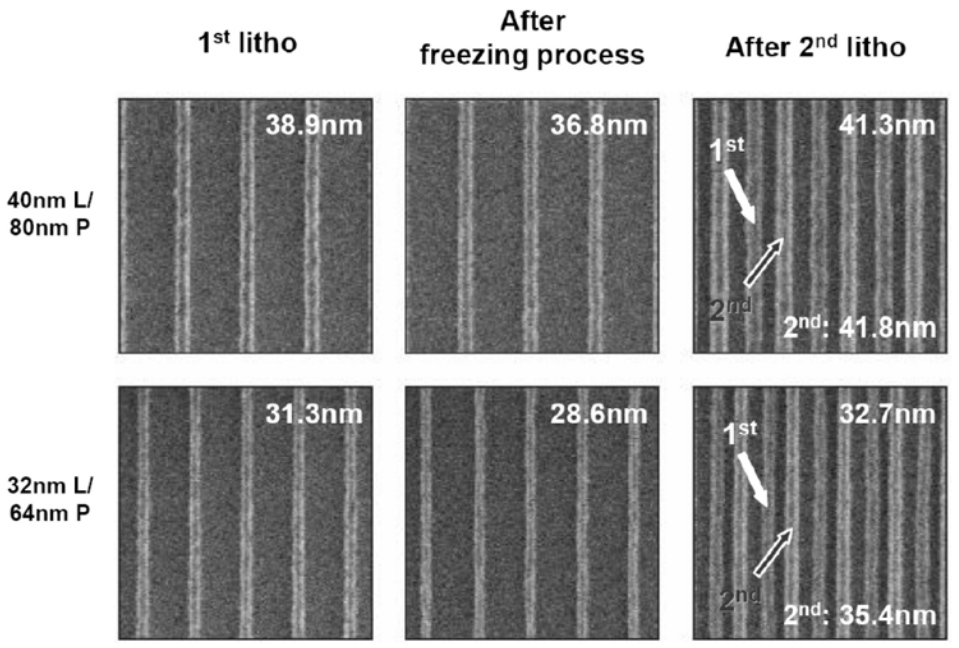

Figure 9.15 Top-down SEM images at each step of the double exposure. The CDs of the resist lines are measured and labeled on the images. (Reprinted by permission from Ref. 15.)

The surface-protective layer approach has also been proposed for double exposures of contact holes (Fig. 9.16(a)).[15] First, vertical line and space patterns are printed, then they are frozen. Next, horizontal line and space patterns are printed. An array of contact holes is formed between the resist lines. The size and pitch of the contact holes are related to the CDs of the lines and spaces. Fig. 9.16(b) shows top-down SEM images of hole patterns formed by this method. The printing of perpendicular 70-nm lines produced 51-nm holes with 120-nm pitch; printing of perpendicular 60-nm lines produced 46-nm holes with 104-nm pitch.

9.3.2.2 Freezing technique with thermal cross-link resist

Freezing the 1st resist pattern by a higher temperature bake (post-develop bake) is another approach to preserving the resist pattern.[17] For example, a thermally activated cross-linker can be added to the 1st resist. The cross-linking temperature must be higher than the PAB and PEB temperatures. After the 1st development, the resist patterns are baked at high temperature to cross-link the resist. The cross-linked resist pattern should be unaffected by the 2nd lithographic process.

The key to the success of this process is the availability of new resists that can be frozen during the high-temperature post-develop bake (PDB). An example of such resists has been reported.[17] The post-develop bake temperature is 200° C. After the bake, the resist film is rinsed with resist solvent and aqueous TMAH

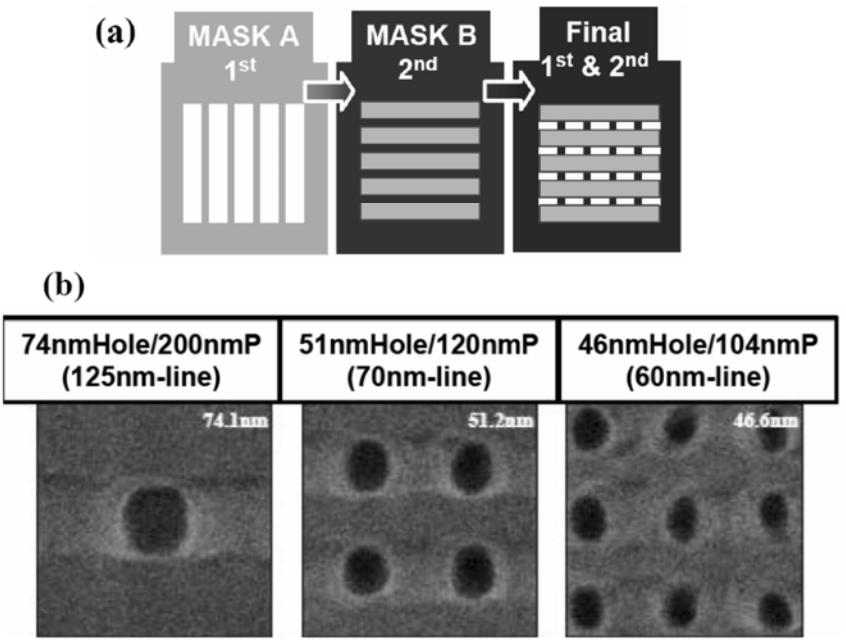

Figure 9.16 (a) Contact holes formed by double exposure. (b) Top-down SEM images of contact holes formed by the double exposure. The size and pitch of the contact holes are related to the CDs of the lines and spaces. (Reprinted by permission from Ref. 15.)

developer to demonstrate a minimum resist loss. Exposures of the resist film before and after the bake are completed to investigate the photosensitivity reduction induced by the bake (Fig. 9.17). In this test, 140-nm contact holes are printed with a dose of 20 mJ/cm^2. The wafer is baked at high temperatures of 150 to 200° C after development. Then, a second set of holes is printed near the first set. However, only small holes are printed, even with a higher dose of 26 mJ/cm^2. This result indicates that the photosensitivity of the resist is reduced by the post-develop bake. The authors found that increasing bake temperatures causes a greater loss in photosensitivity.

The thermally freezable resist is used in combination with a regular 193-nm resist for the double exposure of 35-nm resist lines with 70-nm pitch. Figure 9.18 shows the top-down SEM image of the patterns obtained. The 2nd layer resist images are generated on top of the 1st resist layers to form 35-nm lines in 70-nm pitch. It appears that the 1st resist patterns are unaffected by the 2nd process.

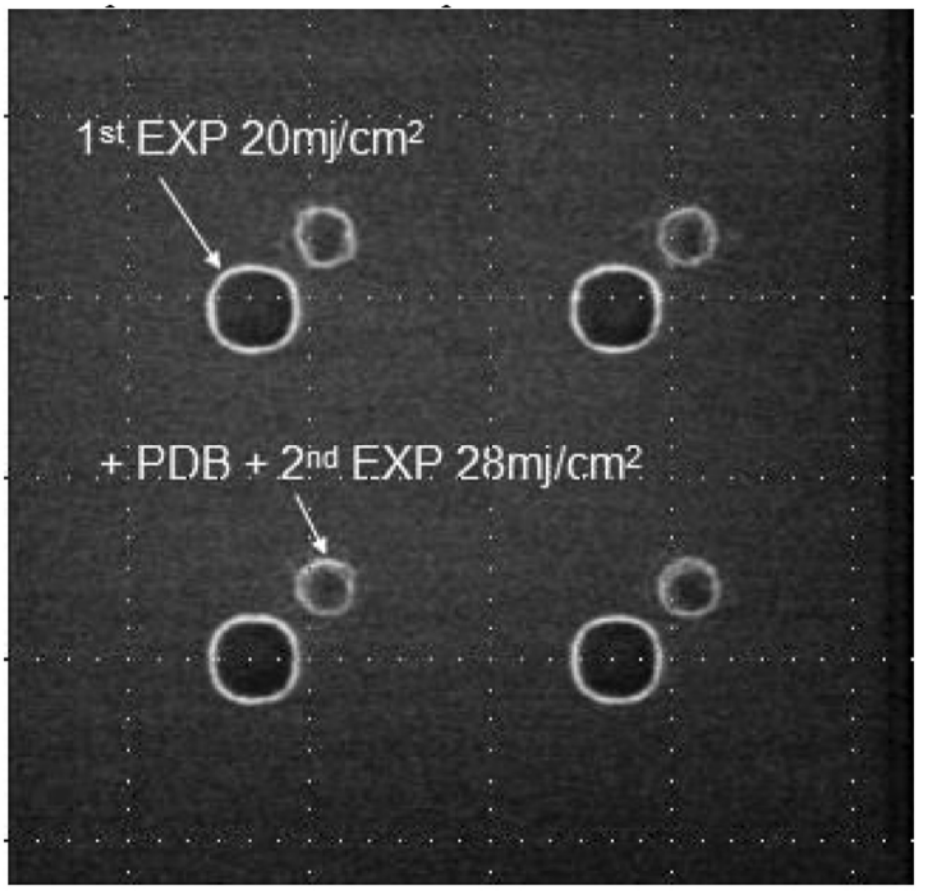

Figure 9.17 Contact holes obtained from exposures before and after the post-develop bake. (Reprinted by permission from Ref. 17.)

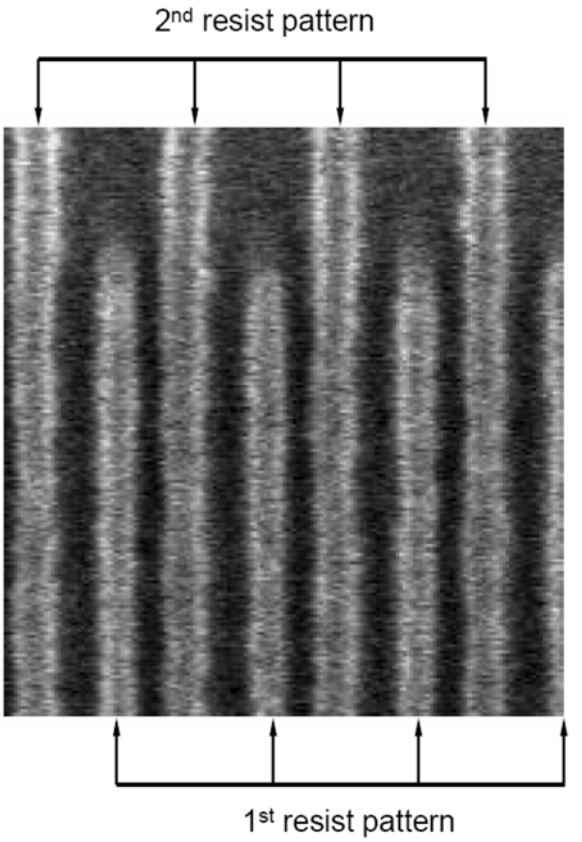

Figure 9.18 Top-down SEM image of 35-nm resist lines with 70-nm pitch obtained by thermal-freezing double exposure. (Reprinted by permission from Ref. 17.)

The great difficulty with the development of thermal-freezing processes is apparently the development of thermally freezable resists with superior lithographic performance. The presence of thermal cross-linkers in the resist formulations should not degrade the pattern profiles, increase defectivity, or lower the etch resistance of the resist. Additionally, the material and process should be track compatible.

9.3.2.3 Other "freezing" approaches

In principle, any semiconductor-friendly process that can freeze resist patterns can be considered for double exposure. Innovative approaches combined with material availability are the keys to bringing new freezing processes to mass production.

In addition to chemical and thermal freezing, ultraviolet (UV) curing methods were investigated for the double exposure of contact holes.[18,19] Recently, UV curing with 172-nm light was evaluated.[20] In this approach, the 1st resist patterns are exposed to 172-nm UV irradiation and baked after the UV curing. It

was proposed that all of the energy of the 172-nm photons would be absorbed at the surface, since they have limited penetration depth in 193-nm resists. The authors proposed that this energy would cause nonselective homolytic bond cleavage in the organic polymers and the resulting radicals would then, in turn, react to form cross-links that would render the resist insoluble. However, CD shrinkage, line-end shortening, and corner feature deformation were the problems observed with these 172-nm treated patterns. In addition, this process needs an extra UV curing chamber, as the double-exposure process cannot be accomplished entirely within the lithography cluster.

The implantation of argon ions (Ar^+) can make resists insoluble in the solvent and unaffected by the 2nd lithographic process.[21,22] The robustness of the resist patterns after ion implantation depends on the energy of the ions. The ions should have at least enough energy to penetrate the entire resist film. To completely harden a conventional 193-nm resist film with a thickness of 150 nm, the ion beam must have energies over 100 keV. However, several issues are associated with this process. First, the resist pattern shrinks during the ion implantation and the shrink value increases with the implantation dose. Second, high-energy ion beams can cause damage to the substrate. Third, the ion implantation process would need to be done outside of the lithography cluster.

9.3.3 Pack and unpack (PAU) for printing contacts

The pack-and-unpack (PAU) process can be used to print arrays of contact holes.[19] Figure 9.19 shows the process flow. The 1st imaging step is optimized to print a dense array of contact holes. Then, the wafer is coated with the 2nd layer resist over the dense contact holes. The 2nd exposure opens only the desired holes. Thus, this process is called pack and unpack. The 2nd layer resist can be negative tone and the 2nd exposure can cover certain areas and open more than one hole. Unlike other double exposure processes, the PAU does not directly provide additional pattern resolution. The pattern resolution is obtained only during the 1st exposure. However, with the help of the unpack exposure, the isolated or random contact holes can be obtained from an array of dense holes. Hence, the 1st exposure illumination can be optimized to give the best resolution for dense holes, without concern for printing isolated holes within the same process window.

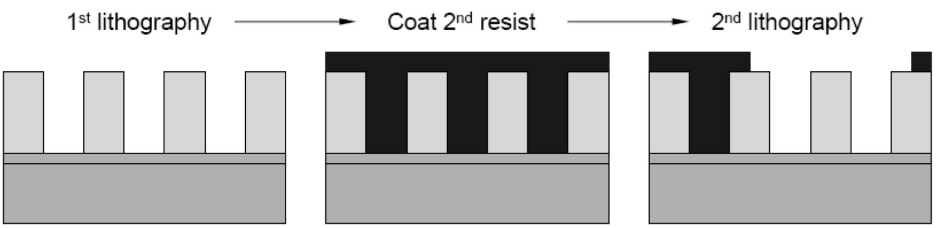

Figure 9.19 Process flow of pack and unpack for printing contacts.

The primary difficulty with this approach occurs in the process of freezing the 1st resist patterns. The 2nd resist can dissolve the 1st resist pattern during coating and the 2nd exposure can deprotect the 1st resist and make it soluble in the 2nd development process. Two solutions have been suggested. One is to use alcohol-based solvents for application of the 2nd layer resist. These solvents should not dissolve the 1st resist, which is soluble in PGMEA. The second solution is to apply a UV curing process to harden the 1st layer resist. The curing process should make the 1st layer resist hard enough so as not to be dissolved by the 2nd layer resist.

9.4 Double Patterning

Double patterning (DP) processes have one more etch step than double-exposure processes. This additional etch is in the process flow. The intermediate etch transfers the 1st resist pattern to a hard mask (HM). The HM can be either an inorganic film deposited by chemical vapor deposition (CVD) or a cross-linked polymer film obtained by spin-coating and high-temperature bake (spin-on HM). The HM preserves the 1st pattern and is unaffected by the solvent, the exposure, and the development occurring during the 2nd lithographic process. Although DP has a complicated process flow, it does not require the development of any new materials. Basically, the materials and the processes used in DP are already available and have been tested in previous technology nodes. Therefore, DP is a more mature process than is the double-exposure process. Double patterning can be implemented in various ways.

9.4.1 Double trench patterning

Double trench patterning etches trenches onto hard masks to form dense line and space patterns. Figure 9.20 shows the process flow of double trench patterning. A hard mask (HM) layer is deposited or coated onto the substrate (e.g., SiN). A resist stack is coated on the HM and the 1st lithographic process is accomplished to generate semidense trenches with a duty ratio (trench/line) of 1:3. The pattern is then transferred to the HM layer by an etch process. After stripping, another resist stack is coated onto the HM. The 2nd resist stack may be identical to the 1st resist stack. A thinner HM film minimizes coating uniformity issues associated with coating of the 2nd resist stack over topography. The 2nd lithographic step is performed to generate the same set of semidense trenches between the previous trenches. Then, the pattern is transferred to the HM by the 2nd etch process. The dense pattern with 1:1 ratio is obtained in the HM layer. Finally, the dense pattern is transferred to the substrate by another etch step.

The exposures in Fig. 9.20 require positive resists and dark-field masks. Unfortunately, the exposure process window for generating the narrow trenches is too small. Simulation results demonstrate that the dark-field mask provides poorer aerial image contrast for the trench and leads to losses in exposure latitude.[23] The aerial image contrast and the process window can be enhanced only by overexposure (i.e., the trenches must be printed larger than the features

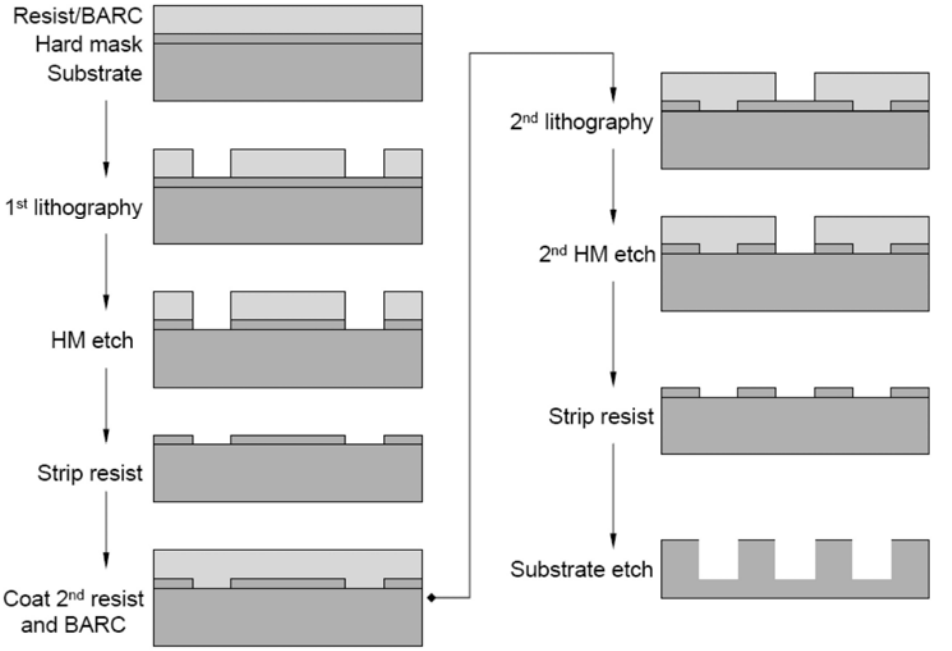

Figure 9.20 Process flow of double trench patterning (dark-field masks with positive resists).

on the mask). To compensate for the CD shift, shrink processes have been used to shrink the trenches so that their CD can meet requirements.[24,25]

In one study,[24] after each of the two development steps, the RELACS process was performed to shrink the trench CDs to their target values. The exposures were performed using a 0.85NA 193i scanner with 150-nm thick resist (PAR IM850) and 33-nm thick BARC (ARC91). The trenches were shrunk 20–40 nm, adjusted by varying the temperature of the mixing bake (see Chapter 8 for details). The HM was TaN film. The target CDs are 50-nm 1:1 dense lines. In this process, both mask bias and RELACS shrinkage values are adjusted to maximize the exposure process window. Simulations and experiments are performed to determine the optimal shrink and optimal mask bias. For the 50-nm trenches with 200-nm pitch, the optimal mask dimension was found to be ~104 nm, resulting in a trench dimension of ~76 nm by underexposure, followed by ~24-nm shrinkage, to reach the final target of ~50 nm with good CD control. Figure 9.21 shows the SEM images of the final pattern etched into the substrate. For the double patterning of contact holes, thermal reflow was used to shrink the contact sizes.[25]

The introduction of shrink processes further complicates the double-patterning process. As an alternative, double trench patterning with bright-field masks and negative resists has been proposed (Fig. 9.22). For the same feature sizes, the aerial image contrast from bright-field masks is much higher than that of dark-field masks, resulting in larger process windows.[26] The challenge lies in

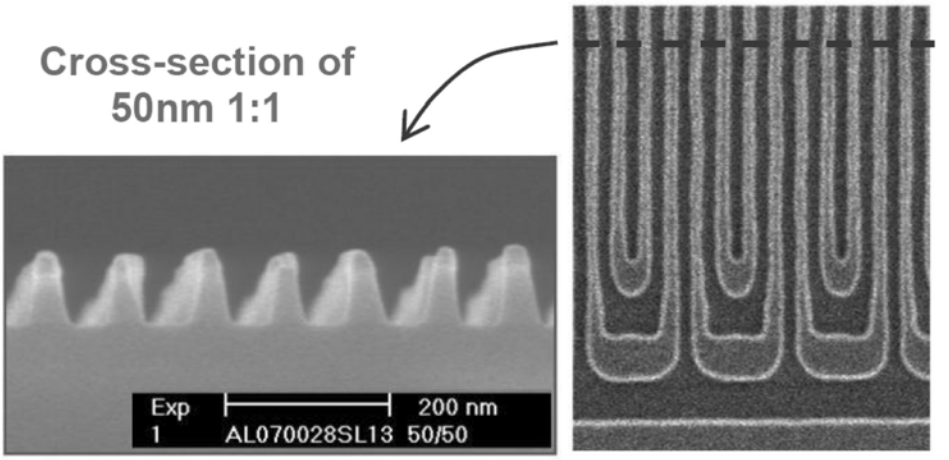

Figure 9.21 SEM images of the final pattern etched into the substrate. The pattern has 50-nm 1:1 dense lines and was obtained by the double trench patterning and RELACS processes. (Reprinted by permission from Ref. 24.)

the fact that a negative resist is required to print the trenches (Fig. 9.22). The 193-nm negative resist must have superior lithographic performance, such as high resolution, low swelling, and small line-edge roughness.

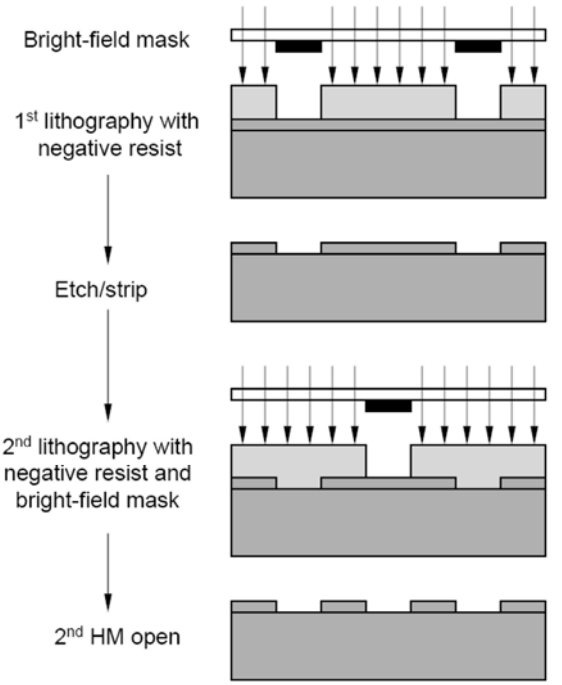

Figure 9.22 Double trench patterning with bright-field masks and negative resists.

A negative resist from TOK was imaged using a 0.85NA scanner and a bright-field mask. The target feature size was a 50-nm trench with 220-nm pitch.[23] Figures 9.23(a) and (b) show the process window and top-down SEM images of the resist pattern. At 5% exposure latitude, the DOF is about 0.17 μm. After etch, the trench pattern is transferred to a SiN HM with a thickness of 35 nm. After the 2nd etch, the final pitch transferred to the HM is 110 nm (Fig. 9.23(c)).

An alternative method using bright-field masks (better aerial image contrast), but without using negative resists, is to use negative-tone developers,[26] which are capable of reversing the tone of positive resists. In this process, the dissolution contrast is derived from the polarity or from the hydrophobicity change

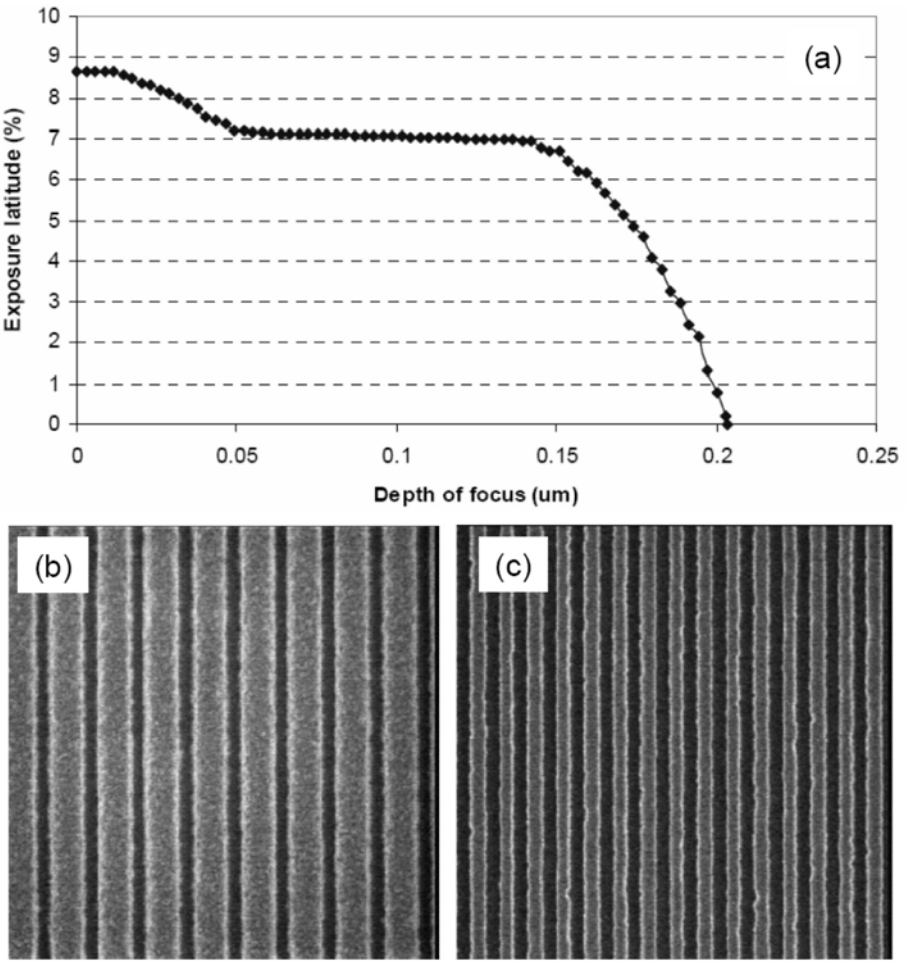

Figure 9.23 (a) Process window and (b) top-down SEM images of a 50-nm trench with 220-nm pitch. The exposure was done at 0.85NA with a bright-field mask and the negative resist is TOK N026. (c) SEM image of the dense lines and spaces in the SiN hard mask after the 2nd etch. The pitch is 110 nm. (Reprinted by permission from Ref. 23.)

of the polymer by the deprotection reaction with the photoacid. Thus, the hydrophobicity or polarity parameter of the developer is the key to controlling dissolution contrast. Several organic solvents have been evaluated as negative developers. A good candidate must quickly dissolve the protected polymers but slowly dissolve the deprotected polymers. Additionally, the developer should not cause the resist to swell and the development rate should be relatively insensitive to the molecular weight (Mw) of the polymers. Figure 9.24(a) shows the dissolution rate of a resist film in a standard aqueous developer and in a negative organic developer. The dissolution rates are compared with and without exposure at a dose of 15 mJ/cm^2. The resist has a dissolution contrast of 1.3×10^3 in the negative-tone developer and a dissolution contrast of 1.3×10^5 in the positive-tone developer. This dissolution contrast is believed to be large enough to obtain fine patterns.

Figure 9.25 shows 60-nm trenches printed using a bright-field mask and a negative developer. The exposure was done with a 0.75NA dry exposure tool and a 6% half-tone mask. The authors predicted that it would be possible to print 45-nm trenches using the same process in combination with a 1.2NA 193i exposure tool.

9.4.2 Double line patterning

In double line patterning, the HM layer is used for transferring only the 1st resist pattern, while the etch mask for the 2nd pattern is the 2nd resist pattern itself (Fig. 9.26). This process has one less etch step compared to the double trench patterning process (Fig. 9.20), since the double line patterning skips the 2nd HM etch.

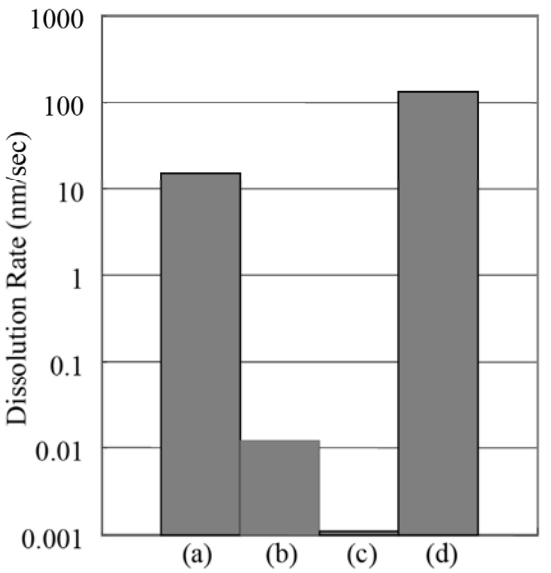

Figure 9.24 Dissolution rate of an ArF resist (a) without exposure and in the negative developer, (b) with exposure (dose = 15 mJ/cm^2) and in the negative developer, (c) without exposure and in aqueous TMAH developer, and (d) with exposure (dose = 15 mJ/cm^2) and in the aqueous TMAH developer. (Reprinted by permission from Ref. 26.)

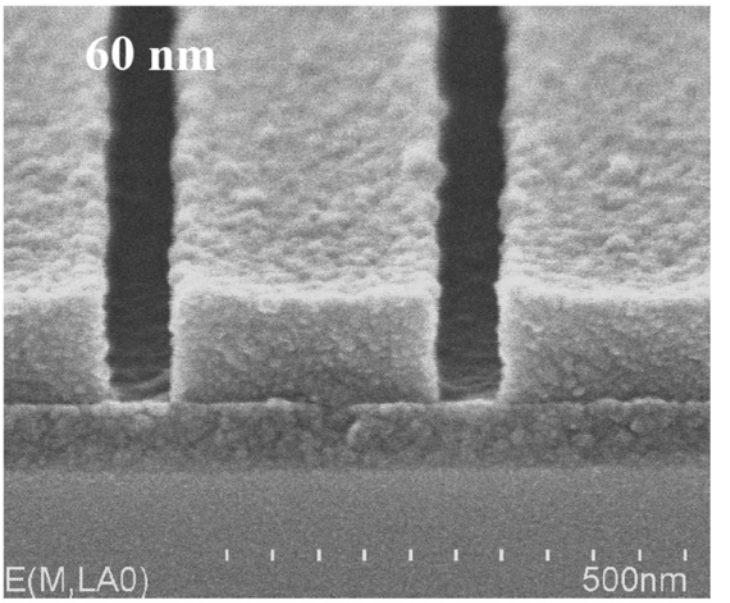

Figure 9.25 Cross-sectional image of a semi-isolated trench with a CD of 60 nm obtained by the process of bright-field exposure and negative development. (Reprinted by permission from Ref. 26.)

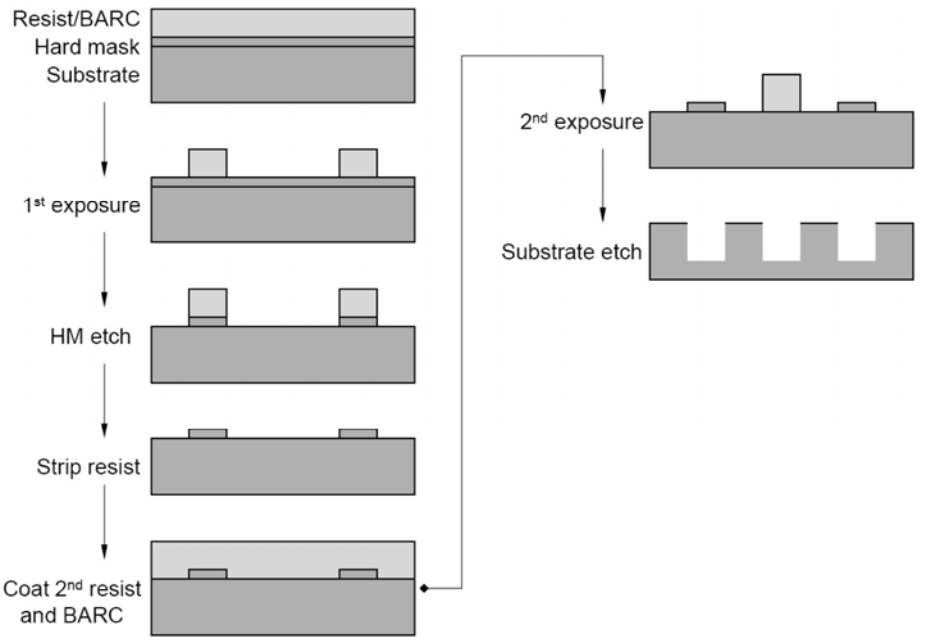

Figure 9.26 Process flow of double line patterning.

The double line patterning process was demonstrated using the poly-Si level (Fig. 9.27).[27] Dense lines with a pitch of 65 nm were printed using a 0.85NA 193-nm immersion scanner and dipole illumination. The cross-sectional images at each process step are also shown in Fig. 9.27. Diagrams of the process steps are included in the figure to explain the film stacks. The substrate is flat during the 1st imaging step, but has uneven topography due to the patterned hard mask during the 2nd imaging step. Another characteristic of this process is the additional etch of the 1st pattern in the HM. Because the 1st pattern must go through two plasma etch steps, the final substrate has two populations of lines. One is etched from the 1st lithographic pattern in the HM and the other is etched from the 2nd resist pattern. These lines correspond to different grayscales in the SEM images in Fig. 9.27. The difference in SEM contrast is perhaps due to the residual HM on the 1st pattern.

A double HM approach was recently developed for double line patterning. In this approach, after the 2nd lithographic process, both the 2nd resist pattern and the 1st HM are used to transfer the pattern into a 2nd HM. Better CD uniformity and process control can be obtained with this double HM approach.[28]

It is worth noting that the overlay errors between the two exposures are transferred into the final CDs differently from the way they are transferred in double trench patterning. In the double line patterning process, the misalignment leads to the CD deviations for *spaces* and image placement errors for *lines*. In the double trench patterning process, the misalignment leads to the CD deviations for *lines* and image placement errors for *spaces* (see Section 9.1.4).

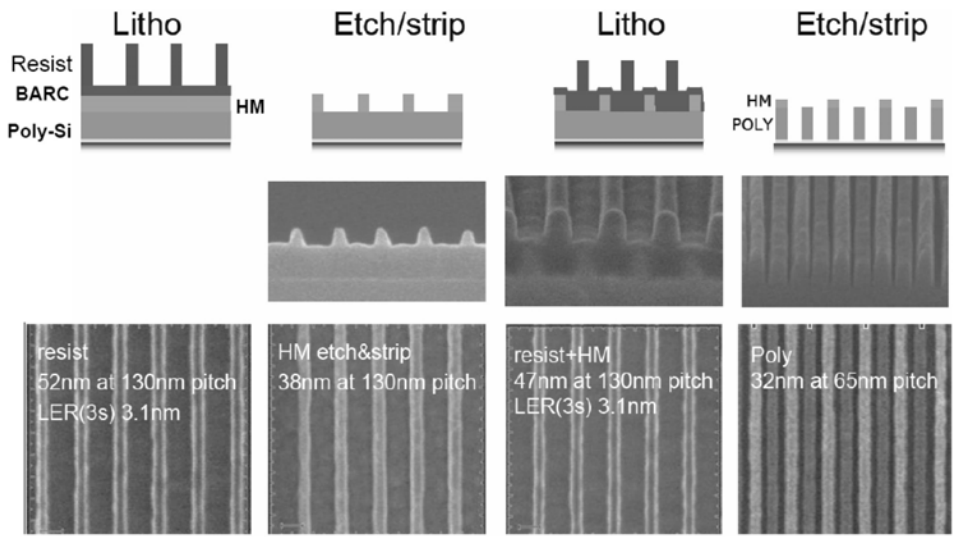

Figure 9.27 Diagram of double line patterning steps with cross-sectional images obtained at each process step. (Reprinted by permission from Ref. 27.)

9.4.3 Si-containing resists used as the 2nd resist in double line patterning

One concern with the double line patterning process is that the 1st HM pattern and the 2nd resist pattern work side by side during the etch. The HM is typically a silicon-containing film (SiN or SiON) and the 2nd resist is typically an organic polymer. The etch rates of these two materials are completely different. To address this issue, Si-containing resists have been evaluated as the 2nd resist,[29] as they have etch rates similar to those of the silicon-containing hard masks. After the 2nd lithographic step, the Si resist pattern together with the HM pattern work as an etch mask for transferring patterns to the poly-Si substrate.

9.4.4 Si-BARC film as a hard mask for double patterning

Spin-on Si-BARC in combination with spin-on carbon (SOC) have been proposed as replacements for the CVD hard mask for DP applications, since they fill the role of both BARC and HM. For double trench patterning, the Si-BARC and SOC are coated over poly-Si substrates. After the 1st lithographic step, the resist pattern is transferred to the Si-BARC by a plasma etch in fluorine chemistry. Then the 1st resist film is removed and the 2nd resist film is coated and imaged. During the 2nd lithographic step, the 1st pattern is preserved by the Si-BARC. A dehydration bake may be needed before application of the 2nd resist. The 2nd resist pattern is transferred to the Si-BARC layer by another etch in fluorine chemistry. Finally, the patterns in the Si-BARC are transferred to the SOC by an oxygen plasma etch and the patterns in the SOC are, in turn, transferred to the poly-Si substrate by the fluorine plasma etch. Figure 9.28(a) shows the process flow.

The Si-BARC/SOC can also be used in the double line patterning process, replacing the CVD hard mask. Figure 9.28(b) shows the process flow. After the 1st lithographic step and etch, another layer of Si-BARC/SOC is coated onto the 1st Si-BARC layer. After the 2nd lithographic step and etch, the patterns in both Si-BARC films work together as an etch mask for the SOC etch. This process has been described in the literature.[30] The 1st Si-BARC and SOC have thicknesses of 82 and 160 nm and the 2nd Si-BARC and SOC have thicknesses of 82 and 90 nm. The stack thicknesses were optimized for the best control of reflectivity. Exposures were performed on a 0.75NA scanner with dipole illumination and dense lines with a pitch of 75 nm were obtained. Figure 9.29 shows the top-down images at each process step. A cross-sectional image after the final etch is also included in Fig. 9.29.

This process has two challenges. First, the Si-BARC must be compatible with the resist and the SOC/Si-BARC/resist stack must have superior lithographic performance. Second, the 1st Si-BARC must be unaffected by the coating of the 2nd Si-BARC/SOC stack and its patterns cannot be degraded during the high-temperature curing processes of the 2nd Si-BARC/SOC.

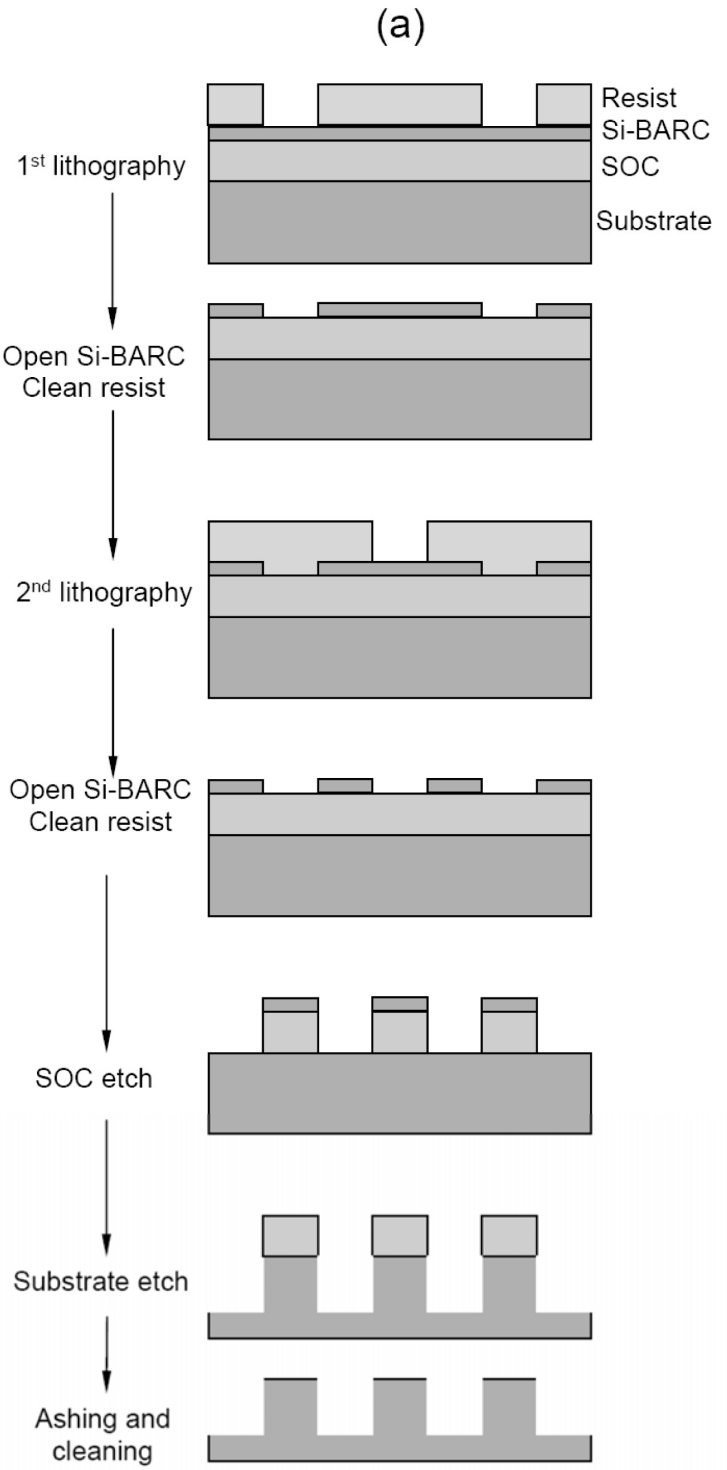

Figure 9.28 (a) Process flow of Si-BARC as a hard mask for double trench patterning.

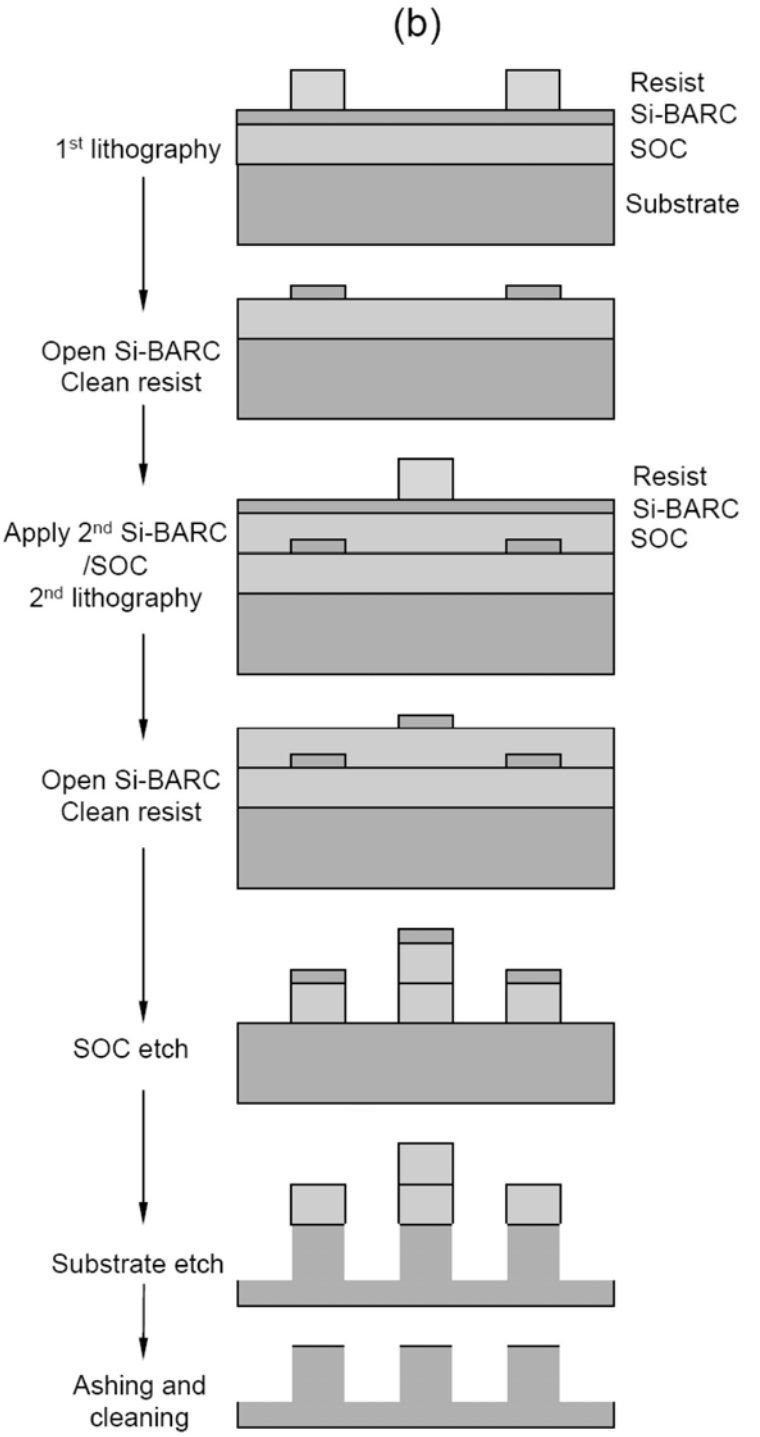

Figure 9.28 (b) Process flow of Si-BARC as a hard mask for double line patterning (with two Si-BARC/SOC layers).

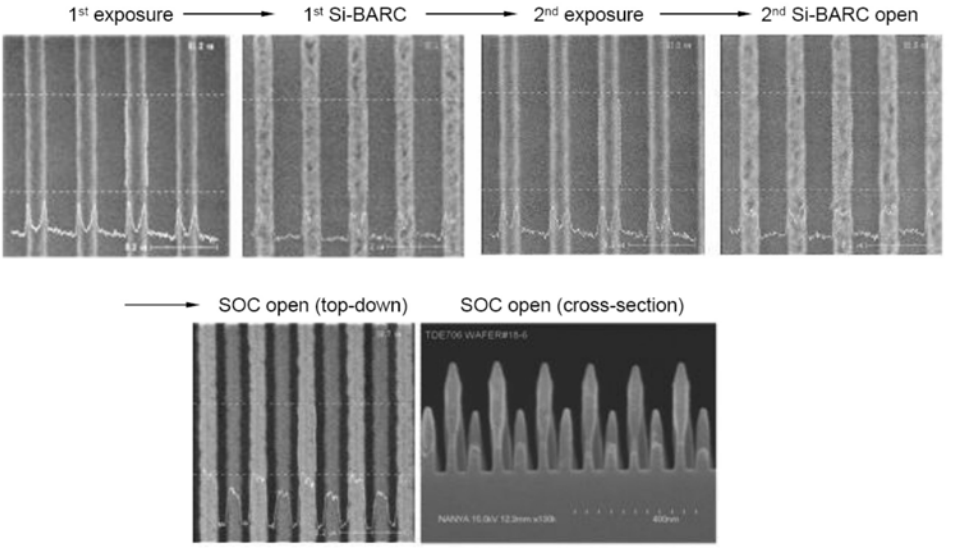

Figure 9.29 SEM images at each process step of double line patterning with Si-BARC. The final pattern has a pitch of 75 nm. (Reprinted by permission from Ref. 30.)

Another way to obtain a SiO_2 HM without using CVD is to use spin-on perhydropolysilazane (PSZ). The formulation, consisting of PSZ, xylene solution, and an amine catalyst, changes to SiO_2 through a reaction with water (with the help of the amine catalyst) during a high-temperature bake.[31]

9.5 Self-Aligned Double Patterning

The patterns produced by double exposure and double patterning processes are both generated by two separate exposures (as described in previous sections in this chapter). Each exposure generates one set of patterns. The two sets of patterns are finally transferred to the substrate and realize spatial frequency doubling. In contrast, self-aligned double patterning (SADP) has a completely different approach, requiring only one exposure. A sequential order of multiple nonlithographic steps (film deposition, etch, and CMP) is capable of doubling the original patterns.[32] Thus, SADP will create new challenges to process engineers of film deposition and etch and create perhaps even greater challenges to designers.

Two approaches to SADP have been developed:[33] positive SADP (Fig. 9.30(a)) and negative SADP (Fig. 9.30(b)). For positive SADP, a resist pattern is first printed with a pitch that is 2x the final pitch. Then, the pattern is transferred to a sacrificial layer by plasma etch. The sacrificial material can be a poly-Si and a trim etch can be employed to make the duty ratio (line/space) 1:3. A spacer material (SiN) is conformably deposited, then etched back to form a spacer pattern with a CD that is almost equal to the CD of the sacrificial line. The sacrificial pattern is removed by an isotropic etch, leaving only the spacer pattern

on the stacked film. Finally, the nitride spacer pattern is transferred to the hard mask. In this process flow, one resist line generates two spacers, creating spatial frequency doubling. The resist line-CD corresponds to the one space-CD for every two spaces in the final pattern.

For the negative SADP (Fig. 9.30(b)), instead of removing the sacrificial pattern, a poly-Si film is deposited to fill the gaps between the spacers. Then, the spacer pattern is etched away and only the sacrificial pattern and gap-fill material remain on the stacked film, working as an etch mask to transfer the pattern to the HM and eventually to the substrate. In the negative SADP process, the original resist line-CD corresponds to the line-CD of the final pattern.

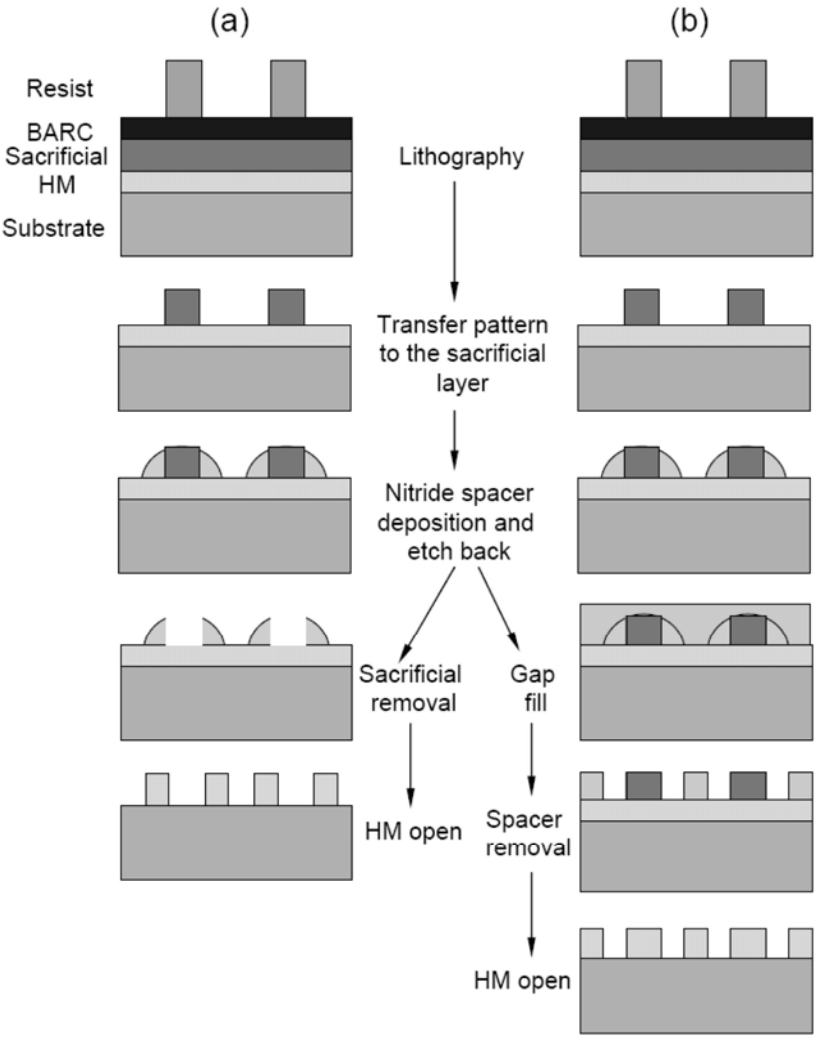

Figure 9.30 Process flow of (a) positive self-aligned double patterning and (b) negative self-aligned double patterning.

The CD of the resist lines has a profound effect on the final feature size. The resist line-CD is determined by the exposure dose. For the positive SADP process, the relationship between the exposure dose and the final CDs has been jointly investigated by ASML and IMEC, and the results are plotted in Fig. 9.31.[34] It appears that the CDs of Line 1 (L1) and Line 2 (L2) are not sensitive to the exposure dose. They are generated by the spacers in both sides of the resist lines, and are, therefore, mainly affected by the height and sidewall of the resist line, not by the width of the resist lines. Space 1 (S1) and Space 2 (S2) are very sensitive to the exposure dose. This is expected, because Space 1 is generated by the resist lines. The four CDs (L1, L2, S1, and S2) must sum to the pitch of the resist lines, which is predetermined by the mask. Decreases in S1 CD lead directly to increases in S2 CD. At an optimum dose, the final CDs are the same and equal lines and spaces are obtained.

The self-aligned double patterning process has attracted a lot of attention and a number of studies have been reported.[35–38] SADP has also been called spacer double patterning (SDP), double patterning with spacer (DPS), or sidewall double patterning (SDP). Further improvements to the process flow have been suggested. For example, instead of using the sacrificial layer, the spacers are directly formed at the sidewall of the resist patterns.[39] The spacer material is an oxide film deposited by novel low-temperature processes. In this study, the lithographic process was started with a film stack of thin nitrogen-free

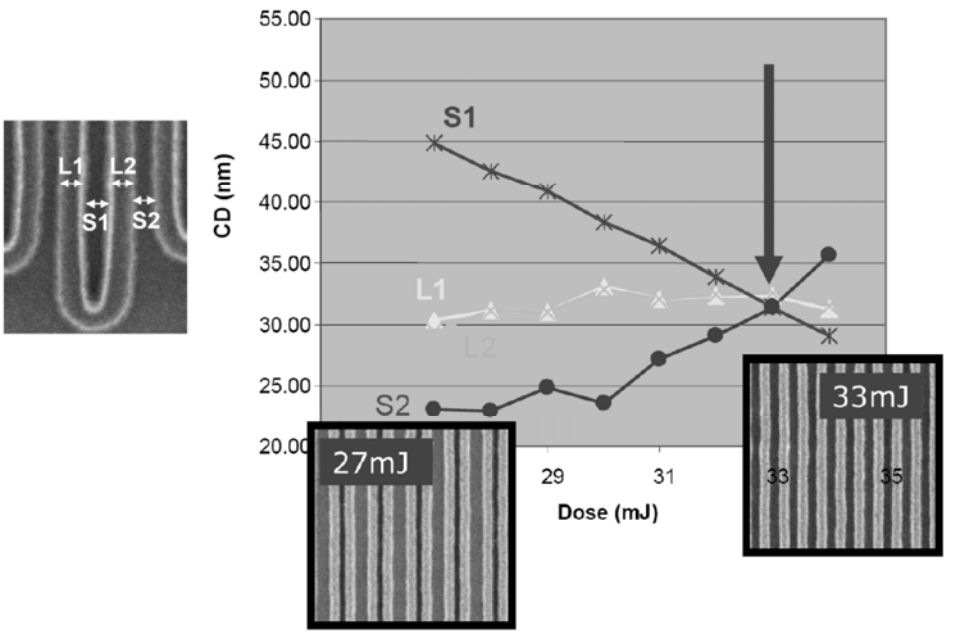

Figure 9.31 For the positive SADP process, the CDs of spaces are sensitive to the exposure dose, while the lines are not. Equal lines and spaces can be obtained at the optimum dose value. (Reprinted by permission from Ref. 34.)

CVD ARC / 100-nm amorphous carbon / dielectric substrate. The 90-nm resist and 80-nm BARC were directly coated onto the thin nitrogen-free CVD ARC layer. Figure 9.32 shows cross-sectional SEM images at each step of this process.

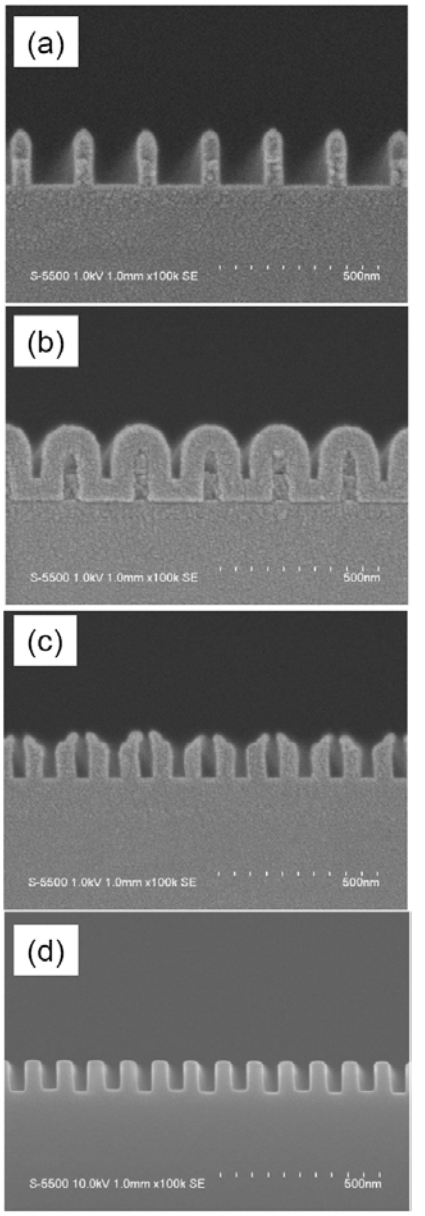

Figure 9.32 Cross-sectional SEM images of: (a) resist pattern after lithography and trim etch (resist thickness = 90 nm, BARC thickness = 80 nm, resist line-CD = 50 nm, pitch = 200 nm); (b) oxide deposited on the resist pattern (oxide thickness = 55 nm and deposition temperature ≤ 100^{o} C); (c) spacer pattern etched in the hard mask (100-nm thick amorphous carbon); and (d) pattern obtained by final etch (pattern height = 120 nm, line width = 50 nm, pitch = 100 nm). (Reprinted by permission from Ref. 39.)

With this process, the primary role of the lithographer is to generate small robust resist patterns with large process windows. A bilayer resist system (Si-containing resist with underlayer) was evaluated and demonstrated a double patterning of $k_1 = 0.15$.[40] The spacer formation is the most critical process step and the CD of the final features depends not only on the resist line-CD obtained by lithography, but also on the resist film thickness, spacer thickness, and etch conditions. Tight control of these process conditions results in good overall CD uniformity. However, it is also difficult to obtain patterns with various feature sizes; therefore, the SADP cannot be applied to random layouts where line widths vary over a wide range.

9.6 Novel Approaches

Since both double exposure and double patterning have many more steps than a traditional single exposure, the simplification of these processes is an important goal of process development. Innovative processes and materials have been proposed and developed.

One innovative approach uses a "dual-tone development."[26] If the deprotection threshold for dissolution in standard aqueous developers is different from that in a negative organic developer, pattern doubling can be obtained by developing the resist film first in an aqueous developer, then in a negative developer (Fig. 9.33). The exposure light intensity changes from a maximum at the center of the space to a minimum at the center of the line. The areas with fewer doses are developed in the negative developer and the areas with more doses are developed in the TMAH developer. Thus, double lines are generated from one line in the mask.

A feasibility test was demonstrated with a 0.75NA ArF dry exposure tool and 120-nm dense lines in the mask.[26] The 1st development was in the negative tone developer for 15 seconds and the 2nd development was in a 0.048% TMAH developer. Dense lines with a pitch of 120 nm were obtained (Fig. 9.34). Potentially, several issues with this process must be addressed. First, the development thresholds of the positive and negative processes must be carefully matched.[41] If the overlap between the positive and negative tone contrast curves is too small (Fig. 9.35(a)), almost all of the resist is developed after the two development steps (Fig. 9.35(b)). A sufficient overlap is needed to generate the correct feature size (Figs. 9.35(c) and (d)). Because the two edges of each resist line are generated by different development processes, the line-edge roughness is likely to be different on each side. The negative organic developer must be handled differently from the way a standard TMAH developer is handled; the dispense cup and drain system must be compatible with this new developer.

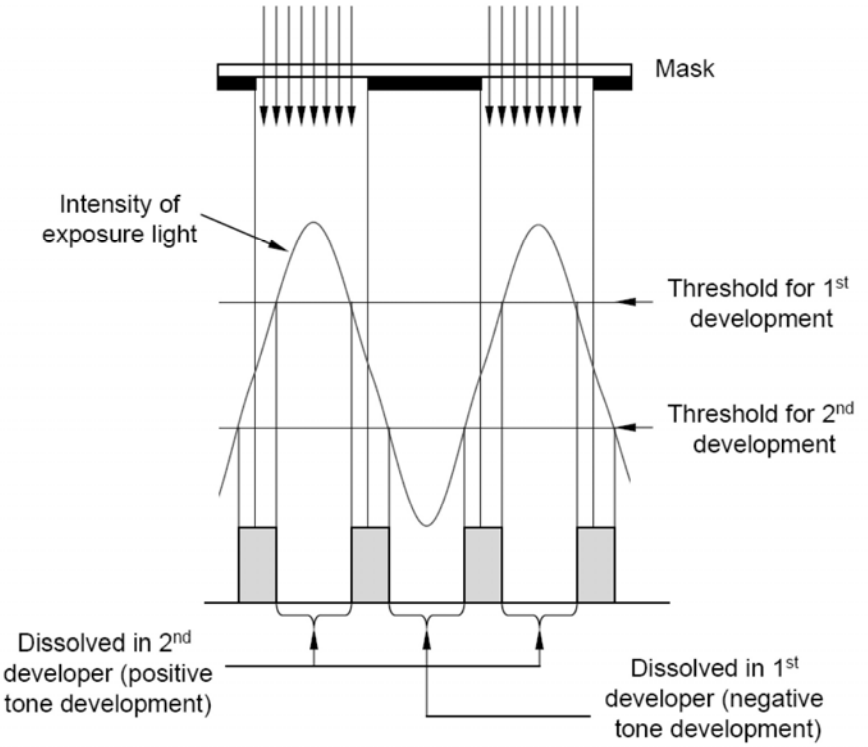

Figure 9.33 Conceptual sketch of the dual-tone development process with a regular resist. Only the slopes of the aerial image are printed.

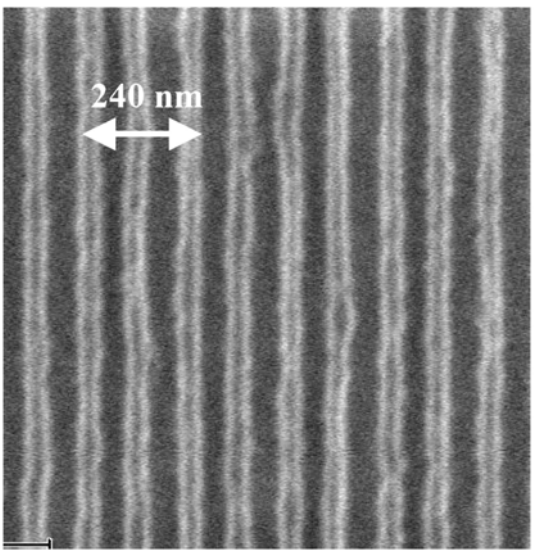

Figure 9.34 Top-down SEM image of the dense lines with a pitch of 120 nm, obtained by dual-tone development. (Reprinted by permission from Ref. 26.)

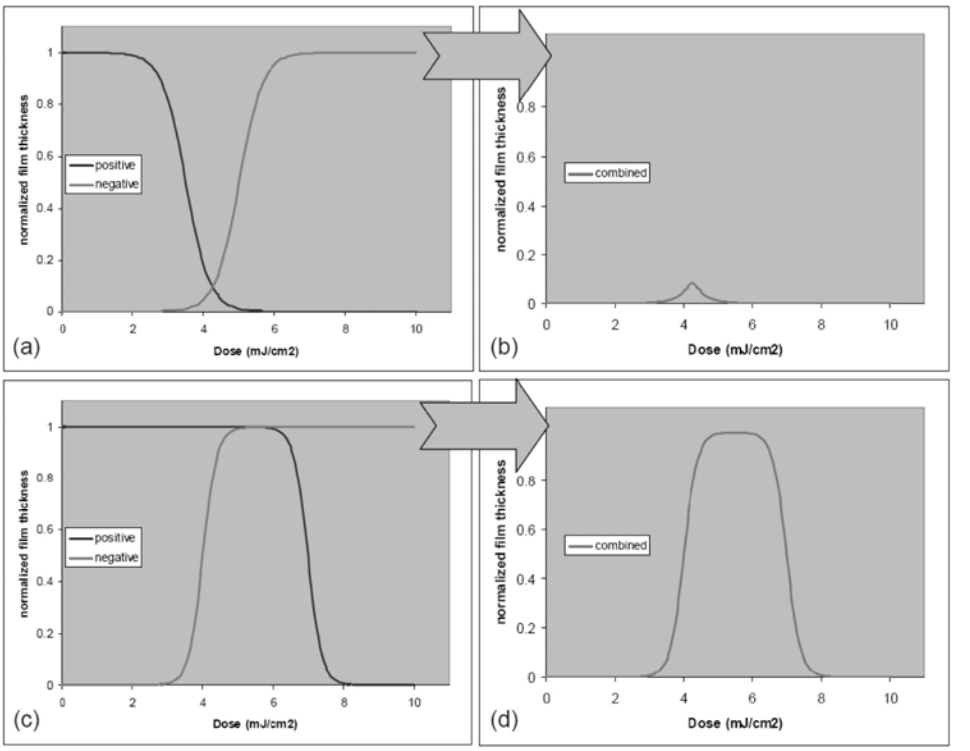

Figure 9.35 Contrast curves in positive and negative developers must be matched for the dual-tone development process. Too little overlap in (a) leads to complete dissolution of the resist film in (b). Sufficient overlap in (c) is needed to generate the correct size feature in (d). (Reprinted by permission from Ref. 41.)

Instead of using two different developers to print dual-tone features, it has been suggested that resists can be designed to respond differently to exposure doses in the higher and lower ranges. At very low doses, the resist is insoluble (like positive-tone resists) and at very high doses, the resist is again insoluble (like negative resists). Only at intermediate doses does the resist dissolve in developer; therefore, the design and manufacture of such resists may be quite a challenge.

9.7 Additional Comments

Various approaches to double exposure and double patterning have been proposed. Process selection must include not only the evaluation of material availability and the simplicity and maturity of the process, but also the pattern layout. For example, a typical DRAM design can be divided into cell, core, and peripheral regions.[42] The cell region has dense lines and spaces, as well as islands. To print the islands, double patterning with bright-field masks appears to give the best process windows. In the core region, the CD is about 1.2–1.6x that of the

cell. Both small lines and pads exist, making pattern decomposition difficult and, therefore, requiring OPC for each exposure.

Due to the success of double exposure and double patterning, some attention has been paid to triple and even quadruple patterning processes.[43] Although triple and quadruple patterning can further boost resolution, the processes are very complicated. In addition to the technical issues, such as material availability and pattern decomposition, the cost of ownership and availability of alternative technologies are the major factors that affect the adoption of these processes.

Regardless of which double patterning processes are used, two groups of lines or two groups of spaces will be obtained. One group is generated by the 1st patterning process and the other group is generated by the 2nd patterning process (except in SADP). The lines and spaces may have different mean CDs, heights, and profiles. Figure 9.36 shows the line-CDs measured from a wafer processed by double line patterning, where an offset is observed between the CD distribution of the 1st group of lines and the 2nd group of lines.[44] This offset causes degradation of wafer line-CD uniformity, which may result from (1) CD differences between the two exposures, (2) the overlay error between the two exposures, or (3) different etch flows between the two groups of patterns. The challenge to metrology is to generate two sets of data so that the appropriate process step can be adjusted to compensate for the offset value.

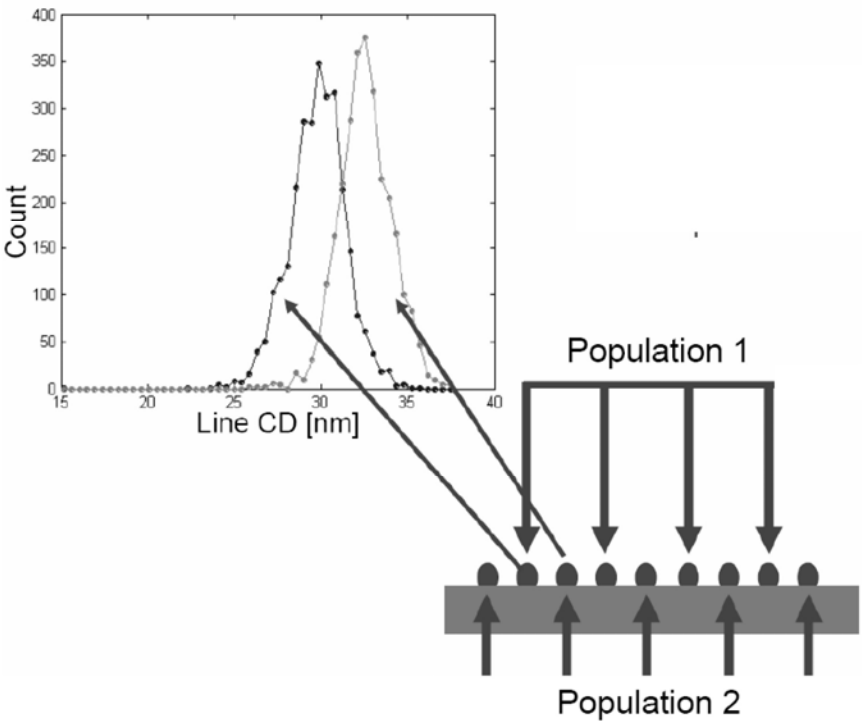

Figure 9.36 Line-CD distribution measured from a wafer processed by double line patterning. (Reprinted by permission from Ref. 44.)

References

1. H. Ooki, D. Coon, S. Owa, T. Sei, and K. Okamoto, "Experimental study on non-linear multiple exposure method," *Proc. SPIE* **3051**, 85–93 (1997).
2. C. Noelscher, M. Heller, B. Habets, M. Markert, U. Scheler, and P. Moll, Double line shrink lithography at $k_1 = 0.16$, *Microelectronic Engineering*, **83**, Issues 4–9, 730–733 (2006).
3. *International Technology Roadmap for Semiconductors*, 2007 Edition, Lithography section.
4. M. D. Levenson, "ASML illuminates a dry path to 40nm," Web report from *Solid State Technology*, Jan. 2007.
5. A. Hand, "Double patterning makes a big debut in roadmap," *Semiconductor International*, p. 30, Feb. 2007.
6. M. Fritze, T. M. Bloomstein, B. Tyrrell, and M. Rothschild, "Extending 193nm immersion with hybrid optical maskless lithography," *Solid-State Technology*, Sept. 2006.
7. Y. Borodovsky, "Marching to the beat of Moore's Law," *Proc. SPIE* **6153**, 615301 (2006).
8. M. Burkhardt, S. Burns, D. Dunn, and T. A. Brunner, "Dark field double dipole lithography (DDL) for back-end-of-line processes," *Proc. SPIE* **6520**, 65200K (2007).
9. S. Hsu, M. Burkhardt, J. Park, D. Van Den Broeke, and J. F. Chen, "Dark field double dipole lithography (DDL) for 45nm node and beyond," *Proc. SPIE* **6283**, 62830U (2006).
10. F. M. Schellenberg, Presentation at Litho Forum 2006, Vancouver, BC, May 2006.
11. A. Poonawala, Y. Borodovsky, and P. Milanfar, "ILT for double exposure lithography with conventional and novel materials," *Proc. SPIE* **6520**, 65202Q (2007).
12. S.-J. Kim, J.-S. Park, T.-Y. Kim, B.-S. Kim, G.-S. Yeo, S.-H. Oh, S.-G. Woo, H.-K. Cho, and J.-T. Moon, "Era of double exposure in 70 nm node DRAM cell," *Proc. SPIE* **5754**, 368–376 (2005).
13. J. Byers, S. Lee, K. Jen, A. Berro, X. Gu, C. G. Willson, N. O'Connor, S. Jockusch, N. J. Turro, P. Zimmerman, and B. J. Rice, "Update on double exposure materials development," Presentation at 4th International Symposium on Immersion Lithography, Keystone, Colorado, Oct. 2007.
14. S. A. Robertson, J. J. Biafore, T. Graves, and M. D. Smith, "Rigorous physical modeling of a materials-based frequency doubling lithography process," *Proc. SPIE* **6923**, 69230I (2008).
15. M. Hori, T. Nagai, A. Nakamura, T. Abe, G. Wakamatsu, T. Kakizawa, Y. Anno, M. Sugiura, S. Kusumoto, Y. Yamaguchi, and T. Shimokawa, "Sub-40nm half-pitch double patterning with resist freezing process," *Proc. SPIE* **6923**, 69230H (2008).
16. A. Vanleenhove and D. Van Steenwinckel, "A litho-only approach to double patterning," *Proc. SPIE* **6520**, 65202F (2007).

17. K.-J. R. Chen, W.-S. Huang, W.-K. Li, and P. R. Varanasi, "Resist freezing process for double exposure lithography," *Proc. SPIE* **6923**, 69230G (2008).
18. H. Nakamura, Y. Onishi, K. Sato, S. Tanaka, S. Mimotogi, K. Hashimoto, and S. Inoue, "Contact hole formation by multiple exposure technique in ultra-low k_1 lithography," *Proc. SPIE* **5377**, 255–263 (2004).
19. D. C. Owe-Yang, S. S. Yu, H. Chen, C. Y. Chang, B.-C. Ho, J. C. Lin, and B. J. Lin, "Double exposure for the contact layer of the 65-nm node," *Proc. SPIE* **5753**, 171–180 (2005).
20. N. Bekiaris, H. Cervera, J. Dai, R. Kim, A. Acheta, T. Wallow, J. Kye, H. J. Levinson, T. Nowak, and J. Yu, "A lithographic and process assessment of photoresist stabilization for double-patterning using 172 nm photoresist curing," *Proc. SPIE* **6923**, 692321 (2008).
21. H. Nakamura, T. Shibata, K. Rikimaru, S. Ito, S. Tanaka, and S. Inoue, "Ion implantation as insoluble treatment for resist stacking process," *Proc. SPIE* **6923**, 692322 (2008).
22. N. Samarakone, P. Yick, M. Zawadzki, and S.-J. Choi, "Double printing through the use of ion implantation," *Proc. SPIE* **6924**, 69242B (2008).
23. R. Kim, T. Wallow, J. Kye, H. J. Levinson, and D. White, "Double exposure using 193nm negative tone photoresist," *Proc. SPIE* **6520**, 65202M (2007).
24. M. Op de Beeck, J. Versluijs, V. Wiaux, T. Vandeweyer, I. Ciofi, H. Struyf, D. Hendrickx, and J. Van Olmen, "Manufacturability issues with double patterning for 50nm half pitch single damascene applications using RELACS shrink and corresponding OPC," *Proc. SPIE* **6520**, 65200I (2007).
25. G. Capetti, P. Cantù, E. Galassini, A. V. Pret, C. Turco, A. Vaccaro, P. Rigolli, F. D'Angelo, and G. Cotti, "Sub $k_1 = 0.25$ lithography with double patterning technique for 45nm technology node flash memory devices at $\lambda =$ 193nm," *Proc. SPIE* **6520**, 65202K (2007).
26. S. Tarutani, H. Tsubaki, and S. Kanna, "Development of materials and processes for double patterning toward 32-nm node 193-nm immersion lithography process," *Proc. SPIE* **6923**, 69230F (2008).
27. V. Wiaux, E. Hendrickx, J. Bekaert, S. Verhaegen, G. Vandenberghe, S. Locorotondo, S. Beckx, J. Finders, M. Dusa, J. Quaedackers, and B. Vleeming, "193nm immersion lithography towards 32nm hp using double patterning," Presentation at 3rd International Symposium on Immersion Lithography, Kyoto, Japan, Oct. 2006.
28. M. Maenhoudt, D. Vangoidsenhoven, T. Vandeweyer, R. Gronheid, J. Versluijs, and A. Miller, "Double patterning process development at IMEC," Presentation at SEMATECH Litho Forum 2008, Bolton Landing, New York.
29. S. Lee, J. Jung, S. Cho, C.-M. Lim, C. Bok, H. Kim, S. Moon, and J. Kim, "Double exposure technology using silicon containing materials," *Proc. SPIE* **6153**, 61531K (2006).
30. H. J. Liu, W. H. Hsieh, C. H. Yeh, J. S. Wu, H. W. Chan, W. B. Wu, F. Y. Chen, T. Y. Huang, C. L. Shih, and J. P. Lin, "Double patterning with multilayer hard mask shrinkage for sub-0.25 k_1 lithography," *Proc. SPIE* **6520**, 65202J (2007).

31. M. Terai, T. Ishibashi, M. Shinohara, K. Yonekura, T. Hagiwara, T. Hanawa, and T. Kumada, "Double patterning using dual spin-on Si containing layers with multilayer hard mask process," *Proc. SPIE* **6924**, 692420 (2008).
32. A. Hand, "Applied's litho scheme: patterning vs. printing," *Semiconductor International*, April 2007.
33. H. Mukai, E. Shiobara, S. Takahashi, and K. Hashimoto, "A study of CD budget in spacer patterning technology," *Proc. SPIE* **6924**, 692406 (2008).
34. D. Flagello, "Evolution of optical lithography towards 22nm and beyond," Presentation at SEMATECH workshop on Approaching the Optical Limit: Practical Methods for Patterning 22nm HP and Beyond, Bolton Landing, New York, May 2008. J. Finders, M. Dusa, B. Vleeming, H. Megens, B. Hepp, M. Maenhouldt, S. Cheng, and T. Vandeweyer, "Double patterning for 32nm and below: an update," *Proc. SPIE* **6924**, 692408 (2008).
35. W.-Y. Jung, S.-M. Kim, C.-D. Kim, G.-H. Sim, S.-M. Jeon, S.-W. Park, B.-S. Lee, S.-K. Park, J.-S. Kim, and L.-S. Heon, "Patterning with amorphous carbon spacer for expanding the resolution limit of current lithography tool," *Proc. SPIE* **6520**, 65201C (2007).
36. A. Carlson and T.-J. Liu, "Negative and iterated spacer lithography processes for low variability and ultra-dense integration," *Proc. SPIE* **6924**, 69240B (2008).
37. U. Iessi, S. Loi, A. Salerno, P. Rigolli, E. De Chiara, C. Turco, R. Colombo, M. Polli, and A. Mani, "Double patterning overlay and CD budget for 32 nm technology node," *Proc. SPIE* **6924**, 692428 (2008).
38. C. Tseng, C. Yang, E. Yang, T. Yang, K. Chen, and C. Lu, "A comprehensive comparison between double patterning and double patterning with spacer on sub-50nm product implementation," *Proc. SPIE* **6924**, 69241Y (2008).
39. N. Shamma, W.-B. Chou, I. Kalinovski, D. Schlosser, T. Mountsier, C. Mui, R. Tarafdar, and B. van Schravendijk, "PDL™ oxide enabled pitch doubling," *Proc. SPIE* **6924**, 69240D (2008).
40. C. Noelscher, F. Jauzion-Graverolle, M. Heller, M. Markert, B.-K. Hong, U. Egger, and D. Temmler, "Double patterning down to k_1=0.15 with bi-layer resist," *Proc. SPIE* **6924**, 69240Q (2008).
41. M. Maenhoudt, R. Gronheid, N. Stepanenko, T. Matsuda, and D. Vangoidenshoven, "Alternative process schemes for double patterning that eliminate the intermediate etch step," *Proc. SPIE* **6924**, 69240P (2008).
42. S.-M. Kim, S.-Y. Koo, J.-S. Choi, Y.-S. Hwang, J.-W. Park, E.-K. Kang, C.-M. Lim, S.-C. Moon, and J.-W. Kim, "Issues and challenges of double patterning lithography in DRAM," *Proc. SPIE* **6520**, 65200H (2007).
43. B. Arnold, "Prospects for further extension of ArF lithography to 32nm and what is next?" Presentation at Interface 2006, 31 October, 2006.
44. B. Vleeming, J. Quaedackers, E. van der Heijden, P. de Haas, S. Uzunbajakau, J. Meessen, G. Dicker, J. Finders, M. Dusa, P. Jaenen, S. Locorotondo, and M. Maenhoudt, "Sub-32nm half pitch imaging with high NA immersion exposure systems using double patterning techniques," Presentation at 4th International Symposium on Immersion Lithography, Keystone, Colorado, Oct. 2007.

Chapter 10
Line-Edge Roughness of Resist Patterns

The edges of resist line patterns are never completely straight; they invariably show deviations from linearity, which is called line-edge roughness (LER). LER may be derived from pattern roughness in the mask, statistical variations in dose along the line edge, or from the chemical properties of the resist. Variation in the width of a line determines its line-width roughness (LWR). LER and LWR are two of the key parameters that determine device performance.[1] Figure 10.1 shows how a single line can be a gate for multiple transistors. Low-frequency variations in LWR can lead to a different gate length for each transistor. These variations, in turn, cause threshold voltage variations between transistors in the same chip. LWR with periodicities shorter than the gate width can result in problems with leakage current. Experimental results show that leakage current increases exponentially with LWR. For devices fabricated at the 65-nm node, LWR (3σ) < 8% of gate CD leads to < 1% performance degradation, while LWR (3σ) < 10% of gate CD leads to < 2% of performance degradation.[2] Based on this analysis, the ITRS requires that the low-frequency portion of the LWR be less than 8% of its CD.[3] For the 45-nm half-pitch node, ITRS requires a LWR of 2.4 nm (3σ).

In this chapter, lithographic processes and materials will be analyzed to identify the root causes of LER and LWR within printed features. LER and LWR can be improved through optimization of process parameters and selection of the resist materials. In addition, the roughness can be further reduced by smoothing of the resist patterns after development.[4] These "smoothing processes" will be summarized and assessed. Resist patterns are transferred to substrates using plasma etch processes. The LER and the LWR of final etched patterns are what actually determine device performance. The extent to which roughness is transferred from the resist pattern to the substrate during the etch process will also be discussed in this chapter.

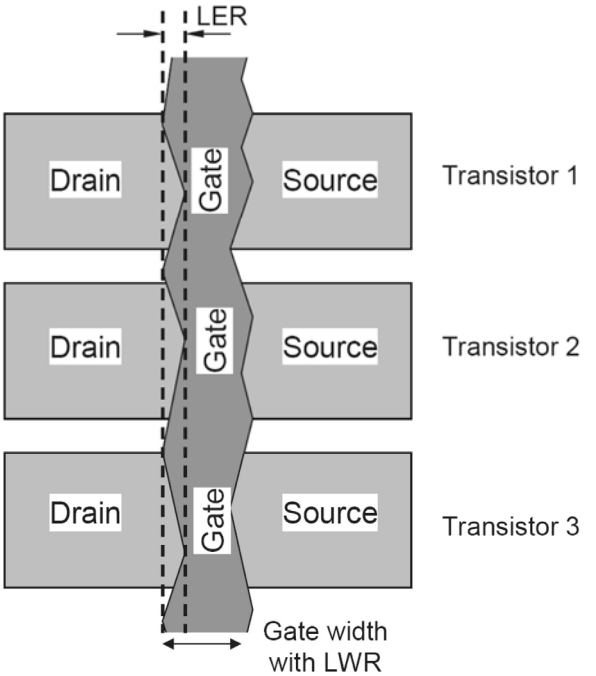

Figure 10.1 Diagram of the gate pattern with LWR and LER.

10.1 Metrology of Line-Edge Roughness (LER) and Line-Width Roughness (LWR)

LER and LWR are currently measured by high-resolution CD-SEMs. The SEMs produce high-resolution images of the patterns, which are evaluated to determine LER or LWR using software installed in the SEM or off-line.

10.1.1 LER

Figure 10.2 shows a top-down diagram of a resist line edge. To measure the LER, a measurement window is defined that covers a certain length L of the resist line. Within the window, the resist line is scanned N times at equal intervals of Δ, so that $L = N\Delta$. The quantity x_i (i = 1, 2,... N) represents the position of the edge detected along the line segment. The averaged edge on the x-axis is defined as

$$\bar{x} = \left(\sum_{i=1}^{N} x_i \right) / N. \tag{10.1}$$

The deviation of the detected edge from the averaged edge is

$$\delta x_i = x_i - \bar{x}. \tag{10.2}$$

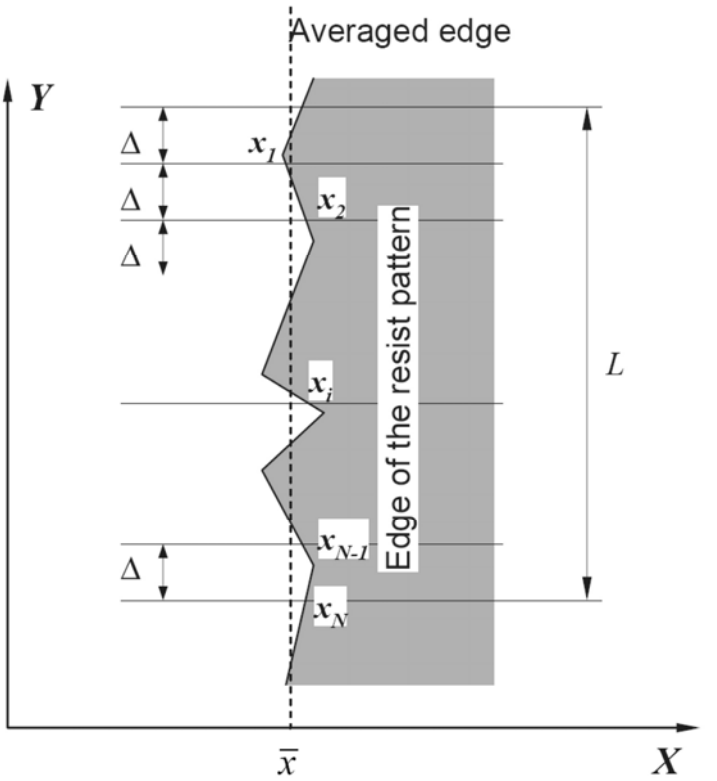

Figure 10.2 Diagram of a resist line edge.

The standard deviation of the edge from the averaged edge is used to describe the line edge roughness:

$$\sigma_{\mathrm{LER}} = \sqrt{\frac{1}{N}\sum_{i=1}^{N}(\delta x_i)^2} = \sqrt{\frac{1}{N}\sum_{i=1}^{N}(x_i - \bar{x})^2}\,. \tag{10.3}$$

In the lithographic community, the LER is usually reported as three standard deviations (i.e., $3\sigma_{\mathrm{LER}}$), to ensure a tight control of line-edge roughness.

10.1.2 LWR

Line-width roughness (LWR) quantitatively describes line-width variation. Figure 10.3 shows a top-down diagram of a resist line. As in the measurement of LER, LWR can also be measured from top-down images. The measurement window covers the resist line length of L. Within the measurement window, the resist line is scanned N times with equal intervals of Δ (i.e., $L = N\Delta$). The quantities $x^{\mathrm{L}}{}_i$ and $x^{\mathrm{R}}{}_i$ (i = 1, 2,... N) represent the coordinates of the left and right edges along the line segment with intervals of Δ. The line width at each measuring grid is

$$w_i = x_i^{\mathrm{R}} - x_i^{\mathrm{L}}. \tag{10.4}$$

The average line width is

$$\overline{w} = \left(\sum_{i=1}^{N} w_i \right) / N. \tag{10.5}$$

The deviation of the measured width from the average width is

$$\delta w_i = w_i - \overline{w}. \tag{10.6}$$

The standard deviation of the measured line width from the averaged edge is used to describe the line-width roughness:

$$\sigma_{\mathrm{LWR}} = \sqrt{\frac{1}{N} \sum_{i=1}^{N} (\delta w_i)^2} = \sqrt{\frac{1}{N} \sum_{i=1}^{N} (w_i - \overline{w})^2}. \tag{10.7}$$

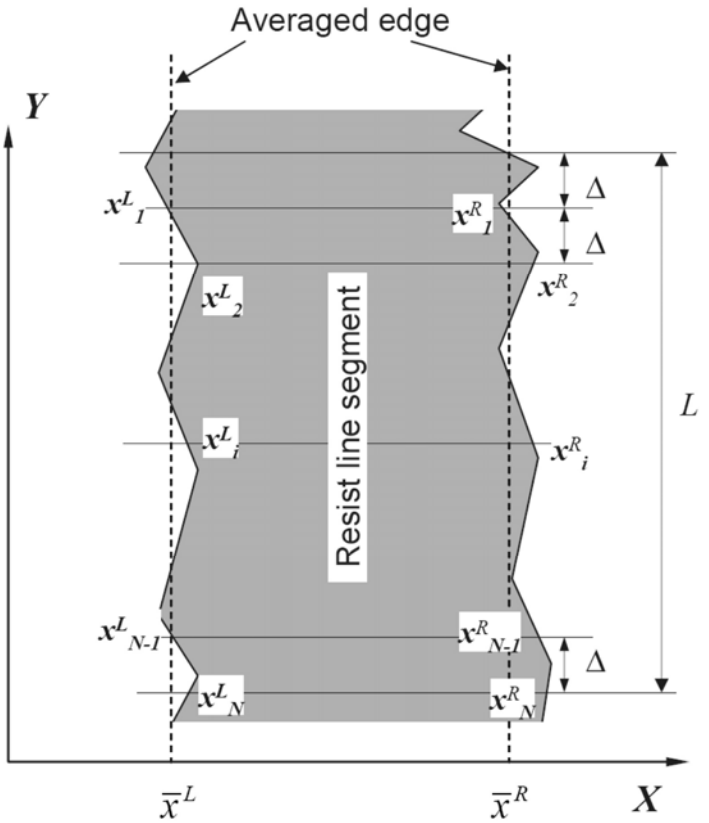

Figure 10.3 Sketched top-down image of a resist line segment.

10.1.3 Relationship between LER and LWR

LWR results simply from the LERs at both the left and right edges of the resist line. The relationship between the σ_{LWR} and the σ_{LER} of the two edges can be calculated as follows:

$$\begin{aligned}\sigma_{LWR}^2 &= \frac{1}{N}\sum_{i=1}^{N}(w_i-\bar{w})^2 = \frac{1}{N}\sum_{i=1}^{N}[(w_i)^2]-(\bar{w})^2 \\ &= \frac{1}{N}\sum_{i=1}^{N}[(x_i^R)^2]-(\bar{x}^R)^2+\frac{1}{N}\sum_{i=1}^{N}[(x_i^L)^2]-(\bar{x}^L)^2+2\bar{x}^R\cdot\bar{x}^L-\frac{2}{N}\sum_{i=1}^{N}(x_i^R\cdot x_i^L) \\ &= (\sigma_{LER}{}^R)^2+(\sigma_{LER}{}^L)^2+2\left[\bar{x}^R\cdot\bar{x}^L-\frac{1}{N}\sum_{i=1}^{N}(x_i^R\cdot x_i^L)\right],\end{aligned} \tag{10.8}$$

where $\sigma_{LER}{}^R$ and $\sigma_{LER}{}^L$ are the standard deviations of the left and right edges (left and right line-edge roughness). From Eq. (10.8), it is obvious that the LWR is strongly related to the LER. The last term in Eq. (10.8) describes the correlation between the two edges. By introducing a correlation factor *c*, equation (10.8) can be written as

$$\sigma_{LWR}^2 = (\sigma_{LER}{}^R)^2+(\sigma_{LER}{}^L)^2+2\cdot c\cdot\sigma_{LER}{}^R\cdot\sigma_{LER}{}^L, \tag{10.9}$$

where the value of the correlation factor *c* is between –1 and 1 ($-1 < c < 1$).

In most situations, the roughness of the two edges is always uncorrelated in the absence of external influences such as optical proximity effects, defects, or topography. If the LERs of the left and right edges are uncorrelated ($c = 0$), as shown in Fig. 10.4(a), Eq. (10.9) can be simplified to

$$\sigma_{LWR} = \sqrt{2}\ \sigma_{LER}{}^L = \sqrt{2}\ \sigma_{LER}{}^R. \tag{10.10}$$

Equation (10.10) is familiar to lithographers and is used frequently. However, if the correlation factor $c = 1$, then the two edges are anticorrelated (Fig. 10.4(b)), and $\sigma_{LWR} = 2\sigma_{LER}{}^L = 2\sigma_{LER}{}^R$, which is the worst situation for LWR. In the opposite situation, if the two edges are perfectly correlated ($c = -1$) (Fig. 10.4(c)), then $\sigma_{LWR} = 0$, which would be ideal for LWR.

For resist lines printed in a single patterning step, the left and right edges are typically uncorrelated and $c = 0$. However, for the SADP process, the left and right edges will be correlated if the spacer is conformal.

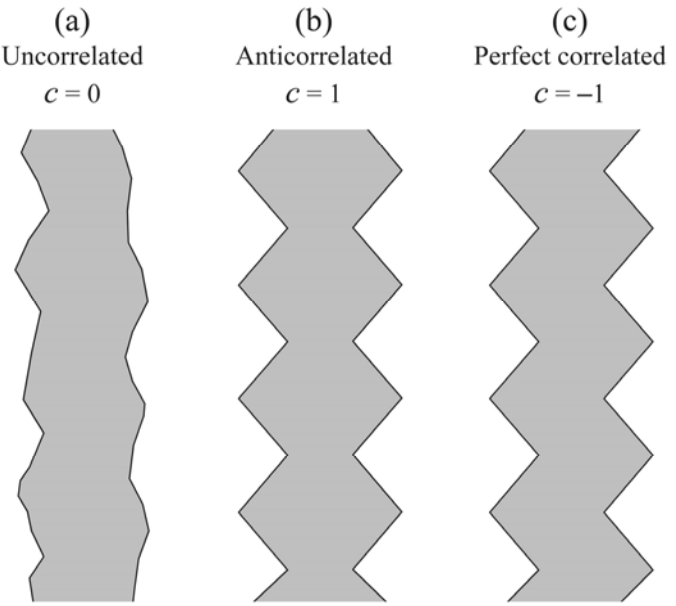

Figure 10.4 Sketch showing correlations between left and right edges of a resist line.

10.1.4 Correlation length of the roughness

The measured values of LER and LWR depend on the length of the evaluation window L (Fig. 10.5).[5,6] For short windows, this dependence can be characterized by a power law where $3\sigma_{LWR} \sim L^{\alpha}$ and α is the roughness exponent. For long windows ($L > L_s$), the LWR is saturated and independent of the length. L_s is the sigma correction length, which is quantitatively defined as

$$\sigma_{LWR}(L_s) = 0.9 \cdot \sigma_{LWR}(\text{inf}), \tag{10.11}$$

where $\sigma_{LWR}(\text{inf})$ is the saturation value measured from a sufficiently large window.

The shape of the curve shown in Fig. 10.5 is determined by the spatial frequency spectrum of the roughness. The LWR consists of both low and high spatial frequency components. Short evaluation windows ($L < L_s$) include information only about roughness with high spatial frequency and neglect information about roughness with low spatial frequency. The roughness exponent, α ($0 < \alpha < 1$), quantifies the relative contribution of high spatial frequency roughness to LWR. Large values of α mean that σ_{LWR} decreases quickly with the reduction of L, since the contribution of high spatial frequency roughness is limited. At large sampling lengths, more low spatial frequency information is included in the measurement and the resulting roughness is stabilized.[7] Similarly, the distance Δ between the scan lines is also very important to LWR and LER measurements. Roughness values with spatial frequencies greater than $1/\Delta$ are not included in the measurements.

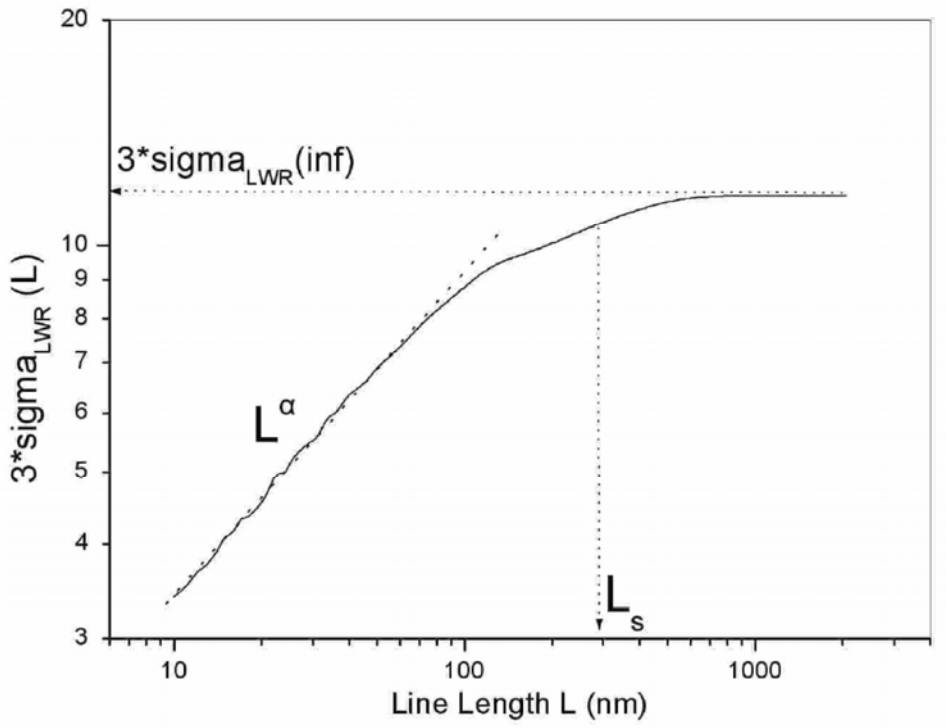

Figure 10.5 Typical dependence of LWR (3σ) on the length of the measuring window (*L*, sampling length), obtained by analysis of a CD-SEM image. (Reprinted by permission from Ref. 6.)

SEMATECH recommends a protocol for measuring LER and LWR in which the sampling distance (distance between scans Δ) is 4 nm up to the 22-nm node, and 2 nm thereafter.[8] The length *L* of the sampled line should be 2000 nm, leading to a stable value for measurement and assuring that all important low frequencies are sampled. The Δ of 4 nm assures frequency sampling well into the high-frequency noise floor. It is better to measure multiple edges when determining an average LER and LWR. By averaging multiple edges, better statistics can be obtained and process comparisons can be conducted with higher confidence.

10.1.5 Spatial frequency spectrum

Roughness consists of a broad band of spatial frequencies. However, the standard deviation σ gives only averaged information on roughness. To investigate the spatial frequency components of roughness, the power spectral density (PSD) must be analyzed.[9] This is done by Fourier transformation of the line-edge measurements (x_i, i = 1, 2,… N) (Fig. 10.2). The PSD covers spatial frequency from $1/L$ to $1/\Delta$ and corresponds to the sampling window size and distance

between scan lines. It also provides information related to how the roughness determined at each spatial frequency contributes to the overall LER.

In general, all PSD curves obtained from 193-nm resist patterns show similar behavior (Fig. 10.6).[8] They have "low frequency plateaus," "mid-frequency roll-offs," and "high-frequency floors."[8] The low frequencies make the largest contribution to total roughness. The roughness in the mid-frequency region can provide information about the causes of the roughness; for example, changes in resist composition can result in distinctive changes in the mid-frequency region. The high-frequency floor is an artifact that results from white noise from the SEM measurement. It is caused by errors in precisely locating the line edge for each sampled point. Use of SEMs with improved image resolution and careful selection of image and line-edge detection parameters will minimize the contributions of the noise floor to LER and LWR measurements.

Although the CD-SEM is a convenient and popular method for measuring LER and LWR, the electron beam can cause resist shrinkage and lead to deviations in CD.[10] Therefore, efforts to develop better measurement tools continue, with the aim of providing better resolution with lower noise. The capability of metrology tools and their improvements are beyond the scope of this book and will not be discussed here.

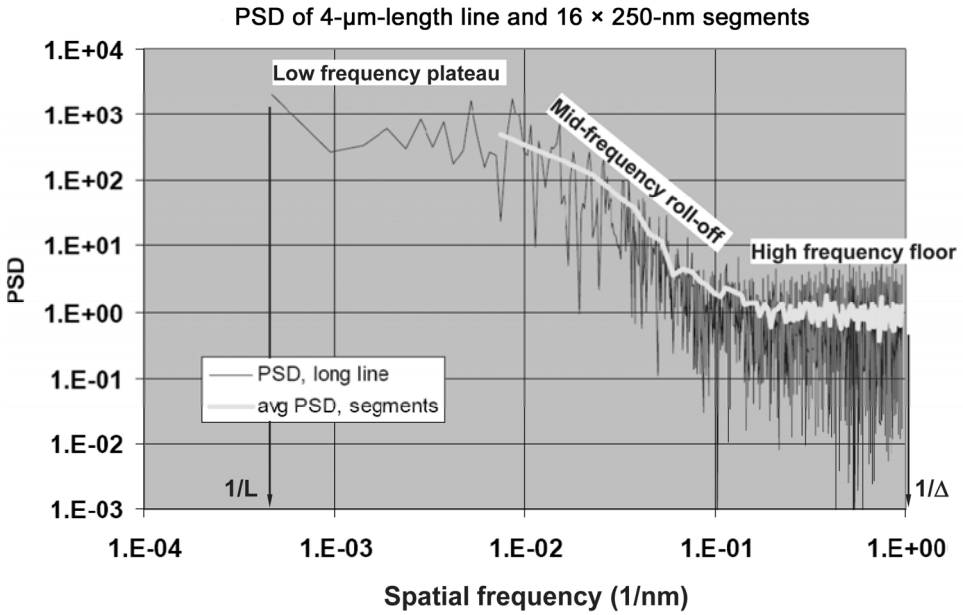

Figure 10.6 Sample power spectral density (PSD) of LER. The whole PSD covers the spatial frequency range from 1/L to 1/Δ. It consists of a low-frequency plateau, a mid-frequency roll-off, and a high-frequency floor. The low-frequency plateau contributes the most to the LER. (Reprinted by permission from Ref. 8.)

10.2 Formation of LER

In the lithographic process, the pattern on the mask is illuminated by light. The diffraction orders are collected by the projection lens and focused on the resist surface. The exposure light generates photoacids in chemically amplified resists and polymer deprotection occurs during PEB. Finally, the portions of the resist that have been deprotected are dissolved in aqueous developer and the resist film is rinsed and dried to produce the resist pattern. Each process step can contribute to the LER of the final resist pattern.

10.2.1 LER of the mask pattern

The pattern on the mask is obtained by imaging resists using e-beam lithography, followed by pattern transfer during etch, which uses processes very similar to those used during the manufacture of integrated circuits. Inevitably, the mask patterns have LER (LER_{mask}). If the optical imaging system has 100% fidelity, then the mask pattern will be projected onto the resist surface without distortion and the LER of the aerial image (LER_{aerial}) in the resist will be the LER_{mask} divided by the demagnification factor of the scanner and multiplied by the MEEF factor (i.e., $LER_{aerial} = MEEF \times LER_{mask}/4$).

However, the LER_{mask} is much smaller than its pattern size. For example, 180-nm half-pitch dense lines in the mask typically have an average LER of < 10 nm (3σ). In reality, such low LER is beyond the resolution capability of current 193-nm optical imaging systems and the details of mask pattern LER are not projected onto the resist surface.

10.2.2 Aerial image contrast at the pattern edge

The projection lens has a limited size and cannot collect all diffraction orders from the mask. Thus, the exposure system has a limited resolution capability. The aerial image of the edge of a pattern projected onto a resist surface is not a step function, but rather, a gradient of light intensity (Fig. 10.7). The image log-slope (ILS) is introduced to quantitatively define the aerial image contrast at the edge of the feature:

$$\mathrm{ILS} = \frac{1}{I_{\mathrm{Edge}}} \cdot \frac{\partial I(x)}{\partial x}\bigg|_{\mathrm{Edge}}, \tag{10.12}$$

where I_{Edge} and $\left.\frac{\partial I(x)}{\partial x}\right|_{\mathrm{Edge}}$ are the light intensity and the intensity slope at the edge.

To single out the role of the optical system in the formation of LER, we assume that the resist follows the simple threshold model in which the resist is sufficiently deprotected to dissolve if the exposure dose is above the threshold value and will not dissolve if the exposure dose is below the threshold dose. The resist edge is formed at the position where the exposure dose equals the threshold value.

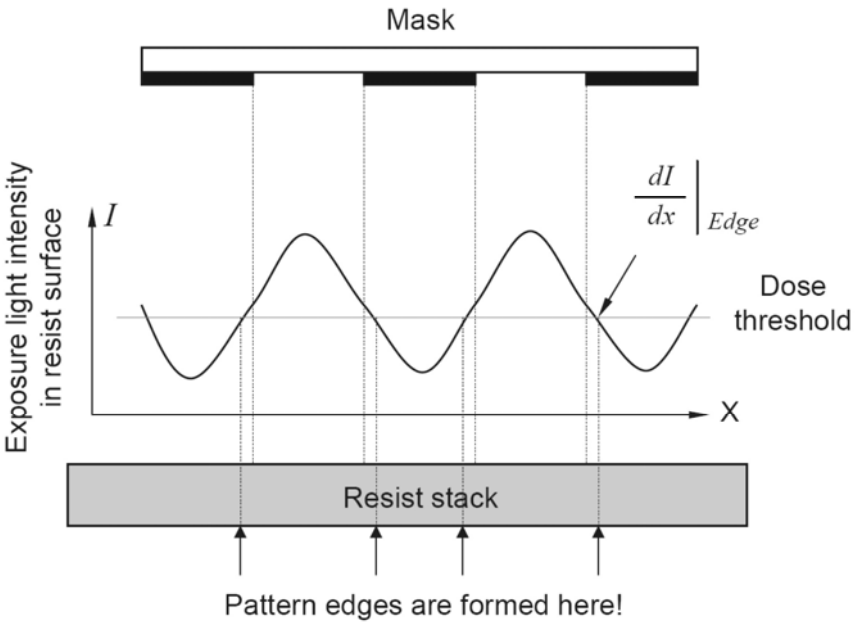

Figure 10.7 At the pattern edge, the aerial image intensity is not a step function.

In practice, however, various factors can cause fluctuations in light intensity, such as fluctuations in laser output power and vibrations of the optical system and of the wafer stage. The fluctuations in exposure light intensity cause shifts in the resist edge in the x-direction, forming LER (Fig. 10.7). These same fluctuations of light intensity ΔI induce smaller shifts in the position of the resist edge Δx when the image contrast is steep. Thus, large aerial image contrast reduces LER. Figure 10.8 shows the experimental results of resist LER as a function of aerial image contrast.[11] With increased aerial image contrast, the LER (3σ) value decreases and levels off at about 5 nm. Further increases in aerial image contrast provide no additional improvements in LER. As a result, it has been suggested that the residual LER originates from the intrinsic material roughness of the resist.[12]

10.2.3 LER generation in positive chemically amplified (CA) resists

For most chemically amplified (CA) resists, the photoacid generators are blended with polymers and other components. Molecules of photoacid generator are distributed randomly in the chemically amplified resists, as shown in Fig. 10.9(a). After absorption of light, these molecules decompose to form acids. For positive resists during PEB, the photoacids catalyze the conversion of developer-insoluble groups on the polymers into developer-soluble groups. This transformation is also referred to as polymer deprotection and results in the dissolution of the regions of the resist film that have received an exposure dose higher than the threshold value. However, in order for the photoacid to catalyze the deprotection of the polymer, it must diffuse from group to group within the polymer.

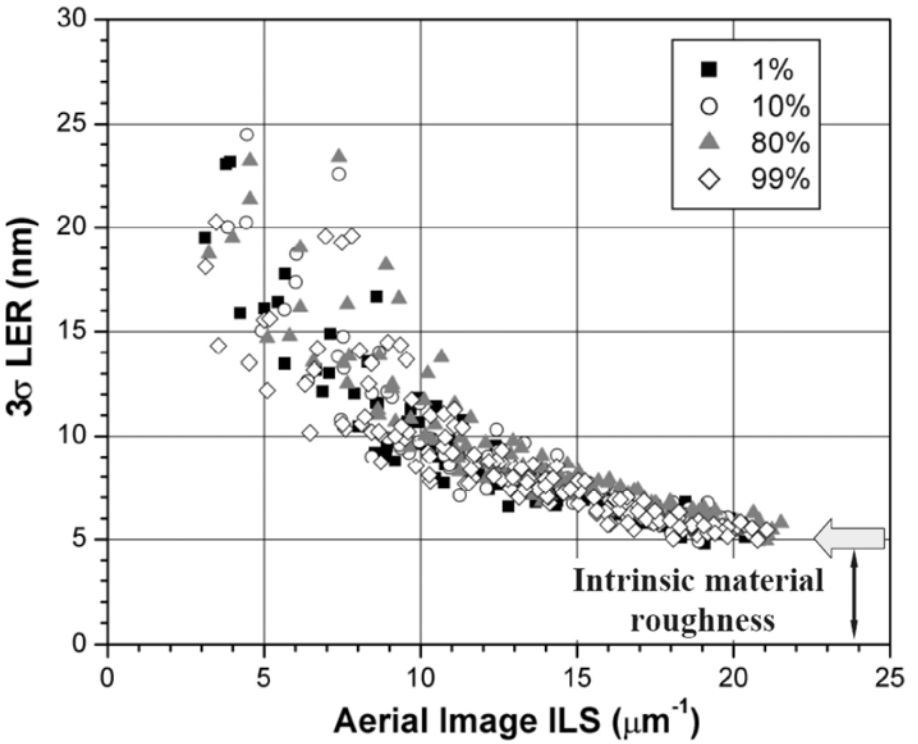

Figure 10.8 Experimentally measured 3σ LER in a resist as a function of the aerial image image log-slope (ILS) for 120-nm lines at 270-nm pitch with global pattern densities of 1%, 10%, 80%, and 99%. (Reprinted by permission from Ref. 11.)

In fact, acid diffusion is a complicated process. The deprotection reactions occur only in the presence of acid; studying the acid diffusion and the deprotection reactions independently of each other is generally difficult. The acid diffusion rate must be slower than the deprotection rate, so that the acid molecules have sufficient time to react with the protecting groups. The diffusion coefficient of the acid molecule is a function of the bake temperature and of the extent of deprotection of the polymer. Because the polymer environment changes over the course of the bake, the diffusion rates of acid molecules also vary.[13] Rigorous calculations suggest that acid molecules can diffuse several tens of nanometers from their original sites during post-exposure bake.[14] Acid diffusion can smooth out the random distribution of acid originating from the random distribution of the PAGs in exposed areas (Fig. 10.9(b)). However, the acid can also diffuse into unexposed areas, thereby increasing the high-frequency components of the LER. Only polymer molecules with deprotection levels greater than the threshold level will be dissolved by the developer. This threshold of deprotection defines both the edge of the resist line and the line-edge roughness (Fig. 10.9(c)).

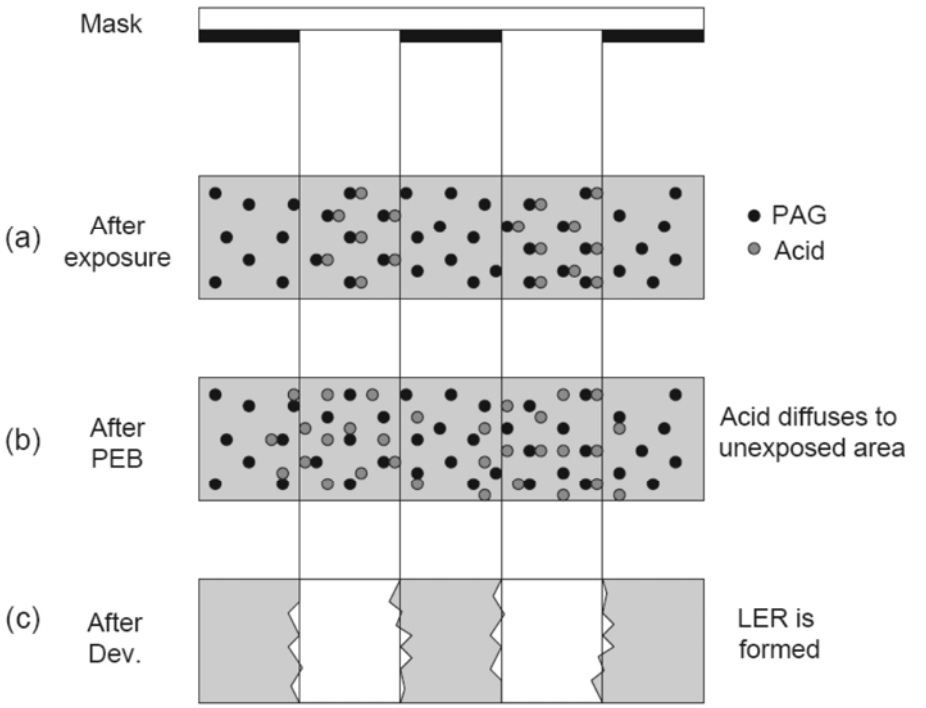

Figure 10.9 (a) Acids are generated near the original locations of the PAG molecules and are randomly distributed throughout the resist. (b) After PEB, the acid molecules in the exposed areas diffuse into the unexposed areas. (c) The edges of the resist lines are formed after development.

Even with ideal optical systems, fluctuations in light intensity still exist. According to Poisson statistics, the number of photons N incident upon a given area fluctuates with an amplitude of $\sqrt{N}$. The resulting dose fluctuation is proportional to $1/\sqrt{N}$ and is typically referred to as shot noise. The shot noise is very pronounced when the number of photons is small, a condition that corresponds to the exposure of highly sensitive resists.

The mathematical model for acid diffusion in chemically amplified resists has been investigated by various groups.[15,16] Three major conclusions have been drawn from this research. First, LER is inversely proportional to the square root of the exposure dose.[17] Second, LER is strongly correlated with aerial image contrast (ILS). Third, longer acid diffusion length leads to smaller LER. These conclusions can be expressed in the formula

$$\sigma_{\mathrm{LER}} \sim \left(\frac{1}{\mathrm{ILS}}\right) \cdot \frac{1}{L_d} \cdot \left(\frac{1}{\sqrt{E_{\mathrm{edge}}}}\right), \tag{10.13}$$

where E_{edge} is the exposure dose at the resist edge, L_d is the diffusion length of the acid, and ILS is the image log-slope at the edge. Experimental results reported by various groups have shown the relevance of Eq. (10.13).[12,18]

Acid diffusion length is directly related to the resolution capability of a resist. High diffusion length smears the aerial image contrast and causes lower resolution. The exposure dose at the resist edge E_{edge} actually represents the deprotection threshold and is dependent on the photospeed of the resist. Thus, Eq. (10.13) correlates LER, resolution, and photospeed of a chemically amplified resist. These three factors are difficult to simultaneously improve. To reduce LER, one could increase quencher concentration, but then the resist gets slower because more photons are needed for the exposure. Increasing the photospeed (which means that the imaging is performed with fewer photons and the shot noise statistics ($\sim N^{-1/2}$) will get worse) results in larger LER. Therefore, Eq. (10.13) is also called the "lithographic uncertainty principle" and the relationship between the LER, the resolution, and the photospeed can be expressed by a triangle (Fig. 10.10).[19]

One frequently studied topic is the dependence of LER on polymer size. The characteristic sizes of polymer molecules are, at most, a few nanometers.[20] However, analysis of the power spectra of typical 193-nm resists demonstrates that the dominant contributions to the LER value are from spatial frequency components of about 20 μm or less.[21] This corresponds to the length scale of 50 nm and above, which is much larger than the molecule size of the resist polymers. As a matter of fact, the resist line edge used for the LER analysis is imaged from the resist pattern by a CD-SEM. Currently, CD-SEMs cannot resolve individual molecules within a resist, thus, any contribution to LER from the molecule size is not captured by the CD-SEM. Similar studies in EUV show that the resist LER is independent of polymer size.[20] However, it is not difficult to foresee that as resolution capability continues to advance, the size of polymer molecules will eventually become an important factor in determining LER.

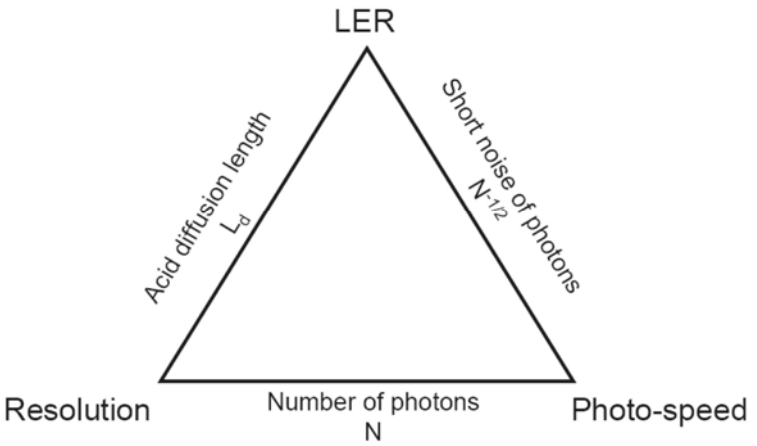

Figure 10.10 Lithographic uncertainty triangle.

10.2.4 Effect of BARC and topcoat on resist LER

BARC films can affect the LER of resist patterns in two distinct ways. The first is mainly an optical effect in which unoptimized BARC thicknesses increase the standing wave effect, leading to losses in aerial image contrast and generating larger LER. The second is a matter of the chemical compatibility, where poor selection of BARC material may result in greater acid diffusion at the BARC–resist interface and cause footing. This resist footing appears in top-down images as the line-edge roughness.

Topcoats applied to resist surfaces also affect the resist LER. Depending on the chemical compatibility of the topcoat and the resist, the topcoat can either increase the resist LER[22] or decrease the resist LER.[23] The chemical interaction between topcoat and resist occurs mainly during PEB.

10.2.5 Resist dissolution behavior

The resist pattern (as well as its roughness) is formed during development. In the center of the exposed area where the dose is high, the resist dissolves quickly. The rate of development is as high as several hundreds of nanometers per second. However, in the transition region at the edge of the exposed area, the resist is not fully exposed and the deprotection reaction is not complete. At the advancing dissolution front, a transition from soluble to insoluble polymer takes place, where the development ceases and the edge forms. At this edge, some of the polymer molecules swell into the developer, while remaining anchored to the rest of the resist film. During the DI water rinse, these partially dissolved polymer chains redeposit on the resist edge. This swelling mechanism has been proposed as one source of LER.[24] The complicated physical and chemical reactions at the edge of the resist pattern have attracted much research interest and are beyond the scope of this book.

10.2.6 Investigation of acid diffusion

Researchers at the National Institute of Standards and Technology (NIST) used a bilayer structure, neutron reflectometry (NR), and infrared spectroscopy (IR) to gain insight into the complex acid deprotection/diffusion mechanism.[18] The bilayer consists of two layers of resist polymers. The top (acid-feeder layer) has PAG and the bottom layer has no PAG. After exposure and PEB, the photoacid catalyzes deprotection reactions that result in the elimination of blocking groups from the film. This reaction is detected by neutron reflectometry as a reduction in hydrogen content. Thus, the deprotection depth profile at the interface can be measured. After development, the surface roughness of the bottom layer corresponds to LER. This experiment was done for different resist polymers with and without base additives. It was concluded that process conditions and molecular details (polymer, PAG, and base) strongly influence the LER. Sharp deprotection fronts result in smaller LER.

10.3 Strategies for Reducing Resist LER

In addition to improving the aerial image contrast of exposure tools, researchers have been attempting to reduce LER of resist patterns. These efforts fall into three categories: (1) development of new resists with smaller intrinsic material roughness, (2) optimization of the lithographic processes, and (3) application of post-development smoothing processes. These smoothing processes can be quite successful in reducing LER.

10.3.1 Developing resists with low intrinsic roughness

The resist is the largest source of roughness; therefore, most efforts to reduce LER/LWR involve the development and optimization of resist formulations. This work has focused on the relationship between LER and each component of the resist.[25–28] For example, increasing the concentration of quencher base can reduce the LER, but will also reduce photosensitivity. Many of the conclusions reached about LER can be difficult to interpret because they are sometimes highly dependent on the specific polymer platform used by different researchers. Developing new resists with high resolution and low LER is currently an important goal of 193-nm resist suppliers.

One interesting approach is to use the surface roughness of the resist to obtain the intrinsic material roughness (IMR).[29] The resist film is exposed at different doses ($< E_0$) and developed. The resist film surface roughness (RMS) is measured by atomic force microscopy (AFM). The measured surface roughness versus dose is plotted as an RMS contrast curve. The authors proposed that the surface roughness corresponds to the intrinsic material roughness. Experimental results demonstrate that the IMR can be improved through optimization of the PAG and the polymer.

To improve the trade-off of resolution, photospeed, and LER, a new resist with anisotropic acid diffusion has been proposed in theory.[30] In this model resist, the horizontal diffusion length is reduced, while the vertical diffusion length is simultaneously increased. The simulation results show that this idea can increase resolution and improve LER, using the same dose.

10.3.2 Optimization of resist process parameters

The LER of resist patterns can be improved by simply optimizing the process parameters. Aerial image contrast can be increased optically by using bright-field masks, aggressive off-axis illumination, or by increasing NA. With such exposure conditions, lower LER can be obtained. These improvements in aerial image contrast will improve LER.

Additionally, PAB, PEB, and development conditions can affect LER values. The relationship between LER and these process parameters will vary from resist to resist. In one experiment, the resist pattern was 80-nm 1:1 dense lines (Fig. 10.11).[31] The LER and LWR of the resist pattern were measured as a function of PAB temperature (Fig. 10.11(a)) and as a function of PEB temperature (Fig. 10.11(b)). Increasing the PAB temperature from 70 to 100^{o} C causes a slight

increase in LER and LWR values. This behavior is believed to be related to the residual solvent in the resist film. It was suggested that more residual solvent in the resist film helps the acid diffusion and results in lower LER.[19,32]

Figure 10.11(b) shows an interesting PEB temperature dependence between LER and LWR. As the PEB temperature increases in value, the roughness decreases to a minimum at ~104^{o} C, and then increases. The authors explain their results by first pointing out that, in general, acid diffusion length increases with increasing PEB temperature, and this, in turn, leads to lower LER. At higher PEB temperatures (> 105^{o} C), the roughness increases with temperature. This behavior was proposed to be caused by the combined effect of decreased resist contrasts and reduced potential for LER improvement by diffusion. Similar results were reported in other studies.[19]

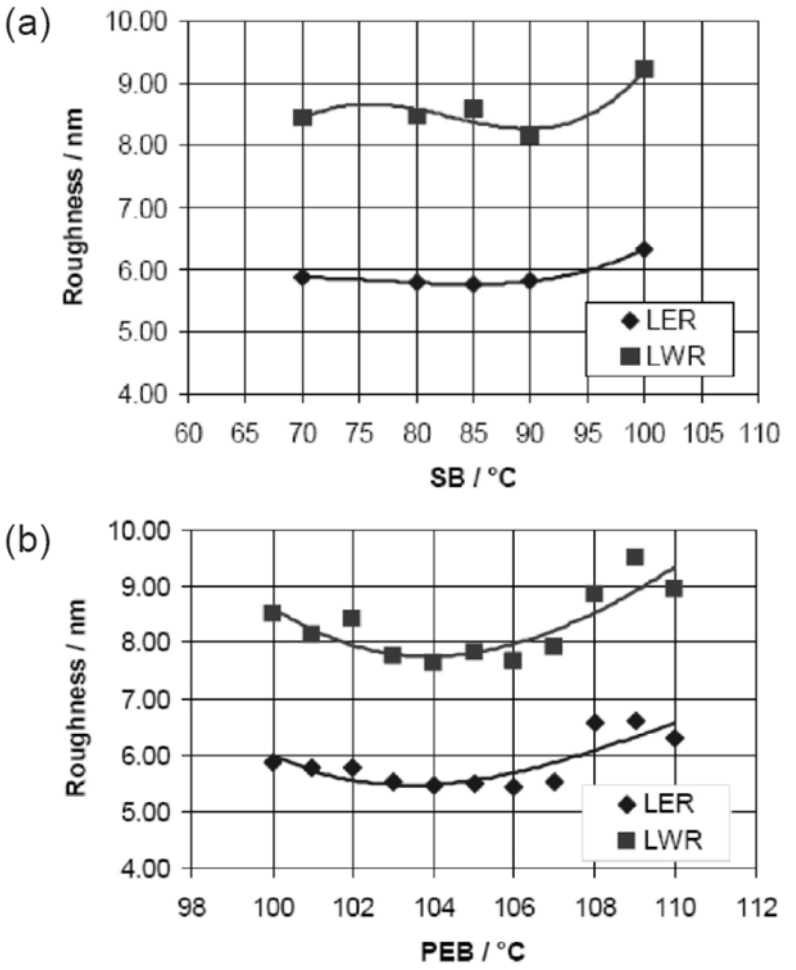

Figure 10.11 LER and LWR (3σ) of 80-nm dense lines measured as a function of (a) PAB temperature and (b) PEB temperature. Resist thickness is 150 nm and baking time is 60 seconds. (Reprinted by permission from Ref. 31.)

The concentration of developer and the development time can also affect roughness. Figure 10.12(a) shows top-down images of resist patterns processed with different development times. The resist line CD is ~85 nm with a pitch of 170 nm. In Fig. 10.12(a), reducing the development time from 60 to 15 seconds increases LER. The resist line CD decreases slightly with development time, as expected. Figure 10.12(b) shows top-down images of resist patterns processed with various developer concentrations. The concentration of the developer and the exposure dose are included in the figure. For this resist, high concentrations of developer help to reduce LER; however, for other resists, opposite results were obtained.[33] These results suggest that the relationship between roughness and development parameters is closely linked to the unique chemistry of each resist platform.

(a)

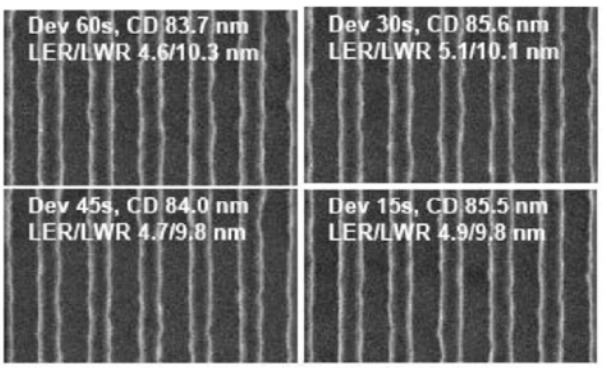

(b)

Developer (N)	0.07	0.13	0.2	0.26	0.3	0.4	0.5
Sensitivity (mJ/cm²)	32	31	30	31	31	31	31
LER (nm)	4.3	5.3	4.7	3.9	2.8	2.5	2.7
Topview							

Figure 10.12 (a) Top-down images of a resist pattern processed with different development times. The resist film has a thickness of 150 nm and the resist pattern has a nominal size of 85 nm with a pitch of 170 nm. The LER of the pattern is included in the images. (b) Top-down images of a resist pattern processed with various developer concentrations. The resist film has a thickness of 210 nm and the nominal size of the pattern is 100 nm with a pitch of 200 nm. The development time is 60 seconds. (Reprinted by permission from Ref. 31.)

10.3.3 Smoothing resist patterns through surfactant rinse and hard bake

Rinsing resist patterns with specially designed surface conditioners after development can reduce LER. These surface conditioners can improve the high to medium spatial frequency portions of the LER. Similarly, baking resist patterns at high temperatures (hard bake) can also reduce the LER of the resist patterns. For most resists, the hard bake temperature is in the range of 150–200° C. At these high temperatures, the resists soften and the rough edges are smoothed.

To obtain even higher reduction in LER, the surfactant rinse and hard bake can be combined.[4,34,35] After development, wafers can be rinsed with a surface conditioner, spun dry, and baked at elevated temperatures. Figure 10.13 shows the results from such rinse and bake processes. In these tests, a set of resist patterns was obtained at best dose but with different focuses. The LER values of the resist patterns with and without treatment were measured and plotted (Fig. 10.13). The process of applying the rinse, together with a 170° C hard bake, provided about 1-nm reduction in LER (3σ)—about a 20% reduction. Without the hard bake, the surfactant rinse process also reduced the LER.

In addition to reducing LER, the surfactant rinse process was reported to provide a solution to the problem of removing the resist scum at the bottom of the

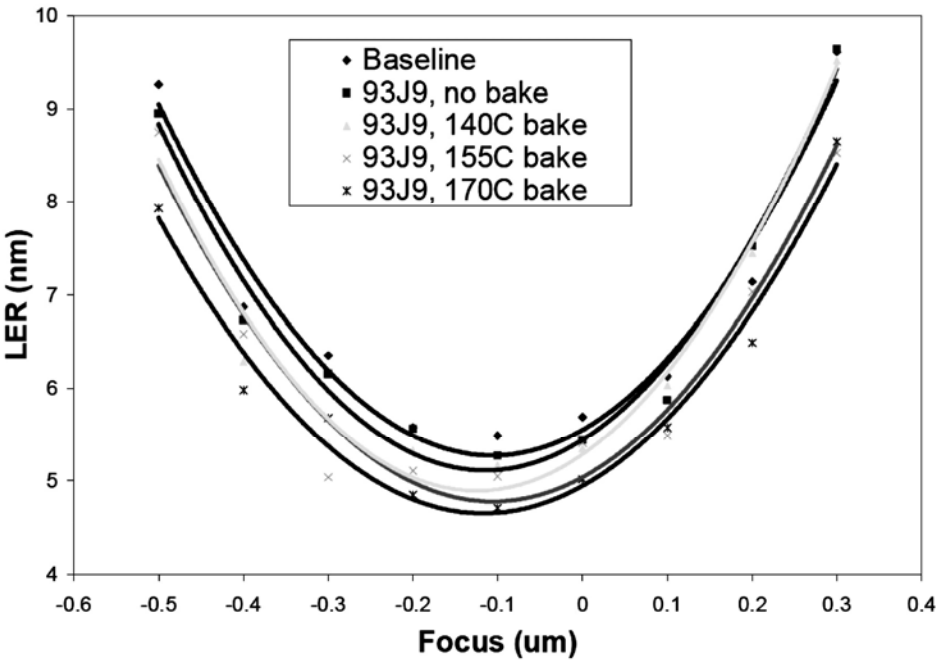

Figure 10.13 LER (3σ) values at the best dose and across focus. The baseline process does not include surfactant rinse and hard bake. Resist thickness is 250 nm and the pattern is 130-nm half-pitch dense lines. Surfactant rinse 93J9 is from Air Products. (Reprinted by permission from Ref. 4.)

contact holes.[36] Resists used in 193-nm immersion lithography are very hydrophobic. Standard aqueous developer and DI water cannot effectively reach the bottom of the contact holes. Residuals from the resist may remain at the bottom and form a scum. According to the authors,[36] because of its lower surface tension, the surfactant rinse is able to penetrate the contact holes and remove the scum from the bottom of the contact holes.

10.3.4 Smoothing resist patterns with solvent vapor

A research group at Tokyo Electron Ltd. (TEL) demonstrated reductions in LER by treating post-development resist patterns with an organic-solvent atmosphere.[37] After development, the wafer is transferred to a chamber supplied with N_2 saturated with solvent vapor. This environment provides the wafer surface with a uniform supply of organic-solvent (Fig. 10.14). The resist surface softens to produce a smooth resist edge and ultimately, lower the LER. The softened regions of the resist surface dry immediately after the process, eliminating the need for a post-bake or any other drying processes. Figure 10.15 shows a dense resist pattern before and after this smoothing process. The resist pattern is very smooth after treatment with solvent vapor.

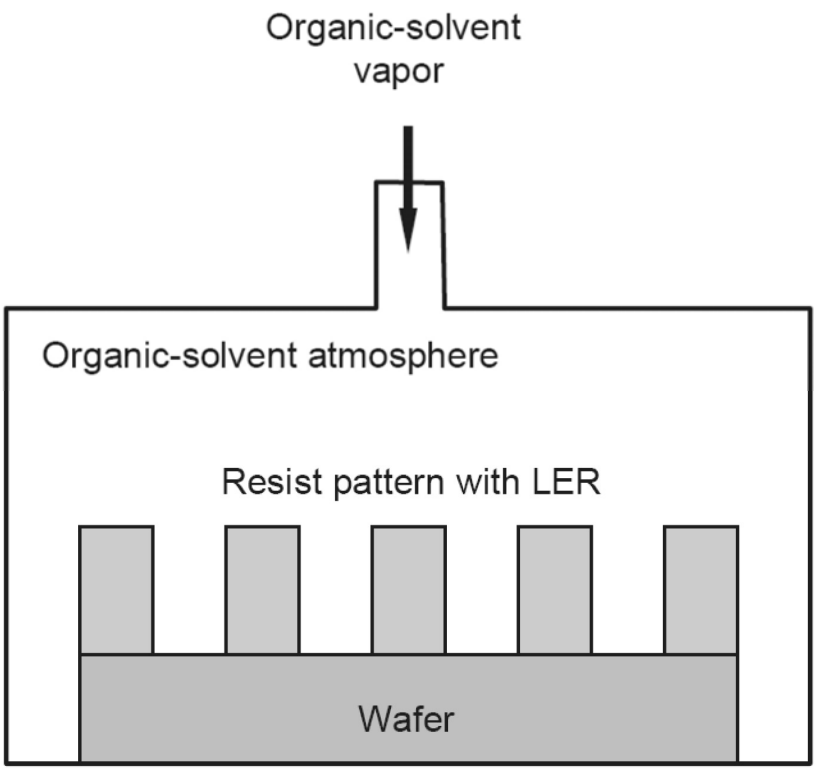

Figure 10.14 Organic solvent vapor is introduced into the resist pattern.

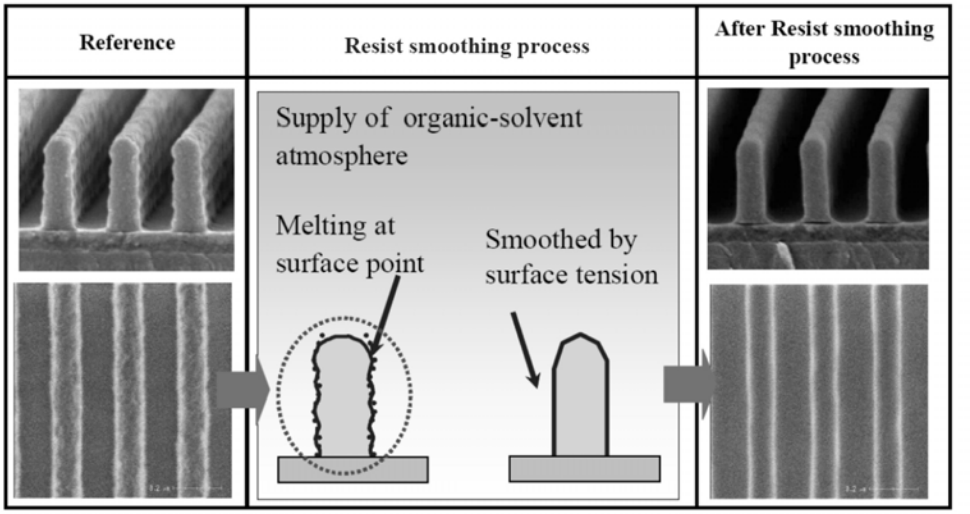

Figure 10.15 Top-down and cross-sectional images before and after the smoothing process. (Reprinted by permission from Ref. 37.)

The solvent vapor method for reducing LER seems to be more effective when used on KrF resist patterns than when used on ArF resist patterns. One possible explanation is that ArF resists are less soluble in organic solvents than KrF resists. Brief exposure to VUV light after development was found to improve the solubility of ArF resist patterns in organic solvents. The combined effects of VUV exposure and solvent vapor exposure can produce a 30% reduction in LWR, the same LWR reduction as seen on KrF resists. Longer treatment times result in better LER, but can also lead to increased degradation of profile.[38]

10.3.5 HBr plasma treatments

Resist patterns can be treated with HBr plasma in an etch chamber,[39] a process that typically involves an additional step at the beginning of the etch recipe. The HBr plasma substantially modifies the resist surface without significantly modifying its bulk properties and structure. XPS data show the formation of a carbon-rich layer at the surface of the HBr-treated resist. In addition to improving LER, the HBr plasma treatment cures the photoresist, hardens the pattern, and suppresses deformation during etch. The insertion of the HBr plasma treatment *after* the BARC opening step is more effective at improving LWR than insertion of the treatment *before* the BARC opening step.

Figure 10.16 shows the LER spectra of resist patterns treated with and without the HBr process. The resist lines have a CD of 130 nm with a pitch of 260 nm. HBr treatment after the BARC opening reduces more LER than treatment before the BARC opening, and reduces both high and low spatial frequency roughness. The experiments in Ref. 39 also showed that LER reduction depends on pattern size. Higher LER reduction is obtained with sparse patterns than is obtained with dense patterns.

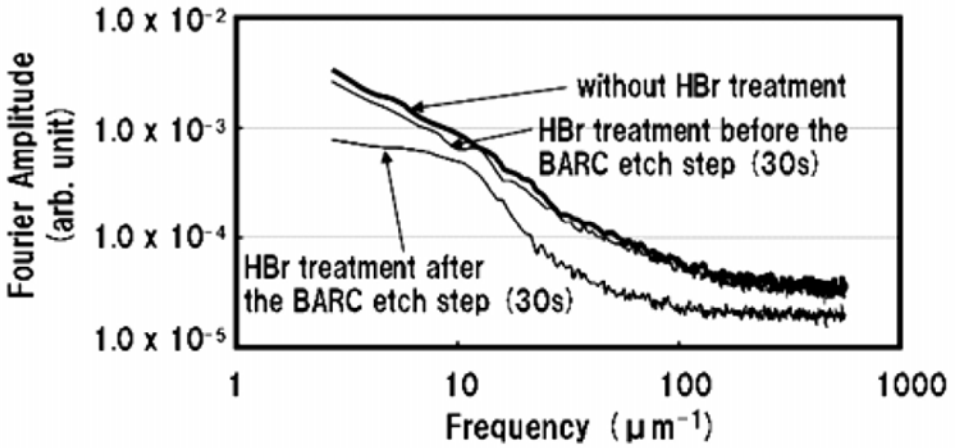

Figure 10.16 LER spectra of resist patterns (line-CD = 130 nm with a pitch of 260 nm) treated with/without HBr plasma. (Reprinted by permission from Ref. 39.)

10.4 Transferring LER from Resist to Substrate: the Effect of Etch

The resist pattern is transferred to the substrate by the etch process. Depending on the film stack, the plasma etch process can consist of several steps and involve several chemicals. The transfer of LER through the etch process is complicated and is affected by the resist material, the substrate film stack, and the etch conditions.

10.4.1 Isotropic versus anisotropic roughness

One interesting observation is that the roughness of sidewalls in resist patterns is isotropic, while the roughness of sidewalls in etched patterns is anisotropic, as shown in the cross-sectional images in Fig. 10.17. The sidewall roughness of resist patterns changes in two directions, both vertically to the substrate and in parallel to the substrate along the resist line (Fig. 10.17(a)). In contrast, the sidewall roughness of the etched pattern appears to change in only one direction: along the resist line (Fig. 10.17(b)). This difference is due to the physical nature of the anisotropic plasma etch. In the etch process, an electric field drives the etch ions perpendicular to the wafer surface and the etching front moves in only one direction into the substrate.

The transfer of LER from resist to substrate was reported by Goldfarb et al.[40] Their technique is to tilt the resist pattern and use AFM to directly image the roughness of the resist sidewall. Figure 10.18 shows the AFM imaging setup and the stack of the substrate. The film stack has resist, BARC, and SiO_2 as the hard mask (HM) on a silicon substrate. The sidewall of the pattern was imaged by AFM after each etch step. Figures 10.19 (a) through (d) show AFM images of pattern sidewalls after development, BARC opening, and HM (SiO_2) etches.

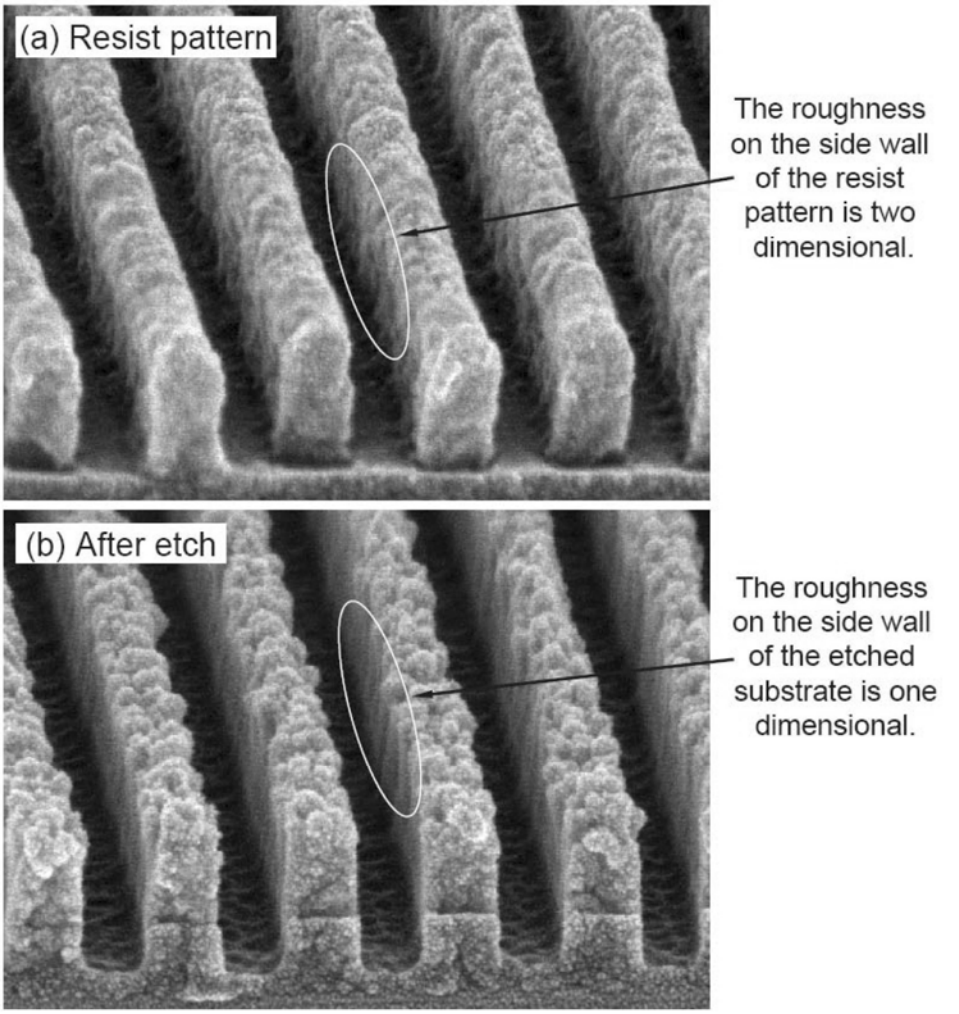

Figure 10.17 Cross-sectional images of (a) resist pattern and (b) Si-lines after plasma etching. The resist residuals have not been removed in (b).

After development, the roughness of the resist sidewall is isotropic, or two-dimensional (Fig. 10.19(a)). After the BARC etch, striations are formed in the resist as well as in the BARC sidewall (Fig. 10.19(b)). The striations are normal to the substrate surface and are generated by the anisotropic plasma etch. Fewer anisotropic etch conditions provide less pronounced striations. These striations act as templates and are transferred to the HM and the substrate. Etch process variables such as polymer deposition, ion bombardment, and wafer temperature can greatly affect the final LER.

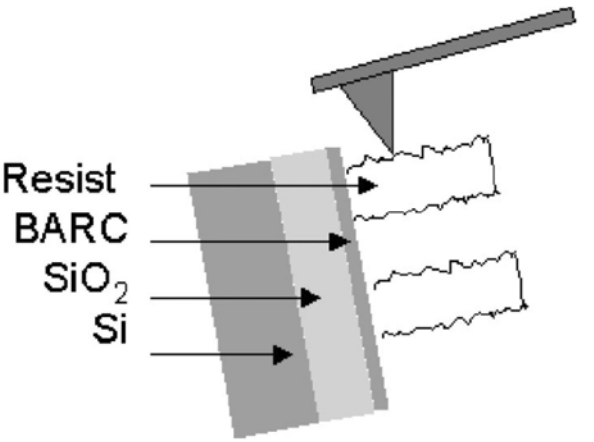

Figure 10.18 AFM is used to image the sidewall of the pattern and as the tapping mode. A specialized sample holder was designed to tilt the die. (Reprinted by permission from Ref. 40.)

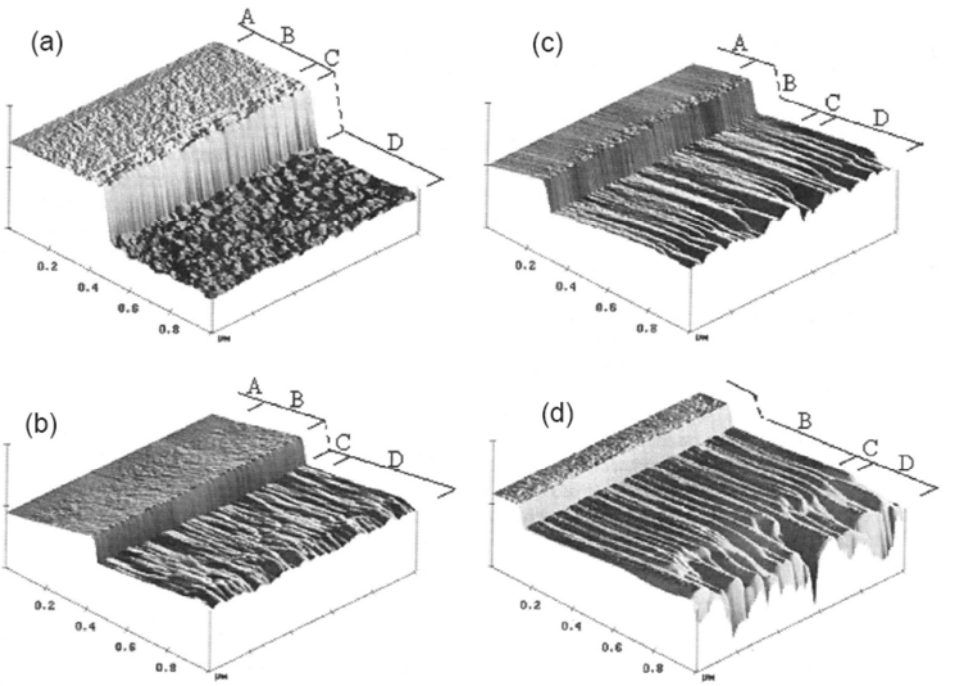

Figure 10.19 AFM images of pattern sidewalls: (a) after development, (b) after BARC open etch (N_2/H_2 plasma), (c) after oxide etch of 0.2 μm (CF_4/CHF_3 plasma), and (d) further oxide etch of 0.5 μm (CF_4/CHF_3 plasma). The film stack is: A = silicon substrate, B = silicon oxide (0.7 μm), C = BARC, and D = photoresist. Height scale is 200 nm/div. (Reprinted by permission from Ref. 40.)

10.4.2 LER reduction after etch

The transfer of LER through the etch process is not straightforward. The plasma etch with optimized conditions appears to transfer less LER from the resist pattern to the etched substrate. The transformation rate depends on the etch conditions and the film stack on the substrate and is also related to the initial resist LER and resist chemistry. Comparison experiments have been carried out at the gate level.[11,41]

At the gate level, the resist and BARC films were coated on the wafer with a poly-Si film. The LER of the resist pattern was measured after the lithographic process. The resist pattern was transferred to the poly-Si film by a plasma etch and the resulting LER in the poly-Si pattern was also measured. Figure 10.20 shows the relationship between the resist LER and the poly-Si LER. It appears that $LER_{poly\text{-}Si} < LER_{resist}$ and that the $LER_{poly\text{-}Si}$ value is a linear function of LER_{resist}.

The LER was analyzed for power spectral density (PSD) as shown in Fig. 10.21.[41] After etch, the low (0.6–5 μm) and high (> 50 μm) spatial frequency regions remain the same. The middle spatial frequency range (5–50 μm) shows distinct improvement in roughness. After etch, the middle to high spatial frequency regions contribute less to the overall LER than the low spatial frequency

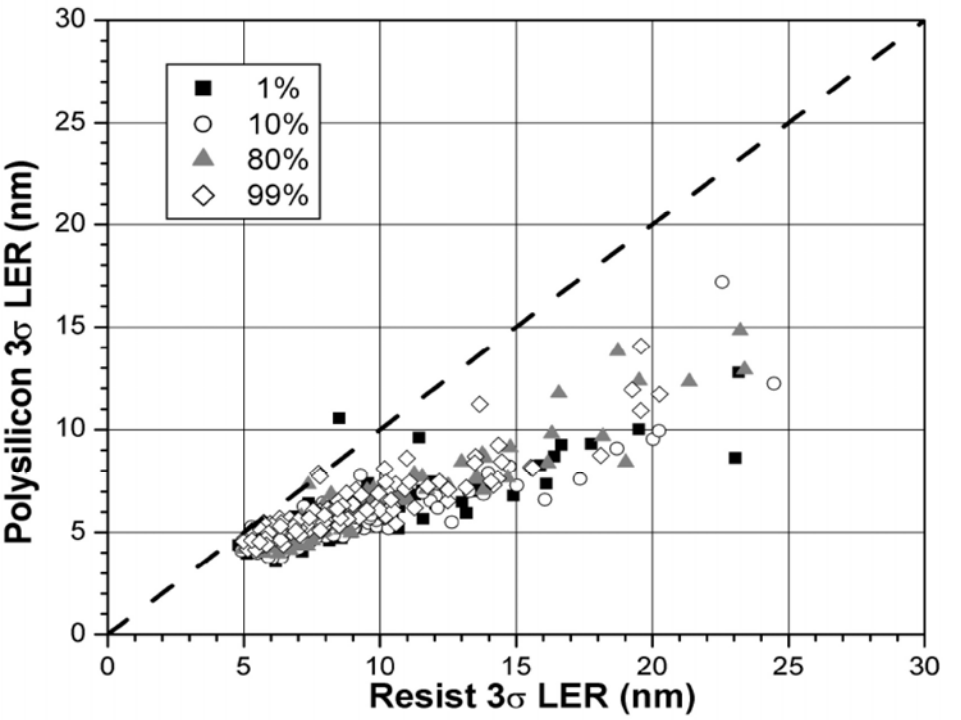

Figure 10.20 Poly-Si LER after etching as a function of the resist LER prior to etch. The dashed line represents a linear slope. The legend labels the global pattern density. (Reprinted by permission from Ref. 11.)

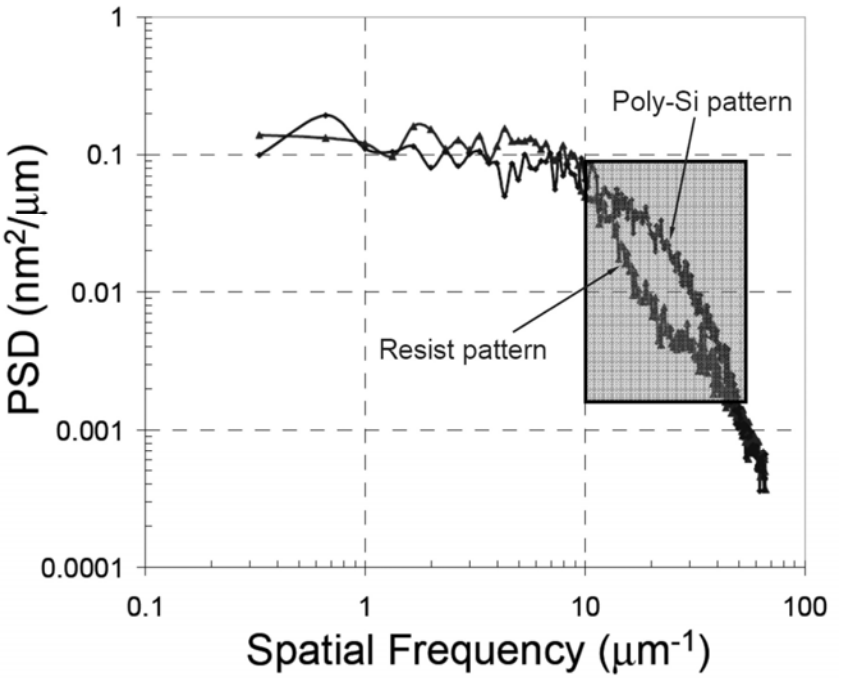

Figure 10.21 Power spectral density of the resist LER and the poly-Si LER. The shaded area indicates the etch-induced LER reduction. (Reprinted by permission from Ref. 41.)

regions contribute. These results raise the following question: How important is reduction of the resist LER? Most of the LER reduction process is only effective at removing the high-frequency resist LER. Thus, the best way to assess these processes is to evaluate the final post-etch LERs. After all, the final LER is the real target and most relevant to the performance of the final device.

References

1. A. Yamaguchi, H. Fukuda, T. Arai, J. Yamamoto, T. Hirayama, D. Shiono, H. Hada, and J. Onodera, "LER effects to devices and low molecule weight resist**,"** *J. Vacuum Sci. Technol. B***, 23**(6), Nov./Dec. 2005, 2711–2715.
2. M. Chandhok, S. Datta, D. Lionberger, and S. Vesecky, "Impact of line width roughness on Intel's 65 nm process devices," *Proc. SPIE* **6519**, 65191A (2007).
3. *International Technology Roadmap for Semiconductors*, 2007 Edition, Lithography section.
4. P. Zhang, M. Jaramillo, S. Cassel, T. Wallow, A. Acheta, A. R. Pawloski, S. Bell, and R. H. Kim, "Post-etch LER performance of novel surface conditioner solutions," *Proc. SPIE* **6153**, 61533Y (2006).
5. V. Constantoudis, G. P. Patsis, and E. Gogolides, "Photo-resist line-edge roughness analysis using scaling concepts," *Proc. SPIE* **5038**, 901–909 (2003).

6. V. Constantoudis and E. Gogolides, "Characterization and modeling of line width roughness (LWR)," *Proc. SPIE* **5752**, 1227–1236 (2005).
7. L. H. A. Leunissen, M. Ercken, J. A. Croon, G. F. Lorusso, H. Yang, A. Azordegan, and T. DiBiase, "Automating investigation of line width roughness," *Yield Management Solutions*, Spring, 2006.
8. B. D. Bunday, M. Bishop, D. McCormack, J. S. Villarrubia, A. E. Vladar, R. Dixson, T. Vorburger, N. G. Orji, and J. A. Allgair, "Determination of optimal parameters for CD-SEM measurement of line edge roughness," *Proc. SPIE* **5375**, 515–533 (2004).
9. See for example, P. P. Naulleau and J. P. Cain, "Experimental and model-based study of the robustness of line-edge roughness metric extraction in the presence of noise," *J. Vacuum Sci. Technol. B*, **25**(5), Sept. 2007, 1647–1657.
10. T. Azuma, K. Chiba, H. Abe, H. Motoki, and N. Sasaki, "Mechanism of ArF resist pattern shrinkage in CD-SEM measurement," *J. Vacuum Sci. Technol. B*, **22**(1), Jan./Feb. 2004, 226–230.
11. A. R. Pawloski, A. Acheta, S. Bell, B. La Fontaine, T. Wallow, and H. J. Levinson, "The transfer of photoresist LER through etch," *Proc. SPIE* **6153**, 615318 (2006).
12. H. Tsubaki, T. Yamanaka, F. Nishiyama, and K. Shitabatake, "A study on the material design for the reduction of LWR," *Proc. SPIE* **6519**, 651918 (2007).
13. M. D. Stewart, H. V. Tran, G. M. Schmid, T. B. Stachowiak, D. J. Becker, and C. G. Willson, "Acid catalyst mobility in resist resins," *J. Vacuum Sci. Technol. B*, **20**(6), Nov./Dec. 2002, 2946–2952.
14. W. Hinsberg, F. Houle, M. Sanchez, J. Hoffnagle, G. Wallraff, D. Medeiros, G. Gallatin, and J. Cobb, "Extendibility of chemically amplified resists: Another brick wall?" *Proc. SPIE* **5039**, 1–14 (2003).
15. G. M. Gallatin, "Resist blur and line edge roughness," *Proc. SPIE* **5754**, 38–52 (2005).
16. R. L. Bristol, "The tri-lateral challenge of resolution, photospeed, and LER: Scaling below 50nm?" *Proc. SPIE* **6519**, 65190W (2007).
17. R. L. Brainard, P. Trefonas, J. H. Lammers, C. A. Cutler, J. G. Mackevich, A. Trefonas, S. A. Robertson, "Shot noise, LER, and quantum efficiency of EUV photoresists," *Proc. SPIE* **5374**, 74–85 (2004).
18. W. L. Wu, V. M. Prabhu, and E. K. Lin, "Identifying materials limits of chemically amplified photoresists," *Proc. SPIE* **6519**, 651902 (2007).
19. D. Van Steenwinckel, J. H. Lammers, L. H. A. Leunissen, and J. A. J. M. Kwinten,"Lithographic importance of acid diffusion in chemically amplified resists," *Proc. SPIE* **5753**, 269–280 (2005).
20. C. A. Cutler, J. F. Mackevich, J. Li, D. J. O'Connell, G. F. Cardinale, R. L. Brainard, "Effect of polymer molecular weight on AFM polymer aggregate size and LER of EUV resists," *Proc. SPIE* **5037**, 406–417 (2003).
21. W. G. Lawrence, "Spatial frequency analysis of line edge roughness in nine chemically related photoresists," *Proc. SPIE* **5039**, 713–724 (2003).

22. Y. Wei, K. Petrillo, S. Brandl, F. Goodwin, P. Benson, R. Housley, and U. Okoroanyanwu, "Selection and evaluation of developer-soluble topcoat for 193nm immersion lithography," *Proc. SPIE* **6153**, 615306 (2006).
23. L. Singh, I. Matthew, A. Pawloski, and A. Minvielle, "Effect of top coat and resist thickness on line edge roughness," *Proc. SPIE* **6153**, 61530W (2006).
24. V. M. Prabhu, B. D. Vogt, S. Kang, A. Rao, E. K. Lin, S. K. Satij, and K. Turnquest, "Direct measurement of the in situ developed latent image: the residual swelling fraction," *Proc. SPIE* **6519**, 651910 (2007).
25. J. M. Roberts, R. Meagley, T. H. Fedynyshyn, R. F. Sinta, D. K. Astolfi, R. B. Goodman, and A. Cabral, "Contributions to innate material roughness in resist," *Proc. SPIE* **6153**, 61533U (2006).
26. T. H. Fedynyshyn, R. F. Sinta, D. K. Astolfi, A. Cabral, J. Roberts, and R. Meagley, "Deconstructing the resist to probe innate material roughness," *Proc. SPIE* **6153**, 615315 (2006).
27. T. Yamaguchi, K. Yamazaki, and H. Namatsu, "Influence of molecular weight of resist polymers on surface roughness and line-edge roughness," *J. Vacuum Sci. Technol. B*, **22**(6), Nov./Dec. 2004, 2604–2610.
28. F. M. Houlihan, D. Rentkiewicz, G. Lin, D. Rahman, D. Mackenzie, A. Timko, T. Kudo, C. Anyadiegwu, M. Thiyagarajan, S. Chiu, A. Romano, R. R. Dammel, and M. Padmanaban, "Study of the effect of amine additives on LWR and LER," *Proc. SPIE* **6153**, 615317 (2006).
29. T. H. Fedynyshyn, D. K. Astolfi, A. Cabral, and J. Roberts, "PAG segregation during exposure affecting innate material roughness," *Proc. SPIE* **6519**, 65190X (2007).
30. G. M. Gallatin, P. Naulleau, and R. Brainard, "Fundamental limits to EUV photoresist," *Proc. SPIE* **6519**, 651911 (2007).
31. T. Kudo, S. Chakrapani, G. Lin, C. Anyadiegwu, C. Antonio, D. Parthasarathy, R. R. Dammel, and M. Padmanaban, "Some non-resist component contributions to LER and LWR in 193 nm lithography," *Proc. SPIE* **6519**, 651941 (2007).
32. M. Watanabe, S. Yabe, S. Machida, and T. Taguchi, *J. Photopolym. Sci. Technol.*, **12**, 643 (1999).
33. M. Ryoo, S. Shirayone, H. Oizumi, N. Matsuzawa, S. Irie, E. Yano, H. Okazaki, *Proc. SPIE* **4345,** 903–911 (2001).
34. P. Wong, W. Gehoel, S. Sinkwitz, P. Zhang, M. Jaramillo, Jr., M. B. Rao, B. Horvath, B. Ross, and S. Cassel, "Linewidth roughness reduction at the 55 nm node through combination of classical process optimization and application of surface conditioner solutions," *Proc. SPIE* **6153**, 61533V (2006).
35. B. Lu, E. Liu, A. Zeng, A. Tseng, S. Wu, B. Lin, C. Yu, L.-J. Meng, M. Jaramillo, and M.-J. Liao, "Line width roughness (LWR) performance of novel surface conditioner solutions for immersion lithography," *Proc. SPIE* **6923**, 69233G (2008).
36. V. Huang, C. C. Chiu, C. A. Lin, C. Y. Chang, T. S. Gau, and B. J. Lin, "Effect of novel rinsing material and surfactant treatment on the resist pattern performance," *Proc. SPIE* **6519**, 65193C (2007).

37. Y. Inatomi, T. Kawasaki, and M. Iwashita, "LWR reduction in ArF resist pattern by resist smoothing process," *Proc. SPIE* **6153**, 61533X (2006).
38. K. Matsunaga, T. Oori, H. Kato, D. Kawamura, E. Shiobara, Y. Inatomi, T. Kawasaki, M. Iwashita, and S. Ito, "LWR reduction in low k_1 ArF immersion lithography," *Proc. SPIE* **6923**, 69231E (2008).
39. H. Kawahira, N. N. Matsuzawa, E. Matsuib, A. Ando, K. A. Salam, M. Yoshida, Y. Yamaguchi, K. Kugimiya, T. Tatsumi, H. Nakano, T. Iwai, and M. Irie, "Changes of chemical nature of photoresists induced by various plasma treatments and their impact on LWR," *Proc. SPIE* **6153**, 615319 (2006).
40. D. L. Goldfarb, A. P. Mahorowala, G. M. Gallatin, K. E. Petrillo, K. Temple, M. Angelopoulos, S. Rasgon, H. H. Sawin, S. D. Allen, M. C. Lawson, and R. W. Kwong, "Effect of thin-film imaging on line edge roughness transfer to underlayers during etch processes," *J. Vacuum Sci. Technol. B*, **22**, Issue 2, 647–653 (2004).
41. T. Wallow, A. Acheta, Y. Ma, A. Pawloski, S. Bell, B. Ward, C. Tabery, B. La Fontaine, R. Kim, S. McGowan, and H. J. Levinson, "Line edge roughness in 193nm resists: lithographic aspects and etch transfer," *Proc. SPIE* **6519**, 651919 (2007).

Chapter 11
Extendibility of 193-nm Immersion Lithography

Immersion lithography based on water has been very successful. The maximum numerical aperture of 1.3 or 1.35 has allowed this technology to be widely used in the production of 45-nm half-pitch devices. Encouraged by this success, researchers are interested in further boosting NA through the use of fluids and lens materials with higher indices of refraction. In theory, these second-generation immersion technologies could be used in the 32-nm half-pitch node. Table 11.1 shows the resolution requirements for the 45- and 32-nm nodes as described by ITRS 2007.[1] Although DRAM, Flash, and Logic have slightly different specifications, the fundamental challenge for the 32-nm node is to print 32-nm dense lines and 35-nm contact holes. According to the Rayleigh equation (resolution = $k_1\lambda$/NA), a numerical aperture larger than 1.55 will be needed in order for k_1 to be larger than 0.25 for the 32-nm half-pitch node. Detailed simulations suggest that numerical apertures of at least 1.65 will be required to print 32-nm patterns with reasonable process windows.

As discussed in Chapter 1, the maximally effective NA of an immersion system is limited by the refractive index (RI) of the lens, the fluid, and the resist. Thus, high refractive index materials are the key to further increases in NA. Currently, the last lens element is composed of fused silica, which has a refractive index of 1.55 at 193 nm. Conventional 193-nm resists have refractive indices around 1.70. The replacement of water with a high refractive index immersion fluid would be the first step in the development of high-RI 193-nm

Table 11.1 Resolution requirement for the 45- and 32-nm nodes.[1]

Technology node	DRAM and Flash			Logic		
	DRAM ½pitch (Dense lines)	Flash ½pitch (Dense lines)	Contact	M1 ½pitch (Dense lines)	Gate width	Contact
45nm node	45nm	36nm	50nm	45nm	30nm	56nm
32nm node	32nm	25nm	35nm	32nm	21nm	39nm

immersion lithography (193i+). However, the replacement of the immersion fluid alone would be insufficient for reaching NA = 1.65. The fused silica lens must also be replaced by a new material with a RI ≥ 1.65.

Table 11.2 summarizes the possible combinations of high-RI immersion fluid, lens material, and resist, along with the NA values that can be achieved in theory. As of today, high-RI fluids with n ~1.60–1.65 are available for early exposure tests.[2,3] These immersion fluids are called second-generation (G2) fluids. The use of G2 fluids with current lens materials and conventional 193-nm resists should be capable of producing 1.55NA full-field scanners. Various potential lens materials have been screened for higher RI values; $BaLiF_3$ with n ~1.64 and LuAG with n ~2.0 show potential.[4,5] Methods for increasing the RI of resist polymers are being explored by basic research organizations.[6] Hopefully, this work will lead to new resist platforms with n ~2.0. The combination of third-generation (G3) fluids with n ~1.8, higher RI lens material, and higher RI resists gives us hope of achieving numerical apertures of 1.80.

In addition to designing high-RI lenses and fluids, projection optics will need to be redesigned for these second- and third-generation systems. As an alternative, a NA > 1.35 can be reached either by reducing the size of the exposure field[7] or by curving the final lens element.[8] Reducing the field size (~12 mm), the water immersion can reach a maximum NA of ~1.40. However, the chip size must also be reduced and chip designers are unlikely to accept a smaller field size. A curved final lens can cover large incident beams, but the exposure beams will need to travel 20–50x farther in the immersion fluid, requiring the fluid to be extremely transparent. If such a fluid is available, then 1.5NA 193i+ can be reached without the use of high-RI lens materials.

Nevertheless, the 193i+ roadmap is full of technical challenges that will be discussed in this chapter. An important question to ask is whether or not 193i+ can compete with other options for the 32-nm node, such as double patterning or EUV lithography. Another drawback of 193i+ is that it can provide lithographic solutions for only one node—the 32nm half-pitch. At this time (Fall 2008), it appears unlikely that 193i+ tools will be available by 2010 and, therefore, will be too late for the 32-nm node. However, 193i+ is still an interesting technology to

Table 11.2 Possible combinations of high-RI immersion fluid, lens material, and resist. High-risk technologies are in shaded boxes.

	Immersion Fluid	Lens Material	Resist	Resolution Capability
NA ≤ 1.35	Water (n = 1.44)	Fused silica (n = 1.55)	Methacrylate (n = 1.70)	45-nm half-pitch node
NA < 1.55	High-RI fluid (n ≈ 1.60)	Fused silica (n = 1.55)	Methacrylate (n = 1.70)	
NA < 1.65	High-RI fluid (n ≈ 1.65)	High-RI lens Material (n ≈ 2.0)	Methacrylate (n = 1.70)	32-nm half-pitch node
NA < 1.80	3G fluid (n ≈ 1.80)	High-RI lens Material (n ≈ 2.0)	High-RI resist (n ≈ 2.0)	

the lithography community that promises to be less costly than double patterning or EUV, and if available, could be used in combination with double patterning.

11.1 Fluids with High Refractive Indices

The development of high-RI immersion fluids preceded the development of high-RI lenses and resists. In addition to having high RI values (> 1.44 at 193 nm), these fluids must also be very transparent and stable to 193-nm light. Although some performance requirements are obvious, detailed specifications for the 193-nm fluid are still being discussed.[9] The best way to assess an immersion fluid is to compare it to water.

11.1.1 Requirements for high-RI fluids

Table 11.3 compares the performance characteristics of water with the performance objectives of second-generation immersion fluid for 193-nm lithography. Water is very transparent to 193-nm light with an absorption coefficient of 0.036 cm^{-1}. The RI of water is ~1.44 with a temperature sensitivity of $dn/dT = -10^{-4}/^{o}C$. This means that a temperature fluctuation of 0.01° C will cause a refractive index change of 10^{-6}, which in turn, will lead to a defocus of ~1 nm at a working distance of 1 mm. Water is a material that is familiar to IC manufacturers and has been used for rinsing after development. Water also exhibits excellent stability toward photodecomposition by 193-nm light.

Tentative "specifications" for second-generation high-RI immersion fluids have also been drafted (Table 11.3). These specifications are not industrial standards, but were developed by leading lithography material and process development engineers.[9] The performance parameters (except for the refractive index) were obtained simply by compromising the performance of water. The absorption coefficient of the fluid must be low (< 0.15/cm) in order to minimize photodecomposition and thermal fluctuations. The fluid must have low viscosity so that the meniscus can move with the exposure head across the wafer. As these high-RI fluids may be mixtures, the light scattering "specification" is imposed to control flare.

For 157-nm light, the best immersion fluid that has been identified is perfluorotriglyme, $CF_3(OCF_2CF_2)_3OCF_3$, which has $\alpha = 0.64 \pm 0.07 cm^{-1}$. For a 350-μm working distance, the transmission is about 95%.[10]

11.1.2 Measuring the RI of immersion fluids

A simple way to measure the refractive index of a fluid is to use a prism cell (Fig. 11.1). A hollow prism cell made of fused silica is filled with an immersion fluid and mounted on a rotational stage. A 193-nm light beam is directed toward the prism and travels through the immersion fluid. The incident angle α is adjusted by rotating the sample stage so that the maximum portion of the outgoing light beam is collected by the detector. The deviation angle β of the detector relative to the

Table 11.3 Performance parameters of water as an immersion fluid for 193-nm lithography and proposed requirements for the high-RI immersion fluid.

	Water	**High-RI fluid (G2)**
Refractive index at 193 nm	$n = 1.44$	$n = 1.60–1.65$
Variation of RI with temperature fluctuation	$dn/dT = -10^{-4}$/°C	$dn/dT \approx 3 \times 10^{-4}$/°C
Absorption coefficient	$\alpha = 0.036\ cm^{-1}$	$\alpha < 0.15\ cm^{-1}$
Viscosity at 20° C	$\mu = 1.002$ cP	$\mu < 2.0$ cP
Light scattering	< 0.03%/mm	< 0.2%/mm
Chemical compatibility with resist and lens	good	No negative impact
Chemical stability under 193-nm irradiation	stable	Not photoactive or degradable
Environmental impact factor	excellent	No negative impact
Cost of ownership		< $1.00 per layer

original light beam is measured by goniometry. The apex angle A of the prism is 45 deg. The refractive index of the fluid (n_{fluid}) can be calculated by applying Snell's law to the air–fluid and fluid–air interfaces as

$$n_{\text{fluid}} = n_{\text{air}} \cdot \sqrt{2\sin^2\alpha + 2\sin^2\beta + 2\sqrt{2}\sin\alpha\sin\beta}\ . \tag{11.1}$$

In this test, the measurement of the deviation angle β is critical. Because the prism and the fluid shift the beam path, large errors can be introduced into this angle.[11] Nevertheless, a report by NIST demonstrated that this method can provide an accuracy of 1×10^{-4}.[12]

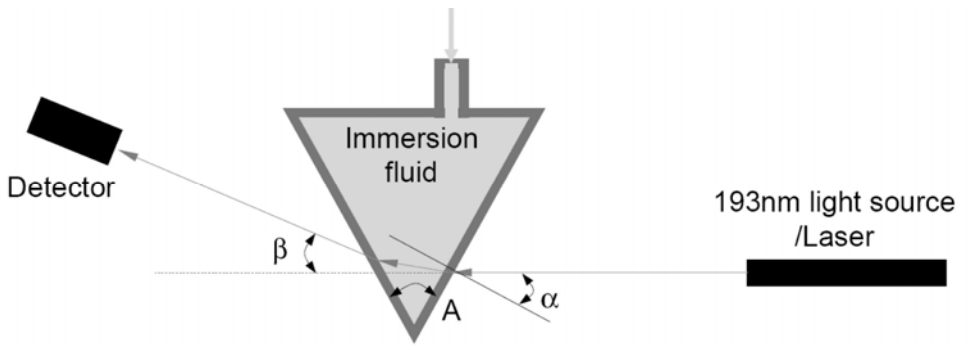

Figure 11.1 Setup for measuring the refractive index of an immersion fluid. The apex angle A is 45 deg.

11.1.3 Development of high-RI fluids

Initial efforts to produce high-RI fluids involved dissolving high-index additives (either organic or inorganic) into water. This approach takes advantage of some favorable properties of water (e.g., density and viscosity) and, indeed, some inorganic salts do increase the refractive index. However, the inorganic salts have limited solubility in water, limiting their ability to increase RI. Crown ethers were added to the water to enhance the solubility of the metal salts. With this approach, an index of 1.6 was obtained with solutions of $CdCl_2$.[13] Unfortunately, high concentrations of heavy metal salts are typically very toxic, making them unacceptable in a production environment. Nontoxic inorganic metal salts of $BaCl_2$ and $CaCl_2$ were also tested. With the help of crown ethers, the solubility was increased, but the increases in RI were very limited. Increasing the additive concentration in water also tends to increase the absorbance of the solution.[14]

Dispensing transparent high-RI nanoparticles into solvents is another approach for developing high-RI fluids. The RI of the fluid can be expressed as

$$\frac{n^2 - n_0^2}{n^2 + 2} = \frac{n_p^2 - n_0^2}{n_p^2 + 2} \cdot \mathrm{NV}, \tag{11.2}$$

where n is the RI of the composite fluid, n_0 is the RI of the liquid host, n_p is the RI of the nanoparticle, and NV is the volume fraction of the particles in the fluid.[15] The refractive index of the composite fluid is proportional to the volume fraction of high-index particles. A volume fraction of at least ~20–30% is needed to reach $n > 1.6$. In an early test, Al_2O_3 nanoparticles were added to water and $n = 1.6$ was reported. However, the application of the composite fluid to 193-nm immersion appears very challenging. First, the exposure light can be scattered by the particles in the fluid. In order to reduce the scattering to an acceptable level, the size of the particles must be ≤ 1 nm, which means that the particles are nearly the size of large molecules. Also, the particles must be monodispersed, since larger particles dominate scattering. Second, the concentrations of additives must be precisely controlled, in order to minimize fluctuations in the refractive index of the fluid. Third, the nanoparticles must not deposit onto the final lens element or scratch it.

Single-component organic liquids show the most promise for meeting the requirements for second-generation fluids. These organic fluids must have both high RI n and low absorption k at 193-nm wavelength; however, n and k are correlated with each other by the Kramers-Kronig relation.[16] Typically, both n and k increase as wavelength decreases and approaches the absorption peak; in fact, n reaches its maximum earlier than k reaches its maximum, as shown in Fig. 11.2. Beyond the peak, the refractive index n decreases with decreasing wavelength. As a result, much effort is focused on finding materials that have strong absorption peaks at wavelengths just below 193 nm to ensure that the indices will be high while the absorbance will be low (at 193 nm).[17]

Single-component organic fluids with RI in the range of 1.60–1.67 have been developed by several suppliers. Table 11.4 summarizes the key performance parameters of these fluids. Detailed results and names of these fluids can be found in several publications.[2,3,18,19] One critical parameter is photostability, which is evaluated by exposing the fluid to a high dose of 193-nm light while monitoring changes in *n* and *k*.[19,20] Similarly, the solubility of air in these fluids is important, since oxygen dissolved in the fluids causes high absorption at 193 nm. Purification systems have been designed to recycle the fluids (Fig. 11.3) and to remove foreign materials coming from the resist, photodecomposition components, and oxygen from the exposure head. By passing through the purification system, the transmittance of the fluid can be largely recovered. However, even with purification, transmission continues to decrease after the accumulation of large doses.[21] Therefore, even with purification, high-RI fluids have finite lifetimes. Better purification systems may be needed in order to extend the lifetime of these G2 fluids.

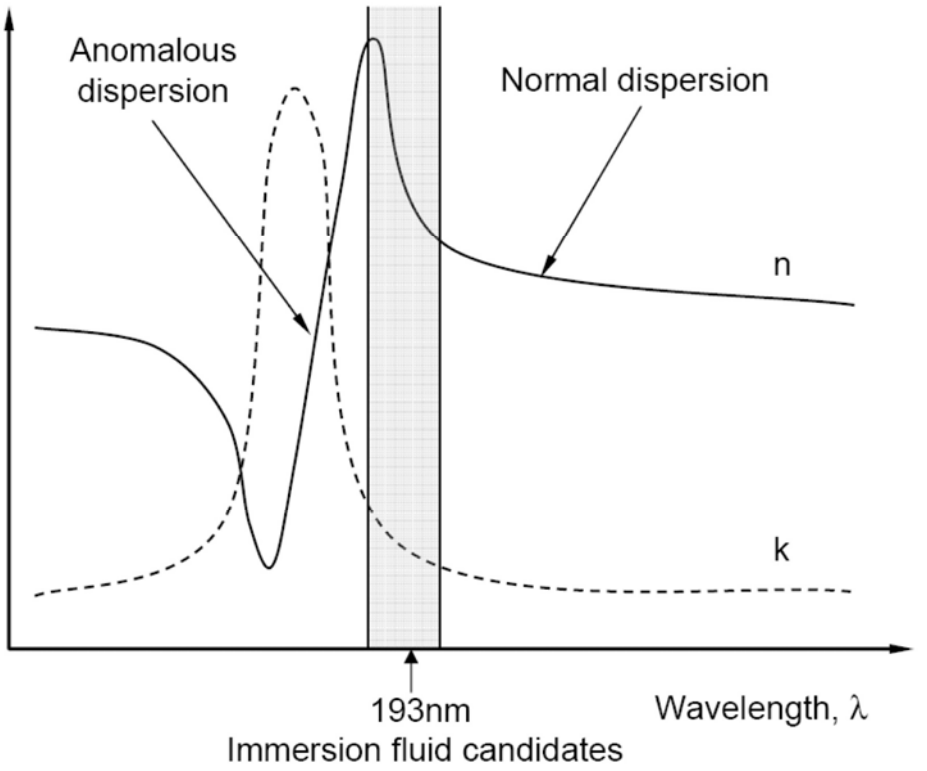

Figure 11.2 Sketch of the dispersion relationships of materials. Immersion fluid candidates must be located at the absorption peak where $\lambda < 193$ nm.

Table 11.4 Performance parameters of currently available G2 high-RI fluid.

	Water	High RI fluid (G2) (publicly reported)
Refractive index at 193 nm	$n = 1.44$	1.60 – 1.67
Absorption coefficient at 193 nm	$\alpha = 0.036\ cm^{-1}$	$0.01 – 0.038\ cm^{-1}$
Transmittance at 193 nm	99.17 %/mm	99.10 – 99.70 %/mm
dn/dT	– 93 ppm/K	– 560 to – 540 ppm/K
Viscosity at 20° C	$\mu = 1.0$ cP	2.1 – 3.7 cP
Vapor pressures at 25° C	3200 Pa	5.9 – 164 Pa

The development of high-RI organic fluids continues around the globe, where researchers have proposed and pursued various approaches.[22–24] For example, *ab initio* and empirical methods have been applied to the search for new chemical compounds with high refractive indices and low absorption at 193-nm wavelength. Modeling has predicted that SO_2-containing compounds with five- and six-membered rings could give increases in the refractive index at relatively low absorption at 193 nm. Fluids consisting of LuAG nanoparticles dispersed in decalin are being investigated for use as 3G high-index fluids.[25]

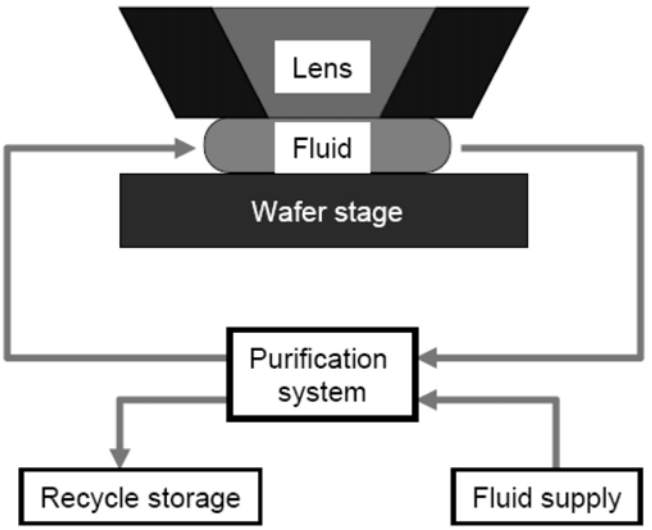

Figure 11.3 Diagram of fluid handling system.

11.1.4 Leaching and contact angle

The tendency of high-RI fluids to leach resist components has been evaluated and compared with the same tendency in water. In general, conventional 193-nm resist components show equivalent or less leaching into high-RI fluids than into water. The time dependence of leaching (dynamic leaching behavior) is similar to that demonstrated by water and most leaching occurs within the first minute.[19] Figure 11.4 shows the PAG leaching level in various high-RI fluids from different suppliers.[26] Samples HIL B and C show less leaching than water shows, because of the low solubility of PAGs in these G2 fluids.

Resists were treated with G2 fluids before and after dry exposure.[26] These treatments can reduce the thickness of the resist and can change the CDs in the printed features, raising concerns that organic fluids might dissolve or swell photoresist films. Hence, the assessment of high-RI fluids must include measurements of resist film thicknesses before and after immersion in the fluid.

The contact angle of the fluid on the resist surface is another major concern for G2 fluids, since it directly dictates how the fluid would be confined during exposure. Figure 11.5 shows the static and dynamic contact angles measured from various high-RI fluids on a typical ArF resist (PAR817). The high-RI fluids have static contact angles of < 20 deg, while water has a static contact angle of ~75 deg on the same resist. This means that the fluid meniscus cannot be confined by surface tension and completely new approaches for exposure heads will need to be developed if these contact angles cannot be increased.

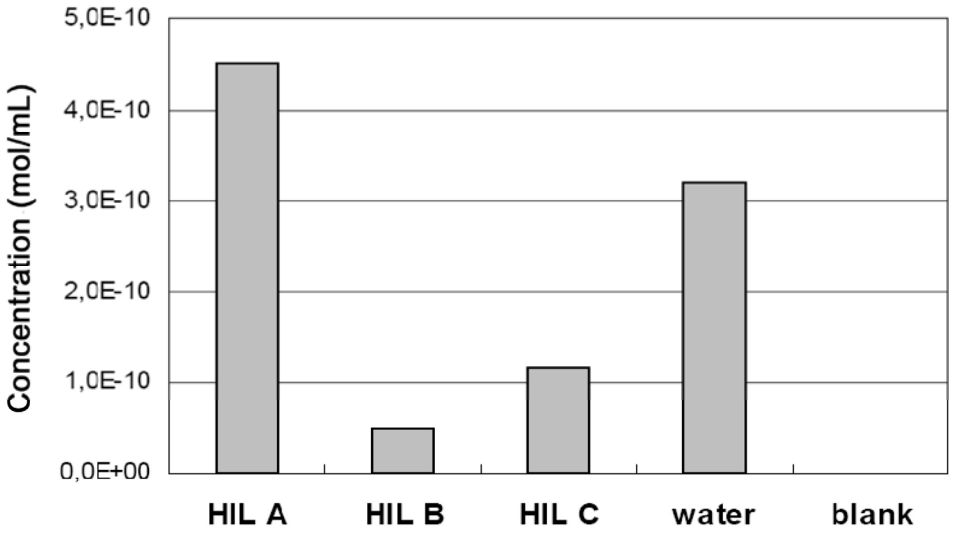

Figure 11.4 PAG leaching level in various high-RI fluids. HIL A, B, and C are the G2 high-RI fluids from different suppliers. (Reprinted by permission from Ref. 26.)

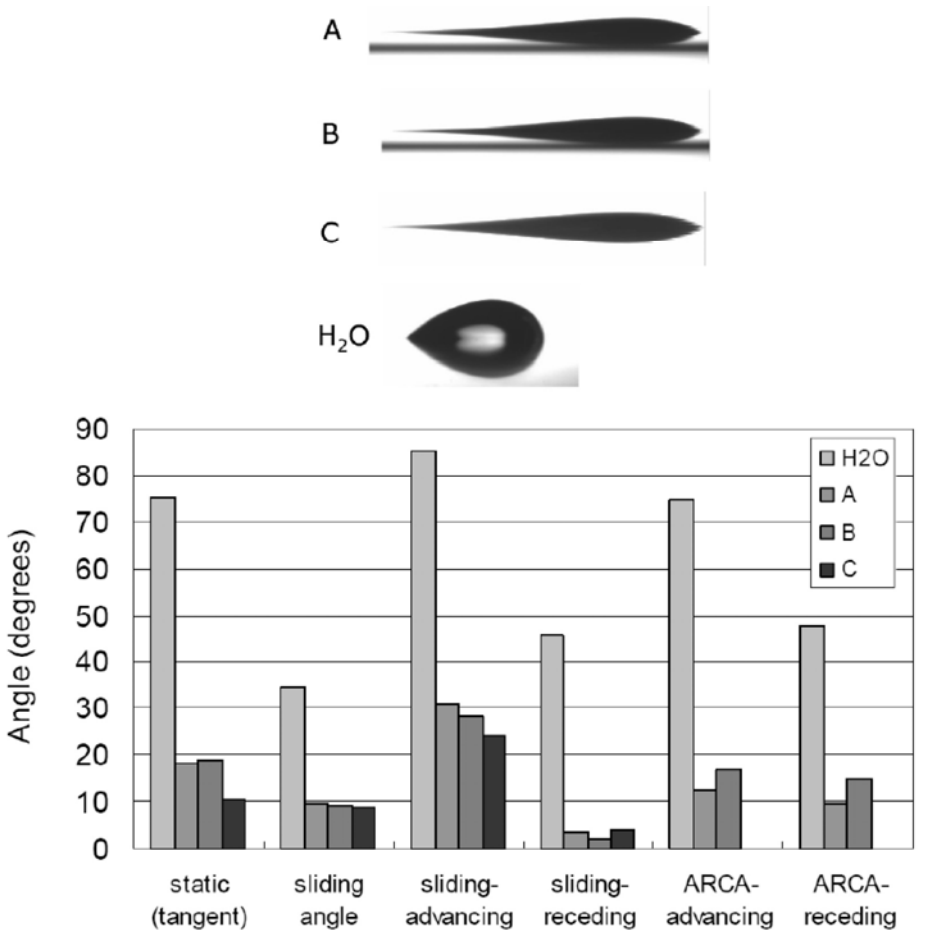

Figure 11.5 Static and dynamic contact angles of high-RI fluids (A, B, C) on a typical ArF resist. The dynamic contact angles (receding and advancing contact angles) were measured by both the sliding wafer method (sliding-advancing and sliding-receding) and the captive method (ARCA-advancing and ARCA-receding). (Reprinted by permission from Ref. 26.)

To overcome these contact angle issues, topcoats designed to work in combination with high-RI fluids have been proposed. These topcoats must have high contact angles for the high-RI fluid as well as high refractive indices for good optical performance. A prototype topcoat has demonstrated a 70-deg static angle for high-RI fluids.[21]

11.2 Materials with High Refractive Indices

A material with a high refractive index is needed for the last lens element in 193i+ scanners. Table 11.5 shows target specifications for high-index lens materials given by scanner suppliers.[27] In addition to high RI, the new lens materials must be highly transparent and have low intrinsic birefringence (IBR).

The absorption coefficient of < 0.01/cm means that > 90% of 193-nm light can pass through a 3-cm lens. Additionally, these materials must be highly homogeneous and be available in large sizes.

Theoretically, large-band-gap ionic materials that are highly polarizable should be relatively transparent to 193-nm light and have high refractive indices. These theoretical predictions narrow the search to group II metal oxides. Currently, several candidates have been identified: $BaLiF_3$, ceramic spinel, LuAG, and germanate garnets.[28] The current final lens material, SiO_2, is also included for reference in Table 11.5, which provides key performance characteristics of these candidates.

Although the refractive index of $BaLiF_3$ (1.64) falls short of the index needed for the final lens element, its transparency, laser durability, and intrinsic birefringence are better than those of the other candidate materials. Additionally, large single crystals of $BaLiF_3$ with diameters of 150 mm have been successfully produced by controlling the ingredient composition and by optimizing its zone-refining process.[4,29] Ceramic spinel ($MgAl_2O_4$) has no IBR problem, but its poor crystallinity leads to high absorption and poor RI uniformity. These properties are unlikely to improve. LuAG ($Lu_3Al_5O_{12}$) has a high RI (~2.1), but its absorption (0.11 cm^{-1}) is still beyond the target. The stress birefringence and homogeneity of LuAg continue to improve and are closer to the final target, and the high IBR (3x the specification) is manageable for the optics maker.[5,30] Germanate garnets ($X_3Y_2Ge_3O_{12}$) have potential, and further investigation of these types of materials is ongoing.

Another approach to developing high-RI lens material is to dope fused silica (SiO_2) with lanthanum.[31] Because silica glass is commonly used in scanners, the doping approach could have a number of advantages. For example, the doped lanthanum forms La_2O_3 in the glass and high lanthanum concentrations result in

Table 11.5 Tentative targets and key performance data for high-RI lens material candidates.[27,28]

	Refractive index at 193nm	Intrinsic birefringence (IBR) (nm/cm)	Absorption coefficient (A_{10}, cm^{-1})	Stress birefringence (SBR) (nm/cm)	Scattering	Manufacturing capability
Target	≥ 1.8	< 10	≤ 0.003	≤ 1	Uncritical	Large scale manufacturing
SiO_2	1.55	None	0.00087		Uncritical	Large scale manufacturing
LuAG	2.1	30	0.11	~ 1	Uncritical	R&D scale
$BaLiF_3$	1.64	25	0.005	< 2.5	Uncritical	R&D scale
Ceramic Spinel	1.92	None	0.2	< 5	10x too high	R&D scale
Germanate Garnets	2.0 – 2.2	?	?	?		

high RI. Currently, lanthanum-doped silica can reach refractive indices near 1.58. Further improvement in the doping process and in the use of high purity raw material is ongoing.

11.3 Resists with High Refractive Indices

11.3.1 Development of high-RI resists

High-RI resists must have indices of ~2.0 and must additionally have imaging, etch, and cost properties similar to current 193-nm dry resist properties. The RI of polymers can be increased by introducing high-RI functional groups into the polymers; however, many of these functional groups are coupled with undesirable properties. For example, the addition of chlorine, bromine, or iodine would significantly increase the RI, but are inappropriate for use in 193-nm resists because of absorbance or photoinduced chemical reactions.[32]

Sulfur-containing polymers show more promise.[33–35] Whittaker and coworkers at the University of Queensland designed a sulfur-containing polymer that demonstrates $n = 1.8$, but its absorbance is $> 7\ \mu m^{-1}$, which is much higher than the specification ($< 3\ \mu m^{-1}$).[33] Along with Whittaker's approach, further optimization of sulfur groups in the polymer can lead to increases in n without increasing k.[34] A sulfur-containing resist with $n = 1.76$ and an absorption coefficient of $1.70\ \mu m^{-1}$ has been designed by a group at JSR Micro and is capable of resolving 80-nm dense lines.[35] In general, the RIs of polymers increase with increased sulfur content in the polymer. Sulfur contents of 17–30% will be required to achieve $n = 1.85$. The difficulty is that increased sulfur content also leads to increased absorption and outgassing, while decreasing lithographic performance and etch resistance.

Introduction of silicon into polymers is another approach used to increase the index of refraction. A silicon-containing resist with $n = 1.81$ and an absorption coefficient of $2.43\ \mu m^{-1}$ has been prepared and tested for lithographic performance.[32] However, increasing silicon content results in poor lithographic performance and poor compatibility with the underlayer.

Addition of transparent high-RI nanoparticles to conventional resists is an innovative approach to reaching the target refractive indices. One major advantage of this approach is that only minor modifications to the existing resist platforms will need to be made. The two critical steps are the preparation of the high-RI nanoparticles and their blending into the resist formulations. A polymer film blended with nanoparticles has a demonstrated refractive index of ~2.0 and an absorbance of ~2.5 μm.[36]

A theoretical model, called the quantitative structure property relationship (QSPR), has been developed to predict the refractive index of monomers and polymers.[33,37] This model uses nine descriptors of the RI: heat of formation, translational entropy, minimum partial charge on carbon atoms, number of sulfur atoms, number of fluorine atoms, minimum bond orders of carbon atoms, hydrogen donor-charged surface areas, polarizability, and total enthalpy:

$$\mathrm{RI} = \sum_{i=1}^{9} (k_i \cdot \mathrm{Descriptor}_i) . \tag{11.3}$$

This predictive model allows candidate polymers to be assessed before they are synthesized, so that only those molecules with the desired properties are prepared.[6] Hopefully, this type of approach accelerates development cycles and reduces cost.

11.3.2 Aerial image improvements with high-RI material

High-index resists are necessary for 193i+ because they ensure that exposure beams with NA > 1.7 refract into the resist rather than reflecting off of its interface with the high-index fluid (Fig. 11.6). In addition to enabling the increase of NA, high-RI resists can enhance the aerial image contrast, since for the same pattern, a high-RI resist can provide better aerial image contrast and a larger DOF than can a low-RI 193-nm resist.

Benefits to aerial image contrast by the use of high-RI resists can be explained in terms of the interference between exposure beams. Two exposure beams with the same incident angle (θ_1, $n_{\mathrm{fluid}}\sin\theta_1$ = NA) pass through the immersion fluid and interfere at the resist film, generating patterns (Fig. 11.7). According to Snell's law, the higher the RI of the resist, the smaller will be the refractive angle θ_2. The interference of the transverse electric (TE) components of the refracted beams is not related to the refractive angle, because the TE components have the same orientation. However, the superposition of transverse magnetic (TM) components depends on the refractive angle θ_2. Assuming that the amplitudes of the two beams are the same, i.e., $|\mathbf{E}_1|=|\mathbf{E}_2|$, the image contrast is

$$C = \tfrac{1}{2}(1+\cos^2\theta_2) = 1-\tfrac{1}{2}\sin^2\theta_2 = 1-\tfrac{1}{2}\left(\frac{\mathrm{NA}}{n_{\mathrm{resist}}}\right)^2 . \tag{11.4}$$

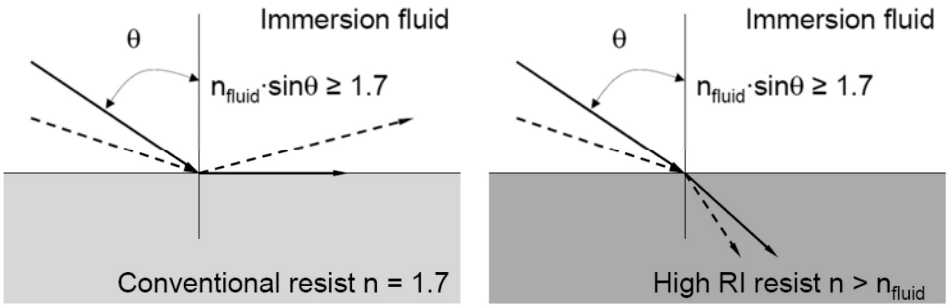

Figure 11.6 Refraction of exposure beams at the interface of resist and fluid. The refractive index of the resists must be higher than the refractive index of the immersion fluid so that all exposure beams can enter the resist film.

In Eq. (11.4), at a fixed NA, the image contrast increases with the RI value of the resist. Compared to the conventional resist (n = 1.7), the improvement of the image contrast is calculated from Eq. (11.4) as a function of n_{resist} and NA, as shown in Fig. 11.8.[38] A higher NA will provide a higher contrast when using high-RI resists.

Exposure latitude (EL) is a measure of a lithographic system's insensitivity to variations in dose and is directly related to the aerial image contrast. The CDs of images printed with poor aerial image contrast will be overly sensitive to changes in dose. Therefore, increasing the refractive index of resists could lead to increases in exposure latitude.

It is also possible to improve DOF by increasing RI, although the arguments are more complicated.[39] To understand this, we need to first review how the DOF is defined; for resist lines, the DOF is usually determined by the CD at the bottom of the line. In other words, the DOF is the focus range in which the bottom CD remains within ±10% of the target value. However, other parameters, such as the line top CD and the pattern sidewall angle (SWA) are also important in defining the process window. As a result, the combined DOF is obtained by overlapping the DOFs of the bottom-CD, the top-CD, and the pattern sidewall angle.

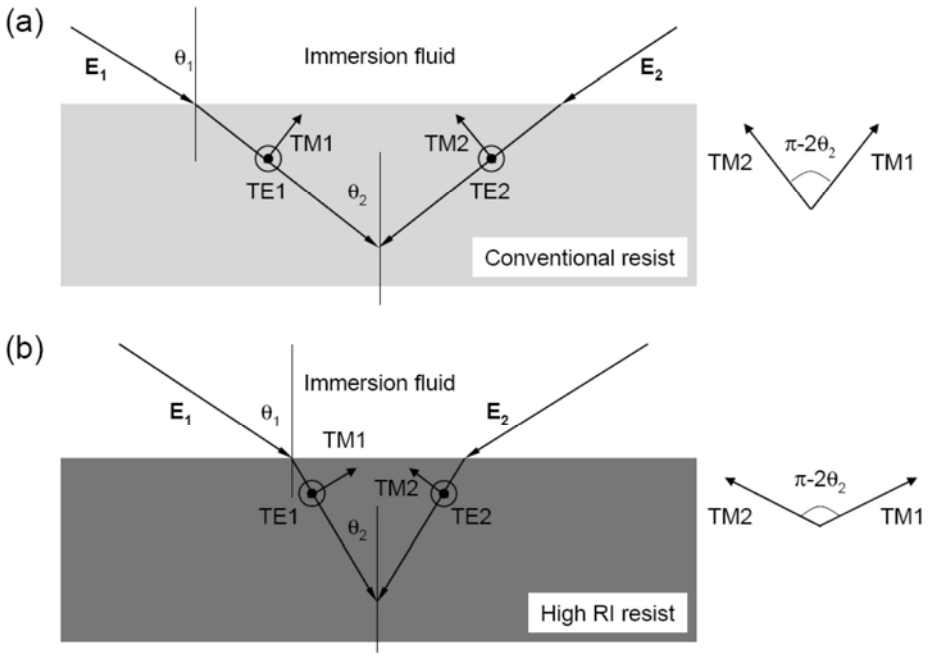

Figure 11.7 Optical path of two-exposure-beam interference with (a) conventional resist and (b) high-RI resist.

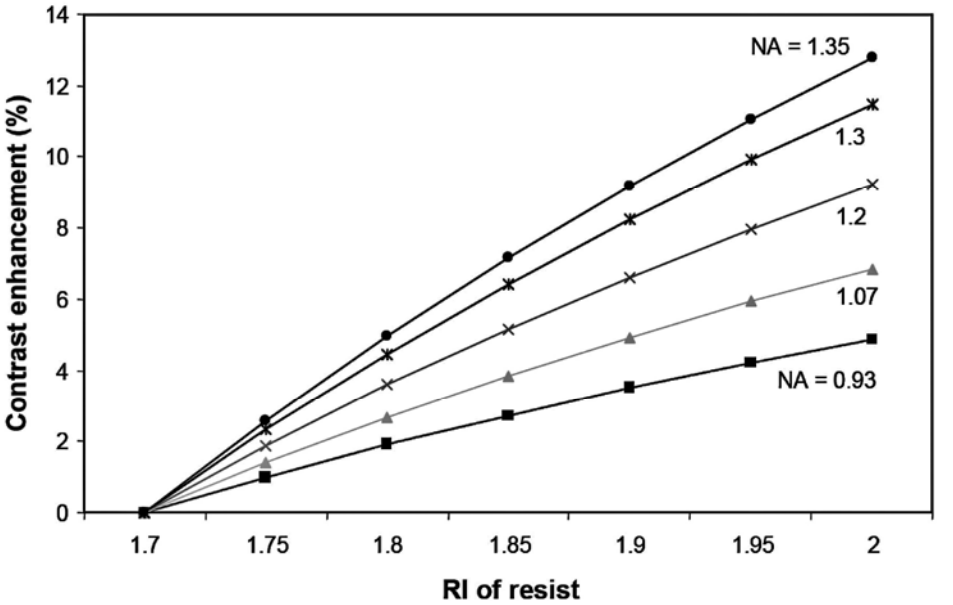

Figure 11.8 Imaging contrast enhancement (relative to the current resist n = 1.7) as a function of resist RI.

Assuming that the exposure beams travel in the fluid and focus at the resist surface, the DOF of the top-CD can be calculated as

$$\mathrm{DOF}_{\text{top-CD}} = \frac{k_2}{4} \cdot \frac{\lambda_0}{n_{\text{fluid}} \sin^2(\theta/2)}, \tag{11.5}$$

where λ_0 is the wavelength in the vacuum and θ is the incident angle in the fluid. In Eq. (11.5), the DOF of the top-CD is unrelated to the resist parameters. Similarly, the DOF of the bottom-CD can be calculated from Eq. (11.5) by replacing n and θ in the resist, as the exposure beams travel in the resist film. Therefore, the top-CD and the bottom-CD will have different DOFs.

Simulation has been used to quantitatively investigate how the RI value of resists will affect the overlap process window of 32-nm dense line and space patterns.[36] The simulation conditions are listed in Fig. 11.9(a). The process windows of bottom-CD, top-CD, and pattern sidewall angles are calculated for the resist RIs of 1.75 (Fig. 11.9(b)) and 1.9 (Fig. 11.9(c)). The bottom-CD is abbreviated as CD in the figure and the top-CD is indicated by resist loss. The results of this simulation show that the combined DOF would be 243 nm for an RI of 1.75 (Fig. 11.9(b)) and 276 nm for an RI of 1.9 (Fig. 11.9(c)). This improvement in DOF is mainly due to the reduction in top loss, since the top resist surface remains in focus longer when the RI is higher.

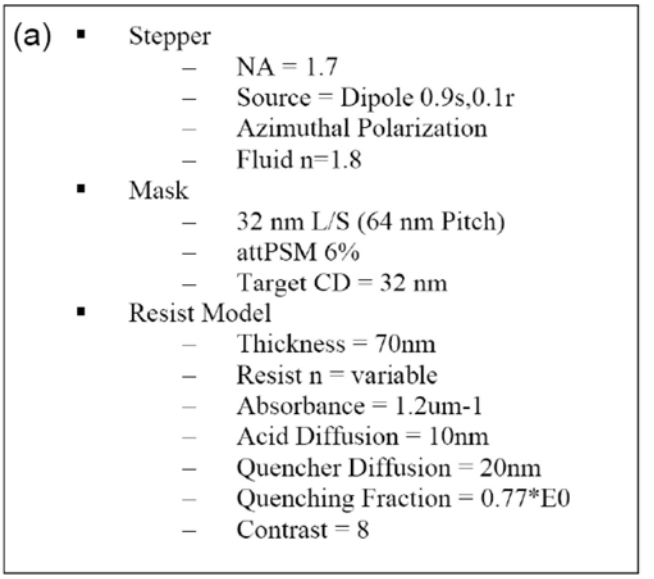

Figure 11.9(a) Simulation of a 32-nm dense line and space pattern: (a) simulation condition and the obtained process windows for the resist RI value of (b) 1.75 and (c) 1.9. (Reprinted by permission from Ref. 36.)

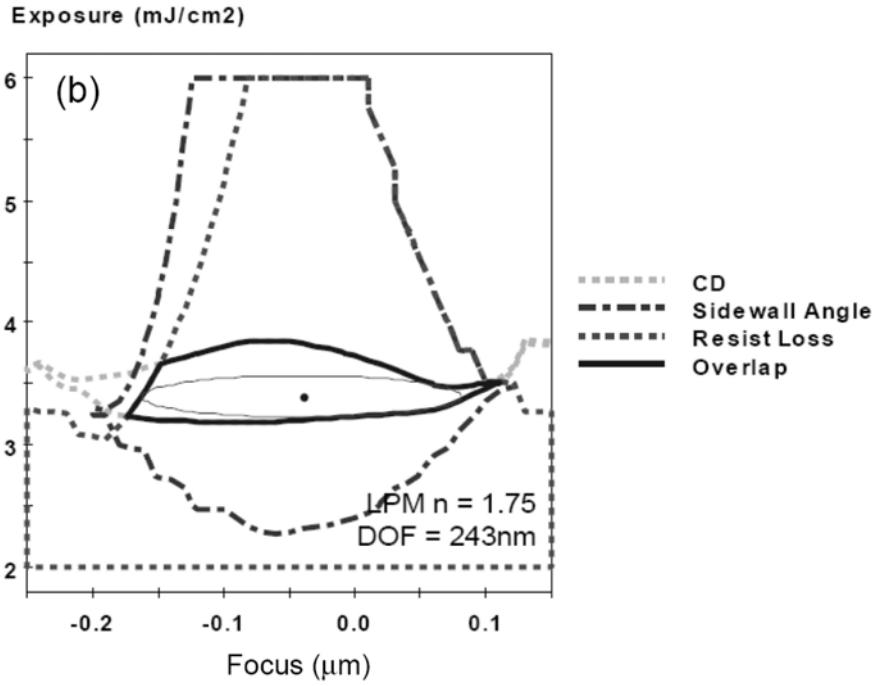

Figure 11.9(b) Simulation of a 32-nm dense line and space pattern: (a) simulation condition and the obtained process windows for the resist RI value of (b) 1.75 and (c) 1.9. (Reprinted by permission from Ref. 36.)

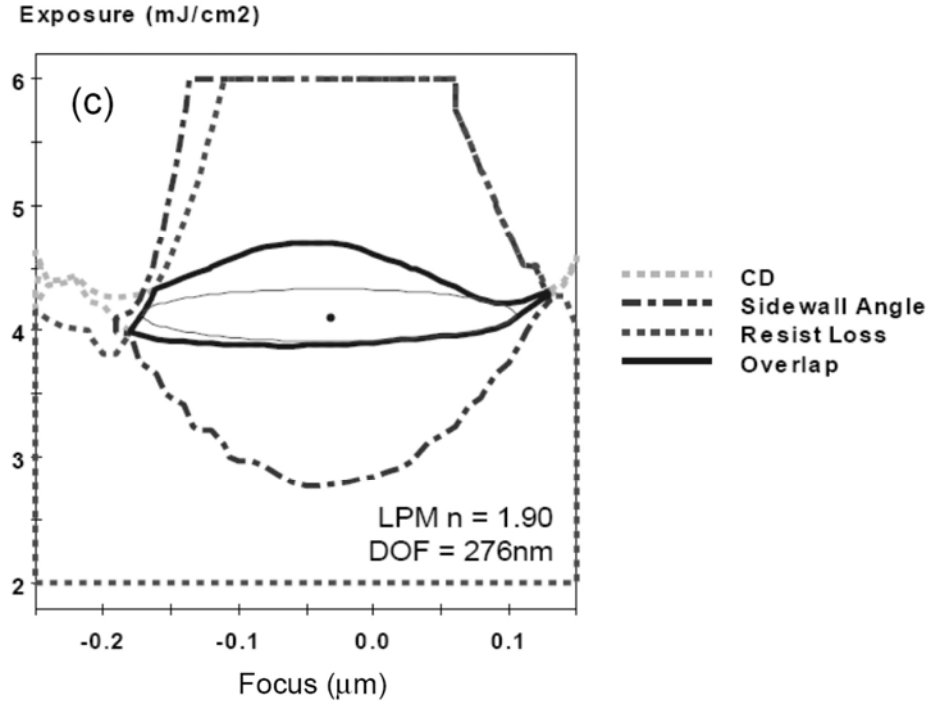

Figure 11.9(c) Simulation of a 32-nm dense line and space pattern: (a) simulation condition and the obtained process windows for the resist RI value of (b) 1.75 and (c) 1.9. (Reprinted by permission from Ref. 36.)

11.4 Solid Immersion

Solid immersion in combination with 193-nm interference lithography was demonstrated by the Smith group at Rochester Institute of Technology.[40] Figure 11.10 shows the setup in which a sapphire prism is pressed against a resist stack. The RI of sapphire (Al_2O_3) is 1.92 at 193 nm. Two exposure beams reflected by the turning mirrors enter the prism and form interference patterns at the interface of prism and resist. During exposure, light is propagated in the solid medium before entering the resist. This technique is therefore called solid immersion lithography.

In solid immersion, the maximum NA is basically determined by the RIs of the prism material and the resist. Current 193-nm resists (n = 1.7) have much smaller RIs than has sapphire (n = 1.92). When the incident angle is beyond a certain value at the interface of sapphire and resist ($> \sin^{-1}(n_{resist}/n_{sapphire}) = \sin^{-1}(1.7/1.92)$), the incident beam is totally reflected and cannot enter the resist film. This area of total reflection is called the evanescent region. However, exposure in the evanescent region can occur. By placing the prism directly on the resist film, the interference pattern at the interface can expose the resist film. The Smith group was able to print 25-nm half-pitch dense lines in a conventional 193-nm resist using solid immersion lithography.[40]

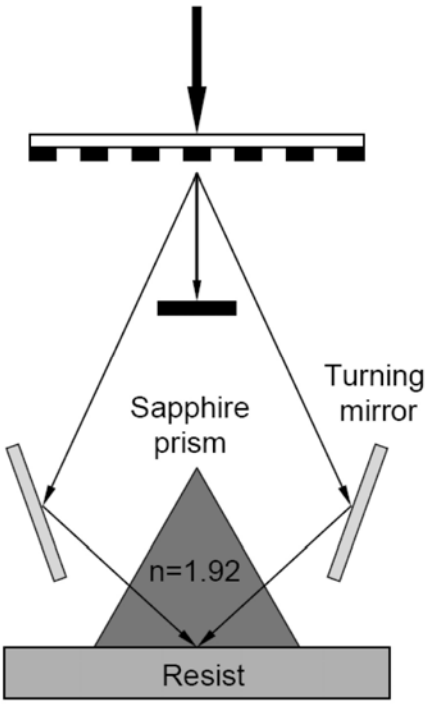

Figure 11.10 Setup of the solid immersion interferometer.

11.5 Other 193i+ Topics

In addition to the development of high-RI materials, other issues must be considered when 193i is extended to 193i+.

11.5.1 Polarization control of exposure light

As explained earlier, when the incident angle of exposure beams in the resist surface approaches 45 deg, the transverse magnetic (TM) component of the exposure beams cannot interfere and image contrast is reduced. Therefore, the control of illumination polarization becomes increasingly important. This has been studied using dry 0.93NA tools, but will become critical for 193i+ tools, since polarization illumination imposes constraints on pattern design and layout.

11.5.2 Reticle-induced polarization

Assuming that the exposure reduction factor remains at 4x, a minimum half-pitch of 128 nm will be needed in the mask to print a 32-nm half-pitch on the wafer. For half-pitches less than the wavelength, the intensity of diffraction orders becomes a strong function of polarization. Masks will transmit light differently, depending on the materials used for the absorber (e.g., Cr, MoSi, and Ta/SiO_2) and the extent of polarization of the light.[41]

Simulations show that at hyper-NA, binary intensity mask (BIM) has better aerial image contrast than has regular MoSi attenuated phase shift mask. In Cr-based BIM, Cr will absorb the TM-polarized light. This is due to the surface plasmon effects that reduce the transmittance of the TM-polarized light. In this case, the BIM acts as a transverse electric (TE) polarizer. Penetration of the TE-polarized light into the MoSi sidewall reduces transmittance, due to the continuous interfacial condition of the electromagnetic field. Thus, the MoSi acts as a TM polarizer and the mask stack must be optimized or redesigned for 193i+.

Increasing the exposure reduction factor has also been proposed. For example, changing the reduction factor by 8x will certainly double the feature sizes in the mask and relieve the mask polarization effect. This change may also reduce the mask price by 60–75%. However, the smaller field size at 8x would reduce throughput by 60–65% and would require stitching in order to achieve larger die sizes.

References

1. *International Technology Roadmap for Semiconductors* (ITRS) 2007, Lithography section.
2. T. Furukawa, T. Kishida, K. Yasuda, T. Shimokawa, Z. Liu, M. Slezak, and K. Hieda, "High refractive index materials design for the next generation ArF immersion lithography," *Proc. SPIE* **6924**, 692412 (2008).
3. R. H. French, V. Liberman, H. V. Tran, J. Feldman, D. J. Adelman, R. C. Wheland, W. Qiu, S. J. McLain, O. Nagao, M. Kaku, M. Mocella, M. K. Yang, M. F. Lemon, L. Brubaker, A. L. Shoe, B. Fones, B. E. Fischel, K. Krohn, D. Hardy, and C. Y. Chen, "High index immersion lithography with second generation immersion fluids to enable numerical apertures of 1.55 for cost effective 32 nm half pitches," *Proc. SPIE* **6520**, 65201O (2007).
4. T. Nawata, Y. Inui, I. Masada, E. Nishijima, T. Mabuchi, N. Mochizukia, H. Satoh, and T. Fukuda, "High-index fluoride materials for 193 nm immersion lithography," *Proc. SPIE* **6520**, 65201P (2007).
5. L. Parthier, G. Wehrhan, D. Keutel, T. Aichele, and M. Ansorg, "Development progress of high refractive LuAG for hyper NA immersion systems," Presentation at 4th International Symposium on Immersion Lithography, Keystone, Colorado, Oct. 2007.
6. I. Blakey, L. Chen, B. Dargaville, H. Liu, A. Whittaker, W. Conley, E. Piscani, G. Rich, A. Williams, and P. Zimmerman, "Novel high-index resists for 193 nm immersion lithography and beyond," *Proc. SPIE* **6519**, 651909 (2007).
7. M. van den Brink, "The only cost effective extendable lithography option: EUV," Presentation at EUV Symposium, Barcelona, Spain, October 17, 2006.
8. J. Mulkens, P. Graupner, H. Sewell, and D. McCafferty, "Immersion lithography beyond water," Presentation at 2nd International Symposium on Immersion Lithography, Brugge, Belgium, Sept. 2005.

9. See various proceedings from the International Symposia for Immersion Lithography: 1st Symposium in Vancouver, BC, Canada, Aug. 2004; 2nd Symposium in Brugge, Belgium, Sept. 2005; 3rd Symposium in Kyoto, Japan, Oct. 2006; 4th Symposium in Keystone, CO, USA, Oct. 2007; 5th Symposium in The Hague, Netherlands, Sept. 2008.
10. M. Switkes, R. R. Kunz, M. Rothschild, R. F. Sinta, M. Yeung, and S.-Y. Baek, "Extending optics to 50nm and beyond with immersion lithography," *J. Vacuum Sci. Technol. B*, **21**(6), Nov./Dec. 2003, 2794–2799.
11. B. W. Smith, Y. Fan, J. Zhou, A. Bourov, L. Zavyalova, N. Lafferty, F. Cropanese, and A. Estroff, "Hyper NA water immersion lithography at 193nm and 248nm, *J. Vacuum Sci. Technol. B*, **22**(6), Nov./Dec. 2004, 3439–3443.
12. J. Burnett and S. Kaplan, "Measurement of the refractive index and thermo-optic coefficient of water near 193 nm**,"** *J. Micro/Nanolith. MEMS MOEMS*, **3**, Issue 1, 68–72 (2004).
13. J. López-Gejo, J. T. Kunjappu, N. J. Turro, and W. Conley, "Amplification of the index of refraction of aqueous immersion fluids with crown ethers," *J. Micro/Nanolith. MEMS MOEMS*, **6**, 013002 (Mar. 9, 2007).
14. E. Costner, J. C. Taylor, S. Caporale, W. Wojtczak, D. Dewulf, W. Conley, and C. G. Willson, "New high index fluids for immersion lithography," *Proc. SPIE* **6153**, 61530B (2006).
15. J. Hoffnagle, D. Milliron, S. Swanson, D. Sanders, and B. Hinsberg, "Fundamental analysis of nanoparticle-based high index immersion fluids," Presentation at 4th International Symposium on Immersion Lithography, Keystone, Colorado, Oct. 2007.
16. F. Wooten, *Optical Properties of Solids*, Academic Press, New York (1972).
17. E. A. Costner, K. Matsumoto, B. K. Long, J. C. Taylor, W. Wojtczak, and C. G. Willson, "New high index fluids: exploiting anomalous dispersion for immersion lithography," *Proc. SPIE* **6923**, 69230B (2008).
18. Y. Wang, T. Miyamatsu, T. Furukawa, K. Yamada, T. Tominaga, Y. Makita, H. Nakagawa, A. Nakamura, M. Shima, S. Kusumoto, T. Shimokawa, and K. Hieda, "High-refractive-index fluids for the next generation ArF immersion lithography," *Proc. SPIE* **6153**, 61530A (2006).
19. R. H. French, H. V. Tran, D. J. Adelman, N. S. Rogado, W. Qiu, J. Feldman, O. Nagao, M. Kaku, M. Mocella, R. C. Wheland, M. K. Yang, M. F. Lemon, L. Brubaker, B. Fones, B. E. Fischel, and C. Y. Chen, "Cost effective single exposure immersion lithography with second generation immersion fluids for numerical apertures of 1.55 and 32 nm half pitches," Presentation at 4th International Symposium on Immersion Lithography, Keystone, Colorado, Oct. 2007.
20. T. Furukawa, T. Kishida, T. Miyamatsu, K. Kawaguchi, K. Yamada, T. Tominaga, M. Slezak, and K. Hieda, "High refractive index material design for ArF immersion lithography," *Proc. SPIE* **6519**, 65190B (2007).

21. T. Furukawa, T. Kishida, T. Miyamatsu, K. Kawaguchi, K. Yamada, T. Tominaga, Z. Liu, M. Slezak, and K. Hieda, "High refractive index fluids and top coat design for next generation ArF immersion lithography," Presentation at 4th International Symposium on Immersion Lithography, Keystone, Colorado, Oct. 2007.
22. R. L. Brainard, S. Kruger, and E. Block, "Models for predicting the index of refraction of compounds at 193 and 589 nm," *Proc. SPIE* **6519**, 651920 (2007).
23. J. López-Gejo, J. T. Kunjappu, J. Zhou, B. W. Smith, P. Zimmerman, W. Conley, and N. J. Turro, "Outlook for potential third-generation immersion fluids," *Proc. SPIE* **6519**, 651921 (2007).
24. J. Irisawa, T. Okazoe, T. Eriguchi, and O. Yokokoji, "The modeling of immersion liquid by quantum chemical calculation," *Proc. SPIE* **5754**, 1040–1048 (2005).
25. P. A. Zimmerman, B. Rice, R. Rodriguez, M. F. Zettel, M. Trikeriotis, D. Wang, Y. Yi, W. J. Bae, C. K. Ober, and E. P. Giannelis, "The use of nanocomposite materials for high refractive index immersion lithography," *J. Photopoly. Sci. Tech.* **21**(5), 621–629 (2008).
26. E. Hendrickx, S. Postnikov, P. Foubert, R. Gronheid, and B. S. Kim, "Screening of second-generation high-index liquids," *Proc. SPIE* **6519**, 65190A (2007).
27. H. Sewell, J. Mulkens, D. McCafferty, L. Markoya, C. Wagner, and P. Graeupner, "High-n immersion lithography," Presentation at 4th International Symposium on Immersion Lithography, Keystone, Colorado, Oct. 2007.
28. J. H. Burnett, "High-index materials for 193-nm immersion lithography," Presentation at 3rd International Symposium on Immersion Lithography, Kyoto, Japan, Oct. 2006.
29. T. Nawata, Y. Inui, I. Masada, T. Mabuchi, E. Nishijima, H. Sato, and T. Fukuda, "High-index fluoride materials for 193 nm immersion lithography," Presentation at 3rd International Symposium on Immersion Lithography, Kyoto, Japan, Oct. 2006.
30. L. Parthier, G. Wehrhan, D. Keutel, J. Alkemper, and K. Knapp, "Starting the full scale development of optical material LuAG for 193nm lithography," Presentation at 3rd International Symposium on Immersion Lithography, Kyoto, Japan, Oct. 2006.
31. H. Hayashi, M. Kawata, N. Sugimoto and S. Kikugawa, "Silica glass based high refractive index lens material for 193 nm immersion lithography," Presentation at 3rd International Symposium on Immersion Lithography, Kyoto, Japan, Oct. 2006.
32. R. Sooriyakumaran, D. P. Sanders, H. Truong, R. D. Allen, M. E. Colburn, and G. R. McIntyre, "High refractive index polymer platforms for 193nm immersion lithography," Presentation at 4th International Symposium on Immersion Lithography, Keystone, Colorado, Oct. 2007.

33. I. Blakey, W. Conley, G. A. George, D. J. T. Hill, H. Liu, F. Rasoul, and A. K. Whittaker, "Synthesis of high refractive index sulfur containing polymers for 193nm immersion lithography: a progress report," *Proc. SPIE* **6153**, 61530H (2006).
34. K. Matsumoto, E. Costner, I. Nishimura, M. Ueda, and C. G. Willson, "High index resists for 193 nm immersion lithography," *Proc. SPIE* **6923**, 692305 (2008).
35. Y. Nishimura, T. Kawakami, K. Hoshiko, T. Tominaga, M. Shima, S. Kusumoto, T. Shimokawa, and K. Hieda, "Novel photoresist materials development with high refractive index at 193nm for next generation immersion lithography," Presentation at 3rd International Symposium on Immersion Lithography, Kyoto, Japan, Oct. 2006.
36. P. A. Zimmerman, J. Byers, E. Piscani, B. Rice, C. K. Ober, E. P. Giannelis, R. Rodriguez, D. Wang, A. Whittaker, I. Blakey, L. Chen, B. Dargaville, and H. Liu, "Development of an operational high refractive index resist for 193nm immersion lithography," *Proc. SPIE* **6923**, 692306 (2008).
37. I. Blakey, L. Chen, B. Dargaville, H. Liu, D. Hill, G. A. George, F. Rasoul, A. K. Whittaker, W. E. Conley, B. Rice, and P. Zimmerman, "Strategies for the generation of high refractive index polymers for 193 nm immersion photoresist formulations polymers," Presentation at 3rd International Symposium on Immersion Lithography, Kyoto, Japan, Oct. 2006.
38. W. Conley and R. Socha, "Everything you ever wanted to know about why the semiconductor industry needs a high refractive index photoresist…but were afraid to ask, Part 1," *Proc. SPIE* **6153**, 61531L (2006).
39. G. McIntyre, D. Sanders, R. Sooriyakumaran, H. Truong, and R. Allen, "The limitations of high index resists for 193nm hyper-NA lithography," *Proc. SPIE* **6923**, 692304 (2008).
40. B. W. Smith, Y. Fan, M. Slocum, and L. Zavyalova, "25nm immersion lithography at a 193nm wavelength," *Proc. SPIE* **5754**, 141–147 (2005).
41. M. Yoshizawa, V. Philipsen, L. H. A. Leunissen, E. Hendrickx, R. Jonckheere, G. Vandenberghe, U. Buttgereit, H. Becker, C. Koepernik, and M. Irmscher, "Comparative study of bi-layer attenuating phase-shifting masks for hyper-NA lithography," *Photomask BACUS News*, Aug. 2006, **22**, Issue 8.

Index

Yayi Wei received his Masters Degree in Engineering from the Electronics Institute, Chinese Academy of Sciences, Beijing, China in 1992 and his Doctorate (Doktor der Naturwissenschaften) from the Max Planck Institute for Solid State Research, Stuttgart, Germany in 1998. As a graduate student in the Max Planck Institute for Solid State Research, Dr. Wei specialized in the electronic transportation of low-dimensional structures and microfabrications. After receiving his Doctorate, Dr. Wei worked for Oak Ridge National Laboratory (ORNL) on electron-beam lithography and nanofabrications; Infineon Technologies, which later became Qimonda, on the process development and material evaluation of advanced lithography in 193-, 157-, and 193-nm immersion, as well as EUV; and AZ Electronic Materials on lithographic materials applications. Dr. Wei has numerous publications and holds several patents in the field of lithography.

Robert L. Brainard received his B.S. in Chemistry from U.C. Berkeley in 1979. He synthesized and studied the reaction mechanisms of organoplatinum compounds during his graduate studies with George Whitesides at MIT and Harvard University. After receiving his Ph.D. in 1985, he studied the reaction mechanisms on copper and silver surfaces under ultrahigh vacuum conditions as a post-doctoral student at Stanford University. Robert worked for Polaroid 1987–1990, where he developed new gold and sulfur chemistry for use in the chemical sensitization of silver halide photographic emulsions. He worked at Shipley/Rohm & Haas 1990–2005, where he did product development research in the areas of: electrodeposited, dielectric, color filter, DUV, EUV, x-ray and e-beam photoresists. Robert is now an Associate Professor at the College of Nanoscale Science and Engineering, UAlbany, investigating new materials for use in EUV and 193-nm lithography.

(Photo of Robert Brainard by Mia Ertas, UAlbany College of Nanoscale Science and Engineering.)